

Oceanologia



Official Journal of the Polish Academy of Sciences: Institute of Oceanology and Committee on Maritime Research

EDITOR-IN-CHIEF

Prof. Janusz Pempkowiak
Institute of Oceanology, Polish Academy of Sciences, Sopot, Poland

MANAGING EDITOR

Agata Bielecka - abielecka@iopan.pl

Editorial Office Address

Institute of Oceanology, Polish Academy of Sciences (IO PAN)
Powstańców Warszawy 55
81-712 Sopot, Poland
Mail:editor@iopan.pl

ADVISORY BOARD

Prof. Xosé Antón Álvarez Salgado
Marine Research Institute, Spanish Research Council (CSIC), Vigo, Spain

Dr Boris Chubarenko
P.P. Shirshov Institute of Oceanology, Russian Academy of Sciences,
Kaliningrad, Russia

Prof. Mirosław Darecki
Institute of Oceanology, Polish Academy of Sciences, Sopot, Poland

Prof. Jerzy Dera
Institute of Oceanology, Polish Academy of Sciences, Sopot, Poland

Prof. Agnieszka Herman
Institute of Oceanography, University of Gdańsk, Gdynia, Poland

Prof. Genrik Sergey Karabashev
P.P. Shirshov Institute of Oceanology, Russian Academy of Sciences,
Moscow, Russia

Prof. Alicja Kosakowska
Institute of Oceanology, Polish Academy of Sciences, Sopot, Poland

Prof. Zygmunt Kowalik
Institute of Marine Science, University of Alaska Fairbanks (UAF), USA

Prof. Matti Leppäranta
Institute of Atmospheric and Earth Sciences, University of Helsinki, Finland

Prof. Ewa Łupikasza
Faculty of Earth Sciences, University of Silesia, Sosnowiec, Poland

THEMATIC EDITORS

Prof. Małgorzata Stramska – Institute of Oceanology, Polish Academy of Sciences, Sopot, Poland

Prof. Tymon Zieliński – Institute of Oceanology, Polish Academy of Sciences, Sopot, Poland

Prof. Hanna Mazur-Marzec
Institute of Oceanography, University of Gdańsk, Gdynia, Poland

Prof. Dag Myrhaug
Norwegian University of Science and Technology (NTNU), Trondheim, Norway

Prof. Sergej Olenin
Coastal Research and Planning Institute, Klaipeda University CORPI, Klaipeda,
Lithuania

Prof. Tarmo Soomere
Tallinn University of Technology, Estonia

Prof. Hans von Storch
Institute of Coastal Research, Helmholtz Center Geesthacht, Germany

Prof. Dariusz Stramski
Scripps Institution of Oceanography, University of California, San Diego, USA

Prof. Piotr Szefer
Department of Food Sciences, Medical University of Gdańsk, Poland

Prof. Antoni Śliwiński
Institute of Experimental Physics, University of Gdańsk, Poland

Prof. Muhammet Türkoğlu
Çanakkale Onsekiz Mart University, Turkey

Prof. Jan Marcin Węslawski
Institute of Oceanology, Polish Academy of Sciences, Sopot, Poland

This journal is supported by the Ministry of Science and Higher Education, Warsaw, Poland

Indexed in: ISI Journal Master List, Science Citation Index Expanded, Scopus, Current Contents, Zoological Record,
Thomson Scientific SSCI, Aquatic Sciences and Fisheries Abstracts, DOAJ

IMPACT FACTOR ANNOUNCED FOR 2019 IN THE 'JOURNAL CITATION REPORTS' IS 2.198; 5-year IF is 2.231. CITESCORE ANNOUNCED FOR 2019 IS 3.4

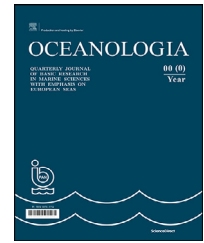
Publisher
Elsevier B.V.
Radarweg 29
1043 NX Amsterdam
The Netherlands

Associate Publisher
Chen Lin
c.lin@elsevier.com
+86-10-8520 8768

ISSN 0078-3234

Available online at www.sciencedirect.com

ScienceDirect

journal homepage: www.journals.elsevier.com/oceanologia

ORIGINAL RESEARCH ARTICLE

Inhomogeneity detection in phytoplankton time series using multivariate analyses

Oihane Muñiz^{a,*}, José Germán Rodríguez^a, Marta Revilla^a,
Aitor Laza-Martínez^{b,c}, Sergio Seoane^{b,c}, Javier Franco^a

^a AZTI, Marine Research Division, Pasaia, Spain

^b Department of Plant Biology and Ecology, Faculty of Science and Technology, University of the Basque Country, UPV/EHU, Leioa Spain

^c Technology and Research Centre for Experimental Marine Biology and Biotechnology (PiE-UPV/EHU), 48620 Plentzia, Spain

Received 17 July 2019; accepted 30 January 2020

Available online 12 February 2020

KEYWORDS

Phytoplankton assemblages;
Fixative;
Variability;
Uncertainty;
Taxonomist;
Long-term series

Summary Phytoplankton communities have long been used as water quality indicators within environmental policies. This has fostered the development of national and international phytoplankton monitoring programs, but these networks are subject to sources of uncertainty due to laboratory issues. Nevertheless, studies regarding the interference associated with these aspects are not well-documented. Hence, a long time series (2003–2015) from the Basque continental shelf (southeastern Bay of Biscay) was analyzed to evaluate the uncertainty given by laboratory strategies when studying phytoplankton variability. Variability in phytoplankton communities was explained not only by environmental conditions but also by changes in fixatives (glutaraldehyde and acidic Lugol's solution) and laboratory staff. Based on Bray-Curtis distances, phytoplankton assemblages were found to be significantly dissimilar according to the effect of changes in the specialist handling the sample and the employed fixative. The pair-wise permutational multivariate analysis of variance (PERMANOVA) showed significant differences between the two fixatives utilized and also between the three taxonomists involved. Thus, laboratory-related effects should be considered in the study of phytoplankton time series.

© 2020 Institute of Oceanology of the Polish Academy of Sciences. Production and hosting by Elsevier B.V. This is an open access article under the CC BY-NC-ND license (<http://creativecommons.org/licenses/by-nc-nd/4.0/>).

* Corresponding author at: AZTI, Marine Research Division, Herrera Kaia Portualdea s/n, E-20110 Pasaia, Spain. Tel.: +34 946 574 000.

E-mail addresses: omuniz@azti.es, oihanemp@hotmail.com (O. Muñiz), grodriguez@azti.es (J.G. Rodríguez), mrevilla@azti.es

<https://doi.org/10.1016/j.oceano.2020.01.004>

0078-3234/© 2020 Institute of Oceanology of the Polish Academy of Sciences. Production and hosting by Elsevier B.V. This is an open access article under the CC BY-NC-ND license (<http://creativecommons.org/licenses/by-nc-nd/4.0/>).

(M. Revilla), aitor.laza@ehu.eus (A. Laza-Martínez), sergio.seoane@ehu.eus (S. Seoane), jafanco@azti.es (J. Franco).

Peer review under the responsibility of the Institute of Oceanology of the Polish Academy of Sciences.



Production and hosting by Elsevier

1. Introduction

Phytoplankton has long been studied as a key environmental quality indicator within several international policies including European directives, such as the Water Framework Directive (WFD, 2000/60/EC) and the Marine Strategy Framework Directive (MSFD, 2008/56/EC) (Borja et al., 2008; Garmendia et al., 2013). These policies require large monitoring networks in order to assess water quality and involve indicators that reflect different phytoplankton attributes, such as composition (Devlin et al., 2009; Domingues et al., 2008). Additionally, bivalve mollusk culture areas worldwide require phytoplankton monitoring programs in order to manage potential toxicity (Bricelj and Shumway, 1998).

Phytoplankton assemblages depend on species succession, which is influenced in turn by environmental changes (Huisman et al., 1999). However, there are also several sources of variation associated with the analysis of phytoplankton communities (Dromph et al., 2013). The microscope-based method following the Utermöhl technique is the standardized method for phytoplankton identification and counting within the European Union (EN 15204 2006). This method requires highly specialized taxonomists, yet most studies show a bias due to variation in the level of expertise exercised by each taxonomist (Culverhouse et al., 2003; Dromph et al., 2013; Jakobsen et al., 2015; Peperzak, 2010; Straile et al., 2013; Wiltshire and Dürselen, 2004). An exception was found for diatom indices for which some studies have concluded that, as long as a harmonized methodology is followed, the error associated with taxonomist variation has little effect (Kahlert et al., 2009, 2012). The preservation of plankton samples can also introduce artifacts on species abundance, as well as cell volume estimates. Traditional fixatives, such as Lugol's iodine and glutaraldehyde, have been reported to produce shrinkage, swelling, or even breakage of phytoplankton cells, which can bias estimates of abundance and biomass (Booth, 1987; Menden-Deuer et al., 2001; Verity et al., 1992; Yang et al., 2016).

In order to develop more accurate phytoplankton counting protocols and be able to interpret their results, it is essential to estimate the variability given by each source of uncertainty. To the best of our knowledge, such studies are scarce. Some of the existing literature focused on specific issues, such as the need of a harmonized methodology (Kahlert et al., 2009, 2012, 2016), or specifically on a concrete taxonomic group (Heino and Soininen, 2007), or on the influence of taxonomic resolution (Carneiro et al., 2010, 2013).

In this context, the aim of the present study is to investigate the detection of inhomogeneities in phytoplankton time series and assess how these differences can be caused by factors other than the environment. This work does not attempt to be a methodology or inter-laboratory comparison, but it shows the importance of a previous data analysis when studying long-term trends or patterns in phytoplankton composition and abundance. Phytoplankton time-series can contain relevant ecological information (e.g., to address the effect of climate change) (Martinez et al., 2009), but can also be subject to methodological interferences (Kahler et al., 2012; Menden-Deuer et al., 2001). Hence,

a complete overview of the potential interference in phytoplankton inter-annual variability given by taxonomist experience and fixative type is addressed. We use a long time series (>10 years), which involves both coastal and offshore areas and takes into account the whole nano- and microplankton community.

2. Material and methods

2.1. Study area, sampling and laboratory strategies

This study draws on data from the Littoral Water Quality Monitoring and Control Network of the Basque Water Agency, which has been used for the implementation of the Water Framework Directive in the Northeast Atlantic ecoregion (Borja et al., 2004, 2016; Revilla et al., 2009). The dataset consists of 16 stations along the Basque coast and three offshore stations in the southeastern Bay of Biscay (Figure 1). The climate in the study area is temperate and oceanic with moderate winters and warm summers. Coastal water bodies are euhaline and exposed. A detailed description of hydrographical conditions is given in Valencia et al. (2004).

The analyzed time series was collected over 13 years (from 2003 to 2015), except for two offshore stations with seven-year datasets (RF20 and RF30, from 2009 to 2015). Although phytoplankton samples have been obtained quarterly since 2007, only the spring and summer data were analyzed (i.e., two surveys per year) as these were the seasons sampled during the complete time series.

The following environmental variables were used in the analysis: temperature, salinity, Secchi depth, suspended solids, ammonium, nitrate, phosphate and silicate. In the field, the temperature and salinity were recorded in surface waters using a conductivity, temperature and depth multiparametric probe (CTD) (Seabird25), the Secchi disk depth was measured as an estimator of the water transparency, and surface water samples were taken for subsequent laboratory analyses. The concentration of suspended solids was estimated following the procedure described in Clesceri et al. (1989) after the filtration of water through Whatman GF/C filters. Inorganic nutrients (ammonium, nitrate, silicate, phosphate) were measured using a continuous-flow autoanalyzer (Bran + Luebbe Autoanalyzer 3, Norderstedt, Germany) according to colorimetric methods described in Grasshoff et al. (1983). When nutrient concentrations were below the quantification limit ($1.6 \mu\text{mol L}^{-1}$ for ammonium, nitrate or silicate; $0.16 \mu\text{mol L}^{-1}$ for phosphate), the value used for statistical analyses was equal to one half of that limit.

For phytoplankton, surface water was preserved immediately and maintained in 125 mL borosilicate bottles under dark and cool conditions (4°C) until analysis. Glutaraldehyde (0.1% v/v) was used for preservation until 2011 and acidic Lugol's solution (0.4% v/v) from then on. Taxonomic identification and cell counting were performed on subsamples of 50 mL (occasionally, particle density was too high and 10 mL samples were used instead), following the Utermöhl method (Edler and Elbrächter, 2010; Hasle, 1978; Utermöhl, 1958) under a Nikon diaphot TMD inverted microscope. Depending on the organism size, 100x or 400x

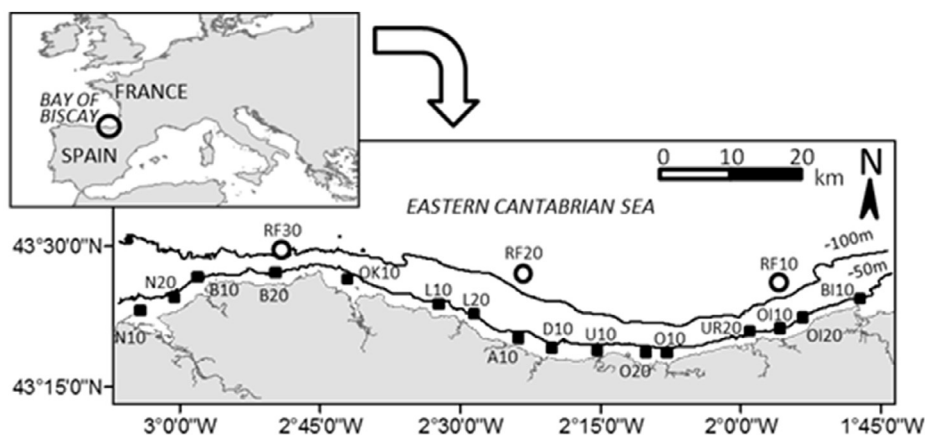


Figure 1 Map of the study area and sampling stations. Squares correspond to nearshore sampling sites and circles to offshore sampling sites.

Table 1 Fixatives and taxonomists associated with the analyses in the time series. In both the spring and the summer data sets, the number of samples is shown, together with the arithmetic mean \pm standard deviation for the total number of taxa, as well as for the number of taxa identified at species or genus levels and at higher level. The rare taxa are excluded (i.e., those occurring in less than 1% of the samples). In addition, the samples from stations RF20 and RF30 are not included, as these stations were monitored only from 2009 onwards.

| Fixative | Taxonomist | Year | Season | Samples | Total taxa | Species or genus | Higher ranks |
|----------------|------------|------------------------------|--------|---------|-----------------|------------------|---------------|
| Glutaraldehyde | #1 | 2003, 2008, 2009 | Spring | 51 | 24.4 \pm 7.1 | 20.2 \pm 7.5 | 4.2 \pm 1.1 |
| | | | Summer | 51 | 25.2 \pm 8.3 | 20.9 \pm 7.9 | 4.3 \pm 1.0 |
| | #2 | 2005, 2006, 2007, 2010, 2011 | Spring | 83 | 21.4 \pm 5.8 | 16.0 \pm 5.6 | 5.5 \pm 1.2 |
| | | | Summer | 82 | 21.1 \pm 5.0 | 15.4 \pm 5.0 | 5.8 \pm 1.0 |
| | #3 | 2004 | Spring | 16 | 12.2 \pm 3.4 | 11.9 \pm 3.5 | 0.3 \pm 0.5 |
| | | | Summer | 16 | 7.0 \pm 5.2 | 6.8 \pm 5.0 | 0.3 \pm 0.4 |
| Acidic Lugol | #1 | 2012, 2013, 2014, 2015 | Spring | 68 | 36.3 \pm 7.6 | 31.8 \pm 7.2 | 4.6 \pm 1.3 |
| | | | Summer | 68 | 36.4 \pm 11.5 | 31.6 \pm 11.3 | 4.8 \pm 0.9 |

magnification was used; the detection limit of microscope counts for microplanktonic organisms was 20 cells L^{-1} . Small nanophytoplankton cells that could not be assigned to any taxonomic group were clumped together into a group named “unidentified forms $<10 \mu m$ ”. Three different taxonomists belonging to the same laboratory took part in the identification and counting of phytoplankton. Taxonomist #1 handled samples corresponding to years 2003, 2008, 2009 and from 2012 to 2015. Taxonomist #2 handled samples from 2005, 2006, 2007, 2010 and 2011, and Taxonomist #3 identified and counted samples from 2004. No changes in the staff took place within the year of analysis. The experience of the taxonomists increased from the beginning of the time series, reaching more specific taxonomic levels. In most of the identifications, and particularly in those made by Taxonomist #3, the levels of species or genus were reached (Table 1).

2.2. Data analysis

2.2.1. Environmental variables

Environmental data were transformed and standardized in order to achieve the assumptions of normality and homoscedasticity. All analyses were performed separately for

spring and summer. Each individual variable was subjected to one-way analysis of variance (ANOVA) and a multiple range test (95% least significant difference, LSD) to check for significant differences among years. Additionally, based on Euclidean distance matrices, nonmetric multidimensional scaling (MDS) ordination and cluster analyses were performed to study the variability of all environmental variables together. Similarity profile analysis (SIMPROF) at $\alpha = 0.05$ was included to test for significant differences at each cluster dendrogram node (Clarke and Gorley, 2006).

The MDS analyses were carried out with the (i) 19 sampling sites and (ii) average values of each variable per season and year (i.e., average between the sampling stations), excluding stations RF20 and RF30 because they were only sampled from 2009 on. Additionally, for the analysis of the 19 sampling sites, permutational multivariate analysis of variance (PERMANOVA) was used to test for significant differences between years. A PERMANOVA with 9999 permutations was carried out with “year” as a fixed factor. A second PERMANOVA, applying the same settings, was used as a post-hoc test for pair-wise comparisons between the 13 different years. Statgraphics Centurion XVI was used for ANOVA, PRIMER 6 statistical software (Primer-E Ltd., UK) for cluster analyses, and MDS and RStudio (R Core Team, 2015) for PERMANOVA.

2.2.2. Phytoplankton community

Prior to mathematical analysis, the phytoplankton species list was standardized according to AlgaeBase (Guiry and Guiry, 2015). Rare taxa, defined here as those occurring in less than 1% of the samples, were excluded in the analyses to reduce noise in the data. A total of 129 of the 336 taxa were left out of the analysis.

Phytoplankton abundance data (cell L⁻¹) were log ($x + 1$) transformed. Separate analyses were performed for spring and summer. MDS and cluster analyses were performed equally to the environmental data but based on zero-adjusted Bray-Curtis matrices (Clarke et al., 2006). These matrices were used to study the inter-annual variability of community assemblages. MDS is a powerful ordination method for ecological community analysis that allows a large presence of zero values and does not assume a linear relationship between variables (McCune et al., 2002). Similar to the environmental data, analyses were carried out with the (i) 19 sampling sites and (ii) average cell density values per season and year. At the level of virtual sampling units, analyses were performed based on densities of (i) the lowest taxonomic level available and (ii) major taxonomic groups (i.e., autotrophic coccoids, chlorophytes, *Mesodinium* spp., cryptophytes, diatoms, dinoflagellates, euglenophytes, haptophytes, ochrophytes, and unidentified forms). Moreover, a PERMANOVA (9999 permutations) was performed to test for significant differences associated with “fixative” as a fixed factor. The dataset was then split into two subsets based on the two fixatives. The first subset, which corresponded to glutaraldehyde and included data for the three taxonomists (i.e., period 2003–2011), was subjected to a second PERMANOVA (9999 permutations) with “taxonomist” as a fixed factor. An additional PERMANOVA was used as a post-hoc test for pair-wise comparisons between the three different taxonomists. The second subset (i.e., period 2012–2015), where the acidic Lugol’s solution was used, could not be subjected to a second PERMANOVA since it only included information for a single taxonomist.

Finally, partial Canonical Correspondence Analyses (pCCA) (Borcard et al., 1992; Legendre and Legendre, 1998) were applied to test if the variability in the abundance of the phytoplankton taxa could be associated with changes in the environmental conditions and/or in the laboratory staff. Two pCCA were carried out for the period 2003–2011: one with spring data and another one with summer data. The pCCA were carried out with CANOCO for Windows 4.5 (Braak and Smilauer, 2002). The log-transformed phytoplankton abundance at each sampling site was used as the dependent data set. The independent data consisted of two sets of explanatory variables: (i) the environmental variables (temperature, salinity, Secchi depth, suspended solids, ammonium, nitrate, phosphate, and silicate), and (ii) the factor ‘taxonomist’, using dummy coding (Legendre and Legendre, 1998). Previously, the environmental variables were Box-Cox transformed and normalized. The pCCA parted the explained variance of the phytoplankton abundance into the following components: (i) the variance uniquely described by the environment (but not by the taxonomist effect), (ii) the variance uniquely described by the taxonomist effect (but not by the environment), (iii) the variance jointly described by the environment and the taxonomist

effect, and (iv) the unexplained variance. The significance of the pCCA models was tested with the Monte-Carlo test.

3. Results

3.1. Environmental variables

All of the investigated environmental variables showed statistically significant differences in mean values among some years, both in spring and summer (ANOVA test, alpha = 0.05). Results for the individual environmental variables are summarized in Figure 2, which shows the means and standard deviations, and Table 1 of the Supplementary Electronic Material, which includes results of the multiple range tests.

Secchi disk depth showed seven homogeneous groups (i.e., statistically significant different groups) both in spring and summer. The groups with the lowest values were obtained from data collected in spring 2003, 2007 and 2011, and summer 2003, 2005 and 2010. The highest values occurred in 2012 and 2015 in spring, and 2004, 2013 and 2015 in summer. Mean Secchi depths ranged from 5.1 to 13.7 m. Mean temperature showed its minimum in spring 2010 (14.6°C) and its maximum in summer 2003 (23.4°C). Apart from that, spring 2011 was relatively warm (18.1°C) and summer 2015 was relatively cold (20.0°C). Based on temperature, each of these years formed a separate homogeneous group, statistically different from the others. Salinity mean values ranged from 34.1 to 35.7. In spring, minimum mean values were given by the homogeneous group formed by the years 2003, 2004, 2005, 2013 and 2014, whereas the maximum was represented by the group from years 2008, 2010 and 2011. In summer, maximum values occurred during 2012. Suspended solids mean concentrations ranged from 1.2 to 9.1 mg L⁻¹ with a general increasing trend from the beginning towards the end of the time series, both in spring and summer.

With regard to nutrients, mean ammonium values were significantly lower during 2003. In spring, the years 2007 and 2013 formed the group with the highest ammonium concentrations, whereas in summer, 2006 and 2013 were the years with the highest values. Mean nitrate concentrations ranged from 0.8 to 4.3 μmol L⁻¹. Compared with spring, where six significant groups of years were found, mean summer values showed lower variability, as shown by the four groups of years. Phosphate concentrations presented mean values between 0.05 and 0.37 μmol L⁻¹. Maxima were found in spring during 2007–2008. 2003 and 2005 presented especially low concentrations in summer. Silicate showed five significantly different homogeneous groups of years. In spring, mean concentrations ranged from 1.0 to 5.3 μmol L⁻¹ and in summer from 1.0 to 4.7 μmol L⁻¹.

MDS biplots represent the samples as points in low-dimensional space such that the larger the distance between two points in the plot, the more dissimilar they are with regard to the environmental variables and vice versa. Hence, when analyzing the variability of all environmental variables together, some years appeared substantially different from the others in the MDS (e.g., spring 2003 and summer 2003, 2005, 2013 and 2014) (Figure 3). The

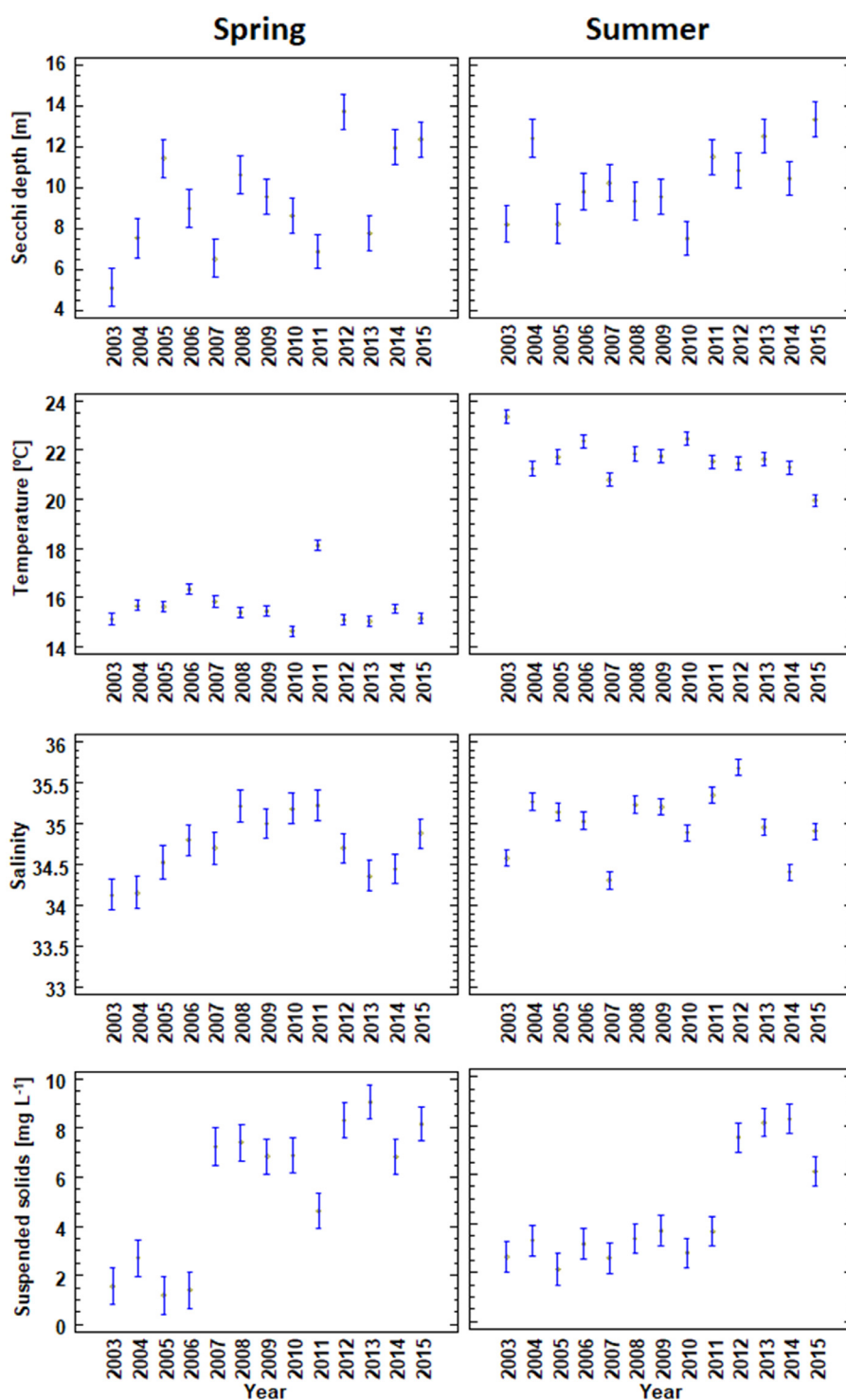


Figure 2 Mean plots for the environmental variables in each year during the period 2003–2015, with spring and summer shown in the left and right columns, respectively. Vertical error bars represent the standard deviation.

pair-wise PERMANOVA revealed significant differences between all years, both in spring and summer (Table 2 of the Supplementary Electronic Material).

In the MDS analysis of environmental variables using average values per season and year, the chronological trajectory showed great dissimilarities between some consecutive years, such as spring 2006–2007 or summer 2003–

2004, 2012–2013 and 2014–2015 (Figure 4). In contrast, some years appeared close to each other indicating similar mean environmental conditions. However, cluster analyses (SIMPROF test, $\alpha = 0.05$) for average values of environmental data did not find any significant group, either in spring or summer (Figure 1 of the Supplementary Electronic Material).

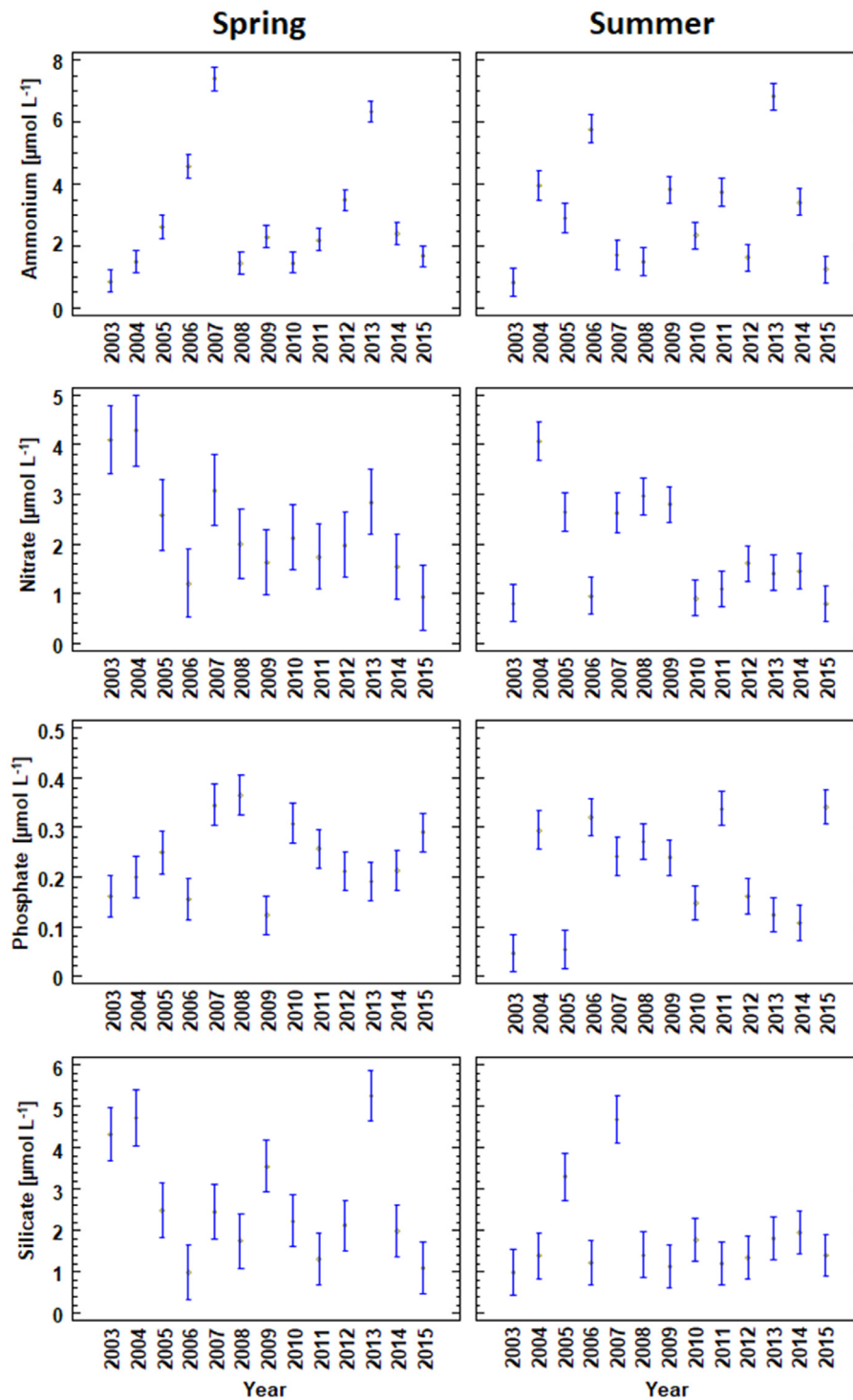


Figure 2 Continued.

3.2. Phytoplankton assemblages

As shown in Table 1, the samples fixed with glutaraldehyde differed little in the number of taxa if analyzed by Taxonomist #1 or by Taxonomist #2. The average richness of these samples (21–25 different taxa, approximately) was very similar between spring and summer. However, the glutaraldehyde-fixed samples analyzed by Taxonomist #3

resulted in a much smaller number of taxa (7–12), especially in summer. The highest number of taxa corresponded to the samples fixed with Lugol and analyzed by Taxonomist #1 after increased experience (36, in average, in spring as well as in summer).

As for the cell density, in general, it was higher in spring compared to summer (Figure 2 of the Supplementary Electronic Material). However, some exceptions can be noticed

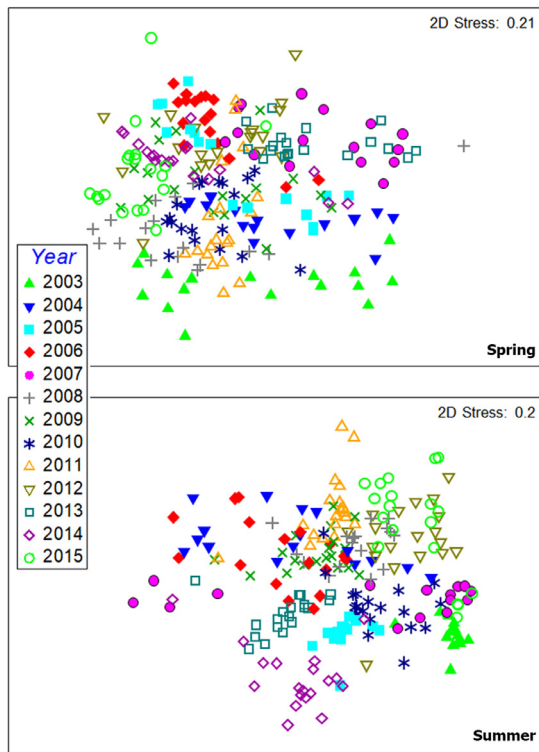


Figure 3 Multidimensional scaling (MDS) of the transformed environmental data in spring and summer using Euclidean distances for the period 2003–2015.

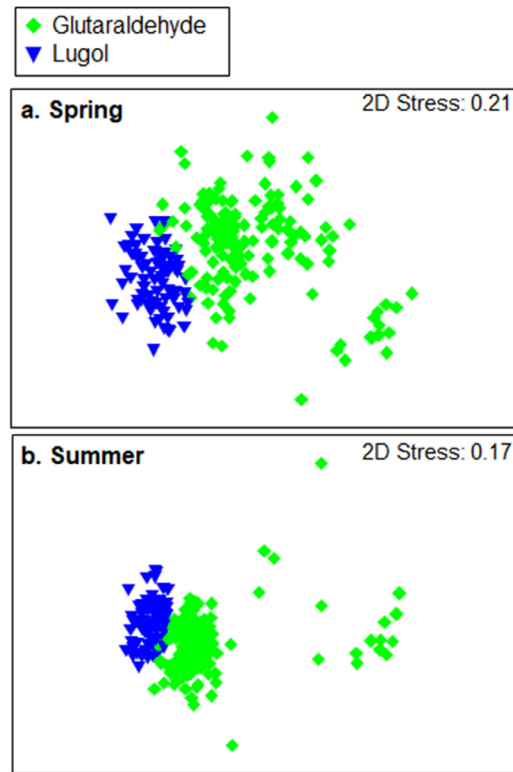


Figure 5 Multidimensional scaling (MDS) for phytoplankton abundance (log (x + 1) transformed data using zero-adjusted Bray-Curtis distances) for the period 2003–2015. Data are shown separately for spring (a) and summer (b). Different symbols represent the different fixatives employed.

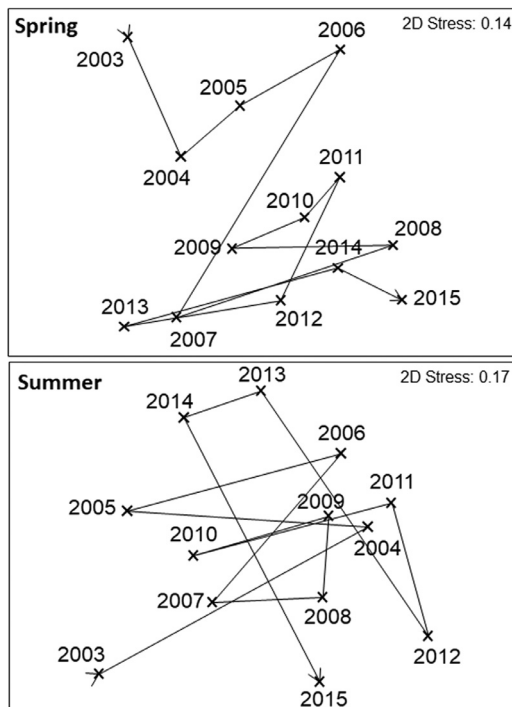


Figure 4 Multidimensional scaling (MDS) of the transformed environmental data (mean values of 17 sampling sites) using Euclidean distances. Cluster analyses did not find any significant group of years (SIMPROF test, alpha = 0.05).

for dinoflagellates and for other non-diatom taxa. Although the dinoflagellates usually contributed very little to the total cell abundance, their almost zero presence in several samples analyzed by Taxonomist #3 is remarkable (Figure 2b of the Supplementary Electronic Material). The other non-diatom cells, all together, were the most abundant in the data sets associated with Taxonomists #1 and #2, but not in many of the summer samples analyzed by Taxonomist #3 (Figure 2c of the Supplementary Electronic Material). In the groups of samples analyzed by Taxonomist #1, the cell abundance (estimated as geometric mean) was very similar between the two types of fixatives (Figure 2 of the Supplementary Electronic Material).

When the complete dataset (19 sites) was analyzed, the MDS showed two separate groups with regard to inter-annual variability of community composition: one referring to the year 2004 and the other referring to the remaining years (Figure 3 of the Supplementary Electronic Material). Separate MDS were conducted for spring and summer considering, firstly, the influence of the fixative (Figure 5). In the MDS biplots, a separation based on the type of fixative used can be observed in both seasons. Moreover, the PERMANOVA analysis indicated that phytoplankton variability was explained by the utilized fixative ($p = 0.0001$).

The influence of the taxonomist was then studied in the subset where one unique fixative was employed (i.e., glutaraldehyde during the period 2003–2011). The MDS biplots showed two main groups: one associated with Taxonomist #1

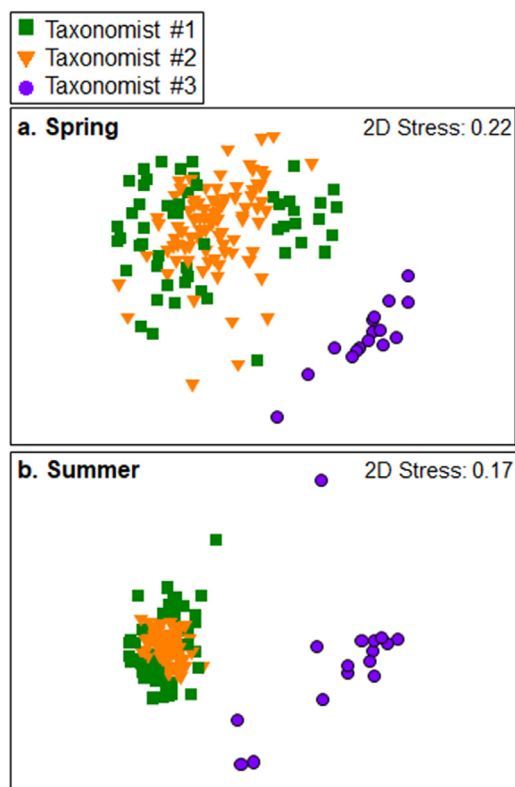


Figure 6 Multidimensional scaling (MDS) for phytoplankton abundance ($\log(x + 1)$ transformed data using zero-adjusted Bray-Curtis distances) for the period 2003–2011. Data are shown separately for spring (a) and summer (b). Different symbols represent different taxonomists handling the samples.

and Taxonomist #2 and the other associated with Taxonomist #3 (Figure 6). The pair-wise PERMANOVA for this subset revealed significant differences between the three different taxonomists handling the samples (Table 3 of the Supplementary Electronic Material). Similar results were obtained for spring and summer.

Inter-annual variability was also studied based on average values per season and year. Here, the MDS and cluster analyses for phytoplankton assemblages showed several significant groups according to changes both in the utilized fixative and taxonomist handling the samples (Figure 7).

At the lowest taxonomic level, 2004 (associated with Taxonomist #3) was the most different (Figure 7a, 7b). In spring, significant groups formed between years associated to the same fixative, such as the period 2012–2015 (Figure 7a). In summer, years were grouped not only according to the fixative, but also to the taxonomist, as shown by the group formed by the years identified by Taxonomist #2. The similarity of the significant groups of years was approximately 60%.

At the level of major taxonomic groups, the year 2004 also showed different phytoplankton assemblages compared to other years. At this taxonomic level, spring in all years appeared significantly grouped in accordance to the utilized fixative, except for 2004 that was also associated with a change in the taxonomist (Figure 7c). In summer, except for 2008, years were grouped in agreement with the

specialist doing the identification, even if the employed fixative was different (Figure 7d). The observed groups of years presented a similarity of around 90%.

Not only were differences among taxonomists observed, but also among different years with the same taxonomist. However, when looking at the years identified by Taxonomist #1 and Taxonomist #2 separately, the dissimilarities in community assemblages between years become smaller, particularly for Taxonomist #2. Cluster analyses of phytoplankton data are described in further detail in the Electronic Supplementary Material (Figure 4 of the Supplementary Electronic Material).

By using the pCCA (Table 2), the variability in the species densities explained by the sum of the environmental conditions and the taxonomist effect was 29.1% (spring) and 25.9% (summer). The percentage of variability uniquely explained by the environment was 15.8% and 12.8%, whereas that of the taxonomist effect was 10.8% and 9.6% (for spring and summer, respectively). The part of the variation that was explained jointly by the environment and the taxonomist effect was 2.5% (spring) and 3.5% (summer). Hence, the two sets of independent variables were not very redundant in explaining the spatio-temporal variability of species densities (i.e., each set of independent data was largely explaining different aspects of the observed variability in the phytoplankton).

4. Discussion

Yearly variation in phytoplankton communities can be explained not only by changes in nutrient concentrations and climatic factors (Cloern and Jassby, 2010; Cloern et al., 2013), but also by the employed fixative (e.g., Zarauz and Irigoien, 2008) and uncertainty introduced by the taxonomists even if the methodology was similar (Peperzak, 2010). This study presents evidence of the effect of these two laboratory-associated factors.

Different fixatives have been found to produce several effects on phytoplankton cells, such as diameter shrinkage, size changes and reduction in the abundance of detected cells (Leakey et al., 1994; Mukherjee et al., 2014; Zarauz and Irigoien, 2008). Thus, the identification and counting of cells can be biased and lead to distorted results. The results presented here show evidence of the bias introduced by changes in the utilized fixative, as in the analysis of phytoplankton communities from 19 sampling sites a clear differentiation was found from the year 2012 onwards (i.e., when the change from glutaraldehyde to Lugol's solutions occurred).

Additionally, evidence of interference arising from changes in the taxonomist performing the identification was identified. This could be explained in part by the risk of misidentification of small and cryptic species that is likely when using traditional techniques, such as that of Uthermöhl, which require a high level of expertise of the taxonomist (Mouillot et al., 2006). The clearest finding was observed for phytoplankton assemblages from 2004, which appeared notably differentiated from the others in the MDS plots. These results could not be linked to the previously mentioned effect of the fixative because the same fixative was employed in other years and such differences were not

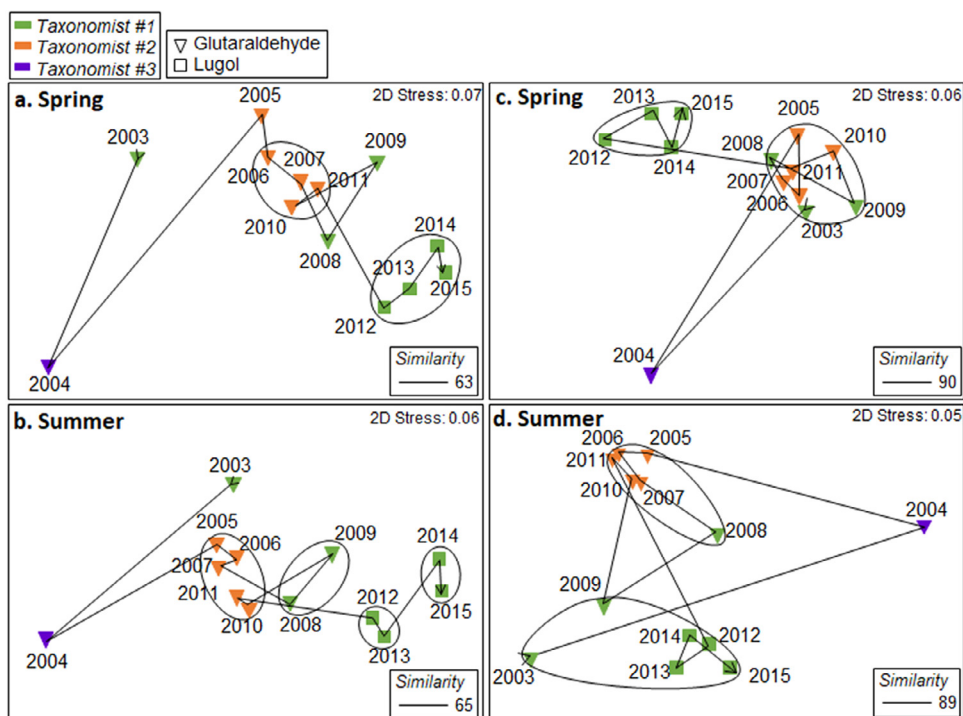


Figure 7 Multidimensional scaling (MDS) of the annual phytoplankton community assemblages ($\log(x + 1)$ transformed data using zero-adjusted Bray-Curtis distances). Average values per year and season (i.e., mean values of 17 sampling sites) are shown for spring (a, c) and summer (b, d). Panels a and b show data at the lowest taxonomic level available, and panels c and d at the major group level. Symbols represent different fixatives, colors show different taxonomists, and contour lines indicate significantly different groups (SIMPROF test, $\alpha = 0.05$). See Figure 4 of the Supplementary Electronic Material for cluster analyses.

Table 2 Results of two partial Canonical Correspondence Analyses (pCCA) carried out within the period 2003–2011; one for spring data and other one for summer data.

| | Spring | | | Summer | | |
|--|-----------------------|---------|---------|-----------------------|---------|---------|
| | explained inertia (%) | F-Ratio | p-value | explained inertia (%) | F-Ratio | p-value |
| Environmental data (1) | 18.3 | 4.12 | <0.01 | 16.4 | 3.57 | <0.01 |
| Taxonomist (2) | 13.3 | 11.7 | <0.01 | 13.1 | 11.43 | <0.01 |
| Environmental data – [taxonomist] (3) | 15.8 | 4.05 | <0.01 | 12.8 | 3.12 | <0.01 |
| Taxonomist – [environmental data] (4) | 10.8 | 11.02 | <0.01 | 9.6 | 9.27 | <0.01 |
| Environmental + taxonomist (shared variance) | 2.5 | | | 3.5 | | |
| Total (5) | 29.1 | 5.95 | <0.01 | 25.9 | 5.03 | <0.01 |

(1) CCA carried out with environmental data as independent data, (2) CCA carried out with taxonomist data as independent data, (3) CCA carried out with environmental data as independent data and taxonomist data as covariable; (4) CCA carried out with taxonomist data as independent data and environmental data as covariable, (5) CCA carried out with taxonomist data and environmental data as independent data. Note: the results of (1) and (2) are not part of the pCCA.

observed. In addition, the environmental variables in 2004 did not present extreme values that could explain such differentiation in the phytoplankton assemblages. Thus, the observed phytoplankton assemblages for 2004 were suspected to be artifacts of the change in the taxonomist (e.g., Dromph et al., 2013; Peperzak, 2010).

However, it must be noted that not only extreme values can shape the composition of phytoplankton communities (e.g., Remy et al., 2017). As shown in previous studies (Bode et al., 2015; Devlin et al., 2019; Hernández et al., 2015), phytoplankton variability is also influenced by gradual changes of several variables, such as water temperature,

turbidity, salinity or nutrient concentration, at the long-term. In the present study, environmental conditions in surface waters were studied to check if they could explain the inter-annual variability of phytoplankton community. In general, dissimilarities found in the environmental conditions did not explain the main dissimilarities observed in the phytoplankton communities. As an example, apart from the above explanation regarding 2004, 2003 was found to be one of the most different years in terms of environmental variables, both in spring and summer. Spring 2003 was characterized by minimum values in water transparency (Secchi depth) and salinity, and relatively high values in

nitrate and silicate. Summer 2003 presented the maximum water temperature and the minimum in all nutrients (ammonium, nitrate, nitrite, phosphate and silicate). However, these findings were not consistently accompanied by great dissimilarity in phytoplankton assemblages between 2003 and other years. In addition, along the chronological trajectory, the largest dissimilarities in environmental conditions between years, with respect to average values per season and year, did not reflect such changes in community assemblages for the same years. In fact, one of the largest dissimilarities in phytoplankton communities between consecutive years, apart from 2004, was associated with changes in the both the fixative and the taxonomist (i.e., 2011 to 2012). Therefore, these laboratory-induced artifacts are confirmed as significant factors in introducing uncertainty to the study of phytoplankton communities.

It could be possible that the error in the taxonomic determinations and counts derived from the taxonomist change caused (at least partially) the lack of correlation of the environmental variables with the structure of the communities observed in the MDS results. Muñiz et al. (2018) found that, for this same studied area, the spatio-temporal variability in the phytoplankton densities was significantly explained by environmental data in the period 2012–2015, in which the taxonomist handling the samples and the fixative used were the same. Considering a longer period (2003–2011) with the same fixative, but including three different taxonomists, the pCCA results show that the variability in the phytoplankton densities was also significantly explained by environmental data, once removed the taxonomist effect (Table 2). Nevertheless, it is important to remark that the percentage of the variability explained by the environmental variables in the 2003–2011 period increases considerably when the taxonomist effect is taken into account. This implies that, at least in our case study, it is relevant to take into account appropriate measures when phytoplankton time series involving different taxonomists are studied.

Although data obtained by different taxonomists in the same samples were not compared in this study, Taxonomist #1 and Taxonomist #2 took part in a previous study that assessed the variability in total cell counts within a similar set of samples analyzed by different taxonomists (Dromph et al., 2013). That study involved several localities, including the Basque coast, and concluded that in all cases, important differences were observed due to the taxonomists' effect. When data from different monitoring programs are integrated, inter-laboratory biases are added to intra-laboratory ones. Intercomparison exercises among laboratories (for example, the International Phytoplankton Intercomparison, <https://www.iphyi.org>) arise as a good strategy to reduce uncertainty related to taxonomists and other analytical protocols.

It is also interesting to assess this effect not only at the lowest taxonomic level available, but also at other taxonomic levels. At the level of major taxonomic groups, the bias due to the experience of the taxonomist was found to be much lower compared with that of species level, as shown by the similarity percentages of significant groups (Figure 3c, 3d). Consequently, for studies or monitoring networks in which a high taxonomic detail is not required, it would be desirable to work at a higher taxonomic level in

order to minimize identification errors. However, interpretation of this finding should be taken with care as Straile et al. (2015) found that, at least in lakes, taxonomic aggregation does not always imply more robust results.

It should be noted that studies focused on inhomogeneity detection in phytoplankton time series are relatively scarce. This is not the case for climate datasets, for which several methodologies have been developed for the detection of inhomogeneities (e.g., Buishand, 1982; Costa et al., 2008; Ribeiro et al., 2016). Thus, it is necessary to test the usefulness of the methodology employed in the present study (i.e., detection of changes in biological assemblages by means of multivariate analyses, such as PERMANOVA and SIMPROF tests) to other long-term phytoplankton datasets.

5. Conclusions

Evidence of the uncertainty due to laboratory issues (i.e., changes in fixatives, experience or changes in the taxonomist) is demonstrated and should be considered when studying long-term phytoplankton time series. Interference introduced by changes in the taxonomists was lower at the level of major taxonomic groups and thus, we suggest that community studies be conducted at higher taxonomic levels when possible. Continuous learning should be combined with detailed protocols and strict standards, and further research should be done regarding the detection of inhomogeneities in phytoplankton time series.

Acknowledgements

The data for this study were obtained from the project “Program for the monitoring and assessment of the ecological status of transitional and coastal waters of the Basque Country” funded by URA, the Basque Water Agency, through a convention with AZTI. This work was supported by the project “IM17MUSSELS”. The participation of O. Muñiz was funded by a grant from the Department of Economic Development and Competitiveness of the Basque Government (BOPV num. 201; 2013/4467). This paper is contribution number 956 from AZTI (Marine Research Division). We also thank Proof-Reading-Service for their great professional proof reading and editing service, as well as the anonymous reviewers for their comments and suggestions.

Supplementary materials

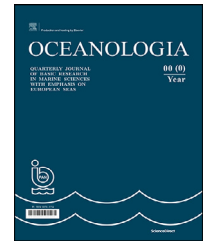
Supplementary material associated with this article can be found, in the online version, at <https://doi.org/10.1016/j.oceano.2020.01.004>.

References

- Bode, A., Estévez, M.G., Varela, M., Vilar, J.A., 2015. Annual trend of phytoplankton species abundance belie homogeneous taxonomical group responses to climate in the NE Atlantic upwelling. *Mar. Environ. Res.* 110, 81–91.

- Booth, B., 1987. The use of autofluorescence for analyzing oceanic phytoplankton communities. *Bot. Mar.* 30, 101–108.
- Borcard, D., Legendre, P., Drapeau, P., 1992. Partialling out the spatial component of ecological variation. *Ecology* 84, 511–525.
- Borja, A., Bricker, S.B., Dauer, D.M., Demetriades, N.T., Ferreira, J.G., Forbes, A.T., Hutchings, P., Jia, X., Kenchington, R., Marques, J.C., 2008. Overview of integrative tools and methods in assessing ecological integrity in estuarine and coastal systems worldwide. *Mar. Pollut. Bull.* 56, 1519–1537.
- Borja, A., Chust, G., Rodríguez, J.G., Bald, J., Belzunce-Segarra, M.J., Franco, J., Garmendia, J.M., Larreta, J., Menchaca, I., Muxika, I., Solaun, O., Revilla, M., Uriarte, A., Valencia, V., Zorita, I., 2016. ‘The past is the future of the present’: Learning from long-time series of marine monitoring. *Sci. Total Environ.* 566–567, 698–711.
- Borja, A., Franco, J., Valencia, V., Bald, J., Muxika, I., Jesús Belzunce, M.A., Solaun, O., 2004. Implementation of the European water framework directive from the Basque country (northern Spain): a methodological approach. *Mar. Pollut. Bull.* 48, 209–218.
- Braak, C.J.F., Smilauer, P., 2002. *CANOCO Reference manual and CanoDraw for Windows user’s guide: software for canonical community ordination (version 4.5)*. Ithaca NY, USA: www.canoco.com (Microcomputer Power). *Mathematical and Statistical Methods – Biometrics*.
- Bricejaj, V.M., Shumway, S.E., 1998. Paralytic shellfish toxins in bivalve molluscs: occurrence, transfer kinetics, and biotransformation. *Rev. Fish. Sci.* 6, 315–383.
- Buishand, T.A., 1982. Some methods for testing the homogeneity of rainfall records. *J. Hydro.* 58, 11–27.
- Carneiro, F.M., Bini, L.M., Rodrigues, L.C., 2010. Influence of taxonomic and numerical resolution on the analysis of temporal changes in phytoplankton communities. *Ecol. Indic.* 10, 249–255.
- Carneiro, F.M., Nabout, J.C., Vieira, L.C.G., Lodi, S., Bini, L.M., 2013. Higher taxa predict plankton beta-diversity patterns across an eutrophication gradient. *Nat. Conservação* 11, 43–47.
- Clarke, K., Gorley, R., 2006. *User manual/tutorial*. Primer-E Ltd., Plymouth, 93 pp.
- Clarke, K.R., Somerfield, P.J., Chapman, M.G., 2006. On resemblance measures for ecological studies, including taxonomic dissimilarities and a zero-adjusted Bray–Curtis coefficient for denuded assemblages. *J. Exp. Mar. Biol. Ecol.* 330, 55–80.
- Clesceri, L., Greenberg, A., Trussell, R., 1989. *Standard methods for the examination of water and wastewater*, 17th edn., Port City Press, Baltimore 232 pp.
- Cloern, J., Foster, S., Kleckner, A., 2013. Review: phytoplankton primary production in the world’s estuarine-coastal ecosystems. *Biogeosciences Discuss* 10, 17725–17783.
- Cloern, J.E., Jassby, A.D., 2010. Patterns and scales of phytoplankton variability in estuarine-coastal ecosystems. *Estuar. Coast.* 33, 230–241.
- Costa, A.C., Negreiros, J., Soares, A., 2008. Identification of inhomogeneities in precipitation time series using stochastic simulation. *geoENV VI—Geostatistics for Environmental Applications*. Springer, Berlin, 275–282.
- Culverhouse, P.F., Williams, R., Reguera, B., Herry, V., González-Gil, S., 2003. Do experts make mistakes? A comparison of human and machine identification of dinoflagellates. *Mar. Ecol. Prog. Ser.* 247, 17–25.
- Devlin, M., Barry, J., Painting, S., Best, M., 2009. Extending the phytoplankton tool kit for the UK Water Framework Directive: indicators of phytoplankton community structure. *Hydrobiologia* 633, 151–168.
- Devlin, M.J., Breckels, M., Graves, C., Barry, J., Capuzzo, E., Huerta, F.P., Al-Ajmi, F., Al-Husain, M., LeQuesne, W., Lyons, B.P., 2019. Seasonal and temporal drivers influencing phytoplankton community in Kuwait marine waters, documenting a changing landscape in the Gulf. *Frontiers Mar. Sci.* 6, 1–22.
- Domingues, R.B., Barbosa, A., Galvão, H., 2008. Constraints on the use of phytoplankton as a biological quality element within the Water Framework Directive in Portuguese waters. *Mar. Pollut. Bull.* 56, 1389–1395.
- Dromph, K.M., Agusti, S., Basset, A., Franco, J., Henriksen, P., Icely, J., Lehtinen, S., Moncheva, S., Revilla, M., Roselli, L., 2013. Sources of uncertainty in assessment of marine phytoplankton communities. *Hydrobiologia* 704, 253–264.
- Elder, L., Elbrächter, M., 2010. The Utermöhl method for quantitative phytoplankton analysis. In: Karlson, B., Cusack, C., Brennan, E. (Eds.), *Microscopic and Molecular Methods for Quantitative Phytoplankton Analysis*, 110. Intergovernmental Oceanographic Commission of UNESCO, 13–20.
- Garmendia, M., Borja, A., Franco, J., Revilla, M., 2013. Phytoplankton composition indicators for the assessment of eutrophication in marine waters: Present state and challenges within the European directives. *Mar. Pollut. Bull.* 66, 7–16.
- Grasshoff, K., Ehrhardt, M., Kremling, K., 1983. *Methods of seawater analyses*. Verlag Chemie, Weinheim, 342–355.
- Guiry, M., Guiry, G., 2015. *AlgaeBase*. World-wide Electronic Publication. Nat. Univ., Ireland, Galway, <http://www.algaebase.org>.
- Hasle, G., 1978. *The inverted microscope method*. Phytoplankton Manual. UNESCO, Paris, 337 pp.
- Heino, J., Soininen, J., 2007. Are higher taxa adequate surrogates for species-level assemblage patterns and species richness in stream organisms? *Biol. Conserv.* 137, 78–89.
- Hernández, T., Bacher, C., Soudant, D., Belin, C., Barillé, L., 2015. Assessing phytoplankton realized niches using a French national phytoplankton monitoring network. *Estuarine, Coast. Shelf Sci.* 159, 15–27.
- Huisman, J., van Oostveen, P., Weissing, F.J., 1999. Critical depth and critical turbulence: two different mechanisms for the development of phytoplankton blooms. *Limnol. Oceanogr.* 44, 1781–1787.
- Jakobsen, H.H., Carstensen, J., Harrison, P.J., Zingone, A., 2015. Estimating time series phytoplankton carbon biomass: Inter-lab comparison of species identification and comparison of volume-to-carbon scaling ratios. *Estuarine, Coast. Shelf Sci.* 162, 143–150.
- Kahlert, M., Ács, É., Almeida, S.F., Blanco, S., Drefßler, M., Ector, L., Karjalainen, S.M., Liess, A., Mertens, A., van der Wal, J., 2016. Quality assurance of diatom counts in Europe: towards harmonized datasets. *Hydrobiologia* 772, 1–14.
- Kahlert, M., Albert, R.L., Anttila, E.L., Bengtsson, R., Bigler, C., Eskola, T., Gälman, V., Gottschalk, S., Herlitz, E., Jarlman, A., 2009. Harmonization is more important than experience—results of the first Nordic–Baltic diatom intercalibration exercise 2007 (stream monitoring). *J. Appl. Phycol.* 21, 471–482.
- Kahlert, M., Kelly, M., Albert, R.-L., Almeida, S.F., Bešta, T., Blanco, S., Coste, M., Denys, L., Ector, L., Fránková, M., 2012. Identification versus counting protocols as sources of uncertainty in diatom-based ecological status assessments. *Hydrobiologia* 695, 109–124.
- Leakey, R.J.G., Burkill, P.H., Sleight, M.A., 1994. A comparison of fixatives for the estimation of abundance and biovolume of marine planktonic ciliate populations. *J. Plankton Res.* 16, 375–389.
- Legendre, P., Legendre, L., 1998. *Numerical Ecology*, 2nd edn., Amsterdam, 853 pp.
- Martinez, E., Antoine, D., D’Ortenzio, F., Gentili, B., 2009. Climate-driven basin-scale decadal oscillations of oceanic phytoplankton. *Science* 326, 1253–1256.
- McCune, B., Grace, J.B., Urban, D.L., 2002. *Analysis of ecological communities*. MjM software design Gleneden Beach, OR.

- Menden-Deuer, S., Lessard, E.J., Satterberg, J., 2001. Effect of preservation on dinoflagellate and diatom cell volume and consequences for carbon biomass predictions. *Mar. Ecol. Prog. Ser.* 222, 41–50.
- Muñiz, O., Rodríguez, J.G., Revilla, M., Laza-Martínez, A., Seoane, S., Franco, J., 2018. Seasonal variations of phytoplankton community in relation to environmental factors in an oligotrophic area of the European Atlantic coast (southeastern Bay of Biscay). *Reg. Stud. Mar. Sci.* 17, 59–72, <http://dx.doi.org/10.1016/j.rsma.2017.11.011>.
- Mouillot, D., Spatharis, S., Reizopoulou, S., Laugier, T., Sabetta, L., Basset, A., Do Chi, T., 2006. Alternatives to taxonomic-based approaches to assess changes in transitional water communities. *Aquat. Conserv.* 16, 469–482.
- Mukherjee, A., Das, S., Bhattacharya, T., De, M., Maiti, T., Kumar De, T., 2014. Optimization of phytoplankton preservative concentrations to reduce damage during long-term storage. *Biopreserv. Biobank.* 12, 139–147.
- Peperzak, L., 2010. An objective procedure to remove observer-bias from phytoplankton time-series. *J. Sea Res.* 63, 152–156.
- R Core Team, R.C., 2015. R: A language and environment for statistical computing. R Foundation for Statistical Computing, Vienna, Austria.
- Remy, M., Hillebrand, H., Flöder, S., 2017. Stability of marine phytoplankton communities facing stress related to global change: Interactive effects of heat waves and turbidity. *J. Exp. Mar. Biol. Ecol.* 497, 219–229.
- Revilla, M., Franco, J., Bald, J., Borja, Á., Laza, A., Seoane, S., Valencia, V., 2009. Assessment of the phytoplankton ecological status in the Basque coast (northern Spain) according to the European Water Framework Directive. *J. Sea Res.* 61, 60–67.
- Ribeiro, S., Caineta, J., Costa, A.C., Henriques, R., Soares, A., 2016. Detection of inhomogeneities in precipitation time series in Portugal using direct sequential simulation. *Atmos. Res.* 171, 147–158.
- Straile, D., Jochimsen, M.C., Kümmerlin, R., 2013. The use of long-term monitoring data for studies of planktonic diversity: a cautionary tale from two Swiss lakes. *Freshwater Biol.* 58, 1292–1301.
- Straile, D., Jochimsen, M.C., Kümmerlin, R., 2015. Taxonomic aggregation does not alleviate the lack of consistency in analysing diversity in long-term phytoplankton monitoring data: a rejoinder to Pomati et al. (2015). *Freshwater Biol.* 60 (5), 1060–1067, <https://doi.org/10.1111/fwb.12552>.
- Utermöhl, H., 1958. Zur vervollkommnung der quantitativen phytoplankton-methodik. *Mitteilungen der Internationale Vereinigung für Theoretische und Angewandte Limnologie* 9, 1–38.
- Valencia, V., Franco, J., Borja, Á., Fontán, A., 2004. Hydrography of the southeastern Bay of Biscay. In: Borja, A., Collins, M. (Eds.), *Oceanography and Marine Environment of the Basque Country*, 70. Elsevier Oceanogr. Ser., 159–194.
- Verity, P.G., Robertson, C.Y., Tronzo, C.R., Andrews, M.G., Nelson, J.R., Sieracki, M.E., 1992. Relationships between cell volume and the carbon and nitrogen content of marine photosynthetic nanoplankton. *Limnol. Oceanogr.* 37, 1434–1446.
- Wiltshire, K.H., Dürselen, C.D., 2004. Revision and quality analyses of the Helgoland Reede long-term phytoplankton data archive. *Helgol. Mar. Res.* 58, 252–268.
- Yang, Y., Sun, X., Zhao, Y., 2016. Effects of Lugol's iodine solution and formalin on cell volume of three bloom-forming dinoflagellates. *Chin. J. Oceanol. Limn.* 35, 858–866.
- Zarauz, L., Irigoien, X., 2008. Effects of Lugol's fixation on the size structure of natural nano–microplankton samples, analyzed by means of an automatic counting method. *J. Plankton Res.* 30, 1297–1303.



ORIGINAL RESEARCH ARTICLE

Imprints of atmospheric waves on the Black Sea surface in data of ocean color scanners

Marina A. Evdoshenko*

P.P. Shirshov Institute of Oceanology, Russian Academy of Sciences, Moscow, Russia

Received 16 August 2019; accepted 28 January 2020

Available online 12 February 2020

KEYWORDS

Remote sensing;
Ocean Optics;
Atmospheric gravity
waves;
Black Sea

Summary Data from MERIS onboard Envisat and MODIS onboard Terra and Aqua for 15–16 May 2010 were used to study powerful imprints of atmospheric gravity waves (AGWs) on the western part the Black Sea surface. Two cold fronts crossed the sea following the warm front and caused the AGWs which modulated the sea surface. Imprints of AGWs appeared as stripes of alternating brightness, they had crest length more than a hundred kilometers and wavelength of units of kilometers. Wave amplitude of AGWs imprints, evaluated by a 90%-depth of light penetration into the sea at 490 nm z_{90} , the value inverse to the diffuse attenuation coefficient Kd_{490} , was units of decimeterxs. MODIS 250-m data of remote sensing reflectance, wind components and atmospheric pressure near the sea surface were obtained by processing the top of atmosphere data with the SeaDAS software package. Negative correlations of fluctuations of z_{90} with fluctuations of wind stress and atmospheric pressure were found on the transects of more than ten kilometers. The impact of wind stress on the origination of AGW imprints was found to be determinant, while the impact of atmospheric pressure was not more than units of percent.

© 2020 Institute of Oceanology of the Polish Academy of Sciences. Production and hosting by Elsevier B.V. This is an open access article under the CC BY-NC-ND license (<http://creativecommons.org/licenses/by-nc-nd/4.0/>).

* Corresponding author at: P.P. Shirshov Institute of Oceanology, Russian Academy of Sciences, 36 Nakhimovski prospect, 117997 Moscow, Russia.

E-mail address: maarsio@bk.ru

Peer review under the responsibility of the Institute of Oceanology of the Polish Academy of Sciences.



Production and hosting by Elsevier

1. Introduction

Investigations of the footprints of atmospheric phenomena on the sea surface are traditionally carried out with the help of satellites equipped with devices termed synthetic aperture radar (SAR) systems. The microwave radiation of SAR freely penetrates through clouds into the sea to a distance of about several millimeters (Knyazev et al., 2003; Valenzuela, 1978). Atmospheric gravity waves (AGWs) which are generated in the marine planetary boundary layer (PBL), backscatter from the sea surface roughness and create a

<https://doi.org/10.1016/j.oceano.2020.01.002>

0078-3234/© 2020 Institute of Oceanology of the Polish Academy of Sciences. Production and hosting by Elsevier B.V. This is an open access article under the CC BY-NC-ND license (<http://creativecommons.org/licenses/by-nc-nd/4.0/>).

periodic signal that is perceived by the radar (Alpers et al., 2008). AGWs are known to be generated by atmospheric fronts, horizontal or vertical wind shear or by airflow over mountain ranges, in which case they are called atmospheric lee waves. Imprints of AGWs with SAR devices installed onboard different satellites have been studied for several decades (Alpers and Brummer, 1994; Cheng and Alpers, 2010; Li et al., 2011; Vachon et al., 1994; Zheng et al., 1998).

AGWs are usually invisible but become visible at sufficiently high humidity appearing as “cloud streets” on top-of-the-atmosphere (TOA) reflectance images obtained from ocean color scanners. TOA data enable detailed investigations of cloud manifestations of atmospheric waves in the PBL (Da Silva and Magalhaes, 2009; Li et al., 2008; Liu et al., 2004).

Optical and near-infra-red radiance does not penetrate clouds, however, under a clear sky, ocean color scanners perceive the changing reflectance of the sea surface which AGWs modulate. Images from Envisat-ASAR and near-infrared images from MODIS-Terra revealed AGWs in different ocean regions (Li et al., 2011; Magalhaes et al., 2011). In (Evdoshenko, 2016) it was shown that the superimposition in a difference mode of MODIS TOA level 1 radiance image with signatures of AGWs in cloud, and remote sensing reflectance (R_{rs}) image of level 2 with signatures of AGWs on the sea surface, both at 859 nm, revealed that crests of the surface AGW imprints were similar the prolongations of AGW cloud stripes. Similar results were shown to be valid for different ocean regions. Numerical simulations and water tank experiments described by Sachspurger et al. (2017) showed that the vertical amplitudes of atmospheric gravity lee waves with wavelengths ~ 2 -6 km depend on the inversion strength on the vertical temperature profiles measured in the PBL and can reach 300 m in size.

In the present paper, the numerous highly expressed long imprints of AGWs revealed by ocean color data on 15–16 May of 2010 which covered the western part of the Black Sea are analyzed. Such powerful AGW imprints in the Black Sea were found only once for the time period from the beginning of measurements with the ocean color scanner SeaWiFS in 1998 and MODIS in 2002, until 2015. Evidently, they were connected with the very specific weather conditions produced during the passing of the warm and cold fronts over the sea. As a result, the intense AGWs were created in PBL; they spread down to the sea surface and modulated it. Vertical amplitudes of AGW imprints are evaluated and dependencies of the amplitudes from the atmospheric pressure and wind stress above the sea surface are stated.

The included ocean color satellite data, methods of their processing and data presentation are listed in section 2. Characteristics of AGW imprints and correlations of their amplitudes with some atmospheric characteristics are reflected in section 3. The main results obtained on the basis of the used satellite data are stated in section 4.

2. Material and methods

Data were obtained from three ocean color scanners: a medium resolution imaging spectrometer (MERIS) onboard Envisat and moderate resolution imaging spec-

troradiometers (MODISes) onboard EOS AM-1 Terra and EOS AM-2 Aqua satellites. We used the following data for 16 May 2010: MERIS full resolution (300-m) data M2010136084011.L2_FRS_OC, 1-km data of MODIS-Terra T2010136092000.L2_LAC_OC, MODIS-Aqua 250-m data A2010136110000.L1A_LAC and 1-km of MODIS-Aqua data A2010136110000.L2_LAC_OC. All these data are available at <http://oceancolor.gsfc.nasa.gov>. True-color level 1 TOA images from MODIS-Terra and -Aqua at 250-m resolution with no projection for 15–16 May 2010 are accessible at <https://earthdata.nasa.gov/earth-observation-data>.

R_{rs} at 859 nm originates in the thin topmost layer of about several centimeters owing to high absorption of pure water (Hale and Querry, 1973; Pegau et al., 1997), so it provides good reproduction of the imprints of atmospheric waves in water. Ocean color data of level 2: 250-m R_{rs} 859 and some atmospheric (meteorological) characteristics were generated from level 1 data with the SeaDAS software package. The process included several generation steps: 1 – the geolocation file, 2 – calibrated geolocated level 1b file and 3 – level 2 data. Meteorological data were initially obtained from the National Centers for Environmental Prediction (NCEP) and then processed with SeaDAS as level 2 products, namely: wind components at a height of 10 m above the ocean and atmospheric pressure near the sea surface; these data were automatically interpolated for a given time and place with the ocean color data. The SMCS software package (Sheberstov and Lukyanova, 2007) was used to plot the geographical maps of the obtained characteristics in the Mercator projection.

3. Results

We considered unusually long and intensive atmospheric waves and their imprints on the sea surface manifested over the Black Sea for two days. The Black Sea is a tideless marginal sea of the Atlantic Ocean that is divided into two sub-basins by a convexity extending south from the Crimean Peninsula. The maximum depth of 2212 m occurs in the center of the sea and the largest shelf is to the north of the basin which extends up to 190 km.

A map of the Black Sea with bathymetric contours of 50, 100, 500, 1000, and 2000 m is shown in Fig. 1. A polygon where imprints of AGWs were clearly manifested on all scanners images on 16 May 2010 is denoted by a black rectangle. A black circle designated the meteo-station Samsun, Turkey, on the southern shore of the sea where the radiosonde measurements were performed on those days.

On 15 May 2010 intensive atmospheric waves manifested as cloud structures of different forms over the entire Black Sea. The cloud patterns reflected atmospheric waves, convective cells and undular bores. Desaturated true-color TOA images of the sea with no projection at 250-m resolution from Terra-MODIS at 8:35 and from Aqua-MODIS at 10:20 2010 are shown in Fig. 2a and b. True-color images combine three spectral bands: band 1 (620–670 nm), band 3 (459–479 nm) and band 4 (545–565 nm). Fig. 2 shows that the western part of the sea was covered with fog and that against this background numerous AGWs signatures were observed as thick, near-linear cloud formations in the form

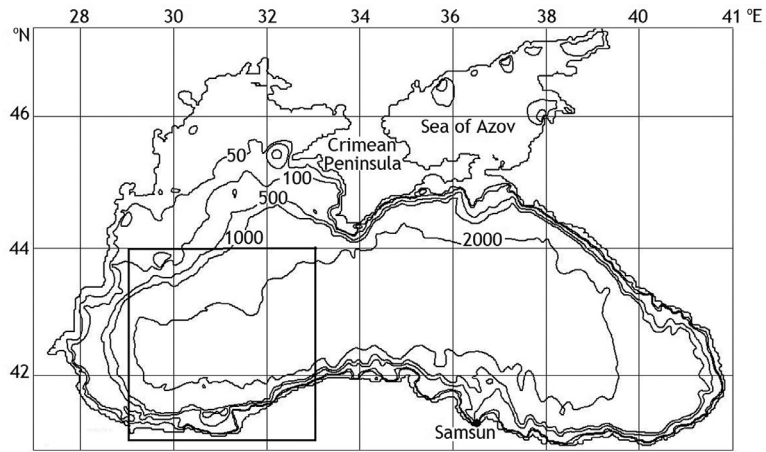
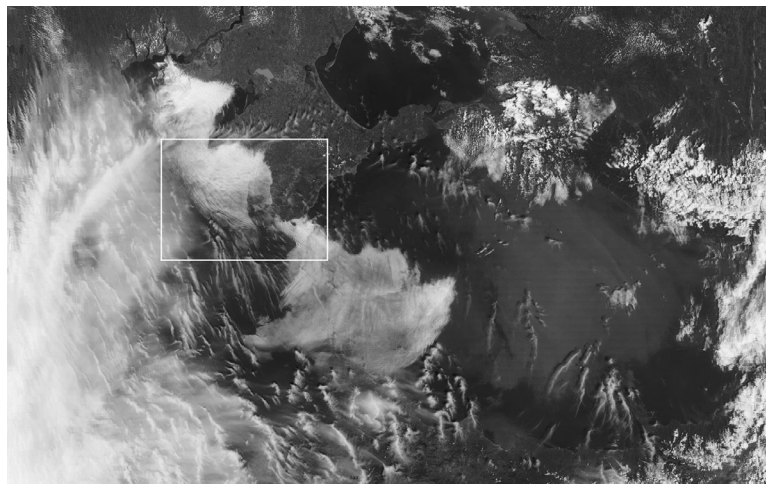
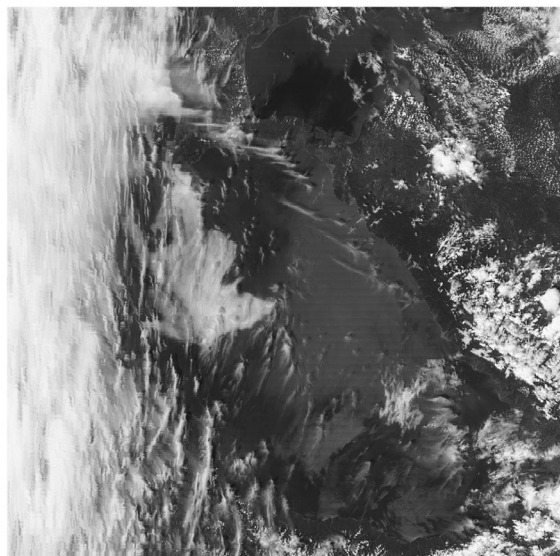


Figure 1 Map of the Black Sea with bathymetric contours Figure 8.



a



b

Figure 2 Desaturated true-color 250-m images of the Black Sea from: a – Terra-MODIS at 8:35, and b – Aqua-MODIS at 9:20 on 15 May 2010. The white square restricts an area with undular bores.

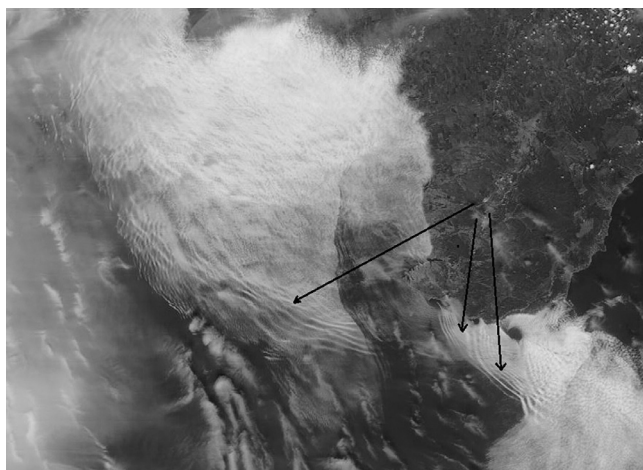


Figure 3 Desaturated true-color 250-m image of a series of undular bores (indicated by black arrows) to the south of the Crimean Peninsula obtained from Terra-MODIS at 8:35 on 15 May 2010.

of separate cloud streets in the north-eastern part of the sea.

The northern central part of the Black Sea, which contains undular bore clouds (is bound by a white square in Fig. 2a) is scaled up in Fig. 3. A series of low-level clouds in the form of narrow, arched stripes of atmospheric wave manifestation (indicated by black arrows in Fig. 3) is clearly seen propagating toward the southern Crimean Peninsula; undular bore clouds were imposed on each other. It is known that a thunderstorm may assist with the occurrence of undular bores and that undular bores can, in turn, intensify a thunderstorm because they further disturb the atmosphere (Chanson, 2010). Seemingly, there was a thunderstorm or hurricane on 15 May 2010.

On the following day, 16 May 2010, the cloudiness dispersed above almost the entire Black sea. Three ocean color sensors – MERIS at 8:40, Terra-MODIS at 9:20 and Aqua-MODIS at 11:00 – recorded unusual surface imprints of AGWs in the Black Sea on that day only. Apparently, imprints of

AGWs on the sea surface existed for two days – on 15 and 16 May 2010, but a strong fog on 15 May prevented their observation with ocean color scanners, as the light in the visible range does not penetrate through strong fog or haze. A picture showing clear AGW signatures in the Black Sea on 16 May 2010 was unique for the period from 1998 until 2015.

The desaturated true-color TOA images of the western part of the Black Sea at 250-m resolution obtained on 16 May 2010 from Terra-MODIS at 9:20 and Aqua-MODIS at 11:00 are shown in Fig. 4a and b. These figures show practically the same western part of the Black Sea but have different sizes because they are represented without any projection and with no latitude-longitude axes (available at <https://earthdata.nasa.gov/earth-observation-data>). On both images numerous AGWs of different directions are seen on the background of sun glitter. They most clearly appeared in the left western part of the sea. Imprints of AGWs in the form of long waves are evident; they represented AGWs because they were very long, narrow and close to rectilinear; a width of their crests expressed as light stripes was significantly less than the width of troughs expressed as dark stripes. These characteristics differentiate AGWs from the signatures of internal surface waves, according to Alpers and Huang (2011). The wave pattern very likely originates from AGWs if a sea area has no shallow underwater bottom topography, no strong tidal currents, and no upwelling – conditions satisfied by the Black Sea. Most of the manifested waves were oriented SW–NE, while others were oriented in different directions. Imprints of AGWs are observed to intersect each other. These phenomena could be caused by the imposition of traces of AGWs propagating at different levels of the marine PBL.

Similar surface imprints were also apparent at a pattern of Rrs at wavelengths of the optical and near-infrared ranges. They were also visible on images of standard ocean color products, as the diffuse attenuation coefficient of sunlight in the sea – Kd_{490} , and other products (accessible at <http://oceancolor.gsfc.nasa.gov>).

The empirical algorithm for an indicator of the turbidity of the water column in the transparency window Kd_{490} , in m^{-1} , returns the diffuse attenuation coefficient for downwelling irradiance at 490 nm, calculated using a

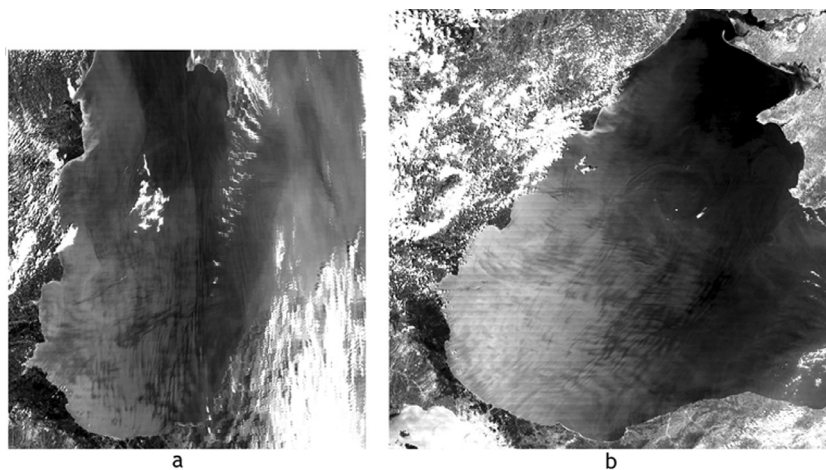


Figure 4 Desaturated true-color 250-m TOA images of the western part of the Black Sea on 16 May 2010: a – at 9:20 from Terra-MODIS, and b – at 11:00 from Aqua-MODIS.

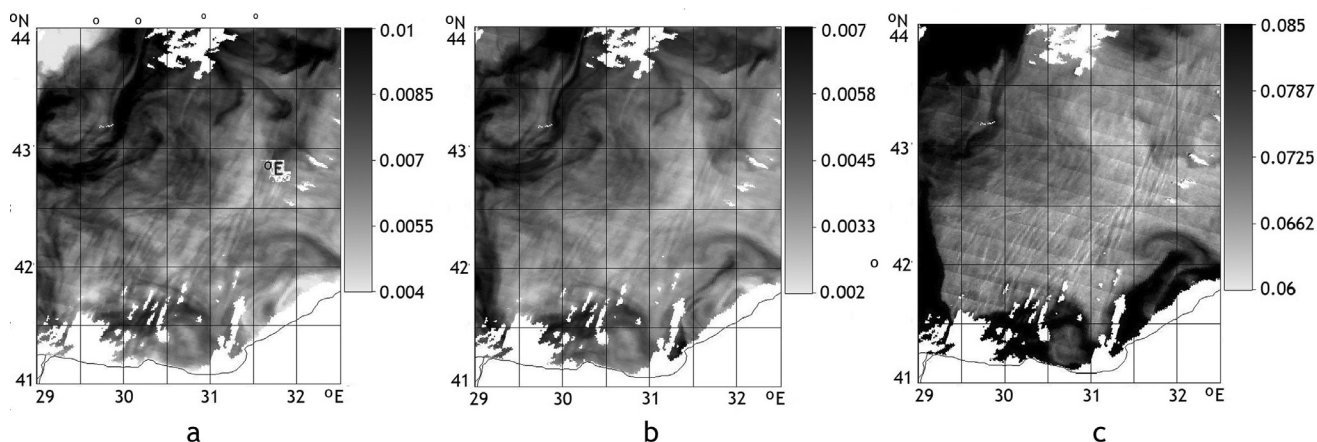


Figure 5 Images obtained from Terra-MODIS on 16 May at 9:20 of the testing area restricted by a black rectangle in Fig. 1: a – Rrs_{488} , sr^{-1} ; b – Rrs_{547} , sr^{-1} ; c – Kd_{490} , m^{-1} .

relationship derived from in situ measurements of Kd_{490} and the blue-to-green band ratios of Rrs (Lee et al., 2005, Morel et al., 2007). Kd_{490} over the first optical attenuation layer is calculated based on the following fourth-order polynomial relationship:

$$\log_{10}(K_{bio_490}) = a_0 + \sum_{(i=1)}^4 a_i (\log_{10}(Rrs_{\lambda_{blue}}/Rrs_{\lambda_{green}}))^i,$$

$$Kd_{490} = K_{bio_490} + 0.0166. \quad (1)$$

For MODIS, $\lambda_{blue} = 488$ nm and $\lambda_{green} = 547$ nm; for MERIS, $\lambda_{blue} = 490$ nm and $\lambda_{green} = 560$ nm; the coefficients a_0 , a_1 , a_2 , a_3 , and a_4 are also sensor-specific (https://oceancolor.gsfc.nasa.gov/atbd/kd_490).

Suslin et al. (2017) showed that for the clear waters ($Kd_{490} \leq 0.07$) of the western Black Sea, MODIS Kd_{490} data calculated for different seasons differed weakly with sea measurements made with an immovable Bulgarian buoy *basbio001d*. For the more turbid waters ($Kd_{490} \geq 0.12$) of the western Black Sea, the discrepancy with sea measurements was minimal in the warm season – from the second half of May to the end of September, whereas for the cold period of a year, the standard satellite values of Kd_{490} were reduced by approximately $\sim 20\%$. Thus, on 16 May, the standard values of Kd_{490} were close to the real ones even for more turbid waters with $Kd_{490} \geq 0.12$.

Kd_{490} in the Black Sea originates at a depth of 10–20 m (Karabashev et al., 2007), so factors such as eddies, fronts and increased concentrations of phytoplankton may play a dominant role and mask possible traces of AGWs in the surface layer. In deep-sea regions, where the amount of phytoplankton is significantly less, the signatures of AGWs on the sea surface can be quite noticeable.

Images of Rrs_{488} , Rrs_{547} , and Kd_{490} from Terra-MODIS obtained on 16 May at 9:20 for the deep central south-west part of the sea, enclosed in the black rectangle in Fig. 1, are shown in Fig. 5a,b and c. Values of Kd_{490} in Fig. 5c did not exceed 0.09, so sea waters in the considered region were clean. Thus values of the standard NASA product Kd_{490} calculated by the relationship (1) is valid for the considered time of the year and south-west region of the Black Sea. On all three images, the traces of AGWs as

narrow stripes elongated in a SW–NE direction are clearly observed in the testing area; best of all, they appeared on the image of Kd_{490} (Fig. 5c). Lee et al. (2005) points out that Kd_{490} depends not only on optical properties of the water (hydrosol, pigments, dissolved matter etcetera), but also varies to some extent with surface conditions.

The diagonal strips manifested on the Kd_{490} image (Fig. 5c) are caused by an imperfect relative correction between the along-track detectors of the scanner MODIS, apprehending the upcoming radiation (Frantz, 2006).

We evaluated a vertical scale of AGW imprints in the sea surface or amplitudes of surface waves induced by AGWs. For this aim we used an approximate relation between Kd and a penetration depth of light in the sea corresponding to the first irradiance attenuation length z_{90} . Gordon and McCluney (1975) defined the value z_{90} as the depth above which 90% of the diffusely reflected irradiance (excluding specular reflectance) originates:

$$z_{90} \approx 1/Kd. \quad (2)$$

Values of z_{90} have a dimension of meter. For the clear deep water of the Black Sea, it is acceptable to consider that fluctuations of the light penetration depth in the sea correspond and equal to fluctuations of the sea level under the impact of AGWs. This allows the ability to estimate vertical amplitudes of AGWs in the sea by the fluctuations of z_{90} . Using Eq. (2), we calculated approximate values z_{90} at 490 nm from data of Kd_{490} . The presented method of evaluation of z_{90} at 490 nm by data of Kd_{490} in the northeastern part of the Black Sea surface obtained from MODIS-Terra and -Aqua on 21 April 2007 was used earlier in (Evdoshenko, 2014).

Calculations were made for three ocean color scanner data for 16 May 2010: MERIS at 8:40, Terra-MODIS at 9:20 and Aqua-MODIS at 11:00. Images of z_{90} from the scanners for the rectangular region shown in Fig. 1 are presented in Fig. 6a,b, and c. Signatures of AGWs on the images of z_{90} were noticeable on the background of the underlying eddies and mushroom-like structures. Transects A, B, and C across clear imprints of AGWs were made for the regions, which were mostly free of sea eddies. This made it possible to minimize errors in the depth of light penetration into the

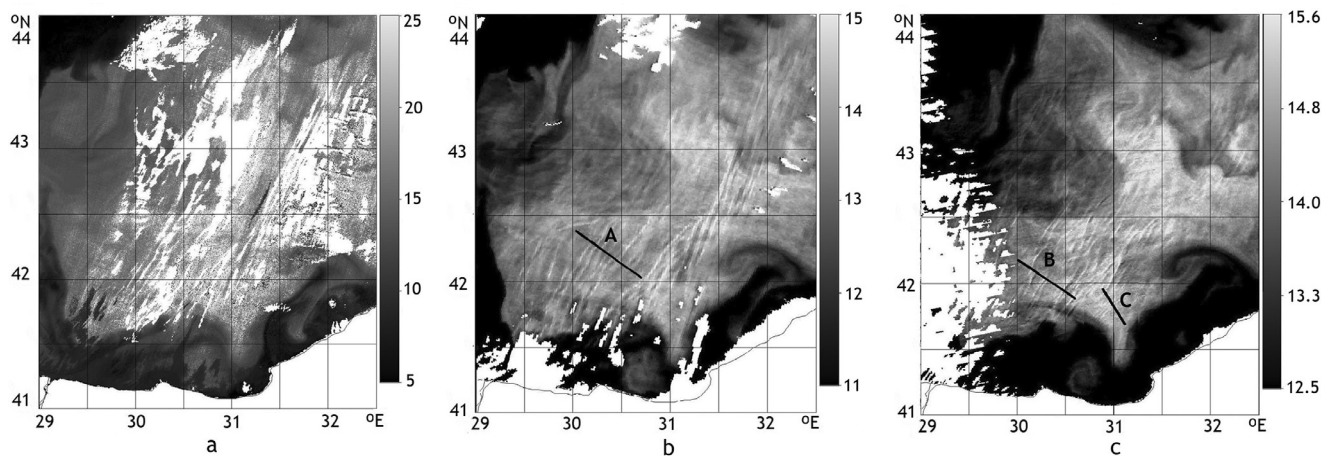


Figure 6 Images of z_{90} of the western part of the Black Sea from: a – MERIS at 8:40; b – Terra-MODIS at 9:20; c – Aqua-MODIS at 11:00; all on 16 May 2010. Transects across imprints of atmospheric waves are shown by black lines; transect A: 42.301°N, 30.102°E–42.170°N, 30.458°E; transect B: 42.036°N, 30.032°E–41.897°N, 30.273°E; transect C: 41.880°N, 30.951°E–41.787°N, 31.030°E.

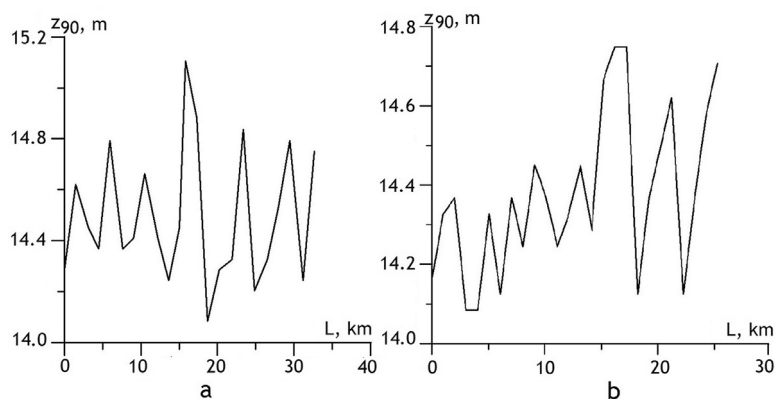


Figure 7 Distributions of $z_{90}(L)$ across AGW imprints at 11:00 on 16 May 2010 (see Fig. 6b and c): a – at the transect A; b – at the transect B.

sea connected with other mesoscale structures that were distinct from AGWs. Transects are indicated by black lines.

The AGW pattern appeared in z_{90} images in the deep sea at depths greater than 1 km. Towards 8:40, cloudiness was intermittent, so imprints of atmospheric waves alternated with cloudy manifestations. Fig. 6b, and c show that AGWs effectively modulated the sea surface to cause changes in the sunlight penetration depth. The main direction of the imprints are SW–NE, but several signatures of AGWs in directions NW–SE are also noticeable in Fig. 6b; these multi-directional imprints are superimposed on each other. Comparison of the patterns of AGW signatures on the images of z_{90} shown in Fig. 6b, and c allows us to conclude that, from 9:20 to 11:00, the wavelength and crest length of the imprints became smaller, but the number of imprinted waves increased; that is, the AGWs began to break up into smaller ones. The length of the wave imprints exceeded 150 km in some cases.

Plots of the surface wave at the transects $z_{90}(L)$ A and B, where L is distance, for 9:20 and 11:00 on 16 May 2010, are shown in Fig. 7a, and b. Fig. 7a shows that the imprints of AGWs at the transect A at 9:20 had a wavelength of more than 5 km, while at the transect B at 11:00, the mean wavelength was 3.3 km. We evaluated a modulation depth, or a

vertical scale of imprinted waves at the transects, using the plots of z_{90} for dimensional considerations. A value of $z_{90 \max}$ corresponds to a wave crest, while the value of $z_{90 \min}$ corresponds to the wave trough; a discrepancy Δz_{90} between $z_{90 \max}$ and $z_{90 \min}$ corresponds to the wave height. The wave amplitude, as a half of the wave height, was 10–50 cm at the transect A, and 5–33 cm at the transect B. Thus, during the 100 min period between the Terra and Aqua flights, the surface wave amplitude and wavelength decreased; that is, the AGWs became weaker.

Fig. 8 shows the image of the 250-m Rrs_{859} from Aqua-MODIS at 11:00 for the western part of the Black Sea. Traces of atmospheric waves of different forms and wavelengths are seen in the deep sea, as well as in the coastal regions, as Rrs_{859} reflects phenomena in the upper layer of several centimeters. Signatures of smaller AGWs of different forms and directions are seen. Imprints of AGWs with a SW–NE direction are intersected by imprints of AGWs directed approximately W–E which evidently spread at a higher altitude. Near 44°N, 30°E, a circular structure is observable, caused possibly by an atmospheric eddy with a diameter of about 100 km which modulated the AGW packet.

Wind speed and direction at a height of 10 m and air pressure near the sea surface for the western part of the

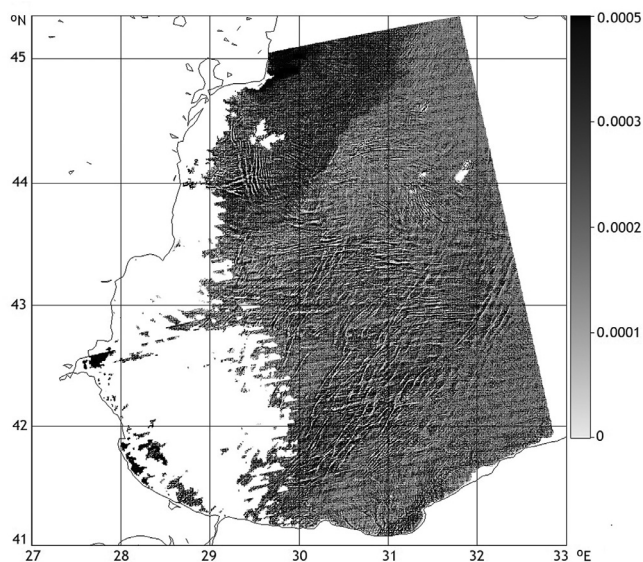


Figure 8 Image of 250-m $Rrs(859)$, sr^{-1} from Aqua-MODIS at 11:00 on 16 May 2010.

Black Sea at 11:00 on 16 May 2010 were calculated, they are shown in Fig. 9a, and b respectively. Wind generally blew from the south-west and reached 10 ms^{-1} in the middle of the western part of the sea, decreasing to $5\text{--}8\text{ ms}^{-1}$ near the shore. A comparison of Fig. 9a and Fig. 6a, b, and c suggests that the AGW signatures were oriented mainly downwind: i.e. SW–NE. The air pressure increased almost monotonically in the NW–SE direction from 1000.5 to 1006.5 mb, as seen in Fig. 8b. Transects along the 9 ms^{-1} isotach and along the isobar of 1006 mb which cross clear imprints of AGWs, are shown by thick black lines in Fig. 9a and b, respectively.

Atmospheric forcing could be expressed by way of pressure and wind stress on the sea surface (Rabinovich, 2008). For confirmation of the interrelationship between signatures of long surface waves and the atmospheric impact, we compared the fluctuations z_{90} , air pressure P above the sea surface, wind speed U , and wind stress τ . For this purpose we chose transects that crossed the sea surface imprints and passed approximately along the isolines of the atmospheric

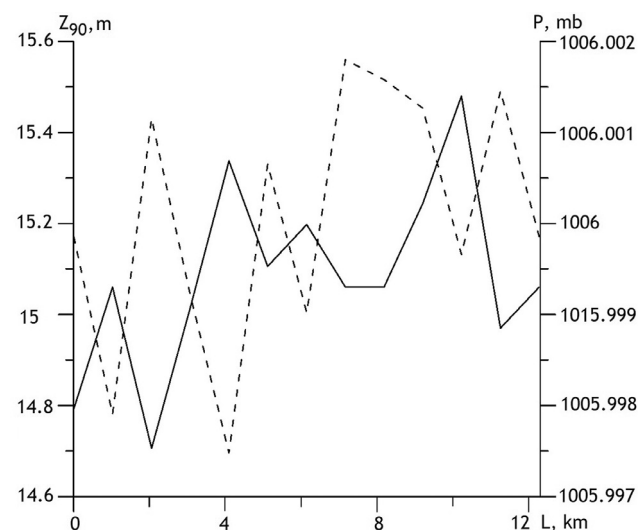


Figure 10 Depth of light penetration into the sea z_{90} (solid line) and air pressure near the sea surface P (dotted line) depending on the distance L at the transect which passes approximately along the isobar $P = 1006\text{ mb}$ at 11:00 on 16 May 2010.

characteristics; it was done with the aim to eliminate low-frequency atmospheric trends in the best way.

A 12-km transect C (41.880°N , 30.951°E – 41.787°N , 31.030°E) that intersected the z_{90} signatures at 11:00 on 16 May 2010 (see Fig. 6c) was chosen along the isobar of 1006 mb; it is also shown in Fig. 9b. The transect crosses the AGW imprints at an angle of approximately 25° normal of them. The distributions of z_{90} and P at the transect are shown in Fig. 10. The vertical amplitude of AGW imprints was $15\text{--}33\text{ cm}$; a negative cross-correlation was evident between z_{90} and P .

Before calculating a cross-correlation between the modulation depth and atmospheric pressure, the polynomial low pass trends of the second order were removed from the z_{90} and P series. The resulting cross-correlation was -0.63 . Note, however, that the data used were obtained in various ways: z_{90} or Kd_{490} – from MODIS data with resolution of 1 km, and surface pressure P – from meteo-observations combined with data from meteorological satellites, with a general resolution of 5 km. The obtained negative cross-

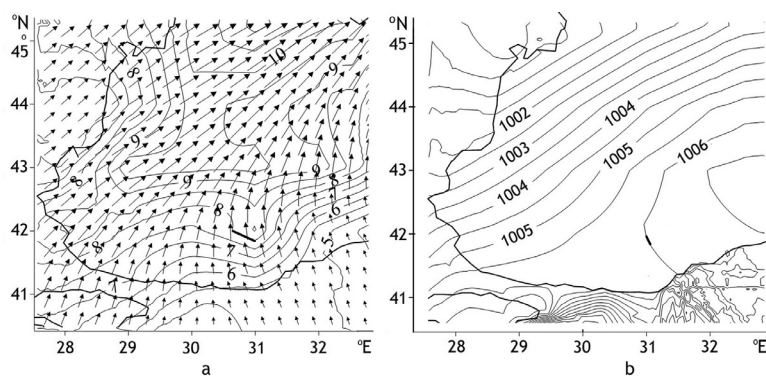


Figure 9 a – wind speed in ms^{-1} (isolines) and direction (arrows) at 10 m above the surface, b – air pressure in mb near the surface for the western Black Sea at 11:00 on 16 May 2010.

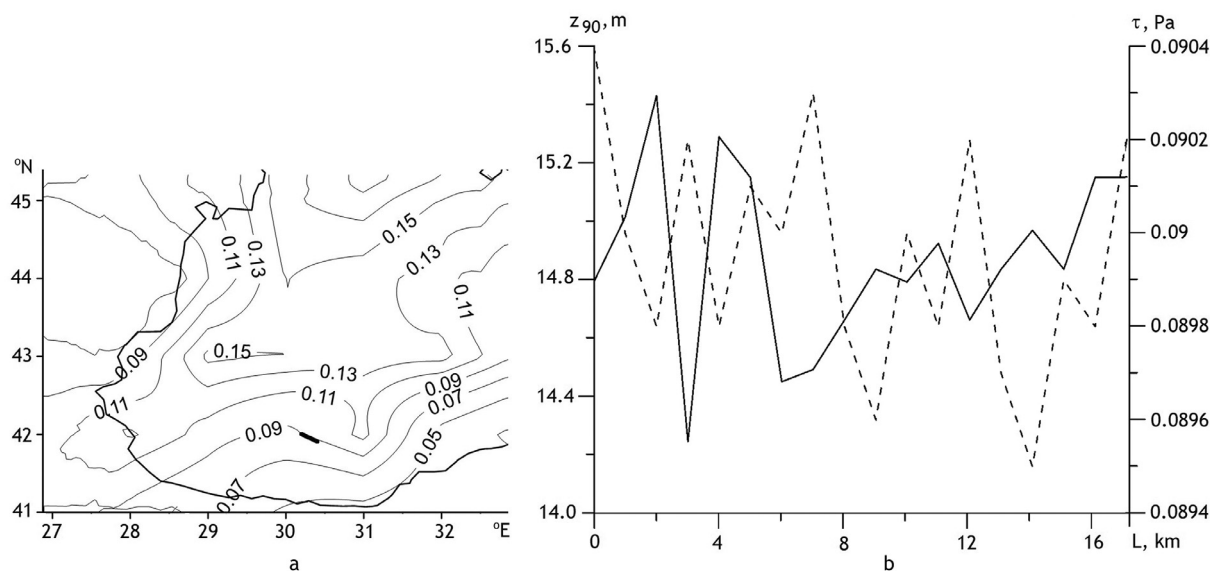


Figure 11 a – isolines of wind stress τ at the height of 10 m, transect passing approximately along the part of the isoline $U = 0.09$ Pa is shown by a thick line; b – depth of light penetration into the sea z_{90} (solid line) and wind stress τ at 10 m above the sea surface (dotted line) depending on the distance L at the transect at 11:00 on 16 May 2010.

correlation would be much more of an absolute value if errors connected with inconsistency caused by the different acquisition methods were also taken into account.

It is known that the inverted-barometer response to air pressure forcing fulfills the condition whereby an atmospheric pressure of 1 mb causes a negative response in the sea level of 1 cm (Wunsch and Stammer, 1997). It is seen from Fig. 10 that the relations of pairs of anticorrelated amplitudes of $A(z_{90})/A(P)$ greatly exceed the inverted-barometer response. Similar cases of the exceeding of the inverted-barometer relation was noted long ago. For example, Donn and McGuiness (1960) recorded a continuous and simultaneous series of oceanic oscillations of sea water level measured by a tsunami detector and oscillations of atmospheric pressure measured by a microbarovariograph with a period of 4–10 min, recorded on 20 September 1958 on the continental shelf southeast of New York at the forth Texas Tower. Air-pressure oscillations of 0.05 mb caused sea-level oscillations of 1.5–4 cm, with a magnification of 80–115 times relative to the inverted barometer. At the time of the measurements, a cold front had passed above the region, causing an inversion of the vertical profile of the air temperature. In the Mediterranean Sea, planetary atmospheric waves caused sea level overshoots far above the inverted-barometer response at subinertial frequencies (Malacic and Orlic, 1993). The authors implied that the Mediterranean Sea level was forced not only by the air pressure, but also by some other agent – most probably wind.

An interrelation between the fluctuations of z_{90} and wind speed U was also examined in the western part of the Black Sea. For this purpose a transect was chosen along the isoch of $U = 8 \text{ ms}^{-1}$ (41.85°N, 31.00°E–42.00°N, 30.64°E) across AGW signatures (Fig. 9a). No correlation was discovered between the fluctuations of z_{90} and of U .

Another characteristic of atmospheric forcing that roughens the sea surface and creates imprints of AGWs could be wind stress. Wind stress is important in air-sea interactions

and forced oceanic variability and is calculated by the following empirical formula (Fairall et al., 2003):

$$\tau = C_d \rho_a U^2, \quad (3)$$

where ρ_a is the air density (about 1.22 kg m^{-3}), and C_d is a dimensionless drag coefficient with a typical value of 0.0013. Wind stress is a square function of wind speed because the wind force depends on the wind speed and sea roughness, which in turn depends on wind speed (Kochanski et al., 2006). Wind stress was calculated using the Eq. (3); a map of τ -isolines is plotted in Fig. 11a, which shows that τ changed from 0.05 to more than 0.17 Pa in the western part of the sea. A transect along $\tau = 0.09$ Pa (42°N, 30.214°E–41.933°N, 30.402°E) is plotted to cross clear imprints of AGWs in the south-western part of the sea. Distributions of z_{90} and τ at the transect are shown in Fig. 11b.

A clear negative correlation is evident between z_{90} and τ at the transect. Before the calculation of a cross correlation, a filtration with low-pass filters in the form of polynomials of the second order was conducted on the compared series; the resulting cross correlation equals -0.53 . The obtained negative cross-correlation would have a much greater absolute value if the errors connected with the inconsistency of the series of U and z_{90} and amplification by U -squaring were taken into account.

Wind stress τ and atmospheric pressure above the sea surface P can be measured in the same units of pressure – pascal, as $1 \text{ mb} = 0.01 \text{ Pa}$. We now compare the relationships of the pairs of negatively correlated amplitudes of values measured at the transects which are shown in Fig. 10 and Fig. 11b. Evaluations revealed a mean relation $A(P)/A(z_{90}) = 6e^{-5} \text{ Pa m}^{-1}$ at the transect shown in Fig. 10, and a mean relation $A(\tau)/A(z_{90}) = 2e^{-3} \text{ Pa m}^{-1}$ at the transect shown in Fig. 11b. Comparing the mean values $A(P)/A(z_{90})$ and $A(\tau)/A(z_{90})$ allows the conclusion that the impact of the wind stress on amplitudes of the imprints exceeded that of atmospheric pressure by about 33 times.

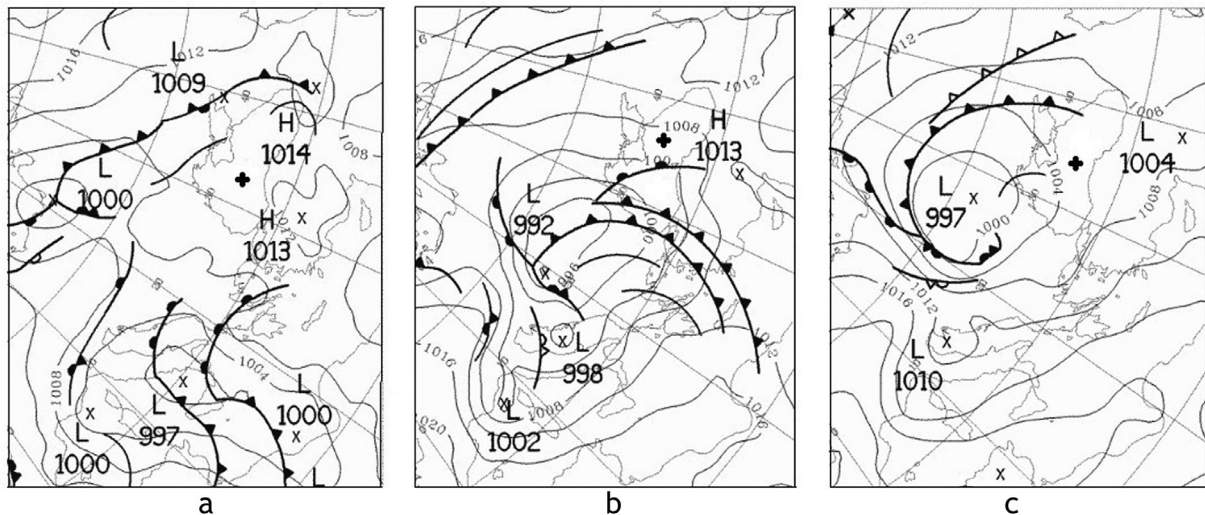


Figure 12 Weather maps for Europe at 00:00 UTC on: a – 15 May, b – 16 May, c – 17 May 2010; the Black Sea is indicated with a four-pointed star.

That is, the contribution of wind stress to induced surface waves was predominant, whereas the contribution of atmospheric pressure was only about 3%. The latter circumstance can explain the multiple times the inverted-barometer response appeared at the transect depicted in Fig. 10b, since the main impact on the sea surface caused by AGWs was due to wind stress rather than atmospheric pressure.

Surface weather maps for the European region at 00:00 on three successive days: 15, 16 and 17 May 2010 (available at <http://metoffice.gov.uk>) are shown in Fig. 12a,b, and c (the Black Sea is designated by a four-pointed star). On 15–16 May, a high-pressure area of 1014 mbar was located over the Black Sea, and a low-pressure core of 997 mbar occurred over the Mediterranean Sea near Italy. This pressure distribution is evidence of the existence of atmospheric fronts over the Black Sea. In actuality, the weather map for 16 May shows that a warm front was moving from the south across the Black Sea and that two cold fronts from the west had begun to cross the sea, in accordance with the wind direction shown in Fig. 9a. The angle between the isobars above the sea (Fig. 12b) was nearly normal, indicating that the fronts were moving quickly. Sea regions, which are visible in Fig. 2, were evidently covered by pre-frontal or warm-frontal fog, which often occurs over large regions ahead of warm fronts. The atmospheric waves in the form of strong cloud streets are known to originate in the vicinity of fronts (Plougonven and Zhang, 2014). Fig. 12c shows that the air pressure dropped over the Black Sea on 17 May, and cold fronts turned and formed a cyclone in the north-west area of the sea.

The single available meteo-station located on the Black Sea shore, starting upper air radiosondes, was Samsun (Turkey) on the southern shore of eastern part of the sea (see Fig. 1). The values of the characteristics measured at the Samsun station at 12:00 UTC on 16 May 2010 of the low atmosphere were obtained from <http://weather.uwyo.edu/upperair/sounding.html>. A thermodynamic diagram (tephigram) and vertical distributions of wind speed and wind direction corresponding to those measurements are shown in Fig. 13. A prominent temperature

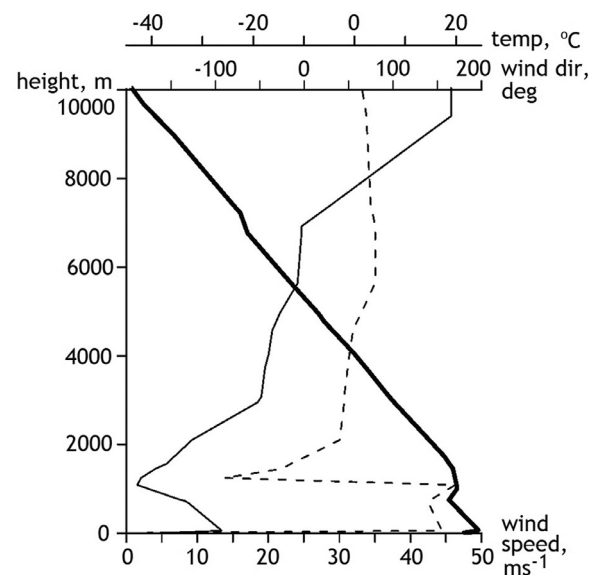


Figure 13 Measurements at the radiosonde station Samsun obtained at 12:00 UTC on 16 May 2010: vertical profiles of temperature (bold solid line), wind speed (solid line), and wind direction (dotted line).

inversion with a potential increase $\Delta\theta$ of 1.6°C , with the base at 746 m and the top at 1001 m, which is seen from Fig. 13, implies that the atmosphere was stably stratified. The inversion shows that the frontal zone represents a transition zone between two distinct air masses, separating the cold, dry air below the inversion from the warmer, moister air above it. Evidently, the cold front(s) crossed the sea and left a mark on the tephigram on 16 May in the form of a frontal inversion. The vertical extent of the frontal inversion was limited to the vertical extent of the frontal zone itself. Similar inversions on vertical profiles of wind direction centered at 1087 m and wind speed centered at 1087 m confirm the atmospheric stability in the layer at about 1 km. AGWs are well known can exist in a stably stratified atmosphere

(Nappo, 2002). An inversion on vertical profiles of low-level air temperature and wind can act like a waveguide and trap the AGWs (Cheng and Alpers, 2010). This is consistent with the situation considered here, where numerous imprints of atmospheric waves appeared on the sea surface. Air temperature and wind speed measured at the station Samsun on 16 May 2010 increased in the vertical layer from about 1000 m up the near water layer (about 60 m), and then decreased up to the sea surface providing significant vertical gradients. These gradients assisted AGWs in spreading downward and modulating the sea surface.

We suppose that the cold front had not yet reached the Samsun station on 15 May at 12:00, so it could not leave a mark on the tephigram that day. The data from Samsun show that the mean wind speed near the surface was 10 ms^{-1} , which is slightly more than the wind speed near the shore, calculated on the base of Aqua-MODIS data from 16 May 2010 at 11:00, but the divergence could be caused by the remoteness of the Samsun meteo-station from the western part of the sea. Comparison of the wind field maps, surface weather maps, and radiosonde data with sea surface imprints on 16 May 2010 leads us to conclude that the wave-like patterns are associated with atmospheric fronts; therefore we define the atmospheric waves as frontal waves (Liu, 2010).

Undular bores can be a result of collision of the warm and cold front, and the cold front moves through the stable atmosphere in the low levels (Coleman et al., 2010). Evidently a similar situation was observed on 15 May 2010 in the north-western part of the sea when several undular bores were spreading to the south-west from the Crimean Peninsula (Fig. 3). An additional reason for bore origination could be that a less expansive cold front passed over the peninsula extending southward from the low-pressure region.

The image of Rrs_{859} (Fig. 8) shows the appearance of AGW imprints on 16 May 2010 on the entire western part of the sea from near the shore regions with depths less than 100 m to the deepest parts with depths about 2200 m (see Fig. 1), and imprints visible on images of z_{90} appeared in the limited region from about 29.30°N , 41.5°E – 32.50°N , 43.5°E (Fig. 6), with depths H from 500 m to 2200 m. A phase speed of ocean surface waves C_{ow} is defined according to Phillips (1977):

$$C_{ow} = \sqrt{\frac{g\lambda}{2\pi} \tanh\left(2\frac{\pi H}{\lambda}\right)}, \quad (4)$$

where λ is the wavelength of wavy imprints, H is the depth, and g is the acceleration due to gravity. The phase speed of C_{ow} for shallow waters with a depth H of 100 m was 31 m s^{-1} , while for deep sea regions it ranged from 68 to 88 m s^{-1} .

Based on the radiosonde data from the Samsun meteo-station, we can define the local atmosphere as a two-layer system with the interface at the inversion layer height of 1000 m (see Fig. 13). A phase speed of atmospheric waves c_0 could be defined by a vertical profile of air temperature below and above the positive inversion $c_0 = \sqrt{g'h_0}$, where g' is the reduced gravity acceleration, and h_0 is the characteristic depth of the waveguide (Magalhaes et al., 2011). The value of h_0 is calculated as $h_0 = d_m d_p / (d_m + d_p)$ where d_m

and d_p are the thicknesses of the lower and upper layers, respectively (Li et al., 2004). We define $d_m = 1000 \text{ m}$, and $d_p = 6000 \text{ m}$, so that $h_0 = 857 \text{ m}$. The reduced gravity acceleration $g' = 0.1 \text{ m s}^{-2}$, so that $c_0 = 9.26 \text{ m s}^{-1}$. As shown in Fig. 9a, c_0 practically coincided with the wind speed in the deep part of the sea.

Thus, as the calculations showed, the phase speed of atmospheric waves c_0 was considerably smaller than the speed of long sea waves C_{ow} , so that the Proudman resonance, when the condition of equal speeds of atmospheric and sea waves are equal (Monserrat et al., 2006), was not fulfilled. Therefore we conclude that sea surface imprints were not caused by a resonance interaction between atmospheric and sea waves, but were caused by instantaneous effect on the sea surface of unusually power atmospheric waves by way of wind stress and atmospheric pressure.

4. Conclusions

The satellite observations at the western Black Sea on 16 May 2016 by Envisat-MERIS, Terra-MODIS, and Aqua-MODIS revealed power imprints of atmospheric gravity waves on the sea surface. These imprints appeared clearly on remote sensing reflectance images of Rrs at different wavelengths, and most strongly on images of Rrs at 859 nm. They were also manifested on images of diffuse attenuation coefficient of light Kd_{490} , and therefore on images of the light penetration depth z_{90} at 490 nm. Wave imprint amplitudes evaluated for the dimensional consideration by values of z_{90} at transects that crossed imprints normal to them changed from less than 5 cm to more than 50 cm. The crests of the imprinted waves exceeded 150 km in length and the wavelength changed from less than 2 to more than 5 km. Distributions at the transect along the isobar P showed a significant negative correlation of fluctuations of z_{90} with P . Similarly, distributions at the transect along the isoline of the wind stress τ showed also a significant negative correlation of fluctuations z_{90} with τ . This statistical analysis confirms the atmospheric nature of the wavy imprints. The wind stress effect on amplitudes of the sea surface imprints was found to be about 30 times more intense than the effect of atmospheric pressure.

Two cold fronts crossed the Black Sea on 16 May 2010. The fronts caused inversions on vertical profiles of air temperature, wind speed, and wind direction at a height of about 1000 m, obtained from radiosonde measurements on the southern shore of the sea. The inversions created a stably stratified layer of atmosphere that could act like a waveguide, trapping the AGWs. Strong vertical stratification of temperature and wind speed from the height of the inversion up to the sea surface promoted the expansion of atmospheric waves downward and impacted the surface to cause imprints.

Acknowledgements

The work was performed within the framework of the Russian state task (topic 0149-2019-0003).

References

- Alpers, W., Brummer, B., 1994. Atmospheric boundary layer rolls observed by the synthetic aperture radar aboard the ERS-1 satellite. *J. Geophys. Res.-Oceans*. 99 (C6), 12613–12621, <https://doi.org/10.1029/94JC00421>.
- Alpers, W., Huang, W., 2011. On the discrimination of radar signatures of atmospheric gravity waves and oceanic internal waves on synthetic aperture radar images of the sea surface. *IEEE T. Geosci. Remote*. 49 (3), 1114–1126, <https://doi.org/10.1109/TGRS.2010.2072930>.
- Alpers, W., Huang, W., Xilin, G., 2008. Observations of atmospheric gravity waves over the Chinese seas by spaceborne synthetic aperture radar. *Proc. Dragon (ESA SP-655, April 2008)*.
- Chanson, H., 2010. Undular bores. In: *Second International Conference on Coastal Zone Engineering and Management*. November 1–3, 2010. Muscat, Oman, 12 pp.
- Cheng, C.M., Alpers, W., 2010. Investigation of trapped atmospheric gravity waves over the South China Sea using Envisat synthetic aperture radar images. *Int. J. Remote Sens.* 31 (17–18), 4725–4742, <https://doi.org/10.1080/01431161.2010.485145>.
- Coleman, T.A., Knupp, K., Herzmann, D.E., 2010. An Undular Bore and Gravity Waves Illustrated by Dramatic Time-Lapse Photography. *J. Atmos. Ocean. Tech.* 27 (8), 1355–1361, <https://doi.org/10.1175/2010JTECHA1472.1>.
- Da Silva, J.C.B., Magalhaes, J.M., 2009. Satellite observations of large atmospheric gravity waves in the Mozambique Channel. *Int. J. Remote Sens.* 30 (5), 1161–1182, <https://doi.org/10.1080/01431160802448943>.
- Donn, W.L., McGuinness, W.T., 1960. Air-coupled long waves in the ocean. *J. Meteorol.* 17, 515–521, [https://doi.org/10.1175/1520-0469\(1960\)017\(0515:ACLWIT\)2.0.CO;2](https://doi.org/10.1175/1520-0469(1960)017(0515:ACLWIT)2.0.CO;2).
- Evdoshenko, M.A., 2014. Meteorological Waves (by Ocean Color Scanner Data). *Dokl. Earth Sci.* 458 (2), 1241–1245, <https://doi.org/10.1134/S1028334X14100043>.
- Evdoshenko, M.A., 2016. Detecting imprints of atmospheric waves in the Bering Sea with MODIS data. *Oceanologia* 58 (4), 264–271, <https://doi.org/10.1016/j.oceano.2016.04.003>.
- Fairall, C.W., Bradley, E.F., Hare, J.E., Grachev, A.A., Edson, J.B., 2003. Bulk parameterization of air-sea fluxes: Updates and verification for the COARE algorithm. *J. Climatol.* 16 (4), 571–591, [https://doi.org/10.1175/1520-0442\(2003\)016\(0571:BPOASF\)2.0.CO;2](https://doi.org/10.1175/1520-0442(2003)016(0571:BPOASF)2.0.CO;2).
- Franz, B.A., Werdell, P., Meister, G., Kwiatkowska, E.J., Bailey, S., Ahmad, Z., McClain, C.R., 2006. MODIS land bands for ocean remote sensing applications. *Proc. P. Soc. Photo-Opt. Ins. XVIII*. Montreal, Canada 9–13 October. <https://www.researchgate.net/publication/234025610>.
- Gordon, H.R., McCluney, W.R., 1975. Estimation of the depth of sunlight penetration in the sea for remote sensing. *Appl. Optics* 14 (2), 413–416, <https://doi.org/10.1364/AO.14.000413>.
- Hale, G.M., Querry, M.R., 1973. Optical constants of water in the 200-nm to 200- μ m wavelength region. *Appl. Optics* 12 (3), 555–563, <https://doi.org/10.1364/AO.12.000555>.
- Karabashev, G.S., Evdoshenko, M.A., Sheberstov, S.V., 2007. Correlation of distributions of normalized spectral radiances as an indication of specific features of water exchange in the Black Sea. *Oceanologia* 47 (3), 325–333, <https://doi.org/10.1134/S0001437007>.
- Knyazev, V.Yu., Kossyi, I.A., Malykh, N.I., Yampolskii, E.S., 2003. Penetration of microwave radiation into water: Effect of induced transparency. *Tech. Phys.* 48, 1489–1492, <https://doi.org/10.1134/1.1626786>.
- Kochanski, A., Koracin, D., Dorman, C.E., 2006. Comparison of wind-stress algorithms and their influence on wind-stress curl using buoy measurements over the shelf off Bodega Bay, California. *Deep-Sea Res. Pt. 53* (25–26), 2865–2886, <https://doi.org/10.1016/j.dsr2.2006.07.008>.
- Lee, Z-P., Darecki, M., Carder, K.L., Davis, C.O., Stramski, D., Rhea, W.J., 2005. Diffuse attenuation coefficient of downwelling irradiance: An evaluation of remote sensing methods. *J. Geophys. Res.-Oceans*. 110 (C02017), <https://doi.org/10.1029/2004JC002573>.
- Li, X., Dong, C., Clemente-Colón, P., Pichel, W.G., Friedman, K.S., 2004. Synthetic aperture radar observation of the sea surface imprints of upstream atmospheric solitons generated by flow impeded by an island. *J. Geophys. Res.-Oceans* 109 (C2), C02016, <https://doi.org/10.1029/2003JC002168>.
- Li, X., Zheng, W., Zou, C.-Z., Pichel, W.G., 2008. A SAR observation and numerical study on ocean surface imprints of atmospheric vortex streets. *Sensors* 8 (5), 3321–3334, <https://doi.org/10.3390/s8053321>.
- Li, X., Zheng, W., Yang, X., Li, Z., Pichel, W.G., 2011. Sea surface imprints of coastal mountain lee waves imaged by synthetic aperture radar. *J. Geophys. Res.-Oceans* 116 (C2), C02014, <https://doi.org/10.1029/2010JC006643>.
- Liu, A.Q., Moore, G.W.K., Tsuboki, K., Renfrew, I.A., 2004. A high-resolution simulation of convective roll clouds during a cold-air outbreak. *Geophys. Res. Lett.* 31 (3), <https://doi.org/10.1029/2003gl018530>.
- Liu, S., Li, Z., Yang, X., Pichel, W., Yu, Y., Zheng, Q., Li, X., 2010. Atmospheric frontal gravity waves observed in satellite SAR images of the Bohai Sea and Huanghai Sea. *Acta Oceanol. Sin.* 29 (5), 35–43, <https://doi.org/10.1007/s13131-010-0061-8>.
- Magalhaes, J.M., Araújo, I.B., da Silva, J.C.B., Grimshaw, R.H.J., Davis, D., Pineda, J., 2011. Atmospheric gravity waves in the Red Sea: a new hotspot. *Nonlinear Proc. Geoph.* 18, 71–79, <https://doi.org/10.5194/npg-18-71-2011>.
- Malacic, V., Orlic, M., 1993. On the origin of the inverted-barometer effect at subinertial frequencies. *Il Nuovo Cimento. Maggio-Glugno*. 16 C (3), 265–288, <https://doi.org/10.1007/BF02524229>.
- Monserrat, S., Vilibic, I., Rabinovich, A.B., 2006. Meteotsunamis: atmospherically induced destructive ocean waves in the tsunami frequency band. *Nat. Hazard Earth Syst.* 6 (6), 1035–1051, <https://doi.org/10.5194/nhess-6-1035-2006>.
- Morel, A., Huot, Y., Gentili, B., Werdell, P.J., Hooker, S.B., Franz, B.A., 2007. Examining the consistency of products derived from various ocean color sensors in open ocean (Case 1) waters in the perspective of a multi-sensor approach. *Remote Sens. Environ.* 111 (1), 69–88, <https://doi.org/10.1016/j.rse.2007.03.012>.
- Nappo, C.J., 2002. *An introduction to atmospheric gravity waves. International Geophysics, Acad. Press*, 276 pp.
- Pegau, W.S., Gray, D., Zaneveld, J.R.V., 1997. Absorption and attenuation of visible and near-infrared light in water: dependence on temperature and salinity. *Appl. Optics* 36 (24), 6035–6046, <https://doi.org/10.1364/AO.36.006035>.
- Phillips, O., 1977. *The dynamics of the upper ocean (2nd edn.)*. Cambridge Univ. Press, 344 pp.
- Plougonven, R., Zhang, F., 2014. Internal gravity waves from atmospheric jets and fronts. *AGU. Rev. Geophys.* 52 (1), 32–76, <https://doi.org/10.1002/2012RG000419>.
- Rabinovich, A.B., 2008. Seiches and Harbour Oscillations. In: Kim, Y. (Ed.), *Handbook of Coastal and Ocean Engineering World Scientific*. California State Univ., Los Angeles, 193–236.
- Sachsperger, J., Serafin, S., Grubi, V., Stiperskic, I., Pacid, A., 2018. The amplitude of lee waves on the boundary-layer inversion. *Q. J. Roy. Meteor. Soc.* 143 (702), 27–36, <https://doi.org/10.1002/qj.2915>.
- Sheberstov, S.V., Lukyanova, E.A., 2007. A system for acquisition, processing and storage of satellite and field biooptical data. In: *Proc. IV Int. Conf.: Current Problems in Optics of Natural Waters. Nizhny Novgorod, September 11–15*, 179–183.
- Sustina, V.V., Slabakova, V.R., Churilova, T.Y., 2017. Diffuse attenuation coefficient for downwelling irradiance at 490 nm and its

- spectral characteristics in the Black Sea upper layer: modeling, in situ measurements and ocean color data. In: Proc. SPIE, 23rd International Symposium on Atmospheric and Ocean Optics: Atmospheric Physics, 10466, 104663H, <https://doi.org/10.1117/12.2287367>.
- Vachon, P.W., Johannessen, O.M., Johannessen, J.A., 1994. An ERS 1 synthetic aperture radar image of atmospheric lee waves. J. Geophys. Res.-Oceans 99 (C11), 22483–22490, <https://doi.org/10.1029/94JC01392>.
- Valenzuela, G.R., 1978. Theories for the interaction of electromagnetic and oceanic waves – a review. Bound.-Lay. Meteorol. 13, 61–85, <https://doi.org/10.1007/BF00913863>.
- Wunsch, C., Stammer, D., 1997. Atmospheric loading and the oceanic "inverted barometer" effect. Rev. Geophys. 35 (1), 79–107, <https://doi.org/10.1029/96RG03037>.
- Zheng, Q., Yan, X.-H., Klemas, V., Ho, C.-R., Kuo, N.-J., Wang, Z., 1998. Coastal lee waves on ERS-1 SAR images. J. Geophys. Res.-Oceans 103 (C4), 7979–7993, <https://doi.org/10.1029/97JC02176>.



ORIGINAL RESEARCH ARTICLE

Investigating the Role of Atmospheric Variables on Sea Level Variations in the Eastern Central Red Sea Using an Artificial Neural Network Approach

Khalid M. Zubier^{a,*}, Lina S. Eyouni^{a,b}

^a Marine Physics Department, Faculty of Marine Sciences, King Abdulaziz University, Jeddah, Saudi Arabia

^b Red Sea Research Center, King Abdullah University of Science and Technology, Thuwal, Saudi Arabia

Received 21 July 2019; accepted 9 February 2020

Available online 24 February 2020

KEYWORDS

Red Sea;
Atmospheric
Variables;
Sea Level Anomaly;
Artificial Neural
Network (ANN);
Non-linear
Auto-Regressive
Network with
eXogenous inputs
(NARX)

Summary Atmospheric variables play a major role in sea level variations in the eastern central Red Sea, where the role of tides is limited to 20% or less. Extensive analysis of daily-averaged residual sea level and atmospheric variables (atmospheric pressure, air temperature, wind stress components, and evaporation rate) indicated that sea level variations in the eastern central Red Sea are mainly contributed to by the seasonal and weather-band variations in the utilized atmospheric variables. The Non-linear Auto-Regressive Network with eXogenous inputs (NARX), a type of Artificial Neural Network (ANN), was applied to investigate the role of the atmospheric variables on the sea level variations at the eastern central Red Sea. Forced by time-delayed daily-averaged observations of atmospheric variables and residual sea level, the constructed NARX-based model showed high performance in predicting the one-step-ahead residual sea level. The high performance indicated that the constructed model was able to efficiently recognize the role played by the atmospheric variables on the residual sea level variations. Further investigations, using the constructed NARX-based model, revealed the seasonal variation in the role of the atmospheric variables. The study also revealed that the role played by some of the atmospheric variables, on sea level variations, could be masked by the role of one or more of the other atmospheric variables. The obtained results clearly

* Corresponding author at: Marine Physics Department, Faculty of Marine Sciences, King Abdulaziz University, P.O. Box 80207, Jeddah 21589, Saudi Arabia.

E-mail address: kzubier@kau.edu.sa (K.M. Zubier).

Peer review under the responsibility of the Institute of Oceanology of the Polish Academy of Sciences.



Production and hosting by Elsevier

<https://doi.org/10.1016/j.oceano.2020.02.002>

0078-3234/© 2020 Institute of Oceanology of the Polish Academy of Sciences. Production and hosting by Elsevier B.V. This is an open access article under the CC BY-NC-ND license (<http://creativecommons.org/licenses/by-nc-nd/4.0/>).

demonstrated that this neurocomputing (NARX) approach is effective in investigating the individual and combined role of the atmospheric variables on residual sea level variations.
© 2020 Institute of Oceanology of the Polish Academy of Sciences. Production and hosting by Elsevier B.V. This is an open access article under the CC BY-NC-ND license (<http://creativecommons.org/licenses/by-nc-nd/4.0/>).

1. Introduction

Sea level variations are of great interest to many oceanographers, marine scientists and coastal engineers as they can significantly affect not only the safety of navigation and coastline facilities but also the coastal environment and marine habitats. Sea level varies spatially according to the shape and geometry of the water body. Temporally, sea level varies according to variations in the affecting processes. Long-term sea level variations are caused by isostatic effects (earth related) and global ice forming/melting events (climate related), both having a temporal scale that ranges from decadal to geological ages (De Lange and Carter, 2014; Milne et al., 2009). Relatively short-term sea level variations are mainly caused by short-term astronomical (tidal) and atmospheric/climatic (non-tidal) effects, temporally ranging from hourly to decadal in scale (Li and Han, 2015; Pugh and Woodworth, 2014; Willis et al., 2008). Owing to their periodic nature, tidal sea level variations can be easily quantified and accurately predicted using Harmonic Analysis methods (Parker, 2007; Pugh, 1987). Except for those associated with climatic modes, non-tidal sea level variations are not periodic and, therefore, require different methods of analysis to quantify (Cox et al., 2002; Deo and Chaudhari, 1998; Makarynska and Makarynsky, 2008).

The Red Sea is a semi-enclosed basin that is geographically located in an arid region and is connected in its southern end to the Indian Ocean through the Strait of Bab Al-Mandab (Figure 1). The climate of the Red Sea is affected by the seasonally reversing monsoon system. The seasonally varying water exchange between the Red Sea and the Gulf of Aden, through the Bab Al-Mandab Strait, is mainly driven by this monsoonal system. The tides in the Red Sea are in the form of a standing wave, indicating that, at the time when high water occurs in the south Red Sea, low water occurs in the north and vice versa (Madah et al., 2015). The central part of the Red Sea is characterized by the lowest tidal variations due to the proximity of the amphidromic point of the M_2 tidal component, which represents the dominant tidal component in the Red Sea (Pugh, 1981; Pugh et al., 2019). According to Ahmad and Sultan (1993), about 15–20% of the sea level variation near Jeddah (eastern central Red Sea) can be attributed to the astronomical tide. In terms of non-tidal sea level variations, Manasrah et al. (2009) showed that sea level varies both spatially and temporally in the Red Sea with an inter-decadal variability of 2.5–7.4 years, depending on both the season and the location. Alawad et al. (2017) showed that the annual and semiannual sea level variabilities in the Red Sea are associated with the Nino3.4 climatic mode. According to previous studies, the Red Sea's long-term sea level variations are mainly influenced by the effect of wind stress, evaporation and water exchange through the Bab Al-Mandab Strait

(Sultan and Ahmad, 2000; Sultan and Elghribi, 2003; Sultan et al., 1995). The monsoonal wind reversal in the southern part of the Red Sea, and its corresponding effects on water exchange patterns, are among the factors that contribute to seasonal sea level variations (Abdelrahman, 1997; Cromwell and Smeed, 1998; Eltaib, 2010; Mohamad, 2012; Osman, 1984; Patzert, 1974; Pugh and Abualnaja, 2015; Sofianos and Johns, 2001; Wahr et al., 2014). The seasonally varying steric effect is another contributing factor to the seasonal sea level variability in the Red Sea (Eid and Kamel, 2004; Patzert, 1974; Sofianos and Johns, 2001; Wahr et al., 2014). For the central part of the Red Sea, several studies have indicated that sea level is affected by the monsoonal system and resulting variations in atmospheric variables, including atmospheric pressure, wind stress, and/or evaporation rate (Ahmad and Sultan, 1993; Maghrabi, 2003; Osman, 1984; Shamji and Vineesh, 2017; Sofianos and Johns, 2001; Sultan and Ahmad, 2000; Sultan and Elghribi, 2003; Sultan et al., 1995a; Sultan et al., 1995b; Sultan et al., 1996; Zubier, 2010). On the shorter-than-seasonal timescale, Sultan and Elghribi (2003) showed relatively large amplitude sea level variations in the central Red Sea, with a range of variability from two days to approximately one month. In a recent investigation, Churchill et al. (2018) showed that along-axis surface wind stress, as well as sub-mesoscale eddies and boundary currents, contribute to the weather-band (~4–30 days) sea level variations in the Red Sea. The cross-axis strong westward wind jets, generated by winds funneling through the Tokar mountain-gap (located on the western side of the Red Sea), also contribute to the sea level variations in the central Red Sea on a relatively shorter timescale (Jiang et al., 2009; Zhai and Power, 2013).

Artificial Neural Networks (ANNs) are among the neurocomputing methods becoming widely utilized, nowadays, in the field of time series analysis. Such methods constitute very powerful tools to conduct analyses on datasets when little information is known regarding the affecting variables and their role in shaping the time series. ANNs have the ability to approximate a continuous function to any desired accuracy without prior implicit assumptions while offering desirable characteristics such as nonlinearity, high parallelism, and robustness (Basheer and Hajmeer, 2000). Applied by Lee et al. (2007) and Tsai and Lee (1999), ANNs have performed efficiently in tidal prediction/forecasting based on previous tidal observations. In numerous studies, ANN techniques have been used to predict/forecast short-term sea level variations (Ghorbani et al., 2010; Karimi et al., 2013; Kisi et al., 2014; Makarynsky et al., 2004; Pashova and Popova, 2010; Sertel et al., 2008). The obtained results of these studies showed that ANN techniques performed satisfactorily, indicating that they can be considered as alternative tools for sea level prediction/forecasting. By using the past seven days sea level anomaly as inputs,

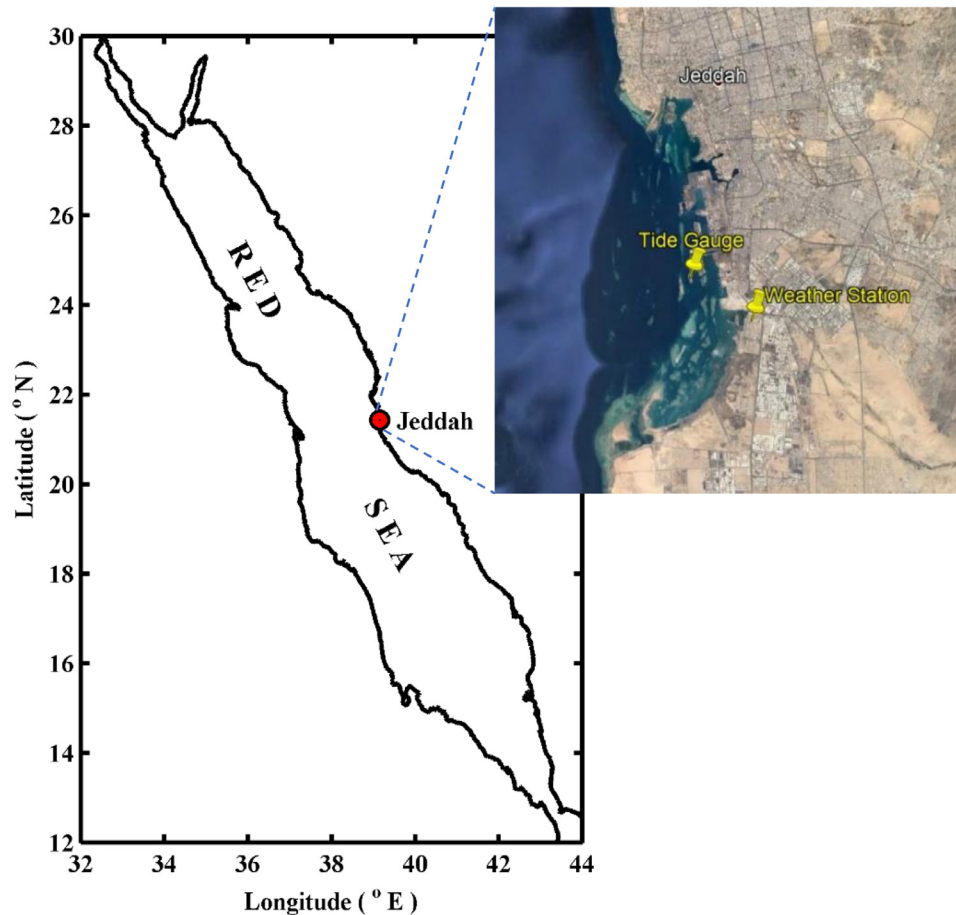


Figure 1 Red Sea map showing the location of Jeddah City (red circle) and the locations of Aramco's tide gauge and weather station (yellow pins).

Londhe (2011) showed that a simple ANN performed reasonably well in predicting the sea level anomaly, which was then added to the harmonically-obtained tidal level to predict total sea level variation. Cox et al. (2002) was able to improve the sea level predictions of a simple linear model by using a neural network approach with wind components, barometric pressure, and the previous sea level anomaly used as inputs. Using wind shear velocity components as inputs, Nitsure et al. (2014) showed that both Genetic Programming (GP) and Artificial Neural Network (ANN) soft-computing techniques performed well in predicting the sea level anomaly. Using an ANN approach, Moghadam (2016) found that wind velocity, sea surface temperature, and atmospheric pressure are the most significant meteorological factors affecting the regional sea level anomaly.

Non-linear Auto-Regressive Network with exogenous inputs (NARX) is one type of Recurrent Neural Network (RNN) that has been recently developed. Through proper training, NARX is able to relate the input data to the past output data (exogenous) without prior knowledge of the relationships between the inputs and the output. Mahmoud (2012) has briefly discussed NARX architecture and the dynamics of data processing. In the study by Rakshith et al. (2014), NARX efficiently predicted the observed tides at two different locations with a high correlation coefficient ($r > 0.96$). In the

comparison between two ANN techniques made by Salim et al. (2015), the NARX method significantly outperformed the Feed Forward with Backpropagation Algorithm (FFBP) method in predicting the tides; it yielded correlation coefficients of 0.914 and 0.564, respectively.

Unlike tidal sea level variations, which can be easily simulated using harmonic models, the simulation of sea level variations induced by a combination of atmospheric variables is challenging. The difficulty is mainly related to the limitations in understanding how this combination of inter-related atmospheric variables physically affect sea level. To resolve such difficulty, one approach is to develop complex physics-based numerical models that require extensive validation/verification procedures, using an enormous amount of actual data, before they can be used for prediction. Another approach is to use neurocomputing techniques (e.g. NARX) that focus on determining the interrelationships between the sea level and these atmospheric variables numerically rather than physically. Such a practical approach is based on the fact that all the physics, through which these atmospheric variables are interrelated and affecting sea level variability, are already impeded in the utilized data.

In this study, an attempt is made to use NARX as an ANN (soft-computing) approach to investigate the role of different atmospheric variables on the sea level variations at the eastern central Red Sea. The outline of this manuscript is

as follows: the utilized data and the methods used are first introduced, then the results are presented and discussed, and finally the concluding remarks are given.

2. Data

Data sets that were utilized in this study consist of sea level and meteorological records that were collected near Jeddah (Figure 1) during the year 2011. Saudi ARAMCO recorded, at an hourly interval, sea level using a tide gauge located at (39°09'17"E, 21°25'52"N) and atmospheric variables (atmospheric pressure, air temperature, and wind speed and direction) using a nearby weather station located at (39°11'33"E, 21°24'22.99"N).

The general representation of the observed temporal variability in sea level is given by the following equation (Pugh, 1987).

$$X(t) = Z_0(t) + T(t) + R(t), \quad (1)$$

where $X(t)$ is the observed level, $Z_0(t)$ is the slowly varying mean sea level, $T(t)$ is the tidal part of the variation, $R(t)$ is the non-tidal (residual) part of the variation, and (t) is time. Eq. 1 indicates that, by subtracting the tidal part $T(t)$ and the mean sea level $Z_0(t)$ from the observed sea level record $X(t)$, the residual (non-tidal) part $R(t)$ can be obtained. Initially, the hourly sea level record was analyzed using the Matlab®-based T-Tide harmonic analysis toolbox (Pawlowicz et al., 2002) to separate the tidal (astronomical) and the non-tidal (residual) sea level variations. The obtained residual sea level (R) was then daily averaged to focus on the daily and longer-term variations.

ARAMCO's hourly records of atmospheric variables consisting of atmospheric pressure (P), air temperature (T), and the 10 m wind speed and direction were daily averaged. Daily cross-shore and along-shore wind velocities (u , v) were calculated using daily-averaged wind speed and direction, taking axis rotation (of 25°) into consideration. Then, the daily wind stress cross- and along-shore components (τ_x , τ_y) were calculated based on the following equations:

$$\begin{aligned} \tau_x &= \rho_a C_D u^2, \\ \tau_y &= \rho_a C_D v^2, \end{aligned} \quad (2)$$

where ρ_a is the air density (1.2 kg/m³), (u , v) represent the cross-shore and along-shore components of wind velocities, respectively, and C_D is the drag coefficient calculated according to U_{10} (10 m wind speed) from the following equation (Large and Pond, 1981):

$$10^3 C_D = \begin{cases} 1.2 & 4 \leq U_{10} \leq 11 \text{ m/s} \\ 0.49 + 0.065 U_{10} & 11 \leq U_{10} \leq 25 \text{ m/s} \end{cases} \quad (3)$$

The daily evaporation rate (E) was calculated based on the Bulk-Aerodynamic Formulation (Herting et al., 2004) using the ARAMCO's daily-averaged atmospheric pressure, wind speed and air temperature records. The daily vapor pressure record, also used in the formula, was collected by the General Authority of Meteorology and Environmental Protection (GAMEP) at a daily interval, using the weather station located at King Abdulaziz International Airport (39°11'00"E, 21°42'00"N).

3. Methods

3.1. Descriptive statistics

Statistical parameters (minimum, maximum, mean, and standard deviations) were used in this study to describe the variations in the daily-averaged residual sea level timeseries and each of the daily-averaged atmospheric variables timeseries (Emery and Thomson, 2001). For every daily-averaged record, these parameters were obtained for the entire year (2011) as well as for four periods of 91 days each, with day numbers 1–91, 92–182, 183–273, and 274–364 representing the Winter, Spring, Summer, and Fall seasons, respectively.

3.2. Fourier analysis

The daily-averaged residual sea level and each of the daily-averaged atmospheric variables timeseries were individually decomposed into 182 sinusoidal timeseries using Fourier analysis (Emery and Thomson, 2001). The number of sinusoidal timeseries (Fourier series) is nearly half the number of data points in the actual (decomposed) timeseries and every single Fourier series corresponds to a Fourier constituent with a specific frequency. The frequency range of the Fourier constituents is limited at its lower end by the fundamental frequency (~ 0.00274 cpd) and at its upper end by the Nyquist frequency (0.5 cpd), that is equivalent to period range of 2–365 days, with a frequency interval of ~ 0.00274 cpd. For every decomposed timeseries, each one of the obtained 182 sinusoidal timeseries (corresponding to a specific Fourier constituent) has an amplitude and a phase. The statistical significance of each obtained amplitude was determined using 90% confidence interval, that verifies the statistical range (minimum and maximum) within which the obtained amplitude can vary with a 90% level of certainty. To verify the efficiency of the applied Fourier Analysis, comparisons were made between each actual (decomposed) timeseries and the corresponding reconstructed timeseries (by the linear summation of the 182 sinusoidal Fourier series). Furthermore, it was verified that the variance of the efficiently reconstructed timeseries equals to the sum of the variances of the 182 sinusoidal Fourier series (used to reconstruct the actual timeseries). Consequently, the variance of any specific Fourier series (corresponding to a specific Fourier constituent) was divided by the variance of the reconstructed timeseries to obtain the percent variance explained by this specific Fourier series. For every Fourier constituent, correlation coefficients (r) were obtained between the residual sea level Fourier series and each atmospheric variable Fourier series (of similar frequency). The obtained correlation coefficients, as well as the comparisons made, in terms of amplitude, phase, and percent variance explained, between the residual sea level timeseries and the time series of each of the atmospheric variables (for every Fourier constituent) allowed for determining the specific frequencies (constituents) at which each atmospheric variable is influencing the residual sea level variations.

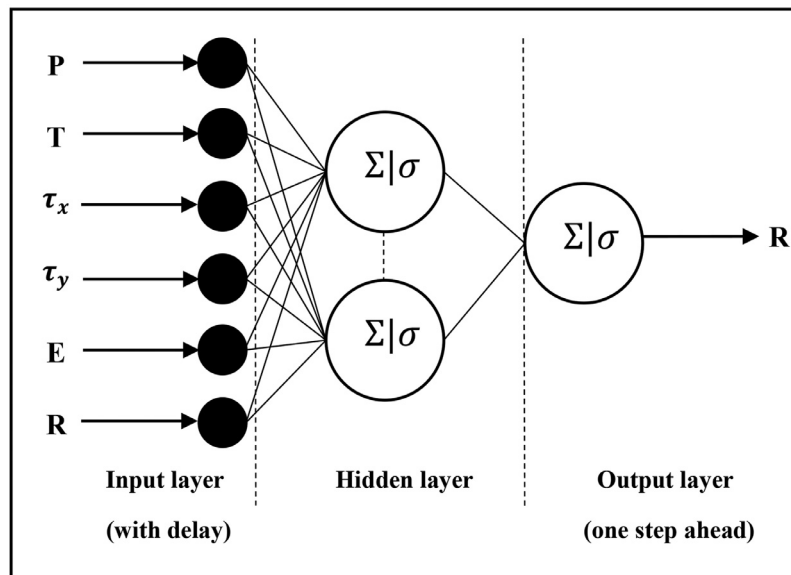


Figure 2 Architecture of constructed Non-linear Auto-Regressive Network with exogenous inputs (NARX).

3.3. NARX model

In the NARX method, a Backpropagation (BP) training algorithm is applied to minimize errors by adjusting weights to allow for the network to learn the behavior of the inputs and for the desired output to be reached. Two Backpropagation (BP) training algorithms, Levenberg–Marquardt (LM) and Resilient Backpropagation (Rprop), were tested and compared in this study to determine the optimum algorithm with the best performance. The functional form for the estimation and simulation of the one-step-ahead residual sea level, based on delayed residual sea level and atmospheric variables, can be expressed by the following equation:

$$R_{(t+1)} = f \left[(R, P, T, \tau_x, \tau_y, E)_{(t)}, (R, P, T, \tau_x, \tau_y, E)_{(t-1)}, (P, T, \tau_x, \tau_y, E)_{(t-2)} \right], \quad (4)$$

where R is the residual sea level (desired target), P is the atmospheric pressure, T is the air temperature, τ_x, τ_y are the cross- and along-shore wind stress components, E is the rate of evaporation, (t) is the current time step, $(t + 1)$ is the next time step, $(t - 1)$, $(t - 2)$ are the two previous time steps (delays).

The open-loop NARX Model that was constructed in this study, using Matlab[®] Neural Network Toolbox (Beale et al., 2014), consists of three layers: input, hidden, and output (Figure 2). The input layer contains time series of the residual sea level as well as all the atmospheric variables with tapped-delays. The output layer contains only the one-step-ahead targeted residual sea level. The used transformation function between the input and hidden layers is sigmoid (tansig), while the function used between the hidden and output layers is linear (purelin).

There is no standard method to find the proper time delays in RNN types (Islam and Morimoto, 2015). However, based on cross-covariance functions computed between the residual sea level and the atmospheric variables (not shown), input and feedback delays of one and/or two

day(s) are suggested. Through trial and error, the minimum network error (i.e. highest performance) and no over-fitted learning are pursued to find the optimal delays. The hidden layer contains a number of hidden neurons, and its range is determined based on the following formulation by Hecht-Nielsen (1990):

$$H_n < 2N^l + 1, \quad (5)$$

where H_n is the number of hidden-layer neurons and N^l is the number of inputs. Then, the optimal number of hidden-layer neurons is determined within this specific range through trial and error, taking into consideration the error measuring criteria.

For each tested training algorithm (LM and Rprop), two different data division sets are considered with each set containing different data percentage for model training, validation, and testing (80%, 10%, and 10%, and 70%, 15%, and 15%, respectively). Considering the input variables and their delays (given in Eq. 4), as an example, the possible number of hidden neurons (based on Eq. 5) would equal to 34, and accordingly the trial and error procedure would involve 136 separate model runs (2 training functions \times 2 data division sets \times 34 possible number of hidden neurons).

The performance of the NARX-based model was evaluated visually using comparison plots and statistically using correlation coefficients (r) and mean squared errors (mse). The difference between the actual and model-obtained residual sea levels was statistically analyzed to describe its variability. Furthermore, this difference was analyzed, using Fourier analysis, to determine the frequencies (Fourier constituents) at which the residual sea level is influenced by other unaccounted-for factors.

Additionally, the constructed NARX-based model was alternatively used to simulate the residual sea level but with each atmospheric variable individually replaced by its own five-degree polynomial fit. For each atmospheric variable, the variability of the difference between the actual and polynomial-fitted timeseries was compared with the variability of the corresponding model-obtained residual sea

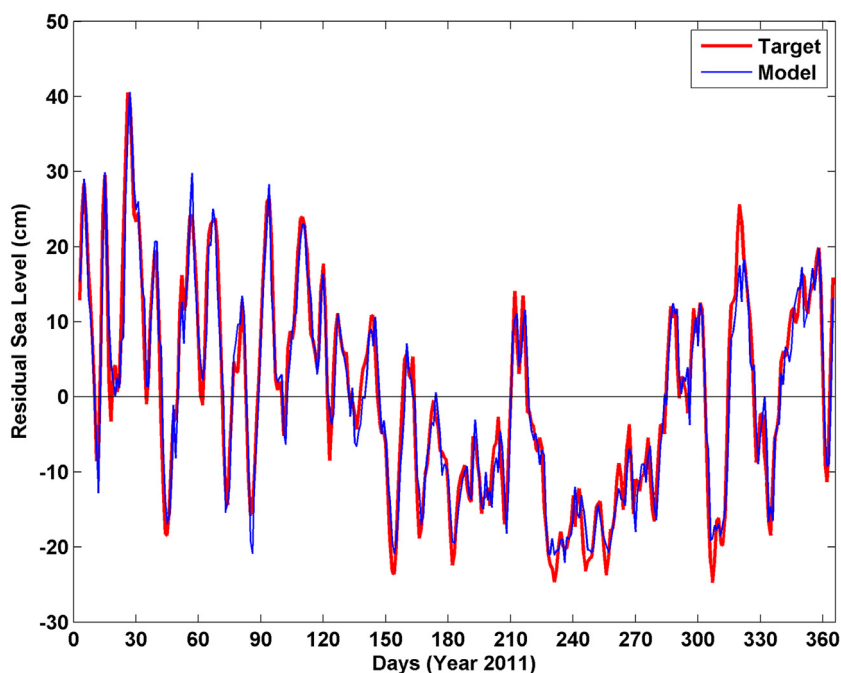


Figure 3 Daily-averaged actual (Target) and predicted (Model) residual sea levels.

level timeseries, on a seasonal basis, to verify that the constructed NARX-based model is recognizing the individual effect of each atmospheric variable on the sea level variations.

For each of the season corresponding periods, the cross-covariance was obtained (for each atmospheric variable) from the difference between a specific atmospheric variable's actual and polynomial-fitted timeseries and the corresponding model-obtained residual sea level timeseries. Additionally, the correlation coefficients (r) were obtained among each pair of differences for the periods corresponding to the different seasons. The obtained cross-covariances and correlation coefficients allowed for determining the extent to which the variations of atmospheric variables, individually and combined, are influencing the variations in residual sea level during each season representing period.

4. Results and discussion

The daily-averaged residual sea level (Figure 3) shows a pronounced increase over the zero mean during the winter and spring seasons and decrease during the summer and early fall seasons before increasing again during the late fall. The difference between the maximum (winter) and minimum (summer) residual sea levels is about 65 cm, a value that exceeds the maximum tidal range (~ 30 cm) obtained through harmonic analysis of the actual sea level record (not shown). Similar residual sea level oscillation patterns and differences have been observed in the central Red Sea by several researchers (e.g. Ahmad and Sultan, 1993; Osman, 1984; Sultan and Ahmad, 2000; Sultan and Elghribi, 2003; Sultan et al., 1995a,b; Sultan et al., 1996; Zubier, 2010) and in the southern Red Sea by Abdelrahman (1997) and

Eltaib (2010). It is also apparent, from Figure 3, that significant short-term variations in the residual sea level do occur within each season. Comparable short-term sea level variations have been found by Sultan and Elghribi (2003).

Similarly, the plots of daily-averaged atmospheric variables, given in Figure 4, show that all the variables do fluctuate on a seasonal basis as well as on a relatively short-term scale within each season. Figure 4 also shows that, for atmospheric pressure and air temperature, the seasonal variations are much larger in magnitude than the short-term variations; while, for wind stress components and evaporation rate, both seasonal and short-term variations are almost of the same magnitude.

To further investigate the magnitude of the seasonal and the short-term (within seasons) variations in the residual sea level and atmospheric variables, their daily-averaged records are statistically analyzed.

4.1. Descriptive statistics

Table 1 shows the results of the statistical analysis applied to the whole year residual sea level timeseries as well as to four 91-day periods representing the different seasons. The residual sea level seasonal means, given in Table 1, confirm the significant seasonal rise (+) and fall (–) in the residual sea level during the winter and summer seasons, respectively, with the difference between the winter and the summer seasonal means reaching 20.5 cm. The spring and fall seasonal means are of the same magnitude (~ 1 cm higher than the annual mean). Based on the range (maximum and minimum) and the standard deviation values, Table 1 also shows that the highest and lowest within-season variations in the residual sea level occur during the winter and summer seasons, respectively.

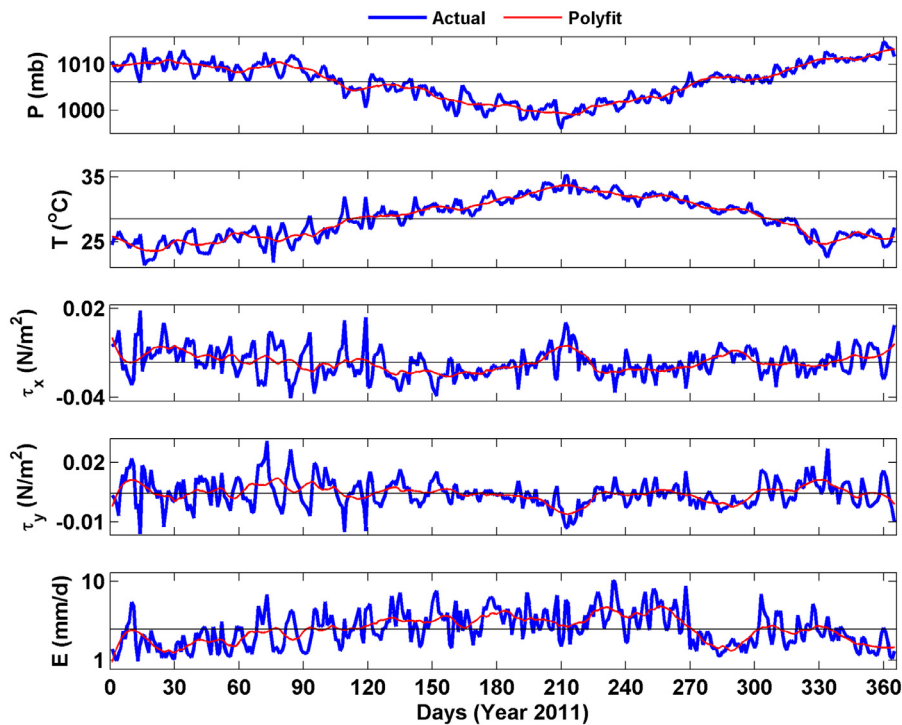


Figure 4 Daily-averaged actual and polynomial-fitted atmospheric variables.

Table 1 Annual and seasonal (91-days) statistical analyses (maximum, minimum, mean, and standard deviation) of residual sea level and atmospheric variables records.

| Parameters | Statistics | Whole Year | Seasons | | | |
|------------------------------------|------------|------------|---------|---------|---------|---------|
| | | | Winter | Spring | Summer | Fall |
| R (cm) | Max | 40.54 | 40.54 | 26.38 | 14.07 | 25.64 |
| | Min | -24.74 | -18.45 | -23.60 | -24.63 | -24.74 |
| | Mean | 0.000 | 8.65 | 1.20 | -11.85 | 1.44 |
| | Stdv | 13.72 | 13.64 | 11.49 | 8.35 | 12.27 |
| P (mb) | Max | 1014.92 | 1013.63 | 1009.67 | 1008.33 | 1014.92 |
| | Min | 996.00 | 1006.08 | 998.46 | 996.000 | 1005.21 |
| | Mean | 1006.15 | 1009.72 | 1004.12 | 1001.46 | 1009.19 |
| | Stdv | 4.13 | 1.65 | 2.57 | 2.24 | 2.34 |
| T (°C) | Max | 35.34 | 27.96 | 32.97 | 35.34 | 31.08 |
| | Min | 21.37 | 21.37 | 24.73 | 30.27 | 22.58 |
| | Mean | 28.57 | 25.06 | 29.28 | 32.39 | 27.57 |
| | Stdv | 3.15 | 1.49 | 1.78 | 1.02 | 2.21 |
| τ _x (N/m ²) | Max | 0.018 | 0.018 | 0.014 | 0.011 | -0.001 |
| | Min | -0.041 | -0.041 | -0.039 | -0.037 | -0.033 |
| | Mean | -0.016 | -0.013 | -0.021 | -0.018 | -0.015 |
| | Stdv | 0.010 | 0.011 | 0.009 | 0.009 | 0.007 |
| τ _y (N/m ²) | Max | 0.031 | 0.031 | 0.020 | 0.016 | 0.027 |
| | Min | -0.016 | -0.016 | -0.015 | -0.013 | -0.005 |
| | Mean | 0.004 | 0.006 | 0.005 | 0.002 | 0.005 |
| | Stdv | 0.007 | 0.009 | 0.006 | 0.005 | 0.006 |
| E (mm/day) | Max | 10.11 | 8.5 | 8.92 | 10.11 | 8.57 |
| | Min | 0.91 | 0.91 | 2.09 | 2.27 | 1.48 |
| | Mean | 4.56 | 3.31 | 5.38 | 5.93 | 3.65 |
| | Stdv | 2.00 | 1.71 | 1.66 | 1.79 | 1.47 |

The statistical analysis applied to all the daily-averaged atmospheric variables provides the magnitudes of their annual and seasonal variations (Table 1). For the atmospheric pressure, the maximum increase in seasonal mean above the annual mean is observed in the winter season, while the minimum decrease in seasonal mean below the annual mean is observed in the summer. Based on standard deviations, the lowest and highest within-season atmospheric pressure variations occur during the winter season and the spring season, respectively. Typically, the lowest and highest air temperature seasonal means, compared to the annual mean, occur in the winter and the summer seasons, respectively; however, the lowest and highest within-season variations occur during the summer and fall seasons, respectively. Compared to the annual mean of the cross-shore wind stress, the lowest seasonal mean occurs in the winter season, while the highest seasonal mean occurs in the spring season. The highest and lowest within-season variations in cross-shore wind stress occur during the winter and fall seasons, respectively. For the along-shore wind stress, the highest seasonal mean above the annual mean occurs in the winter season and the lowest seasonal mean below the annual mean occurs during the summer season. The highest and lowest within-season variations in along-shore wind stress occur during the winter and summer seasons, respectively. In comparison to the annual mean, the evaporation rate reaches its minimum seasonal mean in the winter season and its maximum seasonal mean in the summer season, whereas the maximum and minimum within-season variations occur during the summer and fall seasons, respectively.

The above statistical analyses results confirm that the residual sea level and all the atmospheric variables experience variations not only seasonally but also on a relatively short-term scale (within each season), with the magnitudes of these short-term variations varying with season. To further investigate these variations and their time scales, Fourier analysis is applied.

4.2. Fourier analysis

Tables 2 and 3 show the results of the Fourier analysis of the daily-averaged residual sea level and the daily-averaged atmospheric variables. The obtained amplitudes and phases as well as the percent variance explained (Table 2) correspond to three frequency bins (Fourier constituents) equivalent to periods of 365, 182.5, and 91.25 days, which represent the annual, semiannual, and seasonal constituents, respectively. Table 3 shows the percent variance explained by the combined frequency bins that constitute the weather-band (covering a period of ~4–30 days) Fourier constituents. Figure 5 shows the obtained amplitudes with 90% confidence interval for selected constituents (frequencies) including the annual, semiannual, and seasonal constituents as well as some of the weather-band constituents. The timeseries of the weather-band residual sea level is shown in Figure 6, while Figure 7 shows the normalized timeseries of the weather-band atmospheric variables compared to the normalized timeseries of the weather-band residual sea level. Figure 8 shows plots of the correlation coefficients obtained for the different Fourier constituents (including

weather-band constituents) between the residual sea level and the atmospheric variables.

4.2.1. Residual sea level

More than 43% of the variation in residual sea level is accounted for by the annual, semiannual and seasonal constituents combined, while the combined weather-band constituents account for 42.67% of the variance. The obtained amplitude for the annual constituent is comparable to those found in previous literature for the same region, while the obtained amplitude for the semiannual constituent is somewhat smaller. However, some previous studies (e.g. Eltaib, 2010; Sultan et al., 1996) have clearly shown that the amplitudes of the annual and semiannual constituents do vary significantly from one year to another in the central Red Sea. Figure 6 shows that the weather-band residual sea level variations differ seasonally, with the summer variations being significantly lower in magnitude than those during the winter.

4.2.2. Atmospheric pressure

The annual constituent account for more than 83% of the variance in atmospheric pressure, while the percent variance explained by the weather-band constituents (9.58%) is more than double the percent variance explained by the semiannual and seasonal constituents combined (3.66%). In terms of annual and semiannual constituents, there are apparent phase lags between the atmospheric pressure and the residual sea level, indicating a deviation from the typical inverse (inverter-barometer) relationship between these two variables. This result, which is supported by the relatively strong (+) correlations corresponding to annual and semiannual constituents obtained between these two variables (Figure 8), indicates that atmospheric pressure is likely not a significant contributor to the annual and semiannual sea level variations. The comparison in terms of phase values corresponding to the seasonal constituent, shows that the two variables are almost inversely related; this suggests a contribution of atmospheric pressure to the seasonal sea level variations. This is supported by the high correlation coefficient (-0.86) obtained between the seasonal constituents of the residual sea level and the atmospheric pressure (Figure 8). The timeseries of the combined weather-band constituents of atmospheric pressure, given in Figure 7, experiences its lowest fluctuations during the period corresponding to the mid-summer through late-fall. The obtained correlation coefficients between the residual sea level and the atmospheric pressure, corresponding to weather-band constituents (Figure 8), reveal that the two variables are more negatively than positively correlated. Such results suggest that the atmospheric pressure is a contributing variable to the weather-band sea level variations.

4.2.3. Air temperature

More than 86% of the air temperature variance is accounted for by the annual constituent, while the variance accounted for by the weather-band (8.72%) is more than seven times the variance accounted for by the semiannual and seasonal constituents combined (1.12%). The apparent phase lags between the residual sea level and the air temperature, in terms of annual and semiannual constituents, indicate that

Table 2 Fourier constituents (annual, semiannual, and seasonal): amplitude (A), phase (Phs), and percent variance explained (Var) for residual sea level and atmospheric variables.

| Variable | Parameter | Fourier Constituents | | |
|----------|---|----------------------|------------|----------|
| | | Annual | Semiannual | Seasonal |
| <i>R</i> | A (cm) | 11.82 | 2.04 | 4.42 |
| | Phs (deg.) | 42.58 | −59.82 | 89.32 |
| | Var (%) | 37.19 | 1.11 | 5.20 |
| <i>P</i> | A (mb) | 5.35 | 0.95 | 0.59 |
| | Phs (deg.) | 14.55 | −114.26 | −60.23 |
| | Var (%) | 83.36 | 2.63 | 1.03 |
| <i>T</i> | A (°C) | 4.13 | 0.40 | 0.25 |
| | Phs (deg.) | −149.12 | 126.18 | 101.80 |
| | Var (%) | 86.39 | 0.80 | 0.32 |
| τ_x | A ($\times 10^{-3}$ N/m ²) | 4.13 | 2.80 | 3.60 |
| | Phs (deg.) | −0.63 | 62.95 | 81.02 |
| | Var (%) | 8.87 | 4.07 | 6.72 |
| τ_y | A ($\times 10^{-3}$ N/m ²) | 2.31 | 1.27 | 2.08 |
| | Phs (deg.) | 46.52 | −117.50 | −95.45 |
| | Var (%) | 5.59 | 1.68 | 4.49 |
| <i>E</i> | A (mm/d) | 1.53 | 0.05 | 0.51 |
| | Phs (deg.) | −166.90 | −156.45 | −122.92 |
| | Var (%) | 28.96 | 0.04 | 3.18 |

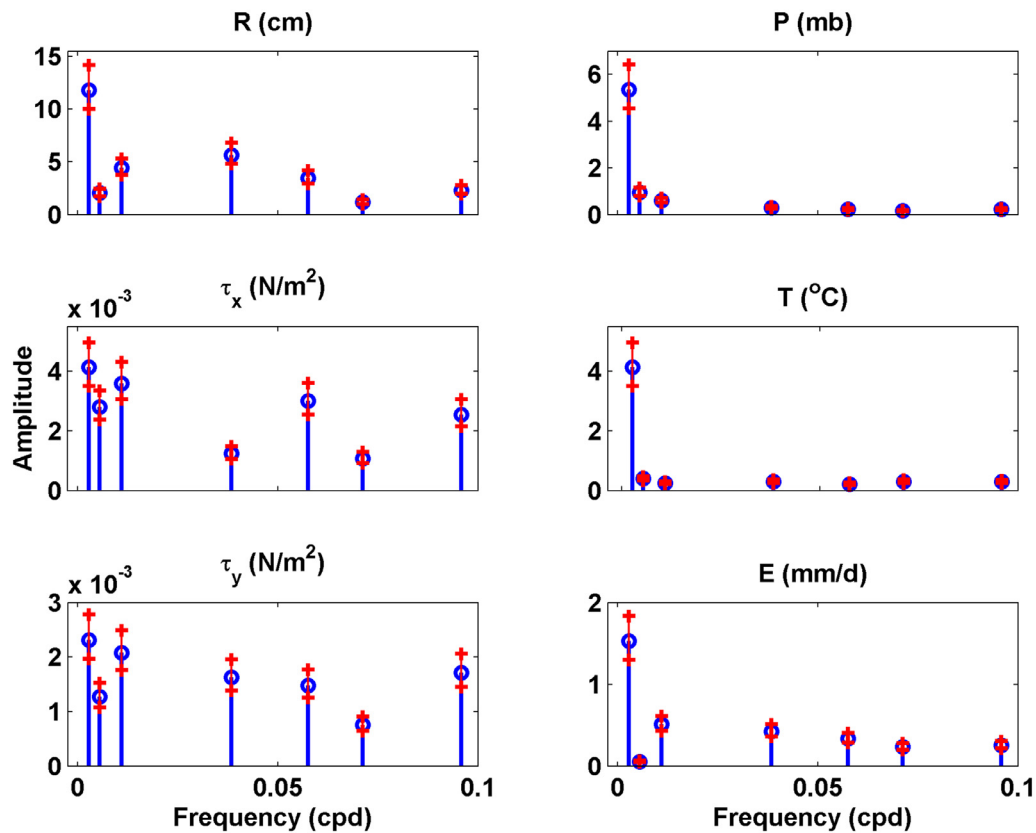


Figure 5 Residual sea level and atmospheric variables amplitudes (o) for selected Fourier constituents (frequencies) with 90% confidence interval (+).

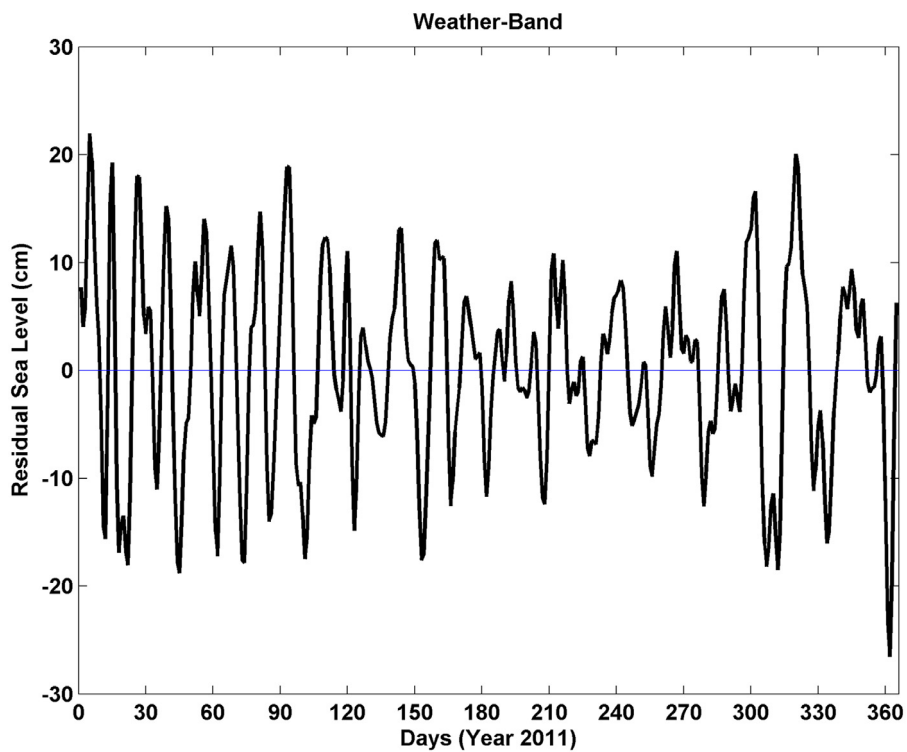


Figure 6 Weather-band residual sea level.

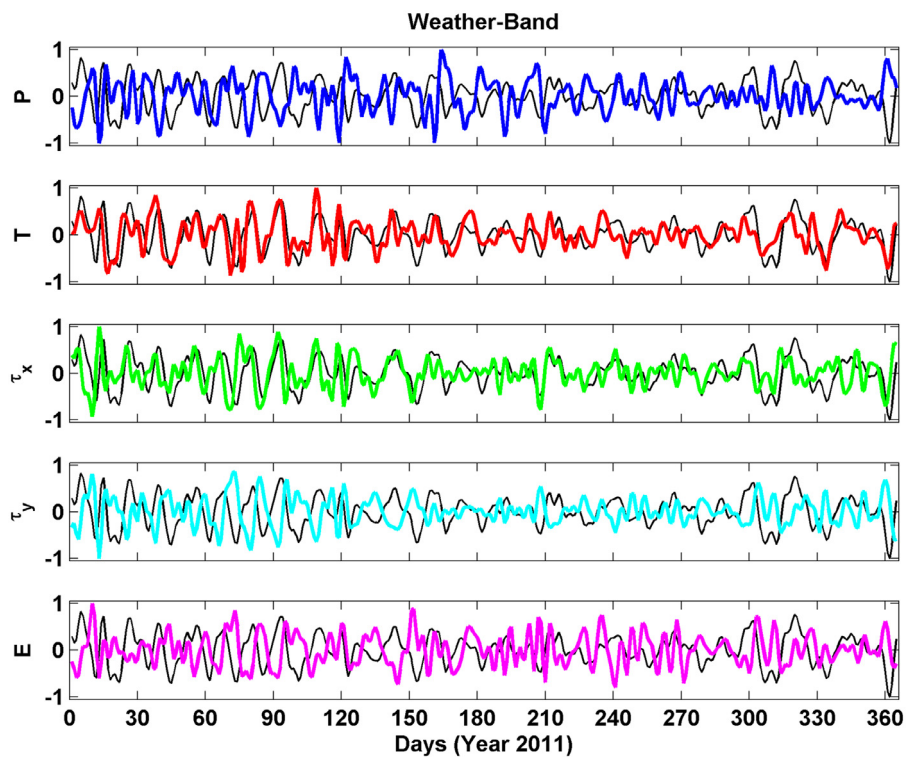


Figure 7 Normalized weather-band atmospheric variables (colored) along with normalized weather-band residual sea level (black).

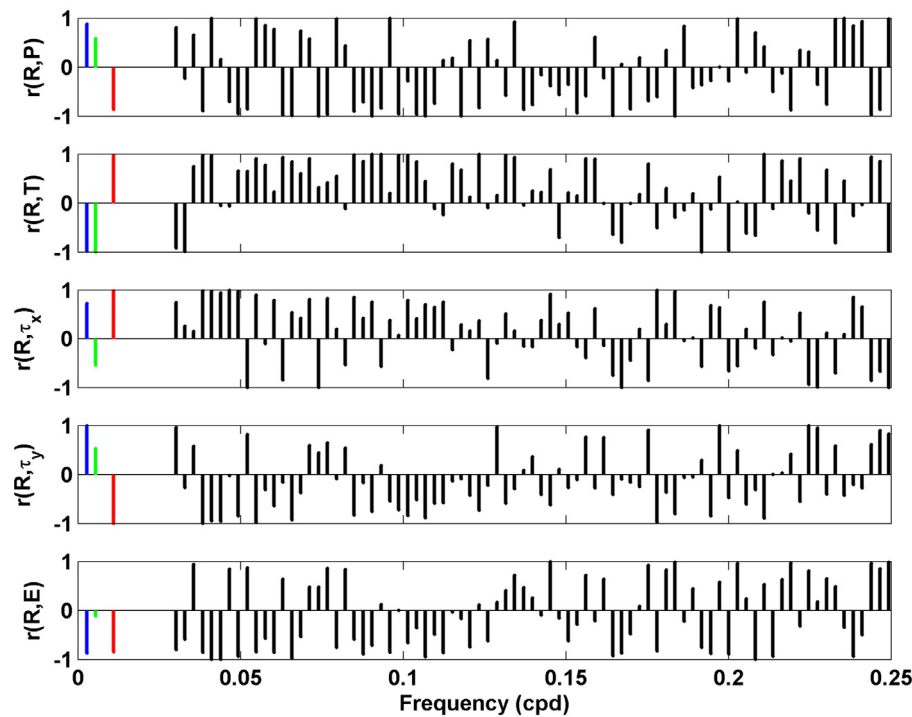


Figure 8 Correlation coefficients between residual sea level and each atmospheric variable for different Fourier constituents (frequencies).

Table 3 Percent variance explained (%) for weather-band residual sea level and atmospheric variables.

| R | P | T | τ_x | τ_y | E |
|-------|------|------|----------|----------|-------|
| 42.67 | 9.58 | 8.72 | 60.07 | 65.39 | 46.86 |

the two variables are inversely related (Table 2). Considering the presumably direct relationship between the two variables, these results indicate that air temperature is, most likely, not a contributing factor to the annual and semi-annual sea level variations. These results are supported by the relatively strong (–) correlations, corresponding to annual and semiannual constituents, obtained between these two variables (Figure 8). The comparison between the residual sea level and the air temperature phase values, corresponding to the seasonal constituent, shows that the two variables are almost directly related; this suggests a possible contribution of air temperature to the seasonal sea level variations. This is supported by the high correlation coefficient (+0.98) obtained between the seasonal constituents of the residual sea level and air temperature (Figure 8). The lowest fluctuations in the timeseries of the combined weather-band, corresponding to air temperature, occur during the summer season (Figure 7). The obtained correlation coefficients between the residual sea level and the air temperature, corresponding to weather-band constituents (Figure 6), reveal that the two variables are more positively than negatively correlated. Such results suggest that the weather-band sea level variations are contributed to by air temperature.

4.2.4. Wind stress

The weather-band accounts for most of the variances in the wind stress components. For the cross-shore wind stress, the variance explained by the weather-band (60.07%) is more than three times the variance explained by the annual, semiannual, and seasonal constituents combined (19.66%). The along-shore wind stress percent variation explained by the weather-band (65.39%) is more than five times than that explained by the annual, semiannual, and seasonal constituents combined (11.76%). The phase comparisons show that each of the two wind stress components have considerable phase lags with the residual sea level, in terms of the annual and semiannual constituents, indicating that the wind stress components are probably not significant contributors to residual sea level annual and semiannual variations. The phase difference corresponding to the seasonal constituent, however, shows that the residual sea level and the along-shore wind stress component are inversely related ($\sim 180^\circ$ out of phase), while the residual sea level and the cross-shore wind stress component are directly related (almost in phase). Considering the wind direction dominance and the associated Ekman transport, such results suggest that both wind stress components contribute to the seasonal variations in sea level. These suggested contributions are supported by the high correlation coefficients (+0.99 and –0.99) obtained, for the seasonal constituent, between the residual sea level and the cross-shore and along-shore wind stress components, respectively (Figure 6). In terms of the combined weather-band, both components of wind stress experience their highest fluctuations during the winter and early spring periods and their lowest fluctuations during the summer (Figure 7). The obtained correlation coefficients, given in Figure 8, show that, in correspondence

Table 4 Correlation coefficients (r) and mean squared errors (mse) as statistical indicators of the NARX-based model performance (overall and data divisions).

| Statistical Parameter | Overall (100%) | Data Divisions | | |
|-----------------------|----------------|----------------|------------------|---------------|
| | | Training (80%) | Validation (10%) | Testing (10%) |
| r | 0.969 | 0.972 | 0.961 | 0.952 |
| mse | 0.00115 | 0.00107 | 0.00107 | 0.00106 |

with weather-band constituents, the residual sea level and the cross-shore wind stress are more positively related while the residual sea level and the along-shore wind stress are more negatively related. These results suggest that the wind stress components contribute to the variations in sea level within the weather-band frequency domain.

4.2.5. Evaporation Rate

The weather-band accounts for 46.86% of the evaporation rate variance, while the annual, semiannual, and seasonal constituents combined account for nearly 32.18% of the variance. The phase comparisons between the residual sea level and evaporation rate, in terms of the Fourier constituents (annual, semiannual, and seasonal), revealed that the annual and seasonal constituents somewhat maintain the typical inverse relationship between sea level and evaporation rate. Such results suggest that evaporation contributes to the residual sea level variations on the annual and seasonal levels. These suggested contributions are supported by the relatively high correlation coefficients (-0.87 and -0.85) obtained between the residual sea level and evaporation rate, corresponding to annual and seasonal constituents, respectively (Figure 8). Based on Figure 7, there are no apparent seasonal differences in the magnitude of fluctuation in the evaporation rate corresponding to the weather-band. The obtained correlation coefficients between the residual sea level and the evaporation rate, corresponding to weather-band constituents (Figure 8), show that the two variables are more negatively than positively correlated. These results suggest that evaporation contributes to the weather-band sea level variations.

Overall, the Fourier analysis results suggest that short-term sea level variations are contributed to mainly by the seasonal and shorter term (weather-band) variations in the considered atmospheric variables.

4.3. NARX Model

4.3.1. Model Performance

Among the large number of NARX-based constructed models, the best performance was obtained using the LM training function with optimal tapped delays of (input: 2, feedback: 1), optimal number of hidden neurons $H_n = 10$, and data division of (training: 80%, validation: 10% and testing: 10%). The comparison between the model-obtained residual sea level and the actual residual sea level, shown in Figures 3 and 9, clearly demonstrates the high performance of the developed NARX-based model. The model performance is also statistically evaluated, in Table 4, using correlation coefficients (r) and mean squared errors (mse).

The high performance strongly suggests that, without any prior interrelation knowledge, the constructed NARX model is able to capture the role played by the utilized atmospheric variables on the residual sea level variations.

Table 5 shows the statistical analysis results for the difference between the actual and model-obtained residual sea levels. Despite the slight model underestimation of the (\pm) residual sea level peaks, shown in Figures 3 and 9, the calculation of the explained percent variance reveals that the model-obtained residual sea level is responsible for nearly 91% of the total variance in the original residual sea level series. The remaining $\sim 9\%$ of the variance corresponds to the difference between the actual and model-obtained residual sea levels, shown in Figure 10, in which the timeseries experiences higher variabilities during the winter and fall seasons and lower variabilities during the spring and summer seasons. This is supported by the greater standard deviations for the winter and fall seasons (Table 5). This difference can be attributed to the role of other contributing (atmospheric/oceanographic) factors that are not presented to the NARX-based model and, therefore, are not accounted for (unmodeled). In order to determine the frequency ranges at which these unaccounted-for factors contribute to the residual sea level variations, the difference between the actual and model-obtained residual sea levels is analyzed using Fourier analysis.

The Fourier analysis results, given in Table 6, show that the annual, semiannual, and seasonal constituents combined are responsible for 1.18% of the variance in the difference between the actual and model-obtained residual sea levels, while the combined weather-band constituents are responsible for more than 67% of the variance. Furthermore, each one of the annual, semiannual, and seasonal constituents has an amplitude of less than 0.5 cm (Figure 11), indicating that their combined contribution to the difference is insignificant. The combined weather-band constituents, however, have varying amplitudes within a range of $\sim \pm 9$ cm. The comparison between the original difference (between the actual and model-obtained residual sea levels) and the reconstructed difference (that corresponds to the weather-band constituents) clearly shows that the original difference is totally in phase with the reconstructed weather-band difference (Figure 10).

These results clearly indicate the presence of other unaccounted-for (atmospheric/oceanographic) factors that are also contributing to the residual sea level variations in this frequency domain (weather-band). Although the presence of lower frequency (longer period) contributing factors is also apparent, their contributions are noticeably

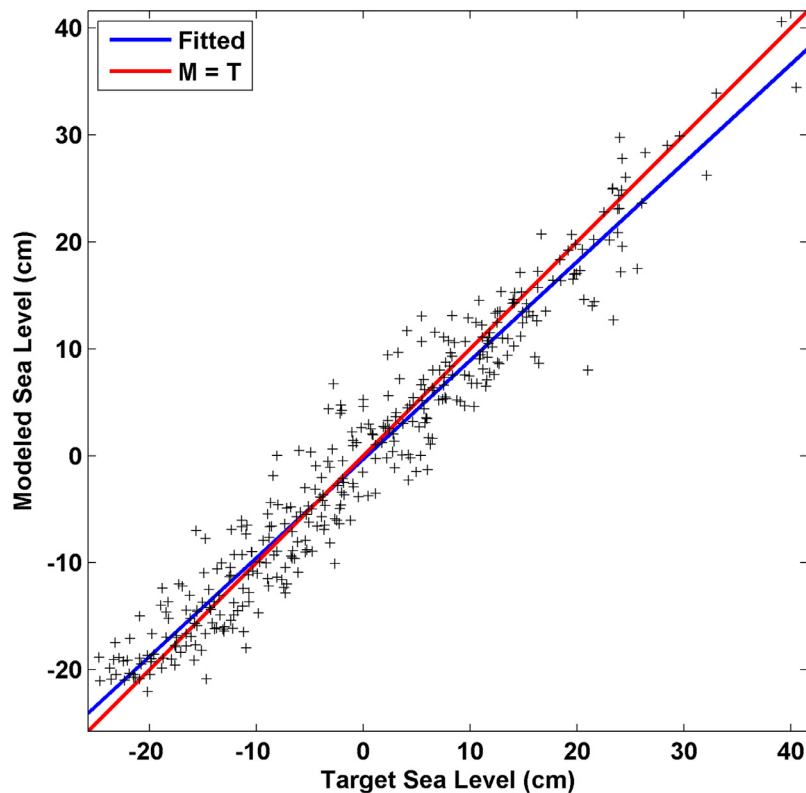


Figure 9 Comparison between actual (Target) and predicted (Model) residual sea levels.

Table 5 Annual and seasonal (91-days) statistical analysis (maximum, minimum, mean, and standard deviation) of the difference between actual (target) and predicted (output) residual sea levels.

| Variable | Statistics | Whole Year | Seasons | | | |
|---------------------------|------------|------------|---------|--------|--------|-------|
| | | | Winter | Spring | Summer | Fall |
| Residuals Difference (cm) | Max | 13.03 | 13.03 | 7.41 | 7.41 | 10.74 |
| | Min | −9.49 | −9.49 | −6.59 | −7.05 | −8.64 |
| | Mean | 0.30 | 0.45 | 0.36 | 0.02 | 0.31 |
| | Stdv | 3.40 | 3.81 | 2.97 | 2.97 | 3.77 |

Table 6 Fourier constituents (annual, semiannual and seasonal): amplitudes (A) and percent variance explained (Var) for the difference between actual (target) and predicted (output) residual sea levels.

| Variable | Parameter | Fourier Constituents | | | Weather Band |
|------------|-----------|----------------------|------------|----------|--------------|
| | | Annual | Semiannual | Seasonal | |
| Residuals | A (cm) | 0.33 | 0.36 | 0.18 | — |
| Difference | Var (%) | 0.48 | 0.56 | 0.14 | 67.54 |

less. A possible unaccounted-for contributor (within the weather-band frequency range) is seawater temperature, which according to [Eid and Abdallah \(1994\)](#) is the dominant factor controlling the steric effect in the central Red Sea. Another possible unaccounted-for short-term contribution is associated with the frequently blowing eastward wind jets from the westerly located Tokar Gap, which acts as an along-axis wind inlet during the summer and outlet during the winter for the Red Sea ([Jiang et al., 2009](#)). Mesoscale

eddies and boundary currents are among the unaccounted-for factors that can significantly contribute to the relatively short-term residual sea level variations ([Churchill et al., 2018](#)). The monsoon-associated water exchange between the Red Sea and the Gulf of Aden, through the southerly located Strait of Bab Al-Mandab, is a possible unaccounted-for low frequency contributing factor to the long-term sea level variations for the entire Red Sea ([Sultan et al., 1995a,b, 1996](#); [Wahr et al., 2014](#)).

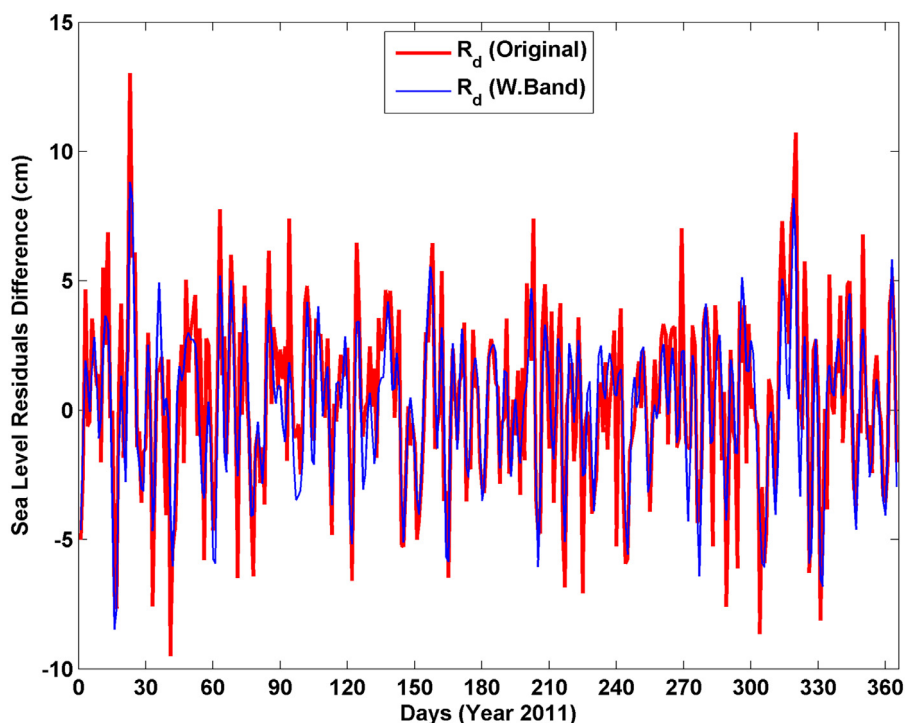


Figure 10 Original and weather-band difference between actual and model-predicted residual sea levels.

4.3.2. Individual and combined effects investigation

Based on its apparent high performance, the developed NARX-based model (with all varying atmospheric variables) was alternatively used to simulate the sea level residual but with each atmospheric variable individually replaced by its own five-degree polynomial fit (Figure 4). Each predicted residual sea level record (with one input polynomial-fitted variable) was subtracted from the original network predicted residual sea level (with all input variables varying). The results of these subtractions are shown in Figure 12, from which the temporal variations in the effect of each atmospheric variable on the residual sea level can be clearly visualized.

In the following subsections, after a holistic description of the role played, individually, by each atmospheric variable on the residual sea level variations was given, a verification procedure was carried out to confirm that the NARX-based constructed model was capturing that individual role. The combined effect of the atmospheric variables on the residual sea level variations is given in the last subsection. **Atmospheric Pressure Effect.** Atmospheric pressure is known to have an inverse influence on sea level (inverted-barometer effect). Based on the hydrostatic hypothesis, an increase in atmospheric pressure by 1 millibar should depress the de-tided sea level by 1 cm and vice versa. On the relatively long-term scale, the comparison between the residual sea level (Figure 3) and the atmospheric pressure (Figure 4) patterns does not reflect the presence of this typical inverse relationship. A similar long-term departure from the isostatic response has also been shown by earlier studies on the sea level variations in the central Red Sea (e.g. Ahmad and Sultan, 1993; Eltaib, 2010; Osman, 1984; Sultan and Elghribi, 2003; Sultan et al., 1995a; Sultan et al., 1995b; Sultan et al., 1996). How-

ever, both Sultan and Elghribi (2003) and Sultan et al. (1995a) have suggested that, over a scale of a few days, the residual sea level variations in the central Red Sea do follow the hydrostatic hypothesis. The Fourier analysis applied earlier in this study revealed that, for the seasonal constituent and for most of the constituents in the weather-band range, the typical inverted-barometer relationship is well-maintained between the residual sea level and atmospheric pressure.

Figure 13 shows seasonal plots of the difference between the actual and the polynomial-fitted atmospheric pressures (Figure 4) as well as the difference between the model-obtained residual sea levels corresponding to the atmospheric pressure effect (Figure 12). These plots (Figure 13) demonstrate that, for all seasons, the typical inverse relationship is highly maintained between the sea level difference and the atmospheric pressure difference. Furthermore, Figure 13 also shows that during the fall season, when the difference between the actual and polynomial-fitted atmospheric pressures is minimal, the difference between the corresponding model-obtained residual sea levels is also minimal. These results indicate that the constructed NARX-based model is efficiently recognizing the effect of the relatively short-term (within seasons) atmospheric pressure variability on the residual sea level variations.

Air Temperature Effect. Air temperature is a major factor influencing seawater temperature which, in turn, influences the sea level through the steric effect – variations of the volume of the seawater due to the thermal effects on its density. Due to such effects, the sea level rises when the seawater is warm and/or less saline and falls when the seawater is cold and/or more saline. Previous studies have suggested that the steric effect is a major contributor to seasonal sea level variations in the Red Sea

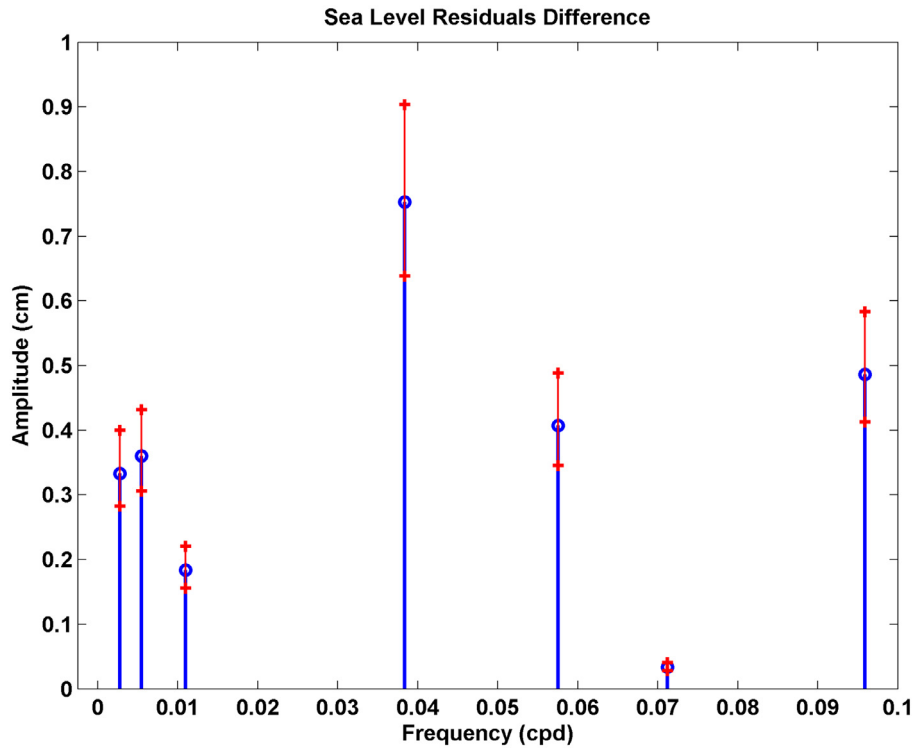


Figure 11 Residual sea levels difference amplitudes (o) for selected Fourier constituents (frequencies) with 90% confidence interval (+).

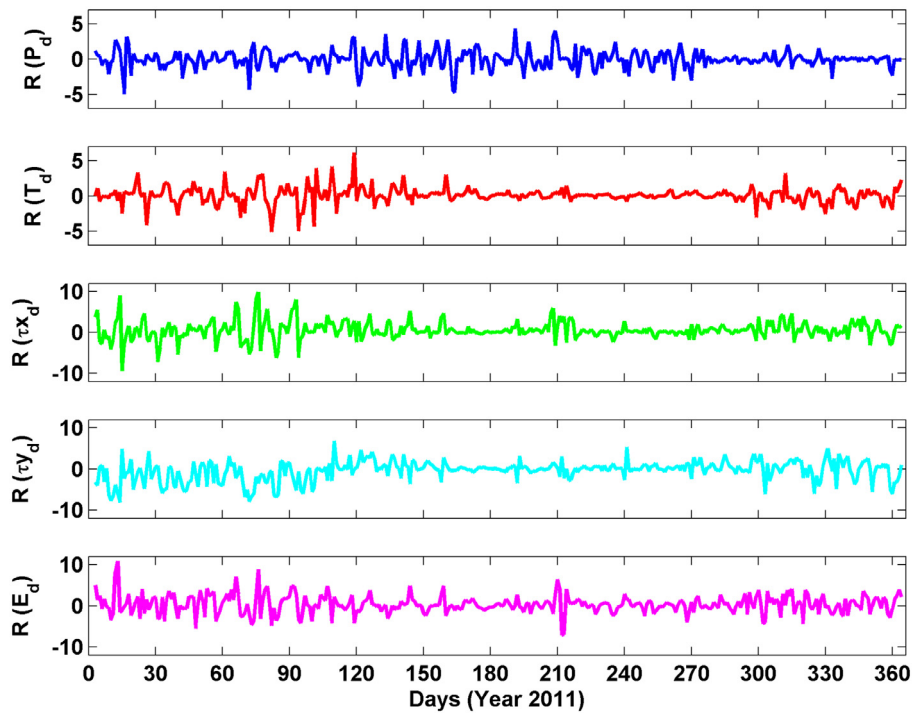


Figure 12 Effect of atmospheric variables on residual sea level represented by the difference between model-obtained residual sea levels (with actual and polynomial-fitted variables).

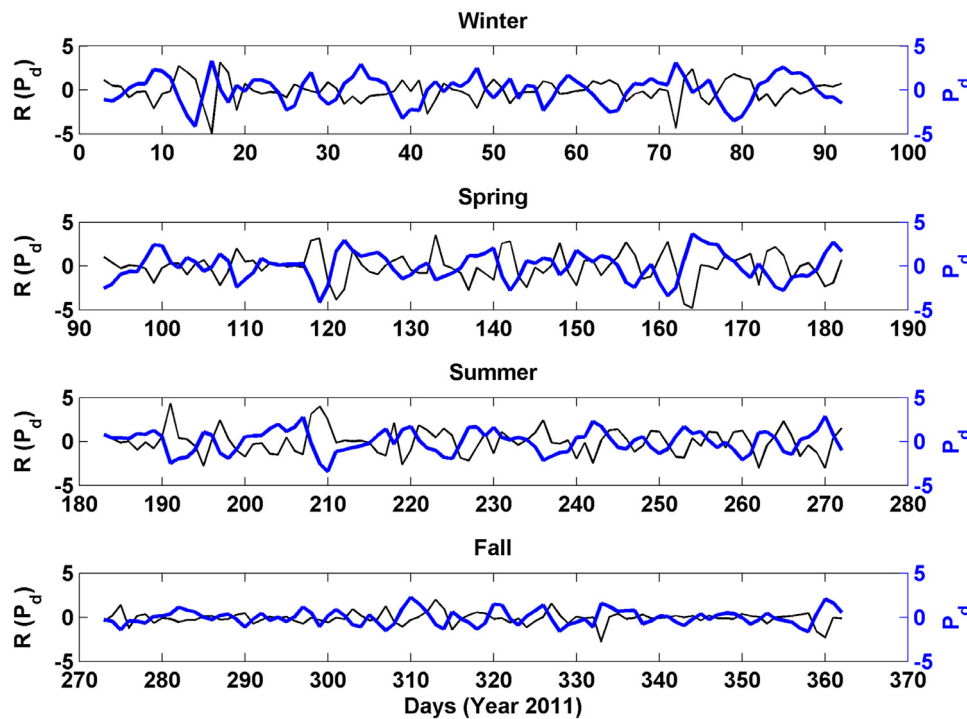


Figure 13 Difference between actual and polynomial-fitted atmospheric pressures (P_d) and difference between the corresponding model-obtained residual sea levels ($R(P_d)$) for the different seasons (91-day period).

(Eid and Kamel, 2004; Mohamad, 2012; Patzert, 1972; Wahr et al., 2014). Other studies have shown that the steric effect on the Red Sea's sea level varies both spatially and temporally (Abdallah and Eid, 1989; Eid and Abdallah, 1994; Eid and Kamel, 2004). According to Eid and Abdallah (1994), the steric effect at the central part of the Red Sea is mainly thermal (minimal salinity effect). Accordingly, air temperature (an influencing atmospheric variable) is used in this study as an indicator due to the lack of sea surface temperature data. The presumably direct relationship between air temperature and residual sea level is not observed when comparing the relatively long-term patterns of the residual sea level (Figure 3) and air temperature (Figure 4). Nevertheless, the earlier performed Fourier analysis showed that, for the seasonal constituents and most of the weather-band constituents, the presumed (typical) direct relationship between sea level and air temperature is maintained.

Figure 14 shows seasonal plots of the difference between the actual and the polynomial-fitted air temperatures (Figure 4) as well as the difference between the model-obtained residual sea levels corresponding to the air temperature effect (Figure 12). The plots (Figure 14) show that, except for the spring season, all seasons are dominated by an inverse relationship between the residual sea level difference and the air temperature difference. For the spring season, the plot shows that a direct (typical) relationship between the two differences is dominant. Figure 14 also shows that, in association with the minimal difference between the actual and polynomial-fitted air temperatures during the fall season, a minimal difference between the corresponding model-obtained residual sea levels is obtained. Such results indicate that the constructed NARX-based model is recognizing the ef-

fect of the short-term air temperature variability on the residual sea level variations mainly during the spring season. During the other seasons, it is highly probable that the air temperature effect on the residual sea level is masked by the role of one or more of the other atmospheric variables.

Wind Stress Effect. Wind is among the atmospheric factors that might directly or indirectly influence sea level, depending on the wind direction. Ekman transports associated with the wind-driven water flows can either pile-up water against the coastline (forcing sea level to rise) or transport water away from coastline (forcing sea level to drop). For the central part of the Red Sea, Patzert (1974) has suggested only a weak contribution of wind stress to sea level variability. However, others have suggested that major parts of sea level variations, in the central part of the Red Sea, can be accounted for by the along-shore wind stress component (Ahmad and Sultan, 1993; Sofianos and Johns, 2003; Sultan et al., 1995b). Furthermore, using daily records of mean sea level and atmospheric variables, studies by Sultan and Elghribi (2003) and Zubier (2010) have shown some considerable effects of both components of wind stress on the sea level variations at the eastern central Red Sea. In a recent study by Churchill et al. (2018), it was shown that the sea level variations in the central Red Sea are highly correlated with wind stress. Comparing each wind stress component pattern (illustrated in Figure 4) with the pattern of the residual sea level (Figure 3) indicates that, on the relatively long-term scale, the wind stress components have no maintained relationship (direct or inverse) with the residual sea level. The comparison of the results obtained earlier through the Fourier analysis of the residual sea level, as well as both components of wind stress, revealed that,

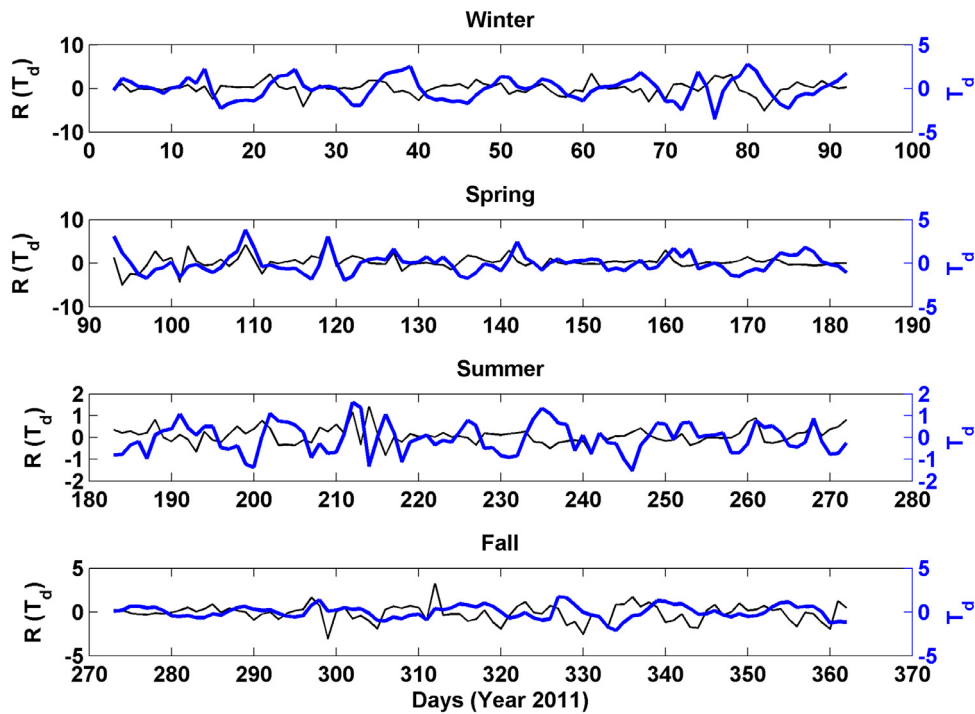


Figure 14 Difference between actual and polynomial-fitted air temperatures (T_d) and difference between the corresponding model-obtained residual sea levels ($R(T_d)$) for the different seasons (91-day period).

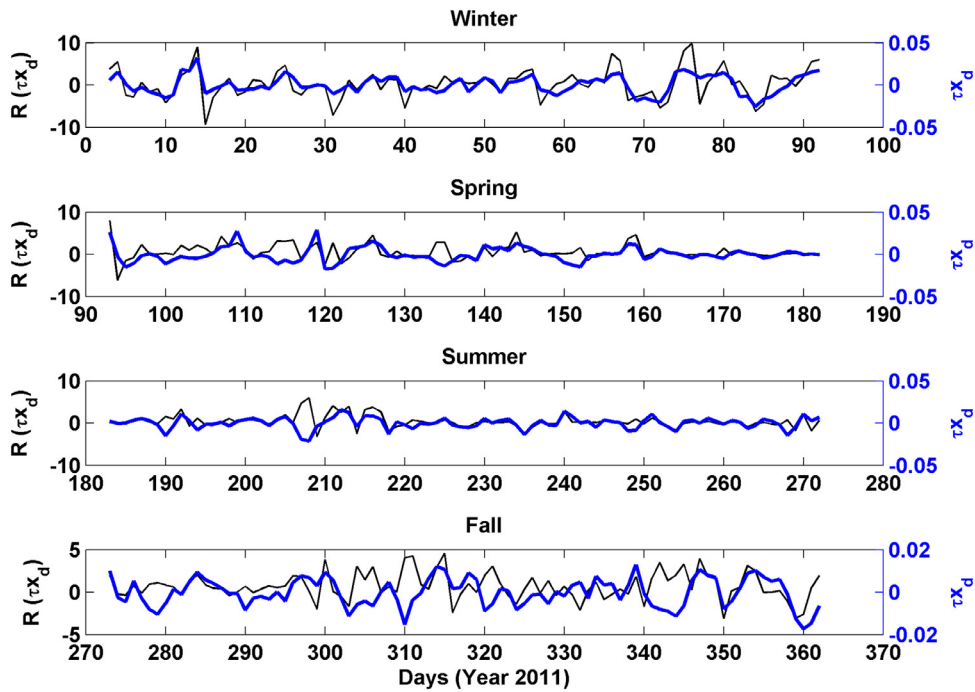


Figure 15 Difference between actual and polynomial-fitted cross-shore wind stresses (τ_{x_d}) and difference between the corresponding model-obtained residual sea levels ($R(\tau_{x_d})$) for the different seasons (91-day period).

the most effective wind stress contributions to the residual sea level variations occur mainly within the weather-band frequency range.

Figure 15 shows seasonal plots of the difference between the actual and the polynomial-fitted cross-shore wind stresses (Figure 4) as well as the difference between

the model-obtained residual sea levels corresponding to the cross-shore wind stress effect (Figure 12). The plots (Figure 15) show that all seasons are dominated by a direct (typical) relationship between the sea level difference and the cross-shore wind stress difference. Figure 15 also shows that the minimal variations in the sea level

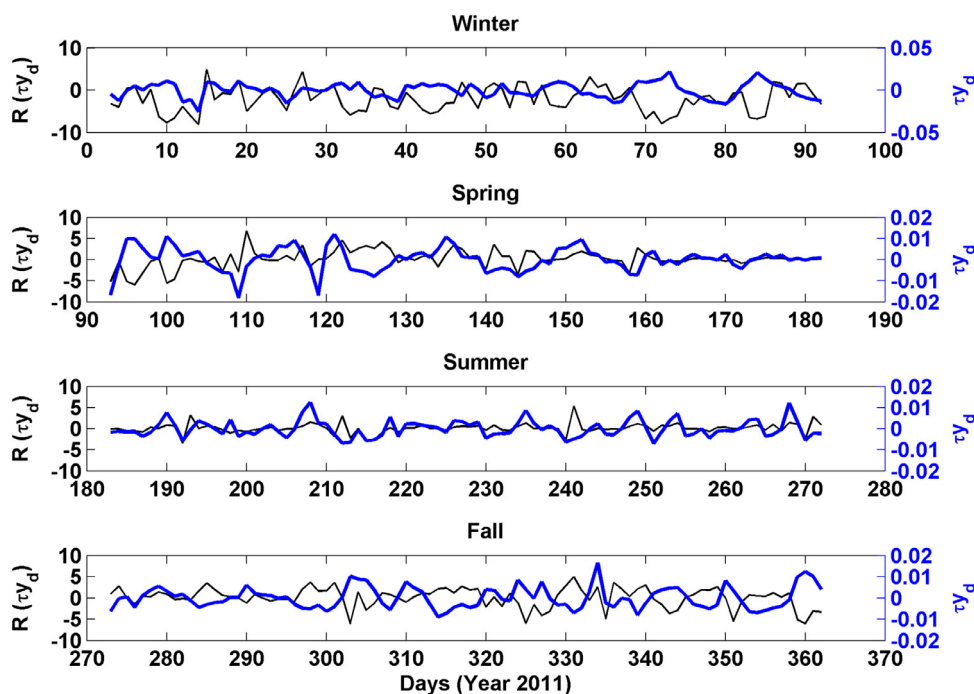


Figure 16 Difference between actual and polynomial-fitted along-shore wind stresses (τ_{y_d}) and difference between the corresponding model-obtained residual sea levels ($R(\tau_{y_d})$) for the different seasons (91-day period).

difference, that occur during the fall season, are associated with the minimal variabilities in cross-shore wind stress difference. Figure 16 shows seasonal plots of the difference between the actual and the polynomial-fitted along-shore wind stresses (Figure 4) as well as the difference between the model-obtained residual sea levels corresponding to the along-shore wind stress effect (Figure 12). The plots (Figure 16) show that, for all seasons, a dominant inverse (typical) relationship between the sea level difference and the along-shore wind stress difference is maintained. Figure 16 also shows that, during the summer season, the minimal variations in the sea level difference and the minimal variations in the along-shore wind stress difference are associated. These results indicate that the constructed NARX-based model is efficiently recognizing the short-term effects of both wind stress components on the residual sea level variations.

Evaporation Rate Effect. Sea level is known to be inversely related to evaporation rate, such that the increase in evaporation rate lowers the sea level and vice versa. Using monthly evaporation rate based on heat flux calculations by Ahmad and Sultan (1989), previous studies have suggested that this inverse relationship is not well-maintained in the central Red Sea on a seasonal level (Ahmad and Sultan, 1993; Sultan and Elghribi, 2003; Sultan et al., 1995a,b). However, some of these studies, as well as the studies by Cromwell and Smeed (1998) and Sofianos and Johns (2003), have suggested that the semiannual sea level variations are possibly related to the evaporation rate. By comparing the patterns of the residual sea level (Figure 3) and the evaporation rate (Figure 4), the typical inverse relationship seems to be somewhat maintained on the relatively long-term scale. The earlier applied Fourier analysis, in this study, revealed that for the annual and seasonal constituents,

as well as for most of the weather-band constituents, the typical inverse relationship between the residual sea level and the evaporation rate is maintained, which is the not the case for the semiannual constituents.

Figure 17 shows seasonal plots of the difference between the actual and the polynomial-fitted evaporation rates (Figure 4) as well as the difference between the model-obtained residual sea levels corresponding to the evaporation rate effect (Figure 12). These plots (Figure 17) show that, for all seasons, a typical inverse relationship is maintained between the sea level difference and the evaporation rate difference. Figure 17 also shows that, whenever the difference between the actual and polynomial-fitted evaporation rate is minimal, the difference between the corresponding model-obtained residual sea levels is also minimal. These results indicate that the constructed NARX-based model is efficiently recognizing the effect of the short-term evaporation rate variability on the residual sea level variations.

Combined Effects. The above investigations have focused mainly on demonstrating the ability of the developed NARX-based model (network) to efficiently recognize the role played by each atmospheric variable individually on the residual sea level variations. In this sub-section, the focus is shifted to investigating the combined effect of atmospheric variables on residual sea level on a seasonal basis.

Taking into consideration the typical relationships between the residual sea level and each of the atmospheric variables, four 30-day periods are visually selected from Figures 13–17 such that each period clearly represents the corresponding season and reflects the typical relationships. In each of these four 30-days periods, the earlier proven significant weather-band variations (~4–30 days) are contained. For each of these four periods (seasons), cross-

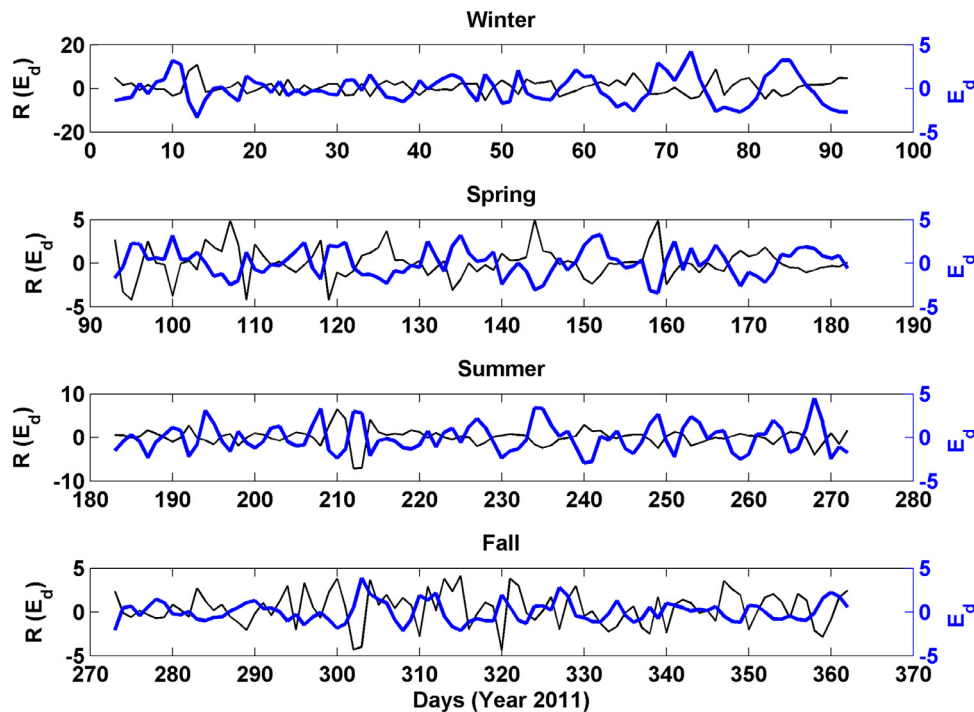


Figure 17 Difference between actual and polynomial-fitted evaporation rates (E_d) and difference between the corresponding model-obtained residual sea levels ($R(E_d)$) for the different seasons (91-day period).

Table 7 Correlation coefficients (r) calculated seasonally (30-day periods) amongst the difference between each atmospheric variable's actual and polynomial-fit timeseries and the difference between the correspondingly obtained residual sea levels.

| Affecting Variable | Seasons | | | |
|--------------------|---------|--------|--------|-------|
| | Winter | Spring | Summer | Fall |
| P | -0.68 | -0.63 | -0.62 | -0.47 |
| T | -0.30 | 0.53 | -0.26 | 0.08 |
| τ_x | 0.73 | 0.36 | 0.82 | 0.02 |
| τ_y | -0.58 | -0.13 | 0.26 | -0.70 |
| E | -0.76 | -0.82 | -0.80 | -0.43 |

covariances are obtained from the difference between the model-obtained sea levels (corresponding to an atmospheric variable effect) and the difference between that specific atmospheric variable's actual and polynomial-fitted records. Figures 18–21 show the results of the cross-covariance analysis for the winter, spring, summer, and fall seasons, respectively. Table 7 shows the correlation coefficients obtained among each pair of differences (effect, variable) for the four 30-day periods corresponding to the different seasons. These obtained cross-covariances and correlation coefficients indicate the extent to which the short-term variations of each of these atmospheric variables are influencing the short-term sea level variations during each (season representing) period.

For the period corresponding to the winter season, Figure 18 shows that, except for the air temperature effect,

relatively high (\pm) cross-covariances are obtained at zero lag between each atmospheric variable difference and the corresponding sea level difference. The cross-covariances (Figure 18) and the correlation coefficients (Table 7) indicate that atmospheric pressure, wind stress components and evaporation rate are the main responsible factors for the weather-band sea level variations during this period. For the air temperature effect, both the ($-$) cross-covariance at zero lag and the ($-$) correlation coefficient indicate that the air temperature effect is probably masked by the apparently significant effect of the cross-shore wind stress component. The significant ($+$) cross-covariance at lag (-2 days) of the air temperature effect can be attributed to the significant drop in the cross-covariance corresponding to the cross-shore wind stress effect at this specific lag. During the winter season, the central Red Sea is characterized by the convergence of the monsoonal NNW and SSW winds in the northern and southern Red Sea respectively. This convergence, which magnitude is affected by the winter intensification of the along-axis wind stress in the northern part, causes a significant rise in the sea level to an extent that masks the combined sea level depressing effects of the high atmospheric pressure and the low air temperature during this season.

The period corresponding to the spring season (Figure 19) is characterized by the air temperature effect's significantly higher ($+$) cross-covariance at zero lag, which can be attributed mainly to the drop (compared to winter) in the ($+$) cross-covariances corresponding to the cross-shore wind stress component. The drop in the ($-$) cross-covariances, corresponding to the along-shore wind stress component (compared to winter), is also probably responsible for the apparently high ($-$) cross-covariance corresponding to the

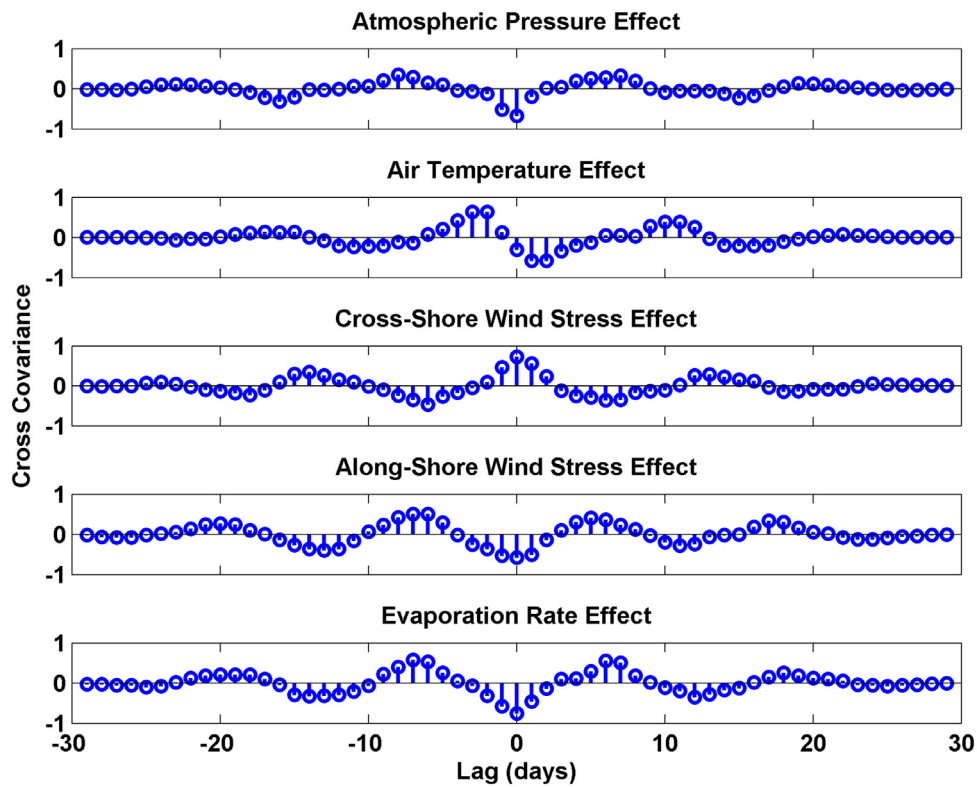


Figure 18 Cross-covariance functions amongst the difference between actual and polynomial-fitted atmospheric variables and the difference between the corresponding model-obtained residual sea levels for the period representing the winter season (30-days).

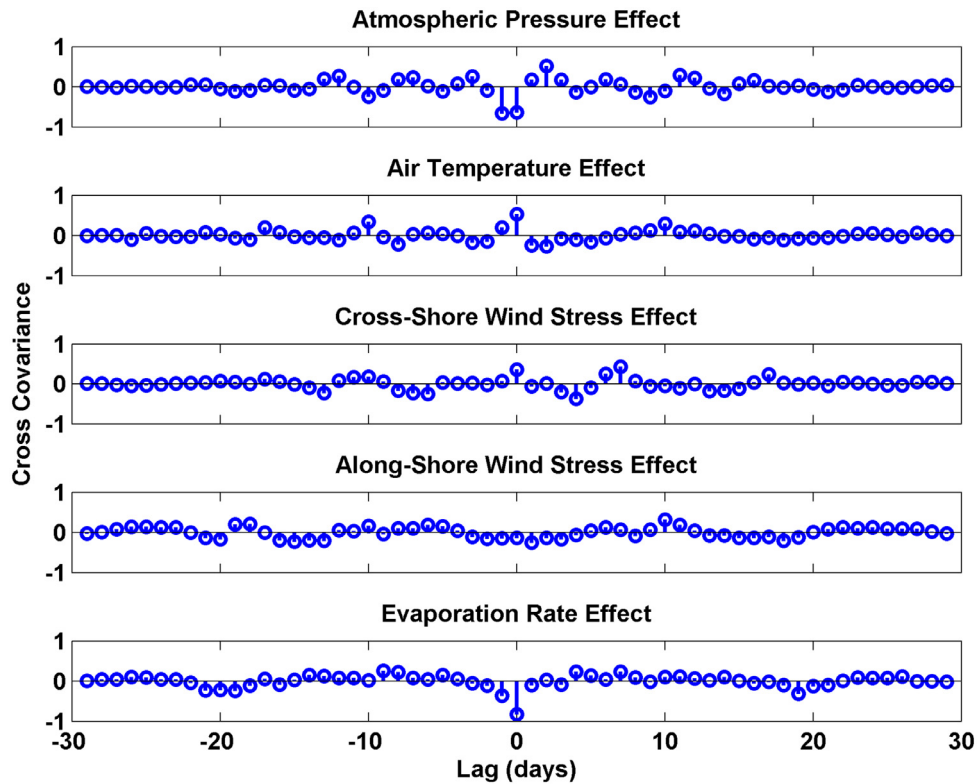


Figure 19 Cross-covariance functions amongst the difference between actual and polynomial-fitted atmospheric variables and the difference between the corresponding model-obtained residual sea levels for the period representing the spring season (30-days).

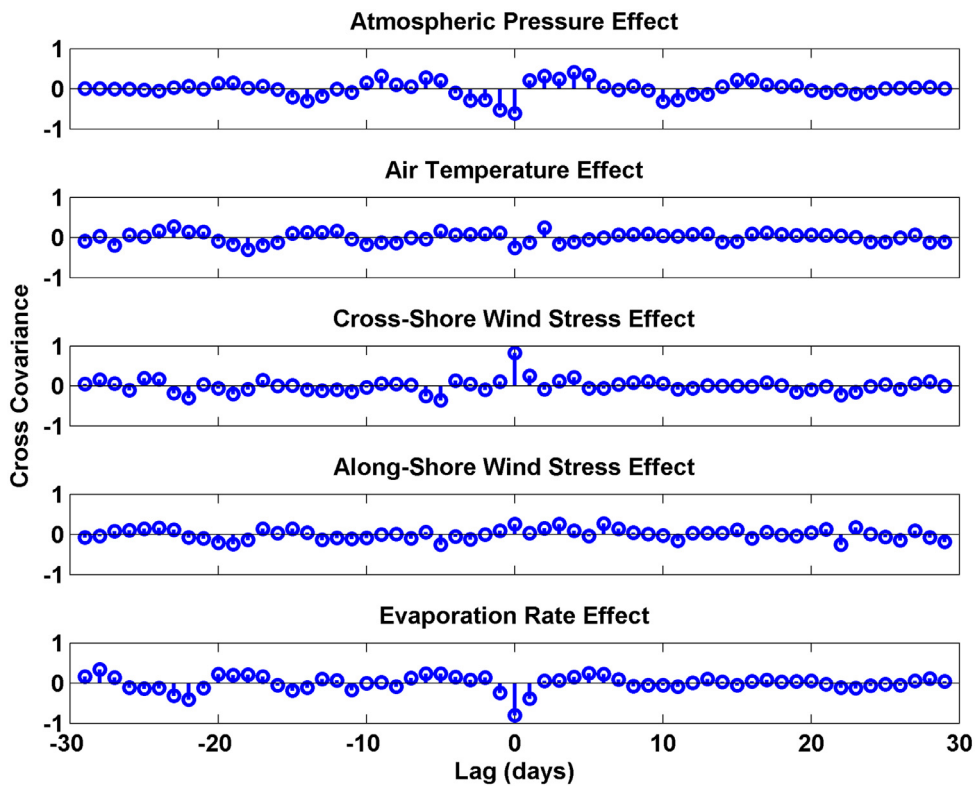


Figure 20 Cross-covariance functions amongst the difference between actual and polynomial-fitted atmospheric variables and the difference between the corresponding model-obtained residual sea levels for the period representing the summer season (30-days).

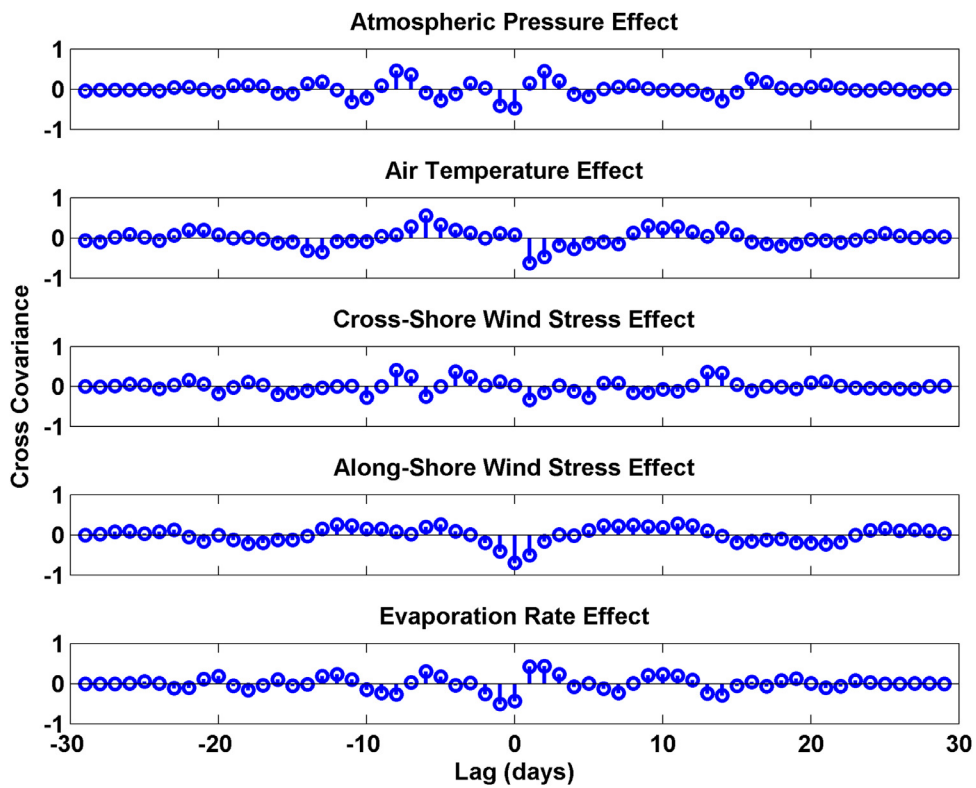


Figure 21 Cross-covariance functions amongst the difference between actual and polynomial-fitted atmospheric variables and the difference between the corresponding model-obtained residual sea levels for the period representing the fall season (30-days).

evaporation rate effect. The cross-covariances (Figure 19) and the correlation coefficients (Table 7) indicate that the short-term variations in atmospheric pressure, air temperature, and evaporation rate are mainly responsible for the short-term sea level variations during this period. During the spring season, the along-axis winds in the central part of the Red Sea weaken and become less variable before the monsoonal-related shift in the wind direction in the southern part. Additionally, during the transition period, sea level variations become more correlated to the evaporation rate variations. Consequently, as a result of this weakening of the along-axis wind, the sea level will start to drop gradually throughout the rest of the season.

The period corresponding to the summer season (Figure 20) is characterized by the significantly high (+) cross-covariance corresponding to the cross-shore wind stress effect at zero lag. In comparison to the other seasons, this period is also characterized by the shift (+) in both the cross-covariance and the correlation coefficient corresponding to the along-shore wind stress effect. The associated drop and shift (–) in the cross covariance (compared to spring) corresponding to air temperature suggests that the air temperature effect is, again, highly masked by the cross-shore wind stress component effect. The cross-covariances (Figure 20) and the correlation coefficients (Table 7) indicate that the short-term variations in atmospheric pressure, cross-shore wind stress, and evaporation rate are mainly responsible for the short-term sea level variations during this period. During the summer season, the central Red Sea is highly affected by the strong wind jets that blow eastward, almost on a daily basis, from the westerly located Tokar Gap. The southward Ekman transport of seawater, associated with such strong winds, will cause the sea level to drop to its lowest level during the summer season. This drop in sea level is significantly large in magnitude to the extent that it masks the combined sea level rising effects of both low atmospheric pressure and high air temperature during this season.

For the period corresponding to the fall season, Figure 21 shows a significant drop in the (–) cross-covariance corresponding to the evaporation rate effect at zero lag (compared with the other seasons). This drop is probably attributed to the masking effect exerted by along-shore wind stress, in which its corresponding effect reaches its highest (–) cross covariance during this period. The slight increase in the cross-covariance corresponding to the evaporation rate effect at lag (–1) days, which is associated with a decrease in the cross-covariance corresponding to the along-shore wind stress effect, at this lag, supports this masking effect possibility. The cross-covariances (Figure 21) and the correlation coefficients (Table 7) indicate that the short-term sea level variations, during this period, are influenced mainly by the along-shore wind stress component and slightly by the atmospheric pressure and evaporation rate. Neither the air temperature nor the cross-shore wind stress component seems to have any influence. During the fall season, the southern part of the Red Sea experiences the monsoonal-related shift in the wind direction, while the northern part experiences the early intensification of the NNW winds. Consequently, the sea level will start rising gradually throughout the rest of the season.

5. Conclusions

Statistical and Fourier analyses of the daily-averaged records of the residual sea level and the utilized atmospheric variables revealed that all these records do vary not only on a seasonal scale but also in a relatively short-term (within the season). The Fourier analysis of these records also revealed that most of the short-term variations are contained within the weather-band range (~4–30 days).

Forced by the tapped-delayed daily-averaged records of atmospheric variables and residual sea level, the constructed NARX-based model showed high performance in accurately predicting the one-step-ahead residual sea level, indicating that the model was able to capture the non-linear relationships between the residual sea level and the forcing atmospheric variables. The statistical analysis of the error (explaining less than 10% of the total variance) revealed the seasonal variations in the magnitude of this error. The Fourier analysis of the error indicated that it is mainly attributed to other unaccounted-for atmospheric and/or oceanographic factors that vary mainly with periods contained within the weather-band range.

Utilizing the developed model to investigate the separate role of the atmospheric variables on the residual sea level revealed that the model efficiently recognizes the typical role of each atmospheric variable. The investigation also revealed that the role played by each atmospheric variable could vary significantly in magnitude from one season to another. The minimum effect of atmospheric pressure on the residual sea level variations occurred during the fall season, while the maximum effect of air temperature occurred in the spring season. The cross-shore wind stress effect on the residual sea level reaches its maximum during the winter season while the along-shore wind stress effect reached its minimum during the summer season. The evaporation rate effect on sea level variation reached its maximum and minimum during the winter and fall seasons, respectively.

The investigation pertaining to the combined effect of atmospheric variables, on the relatively short-term sea level variations, revealed that some atmospheric variables can have significant masking effects on the typical role played by other atmospheric variables in affecting sea level variations. During both winter and summer seasons, the significant effect of the cross-shore wind stress component seemed to be masking the typical air temperature effect on the residual sea level variation. The typical effect of the evaporation rate on the residual sea level variations seemed to be masked by the significant effect of the along-shore wind stress, during both the winter and fall seasons.

The results obtained, in this study, clearly demonstrated the effectiveness of the applied NARX (neurocomputing) approach not only to accurately simulate the residual sea level variations that are induced by the atmospheric variables but also to investigate further the individual and the combined role of these atmospheric variables on residual sea level variations.

Acknowledgement

The authors would like to thank Saudi Aramco for providing the sea level and atmospheric data collected at Jeddah.

Thanks are also due to the General Authority of Meteorology and Environmental Protection (GAMEP) for making available the atmospheric parameters record for Jeddah.

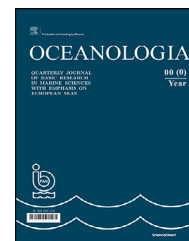
References

- Abdallah, A.M., Eid, F.M., 1989. On the Steric Sea Level in the Red Sea. *International Hydrographic Review*, Monaco LXVI (1), 115–124, <https://journals.lib.unb.ca/index.php/ihr/article/view/23351/27126>.
- Abdelrahman, S.M., 1997. Seasonal Fluctuation of Mean Sea Level at Gizan, Red Sea. *J. Coast. Res.* 13 (4), 1166–1172, https://www.jstor.org/stable/4298725?seq=1#page_scan_tab_contents.
- Ahmad, F., Sultan, S.A.R., 1989. Surface heat fluxes and their comparison with the oceanic heat flow in the Red sea. *Oceanol. Acta* 12 (1), 33–36, <https://archimer.ifremer.fr/doc/00106/21751/19324.pdf>.
- Ahmad, F., Sultan, S.A.R., 1993. Tidal and Sea Level Changes at Jeddah, Red Sea. *Pakistan J. Mar. Sci.* 2 (2), 77–84, <https://core.ac.uk/download/pdf/33719829.pdf>.
- Alawad, K.I., Al-Subhi, A.M., Alsaafani, M.A., Alraddadi, T.M., 2017. Signature of tropical climate modes driven signals on the Red Sea and Gulf of Aden sea level. *Indian J. Geo-Mar. Sci.* 46 (10), 2088–2096, <http://nopr.niscair.res.in/handle/123456789/42751>.
- Basheer, I., Hajmeer, M., 2000. Artificial Neural Networks: Fundamentals, Computing, Design, and Application. *J. Microbiol. Methods* 43 (1), 3–31, [https://doi.org/10.1016/S0167-7012\(00\)00201-3](https://doi.org/10.1016/S0167-7012(00)00201-3).
- Beale, M.H., Hagan, M.T., Demuth, H.B., 2014. *Neural Network Toolbox™ User's Guide*. The MathWorks, Inc., Natick, MA, USA.
- Churchill, J.H., Abualnaja, Y., Limeburner, R., Nellayaputhen-peedika, M., 2018. The Dynamics of Weather-Band Sea Level Variations in the Red Sea. *Reg. Stud. Mar. Sci.* 24, 336–342, <https://doi.org/10.1016/j.rmsa.2018.09.006>.
- Cromwell, D., Smeed, D.A., 1998. Altimetric Observations of Sea Level Cycles Near the Strait of Bab al Mandab. *Int. J. Remote Sens.* 19, 1561–1578, <https://doi.org/10.1080/014311698215351>.
- Cox, D.T., Tissot, P., Michaud, P., 2002. Water Level Observations and Short-Term Predictions Including Meteorological Events for Entrance of Galveston Bay, Texas. *J. Waterw. Port C-ASCE* 128 (1), 21–29, [https://doi.org/10.1061/\(ASCE\)0733-950X\(2002\)128:1\(21\)](https://doi.org/10.1061/(ASCE)0733-950X(2002)128:1(21)).
- De Lange, W.P., Carter, R.M., 2014. *Sea-Level Change: Living with Uncertainty*. The Global Warming Policy Foundation, GWPF Rep. 15, London, UK, 48 pp.
- Deo, M.C., Chaudhari, G., 1998. Tide Prediction Using Neural Networks. *Compu-Aided. Civ. Inf.* 13 (2), 113–120, <https://doi.org/10.1111/0885-9507.00091>.
- Eid, F.M., Abdallah, A.M., 1994. The Relations Between Steric Components and Hydrographic parameters in the Red Sea. *Bull. Fac. Sc. Alex. Univ.* 34 (1), 97–105.
- Eid, F.M., Kamel, M.S., 2004. Contribution of Water Density to Sea Level Fluctuations in Red Sea. *J. KAU. Mar. Sci.* 15 (1), 113–138, https://www.kau.edu.sa/Files/320/Researches/51831_21963.pdf.
- Eltai, E.B.A., 2010. Tides analysis in the Red Sea in port Sudan and Gizan. *Geophys. Insti., Univ., Bergen, Norway*, 61 pp.
- Emery, W.J., Thomson, R.E., 2001. *Data Analysis Methods in Physical Oceanography*. 2nd Edn. Elsevier Sci. B.V., Amsterdam, 638 pp.
- Ghorbani, M.A., Khatibi, R., Aytek, A., Makarynsky, O., Shiri, J., 2010. Sea Water Level Forecasting Using Genetic Programming and Comparing the Performance with Artificial Neural Networks. *Comput. Geosci.* 36 (5), 620–627, <https://doi.org/10.1016/j.cageo.2009.09.014>.
- Hecht-Nielsen, R., 1990. *Neurocomputing*. Addison-Wesley, Boston, 433 pp.
- Herting, A., Farmer, T., Evans, J., 2004. Mapping of the evaporative loss from Elephant Butte reservoir using remote sensing and GIS technology. *New Mexico State Univ. Rep., USA*, 30 pp.
- Islam, P., Morimoto, T., 2015. Performance Prediction of Solar Collector Adsorber Tube Temperature using a Nonlinear Autoregressive Model with exogenous Input. *IJCA* 114 (12), 24–32, <https://doi.org/10.5120/20031-2129>.
- Jiang, H., Farrar, J.T., Beardsley, R.C., Chen, R., Chen, C., 2009. Zonal Surface Wind Jets across the Red Sea due to Mountain Gap Forcing along both sides of the Red Sea. *Geophys. Res. Lett.* 36 (19), art. no. L19605, 6 pp, <https://doi.org/10.1029/2009GL040008>.
- Karimi, S., Kisi, O., Shiri, J., Makarynsky, O., 2013. Neuro-fuzzy and Neural Network Techniques for Forecasting Sea Level in Darwin Harbor, Australia. *Comput. Geosci.* 52, 50–59, <https://doi.org/10.1016/j.cageo.2012.09.015>.
- Kisi, O., Karimi, S., Shiri, J., Makarynsky, O., Yoon, H., 2014. Forecasting Sea Water Levels at Mukho Station, South Korea Using Soft Computing Techniques. *Int. J. Oce. Climate Sys.* 4, 175–188, <https://doi.org/10.1260/1759-3131.5.4.175>.
- Large, W.G., Pond, S., 1981. Open Ocean Momentum Flux Measurements in Moderate to Strong Winds. *J. Phys. Oceanogr.* 11, 324–336, [https://doi.org/10.1175/1520-0485\(1981\)011%3C0324:OOMFM%3E2.0.CO;2](https://doi.org/10.1175/1520-0485(1981)011%3C0324:OOMFM%3E2.0.CO;2).
- Lee, T.L., Makarynsky, O., Shao, C.C., 2007. A Combined Harmonic Analysis-Artificial Neural Network Methodology for Tidal Predictions. *J. Coast. Res.* 23 (3), 764–770, <https://doi.org/10.2112/05-0492.1>.
- Li, Y., Han, W., 2015. Decadal Sea Level Variations in the Indian Ocean Investigated with HYCOM: Roles of Climate Modes, Ocean Internal Variability, and Stochastic Wind Forcing. *J. Clim.* 28, 9143–9165, <https://doi.org/10.1175/JCLI-D-15-0252.1>.
- Londhe, S., 2011. Forecasting Water Levels Using Artificial Neural Networks. *Int. J. Oce. Climate Sys.* 2 (2), 119–135, <https://doi.org/10.1260/1759-3131.2.2.119>.
- Madah, F., Mayerle, R., Bruss, G., Bento, J., 2015. Characteristics of Tides in the Red Sea Region, a Numerical Model Study. *OJMS* 05 (02), 193–209, <https://doi.org/10.4236/ojms.2015.52016>.
- Maghrabi, S.O., 2003. *Variations of Mean Sea Level in the Red Sea SCS thesis*. King Abdulaziz Univ., Saudi Arabia.
- Mahmoud, S., 2012. *Identification and Prediction of Abnormal Behaviour Activities of Daily Living in Intelligent Environments*. Nottingham Trent Univ., UK, 177 pp.
- Makarynska, D., Makarynsky, O., 2008. Predicting Sea-level Variations at the Cocos (Keeling) Islands with Artificial Neural Networks. *Comput. Geosci.* 34 (12), 1910–1917, <https://doi.org/10.1016/j.cageo.2007.12.004>.
- Makarynsky, O., Makarynska, D., Kuhn, M., Featherstone, W.E., 2004. Predicting Sea Level Variations with Artificial Neural Networks at Hillarys Boat Harbour, Western Australia. *Estuar. Coast. Shelf. Sci.* 61 (2), 351–360, <https://doi.org/10.1016/j.ecss.2004.06.004>.
- Manasrah, R., Hasanean, H.M., Al-Rousan, S., 2009. Spatial and seasonal variations of sea level in the Red Sea, 1958–2001. *Ocean. Sci. J.* 44 (3), 145–159, <https://doi.org/10.1007/s12601-009-0013-4>.
- Milne, G.A., Gehrels, W.R., Hughes, C.W., Tamisiea, M.E., 2009. Identifying the Causes of Sea-level Change. *Nat. Geosci.* 2 (7), 471–478, <https://doi.org/10.1038/ngeo544>.
- Moghadam, F.M., 2016. Neural Network-Based Approach for Identification of Meteorological Factors Affecting Regional Sea-Level Anomalies. *J. Hydrologic. Eng-ASCE*. 22 (3), [https://doi.org/10.1061/\(ASCE\)HE.1943-5584.0001472](https://doi.org/10.1061/(ASCE)HE.1943-5584.0001472).

- Mohamad, K.I., 2012. Sea Level Variation in the Red Sea Based on SODA data M.Sc. thesis. Geophys. Inst., Univ., Bergen, Norway, 47 pp.
- Nitsure, S.P., Londhe, S.N., Khare, K.C., 2014. Prediction of Sea Water Levels Using Wind Information and Soft Computing Techniques. *Appl. Ocean. Res.* 47, 344–351, <https://doi.org/10.1016/j.apor.2014.07.003>.
- Osman, M.M., 1984. Variations of Sea Level at Port Sudan. *Int.l Hydrographic Rev.* LXI, 137–144.
- Parker, B.B., 2007. Tidal Analysis and Prediction. National Ocean Service, NOAA Spec. Publ. <https://doi.org/10.25607/OBP-191>.
- Pashova, L., Popova, S., 2010. Daily Sea Level Forecast at Tide Gauge Burgas, Bulgaria Using Artificial Neural Networks. *J. Sea Res.* 66, 154–161, <https://doi.org/10.1016/j.seares.2011.05.012>.
- Patzert, W.C., 1972. Seasonal Variations in Structure and Circulation in the Red Sea Ph.D. thesis. Univ. Hawaii, Honolulu, 186 pp.
- Patzert, W.C., 1974. Wind-induced Reversal in Red Sea Circulation. *Deep-Sea Res* 21, 109–121, [https://doi.org/10.1016/0011-7471\(74\)90068-0](https://doi.org/10.1016/0011-7471(74)90068-0).
- Pawlowicz, R., Beardsley, B., Lentz, S., 2002. Classical Tidal Harmonic Analysis Including Error Estimates in Matlab Using T-tide. *Comput. Geosci.* 28 (8), 929–937, [https://doi.org/10.1016/S0098-3004\(02\)00013-4](https://doi.org/10.1016/S0098-3004(02)00013-4).
- Pugh, D., Woodworth, P., 2014. *Sea-Level Science: Understanding Tides, Surges, Tsunamis and Mean Sea-Level Changes*, 2nd edn. Cambridge Univ. Press, 407 pp.
- Pugh, D.T., 1981. Tidal Amphidrome Movement and Energy Dissipation in the Irish Sea. *Geophys. J. Roy. Astr. Soc.* 67, 515–527, <https://doi.org/10.1111/j.1365-246X.1981.tb02763.x>.
- Pugh, D.T., 1987. *Tides, Surges and Mean Sea Level*. John Wiley & Sons Ltd., 472 pp.
- Pugh, D.T., Abualnaja, Y., 2015. Sea-Level changes. In: Rasul, N.M.A., Stewart, I.C.F. (Eds.), *The Red Sea: the formation, morphology, oceanography and environment of a young ocean basin*. Springer Earth System Sciences, Berlin, Heidelberg, 317–328, https://doi.org/10.1007/978-3-662-45201-1_18.
- Pugh, D.T., Abualnaja, Y., Jarosz, E., 2019. The Tides of the Red Sea. In: Rasul, N.M.A., Stewart, I.C.F. (Eds.), *Oceanographic and Biological Aspects of the Red Sea*. Springer, Cham, 11–40, https://doi.org/10.1007/978-3-319-99417-8_2.
- Rakshith, S., Dwarakish, G.S., Natesan, U., 2014. Tidal-level Forecasting Using Artificial Neural Networks Along the West Coast of India. *JSCE* 2 (1), 176–187, https://doi.org/10.2208/journalofjsce.2.1_176.
- Salim, A.M., Dwarakish, G.S., Liju, K.V., Justin, T., Gayathri, D., Rajeesh, R., 2015. Weekly Prediction of Tides Using Neural Networks. *Procedia Eng.* 116 (1), 678–682, <https://doi.org/10.1016/j.proeng.2015.08.351>.
- Sertel, E., Cigizoglu, H.K., Sanli, D.U., 2008. Estimating Daily Mean Sea level Using Artificial Neural Networks. *J. Coast. Res.* 24 (3), 727–734, <https://doi.org/10.2112/06-742.1>.
- Shamji, V.R., Vineesh, T.C., 2017. Shallow-Water Tidal Analysis at Sharm Obhur, Jeddah, Red Sea. *Arab. J. Geosci.* 10 (3), 11 pp., <https://doi.org/10.1007/s12517-016-2822-y>.
- Sofianos, S.S., Johns, W.E., 2001. Wind Induced Sea Level Variability in the Red Sea. *Geophys. Res. Lett.* 28 (16), 3175–3178, <https://doi.org/10.1029/2000GL012442>.
- Sofianos, S.S., Johns, W.E., 2003. An Oceanic General Circulation Model (OGCM) Investigation of the Red Sea circulation: 2. Three-dimensional Circulation in the Red Sea. *J. Geophys. Res.* 108 (C3), 15 pp., <https://doi.org/10.1029/2001JC001185>.
- Sultan, S.A.R., Ahmad, F., 2000. Annual and Semi-annual Variations of Sea Level at Jeddah, Central Coastal Station of the Red Sea. *Indian J. Mar. Sci.* 29 (3), 201–205, <http://nopr.niscair.res.in/bitstream/123456789/25521/1/IJMS%2029%283%29%20201-205.pdf>.
- Sultan, S.A.R., Ahmad, F., Elghribi, N.M., 1995a. Sea Level Variability in the Central Red Sea. *Oceanol. Acta* 18 (2), 607–615, <https://archimer.ifremer.fr/doc/00096/20766/>.
- Sultan, S.A.R., Ahmad, F., El-Hassan, A., 1995b. Seasonal Variations of the Sea Level in the Central Part of the Red Sea. *Estuar. Coast. Shelf Sci.* 40, 1–8, [https://doi.org/10.1016/0272-7714\(95\)90008-X](https://doi.org/10.1016/0272-7714(95)90008-X).
- Sultan, S.A.R., Ahmad, F., Nassar, D., 1996. Relative contributions of external sources of mean sea-level variations at Port Sudan, Red Sea. *Estuar. Coast. Shelf Sci.* 42 (1), 19–30, <https://doi.org/10.1006/ecss.1996.0002>.
- Sultan, S.A.R., Elghribi, N.M., 2003. Sea Level Changes in the Central Part of the Red Sea. *Indian J. Mar. Sci.* 32 (2), 114–122, [http://nopr.niscair.res.in/bitstream/123456789/4254/1/IJMS%2032\(2\)%20114-122.pdf](http://nopr.niscair.res.in/bitstream/123456789/4254/1/IJMS%2032(2)%20114-122.pdf).
- Tsai, C.P., Lee, T.L., 1999. Back-Propagation Neural Network in Tidal-level Forecasting. *J. Waterw. Port C-ASCE*. 125, 195–202, [https://doi.org/10.1061/\(ASCE\)0733-950X\(1999\)125:4\(195\)](https://doi.org/10.1061/(ASCE)0733-950X(1999)125:4(195)).
- Wahr, J., Smeed, D.A., Leuliette, E., Swenson, S., 2014. Seasonal Variability of the Red Sea, from Satellite Gravity, Radar Altimetry, and in Situ Observations. *J. Geophys. Res.-Oceans* 119, 5091–5104, <https://doi.org/10.1002/2014JC010161>.
- Willis, J.K., Chambers, D.P., Nerem, R.S., 2008. Assessing the Globally Averaged Sea Level Budget on Seasonal to Interannual Timescales. *J. Geophys. Res.-Oceans* 113 (C6), 9 pp., <https://doi.org/10.1029/2007JC004517>.
- Zhai, P., Bower, A.S., 2013. The Response of the Red Sea to a Strong Wind Jet Near the Tokar Gap in Summer. *J. Geophys. Res.-Oceans* 118 (1), 422–434, <https://doi.org/10.1029/2012JC008444>.
- Zubier, K.M., 2010. Sea Level Variations at Jeddah, Eastern Coast of Red Sea. *J. KAU. Mar. Sci.* 21 (2), 73–86, https://www.kau.edu.sa/Files/320/Researches/59382_29726.pdf.

Available online at www.sciencedirect.com

ScienceDirect

journal homepage: www.journals.elsevier.com/oceanologia

ORIGINAL RESEARCH ARTICLE

Rip currents in the non-tidal surf zone with sandbars: numerical analysis versus field measurements

Aleksandra Dudkowska^{a,*}, Aleksandra Boruń^a, Jakub Malicki^b,
Jan Schönhofer^b, Gabriela Gic-Grusza^a

^aUniversity of Gdańsk, Institute of Oceanography, Gdynia, Poland

^bInstitute of Hydro-Engineering, Polish Academy of Sciences, Gdańsk, Poland

Received 14 August 2019; accepted 7 February 2020

Available online 22 February 2020

KEYWORDS

Rip current;
Coastal zone;
Coastal flows;
Wind-wave conditions

Summary Rip currents, which are local seaward-directed jets with their mean velocity exceeding 0.5 m/s, have been a subject of many studies since the 1940s. They are an important part of the nearshore current system and in specific hydro- and geomorphological conditions can cause changes in the local bathymetry. Thus, a detailed analysis of the characteristics of this phenomenon is crucial both to public safety and hydroengineering. The main purpose of this research is to determine the wave conditions of a multi-bar non-tidal coastal zone environment in which rip currents can occur. In this study, we focus on a multi-bar non-tidal coastal zone environment located in the Southern Baltic Sea, where rip current driving forces are mostly reduced to the wind and wind-induced waves. This is one of very few comprehensive approaches to exploring the possibility of rip currents occurrence in such environmental conditions. During two field expeditions, there were carried out in situ measurements exploiting two GPS drifters. The results indicate the formation of irregular non-longshore flows (related to rip currents) in the studied area. To answer the question under what conditions the formation of rip currents takes place, an extended modelling experiment was performed. Deep-water wave conditions typical of the studied area were chosen due to buoy measurements. The total of 589 combinations of the significant wave height, the mean period and wave direction values were examined

* Corresponding author at: University of Gdańsk, Institute of Oceanography, Piłsudskiego 46, 81–378 Gdynia, Poland.

E-mail address: aleksandra.dudkowska@ug.edu.pl (A. Dudkowska).

Peer review under the responsibility of the Institute of Oceanology of the Polish Academy of Sciences.



Production and hosting by Elsevier

<https://doi.org/10.1016/j.oceano.2020.02.001>

0078-3234/© 2020 Institute of Oceanology of Polish Academy of Sciences. Production and hosting by Elsevier B.V. This is an open access article under the CC BY-NC-ND license (<http://creativecommons.org/licenses/by-nc-nd/4.0/>).

as test cases. The coastal flow in the area and tracks of virtual drifters were simulated by XBeach numerical model for all test cases. As a result, 589 nearshore currents fields were generated and two scenarios were indicated: a regular circulation (dominated by the longshore current) which is typical of this area (547 cases), and flows with rip current features (42 cases). This reflects the results of the field measurements carried out. It can be concluded that the wave direction is a dominating factor in the formation of rip currents. Namely the flows of this type may occur in the area of interest when the direction of a deep water wave is almost perpendicular to the shore. Such situations occur rarely. They cover about 7% of the days of the year. Thus, rip currents do not appear to be a significant factor in the reconstruction of the sea bottom in the studied area.

© 2020 Institute of Oceanology of Polish Academy of Sciences. Production and hosting by Elsevier B.V. This is an open access article under the CC BY-NC-ND license (<http://creativecommons.org/licenses/by-nc-nd/4.0/>).

1. Introduction

Coastal zone morphodynamics of the non-tidal inner sea is affected by complex three-dimensional flows of water, generated mostly by waves. Coastal sediment transport is primarily caused by the so-called longshore current, which is the dominating part of the current system. Cross-shore sediment transport is normally induced by the undertow. Such hydrodynamics is directly related to multi-bar seabed forms. Apart from these typical flows, some specific hydro- and geomorphological conditions occasionally form seaward-directed quasi-steady jets. These so-called rip currents originate within the surf zone and broaden outside the breaking region. The physical driving mechanisms crucial to the generation of rip currents is alongshore variability in breaking wave energy dissipation (Pitman et al., 2016). There have been identified a number of different causes of this variability, which is linked to the different types of rip currents along beaches (Castelle et al., 2016; Kirby, 2017). According to the traditional approach, a typical hydrodynamic background is the convergence of the two opposite-directed longshore flows, i.e. feeder currents, resulting from the longshore variability of the wave-induced set-up, caused by the gradients of radiation stresses (Longuet-Higgins and Stewart, 1964). The emerging offshore flow is called a rip current. It may result in a recess in the bar and if the phenomenon lasts long enough, a channel is formed. This so-called energy window is a potential place for the emergence of the next rip current, which deepens the channel. As a result of this positive feedback between waves, currents and morphology (Garnier et al., 2008), a local disturbance of the bathymetry may initiate the generation of a rip current (Sabet and Barani, 2011). This type of rips – channel rip currents – are the most documented in barred surf zones (Castelle et al., 2016). However, complex lito- and hydrodynamics can provide a number of mechanisms driving rip currents, which act simultaneously. Resulting rips are temporary in space and time. Another theoretical approach was applied by (Bruneau et al., 2011) and is based on interpretation of surf zone flows on the basis of their vorticity proposed by (Peregrine, 1998). The authors derived a conservation equation of the vertical vorticity of the mean wave-driven currents, which provides information on rip current circulations that was difficult to interpret using the traditional radiation stress approach.

One of the most commonly used approaches when observing rip currents in the environment are Lagrangian measurements combined with other methods. (Johnson and Pattiaratchi, 2004) recorded transient rip currents, with perpendicular incident swell waves, while carrying out Eulerian and Lagrangian measurements of the nearshore circulation on a longshore uniform beach in Western Australia. (Castelle et al., 2014; Floc'h et al., 2018) used human drifter data (human operators that drifted with the currents, each equipped with a GPS) and video imagery technique. The method based on color processing of video images enables researchers to detect the presence of rip currents via a change of turbidity. They detected numerous rips along the coast of the Gulf of Guinea, exposed to high-energy waves generating strong nearshore currents.

In this paper we focus on the Southern Baltic coastal zone rip currents, which are still a lesser-known phenomenon. The first traces of their occurrence were discovered in 1970 by Rudowski (Rudowski, 1970), who noticed seabed ripple marks arranged in a characteristic pattern. In the following years Furmanczyk (Furmańczyk, 1994) noted some distinctive breaks in bars in the aerial and satellite photographs of the Pomeranian Bay, which he explained by means of rip currents. Also, Pruszek (Pruszek et al., 2008) describes the periodic mega-cusps occurring on the Southern Baltic coast after a storm. Observations conducted by Schönhofer (Schönhofer, 2014), which are regarded as a pioneering study related to the scope of this work, confirmed the occurrence of rip currents in south Baltic shore. During field surveys in Coastal Research Station (CRS) Lubiato, he registered several cases of flow with some features characteristic of rip currents. The measurements with the use of two GPS drifters were carried out during approximately 20 days in years 2011–2013. The rip-current type flows were registered during 4 surveys in which there were similar wave conditions, i.e. the wave was moving from NNW to NNE, and the wave steepness was about 0.025.

These observations confirm the theory that rip currents on the dissipative coasts are induced by long waves, characterized by a small steepness (a small wave height compared to its length), and they can reach the coast without breaking over the bars. Thus, waves bring energy to the coast, the way it can be observed at the steep coasts. A favourable condition is a swell when short-wind waves disappear and long waves occur. Long waves undergo a stronger refraction,

so regardless of the direction in which they approach the shore in the deep water, they are almost perpendicular to the shore in the shallow water (Schönhofer, 2014).

Assessing the risk of rip-current occurrence is important for the scientific as well as the beach-safety purpose. A better understanding of this phenomenon is essential for the development of a predictive system working in an operational mode. Such warning systems, based on a series of measurements of the coastal zone currents were created, among others, for the south-east coast of the USA (MacMahan et al., 2006; 2005), as well as for the Dutch coast (Sembiring et al., 2014). In order to forecast, among other parameters, the possibility of rip current occurrence in the area of the Southern Baltic in selected locations, a pilot predictive system based on XBeach model in 1D mode was implemented (Furmańczyk et al., 2014). This indicator was based on the assumption that rip currents appear when waves break over submerged longshore bars near the shoreline (Short and Aagaard, 1993).

However, to develop an effective system of a rip current forecast for the Baltic, it is necessary to determine the environmental conditions that can be conducive to this phenomenon. Both in situ observations and the theory of rip currents formation suggest that: (1) the wave direction – perpendicular to the shore and (2) the wave steepness – relatively small, are conditions favourable for the generation of rip currents in the studied area. However, a small amount of observational data is insufficient to confirm these hypotheses. Detailed field measurements are difficult, because rip currents are very unpredictable. As it is problematic to observe in situ the nearshore flow in a wide range of hydro- and morphological conditions, the modelling approach seems to be the only way to investigate the phenomenon comprehensively.

Various approaches to the rip currents modelling have been taken. Generally accepted methods applied in simplified basins with regular bathymetry include 3D hydrostatic or Boussinesq modelling. In contrast, a number of modelling studies of coastal zone currents in the real environments with complex topography are based on spectral 2D models. A likely explanation is a compromise between accuracy and the computational cost. An example is the study carried out by (Johnson and Pattiaratchi, 2006) in which a spatially variable wave field was simulated with the model *Funwave* based on the fully nonlinear Boussinesq equations. For a set of different beach slopes and wave spectra variable wave-averaged currents were generated and sometimes transient rip currents were formed. On the other hand (Xie, 2012) showed, that his coupled wave–current 3D model can effectively describe the rip current 3D structures under irregular bathymetry. Apart from successful modelling attempts in artificial basins with a simplified bathymetry, modelling was carried out in the real locations with a complex sea bottom topography. Among others, interesting research was conducted for the region of Egmond aan Zee in The Netherlands, a typical area of the Dutch coast barred coastline. This location is appropriate for studying rip currents in the environment with a strong horizontal tide. A notable example is research conducted by (Winter et al., 2014) based both on (1) in-situ measurements in the surf zone with drifter instruments and (2) modelling with the use of a 2DH numerical model XBeach. Another interesting study in this

location was carried out by (Sembiring et al., 2014) in which an operational model for the nearshore zone provides the prediction of the location, strength and timing of rip currents. The study used a novel approach in which the input to an XBeach model was the video-derived bathymetry.

The aim of this study is to determine whether, under given wave conditions, the generation of rip currents in the multi-bar coastal zone of the Southern Baltic Sea is possible. Our research is the first attempt of a systematic approach to this topic, i.e. it includes all possible wave conditions in the given region. To achieve this, the following assumption was made: the factor responsible for the rip current initiation is the break in the bar – preceding non-linear complex processes leading to the formation of the rip channel are not considered. Thus, we address the research question: What is the minimal frequency of the rip currents occurrence, and whether rip currents are important factors in the processes of seabed and beach rebuilding in the multi-bar coastal zone of the non-tidal inner sea.

Both measurement data and modelling results was used in the presented study. Wave buoy measurements together with other multi-aspect field investigations carried out for many years by the Institute of Hydro-Engineering of the Polish Academy of Sciences (IBW) provided huge amount of data and observations of the coastal zone, which are the background of this study. Long-term buoy measurements provided the basis for determining deep-water wave conditions typical of the studied area. 589 modelling scenarios covers all wave conditions likely in the studied region. Lagrangian field measurements with the use of free GPS drifters were performed to estimate the local coastal flows. During these measurements a flow of rip current type was recorded, similar to this described in the work (Schönhofer, 2014). This registered flow served as an example of the phenomenon in the studied area and its features were then used to verify the results of numerical modeling. Numerical simulations are the optimal way to analyze flows for a wide range of wave conditions. The coastal flow in the area and tracks of virtual drifters were simulated by the numerical model XBeach (Roelvink et al., 2010). The set-up of the model was calibrated firstly by comparison of the modelled wave parameters to the results of SWAN model (Booij et al., 1996), which was validated in previous studies (Reda and Papińska, 2002). Secondly, the tracks of virtual tracers and their velocities were compared to the in situ measured flows. After the model calibration, a nearshore wave and currents fields were simulated for all 589 test cases.

In this work only bathymetry controlled rip currents were simulated. This is the best-documented driving mechanism in barred coastal zones, however, numerous possible scenarios of the rip current initiation are possible. The presented results indicate that the phenomenon of rip currents in the studied area is rare and that it is not a significant factor in the morphodynamic processes.

2. Study area

The study area is located in the Southern Baltic, within Polish Marine Areas (see Fig. 1), adjacent to the coastline in the vicinity of Lubiatowo village, where The Coastal Research Station (CRS) – a field laboratory of the Institute of Hydro-

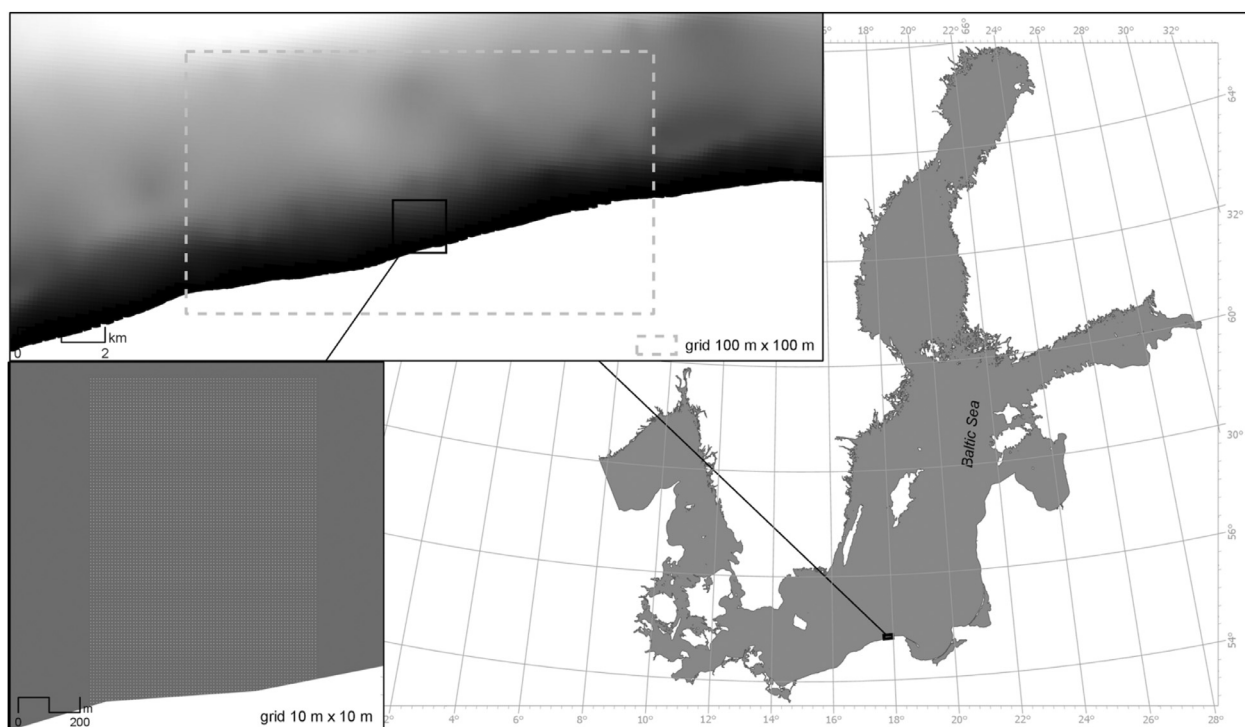


Figure 1 Area of interest and the computational meshes used in numerical modelling: SWAN external grid 100 m × 100 m; SWAN (internal) and XBeach grid 10 m × 10 m.

Engineering of the Polish Academy of Sciences (IBW PAN) – is situated. This area is well-researched and is a representative sample of the Southern Baltic coast. It is characterized by a rather stable shore, with a mild erosive tendency observed over the last years. The slope of the sea bottom is approximately 1.5% (with a value of up to 4% locally, near the shoreline). Along the section of the shore, there can typically be five offshore bars: four permanent and one occurring temporarily, in the distances from the shoreline of approximately: 100–120 m, 200 m, 400–450 m, 650–850 m. As it is difficult to perform bathymetric measurements during strong waves, typical bathymetry for Lubiatowo area was used for modelling, Fig. 2. Principal water depth is about 8 m at 1 km from the shoreline and it increases to about 15–17 m at 2 km and to 25 m at 9 km. The bottom profile is relatively uniform along the coastline (Ostrowski et al., 2016).

3. Material and methods

Nearshore flow measurements

In order to examine nearshore flow in situ, two field surveys in CRS Lubiatowo under different deep water wave con-

Table 2 The technical specification of drifters.

| | ballast [kg] | displacement [dm ³] | height [m] | immersion [m] |
|---|-----------------|------------------------------------|---------------|------------------|
| A | 2 | 2.5 | 0.8 | 0.2 |
| B | 7 | 7.5 | 1.0 | 0.2 |

ditions were carried out: 14.01.2016 the significant wave height H_s was about 1.8 m and the wave steepness ξ was about 0.02, while 15.04.2016 H_s was about 0.5 m and ξ was about 0.01. Other weather and sea conditions during expeditions are summarized in Table 1.

Lagrangian field measurements were carried out with the use of free GPS drifters. Both the preparation of the GPS drifters and the organization of the field expeditions were carried out by IBW. Two drifters (marked A and B) with GPS modules with internal memory attached were used. The drifters were released near the coastline, their positions were recorded and the coastal flows were estimated. For technical details see Fig. 3 and Table 2.

The drifters are built of buoy and ballast that stabilized movement on the water surface. Additionally there was

Table 1 Environmental conditions during field expeditions: wave data from a wave buoy located about 1.5 NM offshore (54°50.360'N, 17°50.301'E), the water depth in the buoy location is about 18 m. The experiments were performed within less than one hour the period in which wind and wave conditions could be considered stable.

| | H_s [m] | T_p [s] | ξ | Θ_{wave} [°] | T_{water} [°C] | T_{air} [°C] |
|------------|-----------|-----------|-------|----------------------------|-------------------------|-----------------------|
| 14.01.2016 | 1.8 | 7.7 | 0.02 | 11 | 0.5 | 4.3 |
| 15.04.2016 | 0.5 | 6.5 | 0.01 | 5 | 7.0 | 13.0 |

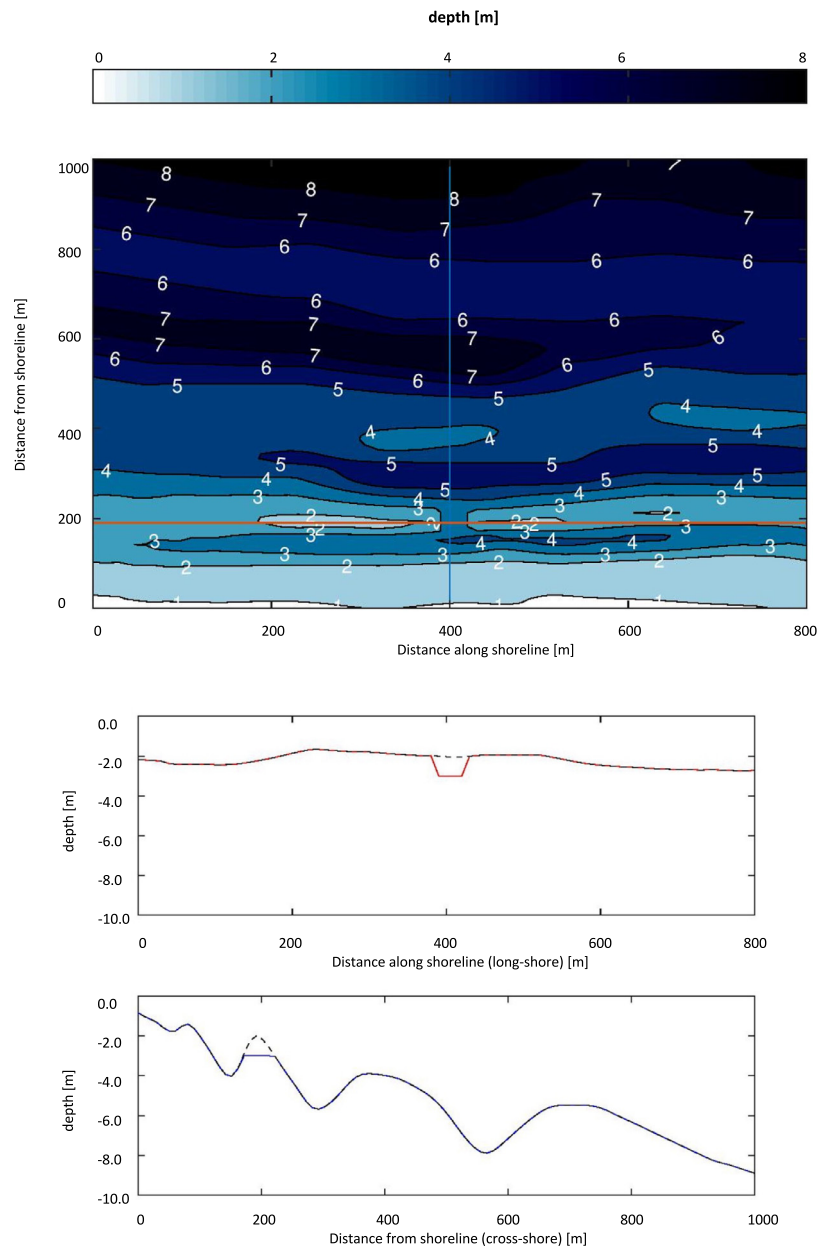


Figure 2 Top panel: bathymetry of CRS in Lubiato, bottom panel: long-shore and cross-shore bottom profiles in the area of rip channel, the black dotted lines are profiles without gap in the bar.

attached a drogue submerged about 0.7 m below the surface of the water, and at shallow depths it floated near the bottom. The underwater drogue ensured the drifter followed the movements of the water and was carried by bottom currents as well as the surface ones. Therefore, it can be assumed that the drifters movement represent a depth-averaged water current. The GPS drifters were released behind the first stable bar, at a distance of 100–150 m from the shoreline, at a depth of about 1.5 m. Typically, they floated along the shore and their positions were recorded continuously and read after removing the device from the water. After some time, they returned to the beach, see Fig. 4, were thrown again and continued the route along the shore. Aerial photo (Head Office of Geodesy and Cartography) is demonstrative and was done

prior to the measurements, so in some cases the drifters' trajectories end at the beach, which actually didn't happen.

This method was used to measure approximately 1700 m of the beach territory. During the first expedition the following data were recorded: (1) six throws of drifter A, and four throws of drifter B; (2) during the second expedition three throws of drifter A.

Determining deep water wave conditions typical of the studied area

Deepwater waves conditions were determined based on measured by wave buoy Datawell BV DWR-7 Mk. III in 2013–2018 parameters. The buoy was anchored in the nearshore

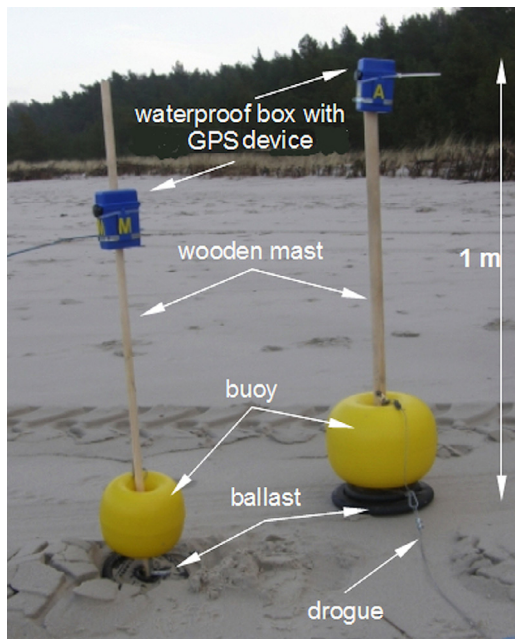


Figure 3 Drifters used for in situ measurements: A (smaller one) and B (bigger one).

beach in Lubiatowo village in the point: 54°50.360'N, 17°50.301'E at a distance of about 1.5 NM. The water depth of the anchored point was about 18 m. The buoy measured such parameters as: significant wave height, wave

period, wave direction, water temperature at prevailing 10 minutes interval. The buoy does not record very short wave periods due to the factory sampling frequency of 1.28Hz. The data were sent to IBW PAN with several longer delivery interruptions. Over the period of six years, using this method as many as 170,189 records were collected. Based on the analysis of this data, 31 pairs of significant wave heights and wave periods (H_s , T) which uniformly cover the domain of typical wave conditions were chosen. More details regarding the selection of this wave conditions are described in the Results section, when describing the measurement results. Each element of this set was considered together with 19 discrete wave directions, from NWW to NEE. This means that the total of 547 wave conditions characterized by (H_s , T , dir) were examined as test cases.

The significant wave steepness was calculated based on the height and the period of the significant wave, Eq. (1).

$$\xi = \frac{H_s}{L} = \frac{2\pi H_s}{gT_p^2}. \quad (1)$$

Numerical modelling of nearshore flows

Two spectral numerical wave models: SWAN (Simulating WAVes Nearshore) cycle III (Booij et al., 1996) and XBeach (Roelvink et al., 2010) were used. These complex models simulate the generation of waves by wind and wave propagation, taking into account a number of physical phenomena determining the wave field, such as shoaling, refraction, non-linear interaction between the waves and

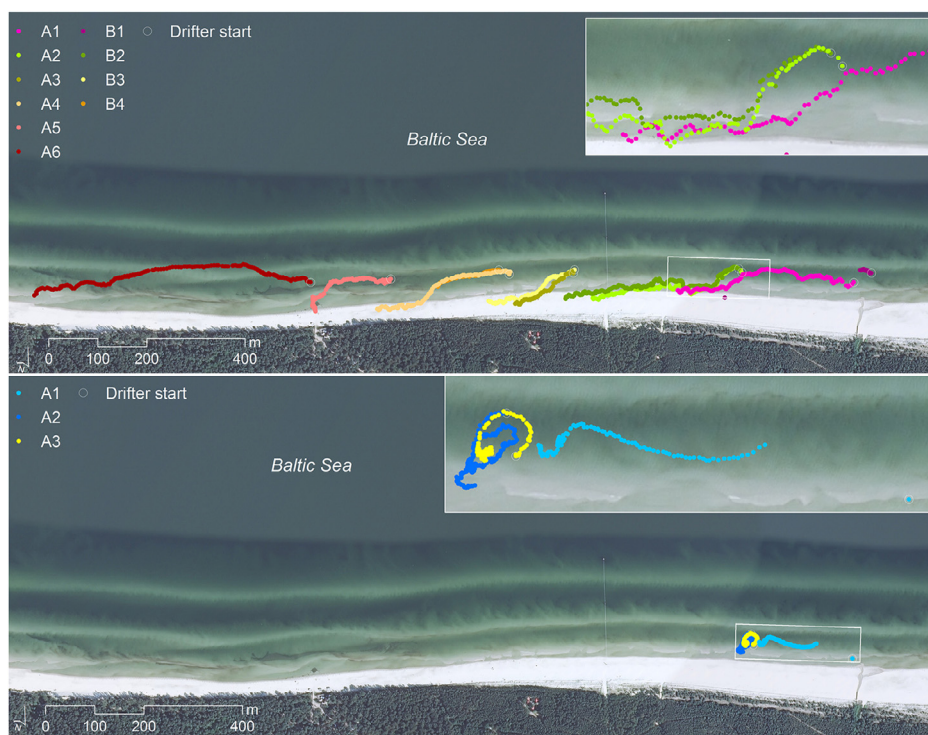


Figure 4 Tracks of drifters measured during field expeditions: 14.01.2016 (the top panel) and 15.04.2016 (the bottom panel). The aerial photo (Head Office of Geodesy and Cartography, retrieved 15.10.2017) is demonstrative and was not done at the same time as measurements, so in some cases the drifters' trajectories end at the beach, which actually didn't happen.

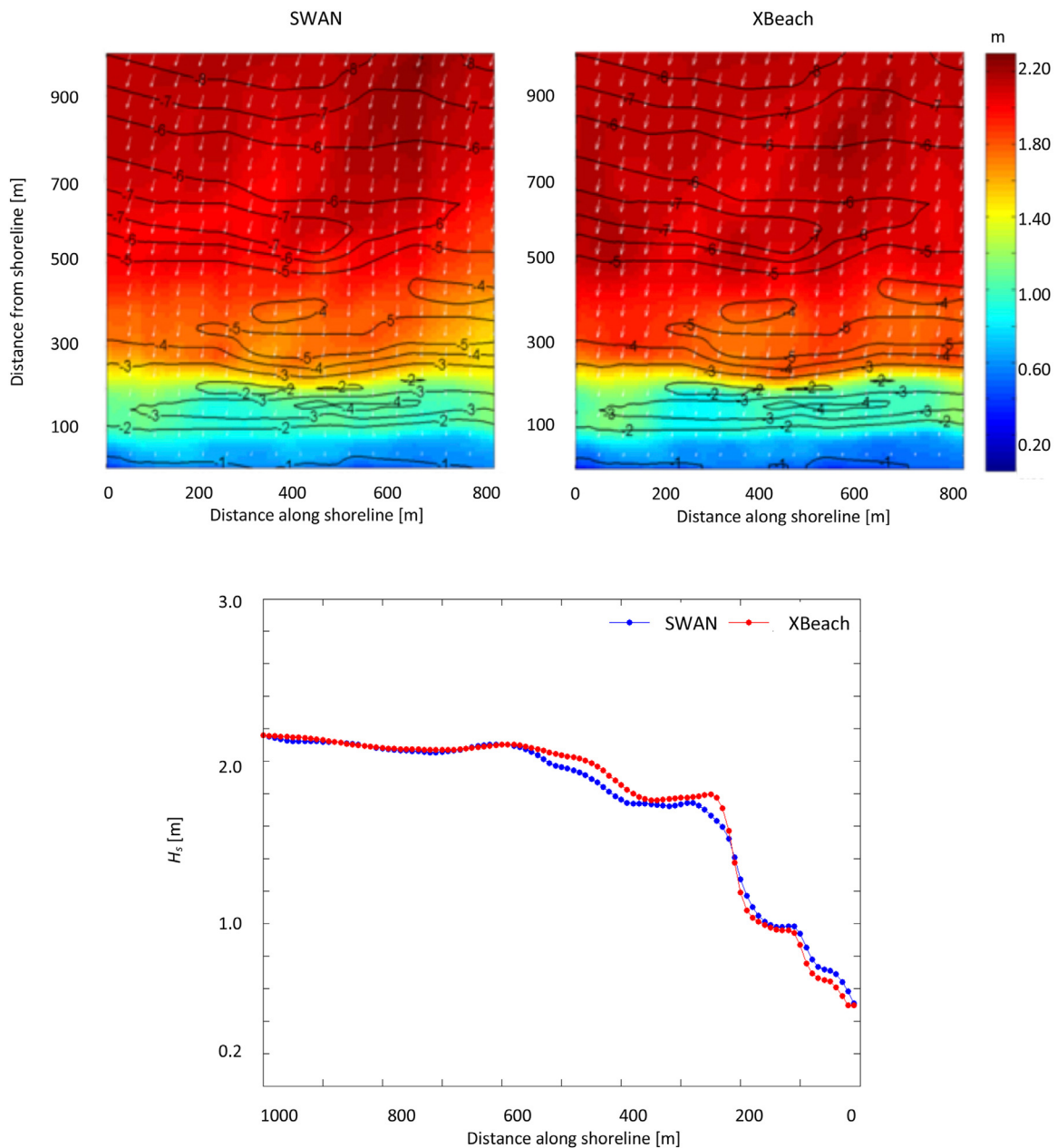


Figure 5 The upper figures: The H_s field modelled by SWAN and XBeach, seaward boundary: $H_s = 2.16$ m, $T = 5.50$ s, $dir = 344^\circ$; the bottom figure: H_s profile along the central transect.

wave energy dissipation. The SWAN model, designed for coastal sea areas, additionally includes energy dissipation by friction at the bottom and refraction due to ocean currents. XBeach, developed to simulate hydrodynamic and morphodynamic processes and impacts on sandy coasts with a domain size of kilometers and on the time scale of storms, takes into account also bottom changes caused by sediment transport. SWAN and XBeach solve the wave action balance equation (for details see e.g. Cieřlikiewicz et al. (2017)).

The SWAN model was used to generate nearshore wind-wave parameters for XBeach model cross-validation. Calculations were done in two steps using numerical meshes presented in Fig. 1:

- The external grid, with spatial resolution of $100 \text{ m} \times 100 \text{ m}$, covering the area between the coastline and a certain location offshore with generalized bathymetric data;
- The internal grid, with spatial resolution of $10 \text{ m} \times 10 \text{ m}$, covering the area up to 1 km offshore, with detailed bathymetric data.

For details, see Grusza (2007). All SWAN parameters were chosen according to the previous extended studies, including the model configuration and results validation in the area of study (Gic-Grusza and Dudkowska, 2014; Reda and Paplińska, 2002).

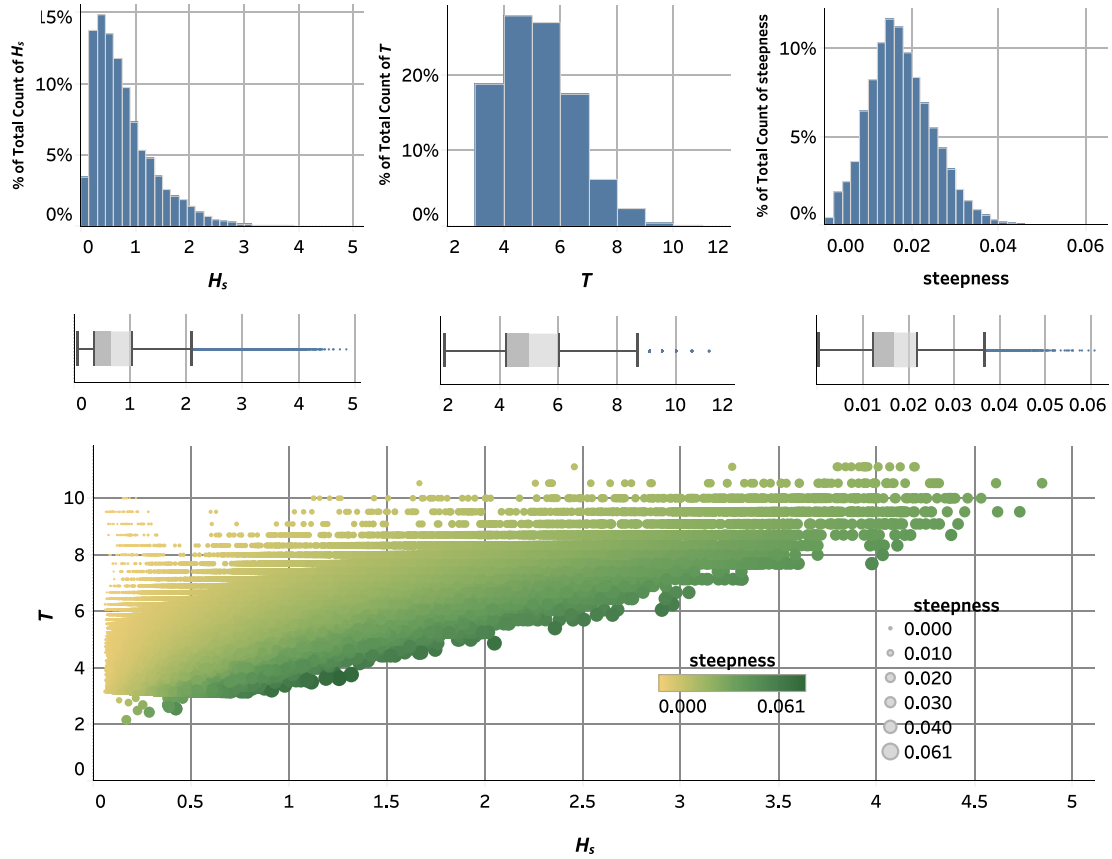


Figure 6 Statistical description of deep water wave conditions in the vicinity of Lubiatowo in years 2013–2018, basing on data from buoy measurements. The upper panel: histograms and box plots of significant wave height, wave period and steepness. Whiskers extend to data within 1.5 times the interquartile range IQR. The bottom panel: scatter plot of significant wave height vs wave period (170,189 points). Wave steepness characteristic for each pair of (H_s, T) is presented as size and colour of marker.

The numerical reconstruction of the coastal flow was performed with the use of XBeach model (Roelvink et al., 2010). The model solves coupled 2D horizontal equations for wave propagation, flow, sediment transport and bottom changes. In this paper sediment transport and bottom changes were not included in calculations. The wave forcing in the shallow water momentum equation is obtained from a time dependent version of the wave action balance equation, Eq. (2).

$$\frac{\partial A}{\partial t} + \frac{\partial c_x A}{\partial x} + \frac{\partial c_y A}{\partial y} + \frac{\partial c_\Theta A}{\partial \Theta} = \frac{D_w}{\sigma}, \quad (2)$$

where A – the wave action, σ – intrinsic wave frequency, Θ – the angle of incidence with respect to x -axis, c_x , c_y , c_Θ – wave action propagation speed in x -, y - and Θ -direction, D_w – total wave dissipation in each directional bin.

Depth-averaged Generalized Lagrangian Mean (GLM) formulation of the shallow water equations are applied to compute the wave induced mass-flux and the return flow (Roelvink et al., 2010). Lagrangian velocity is defined for a water parcel as the average distance traveled during one wave period. The components of Lagrangian velocity: cross-shore u^L and long-shore v^L are related to the components of Eulerian velocity (u^E , v^E) – the fluid velocity at a fixed posi-

tion and to the components of the Stokes drift (u^S , v^S) by:

$$u^L = u^E + u^S \quad v^L = v^E + v^S. \quad (3)$$

The depth-averaged u^L and v^L are obtained from the GLM-momentum and continuity equations in the form of set of equations Eq. (4).

$$\frac{\partial u^L}{\partial t} + u^L \frac{\partial u^L}{\partial x} + v^L \frac{\partial u^L}{\partial y} - f v^L - \nu_h \left(\frac{\partial^2 u^L}{\partial x^2} + \frac{\partial^2 u^L}{\partial y^2} \right)$$

$$= \frac{\tau_{sx}}{\rho h} - \frac{\tau_{bx}^E}{\rho h} - g \frac{\partial \eta}{\partial x} + \frac{F_x}{\rho h},$$

$$\frac{\partial v^L}{\partial t} + u^L \frac{\partial v^L}{\partial x} + v^L \frac{\partial v^L}{\partial y} - f u^L - \nu_h \left(\frac{\partial^2 v^L}{\partial x^2} + \frac{\partial^2 v^L}{\partial y^2} \right)$$

$$= \frac{\tau_{sy}}{\rho h} - \frac{\tau_{by}^E}{\rho h} - g \frac{\partial \eta}{\partial y} + \frac{F_y}{\rho h},$$

$$\frac{\partial \eta}{\partial t} + \frac{\partial h u^L}{\partial x} + \frac{\partial h v^L}{\partial y} = 0, \quad (4)$$

where τ_{bx} , τ_{by} – bottom shear stresses, calculated with the Eulerian velocities, η – the water level, F_x , F_y – the wave induced stresses, ν_h – the horizontal viscosity, f – Coriolis coefficient.

The Lagrangian velocities are used to calculate the wave action propagation speeds according to Eq. (5), which takes

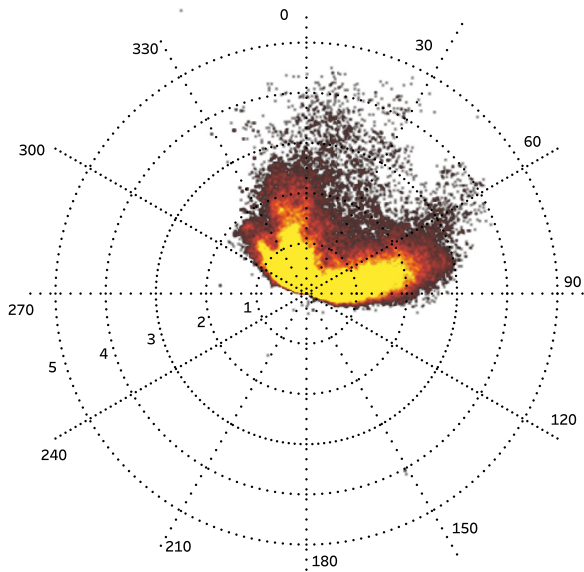


Figure 7 Distribution of wave directions and significant wave height occurring in 2013–2018, basing on data from bouy measurements (170,189 points are shown). Pole system is used – each point of the graph presents the wave direction (angle in the coordinate system) and the significant wave height (distance from the origin). Nautical convention is adopted for wave directions (the direction where the waves are coming from, eg. 270 means that wave is propagating from the west to the east). The colors indicate the frequency of occurrence of wave conditions (H_s, Θ): the yellow points – the most frequent ones, the black points – appearing the least frequently.

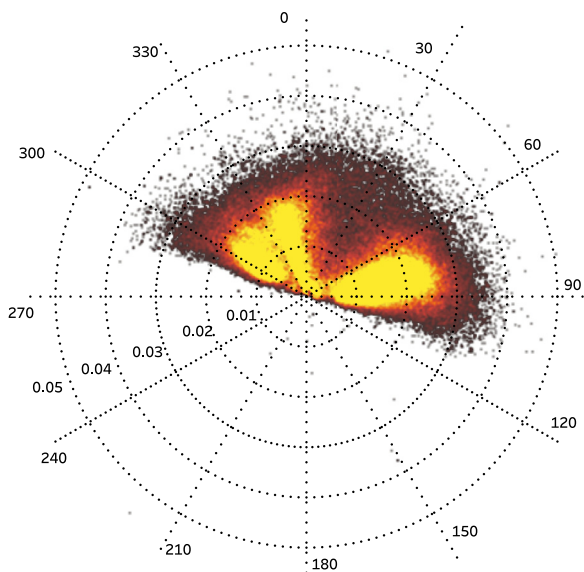


Figure 8 Distribution of wave directions and wave steepness for the data presented in Fig. 7. Each point of the graph presents the wave direction (angle in the pole coordinate system) and the wave steepness (distance from the origin in the pole coordinate system). The colors indicate the frequency of occurrence of wave conditions (ξ, Θ): the yellow points – the most frequent ones, the black points – appearing the least frequently.

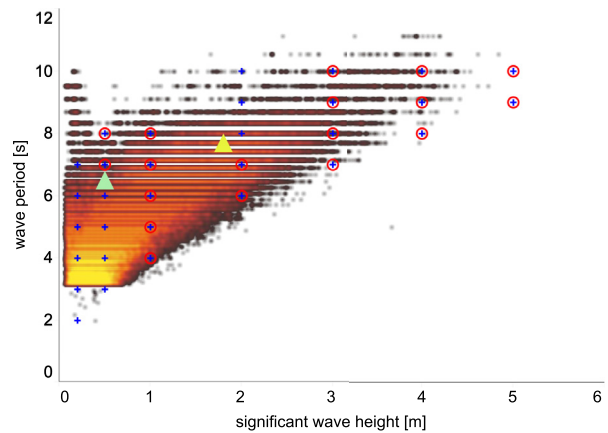


Figure 9 (1) Coloured open circles – distribution of significant wave height and wave period for the data presented in Fig. 7, the colours indicate the frequency of occurrence of wave conditions (H_s, T) analogous to Fig. 7, 170,189 points are shown; (2) blue crosses – 31 test wave conditions (H_s, T) for which coastal flows were examined; (3) red open circles – 18 wave conditions (H_s, T) for which rip currents were modelled; (4) yellow and green triangles – wave conditions during field surveys in CRS Lubiatowo.

into account wave-current interaction.

$$\begin{aligned}
 c_x(x, y, t, \Theta) &= c_g \cos(\Theta) + u^L \\
 c_y(x, y, t, \Theta) &= c_g \sin(\Theta) + v^L \\
 c_\Theta(x, y, t, \Theta) &= \frac{\sigma}{\sinh 2kh} \left(\frac{\partial h}{\partial x} \sin \Theta - \frac{\partial h}{\partial y} \cos \Theta \right) \\
 &+ \cos \Theta \left(\sin \Theta \frac{\partial u}{\partial x} - \cos \Theta \frac{\partial u}{\partial y} \right) \\
 &+ \sin \Theta \left(\sin \Theta \frac{\partial v}{\partial x} - \cos \Theta \frac{\partial v}{\partial y} \right). \quad (5)
 \end{aligned}$$

XBeach model settings which were applied for the purposes of this paper: (i) neglecting of sediment transport and bottom changes, (ii) wave current interaction option, (iii) stationary wave boundary condition at the seaward boundary, which means that a uniform, constant wave energy distribution is set, based on the given values of wave height and period; Neumann lateral boundaries (iv) the roller model which can give a shoreward shift in a wave-induced setup, return flow and longshore current.

In addition, with the use of drifter option there were examined the details of the flow. Drifters are objects that move with Lagrangian mean velocity, and their positions are evaluated at each time step. During numerical simulations drifters were implemented after 600 s of the model spin-up, and the total run duration was set as 1200 s, which was sufficient for the analysis of drifters' behaviour.

The computational grid used in XBeach model (10 m × 10 m, Fig. 2) was rotated clockwise by 17 degrees relative to the original geographical coordinates of the local system, where the x-axis is parallel to the shore, and the y-axis is perpendicular to the shore (Grusza, 2007). Next, the grid was rotated by 90 degrees in order to adjust it to the XBeach convention, where x-axis is perpendicular to the shore. To overcome the artificial wave breaking

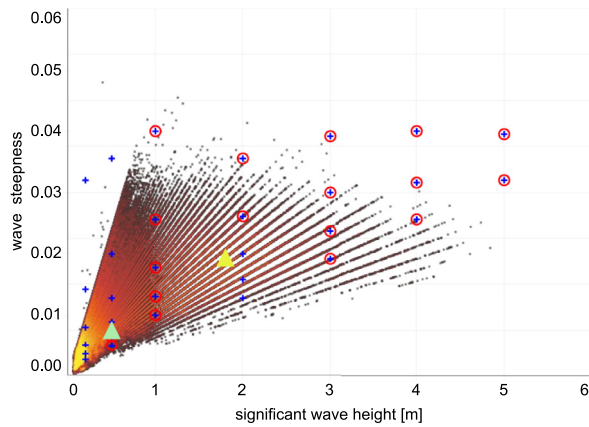


Figure 10 (1) Coloured open circles – distribution of significant wave height and wave steepness for the data presented in Fig. 7, the colours indicate the frequency of occurrence of wave conditions (H_s , ξ) analogous to Fig. 7, 170,189 points are shown; (2) blue crosses – 31 test wave conditions (H_s , ξ) for which coastal flows were examined; (3) red dots – 18 wave conditions (H_s , ξ) for which rip currents were modelled; (4) yellow and green triangles – wave conditions during field surveys in CRS Lubiatowo.

effect on the grid border, the grid was extended to 1400 m in the seaward direction, with uniformly increasing depth up to 20 m. This procedure enabled obtaining the ratio $c_g/c = 0.66$ recommended by XBeach model users on the seaward boundary of the proper computational grid.

The dynamics of water in the model domain is caused by wave coming from the open sea which is defined on seaward open boundary conditions by wave height, period and direction. Among various model output parameters are available fields of significant wave height H_s and vertical

averaged water velocity. Additionally, drifter module allows obtaining trajectories of virtual tracers.

The gap in the bar was artificially introduced into the bathymetry in order to simulate the rip channel. First, the calibration and model validation were conducted by comparison of the modelled wave parameters to the results of SWAN model, which configuration in the study area was discussed in previous studies (Reda and Paplińska, 2002). The second model validation was conducted using the tracks of virtual tracers and their velocities as well as corresponding in situ measured flows. The H_s fields obtained based on XBeach modelling were compared with the H_s field determined by the SWAN model, the results for one chosen wave situation are presented in Fig. 5. The absolute errors of individual H_s values were in the range of 0.08–0.35 m, while the relative errors were in the range of 4%–22%. After model calibration, nearshore wave and currents fields were simulated for all 589 test cases.

4. Results

Deep water waves

The results obtained from the analysis of deep water wave conditions in the vicinity of Lubiatowo in 2014 are presented in Figs. 6–10. Basic statistics are presented as histograms and box plots of significant wave heights H_s , wave period T and resulting wave steepness ξ , Fig. 6. It is visible that in the studied area H_s are typically in the range of about 0.4–1.1 m with the median of about 0.6 m and occasionally occurring waves of height up to 5.0 m. The median of wave period T is 5.0 s, waves of periods between 4.3 and 6.1 s occur most often, the maximal value of T was about 10 s. The most common are waves of steepness in the range 0.012–0.022, with median about 0.017 and

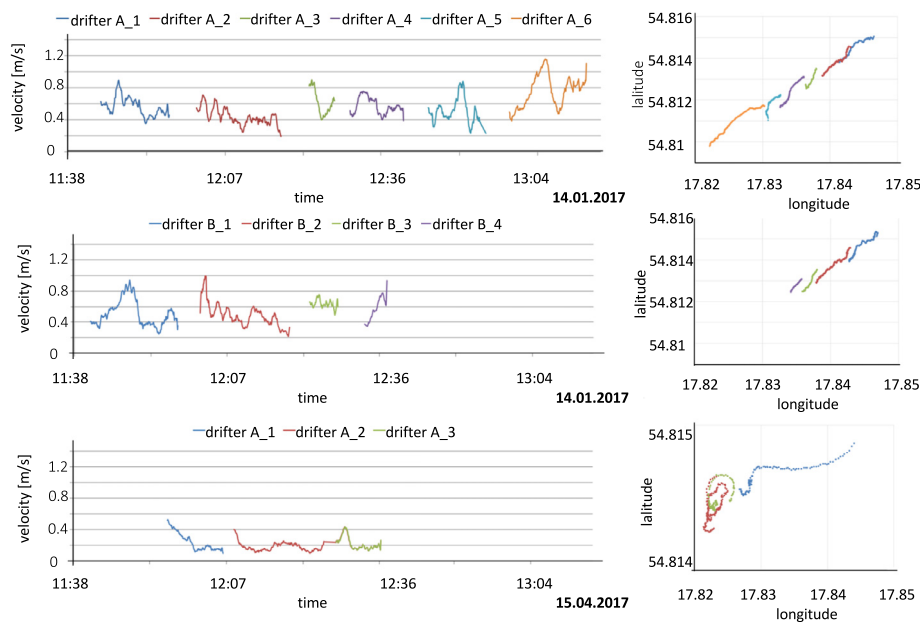


Figure 11 The actual velocities of drifters following their paths presented in Fig. 4 during two expeditions in CRS Lubiatowo.

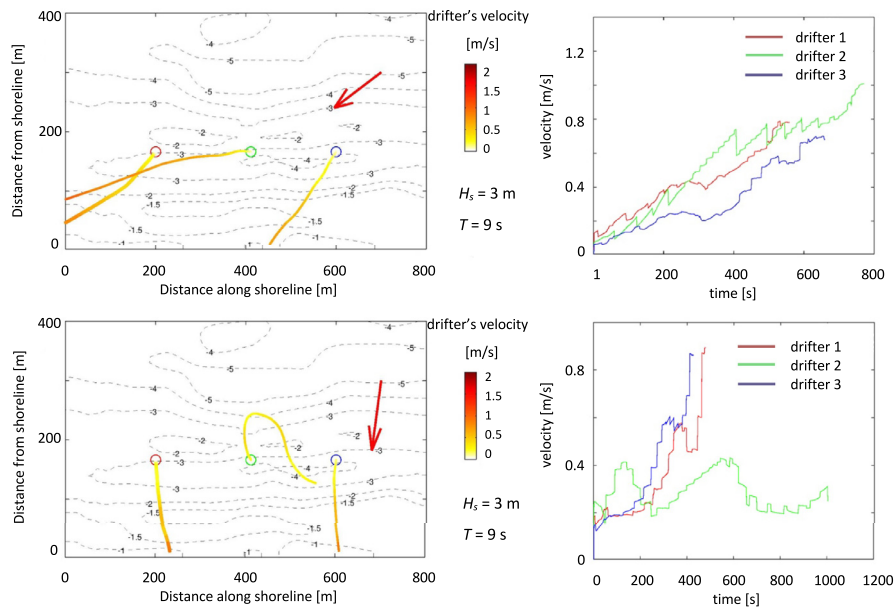


Figure 12 The tracks of virtual drifters obtained by numerical simulation with the use of XBeach model, the simulation time was 1200 s. The red arrow indicates the deep water wave direction, the coloured open circles – the start positions of drifters.

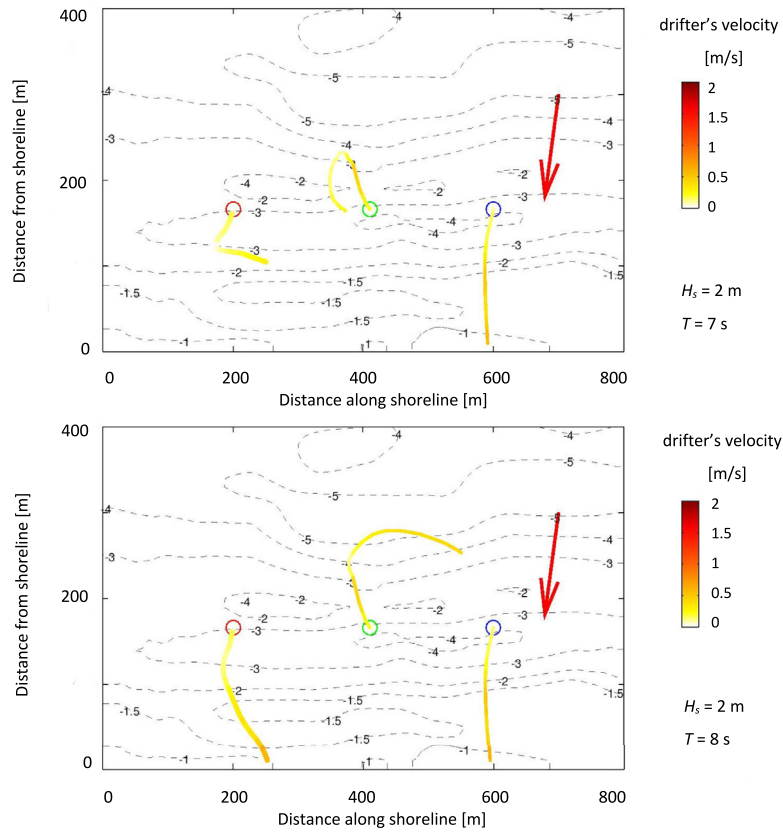


Figure 13 The tracks of virtual drifters (analogous to those shown in Fig. 12). Input wave parameters similar to those prevailing during the expedition in January.

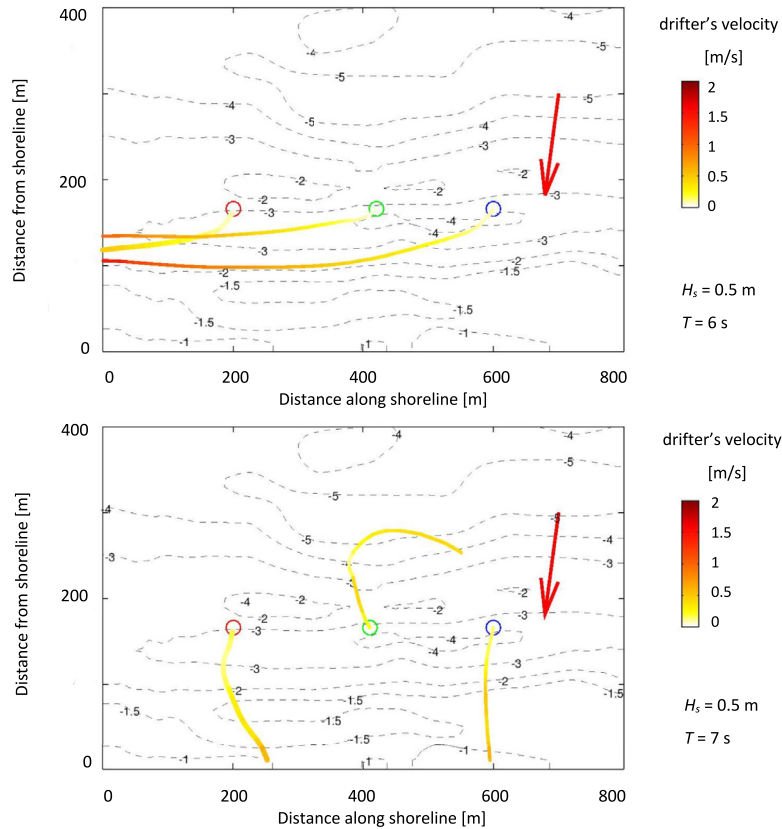


Figure 14 The tracks of virtual drifters (analogous to those shown in Fig. 12), input wave parameters similar to those prevailing during the expedition in April.

maximal value of about 0.06. Such maximal steepness is characteristic of the waves with the lowest periods for the given height, while minimal values are characteristic of the highest periods (Fig. 6), as a direct consequence of Eq. (1).

Offshore waves propagating towards the northern directions are of low heights and occur rarely. Among onshore waves, these propagating towards the west are higher (the most frequent are up to about 2 m) than the waves propagating in the east direction (the most frequent are up to about 1.5 m), Fig. 7. The steepness of onshore waves in typical situations does not exceed the value of 0.04, Fig. 8. Waves with steepness up to about 0.02 are prevailing in the area concerned.

Based on the above analysis, a set of 31 wave conditions given by pairs of H_s and T was selected, which are likely in the studied region. The range and distribution of H_s , T and ξ were taken into account during selection, Figs. 7 and 8.

Lagrangian measurements

Nearshore flows were estimated in situ taking Lagrangian measurements. The routes of the GPS drifters floating freely at the sea surface were tracked during two expeditions. There were six throws of drifter A (the smaller one), four throws of drifter B (the bigger one) on 14.01.2016, and three throws of drifter A on 15.04.2016. The recorded tra-

jectories of drifters are presented in Fig. 4. The wave was higher and steeper during the first expedition in January than during the second one in April. The actual velocities of drifters following their paths along the shoreline are presented in Fig. 11 and the details of the drifters' paths are summarized in Table 3.

It is apparent from the top panel of Fig. 4 that during the first expedition the drifters released at the distance of about 100 m from the shoreline floated along the shore and after several minutes came back to the beach. The trajectory of a drifter does not depend on its size and weight: smaller and bigger drifters thrown close to each other moved along similar routes, and had similar velocities. For example, see throws 1–4 of A and B drifters.

Averaged over the whole route drifters' velocities measured during the first expedition were higher than during the second expedition, see Table 3. The mean velocity of drifters released 10 times on 14.01.2016 was 0.55 m/s with a standard error of 0.03 m/s, and of those released 3 times on 15.04.2016 was 0.23 m/s with a standard error of 0.02 m/s.

The details of the drifters routes, namely their actual velocities and trajectories are presented in Fig. 11. Short-term fluctuations of velocities were smoothed out by a moving average filter with a period of 60 seconds.

Regarding the survey from 14.01.2016, initial velocities of drifters were in the range of about 0.4–0.6 m/s. The

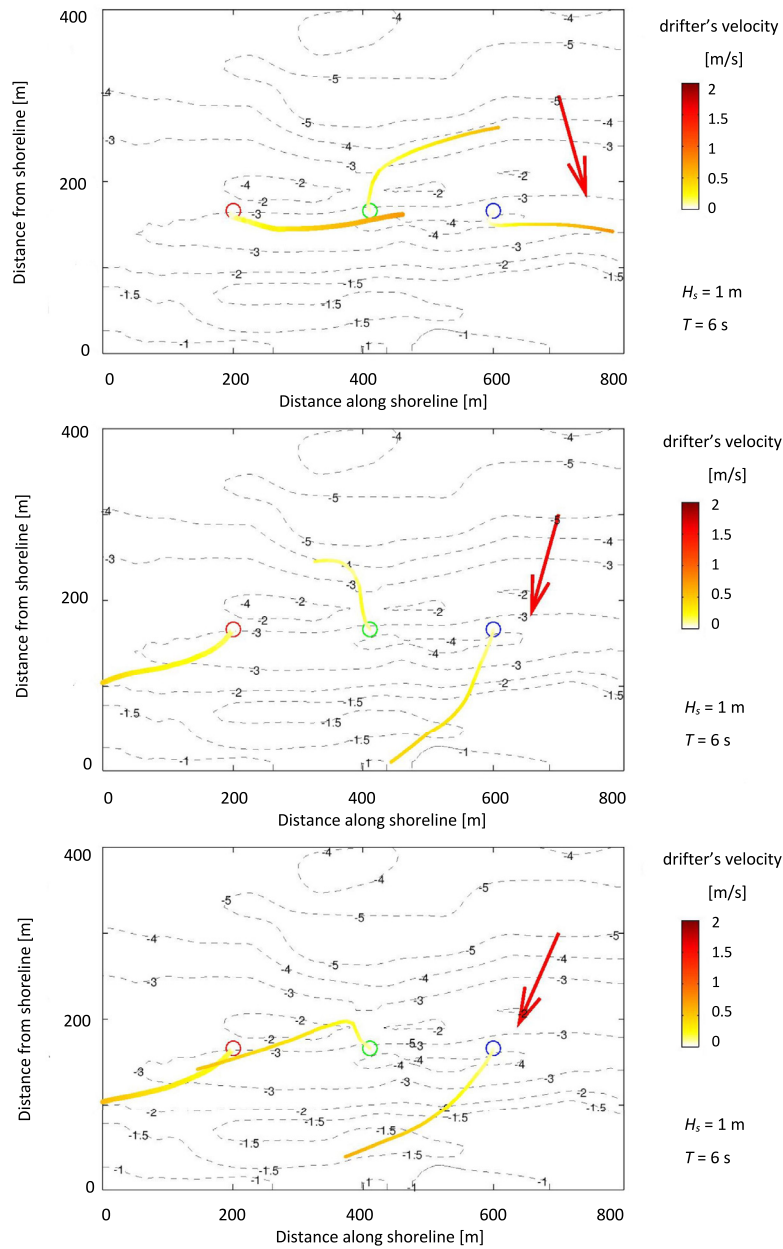


Figure 15 The tracks of virtual drifters (analogous to those shown in Fig. 12), input wave parameters: $H_s = 1$ m, $T = 6$ s, $\xi = 0.018$, $dir: (340, 20, 30)$.

peaks in velocities (up to 1–1.2 m/s) were probably connected to crossing the bar. The changes of the drifters' velocities during their route along the coastline were partly related to the varying depth around bars, but were also caused by an accidental contact with the ground. Thus, a reliable examination of the drifters' velocity changes associated with the nearshore current field in high wave conditions was not possible.

In summary, all the measurements of 14.01.2016 showed a longshore flow typical of this kind of coast, which was quasistationary in the study area (about 1.5 km of coast).

The results of the second expedition (15.04.2016) are the following: the initial velocities of drifters were in the range about 0.2–0.5 m/s, so were smaller than those recorded in January. Also, two trajectories of a drifter observed in April were significantly different from the typical alongshore drifters' routes which were recorded in January. After the first throw, drifter A floated about 250 m for 15 minutes in a typical way, alongshore with the velocity decreasing from about 0.5 to 0.1 m/s. By contrast, after the second throw drifter A moved along the loop about 100 m in diameter. Upon returning to the shore, it was released again and it repeated this loop-shaped route once more.

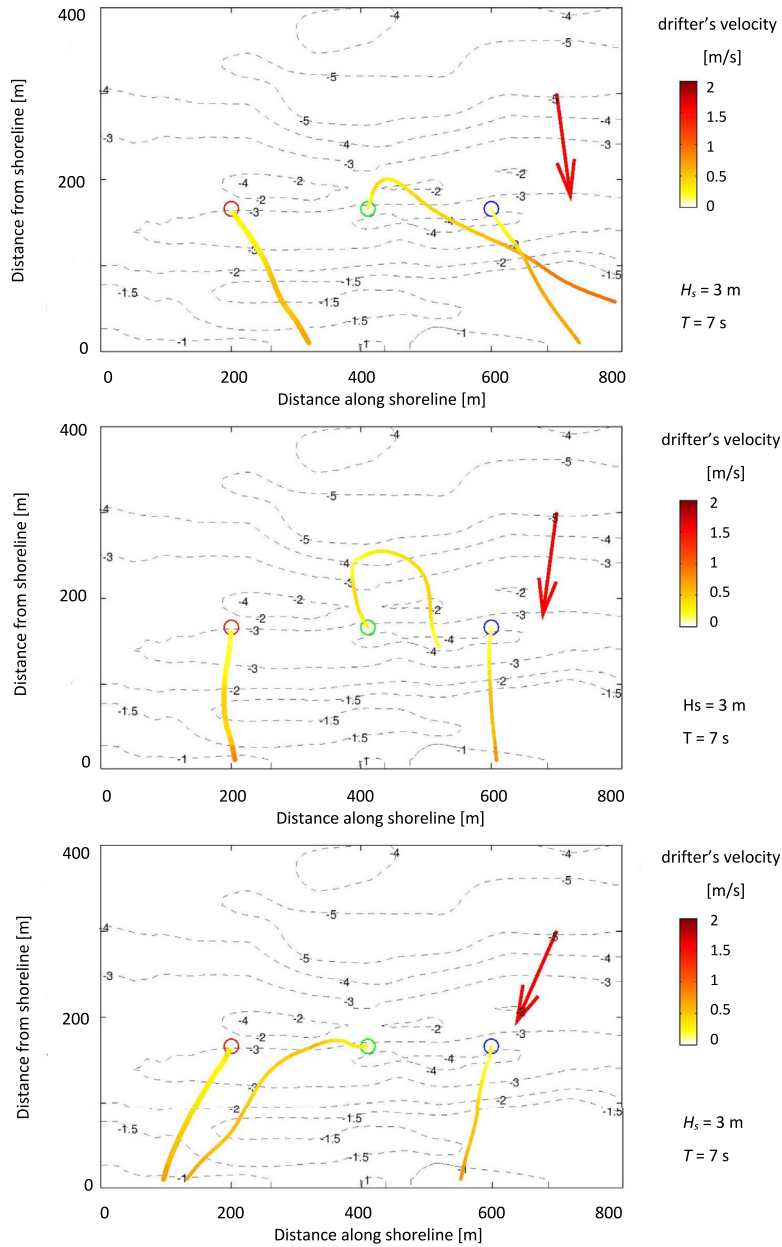


Figure 16 The tracks of virtual drifters (analogous to those shown in Fig. 12), input wave parameters: $H_s = 3$ m, $T = 7$ s, $\xi = 0.039$, $dir: (350, 10, 30)$.

The actual velocities during these untypical flows did not differ from those observed during the first throw, and were about 0.2–0.4 m/s. Taken together, these results provide important insights into two types of nearshore flows.

Modelling approach

In order to confirm hypotheses stated in the Introduction, modelling approach was used. Tracks of virtual tracers were simulated with the use of XBeach model in 589 numerical experiments. The input data for the model are: (1) morphological conditions conducive to rip current generation;

(2) boundary conditions (H_s , T , dir) that represent typical wave fields in the studied area. The set of wave boundary conditions applied in all 589 test cases is presented in Figs. 9, 10, and 18. This set was obtained based on analysis of long term measurements described at the beginning of this section.

There are two subsets of all examined virtual tracers' trajectories. The former contains routes leading directly to the shore with the approach angle dependent on the wave direction to which we refer as regular flows. The latter contains routes with some features typical of rip currents, i.e. offshore flows with increasing velocity. In this paper, we

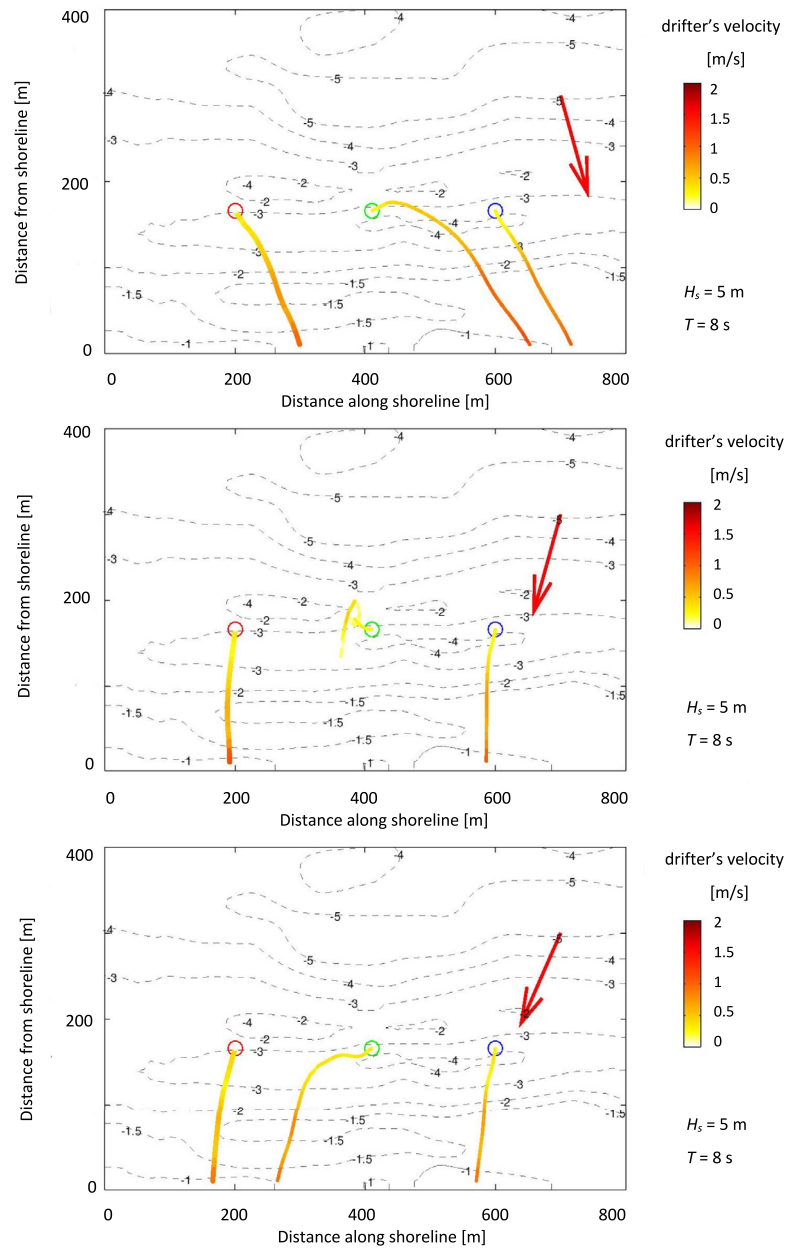


Figure 17 The tracks of virtual drifters (analogous to those shown in Fig. 12), input wave parameters: $H_s = 5$ m, $T = 8$ s, $\xi = 0.05$, $dir: (340, 20, 30)$.

will use the term rip current to describe such type of tracer trajectory. The examples of these two typical flows are presented in Fig. 12, the regular flow in the top panel, and the rip current in the bottom panel. These graphs show that the drifter's velocity changes along its route according to the following rules. In the case of regular flows (all drifters in the top panel and drifter 1 and 3 in the bottom panel) velocity increases as the depth decreases. Occasionally velocity peaks in the areas of rapid change of bathymetry, see for example drifters 1 and 3 during about 300–400 s of simulations. The movement of a rip current type drifter

(drifter 2 in the bottom panel) is characterized by a rapid growth of velocity in the vicinity of rip channel on the way offshore and back along the loop.

Figs. 13 and 14 show results of simulations with wave boundary conditions corresponding to those prevailing during the expeditions in January and in April. A deep sea wave was slightly deviated to the west from onshore direction during both expeditions, while wave steepness were different, about 0.02 during the expedition in January and about 0.01 in April. Virtual tracers' routes in wave conditions similar to those during the first expedition (Fig. 13)

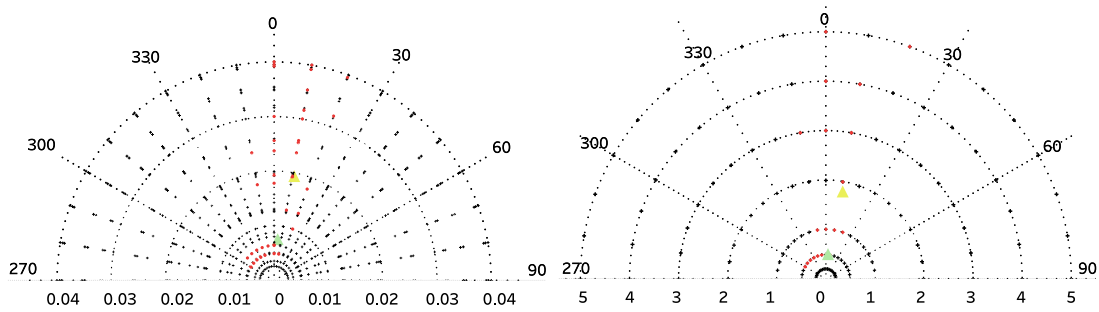


Figure 18 The left diagram: the significant wave steepness with the wave direction (ξ , *dir*). The right diagram: the significant wave height with the wave direction (H_s , *dir*). Pole coordinate system is used in which the angle represents the wave direction, the distance from the origin represents ξ or H_s respectively. Nautical convention is adopted for wave directions (the direction where the waves are coming from, eg. 270 means that wave is propagating from the west to the east). (1) black dots represent $31 \times 19 = 589$ test wave conditions for numerical experiments; (2) red dots – 42 wave conditions for which rip currents were modelled, corresponding to 18 points presented in Fig. 10; (3) triangles – wave conditions during field surveys in Lubiatowo.

Table 3 Drifters' paths characteristics.

| | distance [m] | time | average velocity [m/s] |
|------------|-----------------|----------|---------------------------|
| 14.01.2016 | | | |
| A 1 | 437.5 | 00:12:50 | 0.56 |
| A 2 | 410.4 | 00:15:45 | 0.44 |
| A 3 | 189.4 | 00:05:10 | 0.61 |
| A 4 | 335.4 | 00:09:50 | 0.55 |
| A 5 | 307.4 | 00:11:07 | 0.51 |
| A 6 | 615.4 | 00:14:10 | 0.72 |
| B 1 | 478.4 | 00:16:40 | 0.48 |
| B 2 | 499.9 | 00:16:55 | 0.49 |
| B 3 | 213.5 | 00:05:40 | 0.62 |
| B 4 | 134.7 | 00:04:20 | 0.51 |
| 15.04.2016 | | | |
| A 1 | 243.8 | 00:15:30 | 0.26 |
| A 2 | 333.7 | 00:27:45 | 0.20 |
| A 3 | 115.3 | 00:08:35 | 0.22 |

are of the rip current type. The maximal velocities are up to about 0.6 m/s. It is interesting to note that the direction of rip current 'loop' differs for the wave steepness of 0.03 (counter-clockwise) and 0.02 (clockwise). Simulations for wave conditions similar to those during the second expedition (Fig. 14) are of a regular flow type, with tracers flowing alongshore with increasing velocity.

Figs. 15–17 show exemplary trajectories of drifters for the wave heights of 1, 3, and 5 m and wave directions close to the onshore territory. In these cases an irregular velocity field is more likely to be generated for wave direction closer to normal to the shore.

The total results of all 589 test cases are presented in Fig. 18. It shows that the rip current type of flows were simulated (i) for wave directions in the range from 300 (NW) to 20 (NNE), thus almost normal to the shore; (ii) for all tested wave heights and wave steepness. Among 42 wave conditions for which currents were reproduced there were: the most (18 cases) for wave directions from NNE, 12 cases for wave directions from N, and 12 cases

for wave directions from NW. There is no symmetry in the flow field resulting from corresponding western and eastern wave directions. The rip currents were generated by waves of lower heights ($H_s < 1$) and steepness ($\xi < 0.01$) when approaching from the NNW direction, and by larger (H_s up to 5 m) and steeper (ξ up to 0.04) waves in the other case.

5. Discussion

The wave conditions during both field expeditions were similar in terms of the period and direction of the wave, while the wave heights and the resulting steepnesses were considerably different from each other. The wave directions were almost normal to the shore which, according to theories describing rip currents, are conducive to their formation. Moreover, the wave periods were above the mean value in the studied area. In the case of waves with long periods (long waves), most of the energy reaches the shore and waves break down near the shoreline. The dissipated wave energy is transformed into energy of such phenomena as: turbulence, reflected waves and currents of wave origin. In the case of oblique wave direction longshore current is generated, which has a dominant role in the studied area. In the case of shore-normal waves, a return or rip current is generated.

The example of a rip current was registered in Lagrangian measurements during the second day of measurements. On this day a wave period was slightly shorter than during the first expedition, but with the steepness being about two times lower. It means that during the second expedition the waves dissipated much closer to the shore, thus more wave energy was transported into the close vicinity of the shoreline. That was probably the reason why, under favourable morphological conditions (local lowering of the bar), the onshore stream of water generated close to the shore could not be compensated by the return current, and a more intense rip current was generated.

However, it is not possible to draw conclusions about the prevalence of occurrence of rip currents on the basis of one observation. Admittedly, at the time when a rip current was observed, the wave height, period and steepness were similar to the most typical ones in the studied area, Figs. 9 and

10. But the wave moved from the NE direction, which is not most common (the predominant waves come from NWW directions), Figs. 7 and 8. Therefore it cannot be said that these were the most frequent wave conditions. Given the relatively narrow area of research and a small number of tests, this observation may suggest the universality of rip currents in the studied area. On the other hand, it should be noted that according to the theory, a wave direction almost normal to the shore is favourable for the appearance of rip current. All these arguments suggest that due to the difficulty of estimating the frequency of rip currents occurrence, model studies are necessary.

In order to test the occurrence of rips in a wide range of wave conditions, numerical simulations have been conducted. It appeared that nearshore flows with typical rip currents features occurred in 42 of the 589 test cases, which is about 7% of the analysed wave situations.

The simulations demonstrated that rip currents emerge only for a restricted range of wave directions, i.e. wave approaching from the north, almost perpendicularly to the shore. However, not all wave conditions with favorable wave direction generated rip currents. Simulations did not indicate similar limitations for the wave height or steepness, but, there are some combinations of H_s and T for which currents are not generated. In summary, the only rule that can be specified based on the modelling results is the one associated with the wave direction. Both the observed lack of symmetry due to the east and west wave direction as well as the occurrence of rip currents during certain specific wave conditions may indicate that there is another important factor influencing the formation of rip currents. We assume that it is local bottom topography. It should be mentioned however that there is no significant difference in the volume of water on the left and right of the basin. Waves that are symmetric with respect to shore normal direction propagate asymmetrically and after reaching the shore give asymmetrical results. Therefore, it is advisable to carry out further model tests examining the impact of bathymetry changes, as well as local wind field on the results to determine the causes of asymmetry in the results.

It is interesting that in the numerical experiment with wave conditions corresponding to in situ measurements from January, a rip current was generated which was not observed in situ. It was probably due to the lack of favourable morphological conditions at the bottom – the rip channel did not form in the measured area.

6. Conclusions

The presented numerical simulations confirmed that bathymetry controlled rip currents in the barred coastal zone can emerge during the wave propagating in the almost shore-normal direction (for wave directions in the range from 300 (NW) to 20 (NNE)). According to the model results, there is no restriction as to the wave height and steepness. However, this study is unable to encompass the entire dynamics of nearshore flow due to limitations of 2D XBeach model.

The typical hydrodynamical situation conducive to rip currents is when large masses of water transported towards

the shore by breaking waves are unable to return towards the open sea in the form of a bottom return current. In this case, in favourable locations (e.g. the local break in the bar), a strong stream of water is created uniformly throughout the water column. Thus, a reliable simulation of a rip current is possible with a correct modelling of the return current. Although there is a mechanism of a return current implemented in the XBeach model, it seems that 3D models address this phenomenon better. Thus, more detailed numerical simulations with the use of 3D flow models should be performed, mainly in order to verify the most controversial results, i.e. rip currents occurring in the presence of a wave with a high steepness.

The mechanism of the rip current initiation considered in this work (the initial disturbance of bathymetry) is only one of the possible scenarios. Nevertheless, the results presented indicate that this phenomenon is rare. In addition, the velocities of both measured and modelled rip currents (up to 0.4 m/s) are small comparing to the velocity of longshore current (up to 1.6 m/s, (Ostrowski et al., 2016)), which occurs when waves approach the shore obliquely. Concluding, the dominant factor affecting the reconstruction of the bottom is longshore current. Rip currents are not very common and have low speeds, so they are not a significant factor in the morphodynamic processes.

Determining the conditions under which rip currents may occur is very important for the investigation of the impact of these flows on the seabed reconstruction, and for the safety of bathers. It is difficult to predict the place and time of their appearance, because it depends on dynamically changing local bathymetry.

This work is one of few attempts to exploring the possibility of the appearance of rip currents in the coastal zone of the South Baltic and provides a background for further research on the issue. Primarily, different flow patterns observed during the two Lagrangian experiments may be explained not only by incident wave conditions, but also by other factors.

In order to verify the assumption about the triggering factor of observed irregular flows, during further research more Lagrangian data should be collected simultaneously with morphology data. Although measurements of bottom topography during an intense wave is difficult, it seems to be crucial to properly understand the hydrodynamic and morphological control over rip currents dynamics along the studied coast. As this location is a representative example of multi-barred coast, presented results are also useful for describing the non-tidal mechanism of rip currents formation on similar beaches.

7. Data Availability

The research data required to reproduce the work reported in Manuscript are available at: <https://bit.ly/2CllePv>.

Acknowledgement

This study was supported by the Institute of Hydro-Engineering of Polish Academy of Sciences (IBW PAN)

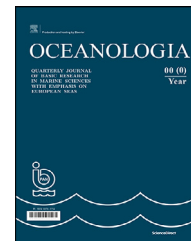
by providing multi-annual measurement data and the organization of field research.

References

- Booij, N., Holthuijsen, L.H., Ris, R.C., 1996. The SWAN wave model for shallow water. In: *Proceedings of the 25th International Conference on Coastal Engineering, Orlando, USA*, 1, 668–676.
- Bruneau, N., Bonneton, P., Castelle, B., Pedreros, R., 2011. Modeling rip current circulations and vorticity in a high-energy mesotidal-macrotidal environment. *J. Geophys. Res.* 116(C7), 17, C07026, <https://doi.org/10.1029/2010JC006693>.
- Castelle, B., Almar, R., Dorel, M., Lefebvre, J.-P., Senechal, N., Anthony, E., Laibi, R., Chuchla, R., du Penhoat, Y., 2014. Rip currents and circulation on a high-energy low-tide-terraced beach (Grand Popo, Benin, West Africa). *J. Coastal. Res.* 70, 633–638, <https://doi.org/10.2112/SI70-107.1>.
- Castelle, B., Scott, T., Brander, R., McCarroll, R., 2016. Rip current types, circulation and hazard. *Earth-Sci. Rev.* 163, 1–21, <https://doi.org/10.1016/2016.09.008>.
- Cieślakiewicz, W., Dudkowska, A., Gic-Grusza, G., Jędrasik, J., 2017. Extreme bottom velocities induced by wind wave and currents in the Gulf of Gdańsk. *Ocean Dynam.* 67(11), 1461–1480, <https://doi.org/10.1007/s10236-017-1098-4>.
- Floc'h, F., Mabilia, G.R., Almar, R., Castelle, B., Hall, N., Du Penhoat, Y., Scott, T., Delacourt, C., 2018. Flash rip statistics from video images. *J. Coastal. Res.* 81, 100–106, <https://doi.org/10.2112/SI81-013.1>.
- Furmańczyk, K., 1994. Strefa brzegowa Półwyspu Helskiego w świetle kompleksowej interpretacji zdjęć lotniczych i satelitarnych. *Mar. Sci.* 134(2), 61–80.
- Furmańczyk, K., Andrzejewski, P., Benedyczak, R., Bugajny, N., Cieszyński, L., Dudzińska-Nowak, J., Giza, A., Paprotny, D., Terefenko, P., Zawisłak, T., 2014. Recording of selected effects and hazards caused by current and expected storm events in the Baltic Sea coastal zone. *J. Coastal. Res.* 70, 338–342, <https://doi.org/10.2112/SI70-057.1>.
- Garnier, R., Calvete, D., Falqués, A., Dodd, N., 2008. Modelling the formation and the long-term behavior of rip channel systems from the deformation of a longshore bar. *J. Geophys. Res. Oceans* 113 (C7), art. no. C07053, 18 pp., <https://doi.org/10.1029/2007JC004632>.
- Gic-Grusza, G., Dudkowska, A., 2014. Modeling of wind wave induced sediment transport in the coastal zone of polish marine areas (southern baltic). *Baltic International Symposium (BALTIC), 2014 IEEE/OES: Measuring and modeling of multi-scale interactions in the marine environment*, May 26–29, 2014, Tallinn, Estonia IEEE/OES, 1–5, <https://doi.org/10.1109/BALTIC.2014.6887860>.
- Grusza, G., 2007. Three-dimensional modelling of wave-generated currents in coastal zone. Ph.D. thesis, Inst. Oceanogr., Univ. Gdańsk, Gdynia, Poland, (in Polish).
- Johnson, D., Pattiaratchi, C., 2004. Transient rip currents and nearshore circulation on a swell-dominated beach. *J. Geophys. Res. Oceans* 109, art. no. C020261, 20 pp., <https://doi.org/10.1029/2003jc001798>.
- Johnson, D., Pattiaratchi, C., 2006. Boussinesq modelling of transient rip currents. *Coast. Eng.* 53, 419–439, <https://doi.org/10.1016/j.coastaleng.2005.11.005>.
- Kirby, J., 2017. Recent advances in nearshore wave, circulation and sediment transport modeling. *J. Mar. Res.* 75(3), 263–300, <https://doi.org/10.1357/002224017821836824>.
- Longuet-Higgins, M., Stewart, R., 1964. Radiation stresses in water waves; a physical discussion, with applications. *Deep-Sea Res. Oceanogr. Abstr.* 11 (4), 529–562, [https://doi.org/10.1016/0011-7471\(64\)90001-4](https://doi.org/10.1016/0011-7471(64)90001-4).
- MacMahan, J., Thornton, E., Reniers, A., 2006. Rip current review. *Coast. Eng.* 53, 191–208, <https://doi.org/10.1016/j.coastaleng.2005.10.009>.
- MacMahan, J.H., Thornton, E.B., Stanton, T.P., Reniers, A.J., 2005. RIPEX: observations of a rip current system. *Mar. Geol.* 218 (1), 113–134, <https://doi.org/10.1016/j.margeo.2005.03.019>.
- Ostrowski, R., Schönhofer, J., Szymkiewicz, P., 2016. South baltic representative coastal field surveys, including monitoring at the Coastal Research Station in Lubiatowo, Poland. *J. Marine Syst.* 162, 89–97, <https://doi.org/10.1016/j.jmarsys.2015.10.006>.
- Peregrine, D., 1998. Surf zone currents. *Theor. Comp. Fluid Dyn.* 10, 295–309, <https://doi.org/10.1007/s001620050065>.
- Pitman, S., Gallop, S.L., Haigh, I.D., Masselink, G., Ranasinghe, R., 2016. Wave breaking patterns control rip current flow regimes and surfzone retention. *Mar. Geol.* 382, 176–190, <https://doi.org/10.1016/j.margeo.2016.10.016>.
- Pruszek, Z., Szymkiewicz, P., Ostrowski, R., Skaja, M., Szymkiewicz, M., 2008. Shallow-water wave energy dissipation in a multi-bar coastal zone. *Oceanologia* 50(1), 43–58.
- Reda, A., Papińska, B., 2002. Application of numerical wave model SWAN for wave spectrum transformation. *Oceanol. St.* 31(1–2), 5–21.
- Roelvink, D., Reniers, A., van Dongeren, A., van Thiel de Vries, J., Lescinski, J., McCall, R., 2010. XBeach Model Description and Manual. Rep.. Unesco-IHE Institute for Water Education, Delft and Delft University of Technology, Delft, Netherlands.
- Rudowski, S., 1970. Smallscale ripples in offshore of the Southern Baltic Sea. *Acta Geol. Pol.* 20(3), 451–483.
- Sabet, B.S., Barani, G., 2011. Field investigation of rip currents along the southern coast of the Caspian Sea. *Sci. Iran.* 18 (4), 878–884, <https://doi.org/10.1016/j.scient.2011.07.017>.
- Schönhofer, J., 2014. Rip currents at beach with multiple bars theoretical description and in-situ observations. Ph.D. thesis, Inst. Hydro-Eng. PAN Gdańsk, Poland, (in Polish).
- Semiring, L., van Dongeren, A., Winter, G., Ormond, M., Briere, C., Roelvink, D.J., 2014. Nearshore bathymetry from video and the application to rip current predictions for the Dutch Coast. *J. Coastal. Res.* 70, 354–359, <https://doi.org/10.2112/SI70-060.1>.
- Short, A.D., Aagaard, T., 1993. Single and multi-bar beach change models. *J. Coastal. Res.* SI 15, 141–157.
- Winter, G., van Dongeren, A., de Schipper, M., van Thiel de Vries, J., 2014. Rip currents under obliquely incident wind waves and tidal longshore currents. *Coast. Eng.* 89, 106–119, <https://doi.org/10.1016/j.coastaleng.2014.04.001>.
- Xie, M., 2012. Three-dimensional numerical modelling of the wave-induced rip currents under irregular bathymetry. *J. Hydrodyn. Ser. B.* 24 (6), 864–872, [https://doi.org/10.1016/S1001-6058\(11\)60314-4](https://doi.org/10.1016/S1001-6058(11)60314-4).

Available online at www.sciencedirect.com

ScienceDirect

journal homepage: www.journals.elsevier.com/oceanologia

ORIGINAL RESEARCH ARTICLE

The demand analysis of oceanic T-S-V 3D reconstruction on wide-swath SSH data features based on ROMS and 4DVAR

Chaojie Zhou^{1,*}, Jie Zhang^{1,2}, Jungang Yang², Lei Cao³¹ China University of Petroleum, College of Oceanography and Space Informatics, Qingdao, China² First Institute of Oceanography, Ministry of Natural Resources, Qingdao, China³ Beijing Research Institute of Telemetry, Beijing, China

Received 13 June 2019; accepted 27 February 2020

Available online 13 March 2020

KEYWORDS

3D Ocean state estimation;
Wide-swath altimeter;
Accuracy;
Spatial-temporal resolution

Summary Future wide-swath altimetry missions will provide high-resolution information about ocean surface elevation, and facilitate the characterization of meso- and sub-mesoscale ocean activities. In this study, the demand analysis of three-dimensional (3D) oceanic state reconstruction on wide-swath SSH data features was evaluated using a data assimilation strategy. Three groups of experiments were performed to determine if the wide-swath altimetry observations would improve the three-dimensional (3D) field estimates of ocean temperature-salinity-velocity (T-S-V), and to evaluate how the spatial and temporal resolution and accuracy of the wide-swath altimetry observations affected the ocean state estimation. The Regional Ocean Modeling System and the four-dimensional variational data assimilation method were used in the experiments, with numerical simulation for the Taiwan region at a resolution of $1/10^\circ$ as the example. The sensitivity of the 3D ocean state construction to the wide-swath altimetry measurements was also investigated. The results showed that the wide-swath sea surface height (SSH) measurements would have an overall positive impact on the 3D T-S-V field and that the positive effect would increase as the resolution and accuracy of the observations increased, but the net benefits would gradually decrease. Among the three examined features

* Corresponding author at: China University of Petroleum, College of Oceanography and Space Informatics, Qingdao 266580, China.

E-mail address: hitzcj@163.com (C. Zhou).

Peer review under the responsibility of the Institute of Oceanology of the Polish Academy of Sciences.



Production and hosting by Elsevier

<https://doi.org/10.1016/j.oceano.2020.02.004>0078-3234/© 2020 Institute of Oceanology of Polish Academy of Sciences. Published by Elsevier B.V. This is an open access article under the CC BY-NC-ND license (<http://creativecommons.org/licenses/by-nc-nd/4.0/>).

of the wide-swath altimetry observations, the temporal resolution had the most influence on the 3D ocean state analysis.

© 2020 Institute of Oceanology of Polish Academy of Sciences. Published by Elsevier B.V. This is an open access article under the CC BY-NC-ND license (<http://creativecommons.org/licenses/by-nc-nd/4.0/>).

1. Introduction

Since 1973, many altimetry missions, such as Skylab, Geosat, ERS, Topex/Poseidon, and the Jason surveys, have been launched to measure sea surface elevation. Information about sea surface height (SSH) collected by altimeters has become an essential element of ocean investigations (Gaspar et al., 1994; Hwang et al., 1998; Martin-Neira et al., 1998; Qiu and Chen, 2005; Tandeo et al., 2014). Altimetry observations can be merged with other data to give the broadest possible interpretation of the mechanisms that drive oceanic processes (Morrow and Birol, 1998; Piecuch and Ponte, 2011; Soto-Mardones et al., 2004; Wang and Liu 2006), and may also be assimilated into ocean and climate models to enhance the accuracy of the predictions (Cooper and Haines, 1996; De Mey and Robinson, 1987; Evensen and Van Leeuwen, 1996; Matsumoto et al., 2000; Mellor and Ezer, 1991). While the resolution and accuracy of the altimetry data are the most important aspects of these modelling applications, to date, few researchers have presented the detailed demand for SSH observations in ocean analysis.

Thanks to these continuous worldwide observations of SSH from satellite altimeters, we have been able to extend our research in various directions and, for example, gain knowledge about the variations in absolute circulation (Chelton et al., 1990; Korotaev et al., 2003; Miller et al., 1988; Nerem et al., 1990; Strub and James, 2002), and map eddies at the global scale (Chaigneau et al., 2008; Le Traon et al., 1990; Traon, 1991; Wang et al., 2003). Generally, ocean circulation occurs at the large-scale (ocean-basin scale) and could be recognized from the altimetry observations easily. Mesoscale eddies have a horizontal scale of between 25 and 500 km and generally move across the ocean at speeds of less than 10 km/day (Koblinsky et al., 1992). However, the sub-mesoscale processes (with scales between 50 and 100 km) are not visible in the images from a traditional altimeter (Klein et al., 2015). It is expected that the future wide-swath altimetry, such as the Surface Water and Ocean Topography (SWOT) mission (to be launched in 2021), would provide the ocean SSH fields in two dimensions at a global scale and make a prominent contribution to the study of sub-mesoscale processes (Bell et al., 2015; Le Traon et al., 2017).

Moreover, the sea surface elevation reflects more than just the surface conditions, and may also benefit for the estimates of three-dimensional (3D) ocean state in ocean modelling system. In some of the previous studies, surface elevation information has been proved to have a positive impact on the ocean model (Fan et al., 2004; Killworth et al., 2001; Kurapov et al., 2011; Martin et al., 2007; Penduff et al., 2002). Conversely, the major challenge for altimetry in the future is how to incorporate data from both wide-swath

and conventional along-track altimeters into high-resolution ocean general circulation models, to facilitate a detailed description and high-resolution forecast of the ocean state (Pujol et al., 2012). Approaching the challenge of using wide-swath altimetry data, Gaultier et al. (2016) underline the need to test their effective impact on ocean analyses and forecasts by performing observing system simulation experiments. Using the simulated observations derived from a fully eddy-resolving free simulation, the contribution of forthcoming wide-swath altimetry missions on the ocean analysis and forecasting system is firstly quantified (Bonaduce et al., 2018).

To further clarify the demand of 3D ocean state estimations on the wide-swath altimetry data, the impact of SSH assimilations was evaluated at various spatial and temporal resolutions and levels of accuracy in this study (Figure 1). The paper is organized as follows. The method for simulating the wide-swath altimetry observations is described in Section 2. Section 3 refers to the main body of the paper, in which we discuss how the future wide-swath SSH observations will influence data assimilation based on the Regional Ocean Modeling System (ROMS) and four-dimensional variational data assimilation (4DVAR). In section 4, the sensitivity analysis of 3D ocean state simulation to the wide-swath SSH

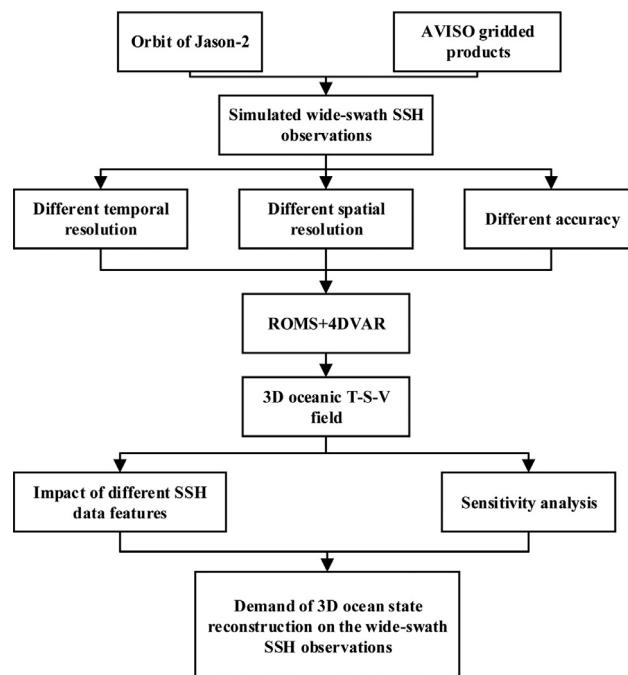


Figure 1 Flowchart of the demand analysis of 3D ocean state on the wide-swath altimeter observations.

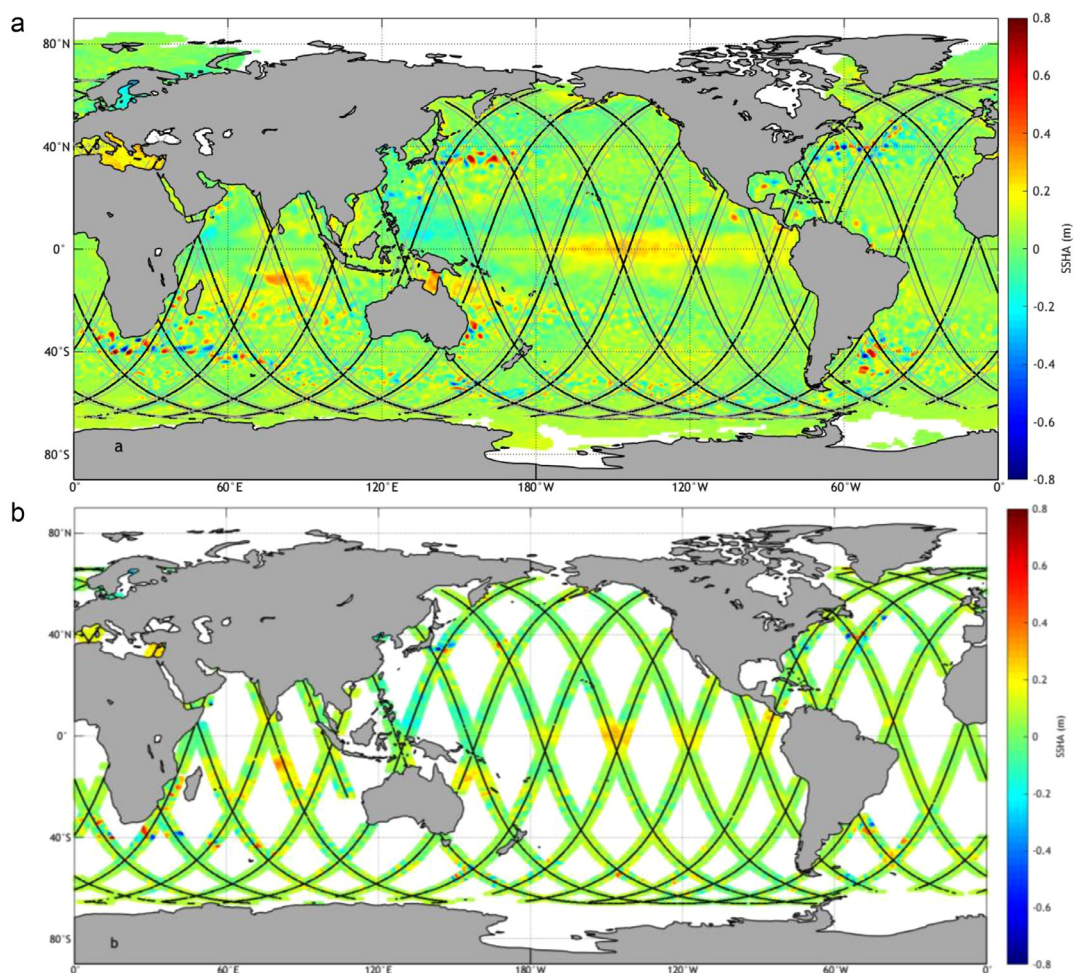


Figure 2 Graph a) is the global sea surface height anomaly (SSHA) from AVISO and the observation orbit of Jason-2 (black lines) on 1 January 2010. The gray lines are the two boundaries of the simulated altimeter's swath, derived by translating the measurements of Jason-2 horizontally. Graph b) presents the simulated altimeter observations with a 6°-wide swath, and the Jason-2 orbit (black lines).

observations, carried out to further validate the conclusion from section 3, are considered. Section 5 comprises a summary and discussion.

2. Simulation of the wide-swath altimetry observations

The wide-swath altimetry observations were extracted from the AVISO gridded products (SEALEVEL_GLO_PHY_L4_REP_OBSERVATIONS_008_047 available at <http://marine.cop-ernicus.eu/>) based on the Jason-2 orbit (see Figure 2). The details of the wide-swath altimetry simulation are presented as follows.

According to previous studies (Ducet et al., 2000; Vélez-Belchí et al., 2013), some detailed characteristics of ocean state could be reconstructed in the gridded SSH products (as shown in Figure 1). To simulate the future altimeter of a certain swath, the measure orbit of Jason-2 were employed and translated horizontally with a desired swath width W . Namely, the zonal boundary of simulated wide-swath orbit

was restricted by the longitude of Jason-2 measurements (Lon) and the swath W , and the SSH data located in $[Lon-W/2, Lon+W/2]$ were extracted from the AVISO gridded products.

The wide-swath altimetry observations using a 6° swath are presented in Figure 1(b). Unfortunately, the extracted SSH measurements were very limited, and we may not find any observations in the study region. Therefore, a track union during the repeat period of Jason-2 (9.9156 days) was considered as the hypothetical orbit of wide-swath altimeter, so that we could make a reasonable coverage for the regional simulation. The 10d and 5d union of observations generated from 1 Jan 2010 to 10 Jan 2010 near Taiwan Island are presented in Figure 3. Here, the 5d union was selected every two days. As shown in Figure 3, the data of both alternatives were sufficiently dense to cover the whole region, but the gaps between the two adjacent orbits of 10d union were too narrow ($\sim 3^\circ$) to specify a wide-swath. Thus, in this study, the 5d union choice was adopted to simulate the wide-swath altimetry observations, and the extracted observations are presented in Figure 3(c).

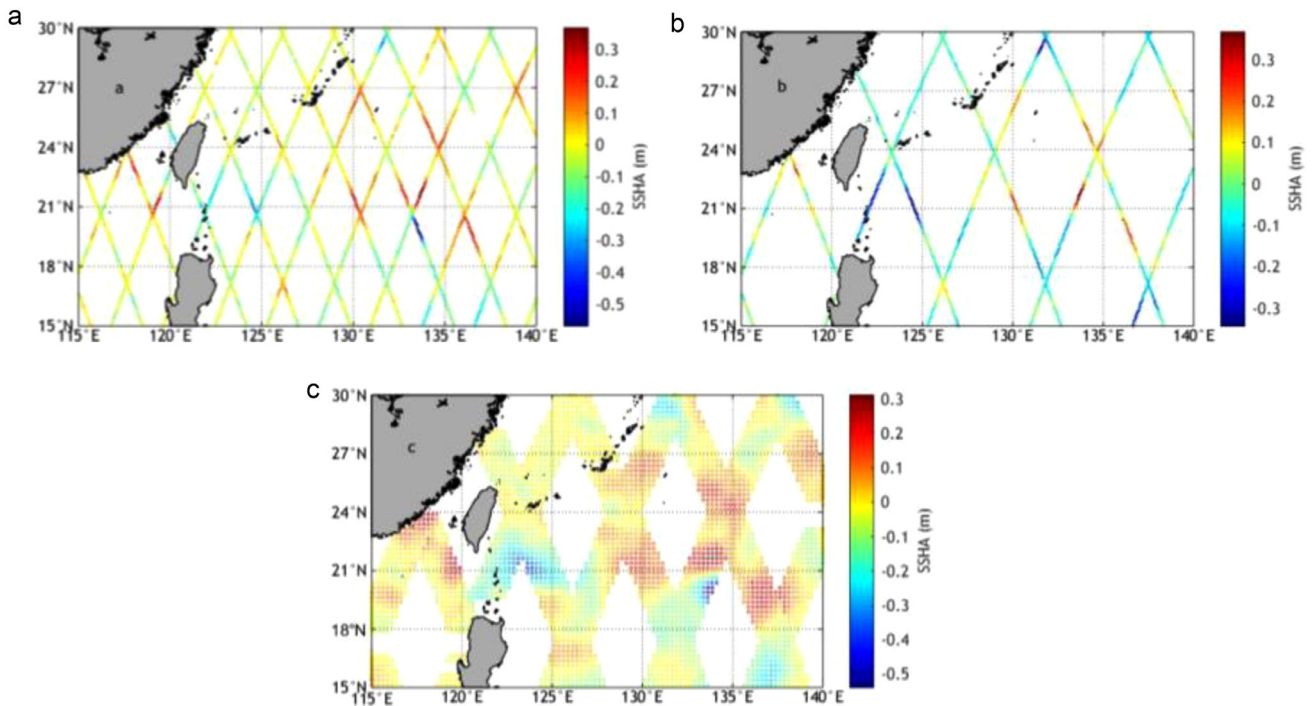


Figure 3 Graph a) and b) are the 10d and 5d orbit simulations based on the Jason-2 measurements. Graph c) represents the simulated altimetry observations with a 2°-wide swath near Taiwan Island.

3. Impact of wide-swath SSH observations on the 3D T-S-V estimates

In section 2, the simulation of wide-swath altimetry observations was performed. In the following, three groups of experiments were carried out with ROMS and 4DVAR, to explore how sensitive the oceanic 3D T-S-V estimates are to the features of the wide-swath SSH data, including the spatial and temporal resolution and accuracy. The configuration of the model and the assimilation were presented at first, and then the impact of the SSH assimilation with different data features is evaluated, respectively.

3.1. Configuration of the model and assimilation

The ocean model ROMS and the 4DVAR scheme were used in the experiments. ROMS is a free-surface, hydrostatic, primitive equation model discretized with a terrain-following vertical coordinate system (Shchepetkin and McWilliams, 2005). The model domain covered the area from 15°N to 30°N, and from 115°E to 140°E (Figure 4), with an eddy-resolved horizontal resolution of $0.1^\circ \times 0.1^\circ$ and 30 S-coordinate layers in the vertical. The level 2.5 Mellor Yamada scheme (Mellor and Yamada, 1982) was used to parameterize the vertical mixing process. The temperature and salinity fields were initialized by the Levitus climatology dataset, and the free surface and velocity were set to 0. The bathymetry field was produced from ETOPO1 data (Amante and Eakins, 2009). The minimum and maximum depths across the whole domain were set at 10 and 5000 m, respectively. A daily mean wind field from the Cross-Calibrated

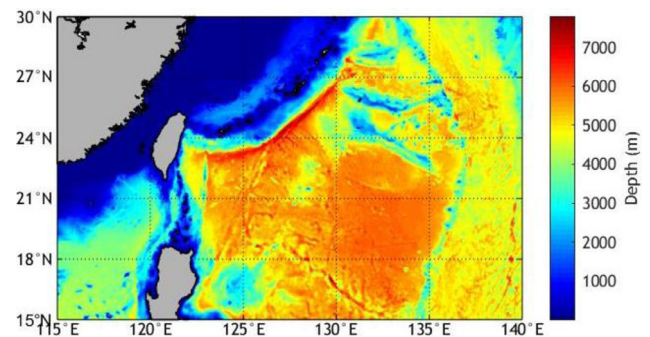


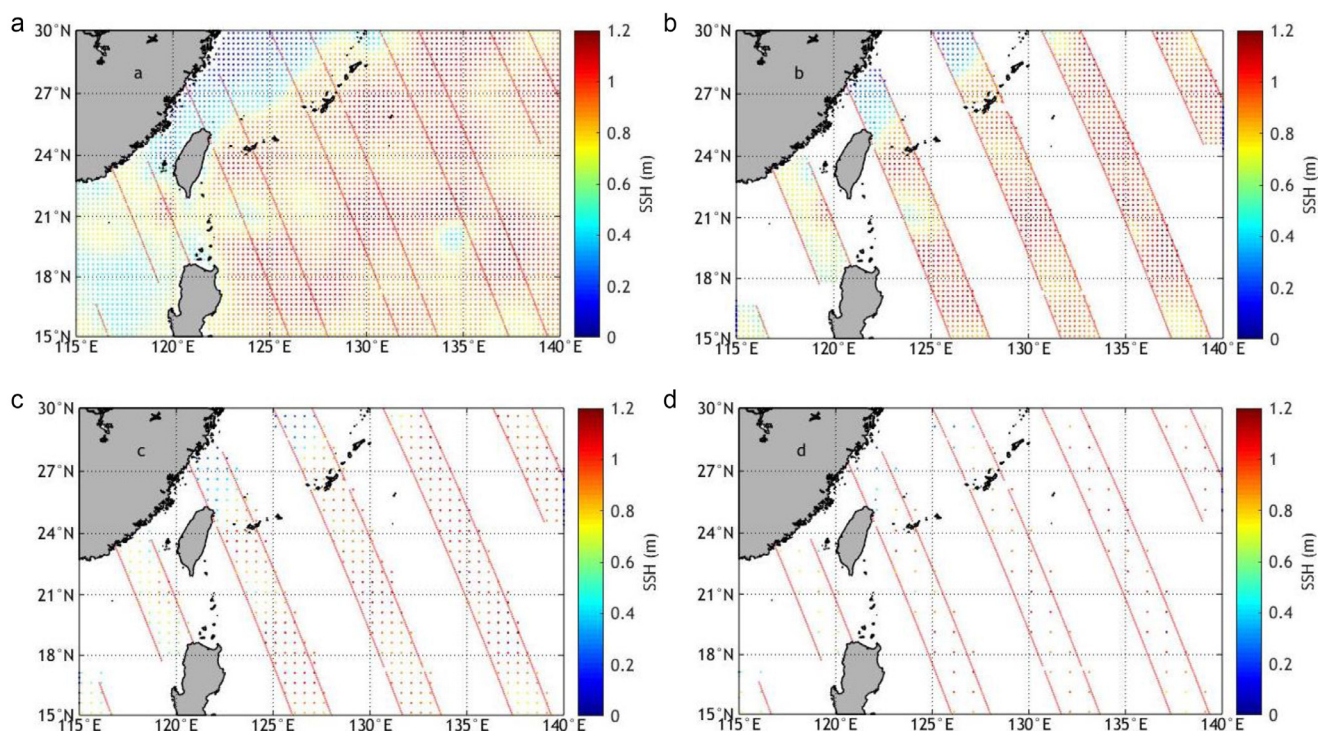
Figure 4 Model domain and bathymetry (m).

Multi-Platform (CCMP) ocean surface wind product (Atlas et al., 2011) with a horizontal resolution of $0.25^\circ \times 0.25^\circ$ was used for the wind field. The other daily atmospheric forcing fields, including heat fluxes, solar radiation fluxes, evaporation-precipitation (E-P), air temperature, and specific humidity, were obtained from the U.S. National Centers of Environmental Prediction (NCEP) reanalysis (Kalnay et al., 1996) at a horizontal resolution of $1.875^\circ \times 1.875^\circ$. The monthly temperature, salinity, sea surface height, and velocity field from simple ocean data assimilation (SODA) were used for the lateral boundary conditions.

Data for 5 years, starting from 1 Jan. 2005, were integrated into the forward model so that a dynamically balanced state was achieved, and then the outcomes were used to calculate the background error covariance matrix. The parameters that were used to model the background error covariance matrix (D) and the observation error covariance

Table 1 Summary of the SSH assimilation cases at different spatial resolutions.

| | Case 1 | Case 2 | Case 3 | Case 4 | Case 5 |
|-----|--------------------------------|--------|---------------------------|-------------------------|---------------------|
| SSH | 0.25° × 0.25° gridded products | No SSH | 0.25° × 0.25° along-track | 0.5° × 0.5° along-track | 1° × 1° along-track |

**Figure 5** Wide-swath SSH observations at different spatial resolutions (a: AVISO gridded products; b: 0.25° × 0.25°; c: 0.5° × 0.5°; d: 1° × 1°). The boundary (red dotted line) is determined by the orbit of Jason-2 using a 2° swath width.

matrix (R) were designed as Moore et al. (2011). The background errors of all initial conditions control variable components of D were 50 km in the horizontal and 30 m in the vertical. Horizontal correlation scales chosen for the background surface forcing error components of D were 300 km for wind stress and 100 km for heat and freshwater fluxes. The correlation lengths for the background open boundary condition error components of D were chosen to be 100 km in the horizontal and 30 m in the vertical. The observation errors were assumed to be uncorrelated in space and time, and the variances along the main diagonal of R were assigned as a combination of the measurement error and the error of representativeness, which are generally additive. A measurement error of 0.02 m was chosen for AVISO SSH.

3.2. Impact of SSH at different spatial resolutions

An experiment with five cases was designed to evaluate the impact of the spatial resolution on the 3D ocean T-S-V field. The details are listed in Table 1. In case 1, the 0.25° × 0.25° gridded SSH observations were assimilated and its outcomes were regarded as the ideal scenario. Due to the verified positive impact of the SSH measurements of our previous study (Zhou et al., 2018), the outcome of case 1 was sufficiently accurate to assess the other cases. In cases 3–5, the SSH

observations with different spatial resolutions were generated by choosing alternately along the satellite track, and the derived observations were assimilated, respectively. To highlight the effect of SSH assimilation, case 2 with no data assimilation was also performed.

In the following, the model outputs of case 1 were denoted as $T(x, y, z, t)$ and the results of the comparative cases were $M_i(x, y, z, t)$ where $i=2, 3, \dots$. Moreover, the temporally and vertically averaged error $H_i(x, y)$, the temporally and horizontally averaged error $V_i(z)$, and the spatially averaged error $S_i(t)$ were calculated as:

$$H_i(x, y) = \frac{1}{l_z l_t} \sum_z \sum_t |M_i(x, y, z, t) - T(x, y, z, t)|,$$

$$V_i(z) = \frac{1}{l_x l_y l_t} \sum_x \sum_y \sum_t |M_i(x, y, z, t) - T(x, y, z, t)|,$$

$$S_i(t) = \frac{1}{l_x l_y l_z} \sum_x \sum_y \sum_z |M_i(x, y, z, t) - T(x, y, z, t)|,$$

where l_x , l_y , l_z , and l_t were the dimensions of the four-dimensional model results, respectively.

For simplicity, only the observations of the ascending orbit were employed. The re-formed wide-swath SSH observations at different spatial resolutions are shown in Figure 5. As we can see, the extracted observations only

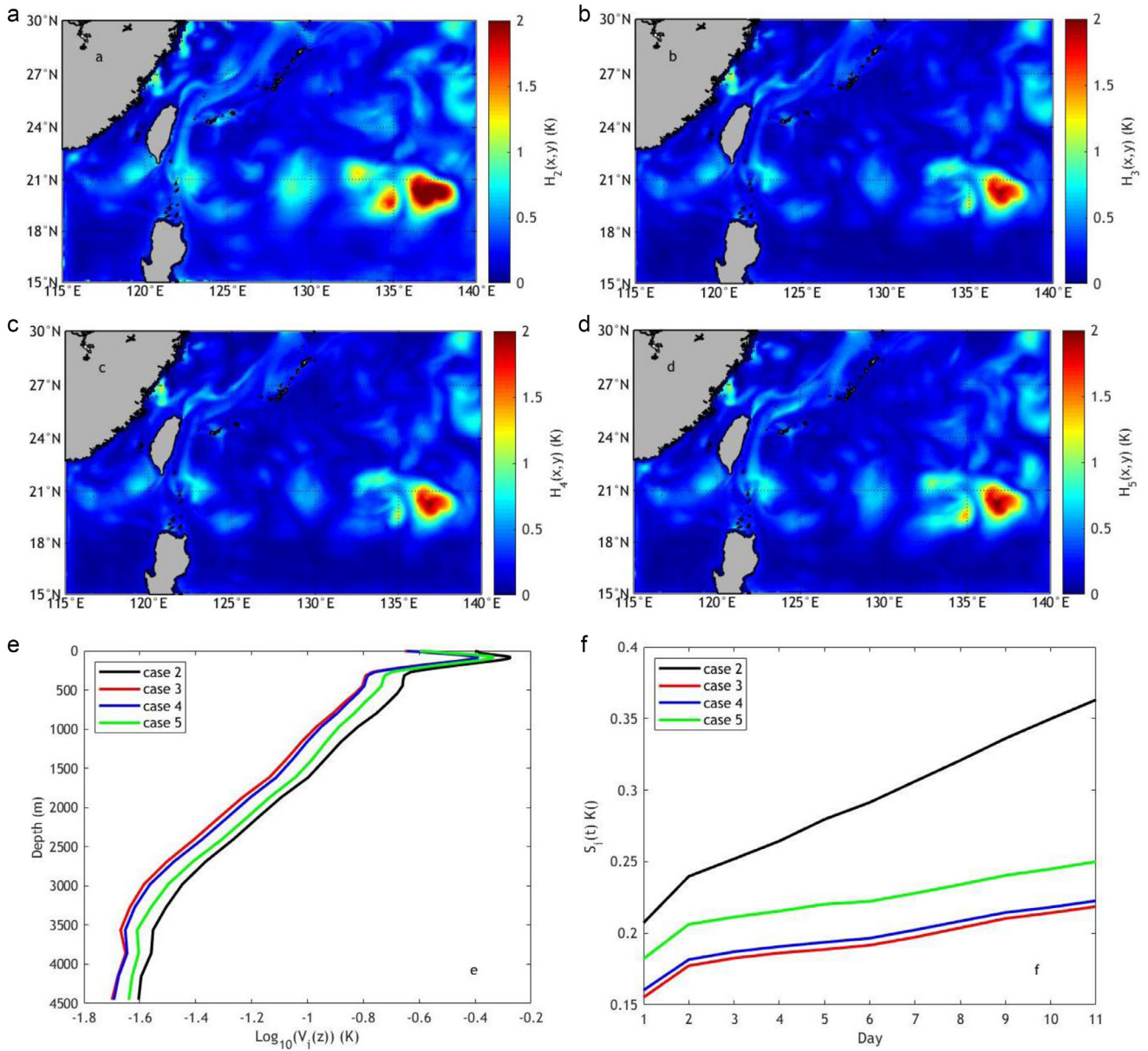


Figure 6 Evaluation of the temperature outcomes of SSH assimilation cases at different spatial resolutions. Here, graphs a)–d) is the temporal and vertical averaged error $H_i(x,y)$ ($i=2, 3, 4, 5$) of the 3D temperature field for cases 2–5. Otherwise, graphs e) and f), each presents the temporal and horizontal averaged error $V_i(z)$ and spatial averaged error $S_i(t)$, in which lines with different color give the results of cases 2–5, respectively.

reflected the local sea level elevation characteristics, and the amount of information contained in the along-track observations varied with the spatial resolution. This suggested that the positive enhancement may decrease considerably if the wide-swath observations became locally sparse.

As shown earlier, the outcomes of case 1 were used as the true states to verify the 3D T-S-V fields derived in cases 2–5. The spatial and temporal errors associated with the 3D temperature field are illustrated in Figure 6. As shown in Figure 6, the accuracy enhancement increased as the spatial resolution increased, but with limited net promotion. Compared with case 2, the outcomes of the

remaining cases were obviously enhanced, and the enhancement of case 3 was the greatest, in which the $0.25^\circ \times 0.25^\circ$ along-track observations were assimilated. Besides, the spatially averaged error tended to increase as the model ran forward, mainly caused by the accumulation of gaps between the ideal gridded and simulated along-track observations.

Meanwhile, the 3D salinity and velocity fields were validated. The error statistics results are presented in Figure 7 and Figure 8, and some similar conclusion was obtained. But the salinity and velocity estimations showed a different sensitivity to the spatial resolution of wide-swath SSH observations. As we can see from Figures 6–8, the temperature

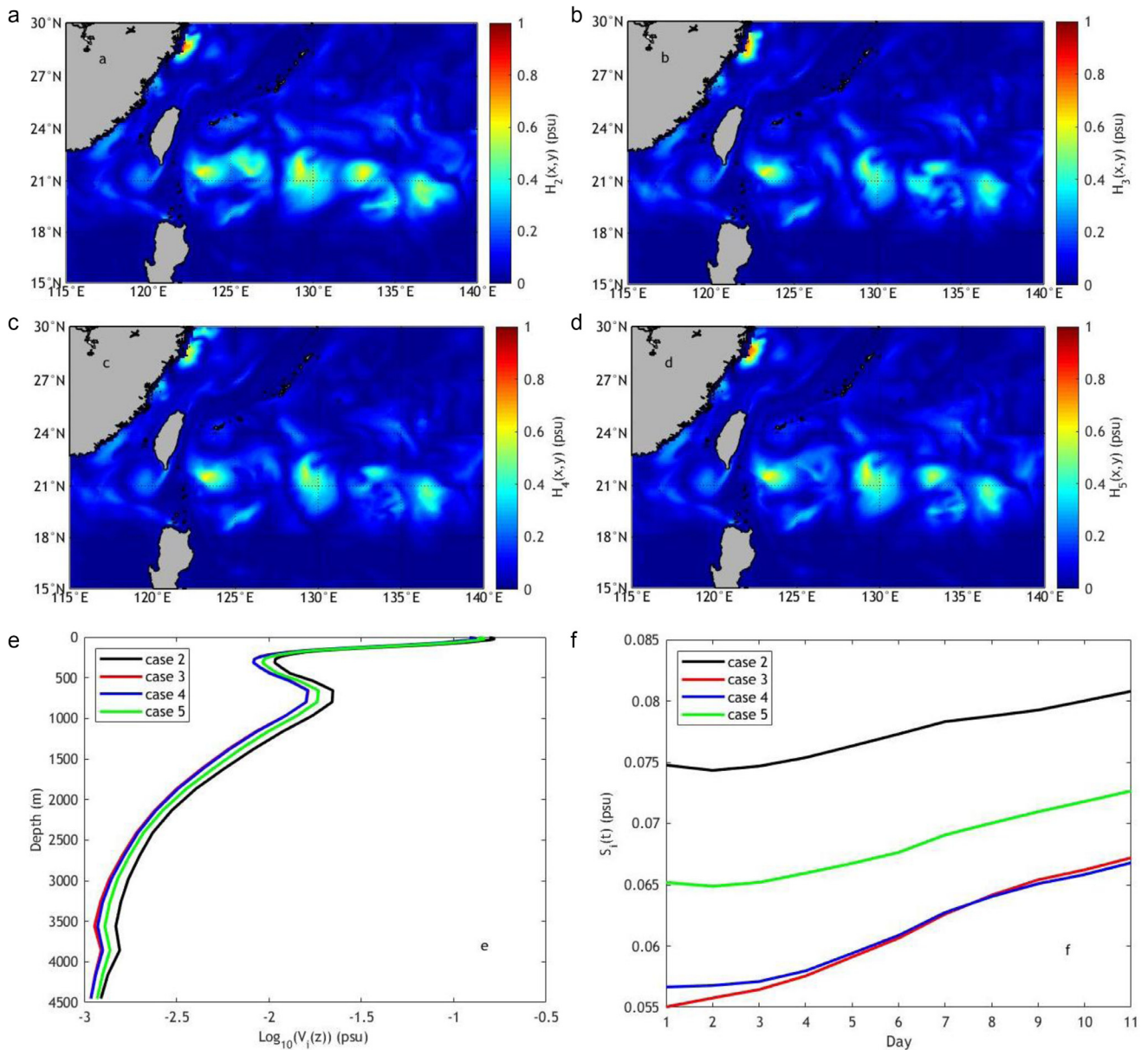


Figure 7 Evaluation of the salinity outcomes of SSH assimilation cases at different spatial resolutions. Graphs a)–f) are presented similarly as Figure 6, but for the 3D salinity field.

estimation was enhanced by a maximum of 0.15°C , but for the salinity and velocity field, the values were 0.02 psu and 0.01 m/s, respectively.

3.3. Impact of SSH at different temporal resolutions

In this section, an experiment with five cases was carried out using different assimilation intervals, to simulate the situation of SSH observations at different temporal resolutions. The daily AVISO SSH gridded products was adopted as the ideal case, and the reduced intervals every 3, 5, or 10 days were considered, respectively (Table 2). As the higher assimilation frequency are more beneficial for ocean analy-

Table 2 Summary of the SSH assimilation cases at different intervals.

| | Case 1 | Case 2 | Case 3 | Case 4 | Case 5 |
|----------|--------|--------|--------|--------|--------|
| Interval | 1-day | No SSH | 3-day | 5-day | 10-day |

sis (Powell et al., 2008), the daily assimilation case (case 1) was applied to verify the outcomes of the remaining cases.

The evaluation was conducted using the similar strategy in section 3.2, and the results are presented in Figure 9–11. As we can see, the 3D T-S-V field estimated by the 3-day assimilation interval (case 3) presents to be the most accurate scenario. Unlike the accuracy promotion caused by

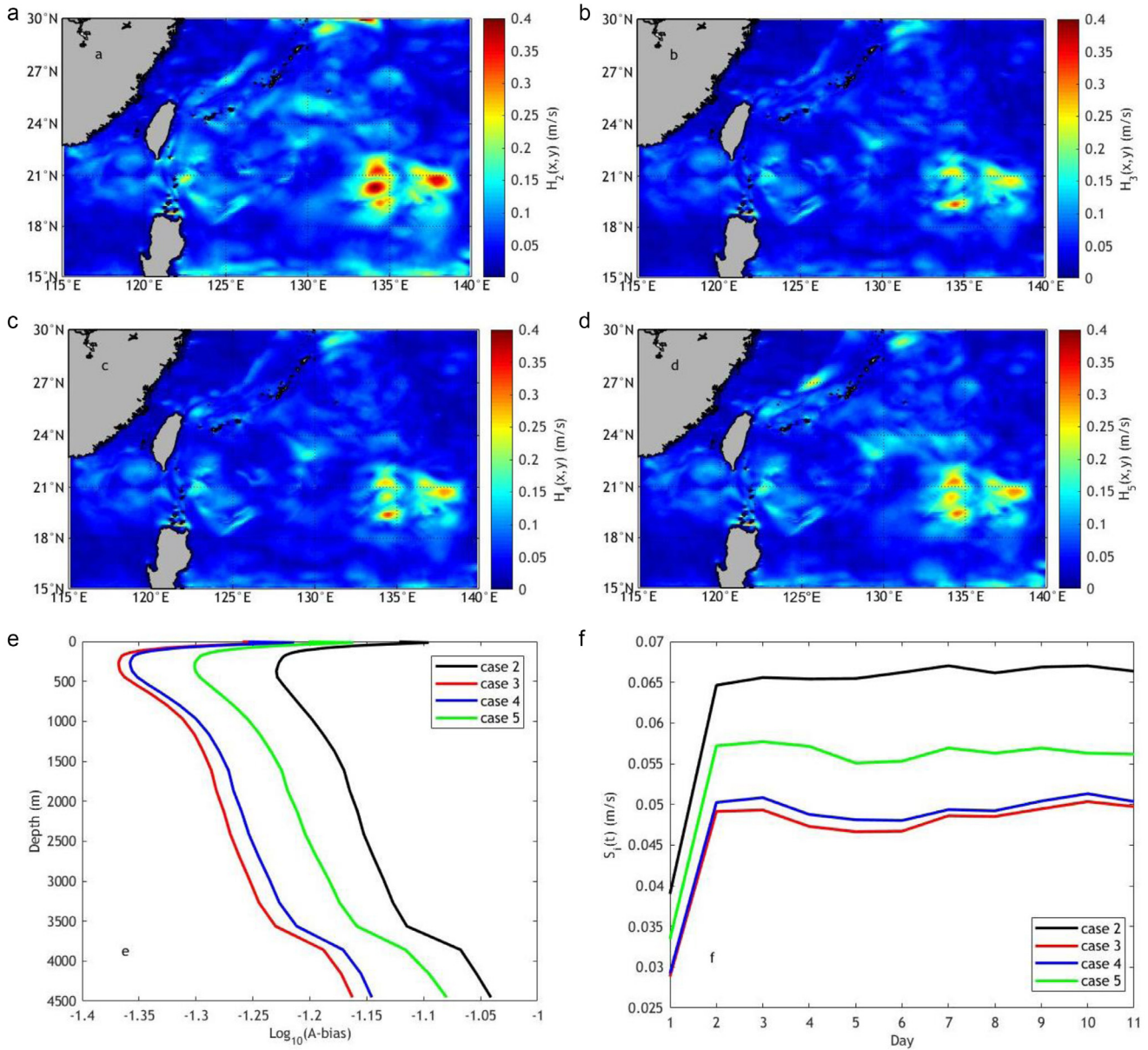


Figure 8 Evaluation of the velocity (eastward component) outcomes of SSH assimilation cases at different spatial resolutions. Graphs a)–f) are presented similarly as Figure 6, but for the 3D velocity field.

the increasement of spatial resolution, more sensitive response was found when the temporal resolution changed. In other words, the temporal resolution of wide-swath altimeter observations seems to be more effective than its spatial features in the data assimilation.

3.4. Impact of SSH at different levels of accuracy

The quality of the observations has an extremely significant role in the data assimilation, and the model solution would be distorted by the inaccurate information. To analyze the impact of the accuracy of wide-swath SSH observations on the 3D T-S-V field construction, some random noise with a fixed mean value was added to the SSH observations. The mean value of added noise was configured as 0.01 m, 0.03

m, 0.05 m, 0.1 m, and 0.15 m. Then the processed SSH observations at different levels of accuracy were assimilated into the ocean model, respectively. The details of the experiment are shown in Table 3, and the assimilation of SSH observations without any noise was taken as the ideal scenario to verify the remaining cases.

The evaluation of 3D T-S-V fields is presented in Figure 12–14. As we can see, the 3D T-S-V simulations were enhanced when the SSH observations were assimilated. However, accuracy of the SSH observations seemed to have less impact than the spatial and temporal resolution, as the difference between cases 3–7 was relatively finite. As shown in Figure 12(h), 13(h), and 14(h), the 3D T-S-V estimations from 0.15 m to 0.01 m were enhanced by less than 0.1°C, 0.05 psu, and 0.03 m/s, respectively. Considering the

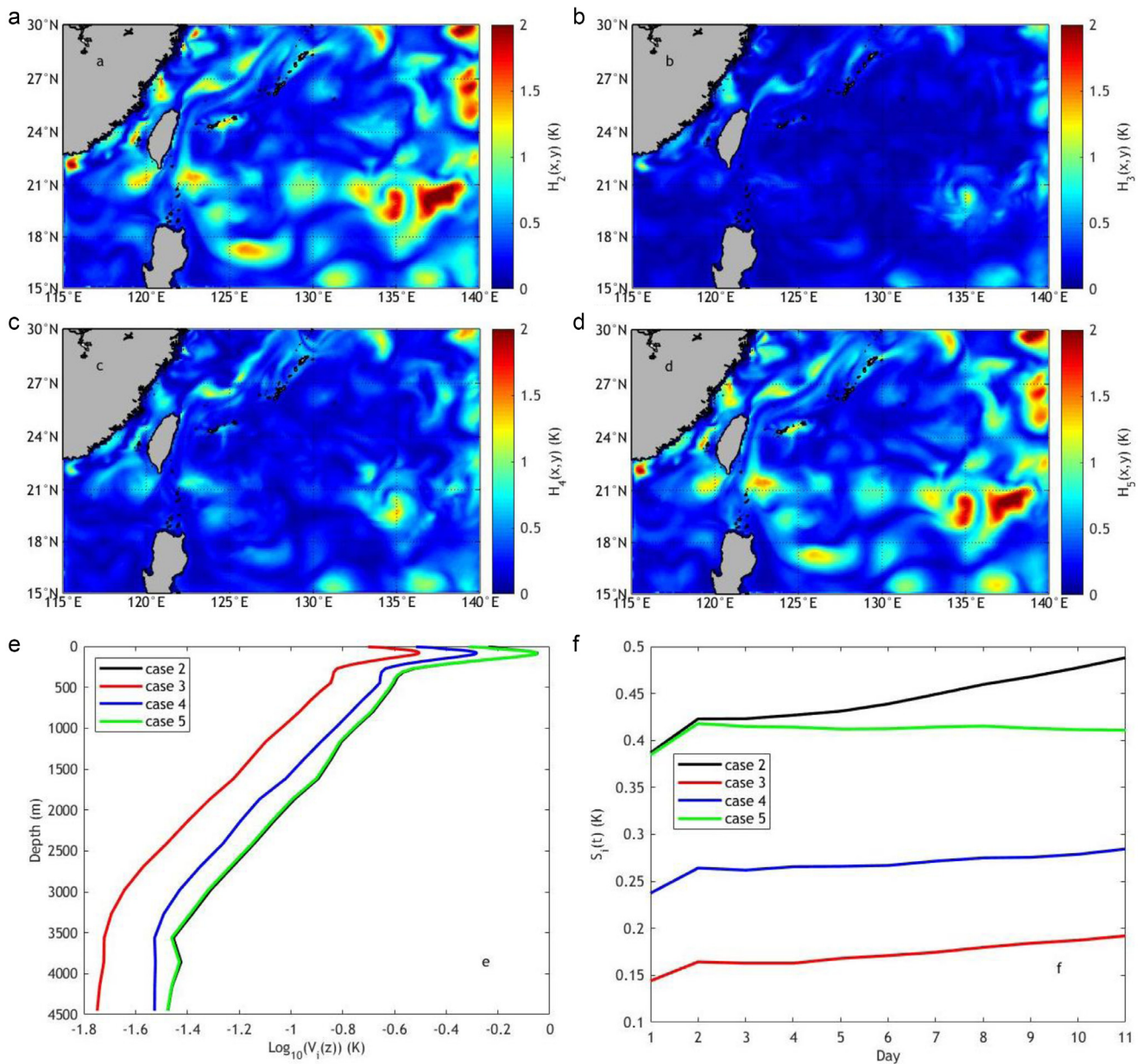


Figure 9 Evaluation of the temperature outcomes of SSH assimilation cases at different temporal resolutions. Here, graphs a)–d), each presents the temporal and vertical averaged error $H_i(x,y)$ ($i=2, 3, 4, 5$) of the 3D temperature field for cases 2–5. Otherwise, graph e) and f) present the temporal and horizontal averaged error $V_1(z)$ and spatial averaged error $S_i(t)$, in which lines with different color give the results of cases 2–5, respectively.

Table 3 Summary of SSH assimilation cases with different noise levels

| | Case 1 | Case 2 | Case 3 | Case 4 | Case 5 | Case 6 | Case 7 |
|-----|--------|---------------------|--------|--------|--------|--------|--------|
| SSH | 0 | No SSH assimilation | 0.01 m | 0.03 m | 0.05 m | 0.1 m | 0.15 m |

addition way of the noise, the abnormal conclusion could be explicated to some degree. The artificial noise was generated with a fixed mean value, which may lead to a similar pattern of the generated observations, and then the characteristics of the sea surface elevation were still contained, more or less.

4. Sensitivity analysis

The above analysis indicated that the 3D T-S-V field estimations could get improved when the wide-swath altimetry observations were assimilated. Among the three discussed features, the temporal resolution was considered to be the

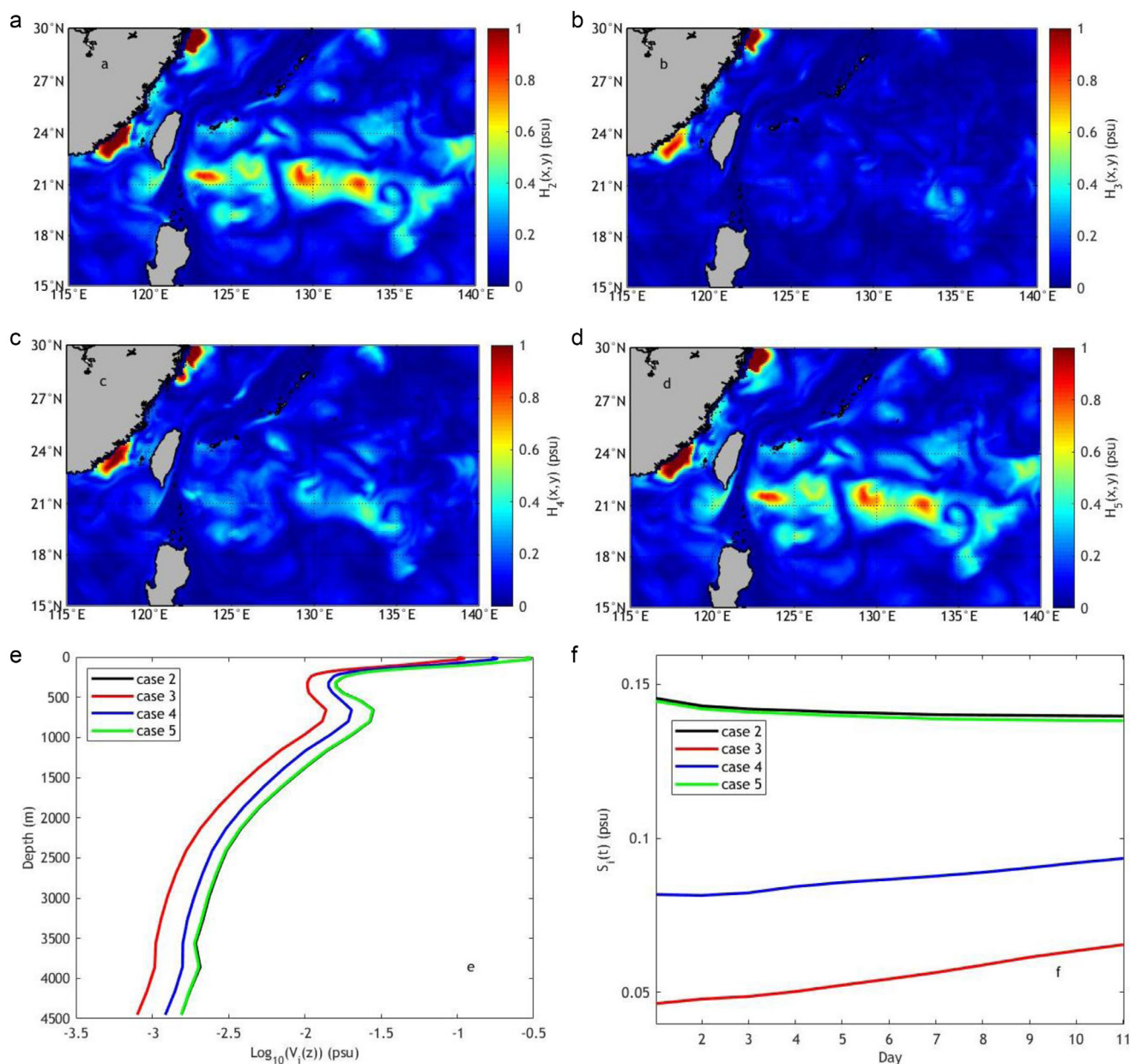


Figure 10 Evaluation of the salinity outcomes of SSH assimilation cases at different temporal resolutions. Graphs a)–f), each presents errors similarly as Figure 9, but for the 3D salinity field.

Table 4 Average absolute bias and the percentage enhancement (in brackets) of the assimilation cases at different spatial resolutions (Sres).

| Sres | 0.25° | 0.5° | 1° | No SSH |
|---------|-------------|-------------|-------------|--------|
| T (°C) | 0.193 (34%) | 0.198 (32%) | 0.223 (24%) | 0.292 |
| S (psu) | 0.06 (22%) | 0.061 (21%) | 0.068 (12%) | 0.077 |
| V (m/s) | 0.047 (27%) | 0.048 (25%) | 0.054 (16%) | 0.064 |

Table 5 Average absolute bias and the percentage enhancement (in brackets) of the assimilation cases at different temporal resolutions (Tres).

| Tres | 3-day | 5-day | 10-day | No SSH |
|---------|-------------|-------------|--------------|--------|
| T (°C) | 0.172 (61%) | 0.268 (40%) | 0.411 (7%) | 0.443 |
| S (psu) | 0.055 (61%) | 0.087 (38%) | 0.14 (7%) | 0.141 |
| V (m/s) | 0.043 (50%) | 0.063 (27%) | 0.085 (1.2%) | 0.086 |

most effective one. In this section, we tried to quantify the impact of the spatial and temporal resolution and the accuracy, and analyze the sensitivity of 3D T-S-V construction to these wide-swath SSH features.

Comparing with the corresponding ideal scenario cases, the absolute bias of the three groups of experiments was averaged and presented in Table 4–6. Besides, the percentage of enhancement was also calculated with respect to the

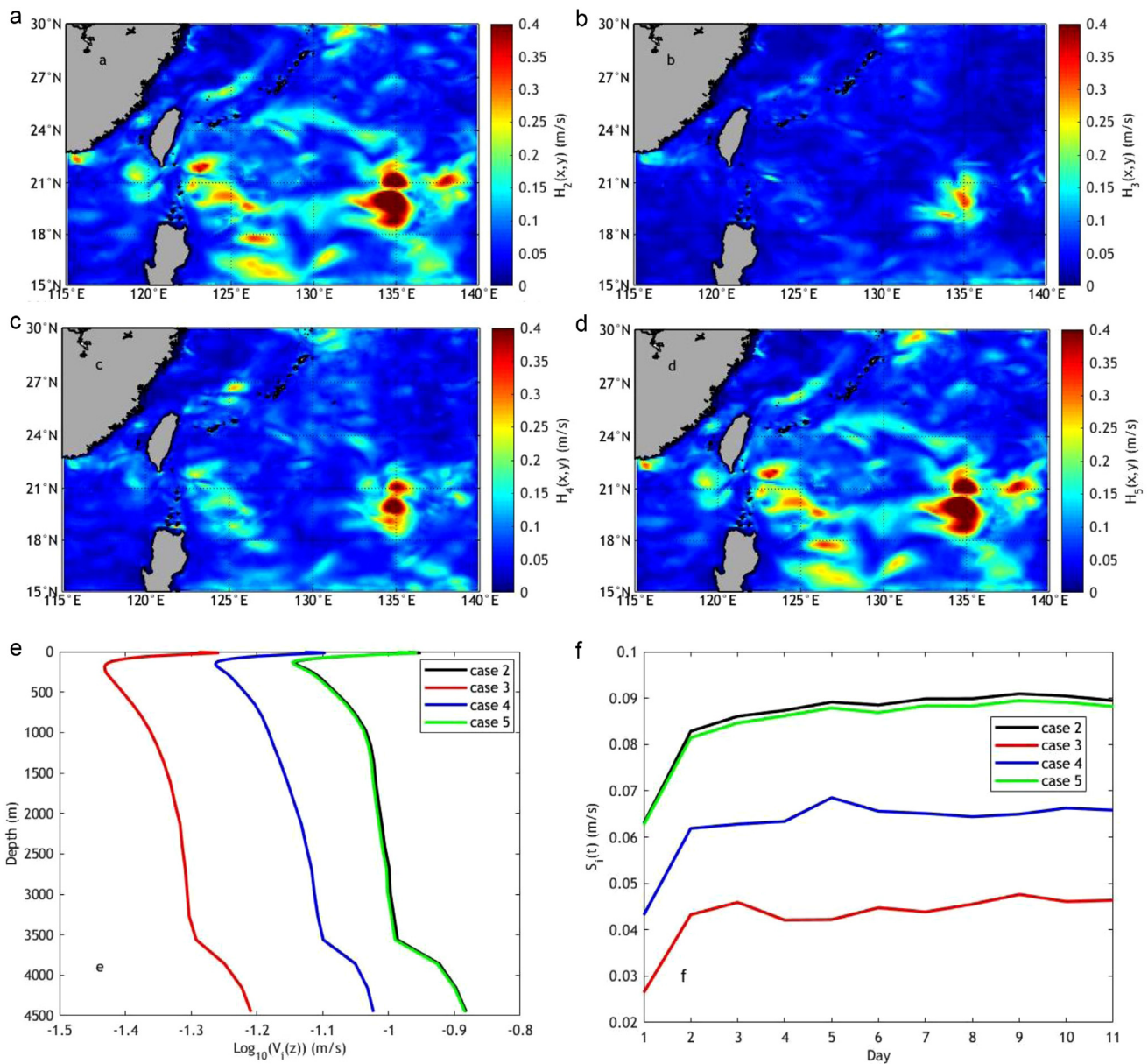


Figure 11 Evaluation of the velocity (eastward component) outcomes of SSH assimilation cases at different temporal resolutions. Graphs a)–f), each presents errors similarly as Figure 9, but for the 3D velocity field.

Table 6 Average absolute bias and the percentage enhancement (in brackets) of the assimilation cases at different accuracy levels.

| Accuracy | 0.01 m | 0.03 m | 0.05 m | 0.1 m | 0.15 m | No SSH |
|----------|-------------|-------------|-------------|-------------|-------------|--------|
| T (°C) | 0.009 (98%) | 0.021 (95%) | 0.034 (92%) | 0.074 (83%) | 0.106 (76%) | 0.441 |
| S (psu) | 0.003 (98%) | 0.006 (96%) | 0.009 (94%) | 0.021 (86%) | 0.032 (78%) | 0.147 |
| V (m/s) | 0.002 (98%) | 0.005 (94%) | 0.009 (89%) | 0.018 (79%) | 0.025 (70%) | 0.084 |

case without data assimilation. In each group, the positive effect of the SSH assimilation increases with better parameter choices. Moreover, the 3D T-S-V fields showed different sensitivity to these three features, and the temporal resolution of the assimilated wide-swath SSH observations seems to be the most attractive one. As shown in Table 5,

the enhancement between two adjacent cases differs by as much as 33%, larger than the variations in Tables 4 and 6.

To make the three groups of experiments comparable, the error scales were normalized accordingly. Firstly, the error of cases without SSH data assimilation and the ideal scenarios were configured as the two extreme values, 1 and

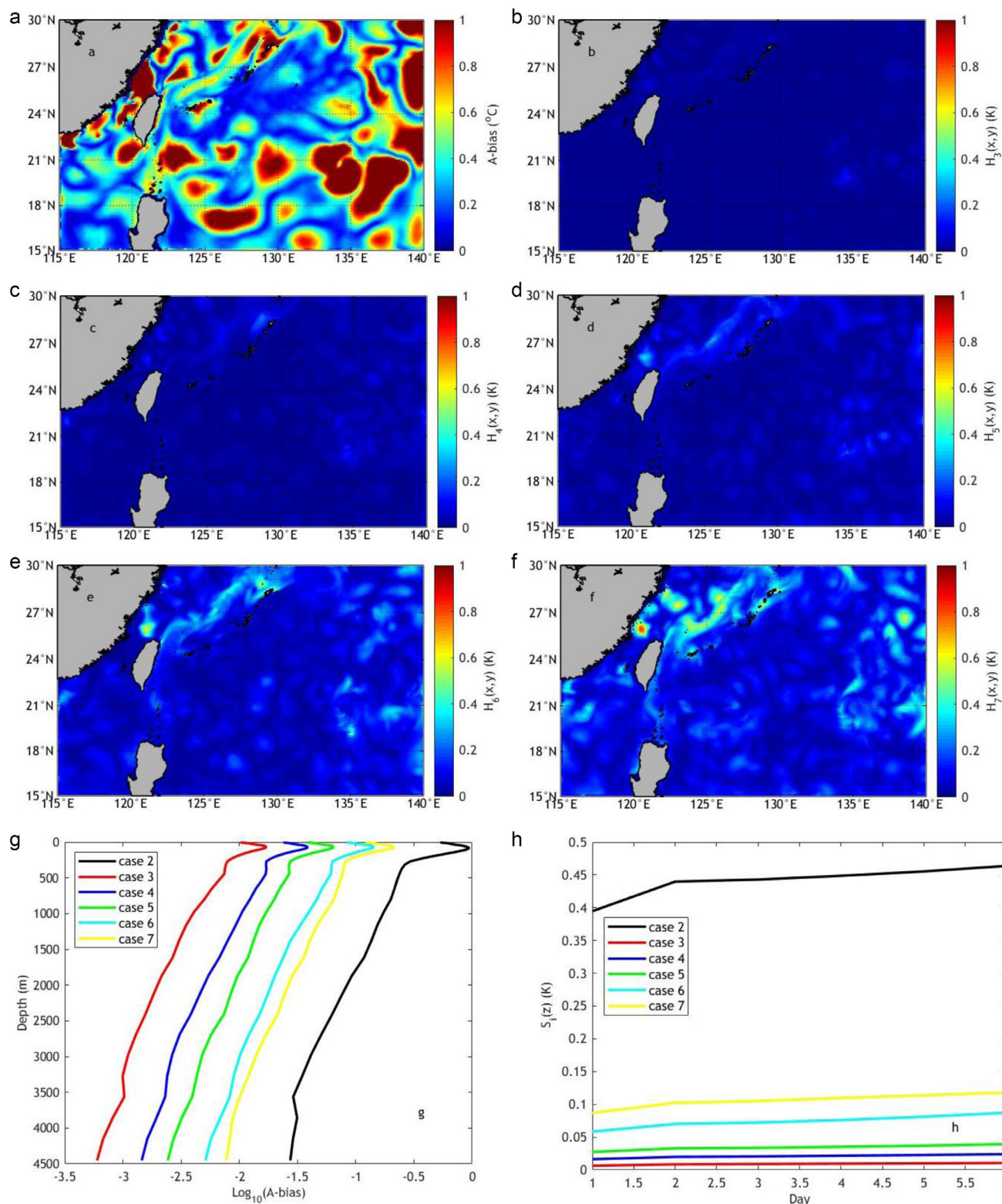


Figure 12 Evaluation of temperature outcomes of SSH assimilation cases at different levels of accuracy. Here, graphs a)–d), each presents the temporal and vertical averaged error $H_i(x,y)$ ($i=2, 3, 4, 5, 6, 7$) of the 3D temperature field for cases 2–7. Otherwise, graph e) and f) present the temporal and horizontal averaged error $V_i(z)$ and spatial averaged error $S_i(t)$, in which lines with different color give the results of cases 2–7, respectively.

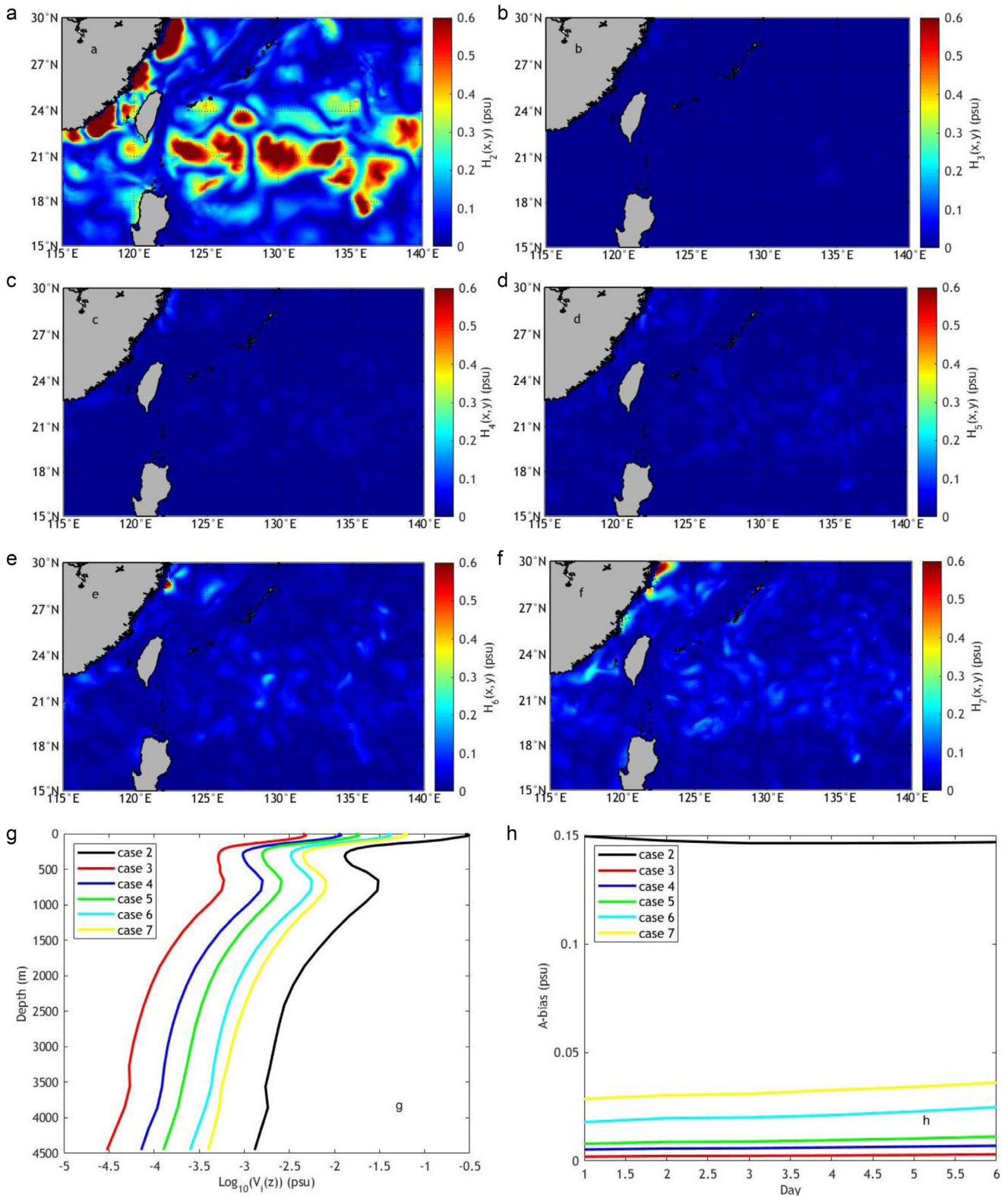


Figure 13 Evaluation of the salinity outcomes of SSH assimilation cases at different levels of accuracy. Graphs a)–h) are presented in the similar way to those in Figure 12, but for the salinity field.

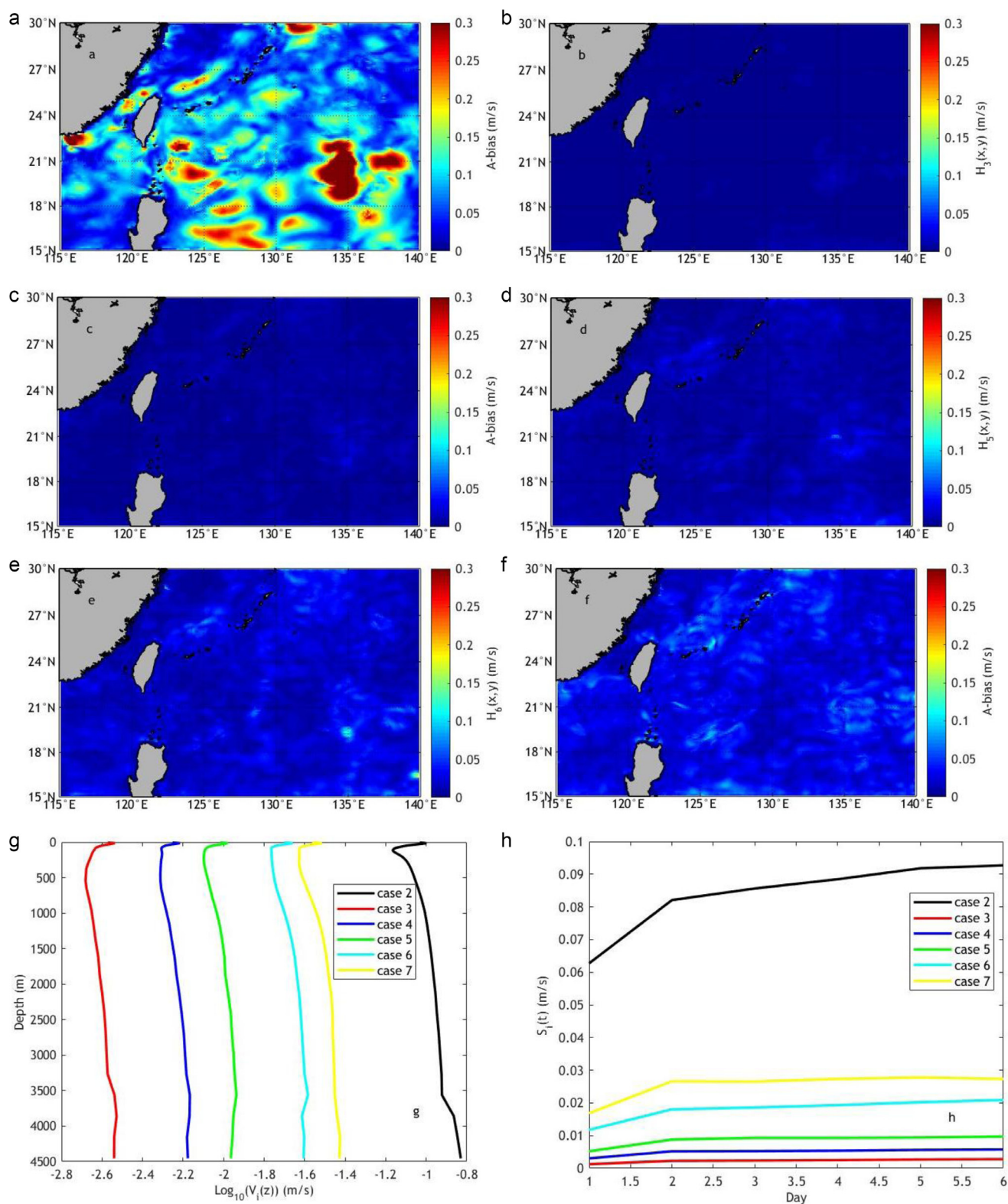


Figure 14 Evaluation of the velocity (eastward component) outcomes of SSH assimilation cases at different levels of accuracy. Graphs a)–h) are presented in the similar way to those in Figure 12, but for the 3D velocity field.

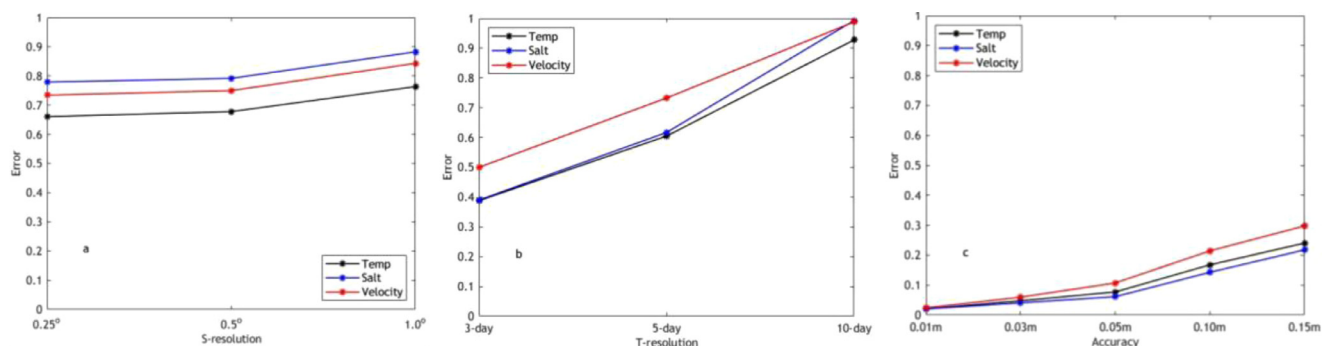


Figure 15 Normalized error statistics. Graphs a)–c) represent the results of SSH assimilation experiments using different spatial and temporal resolutions and different accuracy levels.

0, respectively. Assuming the error series were represented by e_i , then the formula for the normalization is:

$$E_i = \frac{e_i - \min(e_i)}{\max(e_i) - \min(e_i)}$$

After that, all the errors were set between 0 and 1, i.e., $E_i \in (0, 1)$.

The normalized T-S-V errors of the three groups of experiments are shown in Figure 15. In each graph, the slope of the curves is regarded as the sensitivity to the corresponding data feature. Thus, as shown in the figure, the 3D T-S-V field was demonstrated to be the most sensitive to the temporal resolution of wide-swath SSH observations, which confirmed the above conclusion. Thus, if we would like to model the 3D ocean state by assimilating the wide-swath altimeter observations, the temporal resolution or the assimilation interval is the parameter which deserves more attention.

5. Conclusions

In this study, the impact of wide-swath altimeter observations on the construction of the oceanic 3D T-S-V field was investigated, based on ROMS and 4DVAR. Using the AVISO gridded products and the observe orbit of Jason-2, the wide-swath altimetry measurements were simulated and generated at different spatial and temporal resolutions and levels of accuracy. After that, three groups of experiments were performed to examine the impact of these features on the assimilation results. In each group, the derived ocean T-S-V fields were evaluated by the specified ideal scenario. The comparisons indicated that, the estimation of the 3D ocean state obtains an obvious enhancement when the wide-swath SSH information got assimilated, and the effect increased with better parameter choices. Besides, the estimate of the 3D T-S-V fields was demonstrated to be the most sensitive to the temporal resolution, for which the derived 3D T-S-V fields could be improved by up to 54%, and this conclusion was confirmed by analyzing the normalized errors.

The forthcoming wide-swath altimeter observations certainly have a positive effect on the estimates of the ocean 3D state. However, it is unrealistic for the design of the altimeter to hold all the optimal parameters at the same time, and thus some non-essential qualities must

be sacrificed. In such situation, the sensitivity analysis could be applied to evaluate which parameter might be weakened. In the future, we would like to refine the quantitative assessments and evaluate the capacity to detect some ocean dynamical processes. Otherwise, we would also like to thoroughly investigate the potential applications and advantages of the forthcoming wide-swath altimetry observations.

Acknowledgments

The authors would like to thank the AVISO for providing the gridded multi-mission altimeter products (<http://www.aviso.altimetry.fr>). The study is supported by the National Key R&D Program of China under contract no. 2017YFC1405600, the National Natural Science Foundation of China under contract no. 41576176 and the Fundamental Research Funds for the Central Universities under contract no. 19CX05003A-6.

References

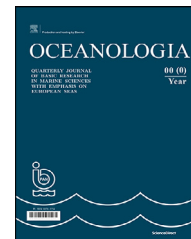
- Amante, C., Eakins, B.W., 2009. ETOPO1 arc-minute global relief model: procedures, data sources and analysis. NOAA Tech. Memo, 19 NESDIS NGDC-24, 25 pp.
- Atlas, R., Hoffman, R.N., Ardizzone, J., Leidner, S.M., Jusem, J.C., Smith, D.K., Gombos, D., 2011. A cross-calibrated, multiplatform ocean surface wind velocity product for meteorological and oceanographic applications. *B. Am. Meteorol. Soc.* 92 (2), 157–174.
- Bell, M.J., Schiller, A., Le Traon, P.Y., Smith, N.R., Dombrowsky, E., Wilmer-Becker, K., 2015. An introduction to GODAE OceanView. *J. Oper. Oceanogr.* 8 (S1), s2–s11.
- Bonaduce, A., Benkiran, M., Remy, E., Traon, P.Y.L., Garric, G., 2018. Contribution of future wide-swath altimetry missions to ocean analysis and forecasting. *Ocean Sci.* 14 (6), 1405–1421.
- Chaigneau, A., Gizolme, A., Grados, C., 2008. Mesoscale eddies off Peru in altimeter records: Identification algorithms and eddy spatio-temporal patterns. *Prog. Oceanogr.* 79 (2–4), 106–119.
- Chelton, D.B., Schlax, M.G., Witter, D.L., Richman, J.G., 1990. Geosat altimeter observations of the surface circulation of the Southern Ocean. *J. Geophys. Res.-Oceans* 95 (C10), 17877–17903.
- Cooper, M., Haines, K., 1996. Altimetric assimilation with water property conservation. *J. Geophys. Res.-Oceans* 101 (C1), 1059–1077.

- De Mey, P., Robinson, A.R., 1987. Assimilation of altimeter eddy fields in a limited-area quasi-geostrophic model. *J. Phys. Oceanogr.* 17 (12), 2280–2293.
- Ducet, N., Le Traon, P.Y., Reverdin, G., 2000. Global high-resolution mapping of ocean circulation from TOPEX/Poseidon and ERS-1 and -2. *J. Geophys. Res.-Oceans* 105 (C8), 19477–19498.
- Evensen, G., Van Leeuwen, P.J., 1996. Assimilation of Geosat altimeter data for the Agulhas current using the ensemble Kalman filter with a quasigeostrophic model. *Mon. Weather Rev.* 124 (1), 85–96.
- Fan, S., Oey, L.Y., Hamilton, P., 2004. Assimilation of drifter and satellite data in a model of the Northeastern Gulf of Mexico. *Cont. Shelf Res.* 24 (9), 1001–1013.
- Gaspar, P., Ogor, F., Le Traon, P.Y., Zanife, O.Z., 1994. Estimating the sea state bias of the TOPEX and POSEIDON altimeters from crossover differences. *J. Geophys. Res.-Oceans* 99 (C12), 24981–24994.
- Gaultier, L., Ubelmann, C., Fu, L.L., 2016. The challenge of using future SWOT data for oceanic field reconstruction. *J. Atmos. Ocean. Tech.* 33 (1), 119–126.
- Hwang, P.A., Teague, W.J., Jacobs, G.A., Wang, D.W., 1998. A statistical comparison of wind speed, wave height, and wave period derived from satellite altimeters and ocean buoys in the Gulf of Mexico region. *J. Geophys. Res.-Oceans* 103 (C5), 10451–10468.
- Kalnay, E., Kanamitsu, M., Kistler, R., Collins, W., Deaven, D., Gandin, L., Iredell, M., Saha, S., White, G., Woollen, J., Zhu, Y., Chelliah, M., Ebisuzaki, W., Higgins, W., Janowika, J., Mo, K.C., Ropelewski, C., Wang, J., Leetmaa, A., Reynolds, R., Jenne, R., Joseph, D., 1996. The NCEP/NCAR 40-year reanalysis project. *B. Am. Meteorol. Soc.* 77 (3), 437–472.
- Killworth, P.D., Dieterich, C., Le Provost, C., Oschlies, A., Willebrand, J., 2001. Assimilation of altimetric data and mean sea surface height into an eddy-permitting model of the North Atlantic. *Prog. Oceanogr.* 48 (2–3), 313–335.
- Klein, P., Morrow, R., Samelson, R., Chelton, D., Lapeyre, G., Fu, L., Qiu, B., Ubelmann, C., Traon, P.L., Capet, X., Ponte, A., Sasaki, H., d'Ovidio, F., Farrar, T., Chapron, B., D'Asaro, E., Ferrari, R., McWilliams, J., Smith, S., Thompson, A., 2015. Mesoscale/sub-mesoscale dynamics in the upper ocean. *NASA Surface Water and Ocean Topography (SWOT)*, <http://www.aviso.altimetry.fr/fileadmin/documents/missions/Swot/WhitePaperSWOTSubmesoscale.pdf>.
- Koblinsky, C., Caspar, P., Lagerloef, G., 1992. Oceans and climate change: The future of spaceborne altimetry. *EOS-T. Am. Geophys. Un.* 73 (38) 403–403.
- Korotaev, G., Oguz, T., Nikiforov, A., Koblinsky, C., 2003. Seasonal, interannual, and mesoscale variability of the Black Sea upper layer circulation derived from altimeter data. *J. Geophys. Res.-Oceans* 108 (C4), 16 pp.
- Kurapov, A.L., Foley, D., Strub, P.T., Egbert, G.D., Allen, J.S., 2011. Variational assimilation of satellite observations in a coastal ocean model off Oregon. *J. Geophys. Res.-Oceans* 116 (C5), 19 pp.
- Le Traon, P.Y., Rouquet, M.C., Boissier, C., 1990. Spatial scales of mesoscale variability in the North Atlantic as deduced from Geosat data. *J. Geophys. Res.-Oceans* 95 (C11), 20267–20285.
- Le Traon, P.Y., Dibarboure, G., Jacobs, G., Martin, M., Rémy, E., Schiller, A., 2017. Use of satellite altimetry for operational oceanography. In: Stammer, D., Cazenave, A. (Eds.), *Satellite altimetry over oceans and land surfaces*. CRC Press, Boca Raton, 581–608.
- Martin, M.J., Hines, A., Bell, M.J., 2007. Data assimilation in the FOAM operational short-range ocean forecasting system: A description of the scheme and its impact. *Q. J. Roy. Meteorol. Soc.* 133 (625), 981–995.
- Martin-Neira, M., Mavrocordatos, C., Colzi, E., 1998. Study of a constellation of bistatic radar altimeters for mesoscale ocean applications. *IEEE T. Geosci. Remote* 36 (6), 1898–1904.
- Matsumoto, K., Takanezawa, T., Ooe, M., 2000. Ocean tide models developed by assimilating TOPEX/POSEIDON altimeter data into hydrodynamical model: A global model and a regional model around Japan. *J. Oceanogr.* 56 (5), 567–581.
- Mellor, G.L., Yamada, T., 1982. Development of a turbulence closure model for geophysical fluid problems. *Rev. Geophys.* 20 (4), 851–875.
- Mellor, G.L., Ezer, T., 1991. A Gulf Stream model and an altimetry assimilation scheme. *J. Geophys. Res.-Oceans* 96 (C5), 8779–8795.
- Miller, L., Cheney, R.E., Douglas, B.C., 1988. GEOSAT altimeter observations of Kelvin waves and the 1986–87 El Niño. *Science* 239 (4835), 52–54.
- Moore, A.M., Arango, H.G., Broquet, G., Edwards, C., Veneziani, M., Powell, B., Foley, D., Doyle, J.D., Costa, D., Robinson, P., 2011. The Regional Ocean Modeling System (ROMS) 4-dimensional variational data assimilation systems: part II – performance and application to the California Current System. *Prog. Oceanogr.* 91 (1), 50–73.
- Morrow, R., Birol, F., 1998. Variability in the southeast Indian Ocean from altimetry: Forcing mechanisms for the Leeuwin Current. *J. Geophys. Res.-Oceans* 103 (C9), 18529–18544.
- Nerem, R.S., Tapley, B.D., Shum, C.K., 1990. Determination of the ocean circulation using Geosat altimetry. *J. Geophys. Res.-Oceans* 95 (C3), 3163–3179.
- Penduff, T., Brasseur, P., Testut, C.E., Barnier, B., Verron, J., 2002. A four-year eddy-permitting assimilation of sea-surface temperature and altimetric data in the South Atlantic Ocean. *J. Mar. Res.* 60 (6), 805–833.
- Piecuch, C.G., Ponte, R.M., 2011. Mechanisms of interannual steric sea level variability. *Geophys. Res. Lett.* 38 (15), 6 art. no. L15605, 6 pp.
- Powell, B.S., Arango, H.G., Moore, A.M., Di Lorenzo, E., Milliff, R.F., Foley, D., 2008. 4DVAR data assimilation in the intra-Americas sea with the Regional Ocean Modeling System (ROMS). *Ocean Model* 23 (3–4), 130–145.
- Pujol, M.I., Dibarboure, G., Le Traon, P.Y., Klein, P., 2012. Using high-resolution altimetry to observe mesoscale signals. *J. Atmos. Ocean. Tech.* 29 (9), 1409–1416.
- Qiu, B., Chen, S., 2005. Variability of the Kuroshio Extension jet, recirculation gyre, and mesoscale eddies on decadal time scales. *J. Phys. Oceanogr.* 35 (11), 2090–2103.
- Shchepetkin, A.F., McWilliams, J.C., 2005. The regional oceanic modeling system (ROMS): a split-explicit, free-surface, topography-following-coordinate oceanic model. *Ocean Model* 9 (4), 347–404.
- Soto-Mardones, L., Parés-Sierra, A., Garcia, J., Durazo, R., Hormazabal, S., 2004. Analysis of the mesoscale structure in the IMECOCAL region (off Baja California) from hydrographic, ADCP and altimetry data. *Deep Sea Res. Pt. II* 51 (6–9), 785–798.
- Strub, P.T., James, C., 2002. Altimeter-derived surface circulation in the large-scale NE Pacific Gyres.: Part 1. Seasonal variability. *Prog. Oceanogr.* 53 (2–4), 163–183.
- Tandeo, P., Chapron, B., Ba, S., Autret, E., Fablet, R., 2014. Segmentation of mesoscale ocean surface dynamics using satellite SST and SSH observations. *IEEE T. Geosci. Remote* 52 (7), 4227–4235.
- Traon, L.P., 1991. Time scales of mesoscale variability and their relationship with space scales in the North Atlantic. *J. Mar. Res.* 49 (3), 467–492.
- Vélez-Belchí, P., Centurioni, L.R., Lee, D.K., Jan, S., Niiler, P.P., 2013. Eddy induced Kuroshio intrusions onto the continental shelf of the East China Sea. *J. Mar. Res.* 71 (1–2), 83–107.

- Wang, G., Su, J., Chu, P.C., 2003. Mesoscale eddies in the South China Sea observed with altimeter data. *Geophys. Res. Lett.* 30 (21) 6-1–6-4.
- Wang, X., Liu, P.L.F., 2006. An analysis of 2004 Sumatra earthquake fault plane mechanisms and Indian Ocean tsunami. *J. Hydraul. Res.* 44 (2), 147–154.
- Zhou, C., Ding, X., Zhang, J., Yang, J., Ma, Q., 2018. An evaluation of sea surface height assimilation using along-track and gridded products based on the Regional Ocean Modeling System (ROMS) and the four-dimensional variational data assimilation. *Acta Oceanol. Sin.* 37 (9), 50–58.

Available online at www.sciencedirect.com

ScienceDirect

journal homepage: www.journals.elsevier.com/oceanologia

ORIGINAL RESEARCH ARTICLE

Unravelling the spatio-temporal variation of zooplankton community from the river Matla in the Sundarbans Estuarine System, India

Tanmoy Nandy, Sumit Mandal*

Marine Ecology Laboratory, Department of Life Sciences, Presidency University, Kolkata, India

Received 20 December 2019; accepted 19 March 2020

Available online 7 May 2020

KEYWORDS

Sundarbans;
Zooplankton;
Copepoda;
Bioindicator;
Seasonal succession

Summary Zooplankton is an important bioindicator of ecosystem functioning. Knowledge of the seasonal fluctuation in the zooplankton population in estuarine waters of the Indian Sundarbans is rather limited. In the present study, we analysed the community structure of zooplankton assemblages and their spatio-temporal variations based on different multivariate statistics and indicator value analysis. A total of 56 taxa were identified and the density was primarily dominated by planktonic copepods and few meroplankton communities during four sampling seasons. The most abundant species were: *Acartia spinicauda*, *Acartia* sp., *Bestiolina similis*, *Euterpina acutifrons*, *Labidocera acuta*, *Paracalanus aculeatus*, *Paracalanus parvus* and *Paracalanus indicus*. Canonical Correspondence Analysis highlighted that temperature, pH, DO, salinity and nutrients were the prevailing environmental parameters associated with significant spatio-temporal changes of zooplankton distribution in this area. The highest abundance of zooplankton was recorded in winter, followed by monsoon, summer and spring. Throughout the study period, different zooplankton indices were observed in good condition. Seasonal occurrence of dominant zooplankton with high *IndVal* index was markedly observed and it might be used as a potential bioindicator for a particular season and environmental condition in this estuarine complex. The results of this study provide evidence for the presence of warm water species in the estuarine waters of the Indian Sundarbans and can be a clear indication of climate change-mediated elevated temperature in the estuarine system. Our results underscore

* Corresponding author at: Marine Ecology Laboratory, Department of Life Sciences, Presidency University, 86/1, College Street, Kolkata-700073, India.

E-mail address: sumit.dbs@presiuniv.ac.in (S. Mandal).

Peer review under the responsibility of the Institute of Oceanology of the Polish Academy of Sciences.



Production and hosting by Elsevier

<https://doi.org/10.1016/j.oceano.2020.03.005>

0078-3234/© 2020 Institute of Oceanology of the Polish Academy of Sciences. Production and hosting by Elsevier B.V. This is an open access article under the CC BY-NC-ND license (<http://creativecommons.org/licenses/by-nc-nd/4.0/>).

the high diversity of zooplankton from mangrove dominated estuarine complex and emphasize the need for long-term monitoring in ecologically fragile ecosystems like the Sundarbans Estuarine System.

© 2020 Institute of Oceanology of the Polish Academy of Sciences. Production and hosting by Elsevier B.V. This is an open access article under the CC BY-NC-ND license (<http://creativecommons.org/licenses/by-nc-nd/4.0/>).

1. Introduction

Estuarine ecosystems have been recognised as a mosaic of habitats exhibiting different biogeochemical processes and act as a transitional ecotone with marked gradients of physical, chemical and biological components (Moderan et al., 2010; Nandy et al., 2018; O'Higgins et al., 2010; Van der Maarel, 1990). Due to their connections with adjoining freshwater and marine ecosystems, estuaries always face a strong physicochemical fluctuation at spatio-temporal scale. Moreover, the fluctuations of numerous physicochemical factors are more evident in the estuarine environment than in other aquatic systems (David et al., 2016). In addition, estuaries act as a nursery ground for different aquatic organisms by providing food and shelter for larvae and juveniles (Dorak and Albay, 2016; Telesh, 2004). Furthermore, estuary acts as a hotspot for many benthic animals larval forms which spend some time, depending upon their larval duration, in the estuarine realm before returning to their benthic mode of life in coastal waters (Morgan, 1995; Shanks, 1995). In estuarine areas, the spatial and temporal variations of different biological communities are always driven by several environmental variables. However, it is essential to improve our knowledge of estuarine ecosystem functioning with a sound understanding of biogeochemical gradients and their interactions with biological entities.

In an estuarine ecosystem, most of the zooplankton are efficient grazers of the phytoplankton and mainly detritus, referred to as living machines transforming plant energy into animal tissue (De Young et al., 2004; Dorak and Albay, 2016; Sampey et al., 2007). Therefore, the zooplankton play a significant role in energy transfer from primary producers to higher trophic levels, occupying a fundamental niche in the estuarine food web (Degerman et al., 2018). Moreover, the estuarine ecotone and profit of coastal fisheries are always influenced by the zooplankton population due to its role as a major food item for fishes (Ayon et al., 2008; Bianchi et al., 2003). Due to the zooplankton large density, shorter life span, drifting nature, high taxa/species diversity and different tolerance to the environmental stress, they are being used as indicator organisms for the physical, chemical and biological processes in the aquatic ecosystem (Longhurst, 2007; Uriarte and Villate, 2004). The seasonal and spatial dominance of certain zooplankton taxa may indicate the relative influence of different water parameters on the estuarine ecosystem and serve as an early indication of a biological response to environmental and climatic changes (Hays et al., 2005; Ziadi et al., 2015). Though zooplankton organisms serve as a good indicator of biodiversity because of high sensitivity to environmental fluctuations (Gorokhova et al., 2016), they have been generally less used in studying biological responses in changing environment

(Gorokhova et al., 2016; Mialet et al., 2011). The identification of indicator species and tracking changes in species composition are essential to detect local and global changes in estuarine biogeochemistry (Fernandez De Puellas et al., 2009).

In the Indian part of the Sundarbans estuarine complex, knowledge about zooplankton communities is relatively limited (Bhattacharya et al., 2015; Nandy et al., 2018) and restricted to the eastern part of this system. We are fortunate enough to get access to the central part of the Sundarbans under the restricted biosphere reserve area for conducting research work funded by MoES. This system is under the influence of southwest monsoon, thus, it is essential to study the seasonal succession of zooplankton communities in order to understand the major influential factors governing the biological productivity of the Sundarban mangrove ecosystem. Nevertheless, knowledge of the zooplankton community is also fundamental in understanding the biogeochemical cycles and energy flows of marine ecosystems because of its roles in the biological pump (Giering et al., 2014; Mitra et al., 2014).

To evaluate the changes in the dynamics of the zooplankton community associated with natural environmental variables, a seasonal observation over a spatial scale is of utmost importance. Studies related to seasonal variation in estuarine waters, particularly in fishing grounds of the Sundarbans, are meagre, hence the present study was carried out and the relationship between zooplankton abundance and hydrological parameters on spatio-temporal scale has been established. Moreover, the effects of some physicochemical variables and seasonal flow patterns on zooplankton community structuring were analyzed. Therefore, the primary goals of the present study were to (i) investigate the seasonal succession and spatial variability of the zooplankton community of the river Matla in the Sundarbans Estuarine System (SES) in terms of composition, abundance and diversity; (ii) evaluate the zooplankton dynamics in relation to environmental variables and (iii) identify the indicator zooplankton species for a particular season as well as for a specific environmental condition.

2. Material and methods

2.1. Study area

The Indian Sundarbans Estuarine System (SES) is a unique bioclimatic zone situated in land-ocean boundaries of the northern coast of Bay of Bengal. The estuarine phase of this macrotidal (tidal amplitude: > 5 m) area is fully covered by true mangrove forest (Biswas et al., 2004). Moreover, the estuarine complex experienced huge monsoonal precipitation (70–80% of annual rainfall) during the summer

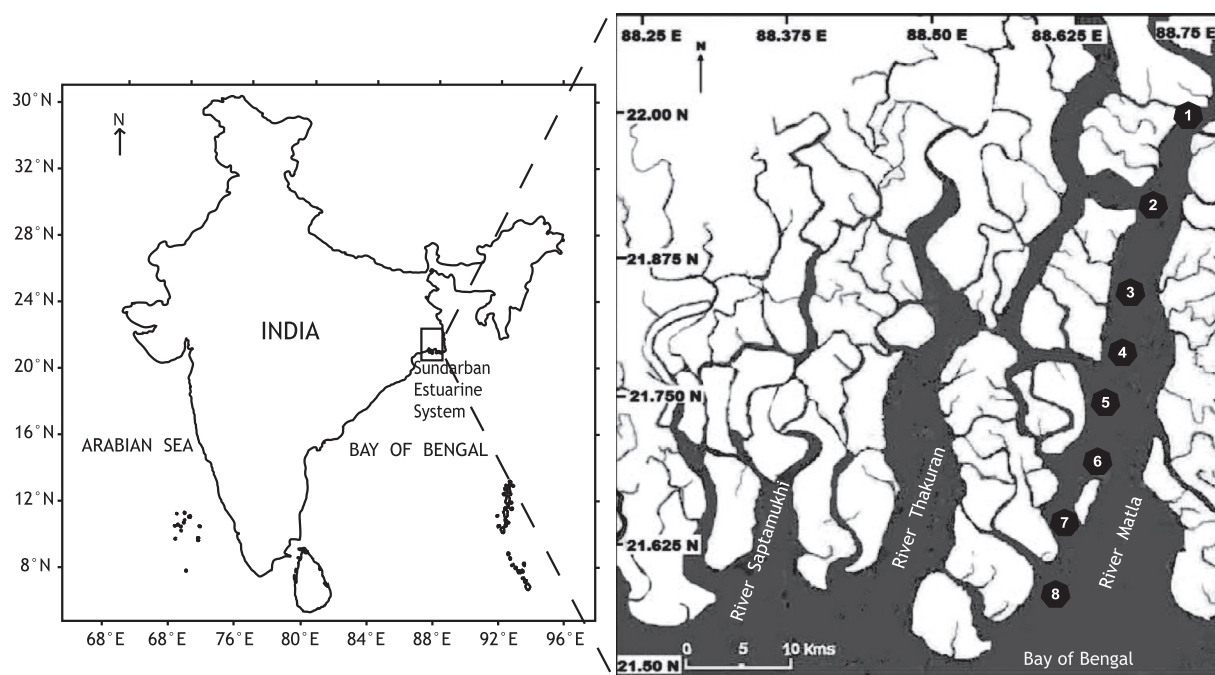


Figure 1 Map of the study area with sampling stations.

monsoon period, i.e. June to September (Mukhopadhyay et al., 2006). The surface water quality of this region is highly influenced by tidal amplitude, particularly during monsoon (Nandy et al., 2018). The SES serves as an important spawning ground and nursery for a wide variety of fishes and crustaceans, due to its ample riverine network with dense mangrove vegetation. It also plays a major role in the natural filtration of anthropogenic pollutants and acts as the most important pathway for nutrients recycling (Chatterjee et al., 2013).

The present study was conducted on the river Matla, situated at the central part of the Indian Sundarbans. A total of 8 study stations were selected according to different salinity gradients at the north-south direction (Fig. 1, Supplementary Table 1). The zooplankton of the river Matla in the Sundarbans Estuarine System was analyzed to determine the response of zooplankton population to contrasting levels of water quality (e.g. temperature, salinity, oxygen, turbidity, nutrients and phytopigments). The surface water sample was collected during four distinct seasons (once per season): monsoon (September, 2016), winter (December, 2016), spring (February, 2017) and summer (May, 2017). The water and zooplankton samples (triplicate) were collected from each station during the overall study period, at day time high tide conditions. Sampling was restricted to the surface layer because of the low (~ 1 m) euphotic depth and spatial variation of river bathymetry in this study area.

2.2. Collection and analysis of water samples

To determine the water quality of the estuary, a water sample was collected at a 0.5 m depth using Niskin's water sampler (Hydro bios). The sample was collected in 500 ml pre-cleaned plastic container (HDPE, Tarsons) and

stored in an ice box for further analysis. Water temperature, salinity, dissolved oxygen (DO) and pH were measured *in situ*. Winkler's titrimetric method and argentometric method (Strickland and Parsons, 1972) were followed to determine the DO and salinity (practical salinity scale) of the water, respectively. Surface water temperature was measured onboard with the help of mercury thermometer and Secchi disc was used to determine the transparency of water at each station. The portable digital pH meter (Model: Orion star A3110, Thermo-Scientific) was used to determine the pH of the water. The dissolved micro-nutrients such as nitrite ($\text{NO}_2\text{-N}$), nitrate ($\text{NO}_3\text{-N}$), ammonium ($\text{NH}_4\text{-N}$), phosphate ($\text{PO}_4\text{-P}$) and silicate ($\text{SiO}_4\text{-Si}$) were analysed using the standard method described by Grasshoff et al. (1999) after filtering the water through GF/F filter paper ($0.07\mu\text{m}$). For the chlorophyll-*a* (Chl-*a*) and phaeopigment (Phaeo) analysis 1000 ml seawater was filtered through GF/F filter paper and the analysis was done by acetone extraction method by Parsons et al. (1984). Suspended particulate matter (SPM) analysis was performed according to the method of Grasshoff et al. (1999).

2.3. Collection and analysis of zooplankton samples

Zooplankton was collected using 200 μm plankton net (60 cm diameter, 2 m length), equipped with a flowmeter (Hydro bios) by horizontal tow at subsurface layer (0.5–1 m); the average volume of water filtered per sample was $100 \pm 23 \text{ m}^3$. The catch was transferred to a plastic bottle and fixed immediately with 10% buffered formaldehyde solution and transported to the laboratory for further analysis. To determine the abundance and composition of zooplank-

ton, subsamples were obtained using Folsom-splitter to give a minimum number of 300 individuals per sample. In the laboratory, the triplicate subsample was taken on to a Sedgwick rafter counting chamber and was enumerated under the stereozoom microscope (Olympus, Magnus: MS24) for their mean abundances expressed as individuals per cubic meter (ind. m^{-3}). Zooplankton were identified up to species level using a compound microscope (Nikon Eclipse: E200) following standard descriptions of Conway et al. (2003), Kasturirangan (1963), Yousif Al-Yamani et al. (2011). The biomass (wet weight) of the zooplankton was determined by weighing one portion of subsample after carefully removing all the adhered water particles using a blotting paper.

2.4. Data analysis

The square root transformed data of zooplankton were used to construct a Bray-Curtis similarity matrix with average linkage group classification (Field et al., 1982) to unravel the significant spatio-temporal variation in the composition of zooplankton. In addition, SIMPER analyses were conducted to investigate which species contributed the most to the groups formed during each season's cluster analysis. To determine the variations among sampling seasons, non-metric multidimensional scaling (nMDS) ordinations were computed (Hunt et al., 2007; Kruskal and Wish, 1978) and Analysis of Similarities (ANOSIM) was applied to detect significant ($p = 0.001$) differences between seasons (Clarke and Warwick, 2001) with respect to zooplankton species composition.

The Canonical Correspondence Analysis (CCA) was conducted to understand the relationship between zooplankton composition and water quality parameters. The outcomes of CCA results were presented as the species and station biplots, in which the biotic and abiotic variables were represented together. The correlations between biological and environmental variables were tested using the Spearman's correlation coefficient.

For assessing the current status and to know the species homogeneity among the populations, different ecological diversity indices, like species richness (d) (Margalef, 1967), species diversity index (H') (Shannon, 1948) and evenness index (J') (Pielou, 1966), were computed.

Indicator species analysis (Dufrene and Legendre, 1997) was performed to identify potential indicator species of zooplankton for particular environmental conditions in each season. When all the individuals of particular taxa occur in a single season, Indicator Value ($IndVal$) index reaches the maximum (100%) indicating the asymmetric distribution of that taxa. However, $IndVal$ index reaches the lowest level when the taxa is symmetrically distributed between seasons (Hunt and Hosie, 2006). According to Dufrene and Legendre (1997) a minimum 25% $IndVal$ can be considered as the threshold limit to determine the indicator species in a group of observations. In our study, $\geq 40\%$ value was used as the threshold to demarcate the $IndVal$ index.

Additionally, a one-way analysis of variance (ANOVA) was applied to identify the significant ($p \leq 0.05$) differences between four distinct seasons for all biotic and abiotic variables. We also conducted the permutation ($1000 \times$) multivariate analysis of variance (PERMANOVA) to find out the significant ($p \leq 0.05$) differences in zooplankton

abundance in terms of the season (monsoon, winter, spring and summer) and site (station 1 to 8).

All the graphs and statistical analysis was carried out using Microsoft Excel (MS Office-2013), PRIMER-version 6.0 (Clarke and Gorley, 2006) software and Multivariate Statistical Package (MVSP) program version 3.1 (Kovach, 1998).

3. Results

3.1. Spatio-temporal variation of hydrological parameters

The hydrological changes in the study area on a spatio-temporal scale are presented in Fig. 2 and Table 1. Physicochemical parameters, like temperature, salinity, Secchi depth, DO, pH, Chl- a , nutrients and SPM showed a wide range of variability among studied stations. The significant ($p \leq 0.05$) seasonal changes of all environmental parameters along with their ANOVA value are presented in Table 1.

The seasonal mean of surface water temperature ranged from $22.34 \pm 1.29^\circ\text{C}$ (winter) to $31.98 \pm 0.94^\circ\text{C}$ (summer) during the study period. The highest (33.4°C) and the lowest value (20.5°C) were observed at station 6 during summer and winter, respectively (Fig. 2a). Salinity varied between 11.93 ± 3.96 and 31.93 ± 1.97 during the overall sampling period (Table 1). Moreover, its range varied at different sampling stations according to their distance from the sea. Upstream stations showed more or less low saline regime in comparison to downstream stations (Fig. 2b). The highest pH value (8.42) was recorded at station 8 and the lowest value (7.40) was recorded at station 5 during monsoon and spring, respectively (Fig. 2c). The DO of surface water varied from $4.77 \pm 0.13 \text{ mg L}^{-1}$ (during summer) to $6.56 \pm 0.80 \text{ mg L}^{-1}$ (during monsoon). A significant spatial variation has been documented during all sampling seasons (monsoon, winter, spring and summer). The upstream stations showed elevated oxygenated water in comparison with the rest of the stations, and a decreasing trend was observed from the riverside to seaside (Fig. 2d). The transparency of water was measured by Secchi depth and it ranged from $55 \pm 7.07 \text{ cm}$ to $20.13 \pm 7.22 \text{ cm}$ during the study period (Fig. 2e). The mean concentration of SPM was recorded at maximum ($261.18 \pm 96.68 \text{ mg L}^{-1}$) during summer and at minimum ($27.38 \pm 9.16 \text{ mg L}^{-1}$) during spring (Fig. 2f).

The essential micronutrients concentrations varied both spatially and temporally in the present study. The average $\text{NO}_2\text{-N}$ concentration varied between $0.31 \pm 0.08 \mu\text{M}$ and $0.61 \pm 0.41 \mu\text{M}$. The maximum value of $\text{NO}_2\text{-N}$ was detected at seaward stations, and the highest value ($1.32 \mu\text{M}$) being recorded at station 6 during spring (Fig. 3a). A similar type of seasonal trend was also noticed for $\text{NO}_3\text{-N}$, $\text{PO}_4\text{-P}$ and $\text{SiO}_4\text{-Si}$. The mean concentration was found to be decreasing from monsoon to spring and again starting to increase during summer (Fig. 3b, c and d). The average $\text{NO}_3\text{-N}$ and $\text{PO}_4\text{-P}$ concentrations were recorded from $17.47 \pm 3.55 \mu\text{M}$ to $4.18 \pm 1.29 \mu\text{M}$ and $1.64 \pm 0.69 \mu\text{M}$ to $0.23 \pm 0.17 \mu\text{M}$, respectively, during the study period. The $\text{SiO}_4\text{-Si}$ value was higher ($53.05 \pm 7.56 \mu\text{M}$) during monsoon and lower ($17.70 \pm 5.55 \mu\text{M}$) during spring. The highest value of $\text{SiO}_4\text{-Si}$ ($64.08 \mu\text{M}$) occurred at station 1 during

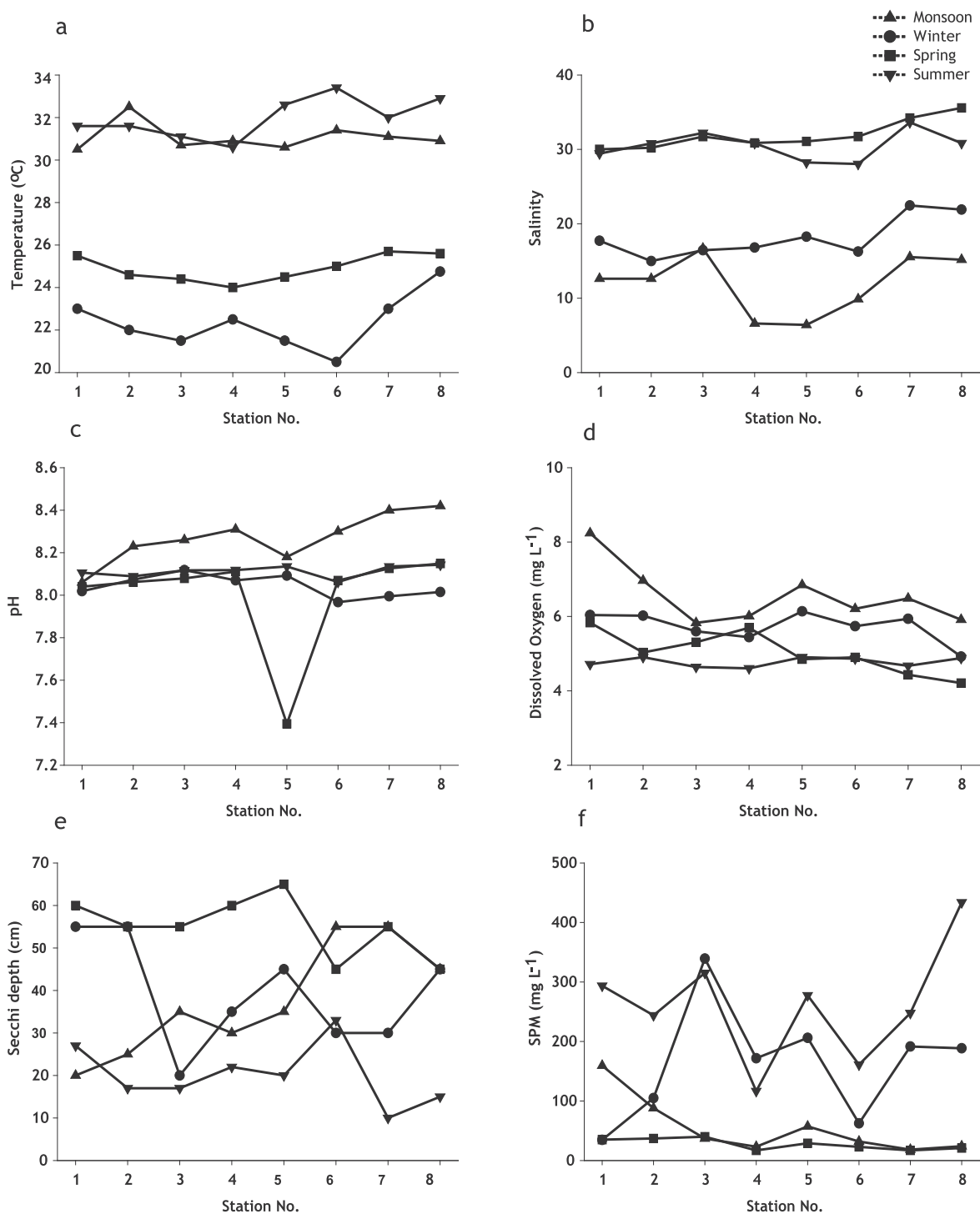


Figure 2 Spatio-temporal variation of hydrological parameters (a – water temperature, b – salinity, c – pH, d – dissolved oxygen, e – secchi depth, f – suspended particulate matter).

monsoon and the lowest value ($11.25 \mu\text{M}$) at station 6 during spring. Lower $\text{NH}_4\text{-N}$ concentration was registered during winter ($0.17 \pm 0.11 \mu\text{M}$) and higher values in summer ($2.32 \pm 0.65 \mu\text{M}$) (Fig. 3e).

During monsoon, the mean concentrations of Chl-*a* and Phaeo were recorded at maximum ($4.14 \pm 1.98 \mu\text{g L}^{-1}$ and

$0.50 \pm 0.47 \mu\text{g L}^{-1}$, respectively). However, minimum values of Chl-*a* and Phaeo ($2.53 \pm 1.12 \mu\text{g L}^{-1}$ and $0.18 \pm 0.14 \mu\text{g L}^{-1}$) were observed during winter and spring, correspondingly. An elevated Chl-*a* concentration was recorded at the middle stretch of the estuary (stations 3–5) during all sampling seasons (Fig. 3f). However, there were no sig-

Table 1 Mean values and standard deviation (SD) of biogeochemical parameters of 8 stations sampled during four seasons. In the last column, results of ANOVA test for the comparison between these four seasons is presented. Asterisks denote significant ($p \leq 0.05$) differences.

| Parameters | Monsoon | | | | Winter | | | | Spring | | | | Summer | | | | <i>(p values)</i> |
|---|---------|---------|---------|--------|--------|---------|---------|---------|--------|---------|--------|--------|--------|---------|--------|--------|-------------------|
| | Min | Max | Mean | SD | Min | Max | Mean | SD | Min | Max | Mean | SD | Min | Max | Mean | SD | |
| Temperature (°C) | 30.50 | 32.50 | 31.08 | 0.64 | 20.50 | 24.75 | 22.34 | 1.29 | 24.00 | 25.70 | 24.91 | 0.63 | 30.60 | 33.40 | 31.98 | 0.94 | 0.0001* |
| Secchi depth (cm) | 20.00 | 55.00 | 37.50 | 13.09 | 20.00 | 55.00 | 39.38 | 12.66 | 45.00 | 65.00 | 55.00 | 7.07 | 10.00 | 33.00 | 20.13 | 7.22 | 0.0025* |
| Salinity | 6.41 | 16.68 | 11.93 | 3.96 | 14.98 | 22.46 | 18.11 | 2.71 | 30.01 | 35.58 | 31.93 | 1.97 | 28.04 | 33.64 | 30.51 | 1.90 | 0.0057* |
| DO (mg L ⁻¹) | 5.83 | 8.24 | 6.56 | 0.80 | 4.92 | 6.14 | 5.73 | 0.40 | 4.21 | 5.83 | 5.03 | 0.57 | 4.61 | 4.91 | 4.77 | 0.13 | 0.0073* |
| pH | 8.06 | 8.42 | 8.27 | 0.12 | 7.97 | 8.12 | 8.04 | 0.05 | 7.40 | 8.15 | 8.00 | 0.25 | 8.06 | 8.14 | 8.11 | 0.03 | 0.0001* |
| Nitrate-N (μM) | 12.12 | 23.10 | 17.47 | 3.55 | 3.44 | 18.14 | 10.22 | 5.13 | 1.94 | 5.88 | 4.18 | 1.29 | 12.23 | 14.17 | 13.40 | 0.54 | 0.0221* |
| Nitrite-N (μM) | 0.21 | 0.40 | 0.31 | 0.08 | 0.21 | 0.59 | 0.39 | 0.11 | 0.13 | 1.32 | 0.61 | 0.41 | 0.28 | 0.56 | 0.41 | 0.10 | 0.0188* |
| Phosphate-P (μM) | 0.90 | 2.93 | 1.64 | 0.69 | 0.81 | 2.17 | 1.42 | 0.38 | 0.04 | 0.53 | 0.23 | 0.17 | 0.91 | 1.88 | 1.37 | 0.35 | 0.1131 |
| Silicate (μM) | 43.67 | 64.08 | 53.05 | 7.56 | 3.44 | 46.98 | 32.38 | 13.35 | 11.26 | 28.22 | 17.70 | 5.55 | 28.32 | 30.90 | 29.56 | 0.91 | 0.006* |
| Ammonium-N (μM) | 0.23 | 0.59 | 0.35 | 0.11 | 0.06 | 0.39 | 0.17 | 0.11 | 0.19 | 0.42 | 0.30 | 0.09 | 1.80 | 3.82 | 2.32 | 0.65 | 0.0827 |
| Chl- <i>a</i> (μg L ⁻¹) | 1.20 | 6.90 | 4.14 | 1.98 | 1.04 | 4.10 | 2.53 | 1.12 | 3.01 | 4.64 | 3.73 | 0.54 | 3.06 | 4.90 | 4.11 | 0.55 | 0.1820 |
| Phaeopigments (μg L ⁻¹) | 0.08 | 1.36 | 0.50 | 0.47 | 0.14 | 1.18 | 0.46 | 0.44 | 0.03 | 0.41 | 0.18 | 0.15 | 0.12 | 0.73 | 0.45 | 0.20 | 0.0179* |
| SPM (mg L ⁻¹) | 18.21 | 159.40 | 54.90 | 48.06 | 34.61 | 339.34 | 162.44 | 95.98 | 17.00 | 40.00 | 27.38 | 9.16 | 116.60 | 433.80 | 261.18 | 96.68 | 0.0598 |
| Zooplankton abundance (ind. m ⁻³) | 324.00 | 2154.00 | 1202.88 | 768.38 | 331.00 | 4185.00 | 1616.00 | 1391.01 | 257.00 | 1126.00 | 573.38 | 270.22 | 428.00 | 1566.00 | 951.38 | 482.40 | 0.0026* |
| Zooplankton biomass (g m ⁻³) | 1.05 | 4.93 | 2.68 | 1.48 | 0.95 | 6.18 | 3.28 | 1.87 | 0.95 | 2.70 | 1.88 | 0.61 | 1.15 | 4.80 | 2.69 | 1.35 | 0.0186* |

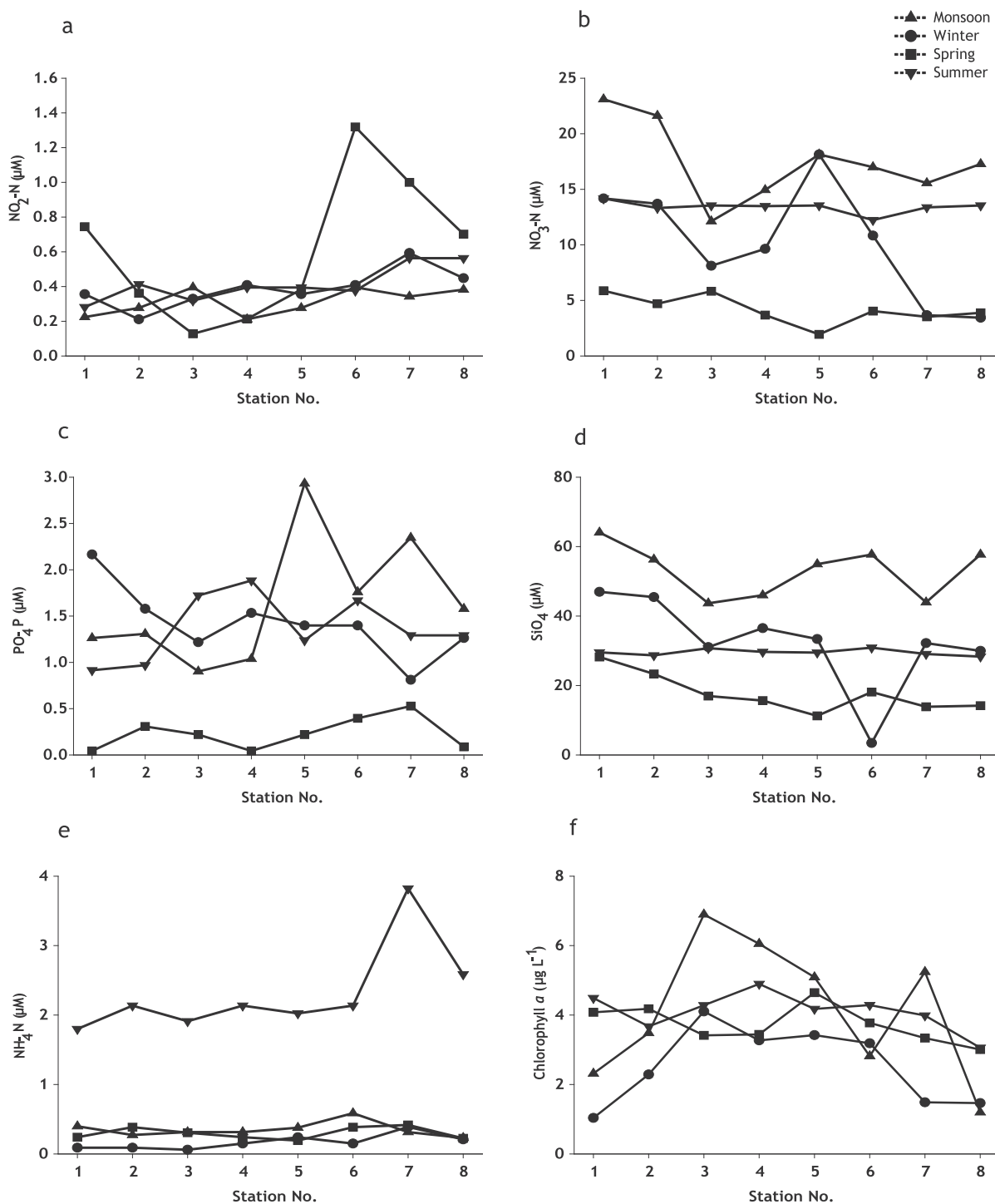


Figure 3 Spatio-temporal variation of nutrients (a – nitrite-N, b – nitrate-N, c – phosphate-P, d – silicate, e – ammonium-N) and f – Chl a concentration.

nificant spatial distribution differences for Phaeo concentration throughout the study period.

3.2. Community structure and composition of zooplankton

In the present study, a noticeable change in the zooplankton community structure with regard to density and diver-

sity was evident among the study stations and between different seasons. The average zooplankton abundance ranged from 573 ± 270 ind. m^{-3} (during spring) to 1616 ± 1392 ind. m^{-3} (during winter). The highest abundance was observed at station 6 during winter (4185 ind. m^{-3}), however, the lowest value was documented during spring at station 6 (257 ind. m^{-3}) (Fig. 4a). Station-wise variations in zooplankton biomass during four sampling seasons are plotted

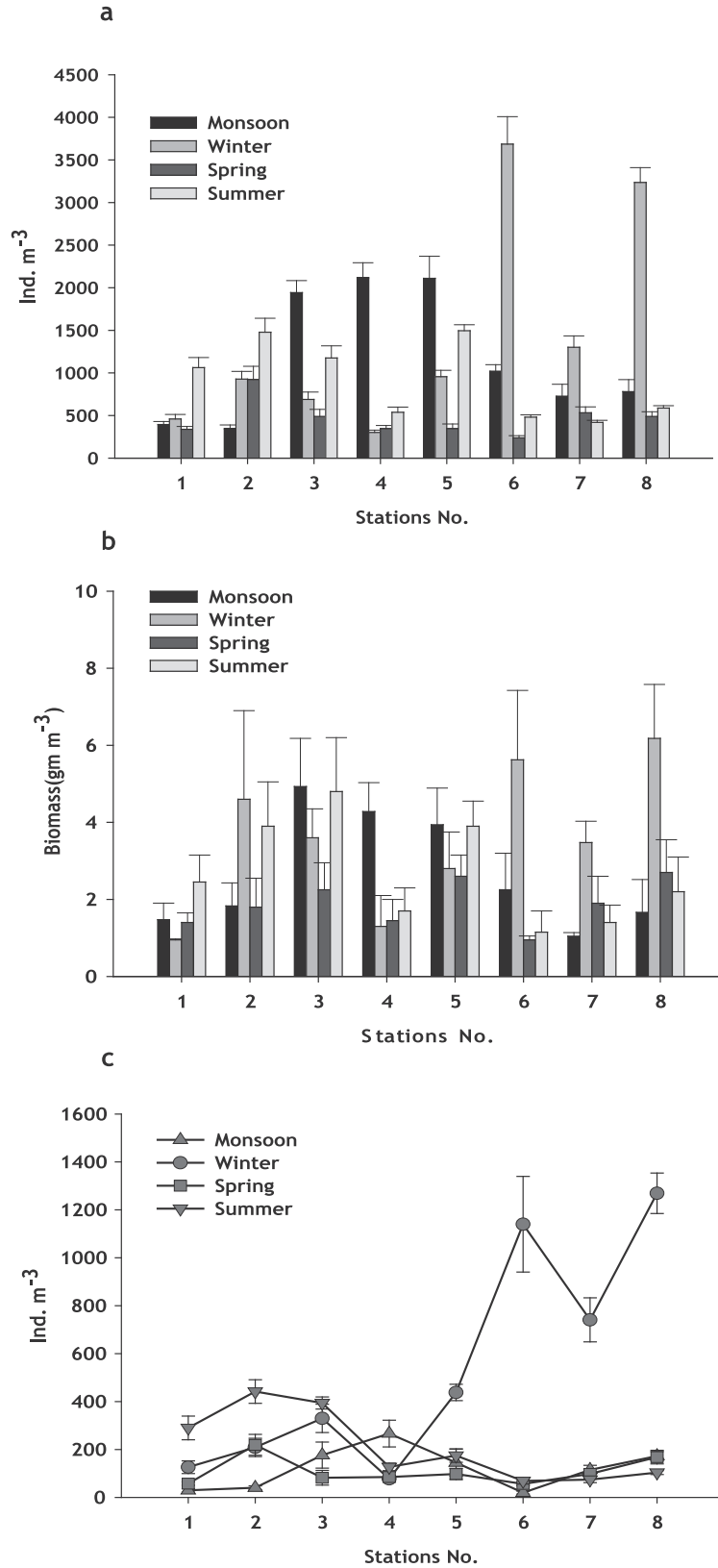


Figure 4 Spatio-temporal variation of a – total zooplankton abundance, b – zooplankton biomass and c – meroplankton population.

in Fig. 4b. The total biomass was recorded higher during winter (ranging from 6.18 to 0.95 gm m⁻³) and lower during spring (ranging from 2.70 to 0.95 gm m⁻³); the variation among seasons was found to be significant with $p=0.0186$ (Fig. 4b).

A total of 56 zooplankton taxa have been documented through the analysis of 32 samples collected from 8 stations during 4 seasons. Copepoda were the most abundant, both quantitatively and qualitatively. They were represented by 36 species belonging to 4 orders. Calanoida emerged as a dominant group with 25 species followed by Cyclopoida (5 species), Harpacticoida (4 species) and Poecilostomatoida (2 species). Out of 36 species of Copepoda recorded, only 8 species had been identified as perennial existing during four sampling seasons. These species are: *Acartia spinicauda*, *Acartia* sp., *Bestiolina similis*, *Euterpina acutifrons*, *Labidocera acuta*, *Paracalanus aculeatus*, *P. parvus* and *P. indicus*. Additionally, 5 taxa of other groups (like: Bivalvia, Gastropoda, Polychaeta, *Zonosagitta bedoti* and Decapoda zoeae) have been recorded as perennial during entire study period. Different larval stages of noncopepods, especially the meroplankton community, have also been observed in a significant amount. The shellfish larval populations (like Bivalve D-larva, Gastropoda veliger larvae, crab zoea larva and shrimp larvae) were documented as a second dominant group of the total zooplankton abundance. Except during the winter period, their mean density declined considerably towards the downstream stations during the overall study period. Among all seasons the maximum shellfish larval population (ranging from 78 ± 13 to 1269 ± 84 ind. m⁻³) was recorded during winter, especially at mouth stations of the estuary facing Bay of Bengal. On the other hand, the minimum shellfish larval density was documented during spring (ranging from 56 ± 8 to 219 ± 44 ind. m⁻³) (Fig. 4c).

The spatio-temporal changes of different diversity indices are presented in Fig. 5. Shannon index of diversity (H') values generally increased in parallel to the species number throughout the study period. The highest diversity ($H'=2.83$) was observed during spring and lowest ($H'=1.78$) during monsoon at station 5 and 6, respectively. The species evenness (J') varied between 0.74 and 0.95 in monsoon; 0.82 and 0.91 in winter; 0.89 and 0.93 in spring and, 0.85 and 0.95 during the summer season. The maximum richness value (d) was recorded during spring ranging from 2.68 to 3.62, however, monsoon samples showed lower values ranging from 1.29 to 2.70 (Fig. 5).

The spatio-temporal changes of zooplankton distribution and cluster formation are shown in Fig. 6. Table 2 is generated from SIMPER analysis of the dendrogram plot (Fig. 6) to determine the contribution percentages of different zooplankton taxa in the formation of a specific cluster. During monsoon, lowest zooplankton abundances (324 ind. m⁻³) were recorded at station 2 and highest (2154 ind. m⁻³) at station 5, with an average of 1203 ± 768 ind. m⁻³. The community was largely dominated (87%) by Copepoda. The cluster analysis revealed a clear spatial distribution of zooplankton during this season. Two distinct groups were formed: group I (station 1–3) and group II (station 4–8) with 72.18 and 73.36% of average similarities, respectively. *B. similis*, *P. parvus*, *P. aculeatus* and *Oithona similis* showed maximum contribution to form group I; however, *P. parvus*, *P. aculeatus*, *Oithona brevicornis* and *A. spinicauda* contributed

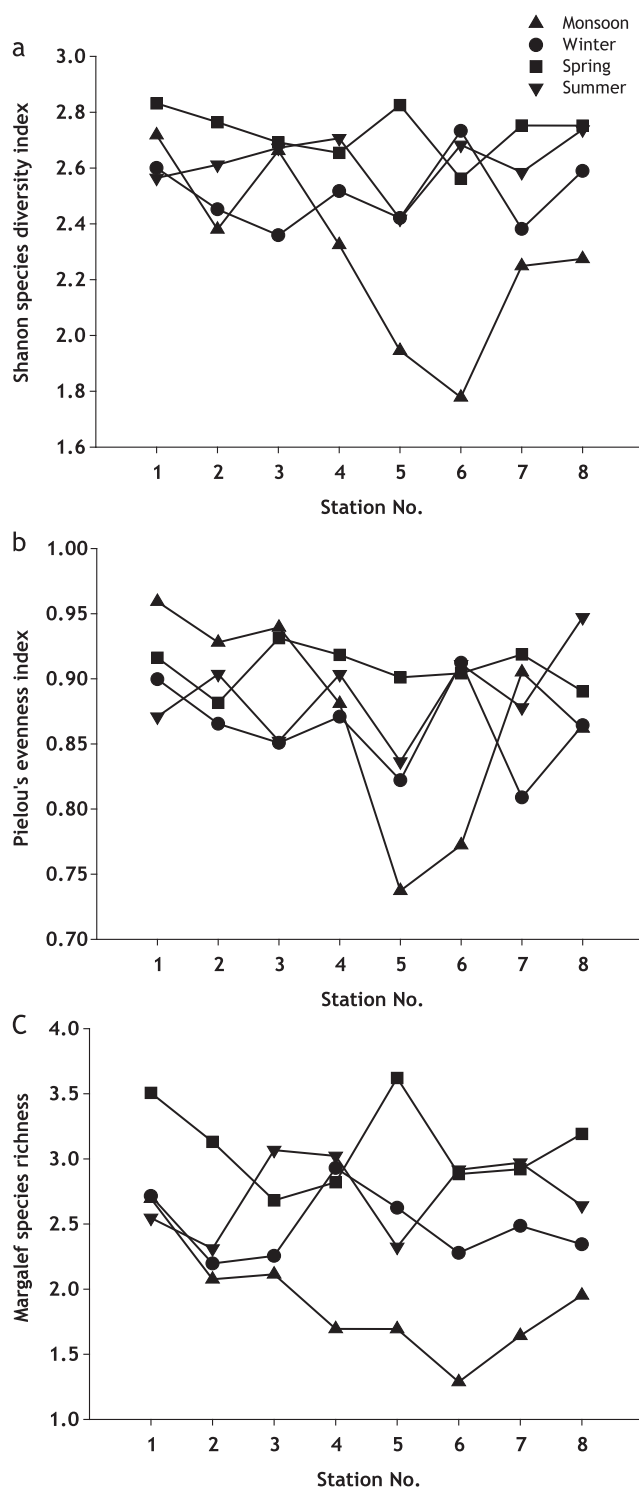


Figure 5 Spatio-temporal variation of different diversity indices.

maximum percentages to form group II. In winter, the zooplankton standing crop increased to reach an average of 1616 ± 1391 ind. m⁻³. It showed high fluctuation between 331 ind. m⁻³ (station 4) and 4185 ind. m⁻³ (station 6). The contribution of Copepoda to the total zooplankton population has been represented by 59%, which drastically dropped compared to the previous season. However, the Mollusca

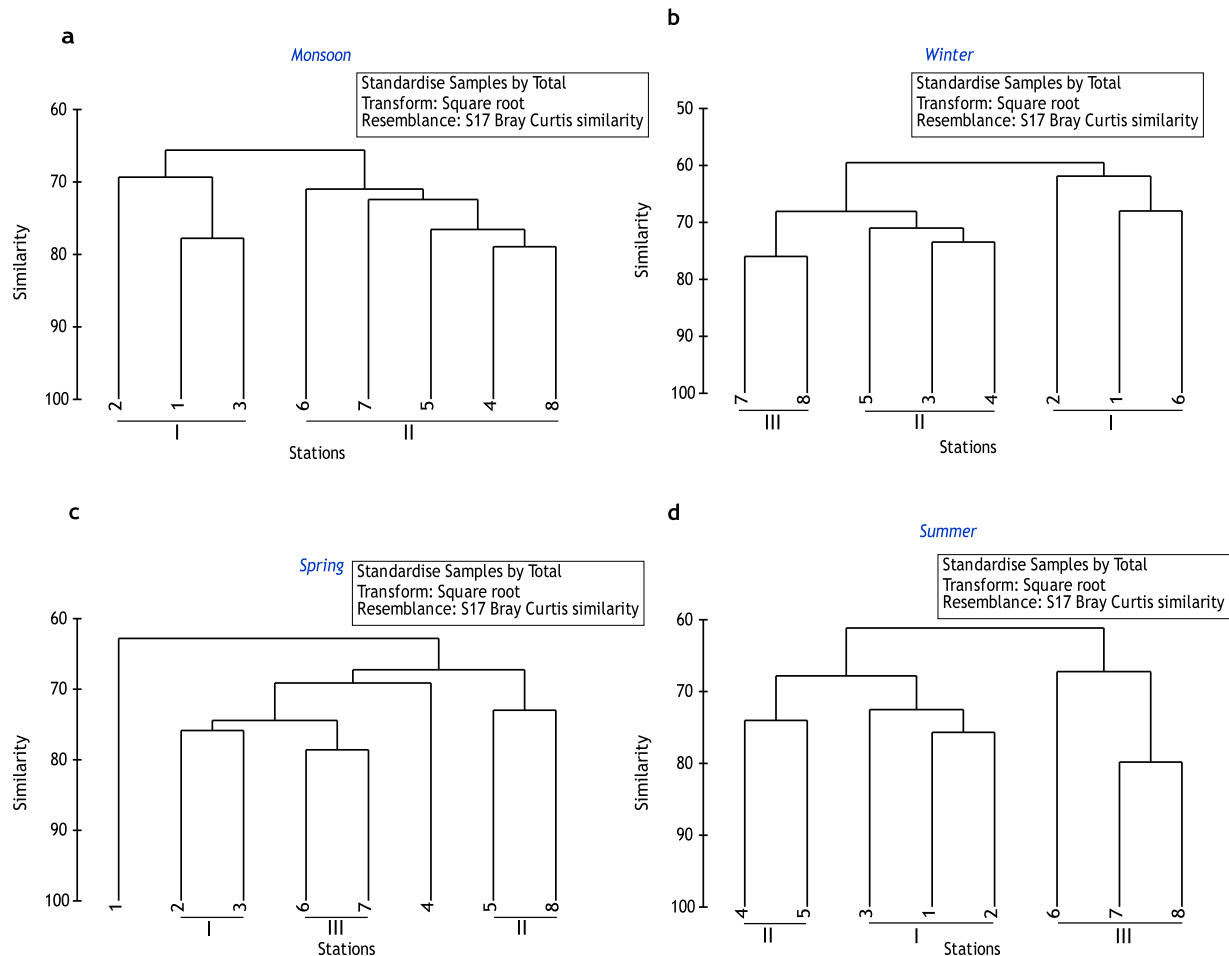


Figure 6 Dendrogram plot of cluster analysis based on total zooplankton abundance during four seasons.

larvae were the second most abundant group and they are dominated by Gastropoda veliger larvae (14%) and Bivalvia-D larvae (9%) of the total zooplankton count. Three separate cluster groups were generated with 63.96%, 71.86% and 76.02% of similarity in group I (station 1, 2 and 6), II (station 3–5) and III (station 7–8), respectively. The major contribution of *P. parvus* and Gastropoda veliger larvae plays a pivotal role to form these groups in conjunction with other zooplankton taxa.

The zooplankton average abundance was the lowest during spring (573 ± 270 ind. m^{-3}) ranging between 257 ind. m^{-3} (station 6) and 1126 ind. m^{-3} (station 2). Mature Copepoda and their nauplii together contributed 66% of the total zooplankton. Three groups (I, II and III) and two separate stations (station 1 and 4) were generated from the cluster analysis. The prevalent distribution of Copepoda nauplii contributed 9.79%, 11.28% and 8.38% in group I (station 2–3), II (station 5 and 8) and III (station 6–7), respectively, during this season. After spring, the zooplankton community increased in number during summer to reach an average of 951 ± 482 ind. m^{-3} . Average zooplankton abundance fluctuated from 420 ± 24 ind. m^{-3} (station 7) to 1495 ± 70 ind. m^{-3} (station 5) and the community was dominated by Copepoda (63%) during this season. A significant spatial dis-

tribution of zooplankton was documented from the cluster analysis, comprising with group I (station 1–3; 73% similarity), group II (station 4 and 5; 74.05% similarity) and group III (station 6–8; 71.46%).

The PERMANOVA analysis was performed to identify the major changes of zooplankton population. There were significant variations documented both spatially ($F = 713.12$, $p = 0.001$) and seasonally ($F = 150.66$, $p = 0.001$). Altogether, the spatio-temporal ($F = 288.33$, $p = 0.001$) variations were found to be significant in the present study.

3.3. Influence of environmental factors on zooplankton distribution

The statistical relationships between the composition of zooplankton and the physicochemical variables were also analysed at different study stations. We used CCA to explore the relationship between environmental variables and zooplankton assemblages and two graphs are generated as station and species biplots (Fig. 7). The station biplot depicts the responsible environmental parameters for clustering different study stations during different seasons. In the present study, all sampling stations distinctly clustered together depending on the particular season as governed

Table 2 SIMPER analysis of zooplankton assemblages determined by dendrogram plot considering each season: average similarity (%) and main taxa contribution (%).

| Groups | | | |
|----------------------------|---|--|--|
| Monsoon | I | II | |
| Average similarity (%) | 72.18 | 73.36 | |
| Main taxa contribution (%) | <i>Bestiolina similis</i> (12.33) <i>Paracalanus parvus</i> (10.52) <i>Paracalanus aculeatus</i> (9.42) <i>Oithona similis</i> (8.75) | <i>Paracalanus parvus</i> (22.47) <i>Paracalanus aculeatus</i> (11.88) <i>Oithona brevicornis</i> (10.31) <i>Acartia (Odontacartia) spinicauda</i> (9.11) | |
| Winter | I | II | III |
| Average similarity (%) | 63.96 | 71.86 | 76.02 |
| Main taxa contribution (%) | <i>Paracalanus parvus</i> (13.80) Gastropoda veliger (11.64) <i>Bestiolina similis</i> (9.99) Bivalvia D larva (9.64) <i>Labidocera minuta</i> (9.26) | Gastropoda veliger (15.72) <i>Paracalanus parvus</i> (11.96) Decapoda Brachyura zoeae (8.11) | Decapoda Brachyura zoeae (15.13) <i>Paracalanus parvus</i> (10.76) Gastropoda veliger (9.09) |
| Spring | I | II | III |
| Average similarity (%) | 75.88 | 73.01 | 78.63 |
| Main taxa contribution (%) | <i>Paracalanus parvus</i> (10.80) Copepoda nauplii (9.79) <i>Zonosagitta bedoti</i> (8.58) | Copepoda nauplii (11.28) <i>Paracalanus parvus</i> (10.45) Gastropoda veliger (9.88) | <i>Paracalanus parvus</i> (12.00) <i>Bestiolina similis</i> (10.08) Gastropoda veliger (8.92) Copepoda nauplii (8.38) |
| Summer | I | II | III |
| Average similarity (%) | 73.6 | 74.05 | 71.46% |
| Main taxa contribution (%) | Gastropoda veliger (12.82) Bivalvia D larvae (10.84) <i>Paracalanus parvus</i> (10.43) | <i>Bestiolina similis</i> (11.74) <i>Paracalanus parvus</i> (9.70) <i>Eucalanus sp.</i> (9.69) | <i>Paracalanus parvus</i> (13.79) <i>Bestiolina similis</i> (10.83) <i>Paracalanus aculeatus</i> (10.09) |

by most responsible physicochemical parameters. For example, the samples collected during monsoon season were regulated by PO₄-P, pH and Phaeo enriched estuarine environment. Winter season showed preferences with respect to salinity, Secchi depth and temperature of the surface water. Furthermore, spring season samples were clustered in close association with DO, NO₂-N and SPM; and summer samples slightly accumulated near the elevated NH₄-N concentration (Fig. 7a). The species biplot was done to investigate the role of environmental parameters on zooplankton species distribution. In this plot, distinct clusters and species associations are formed depending on their preferred environmental conditions. A total of 56 zooplankton taxa were used in the CCA gradient analysis. Eigenvalues for CCA axis 1 and axis 2 represent 30.86% of the cumulative variance in the species data. Species-environment correlations were high for both axes (Axis 1=0.91; Axis 2=0.90) (Fig. 7b). *Acrocalanus longicornis*, *O. similis* and *O. brevicornis* preferred the environment with high pH values during the study period, mostly recorded in monsoon season. Few herbivorous copepods, like *Acartia sp.*, *Acrocalanus gracillis*, *Canthocalanus pauper*, *Oithona simplex* and *Paracalanus sp.* were found to be positively correlated with PO₄-P. Some winter season notable taxa, like Pycnogonida, Bryozoa cyphonautes, *Subeucalanus subcrassus*, *Longipedia weberi* and *Centropages sp.* were favoured by

transparent and high saline estuarine environment. However, few taxa, like nauplius larva, *Belzebub penicillifer*, Crustacea zoeae, and Copepoda, like *Acartia clausi*, *Labidocera acuta*, *L. minuta* and *Temora discaudata*, slightly correlated with water temperature and these species were totally absent during monsoon season. The distribution of carnivorous zooplankton Hydrozoa actinulae, *Corycaeus crassiusculus* and *Labidocera sp.* were associated with SPM of surface water. Species like *Acartia danae*, *E. elongatus elongatus*, *Euterpina acutifrons*, Copepoda nauplii, Euphausiacea calyptopis, Echinodermata larvae and Decapoda larvae were found to prefer moderate to low oxygen and NO₃-N content water mass, recorded during post-monsoon period, especially in spring. Some omnivorous zooplankton, like Polychaeta larvae, fish larvae, *Pseudodiaptomas serriacaudatus* and *Oncaea venusta*, had been associated with NH₄-N enriched water. The Chl-*a* concentration did not exhibit any significant contribution to the distribution pattern of zooplankton population during the present study (Fig. 7b).

3.4. Seasonal occurrences of indicator species

The analysis of nMDS was performed to unravel the seasonal variation on the basis of total zooplankton population dynamics (Fig. 8). Table 3 showed the different dissim-

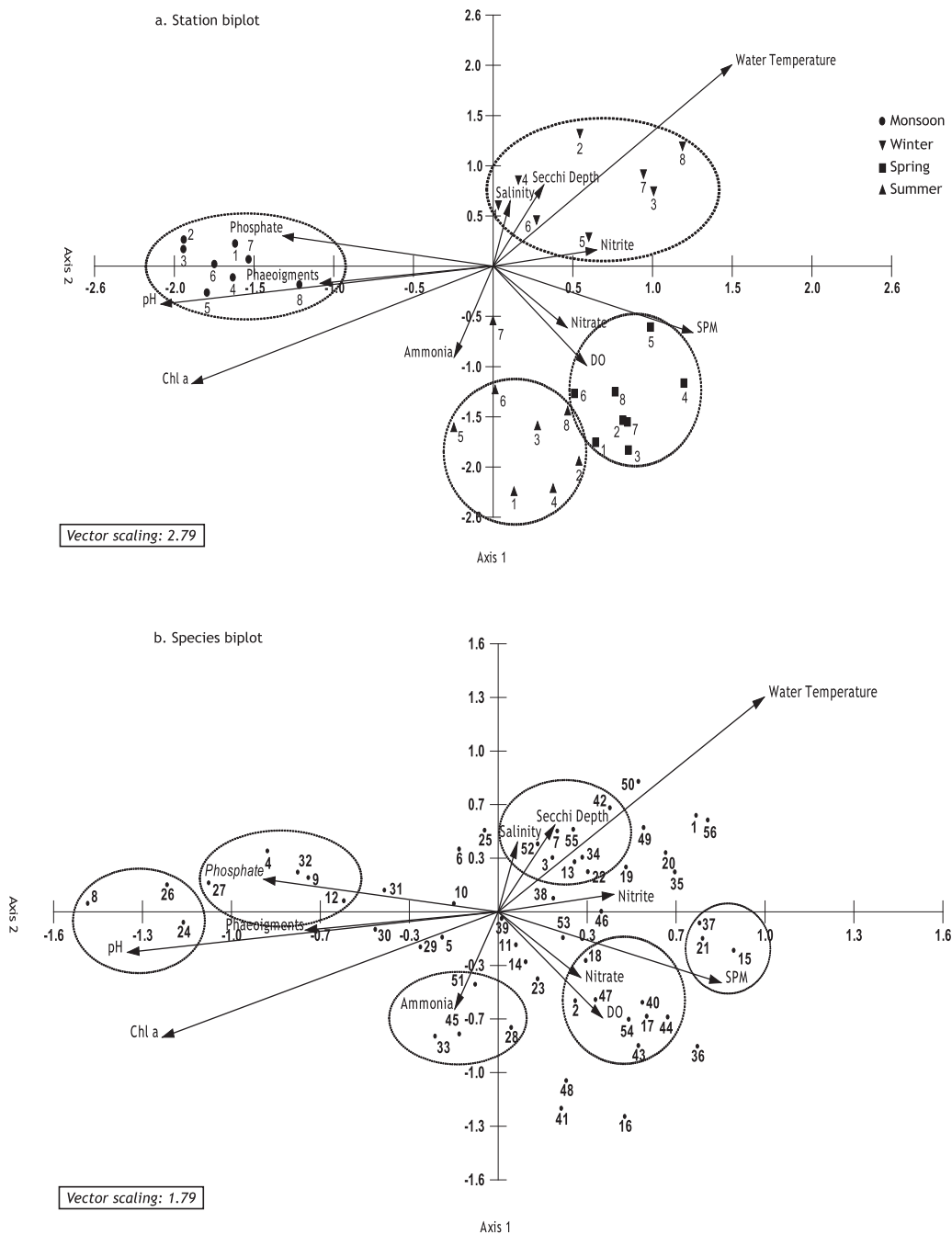


Figure 7 CCA analysis of different zooplankton taxa with associated environmental variables and study stations. (a – station biplot, b – species biplot; Code no. of zooplankton taxa are given in Table 4).

ilarity percentages of four seasons along with their ANOSIM value, indicating the significant variation amongst them. The positive or the value closest to 1 specifies the significant changes between two seasons. The remarkable changes of mean abundances of some zooplankton taxa between different seasons (responsible for seasonal variation) might show the indicator species for the particular season due to their exclusive seasonal occurrences. The result of *IndVal* analysis demarcated altogether 10 Copepoda and 12 non-Copepoda taxa as major indicators of different stud-

ied seasons (Table 4). During the monsoon, *Acartia* sp., *O. brevicornis*, *O. similis*, *O. simplex*, *P. parvus* were the indicator species for all study stations. However, in winter *A. clausi*, *Labidocera minuta*, Bryozoa cyphonautes, Gastropoda veliger, *Zonosagitta bedoti* and Decapoda zoeae were found to be dominant and maximum *IndVal* index was encountered. *C. crassiusculus*, Copepoda nauplii, Euphausiacea calyptopis, Echinodermata larvae and Hydrozoa were the significant indicator species for spring season, lastly high value of *IndVal* index was documented for *Eucalanus* sp., *E.*

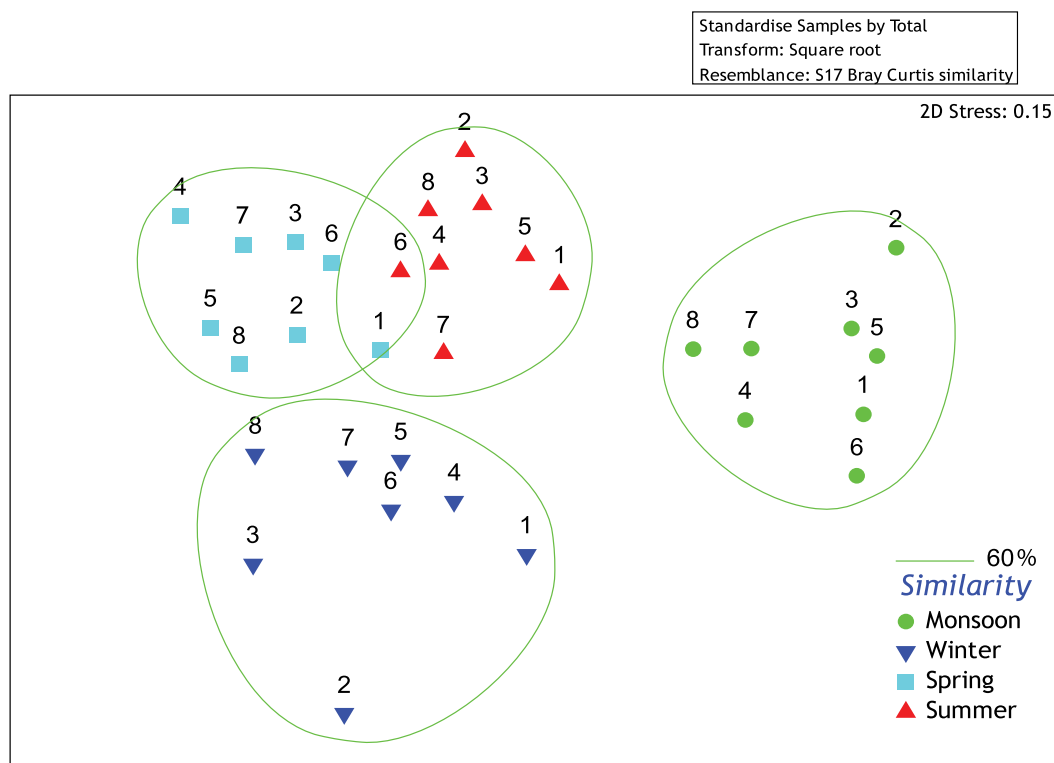


Figure 8 NMDS plot for seasonal zooplankton assemblages sampled in the river Matla.

Table 3 SIMPER analysis for zooplankton assemblages formed by NMDS considering each season: average dissimilarities (%) and ANOSIM results between two seasons are presented.

| Seasons | Average dissimilarity (%) |
|--|---------------------------|
| Monsoon and Winter (ANOSIM, global R=0.956, $p=0.001$) | 55.46 |
| Monsoon and Spring (ANOSIM, global R=0.997, $p=0.001$) | 58.34 |
| Monsoon and Summer (ANOSIM, global R=0.946, $p=0.001$) | 50.13 |
| Winter and Spring (ANOSIM, global R=0.742, $p=0.001$) | 44.33 |
| Winter and Summer (ANOSIM, global R=0.766, $p=0.001$) | 46.06 |
| Spring and Summer (ANOSIM, global R=0.628, $p=0.001$) | 40.77 |

elongatus elongatus, Ctenophora, *Belzebug hansenii* and Decapoda larvae during summer (Table 4).

4. Discussion

4.1. Changes in the environmental variables

Physico-chemical variables in the estuarine ecosystem are subjected to wide temporal variations. The river Matla in

SES is largely influenced by southwest monsoonal rainfall in India. According to Santhosh Kumar and Perumal (2011), the monsoonal rainfall is an important phenomenon in tropical countries as it regulates the biogeochemical characteristics of the coastal and estuarine environment. In the present study, each of the hydrographic parameters such as water temperature, salinity, pH and DO showed remarkable spatio-temporal variations. In general, the higher temperature was recorded in pre-monsoon period at summer season while the lower temperature was observed during winter. SES is located at the north-western coast of Bay of Bengal and the temperature over the bay is primarily regulated by several climatic events, like the atmospheric weather condition and rainfall event (Kannan and Kannan, 1996). Temperature variations throughout the present study period could also be governed by the seasonal changes in atmospheric conditions and monsoonal rainfall.

The salinity acts as a limiting factor in the distribution pattern of marine organisms. Moreover, changes in salinity due to the effect of dilution and evaporation can regulate the faunal composition in the coastal ecosystem (Balasubramanian and Kannan, 2005; Sridhar et al., 2006). In the present study, the lower salinity values during monsoon season could be attributed to the combined effect of precipitation and freshwater influx from surrounding land runoff.

The pH recorded during summer and monsoon period was found to be comparatively higher than in winter and spring season. Influence of seawater inundation and biological activity of photosynthetic organisms might be the possible reason for high summer pH. Furthermore, the observed high pH along with elevated DO during monsoon season might be the

Table 4 List of identified zooplankton taxa with their indicator values for each season. Bold values are considered major indicator species (*IndVal* index ≥ 40) for the present study.

| CCA code | Name of identified zooplankton taxa | Monsoon | Winter | Spring | Summer |
|----------|---|--------------|--------------|--------------|--------------|
| 1 | <i>Acartia (Acartiura) clausi</i> Giesbrecht, 1889 | 0 | 74.47 | 9.31 | 0 |
| 2 | <i>Acartia (Acartia) danae</i> Giesbrecht, 1889 | 0 | 0 | 1.79 | 21.43 |
| 3 | <i>Acartia (Acartia) negligens</i> Dana, 1849 | 0 | 32.29 | 0.69 | 1.04 |
| 4 | <i>Acartia</i> sp. | 56.85 | 6.05 | 1.21 | 0.41 |
| 5 | <i>Acartia (Odontacartia) spinicauda</i> Giesbrecht, 1889 | 33.80 | 20.83 | 6.35 | 29.10 |
| 6 | <i>Acartia sewelli</i> Steuer, 1934 | 6.82 | 32.95 | 0 | 0.85 |
| 7 | <i>Acrocalanus gibber</i> Giesbrecht, 1888 | 0 | 12.5 | 0 | 0 |
| 8 | <i>Acrocalanus gracilis</i> Giesbrecht, 1888 | 26.47 | 0 | 0 | 7.35 |
| 9 | <i>Acrocalanus longicornis</i> Giesbrecht, 1888 | 50 | 0 | 0 | 0 |
| 10 | <i>Bestiolina similis</i> Sewell, 1914 | 29.52 | 34.63 | 11.94 | 1 |
| 11 | <i>Bomolochus</i> sp. | 0 | 0 | 12.5 | 0 |
| 12 | <i>Canthocalanus pauper</i> Giesbrecht, 1888 | 25 | 0 | 0 | 0 |
| 13 | <i>Centropages</i> sp. | 0 | 12.5 | 0 | 0 |
| 14 | <i>Clytemnestra scutellata</i> Dana, 1848 | 0 | 0 | 12.5 | 0 |
| 15 | <i>Corycaeus crassiusculus</i> Dana, 1849 | 0 | 20.46 | 57.58 | 5.68 |
| 16 | <i>Eucalanus</i> sp. | 0 | 0 | 25.68 | 70.65 |
| 17 | <i>Eucalanus elongatus elongatus</i> Dana, 1849 | 0 | 7.72 | 30.39 | 49.02 |
| 18 | <i>Euterpina acutifrons</i> Dana, 1848 | 0.3 | 9.52 | 20.83 | 22.32 |
| 19 | <i>Labidocera acuta</i> Dana, 1849 | 1.09 | 38.43 | 12.5 | 12.5 |
| 20 | <i>Labidocera minuta</i> Giesbrecht, 1889 | 0 | 63.03 | 26.89 | 6.3 |
| 21 | <i>Labidocera</i> sp. | 0 | 0 | 12.5 | 0 |
| 22 | <i>Longipedia weberi</i> Scott A., 1909 | 0 | 19.11 | 5.88 | 0 |
| 23 | <i>Microsetella norvegica</i> Boeck, 1865 | 0 | 0 | 0 | 12.5 |
| 24 | <i>Oithona brevicornis</i> Giesbrecht, 1891 | 83.01 | 0 | 3.75 | 5.5 |
| 25 | <i>Oithona nana</i> Giesbrecht, 1893 | 12.5 | 0 | 0 | 0 |
| 26 | <i>Oithona similis</i> Claus, 1866 | 91.3 | 0.36 | 0 | 1.45 |
| 27 | <i>Oithona simplex</i> Farran, 1913 | 62.19 | 0 | 6.1 | 0.61 |
| 28 | <i>Oncaea venusta</i> Philippi, 1843 | 0 | 0 | 6.25 | 6.25 |
| 29 | <i>Paracalanus aculeatus</i> Giesbrecht, 1888 | 34.45 | 26.72 | 7.84 | 27.17 |
| 30 | <i>Paracalanus indicus</i> Wolfenden, 1905 | 36.02 | 17.72 | 0.2 | 16.54 |
| 31 | <i>Paracalanus parvus</i> Claus, 1863 | 45.94 | 25.7 | 10.52 | 17.84 |
| 32 | <i>Paracalanus</i> sp. | 36.16 | 0 | 3.57 | 0 |
| 33 | <i>Pseudodiaptomus serricaudatus</i> Scott T., 1894 | 0 | 0 | 0 | 37.5 |
| 34 | <i>Subeucalanus subcrassus</i> Giesbrecht, 1888 | 0 | 25 | 0 | 0 |
| 35 | <i>Temora discaudata</i> Giesbrecht, 1889 | 0 | 7.5 | 0.84 | 8.33 |
| 36 | <i>Temora turbinata</i> Dana, 1849 | 0 | 0 | 2.78 | 29.17 |
| 37 | Hydrozoa acrinulae | 0 | 0 | 25 | 0 |
| 38 | Arachnida | 0 | 0 | 0 | 0 |
| 39 | Bivalvia D larvae | 26.16 | 34.77 | 7.95 | 26.16 |
| 40 | Copepoda nauplii | 0 | 17.63 | 45.87 | 13.46 |
| 41 | Ctenophora | 0 | 0 | 0 | 62.5 |
| 42 | Cyphonautes larvae | 0 | 63.59 | 2.17 | 1.63 |
| 43 | Euphausiacea calyptopis | 0 | 0 | 62.5 | 0 |
| 44 | Echinodermata larvae | 0 | 6.48 | 55.55 | 0 |
| 45 | Fish larvae | 2.5 | 0 | 5 | 30 |
| 46 | Gastropoda veliger | 8.52 | 51.31 | 12.12 | 26.84 |
| 47 | Hydrozoa medusae | 0 | 0 | 62.5 | 0 |
| 48 | <i>Belzebub hanseni</i> Nobili, 1906 | 0 | 0 | 0 | 87.5 |
| 49 | <i>Belzebub penicillifer</i> Hansen, 1919 | 0 | 21.4 | 1.78 | 0 |
| 50 | Nauplius larvae (Cirripedia) | 0 | 82.8 | 0.66 | 0 |
| 51 | Polychaeta larvae | 19.85 | 14.34 | 1.11 | 31.25 |
| 52 | Pycnogonida | 0 | 25 | 0 | 0 |
| 53 | <i>Zonosagitta bedoti</i> (Béraneck, 1895) | 9.87 | 44.23 | 16.59 | 28.85 |
| 54 | Decapoda larvae | 0 | 0 | 0 | 87.5 |
| 55 | Star fish juvenile (Echinodermata) | 0 | 37.5 | 0 | 0 |
| 56 | Decapoda Brachyura zoeae | 0.56 | 71.19 | 6.48 | 5.8 |

cumulative effect of higher wind velocity coupled with massive rainwater and the resultant freshwater mixing in the estuarine system (Das et al., 1997).

Nutrients levels are known to be a significant determinant of estuarine productivity and their spatio-temporal variations can play a crucial role by influencing the process of competition and community structure as well as trophic dynamics in the estuarine environment (Gaonkar et al., 2010). Distribution of nutrients in an estuary is principally controlled by season, tidal condition and freshwater runoff from surrounding landmass. Nitrite ($\text{NO}_2\text{-N}$), the most unstable form of nitrogenous nutrients in seawater, exhibited wide range of fluctuation. Its variations in surface water throughout the study period could be ascribed to the excretion of the planktonic organism, oxidation of ammonia, reduction of nitrate and bacterial decomposition of planktonic detritus (Govindasamy et al., 2000). In the present study, the high monsoonal value of major micronutrients ($\text{NO}_3\text{-N}$, $\text{PO}_4\text{-P}$ and $\text{SiO}_4\text{-Si}$) concentration could be influenced by organic matter received from the catchment area (Das et al., 1997). The maximum recorded value of $\text{NO}_3\text{-N}$ during monsoon season and the lowest recorded salinity clearly signifies the freshwater inflow as a major contributor of nitrate in the estuarine system. According to Karuppasamy and Perumal (2000), Santhanam and Perumal (2003) and Sarkar et al. (2007) nitrate level was generally increased by land drainage, precipitation, decomposition of mangrove litter and terrestrial runoff during monsoon season. In contrast, during post-monsoon period, the prevalent lower value of $\text{NO}_3\text{-N}$ is linked to the biological utilization and primary productivity in shallow estuarine water (MacIntyre et al., 1996). Like nitrate, $\text{PO}_4\text{-P}$ concentration also exhibited higher value during monsoon, indicating the influence of freshwater influx in the present study area. Maximum concentration of inorganic phosphates during monsoon might be due to the intrusion of seawater into the mangrove creeks and enrichment by freshwater drainage (Mathew and Pillai, 1990; Nair et al., 1984). The low value of phosphate in spring could be recognized by high salinity and utilization of phosphate by phytoplankton, along with the low freshwater influx in the estuarine system (Senthilkumar et al., 2002). The lower concentration of $\text{SiO}_4\text{-Si}$ during the post-monsoon period, especially in spring, could be connected to its uptake by phytoplankton for their biological activity (Mishra et al., 1993; Ramakrishnan et al., 1999). Furthermore, the high silicate concentration during monsoon might be due to the resuspension of bottom sediment (Rakhesh et al., 2008). The higher concentration of $\text{NH}_4\text{-N}$ recorded during summer could be partially due to the death, subsequent decomposition and excretion of ammonia by planktonic organisms (Segar and Hariharan, 1989).

4.2. Diversity and distribution of the zooplankton population

In the present study, 56 zooplankton taxa have been reported from the river Matla at SES, the number of zooplankton recorded in this river is in accordance with the published report from the river Saptamukhi (Nandy et al., 2018) and the northern part of the Sundarban mangrove wetland (Bhattacharya et al., 2015). Zooplankton commu-

nity changes of the SES indicated a strong seasonal pattern showing lower abundances in the spring-summer period and higher density in monsoon-winter time. In dry weather during spring, lower temperature and the shortest daylight hours coupled with water transparency might have reduced the secondary productivity and had a cascading effect as was mirrored by diminished zooplankton abundance during this period. Contrarily, high to moderate temperature, low salinity and availability of sufficient nutrients were the favourable conditions for increasing the zooplankton abundance during and after the wet season in SES (Nandy et al., 2018) which corroborates present findings.

The high abundance of zooplankton in monsoon and post-monsoon seasons might be attributed to a combination of temperature, salinity and Chl-*a* concentration, which are considered the main factors in regulating the population dynamics (Peterson and Bellantoni, 1987). Seasonal studies in different coastal areas highlighted the similar relationship between the zooplankton abundance and the elevated temperature and Chl-*a* concentration (Biancalana et al., 2014; Vieira et al., 2003), and are also in agreement with present findings. In accordance with earlier studies in the Sundarbans (Bhattacharya et al., 2015; Nandy et al., 2018) as well as Indian coastal belt (Srichandan et al., 2015), our result also recorded high contribution of Copepoda among the total zooplankton. During the present study, the contribution of Copepoda to the total zooplankton population ranged from 59–87% as reported in many estuarine systems and coastal areas where Copepoda dominated the zooplankton community (Marques et al., 2006; Moderan et al., 2010; Mouny and Dauvin, 2002).

In the present study, a noticeable abundance of Copepoda with 87% of the total composition was documented during the peak monsoon season. The versatility of these taxa, which occupy several estuarine habitats is often due to their broad trophic spectrum. According to Jagadeesan et al. (2017), the temporal changes in the abundance of copepod community in a coastal area is generally influenced by the coastal upwelling and associated hydrographical changes of the estuarine environment. During the summer and winter seasons, Calanoida (e.g., *P. parvus*, *P. aculeatus*, *Bestiolina similis*, *Acartia* sp. and *A. spinicauda*) clearly outnumbered other Copepoda species. However, during the monsoon season, along with Calanoida few Cyclopoida (e.g., *Oithona nana*, *O. similis*, *O. simplex* and *O. brevicornis*) were also dominant in the community. The seasonal dominance of Cyclopoida in the SES was clearly highlighting the temporal shift in their composition. The overall ubiquitous dominance of genus *Oithona* during peak monsoon season suggests their high adaptability to trophic and hydrologic conditions, which might be due to their continuous reproduction and reduced mortality rates during this season (Nielsen and Sabatini, 1996; Pages et al., 1996).

SES is characterised by a rich population of Copepoda and meroplankton species adapted to endure changes in salinity and other hydrological parameters during winter. Moreover, the preponderance of meroplankton (e.g., Decapoda zoeae, Bryozoa cyphonautes, Bivalvia and Gastropoda veliger) in the SES suggests that these organisms take an important role in the coupling of benthic-pelagic food webs. The abundance and diversity of different larval forms (e.g., Zoea, nauplius, and veliger) and their enormous contribution to

the total zooplankton population make SES a unique ecosystem during winter. Similar findings have also been reported by [Rakhesh et al. \(2008\)](#) at Kakinada Bay. During winter, different Mollusca veliger populations recorded maximum, especially at mouth stations, probably corresponding with their seaward migration from the estuarine system. These larval forms move into the water column from the bottom layer during tidal flooding, and they are flushed into downstream habitat by the ebb tides ([Zhou et al., 2009](#)). During this season the higher abundance of *Chaetognatha* (*Z. bedoti*), was recorded with high *IndVal* index (44.23). The previous study also reported their high abundance in SES due to their preference of estuarine environment during their development ([Bhattacharya et al., 2015](#)). Similarly, the high abundance of *Chaetognatha* during post-monsoon period was common in the coastal water of Adubidri ([Resmi et al., 2011](#)) and Rushikulla estuary ([Srichandan et al., 2015](#)) which is in agreement with our present observation.

In the present study, the lowest abundance of zooplankton occurred in the spring season. The increase of saline water in SES caused by excess evaporation and lower nutrients concentration during spring season might be the possible reason for recording low zooplankton abundance and biomass. In general, soon after monsoonal precipitation, the river runoff and water temperature start to decrease and cause depleted nutrients supply to the system, which has a cascading effect on lower productivity and might be the reason of less zooplankton abundance during this season. In tropical estuarine system zooplankton generally breed during post-monsoon season (winter). As it takes time for zooplankton to breed and grow, there is a time-lapse for the concentration of zooplankton to increase. For this reason, the abundance of zooplankton is the lowest in spring. However, during the summer season the high turbidity in estuarine waters (wind and tide induced resuspension) might affect the phytoplankton growth and restrain light availability; which may be the causative factor in recording the second-lowest zooplankton abundance in the study area. In agreement with our study, similar observations have also been reported from Kakinada Bay ([Rakhesh et al., 2008](#)) and Quinzhou Bay ([Wang et al., 2014](#)).

In our study salinity seemed to be an important factor in explaining the dynamics of the zooplankton, especially at a spatial scale. [Marques et al. \(2009\)](#) ascribed that salinity of different water masses is closely related to the distribution pattern of zooplankton. In the present study, spatial variation of salinity followed a similar pattern during four seasons. An increasing trend was observed from head to mouth of the estuary. The cluster analysis of four study seasons depicted a clear spatial distribution pattern of zooplankton population along the salinity gradient. During summer and monsoon seasons the upstream stations form a separate cluster apart from the middle and downstream stations. The major contribution of Bivalvia and Gastropoda clustered the upstream stations (station 1–3) during summer, indicating their seasonal recruitment during this time in SES. The upstream to downstream connectivity and directionality influence the passive distribution of zooplankton community. In SES, the significant spatial distribution of zooplankton during wet season could be explained by high river runoffs that create typical north-south river continuum environmental gradient patterns as described by [Vannote](#)

[et al. \(1980\)](#) in the Ying river. Furthermore, the low runoff during dry season (spring) turned the river into numerous interconnected pools in SES, which resulted in a nondirectional spatial distribution of zooplankton (personal observation). Low flows during the dry period partially interrupted the upstream-downstream connection and limited the passive migration of organisms. Similarly to present observation, many researchers documented environmental-changes induced high temporal variation of zooplankton population in estuarine systems around the globe ([Biggs et al., 1998](#); [Peterson, 1996](#)), and robustly heterogeneous spatial distribution of zooplankton ([Giller et al., 1994](#); [Zhao et al., 2017](#)). The significant spatial changes of zooplankton abundance and biomass in SES might be synchronized with the existence of the salinity gradient, as described in the Pearl river estuary by [Li et al. \(2006\)](#).

Shannon species diversity index is one of the broadly used ecological indices for measuring diversity for a particular community. It can vary spatially and seasonally with different ecological factors (e.g., competition, predation and succession) which might change the evenness index albeit any alteration in richness index ([Stirling and Wilsey, 2001](#)). The present study showed a similar pattern in the graphical representation of diversity and evenness indices, but the relation with richness was not clear. Furthermore, the higher values were observed for all diversity indices in upstream stations, indicating this part of the estuary is healthier than the downstream part in terms of zooplankton biodiversity. According to [Wang et al. \(2014\)](#) the diversity threshold of zooplankton in a tropical estuarine system can be divided into 5 stages, like bad (<0.6), average (0.6–1.5), good (1.6–2.5), better (2.6–3.5) and excellent (>3.5). In the present study, the Shannon diversity index of SES was recorded much higher than 1.6 throughout the study period, showing a good to better zooplankton diversity pattern in this area. Moreover, the evenness index exceeded 0.3 during four seasons, indicating a good diversity of zooplankton ([Sun et al., 2004](#)). The species diversity and species richness values were high during the pre-monsoon period (spring and summer), along with high values of the evenness index, suggesting an equal distribution of zooplankton species during these seasons. The present study showed the lowest diversity indices during the monsoon season, which gradually increased after this period. This is consistent with previous works where a similar observation was also reported by [Bhattacharya et al. \(2015\)](#) at different parts of the Sundarbans.

4.3. Zooplankton response to environmental changes

Our study revealed clear differences in zooplankton community between the different sampling seasons, which can be explained by a combination of environmental variables. From the CCA, the assemblages of zooplankton in the SES are closely related to temperature, salinity, DO and nutrients. It is indicated that the abundance and biomass are obviously related to environmental factors in monsoon and winter seasons. The low salinity, moderate temperature, normoxic water with sufficient nutrients triggered the zooplankton growth during this time in the SES. A similar type

of observation has also been reported in Rushikulla Estuary by Srichandan et al. (2015), where zooplankton density showed a positive correlation with nitrate and DO but negatively correlated with salinity. In terms of zooplankton population, monsoon and winter seasons would be considered as the most productive season for this estuarine system. An elevated Chl-*a* was recorded during monsoon when nutrients were readily available and temperature increased, while a decrease in Chl-*a* was observed during winter. Such seasonal pattern of Chl-*a* has been reported by many researchers in different estuarine complexes around the world (Amin et al., 2011; Biancalana et al., 2014; Gil et al., 2011). The lower concentration of the phytopigments and higher zooplankton population during winter suggests a potential zooplankton (especially meroplankton) grazing in this season (Torres et al., 2009). Moreover, anoxic conditions (during spring and summer) and high turbidity (only during summer) related to organic enrichment could be a causative factor in decreasing zooplankton abundance and accelerating rate of copepod mortality (Drira et al., 2018; Gordina et al., 2001; Park and Marshall, 2000), though the total zooplankton biomass was found to be high during summer due to the dominance of large-sized Decapoda larvae. In the overall study, the predominance of low saline species of genus *Paracalanus*, *Acartia* and *Acrocalanus* clearly indicates the estuarine influence in the study area. Furthermore, subtle changes of detrimental pollutant such as NH₄-N plays a noteworthy role in the seasonal pattern of zooplankton communities. The higher concentration of ammonia-nitrogen during summer had a great impact on the abundance of zooplankton in the present study. Zhao et al. (2013) recognized that too high or low concentration of this parameter results in the reduction of zooplankton density in an estuarine system. The distinct clusters in both stations and species biplot of CCA analysis clearly revealed that the zooplankton spatio-temporal variation may be caused by different environmental variables, which can regulate the overall composition, diversity, distribution of Copepoda and abundance of meroplankton in the estuarine ecosystem. Among all the environmental variables salinity, pH, temperature and micronutrients accounted for the most of spatio-temporal variations of zooplankton population dynamics. As suggested by Dorak and Albay (2016) and Wooldridge (1999), the horizontal salinity and temperature gradients are known to have an important role in determining the spatial and seasonal distribution of zooplankton, respectively.

4.4. Zooplankton as a relevant bioindicator

Due to their short life cycles, drifting habitus and quick reactions to changes of the aquatic environment zooplankton are considered as an excellent bioindicator for investigating and documenting of the environmental influences in estuarine and/or brackish water system (Annabi-Trabelsi et al., 2019; Campos et al., 2017; Drira et al., 2018; Sipkay et al., 2009). In a tropical estuarine complex, dominant zooplankton taxa generally determine the structure of the community and the pathway of material circulation and energy transference into the ecosystem. If a dominant group dies out, the structure of the community will alter along with the ecological environment (Wang

et al., 2014). In the present investigation, the seasonal occurrences of particular zooplankton with significant temporal variation implies that the variation of salinity and other environmental factors in the surface water exerts either a direct or an indirect effect in the appearance or disappearance of some taxa and replacement by others. Mean abundance of some indicator zooplankton taxa varied seasonally and acted as the responsible factor for significant ($p = 0.001$) dissimilarity among four sampling period.

Among zooplankton, Copepoda are considered as most sensitive to even subtle changes in the hydrological characteristics and regarded as suitable ecological indicators of different environmental oscillation and ecosystem functioning (Campos et al., 2017; Jyothibabu et al., 2018). During monsoon, 3 Calanoidea (*P. parvus*, *Acartia* sp. and *A. longicornis*) and 3 Cyclopoida (*O. brevicornis*, *O. simplex* and *O. similis*) species showed high *IndVal* index. Cyclopoida can survive in a wide range of habitats and maintain their population in any adverse condition (Paffenhoffer, 1993). Moreover, their reproductive strategy was the main reason for their significantly high abundance during monsoon season (Keister and Tuttle, 2013). The high *IndVal* index (83.01) of *O. brevicornis* and presence of *O. nana* only during monsoon exhibit a clear indication of organic pollution and anthropogenically disturbed marine system in this period at the river Matla of SES (Drira et al., 2018; Serranito et al., 2016; Uye, 1994). These phenomena probably can be best explained by the fact that this area during monsoon season is under constant anthropogenic stress compared to other seasons. The dominance of meroplankton (especially the Mollusca veliger) during winter is a good indication of the most productive season for their recruitment in SES activated by low temperature and a moderate amount of nutrients and Chl-*a* concentration in the estuarine environment. The higher indicator value of copepod *A. clausi* during this time implies their euryhaline character and the high abundance in the dry season, as reported in earlier studies (Dorak and Albay, 2016; Vieira et al., 2003). During spring, the herbivorous zooplankton like Euphausiacea calyptopis, Echinodermata larvae, Hydrozoa, and Copepoda nauplii indicated their preferences to transparent high saline estuarine water. The peak abundance of Hydrozoa during spring was a very common phenomenon in Indian coasts. Santhakumari and Nair (1999) and Srichandan et al. (2015) also reported such higher population density of Hydrozoa during the pre-monsoon period. Furthermore, maximum *IndVal* index of *C. crassiusculus* (57.58) during spring indicates their feeding preference towards Copepoda nauplii (Turner, 1984), which is most abundant in SES during this period. The highest indicator value (87.5) recorded for the Decapoda larvae and *B. hanseni* during the summer season suggested that SES supports these decapods community during this time for their ingress, growth and reproduction. Similarly, Srichandan et al. (2015) and Venkataramana et al. (2017) have also mentioned that the coastal part of Bay of Bengal remains more productive and supports high decapods density by linear correlation with temperature during pre-monsoon season.

In the present study, the maximum water temperatures 32.5 and 33.4°C were recorded during the monsoon and summer season, respectively, in this part of the

Sundarbans. Mitra et al. (2009) suggested that the effects of global warming can be observed in the Indian Sundarbans as a significant rising trend of the surface water temperature has been detected over the past 27 years. The increment of water temperature is visibly reflected in the present study by perennial dominance of Calanoida (*B. similis*, *P. parvus*, *A. gracilllis*, *Acrocalanus gibber* and *Temora turbinata*) in SES, which are considered warm water preferring species (Bhattacharya et al., 2015; Stephen, 1984; Tseng et al., 2012; Wong et al., 2000). The exclusive appearance of these warm-water species along with high *IndVal* index might be an indication of the climate change-mediated temperature rise in the Indian Sundarbans.

5. Conclusion

The present study provides an overview of the changes in abundance and community structure of zooplankton and strengthens their role as an indicator organism of hydrographical changes in the Sundarbans. A strong spatial, as well as seasonal variation, was observed in the zooplankton community influenced by different hydrological parameters at the river Matla in SES. This is the first in-depth study from the mangrove dominated estuary under a restricted biosphere reserve area in the SES. A clear seasonal compositional shift with the increased percentage of Copepoda during the monsoon season was documented. Copepoda have emerged as the dominant group contributing >50% of the total population. Presence of different larval forms dominated by Crustacea suggested that the Sundarbans estuarine complex acts as a breeding ground for benthos species. Water temperature, DO, salinity and nutrients were the principal factors in affecting spatio-temporal differentiation of zooplankton community structure at the present study area. A clear seasonal cycle was observed in terms of variability in Copepoda composition and recruitment of different zooplankton communities. Such biological changes in zooplankton assemblages are likely to have significant implications on the productivity and functioning of the pelagic ecosystem in SES. Additionally, the present study is a maiden approach, focused on identifying indicator species of different zooplankton taxa at different time-scales. The occurrence of warm water species indicated the area is under the threat of climate change-mediated temperature rise. The present data, based on spatio-temporal scale in the Sundarbans, may help monitor the potential ecological assessment of this estuarine system. Furthermore, the result contributes to a deeper understanding of zooplankton variability and their seasonal succession pattern in this dynamic estuarine environment. Future works should be focused on identifying the indicator species of different zooplankton group at a longer time scale, which may help assess ecological understanding in the climate change-driven hydrological regime.

Acknowledgements

The authors wish to express their gratitude to the Vice Chancellor of the Presidency University, for providing facil-

ities and encouragement to carry out the above research work. The authors are thankful to Dr. Meenakshi Chatterjee of Basanti Devi College, Kolkata for her ever-willing help and cooperation during the study. We are also very thankful to the Directorate of Forest and the Sundarban Biosphere Reserve, Government of West Bengal, for permission to work in some of the restricted reserve forest areas, where human activity is strictly prohibited (permission letters memo no. 3561/WL/4R-6/2016 dated 26.07.2016 and 3837/WL/4R-6/2017 dated 11.08.2017). The authors would also like to express their appreciation to the members of the Marine Ecology Laboratory for the excellent teamwork. The authors also thank anonymous reviewers for their constructive comments.

Data in this paper is a part of a doctoral thesis of T.N. to be submitted in partial fulfilment of the requirements of a degree of Doctor of Philosophy from the Presidency University, Kolkata.

We are also thankful to our funding agency, as this work was fully supported by the MoES (MoES/36/OOIS/Extra/24/2013) and FRPDF grant of the Presidency University.

Supplementary materials

Supplementary material associated with this article can be found, in the online version, at doi:<https://doi.org/10.1016/j.oceano.2020.03.005>.

References

- Amin, O., Comoglio, L., Spetter, C., Duarte, C., Asteasuain, R., Freije, R.H., Marcovecchio, J., 2011. Assessment of land influence on a high-latitude marine coastal system: Tierra del Fuego, southernmost Argentina. *Env. Monit. Assess.* 175 (1–4), 63–73, <https://doi.org/10.1007/s10661-010-1493-5>.
- Annabi-Trabelsi, N., El-Shabrawy, G., Goher, M.E., Subrahmanyam, M.N.V., Al-Enezi, Y., Ali, M., Ayadi, H., Belmonte, G., 2019. Key drivers for copepod assemblages in a eutrophic coastal brackish lake. *Water (Switzerland)* 11. art. no. 363, 20 pp., <https://doi.org/10.3390/w11020363>.
- Ayon, P., Criales-Hernandez, M.I., Schwaborn, R., Hirche, H.J., 2008. Zooplankton research off Peru: A review. *Prog. Oceanogr.* 79 (2–4), 238–255, <https://doi.org/10.1016/j.pcean.2008.10.020>.
- Balasubramanian, R., Kannan, L., 2005. Physico-chemical characteristics of the coral reef environs of the Gulf of Mannar biosphere reserve, India. *International J. Eco. Env. Sci.* 31 (3), 265–271.
- Bhattacharya, B.D., Hwang, J.S., Sarkar, S.K., Rakhsit, D., Murugan, K., Li-Chun, T., 2015. Community structure of mesozooplankton in coastal waters of Sundarban mangrove wetland, India: A multivariate approach. *J. Marine Syst.* 141, 112–121, <https://doi.org/10.1016/j.jmarsys.2014.08.018>.
- Biancalana, F., Dutto, M.S., Berastegui, A.A., Kopprio, G., Hoffmeyer, M.S., 2014. Mesozooplankton assemblages and their relationship with environmental variables: a study case in a disturbed bay (Beagle Channel, Argentina). *Env. Monit. Assess.* 186 (12), 8629–8647, <https://doi.org/10.1007/s10661-014-4032-y>.
- Bianchi, F., Aciri, F., Aubry, F.B., Berton, A., Boldrin, A., Camatti, E., Cassin, D., Comaschi, A., 2003. Can plankton communities be considered as bio-indicators of water quality in the Lagoon of

- Venice? Mar. Pollut. Bull. 46 (8), 964–971, [https://doi.org/10.1016/S0025-326X\(03\)00111-5](https://doi.org/10.1016/S0025-326X(03)00111-5).
- Biggs, B.J.F., Goring, D.G., Nikora, V.I., 1998. Subsidy and stress responses of stream periphyton to gradients in water velocity as a function of community growth form. *J. Phycology* 34 (4), 598–607, <https://doi.org/10.1046/j.1529-8817.1998.340598.x>.
- Biswas, H., Mukhopadhyay, S.K., De, T.K., Sen, S., Jana, T.K., 2004. Biogenic Controls on the air-water carbon dioxide exchange in the Sundarban mangrove environment, northeast coast of Bay of Bengal, India. *Limnol. Oceanogr.* 49 (1), 95–101, <https://doi.org/10.4319/lo.2004.49.1.0095>.
- Campos, C.C., Garcia, T.M., Neumann-Leitao, S., Soares, M.O., 2017. Ecological indicators and functional groups of copepod assemblages. *Ecol. Indic.* 83, 416–426, <https://doi.org/10.1016/j.ecolind.2017.08.018>.
- Chatterjee, M., Shankar, D., Sen, G.K., Sanyal, P., Sundar, D., Michael, G.S., Chatterjee, A., Amol, P., Mukherjee, D., Suprit, K., Mukherjee, A., Vijith, V., Chatterjee, S., Basu, A., Das, M., Chakraborti, S., Kalla, A., Misra, S.K., Mukhopadhyay, S., Mandal, G., Sarkar, K., 2013. Tidal variations in the Sundarbans Estuarine System, India. *J. Earth Syst. Sci.* 4, 899–933, <https://doi.org/10.1007/s12040-013-0314-y>.
- Clarke, K.R., Gorley, R.N., 2006. *PRIMERv6: user manual/tutorial*. PRIMER-E, Plymouth, UK, 192 pp.
- Clarke, K.R., Warwick, R.M., 2001. *Change in marine communities: an approach to statistical analysis and interpretation*, 2nd edn. PRIMER-E, Plymouth, UK, 176 pp.
- Conway, D.V.P., White, R.G., Hugues-Dit-Ciles, J., Gallienne, C.P., Robins, D.B., 2003. *Guide to the coastal and surface zooplankton of the south western Indian Ocean*. Occasional Publication of the Marine Biological Association of the United Kingdom, Plymouth, UK, 354 pp.
- Das, J., Das, S.N., Sahoo, R.K., 1997. Semidiurnal variation of some physico-chemical parameters in the Mahanadi estuary, east coast of India. *Indian J. Mar. Sci.* 26 (3), 323–326.
- David, V., Selleslagh, J., Nowaczyk, A., Dubois, S., Bachelet, G., Blanchet, H., Gouillieux, B., Lavesque, N., Leconte, M., Savoye, N., Sautour, B., Lobry, J., 2016. Estuarine habitats structure zooplankton communities: Implications for the pelagic trophic pathways. *Estuar. Coast. Shelf Sci.* 179, 99–111, <https://doi.org/10.1016/j.ecss.2016.01.022>.
- De Young, B., Heath, M., Werner, F., Chai, F., Megrey, B., Monfray, P., 2004. Challenges of modeling ocean basin ecosystems. *Science* 304 (5676), 1463–1466.
- Degerman, R., Lefebure, R., Bystrom, P., Bamstedt, U., Larsson, S., Andersson, A., 2018. Food web interactions determine energy transfer efficiency and top consumer responses to inputs of dissolved organic carbon. *Hydrobiologia* 805 (1), 131–146.
- Dorak, Z., Albay, M., 2016. Effects of environmental factors on seasonal and spatial changes in surface zooplankton in Golden Horn Estuary (Istanbul, Turkey). *Lakes Reserv. Res. Manage.* 21 (2), 67–81.
- Drira, Z., Kmiha-Megdiche, S., Sahnoun, H., Tedetti, M., Pagano, M., Ayadi, H., 2018. Copepod assemblages as a bioindicator of environmental quality in three coastal areas under contrasted anthropogenic inputs (Gulf of Gabes, Tunisia). *J. Mar. Biol. Assoc. U.K.* 98 (8), 1889–1905, <https://doi.org/10.1017/S0025315417001515>.
- Dufrene, M., Legendre, P., 1997. Species assemblages and indicator species: The need for a flexible asymmetrical approach. *Ecol. Monogr.* 67 (3), 345–366.
- Fernandez De Puelles, M.L., Lopaz-Urrutia, A., Morillas, A., Molinero, J.C., 2009. Seasonal variability of copepod abundance in the Balearic region (Western Mediterranean) as an indicator of basin scale hydrological changes. *Hydrobiologia* 617 (1), 3–16.
- Field, J.G., Clarke, K.R., Warwick, R.M., 1982. *A Practical Strategy for Analysing Multispecies Distribution Patterns*. Mar. Ecol. Prog. Ser. 8, 37–52.
- Gaonkar, C.A., Krishnamurthy, V., Anil, A.C., 2010. Changes in the abundance and composition of zooplankton from the ports of Mumbai, India. *Environ. Monit. Assess.* 168 (1–4), 179–194, <https://doi.org/10.1007/s10661-009-1102-7>.
- Giering, S.L.C., Sanders, R., Lampitt, R.S., Anderson, T.R., Tamburini, C., Boutrif, M., Zubkov, M.V., Marsay, C.M., Henson, S.A., Saw, K., Cook, K., Mayor, D.J., 2014. Reconciliation of the carbon budget in the ocean's twilight zone. *Nature* 507 (7493), 480–483.
- Gil, M.N., Torres, A.I., Amin, O., Esteves, J.L., 2011. Assessment of recent sediment influence in an urban polluted subantarctic coastal ecosystem. Beagle Channel (Southern Argentina). *Mar. Pollut. Bull.* 62 (1), 201–207, <https://doi.org/10.1016/j.marpolbul.2010.10.004>.
- Giller, P.S., Hildrew, A.G., Raffaelli, D.G., 1994. *Proceedings of British Ecological Society and American Society of Limnology and Oceanography Symposium*. Blackwell Sci. Publ., Oxford, 649 pp.
- Gordina, A.D., Pavlova, E.V., Ovsyany, E.I., Wilson, J.G., Kemp, R.B., Romanov, A.S., 2001. Long-term changes in Sevastopol Bay (the Black Sea) with particular reference to the ichthyoplankton and zooplankton. *Estuar. Coast. Shelf Sci.* 52 (1), 1–13, <https://doi.org/10.1006/ecss.2000.0662>.
- Gorokhova, E., Lehtiniemi, M., Postel, L., Rubene, G., Amid, C., Lesutiene, J., Uusitalo, L., Strake, S., Demereckiene, N., 2016. Indicator properties of Baltic zooplankton for classification of environmental status within marine strategy framework directive. *PLoS ONE* 11 (7), art. no. e0158326, 26 pp., <https://doi.org/10.1371/journal.pone.0158326>.
- Govindasamy, C., Kannan, L., Azariah, J., 2000. Seasonal variation in physico-chemical properties and primary production in the coastal water biotopes of Coromandel Coast, India. *J. Environ. Biol.* 21 (1), 1–7.
- Grasshoff, K., Kremling, K., Ehrhardt, M., 1999. *Methods of seawater analysis*. Verlag Chemie, Weinheim Germany, 634 pp.
- Hays, G.C., Richardson, A.J., Robinson, C., 2005. Climate change and marine plankton. *Trends Ecol. Evol.* 20 (6 Sp. Is.), 337–344.
- Hunt, B.P.V., Hosie, G.W., 2006. The seasonal succession of zooplankton in the Southern Ocean south of Australia, part I: The seasonal ice zone. *Deep-Sea Res. Pt. I Oceanogr.* 53 (7), 1182–1202.
- Hunt, B.P.V., Pakhomov, E.A., Trotsenko, B.G., 2007. The macrozooplankton of the Cosmonaut Sea, east Antarctica (30°E–60°E), 1987–1990. *Deep-Sea Res. Pt. I Oceanogr.* 54 (7), 1042–1069.
- Jagadeesan, L., Jyothibabu, R., Arunpandi, N., Karnan, C., Balachandran, K.K., 2017. Dominance of coastal upwelling over Mud Bank in shaping the mesozooplankton along the southwest coast of India during the Southwest Monsoon. *Prog. Oceanogr.* 56, 252–275, <https://doi.org/10.1016/j.pocean.2017.07.004>.
- Jyothibabu, R., Jagadeesan, L., Karnan, C., Arunpandi, N., Pandiyarajan, R.S., Balachandran, K.K., 2018. Ecological indications of copepods to oxygen-deficient near-shore waters. *Ecol. Indic.* 93, 76–90.
- Kannan, R., Kannan, L., 1996. Physico-chemical characteristics of seaweed beds of the Palk Bay, southeast coast of India. *Indian J. Mar. Sci.* 25 (4), 358–362.
- Karuppasamy, P.K., Perumal, P., 2000. Biodiversity of zooplankton at Pichavaram mangroves, South India. *Adv. Biosci.* 19, 23–32.
- Kasturirangan, L.R., 1963. A key for the identification of the more common planktonic copepoda of Indian coastal waters. In: Panikar, N.K. (Ed.), *New Delhi: Council of Scientific and Industrial Research*, 87 pp.
- Keister, J.E., Tuttle, L.B., 2013. Effects of bottom-layer hypoxia on spatial distributions and community structure of mesozooplankton in a sub-estuary of Puget sound, Washington, USA. *Limnol. Oceanogr.* 58 (2), 667–680.
- Kovach, W.L., 1998. *MVSP—multi-variate statistical package for windows*, version 3.0. Kovach Computing Services, Pentraeth, Wales, UK, 127 pp.

- Kruskal, J.B., Wish, M., 1978. Multidimensional scaling. Sage Univ. Paper Ser., Quantitative Applications in the Social Sciences, No. 07011, Sage Publications, Newbury Park, <http://dx.doi.org/10.4135/9781412985130>.
- Li, K.Z., Yin, J.Q., Huang, L.M., Tan, Y.H., 2006. Spatial and temporal variations of mesozooplankton in the Pearl River estuary, China. *Estuar. Coast. Shelf Sci.* 67 (4), 543–552, <https://doi.org/10.1016/j.ecss.2005.12.008>.
- Longhurst, A.R., 2007. *Ecological Geography of the Sea*, 2nd edn., Acad. Press, Amsterdam, Boston, MA, 560 pp.
- MacIntyre, H.L., Geider, R.J., Miller, D.C., 1996. Microphytobenthos: The ecological role of the 'secret garden' of unvegetated, shallow-water marine habitats. I. Distribution, abundance and primary production. *Estuaries* 19 (2 A), 186–201.
- Margalef, R., 1967. Some concepts relative to the organization of plankton. *Oceanogr. Mar. Biol. Annu. Rev.* 5, 257–289.
- Marques, S.C., Azeiteiro, U.M., Marques, J.C., Neto, J.M., Pardal, M.A., 2006. Zooplankton and ichthyoplankton communities in a temperate estuary: Spatial and temporal patterns. *J. Plankton Res.* 28 (3), 297–312.
- Marques, S.C., Azeiteiro, U.M., Martinho, F., Viegas, I., Pardal, M.A., 2009. Evaluation of estuarine mesozooplankton dynamics at a fine temporal scale: The role of seasonal, lunar and diel cycles. *J. Plankton Res.* 31 (10), 1249–1263.
- Mathew, L., Pillai, N., 1990. Chemical characteristics of the waters around Andamans during late winter. In: *Proc. First Workshop Scientist Resul. FORV. Sagar, Sampada*, 15–18.
- Mialet, B., Gouzou, J., Azamar, F., Maris, T., Sossou, C., Toumi, N., Van Damme, S., Meire, P., Tackx, M., 2011. Response of zooplankton to improving water quality in the Scheldt estuary (Belgium). *Estuar. Coast. Shelf Sci.* 93 (1), 47–57.
- Mishra, S., Panda, D., Panigrahy, R.C., 1993. Physico-chemical characteristics of the bahuda estuary (Orissa), East coast of India. *Indian J. Mar. Sci.* 22, 75–77.
- Mitra, A., Gastellani, C., Gentleman, W.C., 2014. Bridging the gap between marine biogeochemical and fisheries sciences; configuring the zooplankton link. *Prog. Oceanogr.* 129 (PB), 176–199.
- Mitra, A., Gangopadhyay, A., Dube, A., Schmidt, A.C.K., Banerjee, K., 2009. Observed changes in water mass properties in the Indian Sundarbans (northwestern Bay of Bengal) during 1980–2007. *Curr. Sci.* 97 (10), 1445–1452.
- Moderan, J., Bouvais, P., David, V., Le Noc, S., Simon-Bouhet, B., Niquil, N., Miramand, P., Fichet, D., 2010. Zooplankton community structure in a highly turbid environment (Charente estuary, France): Spatio-temporal patterns and environmental control. *Estuar. Coast. Shelf Sci.* 88 (2), 219–232, <https://doi.org/10.1016/j.ecss.2010.04.002>.
- Morgan, S.G., 1995. The timing of larval release. In: McEdward, L. (Ed.), *Ecology of marine invertebrate larvae*. Florida. CRC Press, Boca Raton, 157–191.
- Mouny, P., Dauvin, J.C., 2002. Environmental control of mesozooplankton community structure in the seine estuary (English Channel). *Oceanol. Acta* 25 (1), 13–22.
- Mukhopadhyay, S.K., Biswas, H., De, T.K., Jana, T.K., 2006. Fluxes of nutrients from the tropical river Hooghly at land-ocean boundary of Sundarbans, NE coast of Bay of Bengal, India. *J. Marine Syst.* 62, 9–21, <https://doi.org/10.1016/j.jmarsys.2006.03.004>.
- Nair, P.V.R., Gopinathan, C.P., Balachandran, V.K., Mathew, K.J., Regunathan, A., 1984. Ecology of mud banks: Phytoplankton productivity I. Alleppey mud-bank. *CMFRI Bull.* 31, 28–34.
- Nandy, T., Mandal, S., Chatterjee, M., 2018. Intra-monsoonal variation of zooplankton population in the Sundarbans Estuarine System, India. *Environ. Monit. Assess.* 190 (10), <https://doi.org/10.1007/s10661-018-6969-8>.
- Nielsen, T.G., Sabatini, M., 1996. Role of cyclopoid copepods *Oithona* spp. in North Sea plankton communities. *Mar. Ecol. Progr. Ser.* 139 (1–3), 79–93.
- O'Higgins, T.G., Ferraro, S.P., Dantin, D.D., Jordan, S.J., Chintala, M.M., 2010. Habitat scale mapping of fisheries ecosystem service values in estuaries. *Ecol. Soc.* 15 (4), art. no. 7, <http://www.ecologyandsociety.org/vol15/iss4/art7/>.
- Paffenhoffer, G., 1993. On the ecology of marine cyclopoid copepods (Crustacea, Copepoda). *J. Plankton Res.* 15 (1), 37–55, <https://doi.org/10.1093/plankt/15.1.37>.
- Pages, F., Gonzalez, H.E., Gonzalez, S.R., 1996. Diet of the gelatinous zooplankton in Hardangerfjord (Norway) and potential predatory impact by *Aglantha digitale* (trachymedusae). *Mar. Ecol. Progr. Ser.* 139 (1–3), 69–77.
- Park, G.S., Marshall, H.G., 2000. Estuarine relationships between zooplankton community structure and trophic gradients. *J. Plankton Res.* 22 (1), 121–135.
- Parsons, T.R., Maita, Y., Lalli, C.M., 1984. *A Manual of Chemical and Biological Methods for Seawater Analysis*. Pergamon Press, Oxford, 173 pp.
- Peterson, C.G., 1996. Response of benthic algal communities to natural physical disturbance. In: Stevenson, R.J., Bothwell, M.L., Lowe, R.L. (Eds.), *Algal ecology: Freshwater benthic ecosystems*. Acad. Press, San Diego, CA, 375–402.
- Peterson, W.T., Bellantoni, D.C., 1987. Relationships between water-column stratification, phytoplankton cell size and copepod fecundity in long island sound and off central Chile. *South Afr. J. Mar. Sci.* 5 (1), 411–421.
- Pielou, E.C., 1966. The measurement of diversity in different types of biological collections. *J. Theoretical Biol.* 13 (C), 131–144.
- Rakhesh, M., Raman, A.V., Kalavati, C., Subramanian, B.R., Sharma, V.S., Sunitha Babu, E., Sateesh, N., 2008. Zooplankton community structure across an eddy-generated upwelling band close to a tropical bay-mangrove ecosystem. *Mar. Biol.* 154 (6), 953–972, <https://doi.org/10.1007/s00227-008-0991-2>.
- Ramakrishnan, R., Perumal, P., Santhanam, P., 1999. Spatio-temporal variations of hydrographical features in the Pichavaram mangroves and Mohi aqua farm, Southeast coast of India. In: *Proc. International Seminar for Application in Hydro geochemistry*. Annamalai University, Chidambaram, Tamil Nadu, India, 197–203.
- Resmi, S., Reddy, R.V., Venkatesha Moorthy, K.S., Chethan, N., 2011. Zooplankton dynamics in the coastal waters of adubidri, Karnataka. *Indian J. Mar. Sci.* 40 (1), 134–141.
- Sampey, A., McKinnon, A.D., Meekan, M.G., McCormick, M.I., 2007. Glimpse into guts: Overview of the feeding of larvae of tropical shorefishes. *Mar. Ecol. Progr. Ser.* 339, 243–257.
- Santhakumari, V., Nair, V.R., 1999. Distribution of hydromedusae from the exclusive economic zone of the west and east coasts of India. *Indian J. Mar. Sci.* 28 (2), 150–157.
- Santhanam, P., Perumal, P., 2003. Diversity of zooplankton in Parangipettai coastal waters, Southeast Coast of India. *J. Mar. Biol. Assoc. India.* 45, 144–151.
- Santhosh Kumar, C., Perumal, P., 2011. Hydrobiological Investigations in Ayyampattinam Coast (Southeast Coast of India) with Special Reference to Zooplankton. *Asian J. Biol. Sci.* 4 (1), 25–34.
- Sarkar, S.K., Saha, M., Takada, H., Bhattacharya, A., Mishra, P., Bhattacharya, B., 2007. Water quality management in the lower stretch of the river Ganges, east coast of India: an approach through environmental education. *J. Clean. Prod.* 15 (16), 1559–1567.
- Segar, K., Hariharan, V., 1989. Seasonal distribution of nitrate, nitrite, ammonia and plankton in effluent discharge area of Mangalore, West coast of India. *Indian J. Mar. Sci.* 18, 170–173.
- Senthilkumar, S., Santhanam, P., Perumal, P., 2002. Diversity of phytoplankton in vellar estuary, southeast coast of India. In: *Proc. 5th Indian Fisheries Forum, Bhubaneswar, Orissa, India*, 145–248.

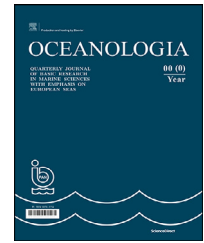
- Serranito, B., Aubert, A., Stemmann, L., Rossi, N., Jamet, J.L., 2016. Proposition of indicators of anthropogenic pressure in the Bay of Toulon (Mediterranean Sea) based on zooplankton time-series. *Cont. Shelf Res.* 121, 3–12.
- Shanks, A.L., 1995. Mechanisms of cross-shelf dispersal of larval invertebrates and fish. In: McEdward, L. (Ed.), *Ecology of marine invertebrate larvae*. Florida. CRC Press, Boca Raton, 323–367.
- Shannon, C.E., 1948. A Mathematical Theory of Communication. *Bell Sys. Tech. J.* 27 (4), 623–656.
- Sipkay, C., Kiss, K.T., Vadadi-Fjilop, C., Hufnagel, L., 2009. Trends in research on the possible effects of climate change concerning aquatic ecosystems with special emphasis on the modelling approach. *Appl. Ecol. Environ. Res.* 17 (2), 171–198.
- Srichandan, S., Sahu, B.K., Panda, R., Baliarsingh, S.K., Sahu, K.C., Panigrahy, R.C., 2015. Zooplankton distribution in coastal water of the north-western Bay of Bengal, off Rushikulya estuary, east coast of India. *Indian J. Geo-Mar. Sci.* 44 (4), 546–561.
- Sridhar, R., Thangaradjou, T., Senthil Kumar, S., Kannan, L., 2006. Water quality and phytoplankton characteristics in the Palk Bay, southeast coast of India. *J. Environ. Biol.* 27 (3), 561–566.
- Stephen, R., 1984. Distribution of calanoid copepods in the Arabian Sea and Bay of Bengal. *Mahasagar Bull. Natl. Inst. Oceanogr.* 17, 161–171.
- Stirling, G., Wilsey, B., 2001. Empirical relationships between species richness, evenness, and proportional diversity. *Am. Nat.* 158 (3), 286–299.
- Strickland, J.D.H., Parsons, T.R., 1972. A practical handbook of seawater analysis. *Fish. Res. Canada*, Ottawa, 328 pp.
- Sun, J., Liu, D.Y., Bai, J., Gao, H.W., Han, X.T., 2004. Phytoplankton community of the Bohai Sea in winter 2001. *J. Ocean Univ. China* 34 (3), 403–422.
- Telesh, I.V., 2004. Plankton of the Baltic estuarine ecosystems with emphasis on Neva Estuary: A review of present knowledge and research perspectives. *Mar. Pollut. Bull.* 49 (3), 206–219, <https://doi.org/10.1016/j.marpolbul.2004.02.009>.
- Torres, A.I., Gil, M.N., Aman, O.A., Esteves, J.L., 2009. Environmental characterization of a eutrophicated semi-enclosed system: Nutrient budget (Encerrada Bay, Tierra Del Fuego Island, Patagonia, Argentina). *Water Air Soil Pollut.* 204 (1–4), 259–270.
- Tseng, L.C., Dahms, H.U., Chen, Q.C., Hwang, J.S., 2012. Meso-zooplankton and copepod community structures in the southern East China Sea: The status during the monsoonal transition period in September. *Helgol. Mar. Res.* 66 (4), 621–634.
- Turner, J.T., 1984. The feeding ecology of some zooplankters that are important prey items of larval fish. *US Dept. Comm. NOAA, Natl. Mar. Fish. Serv.* 28 pp.
- Uriarte, I., Villate, F., 2004. Effects of pollution on zooplankton abundance and distribution in two estuaries of the Basque coast (Bay of Biscay). *Mar. Pollut. Bull.* 49 (3), 220–228, <https://doi.org/10.1016/j.marpolbul.2004.02.010>.
- Uye, S.I., 1994. Replacement of large copepods by small ones with eutrophication of embayments: cause and consequence. *Hydrobiologia* 292–293 (1), 513–519.
- Van der Marrel, E., 1990. Ecotones and ecoclines are different. *J. Veg. Sci.* 1, 135–138.
- Vannote, R.L., Minshall, G.W., Cummins, K.W., Sedell, J.R., Cushing, C.E., 1980. The river continuum concept. *Can. J. Fish. Aquat. Sci.* 37 (1), 130–137.
- Venkataramana, V., Sarma, V.V.S.S., Reddy, A.M., 2017. Impact of river discharge on distribution of zooplankton biomass, community structure and food web dynamics in the Western coastal Bay of Bengal. *Reg. Stud. Mar. Sci.* 16, 267–278.
- Vieira, L., Azeiteiro, U., Re, P., Pastorinho, R., Marques, J.C., Morgado, F., 2003. Zooplankton distribution in a temperate estuary (Mondego estuary southern arm: Western Portugal). *Acta Oecol.* 24 (Suppl. 1), S163–S173, [https://doi.org/10.1016/S1146-609X\(03\)00038-9](https://doi.org/10.1016/S1146-609X(03)00038-9).
- Wang, D., Lu, J., Chen, P., Ma, Y., 2014. Community characteristics and of zooplankton in Qinzhou Bay. *Acta Ecol. Sinica* 34 (3), 141–147, <https://doi.org/10.1016/j.chnaes.2014.03.002>.
- Wong, C.K., Tam, P.F., Fu, Y.Y., Chen, Q.C., 2000. Seasonal succession and spatial segregation of planktonic copepoda in the Zhujiang Estuary in relation to temperature and salinity. *Crustacean Issues* 12, 363–375.
- Wooldridge, T., 1999. Estuarine zooplankton community structure and dynamics. In: Allanson, B.R., Baird, D. (Eds.), *Estuaries of South Africa*. Cambridge Univ. Press, Cambridge, UK, 141–166.
- Yousif Al-Yamani, F., Skyrabin, V., Gubanova, A., Khvorov, S., Prusova, I., 2011. Marine zooplankton practical guide for the Northwestern Arabian Gulf. *Kuwait Inst. Sci. Res.*, Kuwait, 197 pp.
- Zhao, C., Liu, C., Zhao, J., Xia, J., Yu, Q., Eamus, D., 2013. Zooplankton in highly regulated rivers: Changing with water environment. *Ecol. Eng.* 58, 323–334.
- Zhao, K., Songa, K., Pan, Y., Wang, L., Da, L., Wang, Q., 2017. Meta-community structure of zooplankton in river networks: Roles of environmental and spatial factors. *Ecol. Indic.* 73, 96–104.
- Zhou, S., Jin, B., Guo, L., Qin, H., Chu, T., Wu, J., 2009. Spatial distribution of zooplankton in the intertidal marsh creeks of the Yangtze River Estuary. *China. Estuar. Coast. Shelf Sci.* 85 (3), 399–406.
- Ziadi, B., Dhib, A., Turki, S., Aleya, L., 2015. Factors driving the seasonal distribution of zooplankton in a eutrophicated Mediterranean Lagoon. *Mar. Pollut. Bull.* 97 (1–2), 224–233, <https://doi.org/10.1016/j.marpolbul.2015.06.012>.



Available online at www.sciencedirect.com

ScienceDirect

journal homepage: www.journals.elsevier.com/oceanologia



ORIGINAL RESEARCH ARTICLE

Measurements of light transfer through drift ice and landfast ice in the northern Baltic Sea

Elina Kari^{a,d,*}, Arttu Jutila^{b,e}, Anna Friedrichs^c, Matti Leppäranta^b,
Susanne Kratzer^a

^aDepartment of Ecology, Environment and Plant Sciences, Stockholm University, Stockholm, Sweden

^bInstitute for Atmospheric and Earth System Research (INAR), University of Helsinki, Helsinki, Finland

^cInstitute for Chemistry and Biology for the Marine Environment, Carl von Ossietzky University of Oldenburg, Oldenburg, Germany

^dPresent: Institute for Atmospheric and Earth System Research (INAR), P.O. Box 64, 00014 University of Helsinki, Finland

^ePresent: Alfred-Wegener-Institut Helmholtz-Zentrum für Polar- und Meeresforschung, Am Handelshafen 12, 27570 Bremerhaven, Germany.

Received 29 November 2019; accepted 2 April 2020

Available online 20 May 2020

KEYWORDS

Light transfer;
Sea ice;
Diffuse attenuation
coefficient;
Coloured dissolved
organic matter;
Scattering

Summary The aim of this study was to investigate the light transfer through sea ice with a focus on bio-optical substances both in fast ice and in the drift ice zones in the northern Baltic Sea. The measurements included snow and ice structure, spectral irradiance and photosynthetically active radiation below the sea ice. We also measured the concentrations of the three main bio-optical substances which are chlorophyll-*a*, suspended particulate matter, and coloured dissolved organic matter (CDOM). These bio-optical substances were determined for melted ice samples and for the underlying sea water. The present study provides the first spectral light transfer data set for drift ice in the Baltic Sea. We found high CDOM absorption values typical to the Baltic Sea waters also within sea ice. Our results showed that the transmittance through bare ice was lower for the coastal fast ice than for the drift ice sites. Bio-optical substances, in particular CDOM, modified the spectral distribution of light penetrating through the ice cover. Differences in crystal structure and the amount of gas inclusions in the ice caused variation in the light transfer. Snow cover on ice was found to be the dominant factor influencing the light field under ice, confirming previous studies. In conclusion, snow cover dominated

* Corresponding author at: Institute for Atmospheric and Earth System Research (INAR), P.O. Box 64, 00014 University of Helsinki, Finland.
E-mail address: elina.kari@helsinki.fi (E. Kari).

Peer review under the responsibility of the Institute of Oceanology of the Polish Academy of Sciences.



Production and hosting by Elsevier

<https://doi.org/10.1016/j.oceano.2020.04.001>

0078-3234/© 2020 Institute of Oceanology of Polish Academy of Sciences. Published by Elsevier B.V. This is an open access article under the CC BY-NC-ND license (<http://creativecommons.org/licenses/by-nc-nd/4.0/>).

the amount of light under the ice, but did not modify its spectral composition. CDOM in the ice absorbs strongly in the short wavelengths. As pure water absorbs most in the long wavelengths, the light transfer through ice was highest in the green (549–585 nm).

© 2020 Institute of Oceanology of Polish Academy of Sciences. Published by Elsevier B.V. This is an open access article under the CC BY-NC-ND license (<http://creativecommons.org/licenses/by-nc-nd/4.0/>).

1. Introduction

The Baltic Sea is a shallow, brackish sea with an annual sea ice cover lasting between four to seven months (Leppäranta and Myrberg, 2009). In the northernmost basin, the Gulf of Bothnia, river water dominates the water budget, and the salinity of the upper layer is only 2–6 ppt. The river inflow contains high concentrations of coloured dissolved organic matter (CDOM) – a mixture of dissolved, decomposed organic matter and humic substances that absorb light at short wavelengths (e.g. Arst, 2003; Pierson et al., 2008). CDOM absorption is the main factor determining the attenuation of light in the Baltic Sea (Arst, 2003; Pierson et al., 2008) and is also found to be inversely related to salinity (Harvey et al., 2015; Kari et al., 2018; Kowalczyk et al., 2006; Kratzer et al., 2003). Other substances influencing the underwater light field are suspended particulate matter (SPM) and chlorophyll-*a* (Chl-*a*).

The brackish Baltic Sea ice shows similar characteristics to marine sea ice, such as the development of saline brine channels (Kawamura et al., 2001; Palosuo, 1961; Weeks et al., 1990). As saline water freezes, ice grows downwards in elongated, columnar crystals, i.e. congelation ice. Growing ice also locks substances from the underlying (freezing) seawater into saline brine pockets or channels in between ice crystal plates but may also reject them. The resulting brine channel system forms a key habitat for ice-associated organisms (Huttunen and Niemi, 1986; Ikävalko, 1998; Ikävalko et al., 1994). In addition to columnar ice, granular snow-ice forms from flooded seawater on top of the ice surface (Leppäranta, 1983; Palosuo, 1963). Granular frazil ice may also form, but its occurrence and amount is not well known in the Baltic Sea (Leppäranta and Myrberg, 2009). On a larger scale, Baltic Sea ice cover appears either as a stable coastal landfast ice zone, or as a dynamic, broken drift ice field with a large variability in thickness and structure (Leppäranta and Myrberg, 2009, Leppäranta, 2011).

Due to the efficient capturing of dissolved organic matter by growing sea ice (Palosuo, 1961; Weeks and Ackley, 1986; Weeks et al., 1990), one may anticipate that significant amounts of CDOM are captured in Baltic Sea ice. This is supported by the results of Arst et al. (2006) and Leppäranta et al. (2003). For SPM the situation is not quite as clear since the ice captures SPM both from sea water during freezing and from atmospheric deposition. The concentration of SPM in Baltic Sea ice has been observed to vary strongly but is generally in a similar range as found within the water body (Leppäranta et al., 1998). Transfer of photosynthetically active radiation (PAR) through the coastal landfast ice zone in the Gulf of Finland (Baltic Sea) has been examined by Ehn et al. (2004), Leppäranta et al. (2003), Rasmus et al. (2002) and Uusikivi et al. (2011, 2010). PAR is an essen-

tial factor influencing biological processes within and below the sea ice. Snow cover and its properties, sea ice thickness and crystal structure as well as gas inclusions and bio-optical substances within the ice determine the light transfer through the ice.

It is the aim of this study to investigate light transfer through sea ice in the Gulf of Bothnia, both in the fast ice and drift ice zone. Measurements of both spectral irradiance (320–950 nm) and irradiance integrated over the PAR range (400–700 nm) are included. Further studied properties were reflectance, transmittance, diffuse attenuation coefficient, ice and snow structure, and the concentrations of bio-optical substances within the ice and its underlying water. The objective is to compare the local scale properties of fast ice and drift ice and to discuss their effects on the light transfer through ice.

2. Methods

2.1. Study sites

The fieldwork was conducted during March 2016, March 2017 and during May 2018. In 2016, *r/v Aranda* was used to perform ice research in the Bothnian Bay, the northernmost basin of the Baltic Sea. The measurements were taken on 4–8 March 2016 at five drift ice floes (D1–D5; Fig. 1). On 1–3 March 2017, another research campaign was performed within the fast ice zone close to Umeå, Sweden, in the Northern Quark connecting the Bothnian Sea with the Bothnian Bay. The measurements were taken at three locations each visited twice, thus resulting in six measurement stations (sites F1–F6; Fig. 1). General information on the prevailing ice conditions was obtained from the daily ice charts provided by the Swedish Meteorological and Hydrological Institute (SMHI) and the Finnish Meteorological Institute (FMI). On 16 May 2018, a research cruise was performed in the central Bothnian Bay onboard the Swedish Coast Guards' vessel KBV 181 to measure the spectral absorption and scattering properties of sea water and bio-optical substances in the surface water right after the ice melting. During each campaign, temperature and salinity profiles of the water column were obtained with CTD-profilers: RBRconcerto (Ottawa, Canada) at drift ice sites, Aanderaa (Bergen, Norway) at fast ice sites, and SAIV A/S (Bergen, Norway) at the open water site.

2.2. Snow and ice properties

Properties of snow were investigated by digging snow pits (Table 1). On site, the ice structure was visually charac-

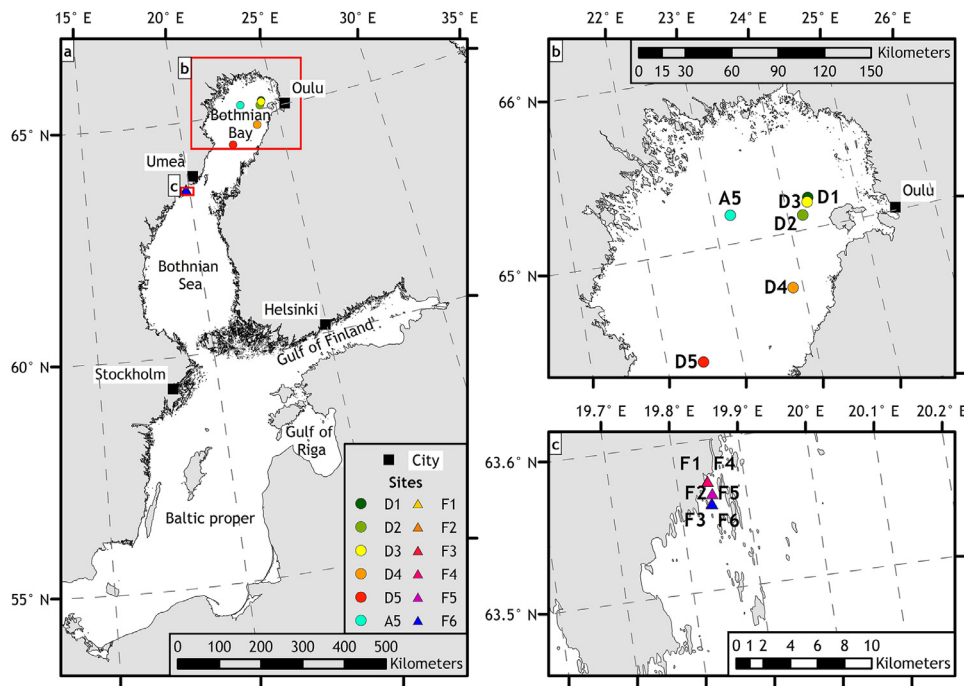


Figure 1 Measurement areas in the Gulf of Bothnia (a). Drift ice sites in the Bothnian Bay (D1–D5) in March 2016 and a site in the open sea (A5) in the central Bothnian Bay in May 2018 (b). Fast ice sites in the northern Bothnian Sea (F1–F6) in March 2017 (c). Background map data: CCM River and Catchment Database © European Commission – JRC, 2007 (Vogt et al., 2007) and SVAR2015 by SMHI.

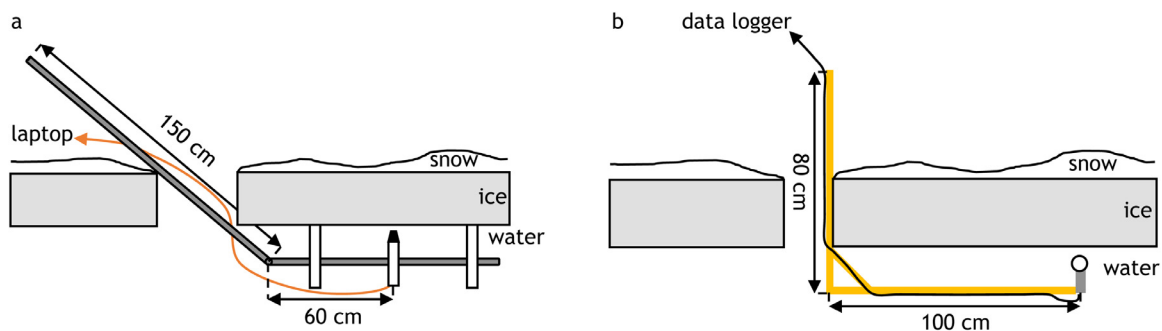


Figure 2 Setups for the irradiance measurements under the ice cover for the drift ice stations (a) and for the landfast ice stations (b). In both cases, the frame kept the sensor vertically levelled and just beneath the bottom of the ice. The frame was directed towards the sun to avoid possible shading.

terised into opaque and transparent ice layers. Ice core samples were taken, placed in plastic tubing, and transported in cold boxes to the freezer (-20°C), where they were stored until further analysis. The fast ice samples were analysed three weeks after sampling and the drift ice samples after 14 months. Ice cores were analysed for their crystal structure. Ice layers were identified from thin sections and classified into granular ice, columnar ice and their transitional form granular/columnar ice (Table 1). The thin sections of ice samples were also photographed. The bulk salinity of the ice cores was measured from the melted ice samples (Table 1). In the fast ice zone, the opaque layer is snow-ice and the transparent layer is columnar congelation ice, but the formation history of the layers in drift ice is not clear.

2.3. Irradiance measurements

Two instrument setups were used for irradiance measurements (Fig. 2; Table 1). At each site, irradiance under the ice was measured both with its natural snow cover and after manually removing the snow. At drift ice sites, the planar spectral irradiance was measured at about 1.5 m above the ice and just beneath the ice (Planar Hyper-spectral radiometer RAMSES ACC-2 VIS, Trios Inc., Germany). At fast ice sites, scalar PAR irradiance was measured at 1 m above the ice and just beneath the ice (Scalar quantum sensor LI-193, LI-COR Biosciences Ltd., UK). The measurements under the ice were first performed with a natural snow surface by lowering the frame through a 40×40 cm hole, with minimum disturbances on the snow surface. The instrument was

Table 1 Overview of measuring methods of each parameter used at drift ice sites (D1–D5), at landfast ice sites (F1–F6), and open sea station (A5).

| Parameter | Stations | Method |
|--|----------------|---|
| Snowpack structure | D1–D5 F1–F6 | Snow pits including snow grain type and size, and layer thickness. |
| Ice structure | D1–D5 F1–F6 | Thin section analysis in a cold room, ‘hard hot-plate’ technique (Shokr and Sinha, 2015; Weeks and Hibler, 2010). |
| Ice salinity | D1–D5 F1–F6 | Bulk salinity of the melted ice core sample: IntelliCAL™ CDC401 Rugged Conductivity Probe (Hach Lange, Düsseldorf, Germany). Bulk salinity of the melted ice core sample: MS-310e Micro-Salinometer (RBR Ltd, Ottawa, Ontario, Canada). Absolute salinity (g kg^{-1} , ppt) was calculated according to the Thermodynamic Equation of Seawater 2010 (TEOS-2010) (McDougall and Barker, 2011). |
| Spectral irradiance [$\text{W m}^{-2} \text{nm}^{-1}$] | D1–D5 | Two planar hyperspectral radiometers RAMSES ACC-2 VIS (Trios Inc., Germany), one as a reference instrument. Wavelength window 320–950 nm with spectral resolution of 3.3 nm. Attached to an aluminium frame with polystyrene floats (Fig. 2a). Sensor vertically levelled, close to the bottom of ice, and at about 1 m distance from the drilled hole (Lei et al., 2011). |
| Quantum irradiance (PAR) [$\mu\text{mol s}^{-1} \text{m}^{-2}$] | F1–F6 | Scalar quantum sensor LI-193 and a planar sensor LI-192 as a reference instrument (LI-COR Biosciences Ltd., UK). Integrated quantum irradiance in PAR band (400–700 nm) attached to a wooden setup with a fixed 90° angle (Fig. 2b). Instrument vertically aligned and at 1 meter distance from the drilled hole. |
| SPM [g m^{-3}] | D1–D5 F1–F6 | Measured gravimetrically (Doerffer, 2002; Kratzer et al., 2000; Strickland and Parsons, 1972) by filtering the water sample through a pre-prepared (rinsed with ultra-pure water and combusted) GF/F-filter with 0.7 μm nominal pore size. Filters were dried at 60°C and weighed, to determine the total SPM concentration and combusted at 480°C to determine also the inorganic and organic fractions of the total SPM. |
| CDOM: g_{440} [m^{-1}] | D1–D5 F1–F6 | Filtered through 0.2 μm membrane filter with a mild vacuum of 200 mbar. Filtered samples were stored cooled (max 6°C). CDOM absorption determined with double beam photospectrometer Shimadzu UVPC 2401 (Kyoto, Japan) (Kratzer and Tett, 2009). |
| Chl- <i>a</i> [$\mu\text{g l}^{-1}$] | D1–D5 F1–F6 | Filtered through Whatman GF/F-filters (glass microfiber filters) with a nominal 0.7 μm pore size with a mild vacuum of 200 mbar. Filters were frozen in liquid nitrogen during the drift ice campaign and in –80°C during the fast ice field campaign. Chl- <i>a</i> was extracted in 5 ml of 90% acetone, sonicated for 30 seconds and centrifuged to separate the Chl- <i>a</i> extract from cell and filter debris. Chl- <i>a</i> absorption determined with a double beam spectrophotometer Shimadzu UVPC 2401 (Kyoto, Japan) (Kratzer and Tett, 2009). |
| Absorption [m^{-1}] Scattering [m^{-1}] | A5 | Absorption and scattering were measured <i>in situ</i> using a Wetlabs AC9 (USA). Absorption and attenuation readings were corrected for salinity and temperature measured with a SAIV-AS CTD (Norway). Spectral scattering was derived for the nine AC9 wavebands from the difference between spectral beam attenuation and absorption (Kratzer and Moore, 2018). |

aligned horizontally by a frame directed towards the sun to avoid possible shading (Fig. 2). Then, the snow was removed from a 3.5×3 m area, elongated towards the sun, and then the irradiance was measured below bare ice. In the highly varying ice and snow conditions of the drift ice sites, it was generally challenging to estimate the shading effect caused by ridges. The measurement points were chosen as to keep sufficient distance from surrounding ridges. Such challenges

did not occur at the fast ice sites as the ice surface was level within short distances (1–2 m).

A reference instrument was placed on ice five meters away from the sampling site, also facing towards the sun in order to account for possible changes in downwelling irradiance during the period of measurement (at drift ice sites: Ramses ACC-2 VIS, Trios Inc., Germany, and at fast ice sites: a planar sensor LI-192 LI-COR Biosciences Ltd., UK).

The proportional change between subsequent control measurements was used to estimate temporal changes in the irradiance field and to adjust the actual measurements of incident irradiance in further calculations. The measured variations caused by clouds were accounted for in the light transfer estimates.

The studied optical properties were reflectance, transmittance, and the diffuse light attenuation coefficient. The analyses of these properties were limited either to PAR or to 320–900 nm range due to the relevance for ecological and ocean colour applications but also in order to ensure the quality of the spectral irradiance data (Ohde et al., 2007; Simis and Olsson, 2013; Simon and Shanmugam, 2016; Zibordi and Darecki, 2006). At drift ice sites, the surface reflectance, $R(0^+, \lambda)$, was obtained directly from the measurements: $R(0^+, \lambda) = E_u(0^+, \lambda) / E_d(0^+, \lambda)$, where $E_u(0^+, \lambda)$ is the upwelling and $E_d(0^+, \lambda)$ the downwelling irradiance, just above the surface, and λ is wavelength. The vertical axis is positive in the upward direction (with zero at the ice surface) and the notation 0^+ refers to just above the surface.

At the fast ice sites, scalar quantum PAR irradiance, q_{PAR} , was measured above and below the ice (Table 1). As a scalar instrument measures the radiance evenly from all directions, upwelling irradiance had to be accounted for when estimating the downwelling irradiance. The downwelling irradiance was assumed diffuse above the ice surface during cloud cover and below the ice due to the high scattering in snow and ice (Arst et al., 2006; Leppäranta et al., 2003). Consequently, we have

$$q_{PAR} = q_{d,PAR} + q_{u,PAR} = (1 + R_{PAR})q_{d,PAR}, \quad (1)$$

where the subscripts d and u refer to downwelling and upwelling irradiance and R_{PAR} is PAR band reflectance. Since no upwelling irradiance measurements were taken, surface reflectance, $R(0^+, \lambda)$, was based on visual evaluation and using literature sources: 0.2 for flooded sea ice, 0.3 for wet ice, 0.5 for wet snow, and 0.85 for new snow (Arst et al., 2006; Leppäranta, 2015; Rasmus et al., 2002). Under ice, the ratio of planar to scalar irradiance, q_p/q_s , was described according to the study by Arst et al. (2006). Backscatter from the water column below was determined in their study as $1 - (q_p/q_s)$. The ratio was assumed to be 0.5 (See Fig. 5a in Arst et al., 2006). Using Equation (1), an estimate of planar downwelling PAR irradiance ($q_{d,PAR}$) can be obtained and this estimate is then used in further calculations of transmittance and light attenuation.

Transmittance of irradiance through the ice cover was defined as the ratio of the downwelling irradiance under the ice, $E_d(-H, \lambda)$, where H is the total ice thickness, to the downwelling irradiance just above the surface, $E_d(0^+, \lambda)$: $T(-H, \lambda) = E_d(-H, \lambda) / E_d(0^+, \lambda)$. Light attenuation through snow and ice was defined in analogy with the Beer-Lambert absorption law (Perovich, 1996), which describes the exponential decay of light with increasing depth:

$$E_d(-H, \lambda) = [1 - R(0^+, \lambda)]E_d(0^+, \lambda) \exp \left[- \int_{-H}^0 K_d(z, \lambda) dz \right], \quad (2)$$

where z is depth and K_d is the diffuse attenuation coefficient. Equation (2) has two apparent optical properties: surface reflectance and diffuse attenuation coefficient, which depend on the inherent optical properties of the ice itself

and the illumination conditions. For the diffuse attenuation coefficient, a layered profile was assumed with fixed values for snow and ice, $K_{d,snow}$ and $K_{d,ice}$, respectively. Thus,

$$\int_{-H}^0 K_d(z, \lambda) dz = K_{d,tot}H = K_{d,snow}h_s + K_{d,ice}h_i, \quad (3)$$

where h_s and h_i are the thicknesses of snow and ice, respectively. $K_{d,tot}$ was calculated based on measurements through the snow and ice cover and $K_{d,ice}$ referring to the measurements after manually removing the snow cover. Next, diffuse attenuation coefficient for snow cover, $K_{d,snow}$, was determined using a specific inversion technique (Eq. 3) by utilising the measured diffuse attenuation coefficients, $K_{d,tot}$ and $K_{d,ice}$ (Leppäranta et al., 2010). The linear regression models, applying the least squares method, were used to solve $K_{d,snow}$ for the drift ice and fast ice groups separately. The calculations were performed over the PAR range and the fit of regression models were tested with a statistical F-test to find out, whether the results are statistically significant (p -value < 0.05).

In order to examine the primary production, the flux of light quanta, or quantum PAR irradiance q_{PAR} , is needed rather than the radiation power. The quantum irradiance was directly measured at the fast ice sites (Table 1), and at the drift ice sites it was calculated from the spectral irradiance measurements according to:

$$q_{PAR} = \frac{1}{hc_0N} \int_{PAR} \lambda E(\lambda) d\lambda, \quad (4)$$

where h is Planck's constant, c_0 is velocity of light in vacuum, and N is Avogadro's number (e.g. Arst, 2003). For white light, the ratio between quantum irradiance and power irradiance is $q_{PAR}/E_{PAR} = 4.6 \mu\text{mol J}^{-1}$.

2.4. Absorption and scattering properties of surface water

The absorption and scattering properties of surface water (at about 1 m depth) were measured using an AC9 (Wet-Labs, Philomath, USA) at station A5 in the central Bothnian Bay on 16 May 2018 (Table 1). The AC9 had been calibrated against pure water in the laboratory prior the measurements (Kratzer and Moore, 2018). The raw data was calibrated using the device file and the absorption and scattering values were then corrected for pure water from laboratory calibration measurements and for temperature. The absorption data was corrected for scattering assuming that the absorption is a fixed proportion of the scattering. Spectral scattering was derived for the nine AC9 wavebands from the difference between spectral beam attenuation and absorption (Kratzer and Moore, 2018). Spectral diffuse attenuation was derived from a formula described in Kirk (2011) and in Kratzer and Moore (2018).

2.5. Bio-optical substances

The concentrations of bio-optical substances were measured both from melted ice samples and from the samples of the underlying water. The ice samples were stored in a freezer and later melted at room temperature. The water samples were collected from just beneath the ice. The samples were filtered and then analysed for Chl- a , SPM, and

CDOM (Table 1). Chl-*a* concentrations and CDOM absorption were obtained from the absorption spectra measured with a spectrophotometer (Kirk, 2011; Kratzer and Tett, 2009). The absorption coefficient at 440 nm, a_{440} , was used for the CDOM absorption. The method and errors are described in detail in Kratzer and Tett (2009) and Harvey et al. (2015). The concentration of SPM was measured gravimetrically. The methodological errors of determining SPM concentration are discussed in Kari et al. (2016). The Chl-*a* concentration was calculated according to the trichromatic method described in detail in Kratzer and Tett (2009) and in Parsons et al. (1984).

3. Results

3.1. Overall ice conditions

The field campaigns were performed during the ice seasons 2015/16 at the drift ice sites and 2016/17 at the fast ice sites. Both seasons were mild as the maximum sea ice extent of the Baltic Sea was 110 000 km² on 22 January 2016 and 88 000 km² on 15 February 2017 (Jouni Vainio, FMI Ice service, 2019), well below the 1971–2000 median of 157 000 km² (Granskog et al., 2006). In March 2016, ice coverage, was high in the Bothnian Bay (90–100%) with large areas of ridged and rafted ice. In the north, the fast ice was 50–65 cm thick. Further out the ice field was consolidated ice of 40–70 cm thickness (Jouni Vainio, FMI Ice service, 2019). Overall, the ice conditions during sampling were quite dynamic at the drift ice sites. In March 2017, ice cover was stable at the fast ice sites with ice thickness of 15–40 cm. During the first sampling day (1 March) drift ice was compressed against the edge of the fast ice but had opened up by the last sampling day (3 March) (Jouni Vainio, FMI Ice service, 2019).

3.2. Temperature and salinity of the water column

At the drift ice sites D1–D4, the water column was mixed down to the bottom to about 30 m depth. At station D5 the water depth was 90 m with a mixed layer down to a thermocline at 35–50 m depth with a temperature step of 1.5°C. A halocline was found at 50–60 m depth, where the salinity increased from 3.0 ppt to 3.5 ppt. At all drift ice sites, the water temperature in the upper 1 m was near the freezing point (from –0.16°C to –0.15°C) with a salinity of 3.0–3.1 ppt. The fast ice sites F1–F6 were located north of the Öre River mouth with a mean discharge of 411 m³ s^{–1} during 2006–2016 (SMHI open data service) There were also some small streams near the sampling sites adding to the freshwater runoff. Due to the stable ice cover, the runoff formed an under-ice plume. This 1–2 m thick plume was distinct closest to the shore, but reached the outermost station as well. The salinity of the upper 1 m layer increased with distance from the shore from 1.4 ppt (F1) to 4.4 ppt (F3). This under-ice plume signal was clearly visible also in the upper 1 m layer with temperatures decreasing from 1.7°C (F1) to 0.5°C (F3). When revisiting the stations F1–F3 after two days (stations F4–F6) similar patterns were found within the upper 1 m layer, where the salinity increased from 0.9 ppt

(F4) to 5.1 ppt (F6) and the temperature decreased from 2.0°C (F4) to 1.9°C (F6). The salinity at F6 corresponds to the normal salinity of the outer basin water.

3.3. Properties of snow and ice

At the drift ice sites, snow thickness varied from less than 1 cm up to 15 cm with distinct spatial variability (Fig. 3). Even at each individual station, the variation was large. At the northernmost stations D1 and D2, there was a 4 cm thick layer of a large-grained depth hoar at the bottom of the snowpack and due to strong adhesion between the snow and ice surface the snow layer could not be fully removed to create a bare ice surface. At most sites, the snow layer consisted of small rounded grains but with a thin layer of freshly fallen new snow at D2 and a thin slush layer at D5. Ice thickness ranged from 23 to 65 cm at the drift ice sites (Fig. 3). Typical drift ice, the structure of ice cores varied from a single columnar congelation ice layer to a seven-layer system caused by ice floes having rafted on top of each other (Fig. 4a). The ice cores consisted of 0–79% granular ice (mean 46%) and 21–100% columnar ice (mean 54%) (Fig. 4a). The bulk ice salinity ranged from 0.5 to 0.8 ppt (mean 0.7 ppt), i.e. on average only about 21% of the salinity of the underlying water.

At the fast ice sites, the snow was thicker than at the drift ice sites, varying from 5 cm to 16.5 cm (Fig. 3). Snow was mostly wet and even some slush layers were found. Between the measurement dates, snowfall had brought a 3–5 cm layer of new snow at stations F4–F6. Freezing temperatures during nights had created frozen slush layers and even an ice lens was found in the snowpack at F5. The thickness of fast ice ranged from 24–42 cm, decreasing with distance to the shore (Fig. 3). The ice structure was characterized by an upper granular snow-ice layer and a lower columnar congelation ice layer (Fig. 4b), which is typical for fast ice. The snow-ice contribution ranged from 8–27% of the total ice thickness (with a mean of 17%) (Fig. 4b). The bulk ice salinity ranged from 0.04 to 0.7 ppt (mean 0.4 ppt), on average amounting to 9% of the salinity of the underlying water.

3.4. Properties of light transfer

At the drift ice sites, the net incoming power irradiance ranged from 38 to 159 W m^{–2} (band 320–950 nm) above ice during the measurements in 2016. Fig. 5 illustrates the spectral distribution of the downwelling irradiance above ice, under ice and snow, and under bare ice after removing the snow. At the fast ice sites, during the measurements in 2017, the net incoming quantum PAR irradiance ranged from 165 to 369 μmol s^{–1} m^{–2} above ice. The solar altitude was about 18–20° at noon at measurement sites. There was total cloud cover during all these sampling occasions, thus, generally, diffuse downwelling irradiance could be assumed.

3.4.1. Light transfer at drift ice sites

The PAR reflectance of natural snow cover on drift ice ranged from 60%–76% (Table 2). After manually removing the snow, it ranged from 30%–70%. The reflectance of the natural snow cover was on average 1.4 times higher than the reflectance of the surface after removing the snow. There

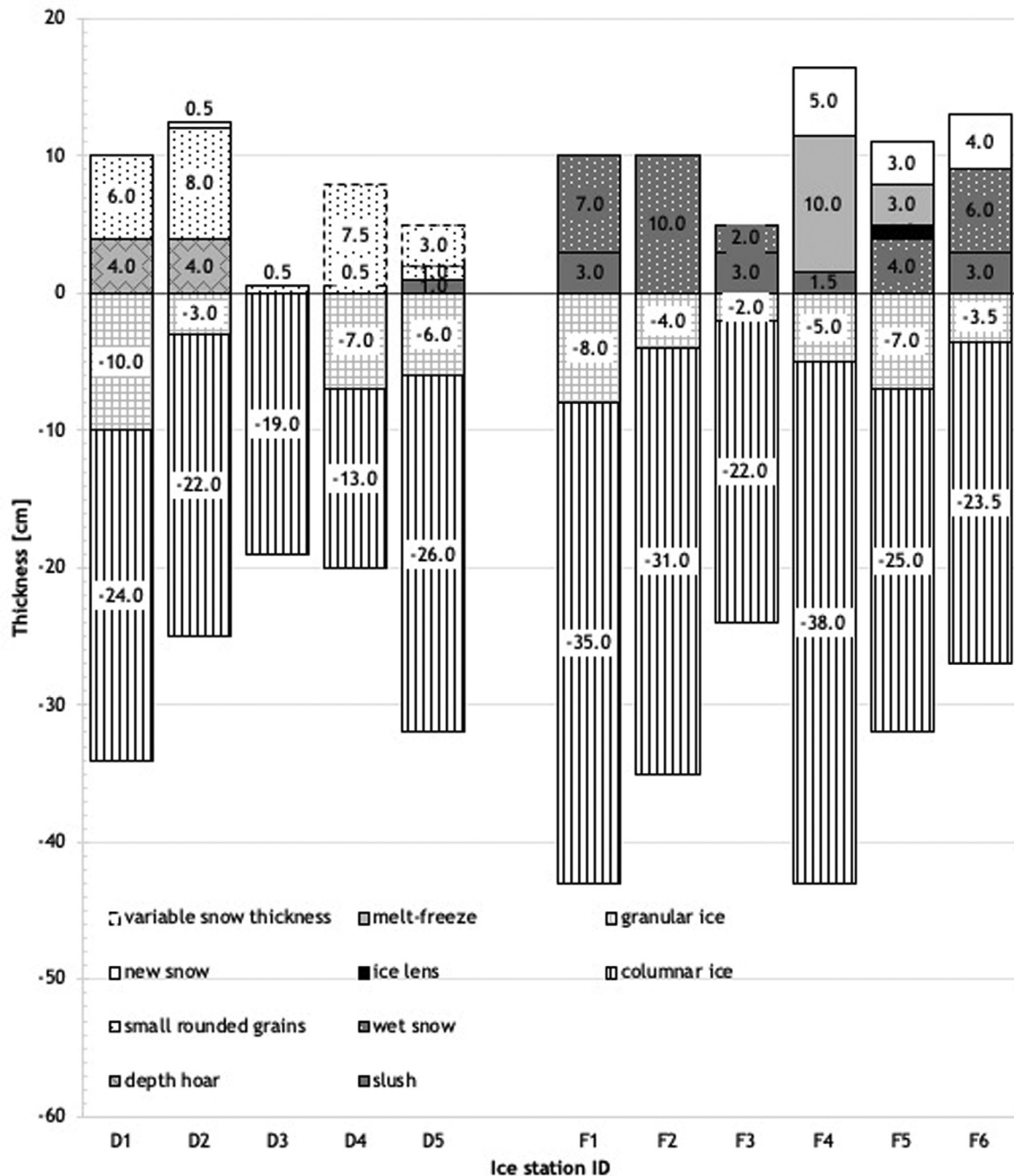


Figure 3 Schematic of the ice and snow structure at drift ice sites (D1–D5) and at fast ice sites (F1–F6). The ice structure was visually characterized into opaque granular ice and clear columnar ice precisely on site with the irradiance measurements. The baseline is the snow-ice-interface as there are no freeboard data available.

was no clear wavelength-dependency over the band 320–900 nm in the reflectance of snow cover (Fig. 6a). At station D1 reflectance without snow was more than twice compared to reflectance at sites D3–D5 (no data at D2, Fig. 6b). The lowest reflectance was measured at D3 above bare ice, where the ice surface was very smooth and the snow could be easily removed. Contrasting snow conditions occurred at D1 and D2, where it was very challenging to remove the snow. Due to incomplete surface reflectance measurements at D1 and D2, the following assumptions were made based on the surface properties. At D1, the reflectance of snow

was estimated to be similar to the reflectance spectra at D2. At D2, the reflectance measurement without snow was not available and as adhesion was similar as observed at D1, the reflectance without snow was assumed to be the same as at D1 (without snow) (Table 2).

Transmittance through snow-covered ice was mostly limited by the presence of snow (Table 2). The PAR transmittance was on average only 1.6% at D1 and D2 due to a thicker snow cover while at D3–D5 the PAR transmittance was on average 21%. After removing the snow cover, the PAR transmittance increased on average about three times (from 13%

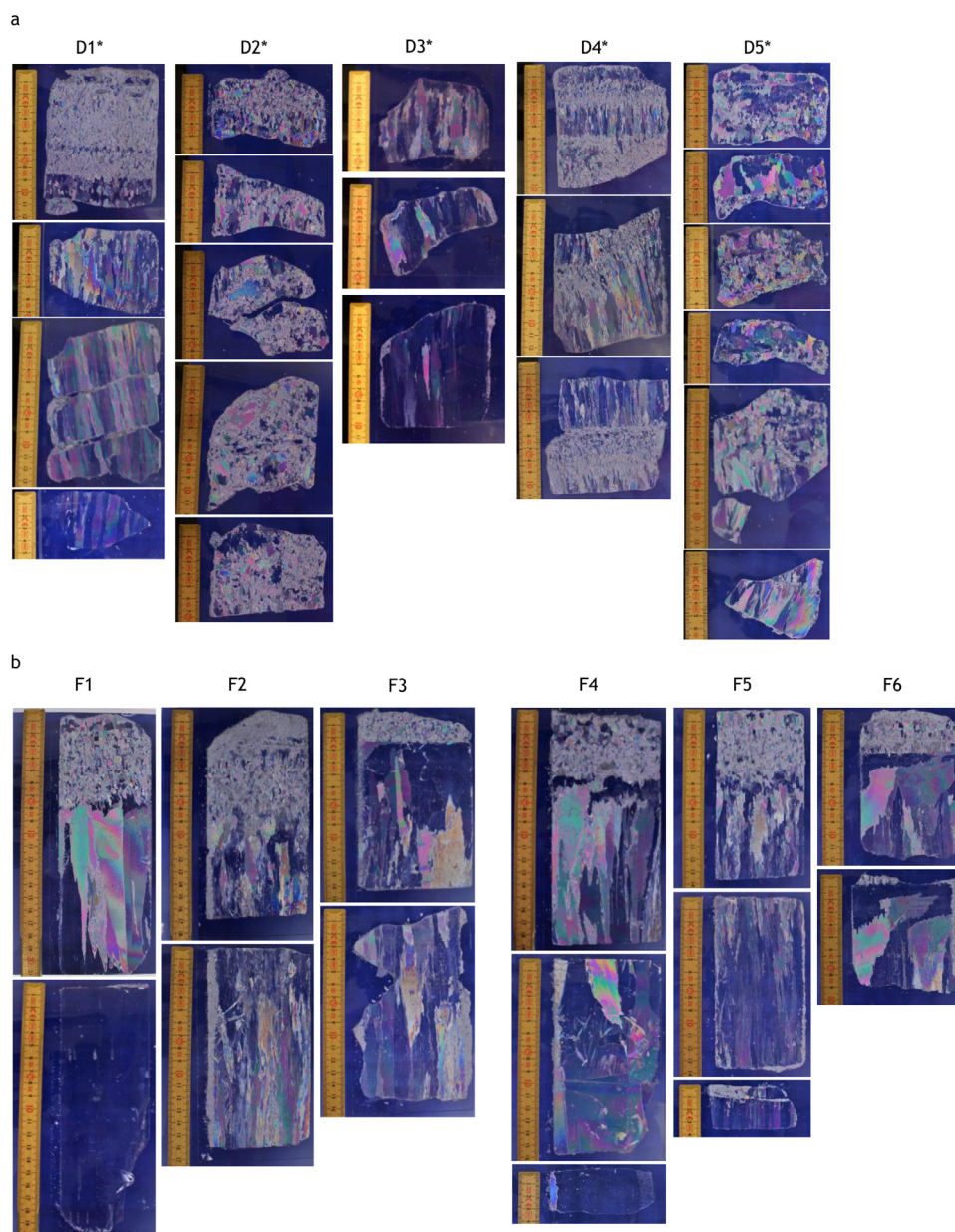


Figure 4 Photographs of the thin sections of ice samples at drift ice sites (D1–D5) and at fast ice sites (F1–F6). At drift ice sites marked with *, the ice core samples were not taken exactly at the point of the irradiance measurements (but within meters).

to 36%). The highest transmittance through bare ice (57%) was measured at D3 with a purely columnar ice structure. Spectral transmittance showed a similar shape, both with and without snow cover. The highest transmittance occurred between 569–582 nm through snow and ice and between 549–585 nm through bare sea ice.

In the presence of snow cover the total PAR diffuse attenuation coefficient, $K_{d,tot}(PAR)$, was on average 4.5 m^{-1} . After removing the snow cover $K_{d,ice}(PAR)$ was 2.5 m^{-1} , i.e. the attenuation was 1.8 times lower without snow (Table 2). $K_d(PAR)$ through ice (both with and without snow) was used to estimate the diffuse attenuation coefficient for snow at each station (Eq. 3). The diffuse attenuation coefficient for snow was $K_{d,snow}(PAR) = 15.7 \text{ m}^{-1}$ (Table 3). The optical thickness of ice and snow was therefore 40 cm and 6.4

cm, respectively, illustrating the strong dependency of light transfer on snow cover thickness. As for the transmittance, the spectral diffuse attenuation coefficient, K_d , showed a clear wavelength dependence (Fig. 7). The minima of the $K_{d,tot}$ (with snow cover) were found in the green (569–588 nm) (Fig. 7a), shifting slightly towards the yellow (569–621 nm) without snow (Fig. 7b). Fig. 8 summarizes the spectral measurements showing the split of incident radiation into reflectance, absorption by ice and snow, and transmittance. When ice is covered by snow, most of the downwelling irradiance (60%) is reflected at the surface. The reflectance is lower for bare ice (40%), and the ice absorption increases in the shorter and longer wavelengths. The site-averaged transmittance was thus highest at 572 nm, both with and without snow cover.

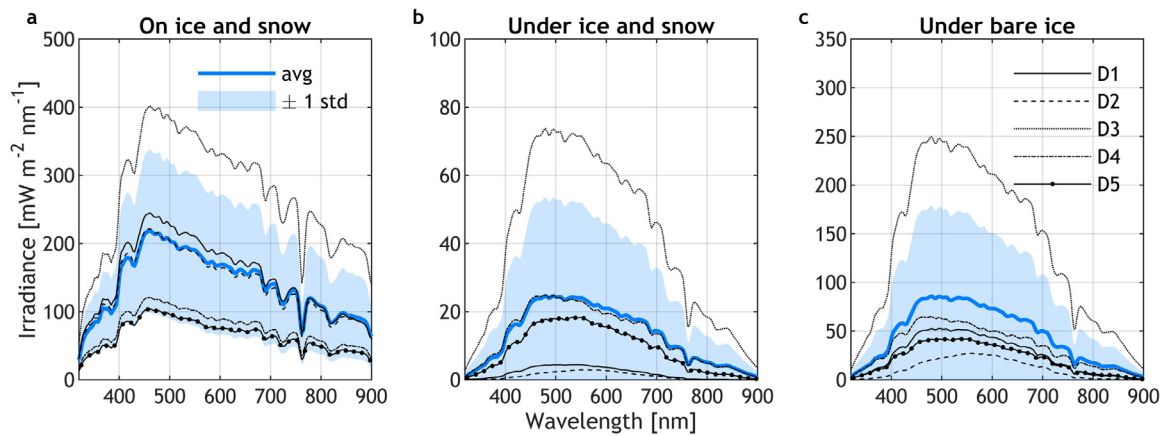


Figure 5 Spectral downwelling irradiance above ice (a), under ice and snow (b) and under bare ice (c) after removing the snow at each station (D1–D5) and their average (blue line) and ± 1 standard deviation (blue shaded area). Note the varying scale of the vertical axes.

Table 2 Overview of the snow and ice stratigraphy and measurement of light transfer. First, the thickness of each layer: snow, opaque granular, and clear columnar ice, at the points of irradiance measurements. Then, reflectance, transmittance and diffuse attenuation coefficient (K_d) in PAR band of ice with natural snow cover (column *total*) and snow manually removed (column *no snow*).

| Station | Date | Thickness [cm] | | | Reflectance (PAR) | | Transmittance (PAR) [%] | | K_d (PAR) [m^{-1}] | |
|-------------|------------|----------------|-----------------|-----------------|-------------------|----------------|-------------------------|----------------|--------------------------|----------------|
| | | <i>snow</i> | <i>granular</i> | <i>columnar</i> | <i>total</i> | <i>no snow</i> | <i>total</i> | <i>no snow</i> | <i>total</i> | <i>no snow</i> |
| D1 | 04/03/2016 | 10 | 10 | 24 | 0.76* | 0.70 | 1.9 | 26.1 | 6.9 | 0.4 |
| D2 | 05/03/2016 | 12 | 3 | 22 | 0.76 | 0.7* | 1.2 | 9.7 | 8.2 | 7.9 |
| D3 | 06/03/2016 | 1 | 0 | 19 | 0.62 | 0.30 | 19.7 | 57.2 | 3.3 | 1.1 |
| D4 | 07/03/2016 | 4 | 7 | 13 | 0.63 | 0.31 | 22.8 | 51.7 | 2.0 | 1.5 |
| D5 | 08/03/2016 | 4 | 6 | 26 | 0.60 | 0.36 | 19.6 | 37.0 | 2.0 | 1.7 |
| <i>Mean</i> | | 6.2 | 5.2 | 20.8 | 0.67 | 0.47 | 13.0 | 36.3 | 4.5 | 2.5 |
| F1 | 01/03/2017 | 10 | 8 | 35 | 0.5* | 0.3* | 0.1 | 8.4 | 11.2 | 4.9 |
| F2 | 01/03/2017 | 10 | 4 | 31 | 0.5* | 0.3* | 0.8 | 13.0 | 9.3 | 4.8 |
| F3 | 01/03/2017 | 5 | 2 | 22 | 0.5* | 0.3* | 2.6 | 21.4 | 10.2 | 4.9 |
| F4 | 03/03/2017 | 17 | 5 | 38 | 0.85* | 0.3* | 0.2 | 8.0 | 6.9 | 5.0 |
| F5 | 03/03/2017 | 11 | 7 | 25 | 0.85* | 0.3* | 0.0 | 13.1 | 11.3 | 5.2 |
| F6 | 03/03/2017 | 13 | 4 | 24 | 0.85* | 0.2* | 0.0 | 16.5 | 10.5 | 6.3 |
| <i>Mean</i> | | 10.9 | 4.9 | 29.1 | 0.68 | 0.28 | 0.6 | 13.4 | 9.9 | 5.2 |

*values estimated from literature, see section 3.3 for details.

Table 3 Diffuse attenuation coefficient for snow, $K_{d,snow}(PAR)$ for drift ice and fast ice sites separately: p-value, coefficient of determination – R^2 , standard error – SE, standard deviation – SD, and sample size – n .

| | $K_{d,snow}(PAR)$ | p-value | R^2 | SE | SD | n |
|-----------|-------------------|---------|-------|-----|------|-----|
| Drift ice | 15.7 | 0.037 | 0.70 | 5.1 | 11.4 | 5 |
| Fast ice | 21.9 | 0.003 | 0.85 | 4.1 | 10.0 | 6 |

The ratio between power irradiance and quantum irradiance was evaluated from the measurements (Eq. 4). The ratio was $4.5 \pm 0.02 \mu\text{mol J}^{-1}$ above ice and slightly higher under the ice, $4.6 \pm 0.05 \mu\text{mol J}^{-1}$. Under the ice, the ratio did not change much after removing the snow and the overall statistics were the same with and without snow.

3.4.2. Light transfer at fast ice sites

Surface reflectance was assumed based on visual evaluation and using literature sources as follows: 0.5 for wet snow (stations F1–F3), 0.85 for fresh snow (stations F4–F6), 0.3 for wet ice (stations F1–F5), and 0.2 when sea water had flooded onto the ice surface (F6) (Arst et al., 2006; Leppäranta, 2015; Rasmus et al., 2002). PAR transmittance through snow and ice was very low, on average 0.6%. After removing the snow, the average transmittance about 22-fold, to an average of 13.4%. The lowest transmittances through bare ice were measured at sites F1 and F4 (8.4% and 8.0%, respectively). At these sites, the ice was the thickest with 8 cm granular ice and 35 cm columnar ice at F1 and 5 cm granular ice and 38 cm columnar ice at F4.

$K_{d,tot}(PAR)$ of snow and ice was on average 9.9 m^{-1} and after removing the snow, $K_{d,ice}(PAR)$ was 5.2 m^{-1} (Table 2). The highest $K_{d,tot}(PAR)$ was measured at F5 (11.3 m^{-1}) and $K_{d,tot}(PAR)$ was also high at F1, F3, and F6, where the snow

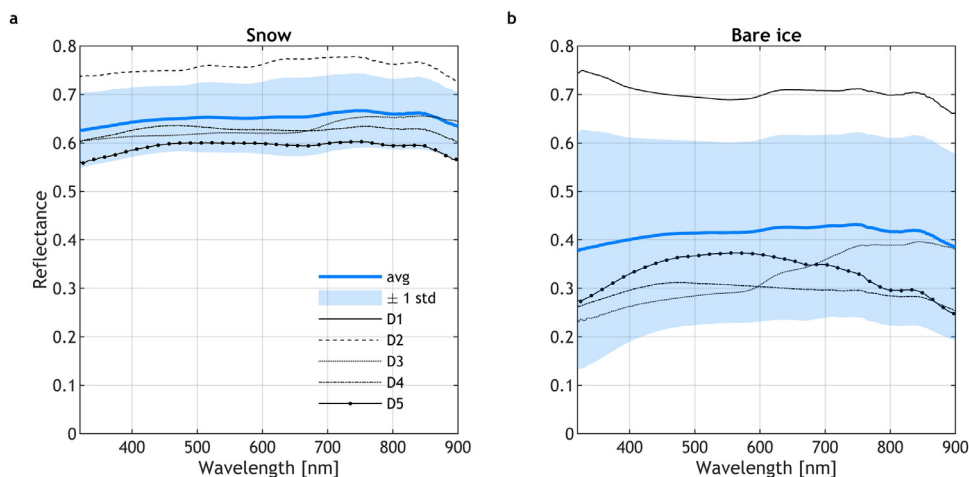


Figure 6 Reflectance of snow cover (a) and bare ice (b) at drift ice stations, their average (blue line) and ± 1 standard deviation (blue shaded area). Reflectance of snow cover at D1 and of bare ice at D2 are missing due to incomplete measurements of upwelling irradiance.

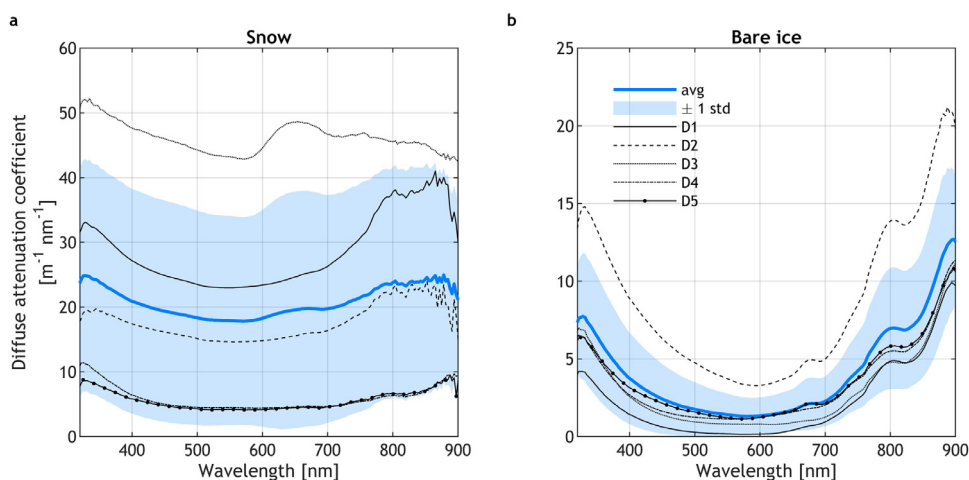


Figure 7 Spectral diffuse attenuation coefficient K_d of snow (a) and bare ice (b) at drift ice stations, their average (blue line) and ± 1 standard deviation (blue shaded area). Note the varying scale of the vertical axes.

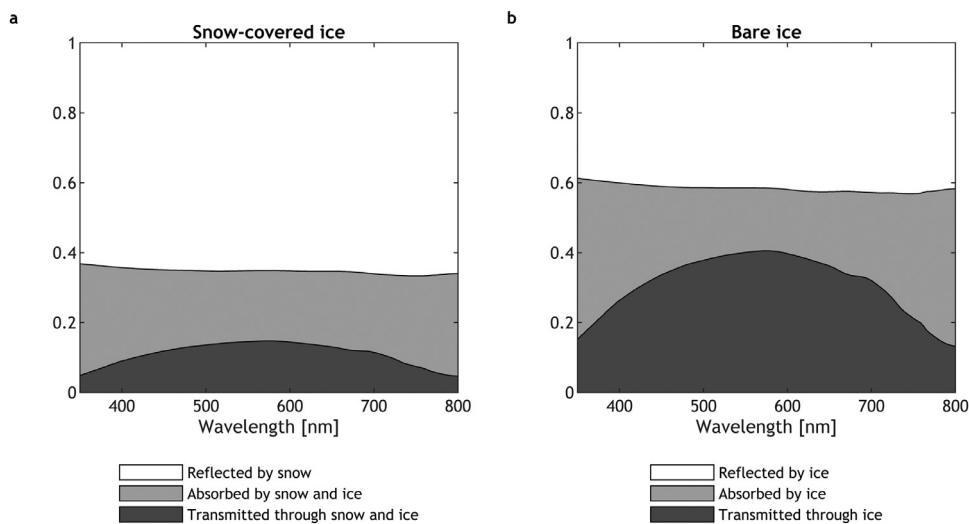


Figure 8 Averaged partitioning of solar radiation at drift ice stations with snow cover (a) and in the case of bare ice (b). Reflectance and transmittance are measured spectra, while absorbed fraction is their residual: $R + A + T = 1$.

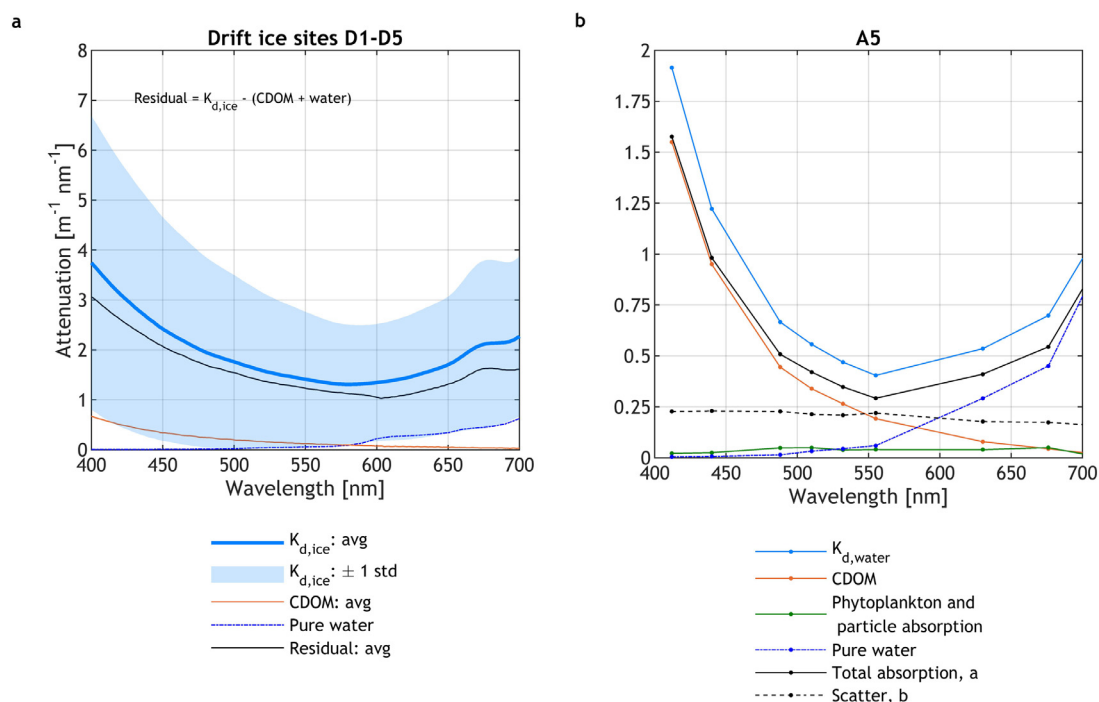


Figure 9 a) Composition of attenuation spectra at drift ice stations showing measured bare ice diffuse attenuation (light blue) against CDOM absorption (orange), pure water absorption (dark blue) (Pope and Fry, 1997) and their residual (black). Solid lines indicate average over the drift ice stations and shaded areas ± 1 standard deviation. The full spectra of $K_{d,ice}$ for each station are shown in Figure 7b. b) CDOM absorption (orange), phytoplankton and particle absorption (green), pure water absorption (dark blue) (Pope and Fry, 1997), total absorption a (black solid line), particle scatter b (black dashed line), and spectral diffuse attenuation coefficient K_d (blue) derived from AC9 measurements in the surface water at station A5, central Bothnian Bay (sea water temperature 1.1°C , CDOM (g_{440}): 0.89 m^{-1} , Chl- a : $0.7 \mu\text{g l}^{-1}$, $K_d(\text{PAR}) = 0.42 \text{ m}^{-1}$). Note the varying scale of the vertical axes.

was wet with a layer of slush. $K_{d,tot}(\text{PAR})$ and $K_{d,ice}(\text{PAR})$ were also used here to calculate the diffuse attenuation coefficients for snow cover separately. The calculated diffuse attenuation coefficient for snow was $K_{d,snow}(\text{PAR}) = 21.9 \text{ m}^{-1}$ (Table 3). Overall, $K_{d,ice}(\text{PAR})$, i.e. without snow, was higher at the fast ice stations compared to drift ice stations.

3.5. Bio-optical substances in sea ice and in surface water

In addition to the ice crystals themselves, the light transfer through the ice and snow also depends on optically active inclusions: gas pockets and bio-optical substances (Chl- a , SPM, CDOM). The gas content was only examined qualitatively at site and from photographs of thick sections. The concentrations of bio-optical substances as well as bulk salinity were determined in the laboratory (Table 1) from melted ice samples and water samples from just below the ice (Table 4). Fig. 9 shows the composition of the measured attenuation, absorption and scattering spectra. In Figure 9a, the measured diffuse attenuation coefficient, K_d , and CDOM absorption spectrum are plotted together with the pure water absorption spectrum (Pope and Fry, 1997) as well as their residual: $K_{d,ice} - (\text{CDOM} + \text{water})$. The residual illustrates the shape of the attenuation spectra without the influence of CDOM and pure water absorption. CDOM absorbs strongly in the short wavelengths, while pure water absorbs in the long wavelengths. The total absorption

and scatter spectra derived from the open water station A5 clearly show that the total absorption is almost entirely dominated by CDOM while water absorbs strongly in the red (Fig. 9b). In surface water, the absorption of phytoplankton in the red part of the spectrum (measured at 676 nm) is hardly detectable. Phytoplankton and particle scatter overall increase the light attenuation within the PAR range, and the effect decreases slightly with increasing wavelength.

At the drift ice sites, Chl- a concentrations were generally higher in the melted ice samples than in the water: within the ice Chl- a concentrations ranged from 0.8 to $14.1 \mu\text{g l}^{-1}$, while in the underlying water concentrations were relatively low, at most $0.5 \mu\text{g l}^{-1}$ (Table 4). At D2 and D5, a clear attenuation peak was visible between 660 – 690 nm , indicating the *in vivo* absorption peak of Chl- a in the red. At the fast ice sites, the Chl- a concentrations in the ice and underlying water did not differ from each other as much, the average Chl- a concentration was $1.9 \mu\text{g l}^{-1}$ both in the melted ice and in the water (Table 4). A comparison between drift ice sites and fast ice sites shows that Chl- a concentrations in ice were clearly higher at drift ice sites than at fast ice sites. However, the opposite was observed in the Chl- a concentrations in the water with lower values at drift ice sites than at fast ice sites.

The SPM concentrations ranged from 0.6 to 11.9 g m^{-3} for melted ice samples while the range was very small in the water samples: 0.2 to 0.7 g m^{-3} at drift ice sites (Table 4). On average SPM concentrations in ice samples were ten times higher than in the water samples. An ex-

Table 4 Overview of bulk salinity and the bio-optical properties within melted *ice* samples and just below ice in underlying *water*. Bulk salinity from melted *ice* samples and averaged over upper 1 m layer for underlying *water*.

| Station | Date | Salinity [g kg ⁻¹] | | Chl- <i>a</i> [μg l ⁻¹] | | g ₄₄₀ [m ⁻¹] | | SPM [g m ⁻³] | | Proportion of inorganic SPM [%] | |
|-------------|----------|--------------------------------|--------------------|-------------------------------------|--------------|-------------------------------------|--------------|--------------------------|--------------|---------------------------------|--------------|
| | | <i>ice (bulk)</i> | <i>water (1 m)</i> | <i>ice</i> | <i>water</i> | <i>ice</i> | <i>water</i> | <i>ice</i> | <i>water</i> | <i>ice</i> | <i>water</i> |
| D1 | 4/3/2016 | 0.7 | 3.0 | 1.7 | 0.4 | 0.43 | 1.19 | 1.6 | 0.7 | 16 | 46 |
| D2 | 5/3/2016 | 0.5 | 3.1 | 9.3 | 0.4 | 0.34 | 1.11 | 11.9 | 0.4 | 66 | 40 |
| D3 | 6/3/2016 | 0.6 | 3.1 | 5.5 | 0.4 | 0.39 | 1.27 | 2.9 | 0.4 | 57 | 45 |
| D4 | 7/3/2016 | 0.6 | 3.1 | 0.8 | 0.5 | 0.47 | 0.92 | 0.6 | 0.4 | 44 | 31 |
| D5 | 8/3/2016 | 0.8 | 3.0 | 14.1 | 0.4 | 0.34 | 0.99 | 3.2 | 0.2 | 45 | 32 |
| <i>Mean</i> | | <i>0.7</i> | <i>3.0</i> | <i>6.3</i> | <i>0.4</i> | <i>0.4</i> | <i>1.1</i> | <i>4.0</i> | <i>0.4</i> | <i>46.0</i> | <i>38.9</i> |
| F1 | 1/3/2017 | 0.1 | 4.1 | 1.2 | 1.1 | 0.82 | 7.37 | 3.0 | 1.5 | 19 | 26 |
| F2 | 1/3/2017 | 0.4 | 4.8 | 3.5 | 3.4 | 0.53 | 1.05 | 1.6 | 1.3 | 18 | 21 |
| F3 | 1/3/2017 | 0.7 | 4.4 | 1.8 | 1.7 | 0.48 | 0.77 | 2.1 | 0.6 | 19 | 36 |
| F4 | 3/3/2017 | 0.0 | 3.7 | 0.6 | 1.2 | 1.00 | 6.55 | 3.4 | 3.2 | 30 | 24 |
| F5 | 3/3/2017 | 0.6 | 4.9 | 2.7 | 1.6 | 0.67 | 0.79 | 2.1 | 1.0 | 29 | 43 |
| F6 | 3/3/2017 | 0.7 | 5.1 | 1.5 | 2.1 | 0.36 | 1.37 | 1.3 | 2.2 | 26 | 30 |
| <i>Mean</i> | | <i>0.4</i> | <i>4.5</i> | <i>1.9</i> | <i>1.9</i> | <i>0.6</i> | <i>3.0</i> | <i>2.3</i> | <i>1.6</i> | <i>23.6</i> | <i>29.9</i> |

ceptionally high SPM value for ice samples occurred at D2 with 11.9 g m^{-3} . At this station Chl-*a* was also relatively high ($9.3 \mu\text{g l}^{-1}$), corresponding well to the observed Chl-*a* absorption peak (660–690 nm) (Fig. 7). At the fast ice sites, the SPM concentration ranged from 1.3 to 3.0 g m^{-3} for the ice samples and from 0.6 to 3.2 g m^{-3} for the water samples (Table 4). Overall, SPM concentrations were higher in the ice samples than in the water samples and differences between ice and water samples were greater at drift than at fast ice sites, similar to Chl-*a* concentrations. The proportions of inorganic SPM varied more within drift ice (16–66%) than within fast ice (18–30%), while in the water the range was similar at both sites, 31–46% at drift ice sites and 21–43% at fast ice sites (Table 4). However, the proportion of inorganic SPM did not show a clear pattern between ice and water samples. At some stations (D2–D5, F4), the proportion was higher in ice than in water, while at other stations (D1, F1–F3, F5, F6) the opposite was true.

At drift ice sites, CDOM absorption, g_{440} , varied only little both in the ice samples ($0.34\text{--}0.47 \text{ m}^{-1}$) and in the water samples ($0.92\text{--}1.27 \text{ m}^{-1}$). CDOM absorption was on average three times lower in ice than in water, indicating CDOM rejection during freezing. This is the opposite behaviour to what is observed for Chl-*a* and SPM. At fast ice sites, CDOM absorption had a larger range for melted ice samples ($0.36\text{--}1.00 \text{ m}^{-1}$) and even larger for the underlying water ($0.77\text{--}7.37 \text{ m}^{-1}$). The large range in the underlying water confirms the observed river plume. At F1 and F4, closest to the shore, the CDOM absorption was highest, both in the ice and in the water. Here, the CDOM absorption was six to nine times higher in the underlying water, while within the ice CDOM absorption was at the most twice as high. CDOM absorption was lower in ice than in water at all stations, and this difference was even more obvious in fast ice than in drift ice (Table 4). The rejection of CDOM from the ice varied much more at the fast ice sites than at the drift ice sites. At the fast ice sites, CDOM absorption in the meltwater was $22 \pm 29\%$ of the CDOM absorption in the underlying water, while at the drift ice sites, CDOM absorption in melted ice samples was $36 \pm 8\%$ of the CDOM absorption in the underlying water.

The transmittance through bare ice was lowest at F1 (8.4%) and F4 (8%). These coastal stations had high amounts of CDOM and SPM both in the ice and the underlying water originating from the river discharge and thus leading to an increase of light attenuation within the ice. Transmittance was also low at D2 (9.7%) with high SPM concentration in ice (11.9 g m^{-3}), contributing to the low transmittance. In fast ice, CDOM absorption and concentration of SPM were higher than in the drift ice, presumably reducing the light transfer through the ice cover.

In order to compare CDOM absorption with salinity concentration, the bulk salinity was determined for melted ice samples and in the upper 1 m layer of the underlying water column. The salinity of ice was very stable: 0.6 ppt and 0.7 ppt in drift ice and fast ice, respectively. The same was true for the water salinity in the upper 1 m, but values differed slightly from one another: on average 3.0 ppt at the drift ice sites and 4.5 ppt at the fast ice sites. Similar to sea water, an inverse correlation between CDOM and salinity was found within the ice, the lower the bulk salinity the higher the CDOM absorption (g_{440}). However, within the ice the ratio of CDOM absorption to salinity was higher than in the

underlying water. The rejection of both CDOM and salinity was more efficient at fast ice sites, the CDOM in ice was on average 22% and salinity 9% of the underlying water. While in drift ice, CDOM was 36% and salinity 21% of the underlying water.

4. Discussion

Drift ice and fast ice properties and the light transfer through different types of snow and ice cover were studied during two consecutive springs, in 2016 and 2017. In addition, salinity and concentrations of bio-optical substances were studied both within the ice and in the underlying water. The fast ice structure was typical for coastal sea ice with a granular upper layer and a columnar lower layer, while the drift ice had a more complex structure. Drift ice is characterized by spatial variability in thickness and structure, due to the dynamics of the ice field and processes such as rafting and ridging as well as seawater flooding and seawater being trapped between ice floes. Differences in ice structure between drift ice and fast ice confirm that the growth history of drift ice is considerably more dynamic than for the coastal fast ice.

A strong freshwater input transports high concentrations of humic substances to the Baltic Sea, especially to its northernmost parts the Bothnian Sea and the Bothnian Bay. CDOM absorption, g_{440} , has been found to be inversely related to salinity in the Baltic Sea (Harvey et al., 2015; Kari et al., 2018; Kowalczyk et al., 2006; Kratzer et al., 2003). We found similar relationships for ice: the lower the bulk salinity the higher the CDOM absorption. However, in ice the ratio of CDOM absorption to salinity was higher than in the underlying water. Müller et al. (2011) found a similar enrichment of CDOM in sea ice. They suggested that the enrichment is caused by the initial freezing process and also by the aggregation of CDOM within the brine. The rejection of both CDOM and salinity was more efficient at the fast ice sites, where also both the CDOM absorption and salinity in the parent sea water were higher than at the drift ice sites.

In order to give a thorough statistical analysis, an increased number of samples would be useful. Due to the limited number of data points ($n = 11$), it was challenging to examine the main or at least significant patterns, as to how bio-optical substances affect the light transfer through the ice cover. The SPM concentration had a positive significant effect on the diffuse attenuation coefficient ($p < 0.001$) at drift ice sites, but when D2 (with comparatively high concentration) was removed, there was no statistically significant effect. Neither SPM nor the other bio-optical substances were shown to affect the light attenuation or transmittance in a statistically significant manner. The lack of quantitative data of gas content hides weaker signals and casts uncertainty onto the results. In order to evaluate the influence of ice structure on light transfer through ice, it is important to note that at the drift ice sites the layer thicknesses were determined visually and measured at site (Fig. 3). Also, the samples for the analysis of the bio-optical substances were collected on site. The ice cores for the ice structure analysis (Fig. 4), however, were not taken exactly at the point of the irradiance measurements (but within metres) at the drift ice sites. Despite these limitations, this

study provides a unique dataset as it compares drift ice and fast ice properties in combination with bio-optical substances.

In contrast to the planar irradiance measurements at drift ice sites, irradiance measurements were performed with a scalar irradiance instrument at the fast ice sites. In order to compare these measurements, we utilised the ratio of planar to scalar irradiance. The ratio was estimated based on a study by Arst et al. (2006), who measured the ratio under ice-covered waters. In their study, the ratio of planar to scalar irradiance (averaged over the upper 2 m layer) ranged from 0.39 to 0.76, depending on the optical quality of the water body, ranging from hypereutrophic to oligotrophic water bodies. The ratio was found to increase with depth under snow and ice cover. Here, 0.5 was selected to represent the ratio just below the ice cover. As the ratio differs between water bodies, the selection of the ratio may cause a difference of -6.8% to $+21\%$ in the calculated transmittance. Selecting minimum and maximum ratios would cause a range from 9.4 m^{-1} to 10.0 m^{-1} in the mean $K_{d,tot}(PAR)$ and from 4.6 m^{-1} to 5.4 m^{-1} in the mean $K_{d,ice}(PAR)$.

The ratio between the power irradiance and quantum irradiance, q_{PAR}/E_{PAR} , allows for the irradiance data to be converted to the same units and also describes the variation of the spectral distribution of the irradiance. Here, q_{PAR}/E_{PAR} was slightly lower on the surface above ice $q_{PAR}/E_{PAR} = 4.5\text{ }\mu\text{mol J}^{-1}$ than the theoretical value for white light ($4.6\text{ }\mu\text{mol J}^{-1}$) indicating more irradiance in the short wavelengths compared to white light. Under ice, the ratio was higher, $q_{PAR}/E_{PAR} = 4.6\text{ }\mu\text{mol J}^{-1}$, whether there was snow or not. The highest value, $q_{PAR}/E_{PAR} = 4.7\text{ }\mu\text{mol J}^{-1}$, was observed at D2 where transmittance was lowest (9.7%). The q_{PAR}/E_{PAR} higher than for white light indicates more irradiance at longer wavelengths compared to white light. Below ice, the light spectrum is modified and typically $q_{PAR}/E_{PAR} > 4.6\text{ }\mu\text{mol J}^{-1}$ (Reinart et al., 1998). Reinart et al. (1998) found that the q_{PAR}/E_{PAR} ratio in lake waters depends on the depth and transparency of the water. The q_{PAR}/E_{PAR} ratio ranged here from $4.7\text{--}5.8\text{ }\mu\text{mol J}^{-1}$.

Surface reflectance is very sensitive to the properties of the surface. At drift ice sites, surface reflectance of the natural snow cover ranged from 0.60 to 0.76 and after removing the snow it was on average 1.4 times lower. This result confirms the dominant role of snow cover on surface reflectance. At the fast ice sites, literature data (Arst et al., 2006; Leppäranta, 2015; Rasmus et al., 2002) were employed to evaluate the PAR reflectance since no reflectance measurements were available. Surface reflectance was assumed to be 0.5 for wet snow, 0.85 for fresh snow, 0.3 for wet ice, and 0.2 when sea water had flooded onto the ice surface. After removing the snow, clear, level ice with only a columnar ice structure had the lowest measured reflectance (0.31), while the ice surface with opaque ice and snow adhered to the surface had the highest reflectance (0.70) due to higher surface scatter. These reflectance measurements fall in the same range as found in previous investigations of fast ice in the Gulf of Finland, where the reflectance of snow cover ranged from 0.42 to 0.76 and from 0.30 to 0.38 without snow (Rasmus et al., 2002).

Transmittance was mostly affected by the snow thickness and type. The optical thickness of snow and ice were 6.4 cm and 40 cm, respectively, and regarding the thickness variations, the high sensitivity of transmittance to snow becomes obvious. Snow cover behaves like a grey light filter changing the spectral shape only slightly. The maximum transmittance through the snow-covered ice was found at 569–582 nm and for bare ice at 548–585 nm. The maximum transmittance of bare ice is similar as of water and bare ice thus might not be detected by optical remote sensing data processors, but could be misinterpreted as surface water instead. This may lead to the detection of erroneously high Chl-*a* concentrations in surface waters (Beltrán-Abauza et al., 2016).

At fast ice sites, the snow cover was mostly wet snow, which absorbs most of the solar radiation. Thus, transmittance through snow and ice was very low. Earlier studies on light transfer through brackish sea ice in the coastal land-fast ice zone in the Gulf of Finland were all conducted in Santala Bay. This needs to be accounted for when comparing the results, since only a small variability of stations is considered due to few available studies. The transmittance results are comparable to previous studies in the fast ice zone in Santala Bay, where the PAR transmittance was 13.6% with 3 cm snow on the ice (Rasmus et al., 2002), and 15% with wet snow patches and 52% for clear ice (Leppäranta et al., 2003). In a study by Ehn et al. (2004) on melting fast ice, the PAR transmittance ranged from 25% to 42%. Rasmus et al. (2002) measured the highest transmittance at 556 nm and Ehn et al. (2004) between 550 and 660 nm. In Arctic sea ice, the maximum transmittance is at 470 nm (blue) (Perovich et al., 1998), but CDOM and Chl-*a* absorption cause a shift in the maximum transmittance towards the green (Arrigo et al., 1991; Kauko et al., 2017). Kauko et al. (2017) measured highest transmittance at 558 nm in a refrozen lead in Arctic sea ice, which corresponds well with the transmittance spectra of Baltic Sea ice.

At fast ice sites the diffuse attenuation coefficient, $K_{d,ice}(PAR)$, was on average 5.2 m^{-1} while at drift ice sites $K_{d,ice}(PAR)$ was on average 2.5 m^{-1} with a more complex, multi-layered ice structure. These results are in agreement with previous studies. Rasmus et al. (2002) measured 6.8 m^{-1} , while in the study by Arst et al. (2006) $K_{d,ice}(PAR)$ ranged from 1.5 to 5.5 m^{-1} (mean 3.2 m^{-1}) in fast ice in the Gulf of Finland. An attempt was made to include a three-layer diffuse attenuation coefficient with separate snow, snow-ice, and congelation ice layers with inconclusive results. The estimates of the diffuse attenuation coefficients for snow were 15.7 m^{-1} at drift ice and 21.9 m^{-1} at fast ice sites which is in the correct order of magnitude. The higher values at the fast ice sites can be explained by the higher liquid water content in snow. Järvinen and Leppäranta (2011) studied the transmission of solar radiation through snow cover and measured the diffuse attenuation coefficient in two layers inside the snowpack, 0–4 cm and 4–8 cm. In their study, the attenuation coefficients varied between 4.0 m^{-1} and 13.0 m^{-1} .

The spectral diffuse attenuation coefficient, K_d , showed minimum values in the wavelength range 569–621 nm, corresponding to the maximum range of transmittance, both with and without snow cover. However, after removing

the snow, the minimum $K_{d,ice}$ decreased from 3.7 m^{-1} to 1.3 m^{-1} (mean of the minima $K_{d,ice}$ at the drift ice sites). At D2 and D5, clear attenuation Chl-*a* peaks were visible between 660–690 nm, these stations had the highest concentrations of Chl-*a*: $9.3 \mu\text{g l}^{-1}$ at D2 and $14.1 \mu\text{g l}^{-1}$ at D5. As the highest measured bulk salinity (0.8 ppt) at D5 suggests, an increased Chl-*a* concentration may imply an increased brine volume as the brine may serve as a habitat for phytoplankton (Huttunen and Niemi, 1986; Ikävalko, 1998; Ikävalko et al., 1994). The high Chl-*a* and SPM concentrations at D2 may have caused the rather low transmittance (9.7%) and high diffuse attenuation coefficient for ice $K_{d,ice}(PAR)$ (7.9 m^{-1}). Concentrations of Chl-*a* and SPM varied among the sampling sites, but the concentrations were generally higher at the drift ice sites than at the fast ice sites. The high concentration of SPM (including phytoplankton) was presumably caused by the dynamics of the drift ice field. The ice floes may have trapped sea water, including the substances within, during ice breakage and deformation processes. Additional attenuation measurements were collected in the surface water in the central Bothnian Bay in May 2018, just after the ice melting. The results confirm that in surface waters the total absorption is almost entirely dominated by CDOM in the short wavelengths, while water absorbs strongly in the longer wavelengths. The residual of $K_{d,ice}$, CDOM, and pure water absorption should correspond to white scatter caused by gas inclusions inside the sea ice. Our results show, however, a clear wavelength-dependency with increasing attenuation towards lower wavelengths and a peak at 660–690 nm which corresponds to the phytoplankton absorption peak. The spectral shape of the K_d is overall dominated by the spectral absorption of CDOM and of pure water.

When comparing the spectral K_d of ice (Fig. 9a) to the one of sea water (Fig. 9b) one can see that the spectral shape is similar but the ice has a much stronger overall attenuation. This is mostly caused by the white scatter of gas inclusion in the ice, increasing the total attenuation spectrum. Additionally, particulate matter included in the ice (Table 4) may add to the scatter. Figure 9b illustrates the spectral slope of scatter in water that slightly decreases from 400 to 700 nm. The main effect, however, is also to shift the total K_d spectrum up to a higher level whilst the spectral absorption of particles and phytoplankton combined is relatively low in this example due to generally low concentrations. In Figure 9a, however, the average K_d shows a clear peak in the red, caused by the extremely high chlorophyll-*a* concentrations in some of the ice melt samples (D2 and D5, see Table 4). It must be noted that spectral K_d is a non-linear function of the absorption and scatter of all optical components (Kirk, 2011), and therefore is not simply additive.

The results shown here are in agreement with those of Uusikivi et al. (2010) who measured the absorption coefficient for CDOM as well as of particulate matter in melted fast ice samples. The high SPM concentration in ice indicates high particulate matter absorption and scatter, which may contribute to the overall high attenuation. In order to develop a full picture of the factors affecting the light transfer and their variability, additional studies will be needed that cover *in situ* measurements of the spectral signature of each bio-optical substance within the ice. However, when mea-

suring the optical properties of melted sea ice, the melting process may influence the concentrations or properties of the bio-optical substances (e.g. Rintala et al., 2014). Seasonal measurements of irradiance inside sea ice would provide valuable additional information with minimum disturbance on the sea ice structure and gas inclusions, e.g. utilising autonomous PAR-sensors (Lei et al., 2011) or fibre optics spectrometry (Wang et al., 2019). A full picture of the light transfer through sea ice and snow cover would provide us with better information about the seasonal changes in the light conditions and light availability under sea ice.

5. Conclusions

Light transfer through the ice and snow cover was studied in the Gulf of Bothnia, northern Baltic Sea. In March 2016, drift ice with multi-layered structure was studied, and in March 2017 the measurements were taken in a landfast ice site where typical coastal sea ice was found with a two-layer structure of granular and columnar ice. An additional study was performed in May 2018 to characterize the effect of CDOM and phytoplankton absorption on the spectral diffuse attenuation coefficient. All study sites were located between 63°N and 66°N . Due to total cloud cover during the field campaigns, the downwelling irradiance could be assumed to be diffuse. Snow cover was the dominant factor influencing the light transfer through sea ice. After manually removing the snow, the transmittance was three times higher at drift ice sites and 22 times higher at fast ice sites. The relation between the power irradiance and quantum irradiance was not affected by the snow cover, indicating that it generally reduces the amount of irradiance under ice but does not markedly change its spectral composition. Strongly scattering gas inclusions in the ice significantly increased the diffuse attenuation coefficient K_d but did not noticeably change the spectral distribution, indicating that they – similar to snow- act as white scatterers. This study presents a unique dataset of bio-optical and physical properties of drift ice and fast ice in the Baltic Sea. Our results confirm the differences in these properties in fast ice and drift ice due to differences both in their growth history and in the properties of their parent sea water. Typical to Baltic Sea, both sea water and sea ice have high concentrations of CDOM and SPM, especially in the vicinity of river outlets. CDOM was found to have a strong effect on the spectral slope of K_d at short wavelengths, while pure water absorbs strongly in the long wavelengths. Generally, the effect of phytoplankton pigments on spectral K_d was hardly detectable, apart from at very high concentrations which lead to an increase of K_d at around 660–690 nm. Thus, bio-optical substances included in the ice increase the light attenuation and alter the spectral distribution of the light transfer through ice. The transmittance through bare ice was lowest at the coastal fast ice sites, where also CDOM absorption and SPM concentration were higher than at the drift ice sites. As our results highlight the critical role of snow cover on the light conditions under ice, we recommend further studies on snow cover properties as well as their temporal and spatial variability, which is also relevant if primary production estimation shall be properly performed.

Acknowledgements

This work was financially supported by the Department of Ecology, Environment and Plant Science at Stockholm University, and by the Swedish National Space Agency [Dnr. 147/12], by Nordforsk [project ref. 80106], and by the German Academic Exchange Service (DAAD) [grant number: 57212311]. Thanks to the marine monitoring group at Umeå University and the Swedish Coast Guards on KBV181 for great support during field work. The Swedish Agency for Water and Marine Management as well as County Board Norrbotten provided financial support via the EU Interreg Nord project SEAmBOTH [contract no. 502-14063-2017]. We are grateful to Dr. Eero Rinne, the chief scientist of the sea ice cruise onboard *r/v Aranda*, for the possibility to join the scientific staff. We want to thank the Finnish Meteorological Institute for the facilities during the research cruise and the scientists at the Finnish Environment Institute for support both in preparations and during the cruise. We also thank professor Jukka Horppila at the Ecosystems and Environment Research Programme, Faculty of Biological Environmental Sciences at the University of Helsinki, Finland, for lending the RAMSES instrument for our field campaign onboard *r/v Aranda*. We thank laboratory technician Kathrin Dietrich at the Institute for Chemistry and Biology of the Marine Environment at the Carl von Ossietzky University of Oldenburg, Germany, for the gravimetric analysis of the SPM samples collected during the *r/v Aranda* cruise. The access to the facilities at the Umeå Marine Research Centre and the support from the station's staff are gratefully acknowledged, as well as the help by Maija Jauhiainen during the field campaign in Umeå. We thank Stefan Svensson at the Department of Ecology, Environment and Plant Science at Stockholm University, Sweden, for the fast ice salinity measurements.

Supplementary material

Supplementary material associated with this article can be found, in the online version, at doi:10.1016/j.oceano.2020.04.001.

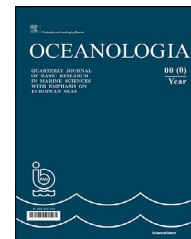
References

- Arrigo, K.R., Sullivan, C.W., Kremer, J.N., 1991. A bio-optical model of Antarctic sea ice. *J. Geophys. Res.* 96 (C6), 10581–10592, <https://doi.org/10.1029/91JC00455>.
- Arst, H., 2003. *Optical properties and remote sensing of multicomponental water bodies*. Springer Science & Business Media.
- Arst, H., Erm, A., Leppäranta, M., Reinart, A., 2006. Radiative characteristics of ice-covered fresh- and brackish-water bodies. *Proc. Est. Acad. Sci. Geol.* 55, 3–23.
- Beltrán-Abaunza, J.M., Kratzer, S., Högländer, H., 2016. Using MERIS data to assess the spatial and temporal variability of phytoplankton in coastal areas. *Int. J. Remote Sens.* 1–25, <https://doi.org/10.1080/01431161.2016.1249307>.
- Doerffer, R., 2002. *Protocols for the validation of MERIS water products – PO-TN-MEL-GS-0043*. ESA Publ. 1–46.
- Ehn, J., Granskog, M.A., Reinart, A., Erm, A., 2004. Optical properties of melting landfast sea ice and underlying seawater in Santala Bay, Gulf of Finland. *J. Geophys. Res.* 109, art. no. C09003, 12 pp. <https://doi.org/10.1029/2003JC002042>.
- Granskog, M.A., Kaartokallio, H., Kuosa, H., Thomas, D.N., Vainio, J., 2006. Sea ice in the Baltic Sea – A review. *Estuar. Coast. Shelf Sci.* 70, 145–160, <https://doi.org/10.1016/j.ecss.2006.06.001>.
- Harvey, E.T., Kratzer, S., Andersson, A., 2015. Relationships between colored dissolved organic matter and dissolved organic carbon in different coastal gradients of the Baltic Sea. *Ambio* 44, 392–401, <https://doi.org/10.1007/s13280-015-0658-4>.
- Huttunen, M., Niemi, Å., 1986. *Sea-ice algae in the Northern Baltic Sea*. *Mem. Soc. Fauna Flora Fenn.* 62, 58–62.
- Ikävalko, J., 1998. Further observations on flagellates within sea ice in northern Bothnian Bay, the Baltic Sea. *Polar Biol* 19, 323–329, <https://doi.org/10.1007/s003000050253>.
- Ikävalko, J., Kristiansen, J., Thomsen, H.A., 1994. A revision of the taxonomic position of *Syncrypta glomerifera* (Chrysophyceae), establishment of a new genus *Lepidochrysis* and observations on the occurrence of *L. glomerifera* comb. nov. in brackish water. *Nord. J. Bot* 14, 339–344, <https://doi.org/10.1111/j.1756-1051.1994.tb00617.x>.
- Järvinen, O., Leppäranta, M., 2011. Transmission of solar radiation through the snow cover on floating ice. *J. Glaciol.* 57, 861–870, <https://doi.org/10.3189/002214311798043843>.
- Kari, E., Kratzer, S., Beltrán-Abaunza, J.M., Harvey, E.T., Vaičiūtė, D., 2016. Retrieval of suspended particulate matter from turbidity – model development, validation, and application to MERIS data over the Baltic Sea. *Int. J. Remote Sens.* 38, 1–21, <https://doi.org/10.1080/01431161.2016.1230289>.
- Kari, E., Merkouriadi, I., Walve, J., Leppäranta, M., Kratzer, S., 2018. Development of under-ice stratification in Himmerfjärden bay, north-western Baltic proper, and their effect on the phytoplankton spring bloom. *J. Mar. Sci.* 186, 85–95, <https://doi.org/10.1016/j.jmarsys.2018.06.004>.
- Kauko, H.M., Taskjelle, T., Assmy, P., Pavlov, A.K., Mundy, C.J., Duarte, P., Fernández-Méndez, M., Olsen, L.M., Hudson, S.R., Johnsen, G., Elliott, A., Wang, F., Granskog, M.A., 2017. Windows in Arctic sea ice: Light transmission and ice algae in a refrozen lead. *J. Geophys. Res. Ocean* 148, 1486–1505, <https://doi.org/10.1002/2016JG003626>.
- Kawamura, T., Shirasawa, K., Ishikawa, N., Lindfors, A., Rasmus, K., Granskog, M.A., Ehn, J., Leppäranta, M., Martma, T., Vaikmäe, R., 2001. Time-series observations of the structure and properties of brackish ice in the Gulf of Finland. *Ann. Glaciol.* 33, 1–4, <https://doi.org/10.3189/172756401781818950>.
- Kirk, J.T.O., 2011. *Light and photosynthesis in aquatic ecosystems*, 3rd edn Cambridge Univ. Press, Cambridge, United Kingdom 662 pp.
- Kowalczyk, P., Stedmon, C.A., Markager, S., 2006. Modeling absorption by CDOM in the Baltic Sea from season, salinity and chlorophyll. *Mar. Chem.* 101, 1–11, <https://doi.org/10.1016/j.marchem.2005.12.005>.
- Kratzer, S., 2000. *Bio-optical studies of coastal waters*. University of Wales, Bangor Ph.D. thesis.
- Kratzer, S., Håkansson, B., Sahlin, C., 2003. Assessing Secchi and photic zone depth in the Baltic Sea from satellite data. *Ambio* 32, 577–585, <https://doi.org/10.1579/0044-7447-32.8.577>.
- Kratzer, S., Moore, G., 2018. Inherent Optical Properties of the Baltic Sea in Comparison to Other Seas and Oceans. *Remote Sens* 10, 1–28, <https://doi.org/10.3390/rs10030418>.
- Kratzer, S., Tett, P., 2009. *Using bio-optics to investigate the extent of coastal waters: A Swedish case study*. *Eutrophication in Coastal Ecosystems*. Springer, Amsterdam, 169–186.
- Lei, R., Leppäranta, M., Erm, A., Jaatinen, E., Pärn, O., 2011. Field investigations of apparent optical properties of ice cover in Finnish and Estonian lakes in winter 2009. *Est. J. Earth Sci* 60, 50–64, <https://doi.org/10.3176/earth.2011.1.05>.

- Leppäranta, M., 2015. Freezing of lakes and the evolution of their ice cover, 1st edn Springer, Praxis, Chichester, 301 pp., <https://doi.org/10.1007/978-3-642-29081-7>.
- Leppäranta, M., 2011. The Drift of Sea Ice, 2nd edn. Springer, Praxis, Chichester, 347 pp., <https://doi.org/10.1007/978-3-642-04683-4>.
- Leppäranta, M., 1983. A growth model for black ice, snow ice and snow thickness in subarctic basins. *Hydrol. Res.* 14, 59–70, <https://doi.org/10.2166/nh.1983.0006>.
- Leppäranta, M., Myrberg, K., 2009. Physical Oceanography of the Baltic Sea. Springer, Praxis, Chichester, 401 pp., <https://doi.org/10.1007/978-3-540-79703-6>.
- Leppäranta, M., Reinart, A., Erm, A., Arst, H., Hussainov, M., Sipilgas, L., 2003. Investigation of Ice and Water Properties and Under-ice Light Fields in Fresh and Brackish Water Bodies. *Nord. Hydrol.* 34, 245–266, <https://doi.org/10.2166/nh.2003.0006>.
- Leppäranta, M., Tikkanen, M., Shemeikka, P., 1998. Observations of Ice and Its Sediments on the Baltic Sea Coast. *Hydrol. Res.* 29, 199–220.
- McDougall, T.J., Barker, P.M., 2011. Getting started with TEOS-10 and the Gibbs Seawater (GSW) Oceanographic Toolbox. SCOR/IAPSO WG127, 28 pp..
- Müller, S., Vähätalo, A.V., Granskog, M.A., Autio, R., Kaartokallio, H., 2011. Behaviour of dissolved organic matter during formation of natural and artificially grown Baltic Sea ice. *Ann. Glaciol.* 52, 233–241, <https://doi.org/10.3189/172756411795931886>.
- Ohde, T., Siegel, H., Gerth, M., 2007. Validation of MERIS Level-2 products in the Baltic Sea, the Namibian coastal area and the Atlantic Ocean. *Int. J. Remote Sens.* 28, 609–624, <https://doi.org/10.1080/01431160600972961>.
- Palosuo, E., 1963. The Gulf of Bothnia in winter. II Freezing and ice forms, Merentutkimuslaitoksen Julkaisu/ Havsforskningsinstitutets Skrift. Finnish Institute of Marine Research, Helsinki, Finland.
- Palosuo, E., 1961. Crystal structure of brackish and freshwater ice. *Bull. Int. Assoc. Sci. Hydrol.* 54, 9–14.
- Parsons, T.R., Maita, Y., Lalli, C.M., 1984. A Manual of Chemical and Biological Methods for Seawater Analysis. Pergamon Press, Oxford 188 pp. <https://doi.org/10.1002/iroh.19850700634>.
- Perovich, D.K., 1996. The Optical Properties of Sea Ice. In: Leppäranta, M. (Ed.), *Physics of Ice-Covered Seas*, 1. Univ. Helsinki, Helsinki, 195–230.
- Perovich, D.K., Roesler, C.S., Pegau, W.S., 1998. Variability in Arctic sea ice optical properties. *J. Geophys. Res. Ocean* 103, 1193–1208, <https://doi.org/10.1029/97JC01614>.
- Pierson, D.C., Kratzer, S., Strömbeck, N., Håkansson, B., 2008. Relationship between the attenuation of downwelling irradiance at 490 nm with the attenuation of PAR (400 nm–700 nm) in the Baltic Sea. *Remote Sens. Environ.* 112, 668–680, <https://doi.org/10.1016/j.rse.2007.06.009>.
- Pope, R.M., Fry, E.S., 1997. Absorption spectrum (380–700 nm) of pure water. II. Integrating cavity measurements. *Appl. Opt.* 36, 8710–8723.
- Rasmus, K., Ehn, J., Granskog, M., Kärkäs, E., Leppäranta, M., Lindfors, A., Pelkonen, A., Rasmus, S., Reinart, A., 2002. Optical Measurements of Sea Ice in the Gulf of Finland. *Hydrol. Res.* 33, 207–226.
- Reinart, A., Arst, H., Blanco-Sequeiros, A., Herlevi, A., 1998. Relation between underwater irradiance and quantum irradiance in dependence on water transparency at different depths in the water bodies. *J. Geophys. Res.* 103, 7749–7752, <https://doi.org/10.1029/97JC03645>.
- Rintala, J.-M., Piiparinen, J., Blomster, J., Majaneva, M., Müller, S., Uusikivi, J., Autio, R., 2014. Fast direct melting of brackish sea-ice samples results in biologically more accurate results than slow buffered melting. *Polar Biol.* 1811–1822, <https://doi.org/10.1007/s00300-014-1563-1>.
- Shokr, M., Sinha, N. (Eds.), 2015. *Laboratory Techniques for Revealing the Structure of Polycrystalline Ice. Sea Ice: Physics and Remote Sensing. Geophys. Monogr.* 209, AGU. John Wiley & Sons, Hoboken, 231–269.
- Simis, S.G.H., Olsson, J., 2013. Unattended processing of shipborne hyperspectral reflectance measurements. *Remote Sens. Environ.* 135, 202–212, <https://doi.org/10.1016/j.rse.2013.04.001>.
- Simon, A., Shanmugam, P., 2016. Estimation of the spectral diffuse attenuation coefficient of downwelling irradiance in inland and coastal waters from hyperspectral remote sensing data: Validation with experimental data. *Int. J. Appl. Earth Obs. Geoinf.* 49, 117–125, <https://doi.org/10.1016/j.jag.2016.02.003>.
- Strickland, J.D.H., Parsons, T.R., 1972. A practical handbook of seawater analysis, 2nd edn. Fisher. Res. Board Canada, Ottawa, Canada, 293 pp., <https://doi.org/10.1002/iroh.19700550118>.
- Uusikivi, J., Granskog, M.A., Sonninen, E., 2011. Meteoric ice contribution and influence of weather on landfast ice growth in the Gulf of Finland. *Baltic Sea. Ann. Glaciol.* 52, 91–96, <https://doi.org/10.3189/172756411795931796>.
- Uusikivi, J., Vähätalo, A.V., Granskog, M.A., Sommaruga, R., 2010. Contribution of mycosporine-like amino acids and colored dissolved and particulate matter to sea ice optical properties and ultraviolet attenuation. *Limnol. Oceanogr.* 55, 703–713, <https://doi.org/10.4319/lo.2010.55.2.0703>.
- Vogt, J., Soille, P., De Jager, A., Rimavičiūtė, E., Mehl, W., Foisneau, S., Bódis, K., Dusart, J., Paracchini, M.L., Haastrop, P., Bamps, C., 2007. A pan-European River and Catchment Database. Rep. EUR 22920 En. [JRC Ref. Rep.], CCM, IES, JCR EU. Office for Official Publ. EU (OPOCE), Luxembourg, 124 pp., <https://doi.org/10.2788/35907>.
- Wang, H., Nan, L., Han, J., Chen, Y., Huang, H., 2019. Long-term measurement of solar irradiance above, within, and under sea ice in polar environments by using fiber optical spectrometry. *J. Atmos. Ocean. Technol.* 36, 1773–1787, <https://doi.org/10.1175/JTECH-D-19-0086.1>.
- Weeks, W.F., Ackley, S.F., 1986. The Growth, Structure, and Properties of Sea Ice. In: Untersteiner, N. (Ed.), *The Geophysics of Sea Ice*. Springer, Boston, 9–164.
- Weeks, W.F., Hibler, W.D., 2010. Appendix E: Thin sections. *On Sea Ice*. Univ. Alaska Press, 566–570.
- Weeks, W.F., Gow, A., Kosloff, P., Digby-Argus, S., 1990. The internal structure, composition and properties of brackish ice from the Bay of Bothnia. In: Ackley, S.F., Weeks, Wilford F. (Eds.), *Sea Ice Properties and Processes: Proc. W.F. Weeks Sea Ice Symp., CRREL Monogr.*, 5–15.
- Zibordi, G., Darecki, M., 2006. Immersion factors for the RAMSES series of hyper-spectral underwater radiometers. *J. Opt. A Pure Appl. Opt.* 8, 252–258, <https://doi.org/10.1088/1464-4258/8/3/005>.

Available online at www.sciencedirect.com

ScienceDirect

journal homepage: www.journals.elsevier.com/oceanologia

ORIGINAL RESEARCH ARTICLE

Surface desalinated layer distribution in the Kara Sea determined by shipboard and satellite data

Dmitry I. Glukhovets^{a,b,*}, Yury A. Goldin^a^a Shirshov Institute of Oceanology, Russian Academy of Sciences, Moscow, Russia^b Moscow Institute of Physics and Technology, Dolgoprudny, Moscow region, Russia

Received 30 November 2019; accepted 8 April 2020

Available online 20 May 2020

KEYWORDS

Surface desalinated layer;
 Interseasonal dynamics;
 Satellite data;
 Kara Sea;
 Fluorescence;
 Absorption

Summary This study reports the propagation dynamics of the Kara Sea surface desalinated layer (SDL) during the summer and autumn seasons. We analysed shipboard measurements data collected in 2013–2018 and MODIS ocean colour data that correlated with the shipboard ones. We formulated a comparatively strict criterion to determine the SDL border based on satellite data. For that, we analyzed the shipboard flow-through measuring system data obtained while crossing the surface desalinated layer border. Further, we used a regional algorithm to process the satellite data and estimate the coloured dissolved organic matter absorption coefficient for the Kara Sea. The results demonstrate a significant effect of the wind regime on the interseasonal and interannual variability of the transformation of the SDL boundaries. The positions of the surface desalinated layer boundaries at different times during 2013–2018 are given. The obtained results are important for calculating the heat balance and analyzing the Kara Sea bio-productivity.

© 2020 Institute of Oceanology of the Polish Academy of Sciences. Production and hosting by Elsevier B.V. This is an open access article under the CC BY-NC-ND license (<http://creativecommons.org/licenses/by-nc-nd/4.0/>).

* Corresponding author at: Shirshov Institute of Oceanology, Russian Academy of Sciences, Nakhimovskiy Prospekt, 36, Moscow, 117218, Russia; Moscow Institute of Physics and Technology, Institutskiy lane 9, Dolgoprudny, Moscow region, 141700, Russia.

E-mail address: glukhovets@ocean.ru (D.I. Glukhovets).

Peer review under the responsibility of the Institute of Oceanology of the Polish Academy of Sciences.



Production and hosting by Elsevier

1. Introduction

The Kara Sea is characterized by the presence of a surface desalinated layer (SDL). It is formed in summer seasons due to river runoff. This layer occupies a significant part of the Kara Sea and has a substantial effect on hydrological, biological, climatic, and geological processes (Burenkov et al., 2010a; Fichot et al., 2013; Osadchiev et al., 2017, 2019; Pasternak et al., 2015; Sukhanova et al., 2012; Zatsepin et al., 2010b). In many cases, the SDL is separated from the sea by sharp fronts (Glukhovets and Goldin, 2014, 2018;

<https://doi.org/10.1016/j.oceano.2020.04.002>

0078-3234/© 2020 Institute of Oceanology of the Polish Academy of Sciences. Production and hosting by Elsevier B.V. This is an open access article under the CC BY-NC-ND license (<http://creativecommons.org/licenses/by-nc-nd/4.0/>).

Table 1 Cruises in which shipboard data were received.

| No. | Cruise and vessel | Measurement period | Track length [km] |
|-----|--|--------------------|-------------------|
| 1 | r/v <i>Professor Shtokman</i> , 125th cruise | 2.09–22.09 2013 | 4050 |
| 2 | r/v <i>Professor Shtokman</i> , 128th cruise | 14.08–14.09 2014 | 4700 |
| 3 | r/v <i>Akademik Mstislav Keldysh</i> , 63rd cruise | 28.08–07.10 2015 | 4750 |
| 4 | r/v <i>Akademik Mstislav Keldysh</i> , 66th cruise | 15.07–18.08 2016 | 5550 |
| 5 | r/v <i>Akademik Mstislav Keldysh</i> , 69th cruise | 24.08–27.09 2017 | 5150 |
| 6 | r/v <i>Akademik Mstislav Keldysh</i> , 72nd cruise | 19.08–17.09 2018 | 7250 |

Zatsepin et al., 2010b, 2015, 2017). Its boundaries can be detected by continuous shipboard measurements, from a flow-through measuring system (Burenkov et al., 2010; Glukhovets and Goldin, 2018) or by satellite ocean colour scanners (Glukhovets and Goldin, 2019, Matsuoka et al., 2017). In addition to measurements of salinity and temperature to trace the freshwater, the CDOM fluorescence characteristics have been recently used to study the mixing of the desalinated and marine waters and to determine their origin (Coble, 2007; Drozdova et al., 2017; Glukhovets and Goldin, 2018, 2019; Goncalves-Araujo et al., 2016). Similar studies of the interaction of desalinated and marine waters were also carried out in other Arctic seas with likewise oceanological conditions – the Laptev and East Siberian seas (Goncalves-Araujo et al., 2015; Pugach et al., 2018). In addition, some authors (Kowalczyk et al., 2019; Reynolds et al., 2019) have studied the optical characteristics of seawater in other Arctic regions.

Shipboard methods provide fairly accurate but fragmented data (Glukhovets and Goldin, 2018; Goncalves-Araujo et al., 2016). At the same time, satellite methods are less accurate in determining the absolute values of the surface layer characteristics. On the other hand, they can regularly obtain spatial distributions for almost the entire studied water area (Matsuoka et al., 2017). Earlier research has identified central, western, and eastern types of the SDL distribution (Moretskii, 1985; Rusanov and Vasil'ev, 1976), and there have been a number of studies on mechanisms determining the transformation of SDL (Kubryakov et al., 2016; Zatsepin et al., 2010b, 2015). Despite its clear relevance to such branches of oceanology as marine biology, climatology, and hydrophysics, the SDL distribution dynamics has, however, not yet been subject to intensive research. Nevertheless, prior work (Pasternak et al., 2015) has shown that the abundance of zooplankton inside the SDL is low and increases sharply at its borders. The species composition of phytoplankton is associated with the distribution of SDL (Sukhanova et al., 2012). The SDL reduces the photic zone depth significantly, which affects bioproductivity (Demidov et al., 2018). The turbid SDL waters absorb more solar radiation, which largely determines the radiation balance (Granskog et al., 2015). The data on the SDL boundaries are important for conducting model hydrodynamic calculations (Zhubas and Zavialov, 2015).

This paper represents a detailed study of the SDL distribution in the summer and autumn seasons between 2013 and 2018. In these years, shipboard research had been carried out using a flow-through measuring complex. Our consideration embraces the period from June to September. At this time, the essential part of the Kara Sea is under the in-

fluence of river runoff, and it is free of ice. When the sea is even partly occupied by ice, this may become another factor affecting the distribution of SDL in some cases. In the studied years, the surface desalinated layer formed by river runoff did not come into contact with sea ice.

2. Material and methods

2.1. Research area

Shipboard measurements were carried out in six cruises of the Shirshov Institute of Oceanology of the RAS (SIO RAS). Table 1 presents some data on the durations and distances of the cruises. The work was mainly conducted in the southwest and central parts of the Kara Sea, which are most affected by SDL (Glukhovets and Goldin, 2014, 2018; Zatsepin et al., 2010b, 2015). The 2014 expedition route is shown as an example in Figure 1b.

2.2. Shipboard data collection

In the current study, we measured salinity (S), temperature, fluorescence intensities (I_f) of coloured dissolved organic matter (CDOM), and chlorophyll a (Chl). The measurements were taken in the seawater surface layer at the depth of 1–2 metres. To carry them out, we used a flow-through measuring complex (Goldin et al., 2015) with a resolution of about 50 m.

The fluorescence intensity is excited with a 373 nm high-brightness LED working in continuous mode ($\text{FWHM}_{\text{CDOM}} = 15$ nm). A photomultiplier is used for the registration of the fluorescence radiation. The fluorescence spectral range (maximum – 480 nm, $\text{FWHM}_{\text{CDOM}} = 150$ nm) is formed by means of a coloured glass optical filter. Due to the combination of excitation wavelength and the registration method we used, the device can primarily register the fluorescence of the terrestrial humic-like dissolved organic carbon component (Coble, 2007). The data-averaging interval was 5–15 s, the relative error in the I_f measurements was $<1\%$, the error in the determination of salinity was <0.25 PSU.

The device provides the I_f measurements in relative units. To calibrate the measurement results into Raman Units, we obtained the seawater fluorescence spectra samples using an Ocean Optics USB4000 spectrometer. Samples for calibration are taken from the water intake system simultaneously with continuous measurements. As a result of their comparison, we derived linear calibration relations. These allow to the conversion of the measured signal to Raman Units.

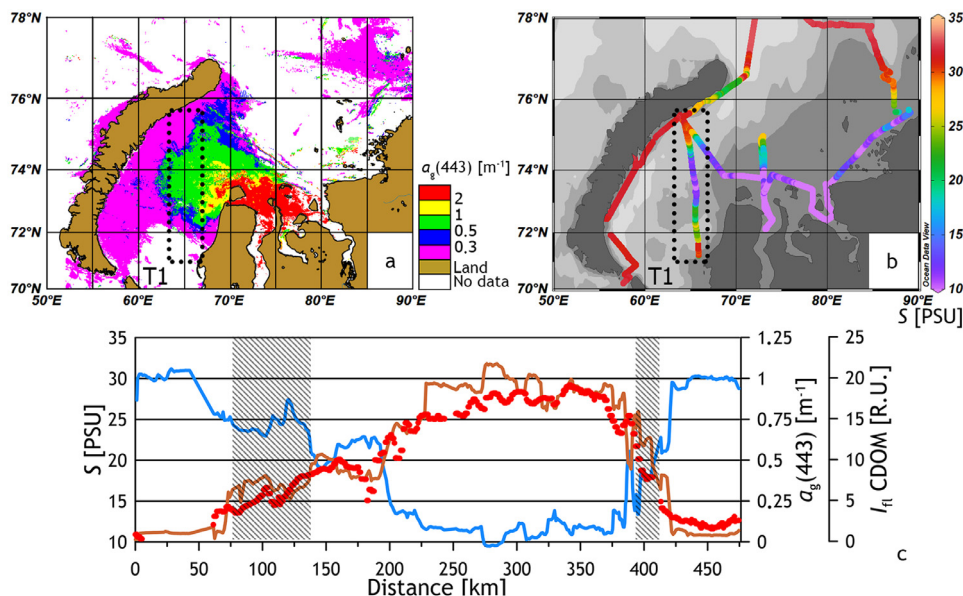


Figure 1 Comparison of satellite and shipboard data: MODIS $a_g(443)$ spatial distribution averaged over the period August 13–19, 2014 (a); the distribution of S along the route of the 128th cruise of the *r/v Professor Shtokman* (b) and the distribution of S (blue), I_{fl} CDOM (brown) and $a_g(443)$ (red) along the T1 transect (c). The fluorescence intensity is given in Raman Units (R.U.). The position of the T1 transect is highlighted by frames; the time of the transect execution is August 11–17, 2014.

2.3. Satellite and complementary data collection

The maps of the CDOM absorption coefficient $a_g(443)$ spatial distribution were drawn using the MODIS ocean colour scanner with the help of the semi-analytical regional algorithm for the Kara Sea (Vazyulya et al., 2014). The algorithm solves the inverse problem of finding absorption values. Low-parametric models applied to MODIS remote sensing reflectance (R_{RS}) are implemented in this algorithm. The absorption coefficient is defined as the sum of the absorption values of pure seawater, CDOM, and the phytoplankton pigments. As a result of solving the inverse problem, $a_g(443)$ is defined. The contribution of chlorophyll is taken into account by using a regional algorithm (Kuznetsova et al., 2013). It implies the following formula to calculate the chlorophyll concentration: $\ln(\text{Chl}) = -3.07 \ln[R_{RS}(531)/R_{RS}(547)] + 0.148$. The development and validation of these algorithms were performed with the shipboard measurement data collected in the Kara Sea in 2007 and 2011.

We processed the satellite data using the SMCS software developed at the SIO RAS (Sheberstov, 2015). In the Kara Sea, it is difficult to obtain satellite data in the visible range of spectrum due to frequent cloud density. Therefore, averaging is necessary to obtain maps with a sufficient degree of coverage. In this work, we used the weekly averaging interval of L2 data on a 3×3 km grid. Data from other ocean colour scanners were not considered, as it does not lead to an increase in coverage. Near-water wind characteristics were estimated from ERA-INTERIM reanalysis data (Dee et al., 2011). River discharge data were taken from the Arctic great rivers observatory archive (<https://arcticgreatrivers.org>).

3. The criterion to determine the desalinated layer boundary from satellite data

The boundary of the river runoff influence can be determined by the isohaline 24.67‰ (Pivovarov, 2000). At this salinity, the freezing temperature is equal to the temperature of the highest density of water. The ice formation regime is different for desalinated waters and seawaters (Fofonoff and Millard, 1983). In a number of studies (Zatsepin et al., 2010b, 2015) the rounded salinity value of 25 PSU is considered to be the SDL boundary. In this paper, we focus on this value.

There exists a strong negative correlation between the salinity and the CDOM concentration due to a united dilution process (Amon, 2003). The data obtained by means of the shipboard flow-through measuring complex showed the presence of a negative correlation between the salinity and the CDOM fluorescence intensity. The negative correlation is an effective indicator of SDL that quickly allows us to determine its presence (Glukhovets and Goldin, 2018).

Previously, satellite Chl concentration maps were used to determine the boundaries of the river runoff influence. This offers a qualitative idea of the SDL distribution in the Kara Sea (Kubryakov et al., 2016) because dissolved organic matter affects the Chl concentration values obtained from satellite data. The standard algorithm is heavily affected by the CDOM absorption, and even the regional one (Kuznetsova et al., 2013) does not seem to completely eliminate its effect. The regional algorithm for the CDOM absorption coefficient $a_g(443)$ (Vazyulya et al., 2014) provides more rigorous results.

Thus, to develop a criterion that identifies the desalinated layer boundary on the basis of the satellite data, we

Table 2 Characteristics of transect parts crossing the SDL boundary.

| No. | Border crossing date | Map date | Boundary position | ρ (I_{fl} , S) | N (I_{fl} , S) | σ (I_{fl} , S) | ΔS [PSU] | Δa_g [m^{-1}] | ρ (a_g , S) | N (a_g , S) | σ (a_g , S) |
|-----|----------------------|-------------------|-------------------|------------------------|-------------------|--------------------------|------------------|---------------------------|---------------------|----------------|-----------------------|
| 1 | 12.08.14 | 13–19 August 2014 | 72.0°N, 65.5°E | −0.99 | 9810 | 1.15 | 20–25 | 0.25–0.5 | −0.94 | 9810 | 2.16 |
| 2 | 15.08.14 | 13–19 August 2014 | 74.6°N, 65.0°E | −0.99 | 9810 | 1.15 | 15–25 | 0.25–0.5 | −0.94 | 9810 | 2.16 |
| 3 | 19.07.16 | 15–21 July 2016 | 75.2°N, 72.8°E | −0.95 | 1920 | 1.74 | 10–25 | 0.5–2 | −0.91 | 1070 | 2.25 |
| 4 | 27.08.17 | 20–26 August 2017 | 75.0°N, 84.0°E | −0.94 | 1251 | 1.33 | 25–27.5 | 0.25–0.5 | −0.82 | 760 | 1.46 |
| 5 | 29.08.17 | 20–26 August 2017 | 74.3°N, 65.0°E | −0.94 | 1251 | 1.33 | 20–25 | 0.25–0.5 | −0.82 | 760 | 1.46 |
| 6 | 21.08.18 | 20–26 August 2018 | 73.5°N, 66.5°E | −0.95 | 7800 | 1.50 | 15–25 | 0.25–0.75 | −0.80 | 7800 | 2.75 |
| 7 | 22.08.18 | 20–26 August 2018 | 76.0°N, 87.5°E | −0.95 | 7800 | 1.50 | 20–25 | 0.25–0.5 | −0.80 | 7800 | 2.75 |

did the following sequence of actions. For the entire period of the study from June to September between 2013 and 2018, weekly averaged satellite maps of the CDOM absorption coefficient were drawn (until June, a significant part of the sea is covered by ice; in October, frequent cloud cover prevents the acquisition of satellite data). Sometimes even a weekly averaging does not allow the complete picture of the SDL distribution to be obtained. In such cases, these data were not taken into account.

The procedure for finding the correspondence of the fronts from shipboard and satellite data is illustrated in Figure 1. We selected averaged satellite maps for the time of shipboard measurements. The top left part of Figure 1 demonstrates areas open from the clouds. The black dotted line on the upper part of Figure 1 indicates the shipboard measurements area, where simultaneously with the satellite data border crossings were recorded. The distributions of the S and I_{fl} CDOM along the ship's route, as well as the $a_g(443)$ values extracted from satellite maps along the ship measurement track, are plotted in Figure 1c.

As it was mentioned above, the S value of 25 PSU can be considered as the SDL boundary. However, the observed spatial structure of the SDL frontal zone displays nonmonotonic change and fragmentation caused by near-surface wind influence (Zatsepin et al., 2017). As a result, this fact does not allow the exact salinity value for unambiguous determination of this layer boundary position to be chosen. Therefore, while formulating the criterion to determine the desalinated layer boundary, we have to specify a certain interval of change in salinity values including the value of 25 PSU. The boundary of this interval in each case is determined, basing on the S and $a_g(443)$ distribution pattern in

a given year. For example, in 2016 it turned out to be 10–25 PSU, while in 2017 it was quite different, being 25–27.5 PSU. The intervals of S values are associated with the corresponding intervals of satellite $a_g(443)$ values. These intervals for matching shipboard and satellite data for all considered years are listed in Table 2.

Table 2 presents the dates of shipboard and satellite measurements, the coordinates of the SDL boundaries positions, the values of the correlation coefficients between S and I_{fl} CDOM (its negative values, close to −1 correspond to the SDL region (Glukhovets and Goldin, 2018)), sample size and root-mean-square errors. It also presents the intervals of salinity and the CDOM absorption coefficient values and the correlation coefficient between them. The example of correlation coefficients calculated for the 2014 data is shown in Figure 2. The results for other years are obtained in a similar way.

It is necessary to note the boundary width is small in comparison with the size of the SDL due to high gradients in the frontal zones. This boundary width is determined by the chosen interval. The analysis showed that the changes in the interval values given in Table 2 do not lead to significant boundary displacements. The SDL border width is estimated from the shipboard data. We considered the angle between the direction of the ship's route and the normal to the border. The position of the normal is determined by satellite maps. In most cases, the border width is about 10 km, but sometimes it can reach 60 km (Figure 1 bottom). These values are consistent with prior work (Zatsepin et al., 2017).

Based on the data in Table 2, we selected the range of absorption coefficient $a_g(443) = 0.25–0.5 m^{-1}$ that corresponds to the SDL boundary. It is important to emphasize

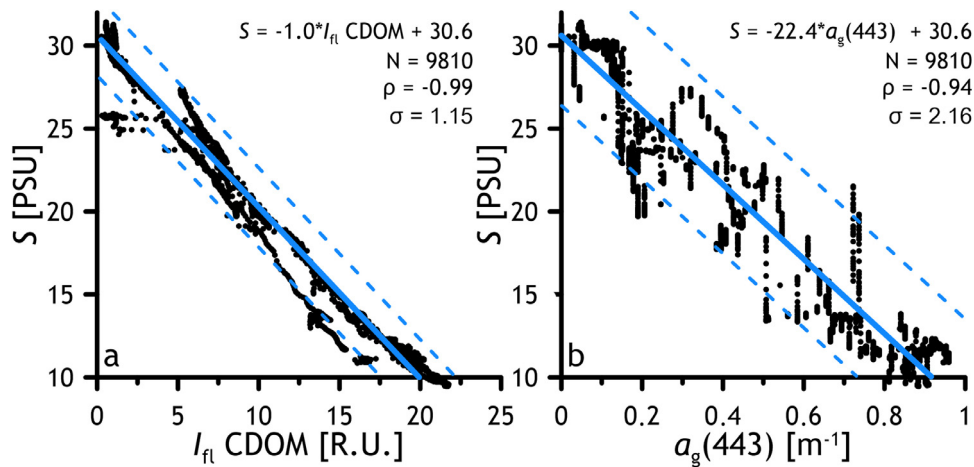


Figure 2 Scatter diagrams of the salinity (S) and coloured dissolved organic matter (CDOM) fluorescence intensity in Raman Units (a) and CDOM absorption coefficients at the 443 nm wavelength (b). Dotted lines represent 95% confidence interval. The T1 transect (see Figure 1), the Kara Sea, August 11–17, 2014.

Table 3 Averaging period for satellite data for the presented contours.

| No. | 2013 | 2014 | 2015 | 2016 | 2017 | 2018 |
|-----|------------|------------|------------|------------|------------|----------|
| 1 | 18–24.06 | 25.06–1.07 | 4–10.06 | 10–16.06 | 11–17.06 | 11–17.06 |
| 2 | 16–22.07 | 30.07–5.08 | 16–22.07 | 1–7.07 | 25.06–1.07 | 18–24.06 |
| 3 | 30.07–5.08 | 20–26.08 | 30.07–5.08 | 15–21.07 | 2–8.07 | 2–8.07 |
| 4 | 24–30.09 | — | 27.08–2.09 | 5–11.08 | 9–15.07 | 16–22.07 |
| 5 | — | — | — | 26.08–1.09 | 16–22.07 | 20–26.08 |
| 6 | — | — | — | 9–15.09 | 13–19.08 | 16–16.09 |
| 7 | — | — | — | — | 20–26.08 | — |
| 8 | — | — | — | — | 24–30.09 | — |

that the maximum $a_g(443)$ values, recorded in the Kara Sea according to satellite data, reach $3.5\text{--}4\text{ m}^{-1}$. It follows from Table 2 that there is some interannual variability. However, this variability does not fall out of the specified range. The derived criterion is valid for the Kara Sea.

4. Results and discussion

We used satellite maps, based on weakly averaging, that show the spatial distribution of the CDOM absorption coefficient. These maps provide sufficient coverage of the Kara Sea and allow us to depict isolines of $a_g(443) = 0.3\text{ m}^{-1}$. This value corresponds to the rounded value of the lower limit of the range selected as the criterion for inclusion of frontal zones in the SDL. The satellite data averaging period for each contour is presented in Table 3. Dashes correspond to the lack of data. In accordance with the developed criterion, the presented contours show the positions of the SDL boundaries in the corresponding time period. When isolines were drawn, the fine structure and the patching effect (Pelevin et al., 2017) in the SDL region were smoothed. The positions of the obtained isolines are reflected in Figure 3. There is a break on the map of 2015 isoline 4 due to continuous cloud cover over the eastern part of the Kara Sea (corresponding to the end of August).

The distributions presented in Figure 3 had been formed by the end of the summer and autumn seasons. These distributions are largely in accordance with existing conceptions (Moretskii, 1985; Rusanov and Vasil'ev, 1976; Zatsepin et al., 2010b, 2015). However, the high interannual variability of the given SDL spreading types and the dynamics of its borders should be taken into account. In some years (for instance, 2013–2015), SDL borders moved throughout the summer-autumn season, although in others (2016–2018), rather long periods of border stability are observed.

The central type of SDL distribution shapes when the water desalinated by river runoff moves to the north and reaches the northern top of Novaya Zemlya by the end of the season. This type was observed in 2013 and at the beginning of 2015. The eastern type of SDL distribution is characterized by the transfer of desalinated water along the coast of the Taimyr Peninsula towards the Laptev Sea. In this case, desalinated waters occupy a rather narrow zone. This type of distribution was observed in 2016 and 2018. The distribution formed by the end of the 2017 season exemplifies the western type of the SDL distribution. Desalinated water reaches the shores of Novaya Zemlya in this case.

However, the existing simplified classification is not enough to describe the SDL distribution in some years. For example, in 2014, the distribution of SDL had the features of the eastern and western types at the same time; in 2015 until mid-July, the central type of distribution was observed,

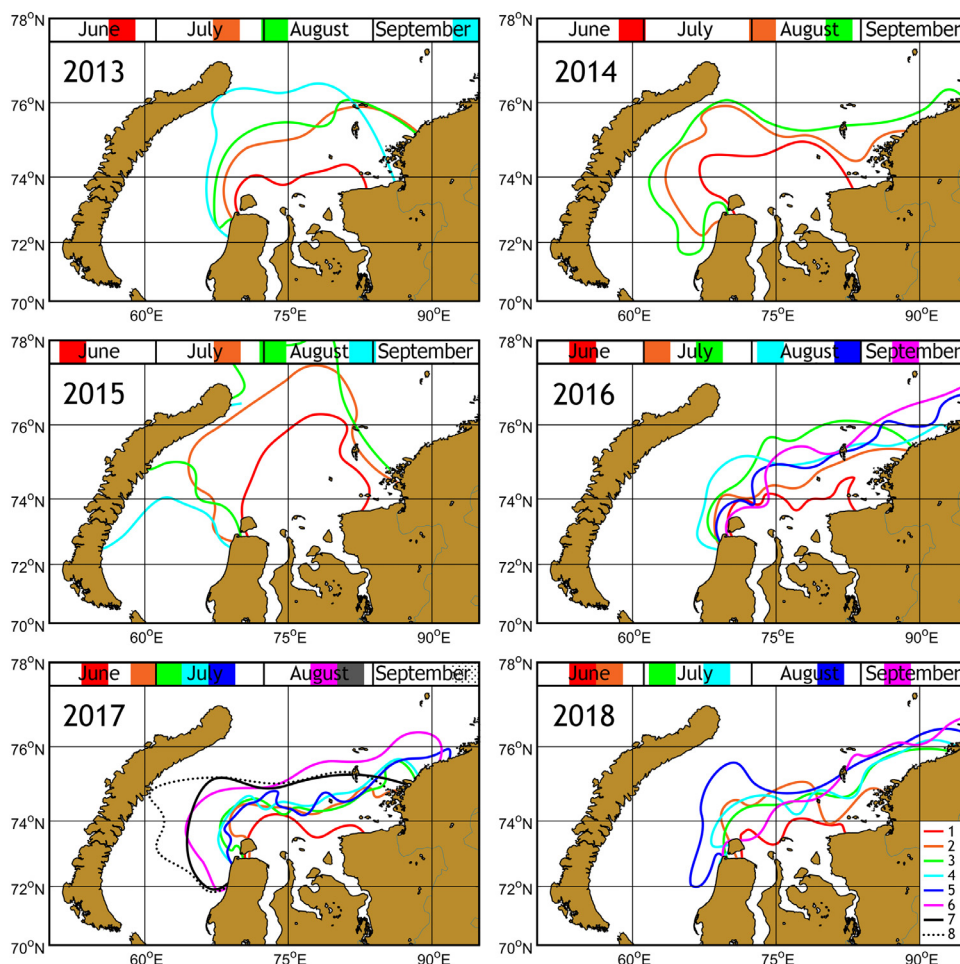


Figure 3 The boundaries positions of the surface desalinated layer at different instants of time, determined by isolines $a_s(443) = 0.3 \text{ m}^{-1}$. Coloured markers in the upper part of the maps indicate the averaging time interval over which the corresponding contours are plotted.

after this period it acquired features of both the central and western ones. This feature has led to the penetration of desalinated continental river runoff waters into the bays of Novaya Zemlya (Glukhovets and Goldin, 2019). Interestingly, the type of SDL distribution may vary during the season. An example comes from the SDL distribution in 2017: the distribution followed the eastern type till the middle of August, but, it had switched to the western type by the end of September. Another example comes from the 2018 season: the properties of the western type were added to the properties of the eastern one over a short period of time (Figure 3).

The type of SDL propagation and the transformation of its boundaries are largely determined by the wind regime (Zatsepin et al., 2015, 2017; Zavalov et al., 2015). To qualitatively demonstrate the effect of wind on the SDL transport, we made time diagrams of wind stress. We calculated the wind stress values by the formulas suggested in (Wu, 1982). For that, we used an air density value of 1.25 kg/m^3 that is characteristic of the region. Weekly averaging was implemented to process the calculations corresponding to the averaging interval of satellite data. The values are calculated for the central part of the Kara Sea and they are

limited to $72\text{--}76^\circ\text{N}$ and $65\text{--}85^\circ\text{E}$. The diagrams are depicted in Figure 4. The direction of the wind is shown in colours.

The diagrams presented in Figure 4 explain well the features of the SDL distribution and the transformation of its boundaries (Figure 3). In 2013, moderate winds were observed during the entire season, mainly from the north and northeast directions. However, these winds had little effect on the SDL distribution. In this case, the central type of propagation was due to river discharge and the Coriolis Effect. Only at the end of September, there was a significant increase in wind stress from the northeast direction, recorded to 0.05 N/m^2 . According to (Zatsepin et al., 2010b), the SDL wind transport in the Kara Sea is directed at $40\text{--}50^\circ$ to the right of the wind direction. This corresponds to the direction of the wind transfer of water to the west. As a result, the SDL boundary (isoline 4) reached the eastern coast of Novaya Zemlya by the end of September (Figure 3).

River discharge and the Coriolis Effect are always present, but their influence dominates only during weak winds. The distribution recorded from June to August 2013 can be considered to be the basic one. Wind exposure leads to various transformations of the SDL boundaries, which were observed in 2014–2018.

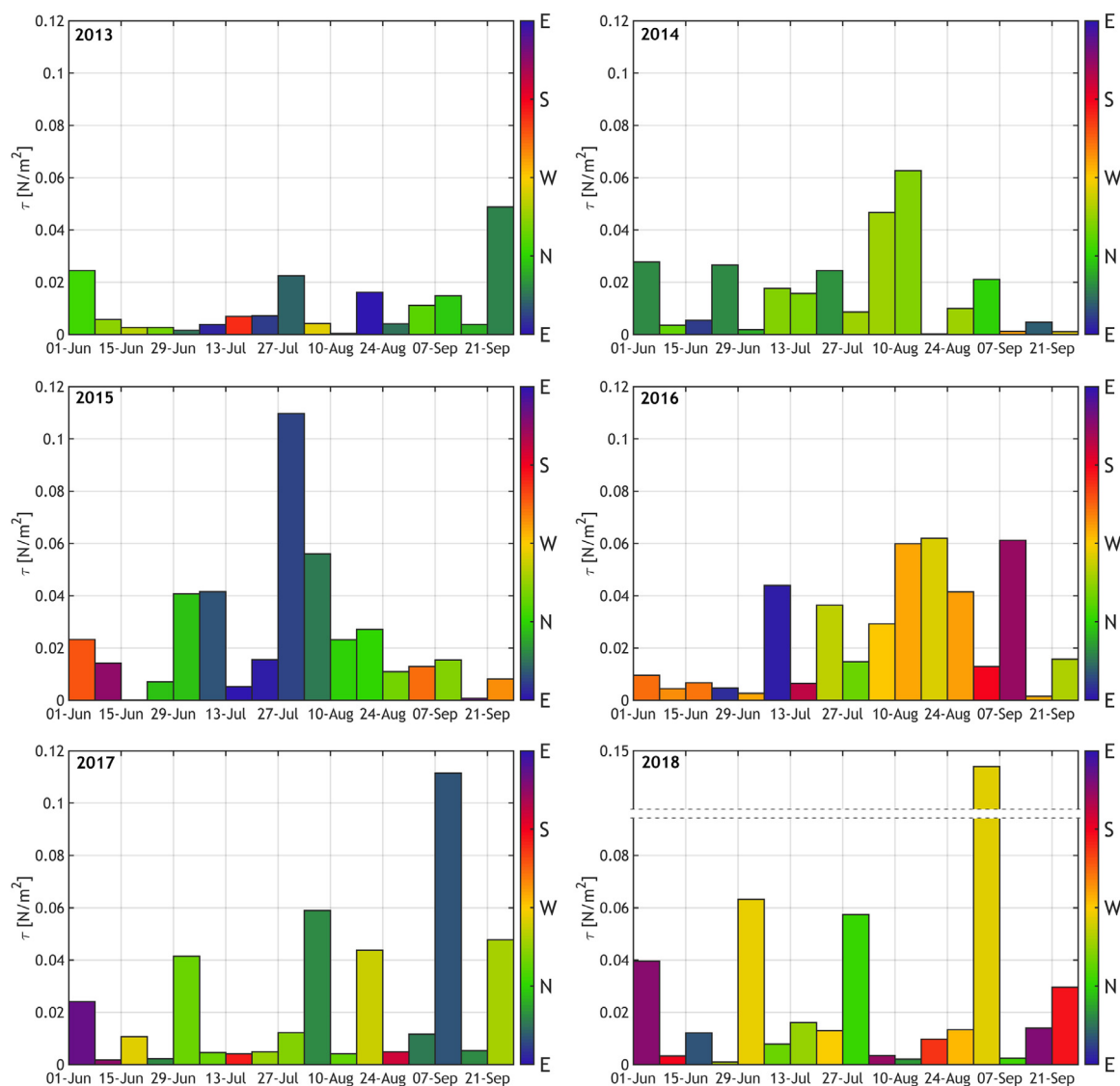


Figure 4 Time diagrams of the wind stress for the central part of the Kara Sea. The averaging interval is 7 days. Wind direction is shown in colours.

Let us consider the main features of the transformation of SDL boundaries under the influence of wind in 2014–2018. The north-northwest wind that blew in mid-August 2014 (Figure 4) caused an SDL shift to the southwest by the end of August (isoline 3 in Figure 3), which led to the western pattern. In 2015, a strong ($\tau > 0.1 \text{ N/m}^2$) east wind at the end of July led to a rapid transfer of the SDL boundary in the northwest direction (contours 2 and 3 in Figure 3). During the second week of July 2016, the eastern wind caused the SDL boundary to move northwest (contours 2 and 3 in Figure 3). Subsequently, stable western winds formed the eastern type of transport (contours 4 and 5 in Figure 3). In the second week of September, the southeast wind moved the SDL boundary to the north (contours 5 and 6). The change in the type of SDL propagation from east to west in 2017 is explained by strong ($\tau > 0.1 \text{ N/m}^2$) northeast winds in the second week of September, which caused the SDL border to shift westward to the shores of Novaya Zemlya by the end of September (isoline 8). The strongest weekly

averaged wind for the considered period was recorded in the first week of September 2018 ($\tau \sim 0.14 \text{ N/m}^2$). This wind led to the displacement of the western part of the SDL, which occupied the central part of the sea (contour 5) to the east (contour 6).

The relations obtained in Ekman (1905) allow us to estimate the magnitude of the SDL displacement under the influence of wind. In the calculations, a characteristic value of $\tau = 0.1 \text{ N/m}^2$ was used (Figure 4), which corresponds to the wind speed of 8 m/s. The thickness of the SDL layer was taken as 10 m (Zatsepin et al., 2010b), the density of water was 1015 kg/m^3 (Zatsepin et al., 2010a, 2010b), and the average latitude was 75°N . In this case, the average velocity of a purely drift current of the SDL will be equal to 7 cm/s, which corresponds to a shift of the layer boundaries by 6 km per day and approximately 40 km per week. The result of the assessment is consistent with Figures 3 and 4.

In addition to the distribution type, one can note the difference in the areas occupied by SDL in different years. This

variability takes place due to the difference in the Ob and Yenisei River runoff. For example, in 2015, the largest runoff volume recorded for the studied period (~850 km³ from May 1 to September 30) led to the largest SDL area. The minimum runoff volume was recorded in 2013 (~640 km³ from May 1 to September 30), which corresponds to a significantly smaller area (Figure 3). A detailed analysis of this effect requires special studies.

5. Conclusions

This paper investigates the dynamics of the SDL distribution processes as it occurs in the Kara Sea. The shipboard data collection took place in the summer and autumn seasons between 2013 and 2018. We also used MODIS ocean colour scanner data. Formulating a criterion to determine the distribution boundary of the desalinated layer from satellite data, these data are compared with the data of simultaneous shipboard measurements. These measurements were made in the indicated years during six cruises of the SIO RAS to the Kara Sea. The positions of the boundaries of the frontal zones defined by both types of data are in good agreement.

As we discussed above, extensive cloud cover does not allow to draw maps with weekly averaging that are good enough to determine the SDL boundaries. The cloud cover over the Kara Sea significantly varied in the considered years. For instance, in 2014, it was possible to draw only three maps with weekly averaging; while in 2017, satellite data provided the opportunity to draw eight contours.

Comparison of the flow-through measuring system data obtained at the moments of crossing the SDL boundaries with the satellite maps allowed us to give a fairly rigorous justification for the use of satellite data. The satellite maps of the CDOM absorption coefficient were drawn with the help of the regional algorithm for the Kara Sea. Our analysis shows that the values of $a_g(443) = 0.25\text{--}0.5\text{ m}^{-1}$ can be taken as a criterion for the SDL boundary. This criterion corresponds to salinity values of about 25 PSU. The use of the interval of values as a criterion arises due to the non-monotonic spatial distribution of salinity in the frontal zones area. The criterion is obtained on the basis of an analysis of shipboard and satellite data for a six-year period, characterized by changing conditions over a wide range. This gives grounds for applying this criterion in other years, for example, for the entire operation period of the MODIS ocean colour scanner.

We also recorded significant interannual variability in the SDL distribution types. The central type of SDL distribution was seen in 2013 and at the beginning of 2015; the eastern type – in 2016 and 2018; the western type was formed by the end of 2017. Sometimes mixed distributions were observed during the season: in 2014, the type of SDL distribution had eastern and western features; in 2015, the features of the western type were subsequently added to the central one, formed at the beginning of the season.

The type of SDL distribution is determined by three main factors. The river runoff determines the area of the desalinated layer, the Coriolis Effect leads to a shift of this layer to the east, and the diversity of the wind intensity and direction determines the variations of this shift. In 2013–

2018, the type of SDL propagation was determined by the wind in most cases. During the years of weak winds in different directions, for example, in 2013, the central type of distribution was observed. The river runoff and the Coriolis Effect were the factors that determined this type of distribution.

Our results can be of value in a number of related fields and issues. For example, as the values of light absorption in SDL are significantly higher than in surrounding seawaters (Burenkov et al., 2010; Granskog et al., 2015), its configuration must be taken into account in modelling calculations. For instance, when calculating the integral solar energy, that enters the water column during the ice-free season. The results can also be used in the analysis of the bio-productivity of the Kara Sea. Finally, based on the obtained data, one can perform short-term forecasting of the desalinated layer transformation, which will prove useful in planning expeditionary works (Flint, 2010).

Acknowledgements

Thematic processing and analysis of shipboard data were carried out as part of the state assignment of SIO RAS (theme No. 0149-2019-0003). The drawing of satellite maps and their comparison with shipboard data was funded by RFBR according to the research project No. 18-35-00525. The grant is provided through the Shirshov Institute of Oceanology of the Russian Academy of Sciences. The authors are grateful to S.V. Sheberstov for the help in satellite data processing, as well as to A.V. Shatravin and E.E. Khimchenko for their help in conducting shipboard measurements and to A.A. Akhmanov for the priceless support in the field of linguistics.

References

- Amon, R.M.W., 2003. The role of dissolved organic matter for the organic carbon cycle in the Arctic Ocean. In: Stein, R., MacDonald, R. (Eds.), *The Organic Carbon Cycle in the Arctic Ocean*. Springer, Berlin, 83–99.
- Burenkov, V.I., Goldin, Y.A., Artem'ev, V.A., Sheberstov, S.V., 2010. Optical characteristics of the Kara Sea derived from shipborne and satellite data. *Oceanology* 50 (5), 675–687, <https://doi.org/10.1134/S000143701005005X>.
- Coble, P.G., 2007. Marine optical biogeochemistry: the chemistry of ocean color. *Chem. Rev.* 107 (2), 402–418, <https://doi.org/10.1021/cr050350>.
- Dee, D.P., Uppala, S.M., Simmons, A.J., Berrisford, P., Poli, P., Kobayashi, S., Andrae, U., Balmaseda, M.A., Balsamo, G., Bauer, D.P., Bechtold, P., 2011. The ERA-Interim reanalysis: configuration and performance of the data assimilation system. *Q. J. R. Meteor. Soc.* 137 (656), 553–597, <https://doi.org/10.1002/qj.828>.
- Demidov, A.B., Gagarin, V.I., Vorobieva, O.V., Makkaveev, P.N., Artemiev, V.A., Khrapko, A.N., Grigoriev, A.V., Sheberstov, S.V., 2018. Spatial and vertical variability of primary production in the Kara Sea in July and August 2016: the influence of the river plume and subsurface chlorophyll maxima. *Polar Biol* 41 (3), 563–578, <https://doi.org/10.1007/s00300-017-2217-x>.
- Drozhdova, A.N., Patsaeva, S.V., Khundzhua, D.A., 2017. Fluorescence of dissolved organic matter as a marker for distribution of desalinated waters in the Kara Sea and bays of No-

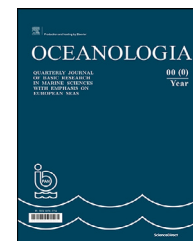
- vaya Zemlya archipelago. *Oceanology* 57 (1), 41–47, <https://doi.org/10.1134/S0001437017010039>.
- Ekman, V.W., 1905. On the influence of the earth's rotation on ocean-currents. *Ark. Mat. Astron. Fys.* 2 (11), 53 pp.
- Fichot, C.G., Kaiser, K., Hooker, S.B., Amon, R.M.W., Babin, M., Bélanger, S., Walker, S., Benner, R., 2013. Pan-Arctic distributions of continental runoff in the Arctic Ocean. *Nature Sci. Rep.* 3. art. no. 1053, 6 pp., <https://doi.org/10.1038/srep01053>.
- Flint, M.V., 2010. Cruise 54th of the research vessel Akademik Mstislav Keldysh in the Kara Sea. *Oceanology* 50 (5), 637–642, <https://doi.org/10.1134/S0001437010050012>.
- Fofonoff, N.P., Millard Jr, R.C., 1983. Algorithms for the computation of fundamental properties of seawater. UNESCO Tech. Pap. Mar. Sci. 44 UNESCO, Paris, 53 pp.
- Glukhovets, D.I., Goldin, Y.A., 2014. Study of bio-optical characteristics of waters of the Kara Sea by using data of satellite and ship measurements. *Curr. Probl. Remote Sens. Earth Space* 11 (4), 346–350, <http://jr.rse.cosmos.ru/article.aspx?id=1359&lang=eng>.
- Glukhovets, D.I., Goldin, Y.A., 2018. Research of the relationship between salinity and yellow substance fluorescence in the Kara Sea. *Fundam. Prikl. Gidrofiz.* 11 (3), 34–39, <https://doi.org/10.7868/S2073667318030048>.
- Glukhovets, D.I., Goldin, Y.A., 2019. Surface layer desalination of the bays on the east coast of Novaya Zemlya identified by shipboard and satellite data. *Oceanologia* 61 (1), 68–77, <https://doi.org/10.1016/j.oceano.2018.07.001>.
- Goldin, Y.A., Shatravin, A.V., Levchenko, V.A., Ventskut, Y.I., Gureev, B.A., Kopelevich, O.V., 2015. Analysis of spatial variability of fluorescent intensity of seawater in western part of the Black Sea. *Fundam. Prikl. Gidrofiz.* 7 (1), 11–20.
- Goncalves-Araujo, R., Granskog, M.A., Bracher, A., Azetsu-Scott, K., Dodd, P.A., Stedmon, C.A., 2016. Using fluorescent dissolved organic matter to trace and distinguish the origin of Arctic surface waters. *Nature Sci. Rep.* 6. art. no. 33978, 12 pp., <https://doi.org/10.1038/srep33978>.
- Goncalves-Araujo, R., Stedmon, C.A., Heim, B., Dubinenkov, I., Kraberg, A., Moiseev, D., Bracher, A., 2015. From fresh to marine waters: characterization and fate of dissolved organic matter in the Lena River Delta region. *Siberia.Front. Mar. Sci.* 2. art. no. 108, 12 pp., <https://doi.org/10.3389/fmars.2015.00108>.
- Granskog, M.A., Pavlov, A.K., Sagan, S., Kowalczyk, P., Raczowska, A., Stedmon, C.A., 2015. Effect of sea-ice melt on inherent optical properties and vertical distribution of solar radiant heating in Arctic surface waters. *J. Geophys. Res.* 120 (10), 7028–7039, <http://dx.doi.org/10.1002/2015JC011087>.
- Kowalczyk, P., Sagan, S., Makarewicz, A., Meler, J., Borzycka, K., Zabłocka, M., Zdun, A., Konik, M., Darecki, M., Granskog, M.A., Pavlov, A.K., 2019. Bio-optical Properties of Surface Waters in the Atlantic Water Inflow Region off Spitsbergen (Arctic Ocean). *J. Geophys. Res.* 124 (3), 1964–1987, <https://doi.org/10.1029/2018JC014529>.
- Kubryakov, A., Stanichny, S., Zatsepin, A., 2016. River plume dynamics in the Kara Sea from altimetry-based lagrangian model, satellite salinity and chlorophyll data. *Remote Sens. Environ.* 176, 177–187, <https://doi.org/10.1016/j.rse.2016.01.020>.
- Kuznetsova, O.A., Kopelevich, O.V., Sheberstov, S.V., Burenkov, V.I., Mosharov, S.A., Demidov, A.B., 2013. Assessment of chlorophyll concentration in the Kara Sea based on the data of satellite scanner MODIS–AQUA. *Curr. Probl. Remote Sens. Earth Space* 5, 21–31.
- Matsuoka, A., Boss, E., Babin, M., Karp-Boss, L., Hafez, M., Chekalyuk, A., Proctor, C.W., Werdell, P.J., Bricaud, A., 2017. Pan-Arctic optical characteristics of colored dissolved organic matter: tracing dissolved organic carbon in changing Arctic waters using satellite ocean color data. *Remote Sens. Environ.* 200, 89–101, <https://doi.org/10.1016/j.rse.2017.08.009>.
- Moretskii, V.N., 1985. Distribution and dynamics of desalinated waters of the Kara Sea. *Tr. Arkt. Antarkt. Nauchno Issled. Inst.* 389, 33–35, (in Russian), <https://www.scopus.com/record/display.uri?eid=2-s2.0-0039119086&origin=inward>.
- Osadchiev, A.A., Izhitskiy, A.S., Zavalov, P.O., Kremenetskiy, V.V., Polukhin, A.A., Pelevin, V.V., Toktamysova, Z.M., 2017. Structure of the buoyant plume formed by Ob and Yenisei river discharge in the southern part of the Kara Sea during summer and autumn. *J. Geophys. Res.* 122 (7), 5916–5935, <https://doi.org/10.1002/2016JC012603>.
- Osadchiev, A.A., Asadulin, E.E., Miroshnikov, A.Y., Zavalov, I.B., Dubinina, E.O., Belyakova, P.A., 2019. Bottom Sediments Reveal inter-Annual Variability of interaction between the Ob and Yenisei plumes in the Kara Sea. *Nature Sci. Rep.* 9 (1), 11 pp., <https://doi.org/10.1038/s41598-019-55242-3>.
- Pasternak, A.F., Drits, A.V., Abyzova, G.A., Semenova, T.N., Sergeeva, V.M., Flint, M.V., 2015. Feeding and distribution of zooplankton in the desalinated “lens” in the Kara Sea: Impact of the vertical salinity gradient. *Oceanology* 55 (6), 863–870, <https://doi.org/10.1134/S0001437015060132>.
- Pelevin, V.V., Zavjalov, P.O., Belyaev, N.A., Kononov, B.V., Kravchishina, M.D., Mosharov, S.A., 2017. Spatial variability of concentrations of chlorophyll *a*, dissolved organic matter and suspended particles in the surface layer of the Kara Sea in September 2011 from lidar data. *Oceanology* 57 (1), 165–173, <https://doi.org/10.1134/S0001437017010131>.
- Pivovarov, S.V., 2000. Chemical Oceanography of the Arctic Seas of Russia. *Gidrometeoizdat, St. Petersburg*, 88 pp., (in Russian).
- Pugach, S.P., Pipko, I.I., Shakhova, N.E., Shirshin, E.A., Perminova, I.V., Gustafsson, Ö., Bondur, V.G., Ruban, A.S., Semiletov, I.P., 2018. Dissolved organic matter and its optical characteristics in the Laptev and East Siberian seas: spatial distribution and interannual variability (2003–2011). *Ocean Sci* 14 (1), 87–103, <https://doi.org/10.5194/os-14-87-2018>.
- Reynolds, R.A., Stramski, D., 2019. Optical characterization of marine phytoplankton assemblages within surface waters of the western Arctic Ocean. *Limnol. Oceanogr.* 64 (6), 2478–2496, <https://doi.org/10.1002/lno.11199>.
- Rusanov, V.P., Vasil'ev, A.N., 1976. Distribution of River Waters in the Kara Sea according to Hydrochemical Determination Data. *Tr. Arkt. Antarkt. Nauchno Issled. Inst.* 323, 188–196. (in Russian) <https://www.scopus.com/record/display.uri?eid=2-s2.0-0005590747&origin=inward>.
- Sheberstov, S.V., 2015. System for batch processing of oceanographic satellite data. *Curr. Probl. Remote Sens. Earth Space* 12 (6), 154–161, (in Russian), http://d33.infospace.ru/d33_conf/sb2015t6/154-161.pdf.
- Sukhanova, I.N., Flint, M.V., Sergeeva, V.M., 2012. Phytoplankton of the surface desalted lens of the Kara Sea. *Oceanology* 52 (5), 635–645, <https://doi.org/10.1134/S0001437012050165>.
- Vazyulya, S.V., Kopelevich, O.V., Sheberstov, S.V., Artemiev, V.A., 2014. Satellite estimation of the coefficients of CDOM absorption and diffuse attenuation in the White and Kara seas. *Curr. Probl. Remote Sens. Earth Space* 11 (4), 31–41, <http://jr.rse.cosmos.ru/article.aspx?id=1348&lang=eng>.
- Wu, J., 1982. Wind-stress coefficients over sea surface from breeze to hurricane. *J. Geophys. Res.* 87 (C12), 9704–9706, <https://doi.org/10.1029/JC087iC12p09704>.
- Zatsepin, A.G., Kremenetskiy, V.V., Kubryakov, A.A., Stanichny, S.V., Soloviev, D.M., 2015. Propagation and transformation of waters of the surface desalinated layer in the Kara Sea. *Oceanology* 55 (4), 450–460, <https://doi.org/10.1134/S0001437015040153>.
- Zatsepin, A.G., Morozov, E.G., Paka, V.T., Demidov, A.N., Kondrashov, A.A., Korzh, A.O., Kremenetskiy, V.V., Poyarkov, S.G., Soloviev, D.M., 2010a. Circulation in the southwestern part of the Kara Sea in September 2007. *Oceanology* 50 (5), 643–656, <https://doi.org/10.1134/S0001437010050024>.

Zatsepin, A.G., Zavialov, P.O., Baranov, V.I., Kremenetskiy, V.V., Nedospasov, A.A., Poyarkov, S.G., Ocherednik, V.V., 2017. On the mechanism of wind-induced transformation of a river runoff water lens in the Kara Sea. *Oceanology* 57 (1), 1–7, <https://doi.org/10.1134/S0001437017010222>.

Zatsepin, A.G., Zavialov, P.O., Kremenetskiy, V.V., Poyarkov, S.G., Soloviev, D.M., 2010b. The upper desalinated layer in the Kara Sea. *Oceanology* 50 (5), 657–667, <https://doi.org/10.1134/S0001437010050036>.

Zavialov, P.O., Izhitskiy, A.S., Osadchiev, A.A., Pelevin, V.V., Grabovskiy, A.B., 2015. The structure of thermohaline and bio-optical fields in the surface layer of the Kara Sea in September 2011. *Oceanology* 55 (4), 461–471, <https://doi.org/10.1134/S0001437015040177>.

Zhurbas, N.V., Zavialov, P.O., 2015. Effect of stratification on wind drift of river runoff in the Kara Sea. *Oceanology* 55 (6), 827–831, <https://doi.org/10.1134/S0001437015060223>.



ORIGINAL RESEARCH ARTICLE

Limitation of lignin derivatives as biomarkers of land derived organic matter in the coastal marine sediments

Janusz Pempkowiak*

Marine Chemistry Department, Institute of Oceanology, Polish Academy of Sciences, Sopot, Poland

Received 5 April 2020; accepted 21 April 2020

Available online 20 May 2020

KEYWORDS

Lignin phenols;
Stable carbon isotopes;
 $\delta^{13}\text{C}$;
End members;
Nonlinear analyses;
Gdańsk Bay;
Southern Baltic

Summary Lignin oxidation products (vanillyl, syringil and cummaryl phenols), and $\delta^{13}\text{C}$ were measured in a variety of land and marine samples collected in Inner Puck Bay – dominated by marine vascular plants, small river run-off, and shallow bottom, and in Gdańsk Bay – characterized by large river run-off, small marine vascular plants population, and the average depth exceeding euphotic zone. Both study areas are parts of the Gdańsk Basin, Southern Baltic. Typical $\delta^{13}\text{C}$ values ($\delta^{13}\text{C} = -28\text{‰}$) and both composition and concentrations of lignin phenols were measured in samples originating from land. Small, yet easily measurable amounts of lignin phenols were found in marine vascular plants biomass ($\Sigma 8 = 90 \mu\text{g}/100 \text{mg}$ organic matter). The biomass was characterized by exceptionally high $\delta^{13}\text{C}$ values (-12‰). No lignin phenols and typical $\delta^{13}\text{C}$ values (-22‰) were measured in marine phytoplankton biomass. $\delta^{13}\text{C}$ and both composition and content of lignin phenols in organic matter of surface sediments collected in the study area fall in the range marked by the end members. The proportion of land derived organic matter calculated using lignin phenols, or $\delta^{13}\text{C}$ in Gdańsk Bay were comparable, while in Puck Bay they differed substantially. It was concluded that a) in areas with substantial bottom coverage with vascular plants the two end members approach, usually employed to establish the contribution of organic matter sources, is insufficient, b) organic matter originating from three sources: riverine, phytoplankton, and vascular plants contribute to sedimentary organic matter in Puck Bay with the respective proportion 30:40:30.

* Corresponding author at: Marine Chemistry Department, Institute of Oceanology, Polish Academy of Sciences, Powstańców Warszawy 55, 81–712 Sopot, Poland.

E-mail address: pempa@iopan.gda.pl

Peer review under the responsibility of the Institute of Oceanology of the Polish Academy of Sciences.



Production and hosting by Elsevier

<https://doi.org/10.1016/j.oceano.2020.04.004>

0078-3234/© 2020 Institute of Oceanology of the Polish Academy of Sciences. Production and hosting by Elsevier B.V. This is an open access article under the CC BY-NC-ND license (<http://creativecommons.org/licenses/by-nc-nd/4.0/>).

© 2020 Institute of Oceanology of the Polish Academy of Sciences. Production and hosting by Elsevier B.V. This is an open access article under the CC BY-NC-ND license (<http://creativecommons.org/licenses/by-nc-nd/4.0/>).

1. Introduction

Organic matter content in marine sediments most often is below 15%. Despite this organic matter is regarded as an important component of sediments. Both contribution to carbon cycling in the earth crust and the influence on physical, biological and chemical properties of sediments are mentioned in this respect (Bianchi et al., 2018; Hedges, 1992).

Amounts and properties of marine sedimentary organic matter depend on the proportion of allochthonous-land derived organic matter, since it differs greatly from autochthonous-marine biota produced organic matter (Jex et al., 2014). The former enters the marine environment mainly with the river run-off, although aerial transport may be of importance in case of specific substances (Chester, 2003; Cragg et al., 2020). Riverine organic matter load is generally composed of organic and organic-mineral, dissolved and particulate matter, washed out from the soil and, to a much smaller extent, from aquatic plants debris. Therefore, it reflects the properties of soil organic matter that is strongly influenced by the regional vegetation and climate (Hedges, 1992; Sun et al., 2017). This organic matter fraction is also relatively biochemically stable.

It has been well documented that terrestrial organic matter makes up a large proportion of sedimentary organic matter in the marine shelf areas (Gordon and Goni, 2003; Hedges et al., 1982; Hedges and van Geen, 1982; Miltner et al., 2005; Winogradow and et al., 2019). For example, in the Baltic Sea it constitutes up to 70 per cent of sedimentary organic matter (Miltner and Emeis, 2000; Pempkowiak and Pocklington, 1983; Staniszewski et al., 2001; Winogradow and Pempkowiak, 2014). This is because most of the terrestrial organic matter transported into the sea is deposited near the mouth of rivers and adjoining areas on the shelf (Gough et al., 1993; Hedges et al., 1988; Ji et al., 2020). Thus, the proportion of terrestrial organic matter in marine sediments decreases with increasing distance from land (Hedges et al., 1988). In the Baltic, most of the riverine organic matter load is transported to depositional basins (Miltner and Emeis, 2001; Pempkowiak and Pocklington, 1983; Staniszewski et al., 2001).

Identifying organic matter origin in sediments of a particular basin is essential in constructing material fluxes and budgets and understanding sedimentary processes. Elemental composition, stable carbon and nitrogen isotopes and chemical markers (chemical compounds that are lacking in either terrestrial or marine environments) have been used in determining the proportion of terrestrial organic matter in sediments (Bordovsky, 1965; Gardner and Menzel, 1974; Hedges and Ertel, 1982; Jex et al., 2014; Pempkowiak, 1983; Staniszewski et al., 2001). A typical component of terrestrial organic matter, believed to be lacking in marine plants, and therefore frequently utilized as a marker,

is lignin (Hautala et al., 1997; Hedges et al., 1988; Miltner and Emeis, 2001; Pradhan et al., 2014).

Lignin bio-macromolecules are high molecular weight phenolic polymers. They are major constituents of vascular plant cell walls (Merdy et al., 2002; Sederoff et al., 1999; Ye et al., 2001). The chemical structure of lignin is troublesome for analysis, owing to difficulties in isolating and de-polymerizing. We do know, however, that they are polyphenols consisting of monomers with a characteristic isopropyl benzoic carbon structure (Donaldson, 2001). Isopropyl benzoic monomers, usually contain methoxy groups bound to aromatic rings (Hedges and Ertel, 1982; Hedges and Mann, 1979).

Lignin polymers in plant tissues, soils, and sediments are not a subject to direct chemical analysis without prior isolation and derivatisation. Samples containing lignin are first subjected to chemical degradation, in order to release small molecules. Then the degradation products are extracted from the reaction mixture and quantified, following derivatization, by a variety of chromatographic techniques (Hedges and Ertel, 1982; Hedges et al., 1982; Staniszewski et al., 2001). When cupric oxide is used as the oxidant the predominant products of lignin oxidation are phenolic aldehydes and phenolic acids. Most often 8 major lignin-derived CuO oxidation products are quantified (Table 1). Chemical structure of the degradation products is presented in Figure 1. These belong to the following groups of phenols: syringyl (S – 3 compounds), vanillin (V, 3), and cynammyl (C, 2) (Farella et al., 2001; Hedges and Ertel, 1982; Hedges et al., 1982; Hu et al., 1999; Miltner and Emeis, 2001; Pempkowiak and Pocklington, 1983; Staniszewski et al., 2001; Wilson et al., 1985). The sum of the 8 lignin oxidation products recalculated to 100 mg of organic material ($\Sigma 8$), or/and to 10 g of sample (Δ) has been used to characterize yield of lignin phenols (Hedges and Mann, 1979). The lignin burden in mineral sedimentary material may be characterized by ' Δ ' – the sum of the 8 lignin phenols recalculated to 10 g of organic matter free material (Pempkowiak et al., 2006).

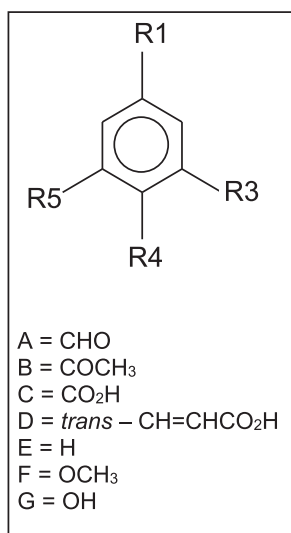
Ratios of specific phenolic aldehydes and phenolic acids may be used to characterize sources of lignin in sedimentary organic matter. The most often applied indexes include: the ratio of syringyl to vanillyl phenols (S/V) – an indicator of angiosperms plants, the ratio of cynammyl to vanillyl phenols (C/V) – an indicator of nonwoody plant tissues, the ratio of vanillic acid to vanillyl aldehyde (Ad/Al)_v – an indicator of diagenetic changes in lignin (Hedges et al., 1982; Miltner et al., 2005). The ratio of methoxyphenols to vanillin phenols (H/V), an indicator of aquatic plant contribution (Wilson et al., 1985), is seldom used.

Lignin phenols are frequently used as markers of land derived material in the aquatic environment in general (Bianchi et al., 1997; Cragg et al 2020; Farella et al., 2001; Hautala et al., 1997; Hedges et al., 1988), and in the coastal marine environment in particular (Gardner and Men-

Table 1 Names and occurrence of lignin degradation products in various plant classes.

| No. | Compound | Name of group | Plant sources* | | | |
|-----|-----------------------|---------------|----------------|---|---|---|
| | | | G | g | A | a |
| 1 | m-hydroxybenzoic acid | H | + | + | | + |
| 2 | p-hydroxybenzaldehyde | | + | + | | + |
| 3 | p-hydroxybenzoic acid | | + | + | | + |
| 4 | vanillin | V | + | + | + | + |
| 5 | acetovanillone | | + | + | + | + |
| 6 | vanillic acid | | + | + | + | + |
| 7 | syringaldehyde | S | | | + | + |
| 8 | syringic acid | | | | + | + |
| 9 | acetosiringone | | | | + | + |
| 10 | p-cumaric acid | C | | + | | + |
| 11 | ferulic acid | | | + | | + |

* Plant sources: G – gymnosperm woods, g – nonwoody gymnosperm tissues, A – angiosperm wood, a – nonwoody angiosperm tissues.



| Typical oxidation products of lignin | Structure | | | |
|--------------------------------------|----------------|----------------|----------------|----------------|
| | R ₁ | R ₅ | R ₃ | R ₄ |
| benzoic acid | C | E | E | E |
| p-hydroxybenzaldehyde | A | E | E | G |
| vanillin | A | E | F | G |
| m-hydroxybenzoic acid | C | E | G | E |
| p-hydroxyacetophenone | B | E | F | G |
| p-hydroxybenzoic acid | C | E | E | G |
| syringaldehyde | A | F | F | G |
| vanillic acid | C | E | F | G |
| acetovanillone | B | F | F | G |
| syringic acid | C | F | F | G |
| p-cumaric acid | D | E | E | G |
| ferulic acid | D | E | F | G |

Figure 1 The chemical structure of lignin phenols.

zel, 1974; Gouth et al., 1993; Hedges et al., 1982; Miltner and Emeis, 1999; Pradhan et al., 2014; Staniszewski et al., 2001). The assumption is that aquatic plants do not comprise lignin units, and therefore organic matter derived from them may dilute lignin phenols concentration (thus influencing both $\Sigma 8$ and Δ) whereas the composition of lignin oxidation products remains unaltered (Gardner and Menzel, 1974; Hedges and Mann, 1979; Merdy et al., 2002). To quantify the proportion of allochthonous organic matter in marine sediments the so-called ‘end members approach’ is adopted (Hedges and Mann, 1979; Thorton and MsManus, 1994). Concentrations of lignin oxidation products (either Σ or Δ) in land-derived (LL), ‘pure’ marine (MM), and actual marine (ML) samples, are combined into a simple formula for the purpose of calculating proportion of allochthonous organic matter component – L (%), in a given sample:

$$L(\%) = \frac{LL - ML}{LL - MM} \cdot 100.$$

Since an assumption was adapted that no lignin phenols are yielded from ‘pure’ marine samples the equation has

been abbreviated to:

$$L(\%) = \frac{LL - ML}{LL} \cdot 100.$$

Based on this approach land derived organic matter was estimated to comprise a substantial proportion of marine sedimentary organic matter: 30–70% in the Baltic Sea (Bianchi et al., 1997; Miltner and Emeis, 1999, 2001; Pempkowiak and Pocklington, 1983; Staniszewski et al., 2001; Winogradow and Pempkowiak 2018; Winogradow et al., 2019), and 10–90% in the Columbia River estuary (Hedges, 1992), Amazon River estuary (Sun et al., 2017) and off India (Pradhan et al., 2014). However, the occurrence of typical lignin derivatives was reported in oxidation products of material originating from marine vascular plants (Cragg et al., 2020; Staniszewski, 2005). Therefore, the applicability of such an approach should be thoroughly investigated.

Estuarine ecosystems are composed of relatively heterogeneous biologically diverse subsystems: water column, mud and sand flats, bivalve reefs and beds, seaweeds and seagrass meadows that are connected by mobile animals

and currents. Together the systems form one of the most productive natural systems in the biosphere. These systems function as traps for all kinds of suspended and dissolved materials, nursery grounds for organisms including many commercially important species and recreational zones for humans. They are also complex systems that exchange matter and energy with terrestrial and marine ecosystems. Unlike seaweeds, submerged hydrophytes (vascular plants, seagrasses) do actually root themselves in the sediments at the bottom of the ocean floor, and they have leaves and flowers, just like terrestrial plants. There are four different groups of seagrasses: Zosteraceae, Hydrocharitaceae, Posidoniaceae and Cymodoceaceae, representing 72 different species.

Seagrass is often characterized as the ‘lungs of the ocean’ because of its capacity for absorbing carbon dioxide and generating oxygen. One square meter of seagrass can generate 10 liters of oxygen every day. Seagrasses tend to live in shallow water about 1 to 3 meters deep, but some can grow at depths of 58 meters (Jørgensen and Fath, 2008). The seafloor area covered by seagrass worldwide is reported in the range of 0.3–0.6 10^6 km² (Duarte and Chiscano, 1999). On the average the seagrass biomass is equal to 460 g dry weight/m², while net production is equal to 2.7 g DW/m² day – more than boreal forest (2.4), and much more than phytoplankton (0.3) (Duarte, 1991). About 25% of the net primary production is exported to beach ecosystems, while 55% is mineralized soon after the plants’ death (Duarte, 2010; Duarte and Cebrián, 1996; Duarte et al., 2005; Haddad and Martens, 1987; Jørgensen and Fath, 2008). It is estimated that 83 g/m² are buried in sediments (Duarte and Cebrián, 1996) – a subject to further mineralization as no accumulation of carbon in shallow, coarse-grained sediments takes place (Winogradow and Pempkowiak, 2019).

The motivation for the survey reported here was twofold. For one thing, it was investigating the occurrence of lignin phenols in the oxidation products of ‘pure’ marine samples: vascular plants, algae, mussels soft tissue. Moreover, the assessment was carried out to what extent this occurrence may affect the land derived organic matter proportion, calculated basing on lignin oxidation products, in actual marine sediments. Stable carbon isotopes ratio $\delta^{13}\text{C}$ was applied to verify the conclusion of the study.

The results indicate that typical lignin phenols do occur at small concentrations in the oxidation products of marine vascular plants. Moreover, their contribution must be taken into account in areas with large loads of organic matter originating from marine vascular plants and a small supply of terrestrial organic matter. A simple three-member approach was applied to establish a proportion of organic matter originating from three different sources in such a system. The sources considered were terrestrial, marine vascular plants, and marine phytoplankton.

2. Study area

The study was performed using samples collected from the Gdańsk Basin, Southern Baltic (Figure 2). Gdańsk Deep, Gdańsk Bay and Puck Bay are parts of the basin (Majewski, 1990).

Gdańsk Bay is a southeastern bay of the Baltic Sea. The western part of Gdańsk Bay, sheltered from the open sea by the Hel Peninsula, is formed by waters of Puck Bay, while the western-most shallow part of the latter is called Inner Puck Bay or the Puck Lagoon. Gdańsk Bay is enclosed by a large curve of the shores of the Hel Peninsula and the Sambian Peninsula. The coast of the bay features two very long sand spits, the Hel Peninsula and the Vistula Spit. The first one defines Puck Bay, the latter one defines the Vistula Lagoon. The maximum depth is 120 m, salinity ranges from 3 to 7 PSU (0.3–0.7%). The major ports and coastal cities are Gdańsk, Kaliningrad and Gdynia.

The main river entering Gdańsk Bay is the Vistula with a yearly run-off of about 40 km³. Gdańsk Bay receives the waters of the Vistula directly via the Przekop, whereas the Śmiała Wisła, and the Martwa Wisła are inactive. To the west of the Vistula river, several streams discharge waters to the bay with the yearly runoff equal to 0.09 km³. The Pregola discharges waters to the bay indirectly, through the Vistula Lagoon. Most of the suspended matter load is retained in the lagoon, influencing the bay to a small extent.

Inner Puck Bay receives waters of several streams. The major ones are the Płutnica and the Zagórska Struga. Total river runoff to Puck Bay equals 0.03 km³/annum.

The surface water circulation in Gdańsk Bay is anticlockwise, and from west to the east. Moreover, there is a sandbar marking the eastern border of the shallow Inner Puck Bay (2.1 m average depth). Since there are no tides in the Southern Baltic the Vistula water is prevented from entering Puck Bay. Thus, two water bodies characterized by different hydrology can be distinguished: Gdańsk Bay and Inner Puck Bay. The former is characterized by large river discharge and substantial depth. The latter is separated from Gdańsk Bay by a sandbar, and is characterized by limited river runoff and shallow bottom (Majewski, 1990).

Puck Bay is characterized by an extensive population of aquatic vascular plants (*Zostera*, *Potamogeton*), and substantial phytoplankton primary production, while Gdańsk Bay has got comparable primary production, while the vascular plants population is of little importance there (Kruk-Dowgiatto, 2008; Majewski, 1990).

3. Material and methods

3.1. Sampling

The surface sediment samples were collected by means of a gravity corer from Gdańsk Bay at locations presented in Figure 2. The uppermost 0–2 cm layers were taken for analyses. Twice (May and October) samples of riverine suspended matter were recovered from about 600 liters of water which were collected from the Vistula river, about 2 km, and the Płutnica – about 0.3 km, upstream from the river mouth. The suspended matter was decanted, centrifuged and freeze-dried to yield 1.8–2.5 g of dry material. Marine suspended matter samples (some 0.3 g each) were collected by filtering some 200 dm³ of water through GF/F glass fiber filters.

Wood, leaf and moss samples were collected in autumn, from typical terrestrial plants (pine, oak, birch, maple) growing along Gdańsk Bay coast. Tissue samples provide, at

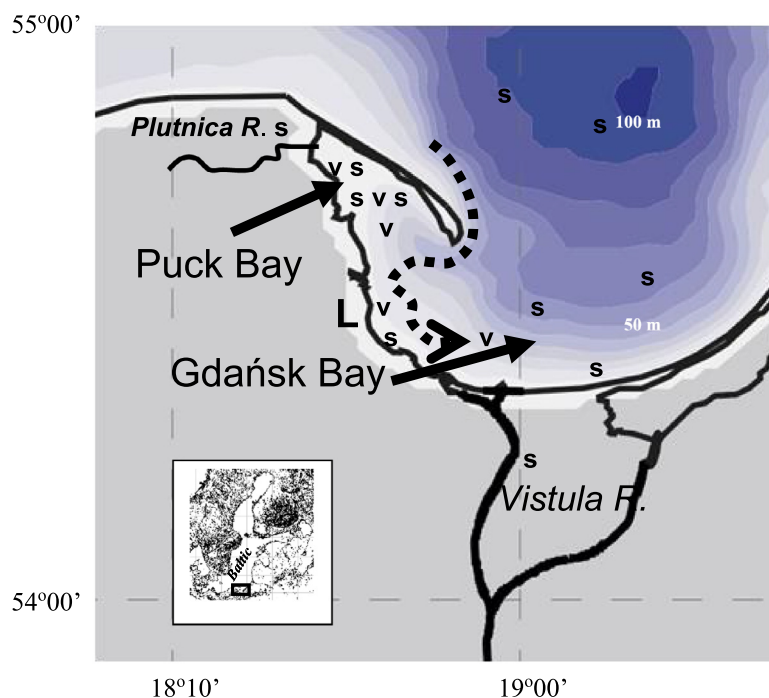


Figure 2 The study area (sampling stations: s – sediment, plankton and suspended matter samples, v – marine vascular plants, L – land vascular plants). Dashed arrow indicates direction of water circulation.

least, three examples from each of four categories of plant tissue types: woody (branch) and non-woody (leaf) tissues of gymnosperms and angiosperms.

Samples of marine biota including vascular plants (*Potamogeton* sp., Charophyta, *Zostera marina*), phytoplankton (*Chlorella vulgaris*, *Scenedesmus* sp., *Pilayella littoralis*, mixed plankton), mussels (*Mytilus trossulus*, *Mya arenaria*) were collected from the study area and stored dry till analyses.

Location of sampling stations is presented in Figure 2, while the characteristics of the collected samples are given in Table 2.

3.2. Analytical methods

The following properties of the collected samples were analyzed in the laboratory: moisture, organic matter, lignin oxidation products (C, V, S, H – phenols), and $\delta^{13}\text{C}$.

Moisture (60°C, 24 h) and loss on ignition (450°C, 4 h) were measured in each sample. Loss on ignition was used as a measure of organic matter (OM) concentration. It was recalculated to organic carbon (C_{org}) using the following formula: $\text{C}_{\text{org}} = 0.45 \times \text{OM}$ (Jonsson and Carman, 1994).

The analysis of lignin-derived phenols was performed after CuO oxidation according to a procedure developed by Hedges et al. (1982) and modified by Staniszewski et al. (2001). In short, steel bombs were loaded with various samples comprising about 50 mg organic matter (0.1 mg accuracy), 400 mg of powdered CuO, 100 mg of $\text{Fe}(\text{NH}_4)_2(\text{SO}_4)_2 \cdot 6(\text{H}_2\text{O})$ and 3 ml of NaOH (2 mol/dm³). After 5 h at 180°C, the contents were centrifuged at $G=2400$ and rinsed with water several times. The combined supernatants were acidified to pH 1.5 with 6M HCl and centrifuged again. The precipitate was rinsed with acidified water. The combined

acidified supernatants were extracted three times with ethyl acetate. The ethyl acetate was then evaporated off and the dry residues were stored in a desiccator at 4°C for derivatization and GC analysis. The dried products were dissolved in pyridine (250 μl) before the addition of 150 μl of the silylating reagent [BSTFA – bis(trimethylsilyl) - trifluoroacetamide] and derivatized for 1 h at room temperature. The derivatised products were analyzed in a gas chromatograph (Shimadzu 17A) on fused silica capillary columns (Phenomenex ZB-5, 30 m x 0.25 mm x 0.50 mm) with flame ionization detection. The GC-FID analyses were performed under the following conditions: initial oven temperature 120°C min, rate of oven temperature increase 3°C/min, final oven temperature 270°C; the temperature of injector and detector: 300°C; carrier gas: helium with a flow rate of 1.5 ml/min.

Degradation products were quantified with commercial type phenolic acids and phenolic aldehydes (Fluka AG). Calibration curves and recovery rates based on internal standards (3-ethoxy,4-hydroxy-benzaldehyde) and standard addition of the analyzed compounds were used for quantitative analyses. The average recovery was $78 \pm 3\%$ ($n=5$). Blanks ran parallel to the samples proved the lack of signal at retention times characteristic of the analyzed samples. The limit of detection ranged from 0.1 to 0.8 $\mu\text{g/g}$ depending on the measured analyte, and never exceeded 2% of the analyte.

Stable carbon isotopes were analyzed according to a procedure described by Jędrysek et al. (2003). In short, a sample comprising some 3 mg of organic matter was combusted with CuO at 900°C in a glass ampoule. The evolving carbon dioxide was cryogenically purified and transferred to a model Finnigan Mat CH7 mass spectrometer equipped with a model Finnigan Mat Delta E detector. The PDB interna-

Table 2 List and short characteristics of collected samples.

| Sampling date | Place of sampling* | Type of sampling | Description |
|------------------|---------------------------------|---|--|
| 04.04. 07.09. | Vistula River Plutnica River | suspended matter | About 600 dm ³ of water was processed |
| 20.10. | Landscape Park | maple – branch maple – leaf oak – branch oak – leaf birch – branch birch – leaf pine – branch | Branches of trees with leaves still attached to them were collected |
| 13.10. 06.06. | Gdańsk Basin | <i>Pilayella littoralis</i> <i>Potamogeton</i> sp. Charophyta <i>Zostera marina</i> <i>Chlorella vulgaris</i> <i>Scenedesmus</i> sp. | Vascular plants were collected by a scuba diver. Phytoplankton samples were collected with a net towed with a speed 1.5 knot, mussels were collected with a dredge towed with a speed of 2.5 knots |
| 04.06. | | Plankton, mixed Tissues of mussels: <i>Mytilus trossulus</i> <i>Mya arenaria</i> | |
| 04.06. | Gdańsk Basin | Suspended matter | About 200 dm ³ were filtered through GF/F glass fiber filters |

* see map in Figure 2 for location of sampling grounds.

tional standard was used for calculating the stable carbon isotope ratio ($\delta^{13}\text{C}$) according to the formula:

$$\delta^{13}\text{C} = \frac{\left[\frac{^{13}\text{C}}{^{12}\text{C}} \right]_{\text{sample}} - \left[\frac{^{13}\text{C}}{^{12}\text{C}} \right]_{\text{standard}}}{\left[\frac{^{13}\text{C}}{^{12}\text{C}} \right]_{\text{standard}}}$$

Stable carbon isotopes ratio was measured with the 0.05‰ accuracy.

3.3. Modeling contribution to sedimentary organic matter from various sources

The contributions of organic matter originating from various sources in the Bay of Puck sediments were established by means of nonlinear estimation (Kulinski and Pempkowiak, 2008; Pempkowiak et al., 2006a). The modelled contributions (**a** – riverine: *R*, **b** – marine vascular plants: *V*, **g** – phytoplankton: *P*) were calculated from linear regression equations independently for values of $\delta^{13}\text{C}$ and $\Sigma 8$ in sedimentary organic matter (OC_M), measured in actual samples.

$$\text{OC}_M \delta^{13}\text{C} = a * \delta^{13}\text{C}_{(R)} + b * \delta^{13}\text{C}_{(V)} + g * \delta^{13}\text{C}_{(P)}$$

$$\text{OC}_M \Sigma 8 = a * \Sigma 8_{(R)} + b * \Sigma 8_{(V)} + g * \Sigma 8_{(P)}$$

This is based on the following assumption: the total concentration of a given property (either $\Sigma 8$ or $\delta^{13}\text{C}$) consists of three portions contributed by each of the members in proportion to the mass contribution of organic matter originating from the sources.

The unknown contributions are calculated applying non-linear estimation. Statistica 5 software package was used to perform calculations.

4. Results and discussion

4.1. Lignin phenols in marine vascular plants

In Table 3 yields of phenolic aldehydes and acids from terrestrial and marine plants, from riverine and marine suspended matter, and from marine sediments are presented.

As for terrestrial plants, the yield of lignin phenols is in the range from 5000 $\mu\text{g/g}$ (maple leaf) to 21000 $\mu\text{g/g}$ (oak leaf), and from 8000 $\mu\text{g/g}$ (pine wood) to 11000 $\mu\text{g/g}$ (birch wood), respectively for soft and hard parts of the investigated plants. Moss was characterized by the exceptionally high yield of phenolic aldehydes and acids (22000 \pm 350 $\mu\text{g/g}$). Yields of the sum of vanillin, syringil, and cynammyl phenols recalculated to 100 mg organic carbon ($\Sigma 8$) are in the same range as reported earlier for plant tissues (Hautala et al., 1997; Hedges and Mann, 1979).

Marine planktonic material yielded none of lignin phenols, and neither did soft tissue of mussels collected in the Gdańsk Basin. It is interesting to see that $\Sigma 8$ phenols are practically lacking in the coastal surface suspended matter. This may be attributed to the lack of lignin phenols ($\Sigma 8=0$) in the planktonic material, dilution of riverine suspended matter by biomass originating from planktonic primary production and transport to the sedimentation basin

Table 3 Yields of lignin phenols and $\delta^{13}\text{C}$ in the analyzed samples.

| Sample | Lignin phenols/ \pm standard deviation | | | | | Lignin indexes | | $\delta^{13}\text{C}$ (‰) |
|---------------------------------|--|---------------|---------------|-----------------|------------------------------|-----------------|---------------|---------------------------|
| | V | C | S | H | $\Sigma 8$ | C/V | S/V | |
| | $\mu\text{g/g}$ | | | | $\mu\text{g}/100\text{ mgC}$ | | | |
| Gymnosperms¹ | | | | | | | | |
| - wood | 2741 \pm 87 | 3576 \pm 93 | 899 \pm 39 | 4911 \pm 112 | 1935 \pm 108 | 0.49 \pm 0.03 | 2.3 \pm 0.4 | -28.7 \pm 0.4 |
| - soft parts | 3576 \pm 118 | 899 \pm 27 | 807 \pm 27 | 11365 \pm 317 | 1450 \pm 36 | 0.06 \pm 0.01 | 2.8 \pm 0.6 | -28.5 \pm 0.3 |
| Angiosperms² | | | | | | | | |
| - wood | 6616 | 694 | 842 | 442 | 1630 | 0.16 | 0.13 | -26.0 |
| - soft parts | 3215 | 1921 | 652 | 892 | 893 | 0.59 | 0.20 | -27.2 |
| Suspended matter | | | | | | | | |
| - Vistula River ³ | 2871 | 2207 | 5536 | 4138 | 2120 | 0.77 | 1.9 | -26.4 |
| - Płutnica River ³ | 2530 | 2230 | 6320 | 1890 | 2350 | 0.90 | 2.5 | -27.1 |
| - Puck Bay ³ | 14 | 8 | BLD | BLD | 4.0 | 0.57 | - | -20.5 |
| - Gdańsk Bay ³ | 25 | 14 | 15 | 8 | 8.1 | 0.56 | 0.60 | -23.7 |
| - Southern Baltic | 14 | 12 | BLD | BLD | 5.2 | 0.86 | - | -22.2 |
| Marine biota | | | | | | | | |
| - vascular plants ^{4a} | 176 | 83 | 177 | 1529 | 89.8 | 0.52 | 1.05 | -11.7 |
| - phytoplankton ^{4b} | BLD | BLD | BLD | BLD | BLD | - | - | -22.0 |
| - mussels ^{4c} | BLD | BLD | BLD | BLD | BLD | - | - | - |
| Marine sediments | | | | | | | | |
| - Puck Bay ^{5a} | 1800 \pm 65 | 790 \pm 41 | 2150 \pm 76 | 1512 \pm 65 | 823 \pm 37 | 0.44 \pm 0.08 | 1.2 \pm 0.1 | -23.0 \pm 0.2 |
| - Gdańsk Bay ^{5b} | 1363 \pm 64 | 870 \pm 26 | 2760 \pm 82 | 1458 \pm 51 | 861 \pm 31 | 0.64 \pm 0.07 | 1.6 \pm 0.2 | -24.8 \pm 0.2 |

BLD – below detection limit.

¹ maple, oak, birch.

² pine.

³ average of 2 samples.

^{4a} *Potamogeton* sp., Charophyta, *Zostera marina*.

^{4b} *Scenedesmus* sp., *Chlorella vulgaris*, mixed phytoplankton.

^{4c} *Mytilus trossulus*, *Mya arenaria*.

^{5a} average of 3 samples.

^{5b} average of 5 samples.

of, lignin-rich, riverine suspended matter in the above bottom, nepheloid layer (Pempkowiak et al., 2002; Winogradow and Pempkowiak, 2018). Organic matter derived from unicellular algae (phytoplankton) constitutes almost 100% of primary production in the marine environment at a global scale, although in the coastal, shallow regions marine vascular plants can contribute substantially to the primary production (Chester, 2003; Cragg et al., 2020; Kruk-Dowgiałto, 2008).

Exceptionally large concentrations of hydroxyl phenols (H) in organic material derived from aquatic plants draw attention. It seems to be a specific feature of aquatic plants biomass. This was reported earlier by Hautala et al. (1997), and Hedges and Mann (1979) who concluded that hydroxyphenols must have yet another source but lignin polymer. In another study the hydroxyphenols were associated with high chlorophyll α concentrations, indicating a possible autochthonous source (Cotrim da Cunha et al., 2001).

It follows from the presented data that marine vascular plants yielded, on average, 435 $\mu\text{g/g}$ compounds in question (V+S+C). The range was from 300 to 500 $\mu\text{g/g}$ ($\Sigma 8=120\ \mu\text{g}/100\ \text{mgCorg}$). Of the three species studied the highest yield resulted from *Zostera marina*, although the differences between species are small. No reports on the occur-

rence of lignin phenols in the oxidation products of biomass produced by marine biota have appeared so far.

Terrestrial suspended organic matter is delivered to the sea, mainly, with river runoff. Composition of suspended matter isolated from river water provides indications on the amount and quality of such material. On average concentrations of particulate lignin phenols in the Vistula water fall in the range from 8000 to 10000 $\mu\text{g/g}$ dry matter. The yield and composition of the phenols derived from the Płutnica suspended matter are similar to these of the Vistula River suspended matter. The riverine suspended matter $\Sigma 8$ index measured in this study is equal to 2223 \pm 250 $\mu\text{g}/100\ \text{mg}$ organic carbon, close to other reported values (Farella, 2001; Staniszewski, 2001). Seasonal variations of both the yield and composition can be observed, possibly, due to the river water flow variations (Cortim da Cunha et al., 2001; Staniszewski et al., 2001; Sun et al., 2017).

4.2. $\delta^{13}\text{C}$ in the analysed samples

In Table 3 the $\delta^{13}\text{C}$ values of the analyzed samples are presented. Except for pine wood ($\delta^{13}\text{C}=-26\%$) terrestrial plants material, and riverine suspended matter falls in the range from -28‰ to -30‰, typical of terrestrial

plants (Maksymowska et al., 2000; Opsahl and Benner, 1995). Organic material derived from marine vascular plants *Zostera marina*, and *Potamogeton* sp. is characterized by much higher $\delta^{13}\text{C}$ values (-12‰) than marine phytoplankton (-22‰), while marine suspended matter and marine sediments are characterized by $\delta^{13}\text{C}$ values falling in the range between marine phytoplankton and riverine suspended matter, except the Bay of Puck, where it is marginally higher (-21.5‰). The exceptionally high values for the marine vascular plants biomass were already reported earlier (Hamminga and Mateo, 1996; Hu and Burdige, 2007), and attributed to the ability of seagrasses to use bicarbonate as an inorganic carbon source (Raven et al., 2002). Sedimentary organic matter $\delta^{13}\text{C}$ signatures in both bays are typical of the Gdańsk Basin (Maksymowska et al., 2000; Winogradow and Pempkowiak, 2018), the Baltic (Miltner et al., 2005; Voss et al., 2000; Winogradow et al., 2019), and worldwide (Gordon and Goni, 2003; Pradhan et al., 2014; Requejo et al., 1986, 2003; Thorton and McManus, 1994).

The occurrence of lignin phenols and abundance of heavy carbon isotope in marine vascular plants biomass may be due to biased estimations of sedimentary organic matter provenience evaluated by means of the end member approach based on lignin residues and/or stable carbon isotopes.

4.3. The influence of marine vascular plants biomass on the sedimentary organic matter properties

Although the yield of $\Sigma 8$ phenols derived from marine vascular plants biomass is 10 to 50 times smaller than that from terrestrial plants biomass, the 'marine' biomass lignin phenols may influence the overall yield ($\Sigma 8$) in sediments comprising organic matter originating from both sources, if a load of marine plants biomass is substantial as compared to organic matter discharged to the sea from land. Therefore, the marine plants contribution cannot be entirely omitted when quantitative relations between marine and land originated organic matter pools are considered. This concerns especially coastal, shallow waters, characterized by restricted water exchange with the open sea, where organic matter derived from vascular marine plants can constitute not only a substantial proportion of primary production, but can overwhelm organic matter load discharged to the sea with river runoff (Kruk-Dowgiatto, 2008). Therefore, a possible influence of the marine vascular plants on the concentration and composition of lignin phenols in the coastal sediments was investigated in some detail in this study.

Not only are lignin phenols used to quantify the proportion of land derived organic matter in marine sediments. Ratios of specific lignin phenols or their groups are used to discriminate between taxonomic plant classes (gymnosperm vs. angiosperm) and tissue types (straw vs. woody tissue) and to diagnose the diagenetic state of lignin material (Jex et al., 2014; Pempkowiak et al., 2006; Reeves, 1995).

In the investigated samples the ratio of syringil to vanillin phenols (S/V) range from 2.8 (gymnosperms, soft parts) to 0.13 (pine wood). The S/V ratio in riverine suspended matter equals 1.9 and 2.5 respectively in the Vistula and the Płutnica suspended matter, indicating gymnosperms woody

material as a source of suspended organic matter, while the S/V ratio in sediments ranges from 1.2 (Puck Bay) to 1.6 (Gdańsk Bay) – values smaller than the ratio in the riverine suspended matter. One explanation for the S/V values could arise from the fact that in the surface sediments, the more degraded organic matter might be contained. It has been shown by several authors (Farella et al., 2001; Hedges et al., 1988; Jex et al., 2014; You et al., 2018) that in the course of degradation, lignin derivatives lose syringil units much faster than vanillin ones. This is unlikely in the presented case, however, considering that based on sedimentation rates in the area (Pempkowiak, 1991; Winogradow and Pempkowiak, 2014), surface sediments not older than 10 years were analysed.

In material derived from marine vascular plants, the S/V ratio equals 1.05 (Table 3), which means that the S/V ratio values in sedimentary organic matter may be influenced substantially in sediments rich with organic matter derived from vascular plants.

The C/V ratios of lignin phenols in the analysed samples are in the range from 0.49 (gymnosperms, wood) to 0.06 (gymnosperms, soft parts). In the riverine suspended matter the C/V ratio equals 0.77 and 0.90, while in the Gdańsk Basin sediments it ranges between 0.29 and 0.44. This indicates that the contribution of nonwoody plant fragments is small (Hedges and Mann, 1979; Opsahl and Benner, 1995). Since the ratio in the marine vascular plants biomass equals 0.55, the contribution of marine vascular plants is likely, although not as obvious an explanation as in the case of the S/V index. Modern pollen yielding high amounts of cinnamyl phenols (Hu et al., 1999) may be another factor influencing C/V ratio values.

The dependence of S/V vs C/V for both marine and terrestrial plants is presented in Figure 3. Terrestrial plants are characterized by large S/V values and small C/V values. Marine plants have small S/V values and both small and large C/V values. S/V ratios in the range from 0.1 to 1.0 are attributed to angiosperm plants material, while C/V ratios in the range from 0.1 to 0.4 are attributed to gymnosperm plants (Cragg et al., 2020; Hedges and Mann, 1979) Since S/V values are used to differentiate between angiosperm vs angiosperm plants, lowering S/V values due to contribution of marine vascular plants phenols may lead to misjudgment in this respect. It must be kept in mind, however, that the yield of lignin phenols from marine plants is smaller than that from terrestrial plants by an order of magnitude. Therefore, the influence will be manifested only in samples comprising a large fraction of V+S+C phenols derived from marine plants biomass.

The distribution of both the S/V and C/V indexes is yet another indication that contribution of marine vascular plants biomass to marine sedimentary organic matter should be taken into account when investigating provenience basing on lignin residues and/or stable carbon isotopes.

The extent of the influence depends both on the actual values of indexes ($\Sigma 8$, C/V, S/V), and on the proportion of organic matter derived from the marine vascular plants in the total sedimentary organic matter. This depends on the bottom coverage by marine vascular plants, biomass production by the plants and hydrology of a given water body. The resistance to biochemical degradation of V, S, and C phenols precursors is also an important factor here. These,

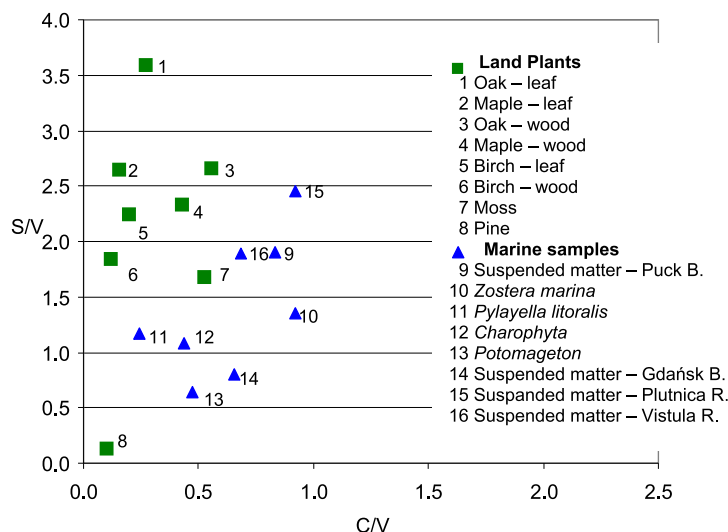


Figure 3 The plot of S/V vs. C/V indexes of the investigated samples.

Table 4 Characteristics of lignin phenols in a two member system (riverine suspended organic matter and marine vascular plants biomass).

| Organic carbon composition RPC ¹ : MVPC ² | Expected ³ $\Sigma 8$ $\mu\text{g}/100 \text{ mgC}$ | Actual ⁴ $\Sigma 8$ | Expected/Actual | | |
|--|---|--------------------------------|---------------------------------|-----------|-----------|
| | | | % Terrestrial organic matter | S/V | C/V |
| 100 : 0 | 2100 | 2100 | 100/100 | 1.93/1.93 | 0.77/0.77 |
| 99 : 1 | 2079 | 2080 | 99/99 | 1.93/1.92 | 0.77/0.77 |
| 95 : 5 | 1995 | 1999.5 | 95/95 | 1.93/1.89 | 0.77/0.76 |
| 90 : 10 | 1895 | 1899 | 90/90 | 1.93/1.84 | 0.77/0.76 |
| 75 : 25 | 1575 | 1597.5 | 75/76 | 1.93/1.71 | 0.77/0.70 |
| 50 : 50 | 1050 | 1095 | 50/52 | 1.93/1.49 | 0.77/0.64 |
| 25 : 75 | 525 | 592.5 | 25/28 | 1.93/1.27 | 0.77/0.57 |
| 10 : 90 | 210 | 291 | 10/14 | 1.93/1.14 | 0.77/0.53 |
| 5 : 95 | 105 | 190.5 | 5/9 | 1.93/1.09 | 0.77/0.51 |
| 1 : 99 | 21 | 110.1 | 1/5 | 1.93/1.06 | 0.77/0.50 |
| 0 : 100 | 0 | 90 | 0/4 | 1.93/1.05 | 0.77/0.50 |

¹ Riverine Particulate Organic Carbon.

² Marine Vascular Plants Organic Carbon.

³ assuming the lack of lignin phenols in marine vascular plants ($\Sigma 8 = 0$).

⁴ assuming $\Sigma 8$ of lignin phenols as in Table 3 ($\Sigma 8 = 90$).

of course, depend on local environmental factors. Assuming just the two organic matter sources, theoretically, composition of sedimentary organic matter may range from 100% land- 0% marine vascular plants derived, to 0% land- 100% marine vascular plants derived. In Table 4, $\Sigma 8$, S/V and C/V indexes are presented of hypothetical sedimentary organic matter consisting, in varying proportions, of land derived and marine vascular plants derived components. Characteristics of the two end members ($\Sigma 8$, C/V, S/V) were taken from Table 3. It follows from the results of calculations presented in Table 4 that, as expected, the extent of the influence depends on the marine vascular plants contribution

to sedimentary organic matter. Up to some 50% contribution, the influence on $\Sigma 8$ is weak. It raises when contribution reaches some 60%. Actual values of both S/V and C/V indexes differ substantially from calculated already when the terrestrial contribution decreases to 75%. It can be concluded that both the calculated proportion of terrestrial organic matter in sedimentary organic matter and origin of lignin, judged by S/V and C/V indexes, can be seriously misjudged based on lignin derivatives alone (Table 4). It has been already pointed out that $\delta^{13}\text{C}$ cannot be trusted in areas with strong vascular marine plants biomass production, either. Therefore, a different approach is necessary for ar-

Table 5 The inflow of lignin phenols to the study area.

| Water body | Input V+S+C (kg/year) | |
|------------|-----------------------|------------------------|
| | Riverine | Marine Vascular Plants |
| Gdańsk Bay | 24750 ¹ | 231.2 ³ |
| Puck Bay | 825 ² | 462.4 ⁴ |

¹ Assuming: river runoff 1060 m³/s, suspended matter concentration 8 mg/dm³, organic matter in suspension 20%, yield of $\Sigma 8$ as in Table 3.

² Assuming: river runoff 2.8 m³/s, suspended matter concentration 7 mg/dm³, organic matter in suspension 14%, yield of $\Sigma 8$ as in Table 3.

³ Assuming: bottom covered by *Potamogeton* + *Zostera marina* + *Zanichella* – 6.1 km², biomass yield g/(m² year) *Potamogeton* – 32, *Zostera marina* – 26, *Zanichella* – 7.5, $\Sigma 8$ yield as in Table 3.

⁴ Assuming: bottom covered by *Potamogeton* + *Zostera marina* + *Zanichella* – 13.2 km², biomass yield as, in footnote no 3, above, $\Sigma 8$ yield as in Table 3.

Table 6 Average values of sedimentary organic matter origin indicators and proportion of land derived organic matter in Gdańsk Bay and Inner Puck Bay sedimentary organic matter (ML%), based on different indicators.

| Indicator | Unit | Gdańsk Bay ¹ | Puck Bay ² |
|--|---------------------------------------|-------------------------|-----------------------|
| $\delta^{13}\text{C}$ | ‰ | -24.8±0.2 | -23.2±0.1 |
| $\Sigma 8$ | mg V + S + C / 100 mgC _{org} | 861±45 | 823±37 |
| S/V | — | 1.60±0.15 | 1.20±0.10 |
| C/V | — | 0.64±0.03 | 0.40±0.02 |
| Proportion of terrestrial organic matter | | | |
| - based on $\delta^{13}\text{C}$ | % | 47 | 20 |
| - based on $\Sigma 8$ | % | 41 | 39 |
| - based on loads of lignin phenols | % | — | 35 |
| - based on the 'three end members' | % | 44 | 30 |

¹ average of 5 samples.

² average of 3 samples.

eas where a strong contribution from marine vascular plants is suspected.

4.4. Origin of sedimentary organic matter in the study area

One such area is Puck Bay, a shallow-bottom and well sheltered, north-west corner of the Gdańsk Basin. In Table 5 estimated inflow of autochthonous and allochthonous suspended organic matter is presented for Puck Bay, and Gdańsk Bay. The load of lignin residues discharged to the sea with the riverine suspended matter is comparable to a load of precursors derived from marine plants in Puck Bay, while in Gdańsk Bay a load of lignin phenols precursors derived from marine plants is two orders of magnitude smaller than the one brought to the bay with the Vistula runoff. Since both bays constitute two separate water bodies, sedimentary organic matter may reflect the mixed origin of lignin phenols precursors in Puck Bay as opposed to practically singular source in Gdańsk Bay.

In Table 6 terrestrial organic matter proportions (ML%) in the sedimentary organic matter, based on lignin phenols and $\delta^{13}\text{C}$, are listed. Values for Gdańsk Bay are close to one another independently of the applied indicator. However, Puck Bay land derived organic matter proportions differ by a factor of 2 (20% – based on lignin vs. 39% – based on $\delta^{13}\text{C}$). The $\Sigma 8$ index suggests a substantial contribution of land derived organic matter to the bay. Since the lignin phenols in the

riverine organic matter originate from woody gymnosperm plants, the S/V and C/V indexes should be equal to 2.6 and 0.49, respectively. However, the actual values are different (Table 3), confirming the substantial contribution of material comprising lignin phenols from a source differing with the quality of phenols from that in river runoff. Biomass of marine vascular plants is an obvious contributor of such material.

It is difficult to quantify the contributions, still there are several approaches to do it. One way of evaluating the contribution is comparing the V+S+C phenols loads derived from the inflow of terrestrial organic matter, and that derived from biomass production of marine vascular plants in the study area. The respective figures are presented in Table 5. The load of the V+S+C phenols originating from marine vascular plants is smaller than the riverine one in both the bays (Table 5). In Gdańsk Bay, the contribution is below 1%. Therefore, as explained earlier, on the regional basis no real threat of misusing lignins as biomarkers of terrestrial organic matter exist. However, in Puck Bay, the contribution is 35%. It may be concluded therefore that locally, in areas with substantial bottom coverage by the underwater meadows, and at the end of the growing season such a possibility exists, as the example of Puck Bay proves. In such an area substantial deviations from results of the two end-members approach based on lignin phenols could be expected and actually take place. Interestingly enough, also stable carbon isotopes ratio measured in samples collected

in the Bay of Puck shows high values. This may be well attributed to the exceptionally low values of $\delta^{13}\text{C}$ in organic material originating from marine vascular plants.

The gathered evidence suggests that in the Bay of Puck a three-member system would better reflect geochemistry of organic matter. The end members are: the riverine organic matter – R ($\Sigma 8=2500$, $\delta^{13}\text{C}=-28.5\text{‰}$), marine vascular plants – V ($\Sigma 8=90$, $\delta^{13}\text{C}=-12.0\text{‰}$), and marine phytoplankton – M ($\Sigma 8=0$, $\delta^{13}\text{C}=-22.0\text{‰}$). Basing on these characteristics the riverine – a, marine vascular plants – b, and marine phytoplankton – g, contributions to the sedimentary organic matter were calculated. The nonlinear estimation used for this purpose (Pempkowiak et al., 2006; Kulinski and Pempkowiak, 2008), proved the contributions to be, on average, 30% – a, 40% – b and 30% – c, for three samples of sediments collected in the bay. A need for introducing a three member approach was suggested earlier. Bianchi et al. (2002) and Gorgon and Goni (2003), noticed that distributions of sedimentary organic matter properties in the northern Gulf of Mexico can be explained by the separation of terrestrial organic matter into two fractions differing with the properties and distribution in sediments; while Requejo et al. (2003) suggested diversified terrestrial lignin sources at the Washington coast. The features may be attributed to fractionation of lignin residues due to specific surface area of sediment particles (Bergamasi et al., 1997), hydrodynamic factors (Ji et al., 2020) and bacterial activity (Yu et al., 2018). The phenomenon described here is based on entirely different mechanism, however.

5. Conclusions

Oxidative degradation of marine vascular plants biomass yields vanillin, cynammyl, and syringil phenols. The average yield of eight analyzed phenols ($\Sigma 8$) is 90 $\mu\text{g}/100\text{ mg}$ organic carbon. In areas characterized by a large supply of marine vascular plants biomass and a small load of riverine organic matter, lignin concentration ($\Sigma 8$) and lignin indexes are strongly modified by phenols derived from marine vascular plants biomass. Since the marine vascular plants biomass is characterized not only by the specific composition of phenols, but by exceptionally high $\delta^{13}\text{C}$ values as well, a three members approach is better suited for evaluation of the sedimentary organic matter provenience in such areas. Using a nonlinear analysis of the sedimentary organic matter $\Sigma 8$ and $\delta^{13}\text{C}$ in Puck Bay, Southern Baltic, the contributions from the three sources in question were calculated to be 40%, 30% and 30% respectively in riverine POM, marine vascular plants, and phytoplankton.

Acknowledgements

This work was performed in the frame of the Institute of Oceanology statutory activities (Theme 3). Participation of the *r/v Oceania* in sampling is acknowledged. The author is grateful to O. M. Jędrysek for performing $\delta^{13}\text{C}$ measurements, and to A. Staniszewski for lignin analysis.

References

- Bergamashi, B., Tsamakidis, E., Keil, G., Eglinton, T., Montlucon, D., Hedges, J., 1997. The effect of grain size and surface area on organic matter, lignin and carbohydrate concentration, and molecular compositions in Peru Margin sediments. *Geochim. Cosmoch. Ac.* 61 (6), 1247–1260.
- Bianchi, T.S., Cui, Blair, X.Q., Burdige, N.E., Eglinton, D.J., Galy, T.I., Galy, V., 2018. Centers of organic carbon burial and oxidation at the land-ocean interface. *Org. Geochem.* 115, 138–155, <https://doi.org/10.1016/j.orggeochem.2017.09.008>.
- Bianchi, T.S., Siddhartha, M., McKee, B.A., 2002. Sources of terrestrially-derived organic carbon in lower Mississippi River and Louisiana shelf sediments: implications for differential sedimentation and transport at the coastal margin. *Mar. Chem.* 64, 211–223.
- Bianchi, T.S., Rolff, C., Lambert, C.D., 1997. Sources and composition of particulate organic carbon in the Baltic Sea: the use of plant pigments and lignin-phenols as biomarkers. *Mar. Ecol. Prog. Ser.* 156, 25–31. <https://doi.org/10.3354/meps156025>.
- Bordovsky, O., 1965. Accumulation and transformation of organic substances in marine sediments. *Mar. Geol.* 3, 3–114.
- Cotrim da Cunha, L., Serve, L., Gadel, F., Blazi, J.-L., 2001. Lignin-derived phenolic compounds in the particulate organic matter of a French Mediterranean river: seasonal and spatial variations. *Org. Geochem.* 32, 305–320.
- Chester, R., 2003. *Marine Geochemistry*. Blackwell Publ., Malden, 357–404.
- Cragg, S.M., Friess, D.A., Gillis, L.G., Trevathan-Tackett, S.M., Terrett, O.M., Watts, J.E., Distel, D.L., Dupree, P., 2020. Vascular Plants Are Globally Significant Contributors to Marine Carbon Fluxes and Sinks. *Ann. Rev. Mar. Sci.* 12, 469–497, <https://doi.org/10.1146/annurev-marine-010318-095333>.
- Donaldson, A., 2001. Lignification and lignin topochemistry – ultrastructural view. *Phytochemistry* 57, 859–873.
- Duarte, C.M., 1991. Seagrass depth limits *Aquatic Botany* 40, 363–377.
- Duarte, C.M., Chiscano, C.L., 1999. Seagrass biomass and production: a reassessment. *Aquat. Bot.* 65 (1–4), 159–174.
- Duarte, C.M., Cebrián, J., 1996. The fate of marine autotrophic production. *Limnol. Oceanogr.* 41, 1758–1766.
- Duarte, C.M., Marbà, N., Gacia, E., Fourqurean, J.W., Beggins, J., Barrón, C., Apostolaki, E.T., 2010. Seagrass community metabolism: Assessing the carbon sink capacity of seagrass meadows. *Global Biogeochem. Cy.* 24 (4), GB4032, <https://doi.org/10.1029/2010GB003793>.
- Duarte, C.M., Middelburg, J.J., Caraco, N., 2005. Major role of marine vegetation on the oceanic carbon cycle. *Biogeosciences* 2, 1–8.
- Farella, N., Lucotte, M., Louchouart, P., Roulet, M., 2001. Deforestation modifying terrestrial organic transport in the Rio Tapajós. Brazilian Amazon. *Org. Geochem.* 32, 1443–1458.
- Gardner, W.S., Menzel, D.W., 1974. Phenolic aldehydes as indicators of terrestrially derived organic matter in the sea. *Geochim. Cosmochim. Ac.* 38, 813–822.
- Gorgon, E., Goni, M., 2003. Sources and distribution of terrigenous organic matter delivered by the Atchafalaya River to sediments in the northern Gulf of Mexico. *Geochim. Cosmochim. Ac.* 67, 2359–2375.
- Gough, M.A., Fauzi, R., Mantoura, C., Preston, M., 1993. Terrestrial plant biopolymers in marine sediments. *Geochim. Cosmochim. Ac.* 57, 645–964.
- Hautala, K., Peuravuori, J., Pihlaja, K., 1997. Estimation of origin of lignin in humic DOM by CuO – oxidation. *Chemosphere* 35, 809–817.
- Haddad, R., Martens, Ch, 1987. Biogeochemical cycling in the organic rich coastal marine basin: 9. Sources and accumulation

- rates of vascular plant-derived organic material. *Geochim. Cosmochim. Ac.* 51, 2991–3001.
- Hamminga, M., Mateo, M., 1996. Stable carbon isotopes in seagrasses: variability in ratios and use in ecological studies. *Mar. Ecol. Prog. Ser.* 84, 9–18.
- Hedges, J.I., 1992. Global biogeochemical cycles: progress problems. *Mar. Chem* 39, 67–93.
- Hedges, J.I., Clark, W.A., Cowie, G.L., 1988. Organic matter sources to the water column and surficial sediments of a marine bay. *Limnol. Oceanogr.* 33, 1116–1136.
- Hedges, J.I., Ertel, J.R., 1982. Characterization of lignin by gas capillary chromatography of cupric oxide oxidation products. *Anal. Chem.* 54, 174–178.
- Hedges, J.I., Ertel, J.R., Leopold, E.B., 1982. Lignin geochemistry of a late Quaternary sediment core from Lake Washington. *Geochim. Cosmochim. Ac.* 46, 1869–1877.
- Hedges, J.I., Mann, D.C., 1979. The characterisation of plant tissues by their lignin oxidation products. *Geochim. Cosmochim. Ac.* 43, 1803–1807.
- Hedges, J.I., van Geen, A., 1982. A comparison of lignin and stable carbon isotope composition in quaternary sediments. *Mar. Chem.* 11, 43–53.
- Hu, F.S., Hedges, J., Gordon, E.S., Brubaker, L.B., 1999. Lignin biomarkers and pollen in postglacial sediments of an Alaska lake. *Geochim. Cosmochim. Ac.* 63, 1421–1430.
- Hu, X., Burdige, D., 2007. Enriched stable carbon isotopes in the pore waters of carbonate sediments dominated by seagrasses; Evidence for coupled carbonate dissolution and reprecipitation. *Geochim. Cosmochim. Ac.* 71, 129–144.
- Jędrysek, O.M., Krąpiec, M., Skrzypek, G., Kałużny, A., 2003. Air-pollution effect and paleotemperature scale versus $\delta^{13}\text{C}$ records in tree rings and in a peat core (Southern Poland). *Water Air Soil Pollut.* 145, 359–373.
- Jex, C.N., Pate, G.H., Blyth, A.B., Spencer, R., Hernes, P.J., Khan, S.J., Baker, A., 2014. Lignin biogeochemistry: From modern processes to Quaternary archives. *Quaternary Sci. Rev.* 87, 46–59.
- Jørgensen, S.E., Fath, B.D., 2008. *Encyclopedia of Ecology*. Elsevier, 1407–1413.
- Ji, Y., Feng, L., Zhang, D., Wang, Q., Pan, G., Li, X., 2020. Hydrodynamic sorting controls the transport and hampers source identification of terrigenous organic matter: A case study in East China Sea inner shelf and its implication. *Sci. Total Environ.* 706, 135699, <https://doi.org/10.1016/j.scitotenv.2019.135699>.
- Jonsson, P., Carman, R., 1994. Changes in deposition of organic matter and nutrients in the Baltic Sea during the twentieth century. *Mar. Pollut. Bull.* 28, 417–426.
- Kruk-Dowgiałło, L., 2008. Przyczyny i skutki wieloletnich zmian fitobentosu Zatoki Gdańskiej. *Inst. Morski, Gdańsk*, 132 pp.
- Kuliński, K., Pempkowiak, J., 2008. Dissolved organic carbon in the southern Baltic Sea: Quantification of factors affecting its distribution. *Estuar. Coast. Shelf Sci.* 78, 38–44.
- Majewski, A., 1990. *Zatoka Gdańska*. Wyd. Geol., Warsaw, 120–311.
- Maksymowska, D., Richard, P., Piekarek-Jankowska, H., Riera, P., 2000. Chemical and isotopic composition of the organic matter sources in the Gulf of Gdańsk (Southern Baltic Sea). *Estuar. Coast. Shelf Sci.* 51, 585–598.
- Merdy, P., Guillon, E., Dumonceau, J., Aplincourt, M., 2002. Characterisation of a wheat straw cell wall residue by various techniques A comparative study with a synthetic and an extracted lignin. *Anal. Chim. Acta* 459, 133–142.
- Miltner, A., Emeis, K., 1999. Origin and transport of terrestrial organic matter from the Oder lagoon to the Arkona Basin. *Southern Baltic Sea, Org. Geochem.* 31, 57–66.
- Miltner, A., Emeis, K.C., 2000. Origin and transport of terrestrial organic matter from the Oder lagoon to the Arkona Basin. *Southern Baltic Sea, Org. Geochem.* 31 (1), 57–66.
- Miltner, A., Emeis, K., 2001. Terrestrial organic matter in surface sediments of the Baltic Sea, Northwest Europe, as determined by CuO oxidation. *Geoch. Cosmochim. Ac.* 65, 1285–1299.
- Miltner, A., Emeis, K.C., Struck, U., 2005. Terrigenous organic matter in Holocene sediments from the central Baltic Sea. *NW Europe. Chem. Geol.* 216 (34), 313–328.
- Opsahl, S., Benner, R., 1995. Early diagenesis of vascular plant tissues: Lignin and cutin decomposition and biogeochemical implications. *Geochim. Cosmochim. Ac.* 59, 4889–4904.
- Pempkowiak, J., 1983. C18 reversed-phase trace enrichment of short- and long-chain (C2-C8-C20) fatty acids from dilute aqueous solutions and sea water. *J. Chromatogr.* 258, 93–102, [https://doi.org/10.1016/S0021-9673\(00\)96401-X](https://doi.org/10.1016/S0021-9673(00)96401-X).
- Pempkowiak, J., 1991. Enrichment factors of heavy metals in the Southern Baltic surface sediments dated with ^{210}Pb and ^{137}Cs . *Environ. Int.* 17, 421–428.
- Pempkowiak, J., Pocklington, R., 1983. Phenolic aldehydes as indicators of the origin of humic substances in marine environments. In: Christman, R.F., Gjessing, E.T. (Eds.), *Aquatic and terrestrial humic materials*. Ann Arbor Sci., Michigan, 371–385.
- Pempkowiak, J., Beldowski, J., Staniszewski, A., Leipe, T., Emeis, K.-Ch., 2002. The contribution of the sediment fraction to the fluffy layer suspended matter. *Oceanologia* 44 (4), 513–527.
- Pempkowiak, J., Tylmann, W., Staniszewski, A., Gołębiowski, R., 2006. Lignin depolymerisation products as biomarkers of the organic matter sedimentary record in ^{210}Pb – ^{137}Cs -dated lake sediments. *Org. Geochem.* 37, 1452–1464.
- Pempkowiak, J., Walkusz-Miotk, J., Beldowski, J., Walkusz, W., 2006. Heavy metals in zooplankton from the Southern Baltic. *Chemosphere* 62, 1697–1708.
- Pradhan, U.K., Wu, Y., Shirodkar, P.V., Zhang, J., Zhang, G., 2014. Sources and distribution of organic matter in thirty-five tropical estuaries along the west coast of India – a preliminary assessment. *Estuar. Coast. Shelf Sci.* 151, 21–33.
- Raven, J.A., Johnston, A.M., Kubler, J.E., Korb, R., McInroy, S.G., Handley, L.L., Scrimgeour, C.M., Walker, D.I., Beardall, J., Vanderklift, M., Fredriksen, S., Dunton, K.H., 2002. Mechanistic interpretation of carbon isotope discrimination by marine macroalgae and seagrasses. *Funct. Plant Biol.* 29, 355–378.
- Reeves, A.D., 1995. The use of organic markers in the differentiation of organic inputs to aquatic Systems. *Phys. Chem. Earth* 2, 133–140.
- Requejo, A., Brown, J., Boehm, P., 1986. Lignin geochemistry of sediments from the Narragansett Bay Estuary. *Geochim. Cosmochim. Ac.* 50, 2707–2717.
- Requejo, A., Brown, J., Boehm, P., Sauer, T., 2003. Lignin geochemistry of North American coastal and continental shelf sediments. *Org. Geochem.* 17, 649–662.
- Sederoff, R.R., MacKay, J.J., Ralph, J., Hatfield, R.D., 1999. Unexpected variation in lignin. *Curr. Opin. Plant Biol.* 2, 145–152.
- Staniszewski, A., 2005. *Pochodzenie materii organicznej w osadach dennych Bałtyku Południowego* PhD Thesis., IO PAN, Sopot, 185 pp.
- Staniszewski, A., Lejman, A., Pempkowiak, J., 2001. Horizontal and vertical distribution of lignin in surface sediments of the Gdańsk Basin. *Oceanologia* 43 (4), 421–439.
- Sun, S., Schefuß, E., Mulitza, S., Chiessi, C. M., Sawakuchi, A. O., Zabel, M., Baker, P. A., Hefter, J., Mollenhauer, G., 2017. Origin and processing of terrestrial organic carbon in the Amazon system: lignin phenols in river, shelf, and fan sediments. *Biogeosciences* 14, 2495–2512, <https://doi.org/10.5194/bg-14-2495-2017>.
- Thorton, S., McManus, J., 1994. Application of organic carbon and nitrogen stable isotopes as indicators of organic matter provenance in estuarine systems: evidence from the Tay estuary. *Scotland. Estuar. Coast. Shelf Sci.* 38, 219–233.

- Voss, M., Larsen, B., Leivuori, M., Vallius, H., 2000. Stable isotope signals of eutrophication in coastal Baltic sediments. *J. Marine Syst.* 25, 287–298.
- Wilson, J.O., Valiela, I., Swain, T., 1985. Sources and concentrations of vascular plant material in sediments of Buzzards Bay, Massachusetts, USA. *Mar. Biol.* 90, 129–137.
- Winogradow, A., Pempkowiak, J., 2014. Organic carbon burial rates in the Baltic Sea sediments. *Estuar. Coast. Shelf Sci.* 138, 27–36, <https://doi.org/10.1016/j.ecss.2013.12.001>.
- Winogradow, A., Pempkowiak, J., 2018. Characteristics of sedimentary organic matter in coastal and depositional areas in the Baltic Sea. *Estuar. Coast. Shelf Sci.* 204, 66–75, <https://doi.org/10.1016/j.ecss.2018.02.011>.
- Winogradow, A., Mackiewicz, A., Pempkowiak, J., 2019. Seasonal changes in particulate organic matter (POM) concentrations and properties measured from deep areas of the Baltic Sea. *Oceanologia* 61 (4), 505–521, <https://doi.org/10.1016/j.oceano.2019.05.004>.
- Ye, Z.H., Zhonga, R., Morrison, W.H., Himmelsbach, D.S., 2001. Caffeoyl coenzyme A O-methyltransferase and lignin biosynthesis. *Phytochemistry* 57, 1177–1185.
- Yu, T., Wu, W., Liang, W., Lever, M.A., Hinrichs, K.U., Wang, F., 2018. Growth of sedimentary *Bathyarchaeota* on lignin as an energy source. *Proc. Natl. Acad. Sci. USA* 115 (23), 6022–6027, <https://doi.org/10.1073/pnas.1718854115>.



ORIGINAL RESEARCH ARTICLE

Characteristics of the grey seal (*Halichoerus grypus*) diet in the Vistula River mouth (Mewia Łacha Nature Reserve, southern Baltic Sea), based on the osteological and molecular studies of scat samples

Śławomir Keszka^a, Remigiusz Panicz^{b,*}, Katarzyna Stepanowska^a,
Marcin Biernaczyk^a, Konrad Wrzecionkowski^c, Mikołaj Zybala^d

^aDepartment of Aquatic Bioengineering and Aquaculture, Faculty of Food Science and Fisheries, West Pomeranian University of Technology, Szczecin, Poland

^bDepartment of Meat Sciences, Faculty of Food Science and Fisheries, West Pomeranian University of Technology, Szczecin, Poland

^cWolin National Park, Międzyzdroje, Poland

^dLaureate of the Duke/Oak Foundation 2013 Mini-grants in Marine Conservation, Marine Laboratory, Nicholas School of Environment, Duke University, Beaufort, N.C., USA

Received 17 December 2019; accepted 17 April 2020

Available online 21 May 2020

KEYWORDS

Diet of marine mammals;
DNA barcoding;
Fish species identification;
Lampetra fluviatilis;
Grey seal (*Halichoreus grypus*)

Summary The study analyses for the first time the diet composition of grey seals inhabiting the Polish Baltic Sea coast. Samples of seal scat were collected in the Mewia Łacha Nature Reserve at the mouth of the Vistula River. Using genetic and osteological methods, the remains of organisms included in the grey seals diet were analysed for their taxonomy (families and species). Based on the analysis of 49 scat samples from grey seals, 761 hard parts that could be identified by taxon were isolated. The predominant species in the samples were perch, *Perca fluviatilis* (almost 78% of samples); pikeperch, *Sander lucioperca* (67%); lamprey, *Lampetra fluviatilis* (almost 35% of samples); Baltic cod, *Gadus morhua callarias* (almost 31% of samples) and sea trout, *Salmo trutta trutta* (26.5%). Genetic analysis confirmed the presence

* Corresponding author at: Department of Meat Sciences, Faculty of Food Science and Fisheries, West Pomeranian University of Technology, Szczecin, Kazimierza Królewicza 4, 71-550 Szczecin, Poland. Tel.: +48 91 449 66 64; fax: +48 91 449 66 54

E-mail address: rpanicz@zut.edu.pl (R. Panicz).

Peer review under the responsibility of the Institute of Oceanology of the Polish Academy of Sciences.



Production and hosting by Elsevier

<https://doi.org/10.1016/j.oceano.2020.04.005>

0078-3234/© 2020 Institute of Oceanology of the Polish Academy of Sciences. Production and hosting by Elsevier B.V. This is an open access article under the CC BY-NC-ND license (<http://creativecommons.org/licenses/by-nc-nd/4.0/>).

of Atlantic cod DNA in 69% and sea trout in 63% of samples. The genetic material of the Atlantic herring, *Clupea harengus* has not been identified in the analysed scat samples. Information on grey seals feeding on river lampreys seems to be valuable in the context of lack of knowledge on the occurrence of lampreys in the Vistula River. The methodology used showed that seals fed on species that were the most abundant in the area which is directly associated with the migration cycle of fish. The results of our study allowed the conclusion that the grey seal is an opportunistic predator and its diet reflects and exploits the variations in its habitat.

© 2020 Institute of Oceanology of the Polish Academy of Sciences. Production and hosting by Elsevier B.V. This is an open access article under the CC BY-NC-ND license (<http://creativecommons.org/licenses/by-nc-nd/4.0/>).

1. Introduction

The grey seal (*Halichoreus grypus*) is the largest predator in the Baltic Sea and its population is estimated to exceed 30 000 individuals in the whole Baltic Sea region (Helcom 2018; Skóra et al. 2014). According to “State of the Baltic Sea – Second HELCOM holistic assessment 2011–2016” the number of grey seals counted in the whole Baltic Sea region in 2016 was 30 000 individuals, compared to the limit reference level of 10 000 individuals, and the population trend is assessed as achieving the threshold value.

The Baltic grey seal population has a complicated history. More than hundred years ago the population exceeded 90 000 individuals but the intensive hunting, and environmental pollutions (ecotoxins) in the 1960s and 1970s caused a rapid decline to about 3000 animals (Harding et al., 2007). At the turn of the 20th century, grey seals were abundant in the Gdańsk Bay. Their estimated population only for Eastern Prussia was approx. 1000 individuals. After a sharp decline in the population from over 90 000 at the beginning of the 20th century to approx. 3000 in the 1980s, grey seals disappeared from the southern Baltic Sea limiting their occurrence to the northern areas above the 58th latitude (Pawliczka et al., 2013). Since the late 1980s the Baltic grey seal population has increased in the whole Baltic Sea and grey seals returned to the Polish Baltic coastal zone. The largest colony of grey seals in Poland inhabits the Vistula River estuary. According to the WWF and Hel Marine Station, their number around a sandbar in the Mewia Łacha Nature Reserve varies from approx. 30 to approx. 300 individuals per observation (HMS, 2017).

With populations of grey seals growing, their impacts on fish stocks and possible exploitative competition with commercial fisheries have become increasingly discussed. Some fishermen demand to cull grey seal populations, while some conservationists advocate for sustained protection. One reason for the strong polarization in the debate is the lack of data on fish consumption and the fishery catch by such predators as the grey seal, as well as the lack of estimated effects of the grey seal predation on fish populations. Information on the diet composition of marine predators is crucial to fully understand the ecological status of the sea and to assess conflicts with fisheries (Hansson et al., 2017; Harrington et al., 2015; Lundstrom et al., 2007; Suuronen and Lehtonen, 2012). In most cases, the diet of grey seals inhabiting the Baltic Sea is known to slightly vary depending on the age of the seal, the season of the year and the region of the sea which individuals inhabit (Lundstrom et al., 2007;

Scharff-Olsen et al., 2018). Nevertheless, the diet of the Polish coastal zone (southern Baltic Sea) grey seals is still poorly recognized and needs further studies. Presumably, analysing the diet of grey seals from this region would be important for elucidating the ecological status of the Baltic Sea, but also for assessing the impact of the fisheries policy on the Polish coastal area of the Baltic Sea and for understanding the competition between seals and commercial fisheries.

An analysis of food consumed by seals can be conducted by direct methods, i.e. analysis of stomachs content of individuals that have died naturally, as well as those that have been culled or by-caught as part of fishery activities (Lundstrom et al., 2007, 2010; Suuronen and Lehtonen 2012). However, non-invasive methods based on the collection and examination of seal scat (analysis of bone fragments of fish and otoliths, genetic analysis) are common and have also been used for years. This indirect analysis can be successfully implemented for strictly protected animal species, such as seals (Tollit et al., 2009).

The aim of this study was a non-invasive examination of the grey seals scats samples in the mouth of the Vistula River (Mewia Łacha Nature Reserve), where their largest (30 to approx. 300 individuals, according to HMS (2017)) population in the Polish coastal zone (southern Baltic Sea) is located.

2. Material and methods

2.1. Study area and scat collection

The study material consisted of 49 fresh grey seal scats collected between August and October of 2013 at Mewia Łacha (54°22'09.4"N, 18°56'51.6"E), southern Baltic coastal zone, Poland (Figures 1 and 2). Each scat was placed separately in a plastic bag, labelled with the date of collection, frozen and stored at -20°C for later examinations.

2.2. Direct and molecular identification of prey species in scats

Samples for molecular studies were collected from each scat (n=49) by low-speed drilling ($\varnothing = 6$ mm) in frozen scats and then used for DNA isolation using GeneMATRIX Stool DNA Purification Kit (EuRx, Gdańsk, Poland), following the manufacturer's instructions. The qualitative and quantitative assessment of the isolates was carried out by electrophoresis



Figure 1 Map of the study site located in the Vistula River mouth, southern Baltic Sea.



Figure 2 Grey seals basking on a sandbar located in the Vistula River mouth (photo by Dariusz Bógdała).

Table 1 Percentage and number of samples in which taxa were identified.

| Taxa identified in seal scats | [%] | Number of scats | Taxon-specific parts (n) | |
|--------------------------------------|-------|-----------------|--------------------------|--------------|
| Cyprinidae | 14.29 | 7 | Scales (6) | Bones (5) |
| Percidae | 14.29 | 7 | Scales (222) | Bones (16) |
| <i>Salmo trutta</i> m. <i>trutta</i> | 26.53 | 13 | Scales (23) | Bones (8) |
| <i>Lampetra fluviatilis</i> | 34.69 | 17 | | Bones (61) |
| <i>Neogobius melanostomus</i> | 2.04 | 1 | Otoliths (1) | Bones (2) |
| <i>Sander lucioperca</i> | 67.35 | 33 | Scales (181) | Bones (15) |
| <i>Perca fluviatilis</i> | 77.55 | 38 | Scales (160) | Bones (20) |
| <i>Gadus morhua callarias</i> | 30.61 | 15 | Otoliths (3) | Bones (37) |
| <i>Osmerus eperlanus</i> | 2.04 | 1 | | Otoliths (2) |

in 1.5% agarose gel followed by spectrophotometric measurements using the NanoDrop 2000 instrument (Thermo Scientific). For all investigated samples, PCR amplification of fish species-specific markers was conducted using the primers Herr16SF and Herr16SR for Atlantic herring, *Clupea harengus* (Deagle et al., 2006), GmoF and GmoR for Atlantic cod, *Gadus morhua* (Marshall et al., 2010), GUT1 and GUT1 for Gadidae (Rosel and Kocher, 2002) and salmcytb7 and salmcytb8, salm16s7 and salm16s18 for Salmonidae (Parsons et al., 2005). All PCR reactions included positive samples from the author's internal repository. The amplification of the selected regions was conducted in accordance with the methodology proposed in the above-mentioned studies and prepared based on the GoTaq®G2 Hot Start polymerase (Promega, Germany), Green Master Mix 12.5 µl, primers 0.5 µl (10 pmol/µl) each, H₂O DEPC 10.5 µl and DNA 1 µl. All PCR amplifications were carried out on a GeneAmp® PCR System 9700 thermocycler (Applied Biosystems), and the results were evaluated by amplicon electrophoresis in 3% agarose gel. Bidirectional Sanger sequencing of the obtained single PCR products, or bands separated, removed from gel and purified using Gel-Out kit (A&A Biotechnology, Poland) was ordered from Genomed, Warsaw, Poland. Analysis of thus obtained sequences was performed using the BioEdit 7.2 software and BLAST.

Next, each scat (n=49) was individually thawed and washed through sieves with gradual mesh sizes (2.5 to 0.5 mm) under running water to collect undigested parts of preys (Daneri et al., 2008). Prey was identified to the lowest possible taxon by direct assessment of sagittal otoliths and other structures, such as vertebrae, chewing pads or pharyngeal teeth (Lundström et al., 2007).

3. Results

3.1. Osteology-based species identification

Based on the analysis of 49 scat samples from grey seals, 761 hard parts, that could be identified by taxon, were isolated (Table 1 and Table 2). Only a few bony residues were intact, including otoliths, fin rays, tooth, and the most abundant scales. The remaining bony elements allowing identification were partially broken and partially digested. These elements usually included vertebrae, preoperculae and premaxillae, as well as pharyngeal bones, but enabled the iden-

tification of fish (Figure 3). The predominant species in the samples, identified mainly based on the abundant presence of scales, were perch (almost 78% of samples) and pikeperch (67%). The third most frequent species in the samples was river lamprey (*Lampetra fluviatilis*) which was identified based on the presence of the characteristic teeth of the sucking disc (almost 35% of samples). The subsequent most frequent species were Atlantic cod (almost 31% of samples), identified based on teeth with fragments of maxillae, and sea trout (26.5%), determined using caudal vertebra, premaxilla and very few otoliths. In single cases, otoliths of round goby (*Neogobius melanostomus*) and smelt (*Osmerus eperlanus*) were found (2% of samples). Based on the partially digested bony elements, 14.3% of samples were identified as belonging to the Cyprinidae family, and the same percent to the Percidae family, without identification of species.

3.2. Molecular identification of species from scats

Assembled sequences were compared to the GenBank database using the BLAST software which enabled prey identification in the collected grey seal scats. In total, two species were identified, i.e. Atlantic cod (*Gadus morhua*) and sea trout (*Salmo trutta*) in 34 and 31 scat samples, respectively. The sequence identified for Atlantic cod showed 100% similarity to the GenBank record KX267089 submitted for the *G. morhua* isolate GEO10. Sequences obtained for sea trout were identical with the cytochrome b sequence submitted to GenBank under accession no. LT617585. The subsequent molecular analysis did not identify other fish species in the analysed scats.

4. Discussion

The seal and human, occupying the top level of the food chain, share the same food niche in many marine ecosystems. The grey seal is an obligate piscivore and is the largest of the three species of seals in the Baltic Sea, i.e. harbour seal, *Phoca vitulina* and ringed seal, *Pusa hispida* (Fjälling, 2006). As fish resources in seas and oceans decrease, a competition between fishermen and seals increases. One of the main complaints, raised by the community of fishermen, is that the grey seal population is growing explosively, which

Table 2 Number of taxon-specific hard parts in collected scat samples.

| Scat number | Otoliths (n) | Bones (n) | Scales (n) |
|-------------|----------------|--|---|
| 1 | Cod (1) | Cod (3), Pikeperch (4) | Perch (11), Pikeperch (16) |
| 2 | Smelt (2) | Cod (2), Perch (4), Lamprey (3) | Percidae (52) |
| 3 | | Perch (3), Seatrout (2) | Seatrout (1), Perch (9), Pikeperch (8) |
| 4 | | Perch (2), Pikeperch (4) | Seatrout (1) |
| 5 | | Cyprinidae (1), Lamprey (3) | Pikeperch (4), Perch (4), Seatrout (2) |
| 6 | | Perch (1), Lamprey (3) | Pikeperch (3), Percidae (46) |
| 7 | Round goby (1) | Seatrout (1), Pikeperch (4), Perch (2), Percidae (3), Round Goby (1) | Cyprinidae (2), Pikeperch (20), Perch (6) |
| 8 | Cod (1) | Perch (1), Lamprey (2) | Pikeperch (6), Perch (4) |
| 10 | | Cod (3) | Pikeperch (7), Perch (7) |
| 11 | | Percidae (4), Pikeperch (3), Lamprey (3), Cyprinidae (1) | Seatrout (1) |
| 12 | | Pikeperch (2), Perch (1) | |
| 13 | | Cod (2), Perch (4) | Pikeperch (3) |
| 14 | | Cod (2) | Perch (3), Pikeperch (5), Seatrout (3) |
| 15 | | | Pikeperch (4) |
| 16 | | Cyprinidae (1) | Seatrout (2), Perch (9), Pikeperch (9) |
| 17 | | Cod (1) | |
| 18 | Cod (1) | Cod (4), Lamprey (3) | Cyprinidae (1) |
| 19 | | | Pikeperch (1) |
| 20 | | Lamprey (6) | Cyprinidae (1) |
| 21 | | Seatrout (1) | Perch (6), Pikeperch (4) |
| 22 | | | Perch (5), Pikeperch (6) |
| 23 | | Lamprey (4) | Perch (4), Pikeperch (5) |
| 24 | | | Seatrout (3) |
| 25 | | | Perch (3), Pikeperch (3) |
| 26 | | Cod (2) | Perch (3), Pikeperch (4) |
| 27 | | Percidae (2) | Perch (5), (Percidae (81) |
| 28 | | Lamprey (3) | Perch (7), Pikeperch (6) |
| 29 | | Seatrout (1) | Perch (4), Pikeperch (4) |
| 30 | | Cod (2) | Perch (3), Pikeperch (3) |
| 31 | | | Pikeperch (3) |
| 32 | | Cod (2) | Perch (5) |
| 33 | | | Perch (4), Pikeperch (4) |
| 34 | | Lamprey (4) | Perch (4) |
| 35 | | Seatrout (1) | Perch (4) |
| 36 | | Cod (2), Lamprey (1) | Perch (3) |
| 37 | | Percidae (4) | Perch (3), Pikeperch (6), Percidae (21) |
| 38 | | Lamprey (3) | Perch (2), Pikeperch (1) |
| 39 | | | Perch (3) |
| 40 | | Cod (3), Seatrout (2) | Perch (2), Pikeperch (4) |
| 41 | | Cyprinidae (2) | Perch (6), Pikeperch (4), Cyprinidae (2) |
| 42 | | Lamprey (5) | Perch (3), Pikeperch (3) |
| 43 | | Lamprey (6) | Seatrout (4), Perch (4) |
| 44 | | Perch (2) | Seatrout (5) |
| 45 | | Cod (4) | Perch (4), Pikeperch (2) |
| 46 | | Lamprey (8) | Perch (2) |
| 47 | | Percidae (3) | Perch (4), Pikeperch (11), Percidae (22) |
| 48 | | Lamprey (3) | Pikeperch (22) |
| 49 | | Lamprey (4) | Seatrout (3), Perch (4) |

is the main cause of declining fish stocks (Olsen et al. 2018). However, the extermination of grey seals could be a short-sighted response and possibly disturb the ecological balance of the Baltic Sea (van Beest et al., 2019). Interactions between fishermen and seals are of interest to both

researchers and institutions/organizations dedicated to biological resource management in waters (Gosch et al., 2014). The largest colony of grey seals in Poland inhabits the estuary of the Vistula River. According to the WWF and Hel Marine Station, their number around a sandbar in the Mewia

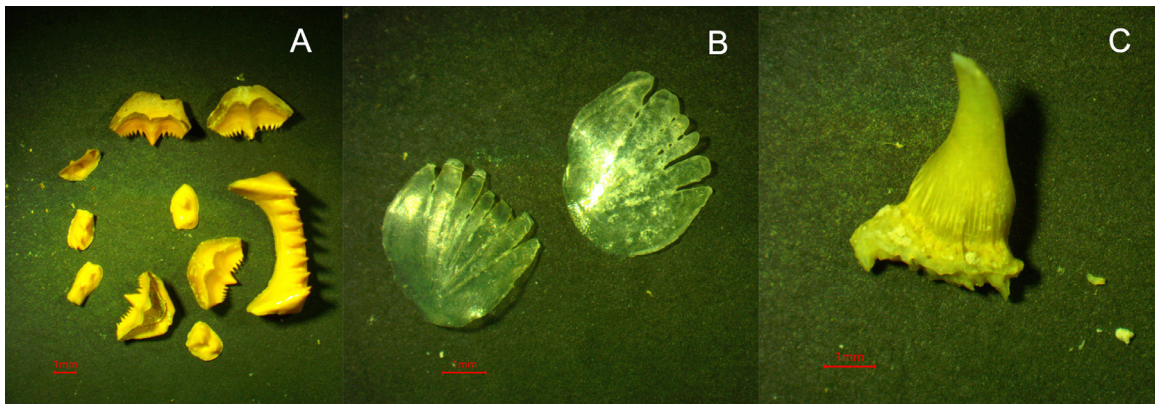


Figure 3 The hard parts of fish, of different sizes and shapes, retrieved from scats of grey seals collected at the Vistula River mouth. A – tooth of *Lampetra fluviatilis*, B – scales of *Perca fluviatilis*, C – teeth of *Gadus morhua*.

Lacha Nature Reserve varies from approx. 30 to approx. 300 individuals per observation (HMS, 2017). Such a great number of seals, observed at or inhabiting one site, creates conflicts between the interest of coastal fishermen and objectives of species protection. This warrants a more detailed investigation into the diet of grey seals at the site of their greatest abundance on the Polish coast of the Baltic Sea. Published data regarding the size of the seal population in Sweden indicate the presence of 17 600 grey seals in 2003. Losses in fisheries in that country caused by seals were assessed at 3.5 million USD in 1996–1997 (Westerberg et al., 2000).

An interesting observation, in the light of the existing knowledge on the occurrence of Petromyzontidae, is the high frequency of river lamprey (*Lampetra fluviatilis*) in the diet of the investigated grey seals from the mouth of the Vistula River. The lamprey is an anadromous species, with different populations living in coastal and fresh waters (Bartel et al., 2010). Spawning, along with larval development, takes place in rivers. The proper period of feeding, and parasitizing, is during their occurrence in the sea. However, their occurrence is limited to brackish coastal waters. The maximum critical salinity tolerated by river lamprey is 22 PSU (Beamish, 1980). In general, there are two spawning cycles of lampreys – autumn and spring (Bartel et al., 2010). The autumn cycle begins in August or September (Raczyński, 2003). Samples for analysis were collected from August to October 2013, which partially explains the frequency of occurrence of this species in the diet of seals. The most opportunistic seals benefited from the abundant presence of lampreys in the mouth of the Vistula River. In the available literature describing the diet of seals, there is information on grey seals feeding on sea lampreys in the North Sea, on the coast of Ireland and the Gulf of Bothnia in the Baltic Sea (Gosch et al., 2014, Scharff-Olsen et al., 2018). The status of the river lamprey population in the Vistula River, in the absence of detailed studies in this area, is not fully understood. Currently, there are only single reports of this species entering the lower Vistula River system and the Vistula Lagoon (Bartel et al., 2010; Radtke et al., 2013). Information on grey seals feeding on river lampreys seems to be valuable in the context of lack of knowledge on the occurrence of lampreys in the Vistula River.

The end of August is also a period of sea trout gathering in estuaries followed by migration toward upper river sections for spawning. This fact probably explains the high proportion of this species in the tested samples which was also confirmed using genetic studies. Sea trout have been reported in the Vistula River and its tributaries: Drwęca and Brda (Radtke et al., 2015). The presence of both trout and salmon in the diet of grey seals in the Baltic Sea was determined by Lundström et al. (2007) and Lundström et al. (2010). Of note, in the context of interactions between fisheries and seals, is the fact that despite the presence of representatives of Salmonidae, such as trout, in the diet of grey seals, salmon was not detected in the tested samples. When historical information is referred to the contemporary data for the investigated area, a significant decrease in the abundance of salmon is noticeable. In the 1980s, salmon was even considered extinct in Poland (Witkowski et al., 2009). However, thanks to the reintroduction of the species, conducted since 1985 under the “Program for the restocking of Polish sea areas”, salmon has been restored in the waters of Poland. It should be noted that despite the good prospects for the maintenance of salmon in the rivers of northern Poland, its local genotype has been irretrievably lost, and the salmon population in Poland is still small, bearing the conservation status EW/CD (Witkowski et al., 2009). The salmon and sea trout are intensively fished by both commercial and recreational fishers, and the closure of commercial offshore fishery for salmon has resulted in increased returns of adult individuals to their spawning rivers (ICES, 2016).

Special attention, in the context of other studies of seal diet in the Baltic region, should be given to the fact that the study did not reveal Atlantic herring in the diet of grey seals. The conducted genetic analyses of faecal samples, in absence of bony residues of Atlantic herrings, did not reveal the presence of this species in the diet of seals inhabiting the Vistula River mouth in the sampling period between August and October. The reason for that is the seasonal occurrence of the Atlantic herring in the Gdańsk Bay, with a peak in March and April (spawning period). Roos and Pawliczka (2010) in their study underlined that during spring season the Atlantic herring individuals were highly abundant and became easy prey for young seals inhabiting coastal wa-

ters. In the study by Lundström et al. (2007) conducted in the Baltic Sea, samples (stomachs and intestines) from grey seals were collected between 2001 and 2004 and the Atlantic herring was found in 81% of the total number of the analysed samples. The relatively high abundance of Atlantic cod remains is not exceptional in the light of the observations by other researchers analysing the food of seals in the Baltic Sea (Lundström et al., 2007). Similarly, the diet of grey seal in the North Sea was dominated by the Atlantic cod, lesser sand eel (*Ammodytes marinus*) and pollock (*Polachius pollachius*) (Hammond and Wilson, 2016). On the other hand, Fjälling (2006) concluded that substitution of the Atlantic cod by other species in the diet of the Baltic Sea seals is caused by a significant reduction in the population of the Atlantic cod. The amount of fish consumed per day depends on its energy value (e.g., fat content), but an average daily intake of 4–7 kg is a commonly accepted figure (Mansfield and Beck, 1977; Rae, 1960). The fact that, in the group of otoliths, only a few (n=3) of them belonged to the Atlantic cod confirms numerous statements of scientists and fishermen that seals eat the soft part of fish but omit head of cod and salmon in their diet (Skóra et al. 2014).

Due to the occurrence of the investigated grey seals in the mouth of the Vistula River, their diet was expected to include the freshwater fish species in addition to the marine species. Taking into account the composition of the ichthyofauna determined in a study by Radtke et al. (2016) using electrofishing in the mouth sections of 19 natural tributaries of the lower Vistula River below the Włocławek reservoir, the presence of freshwater ichthyofauna species in the diet of seals is highly probable. The aforementioned study of the ichthyofauna composition in the Vistula River mouth revealed the presence of 37 fish species and, possibly, two lamprey species, with the highest share of eurytopic species: perch *Perca fluviatilis*, roach *Rutilus rutilus* and white bream *Blicca bjoerkna* (Radtke et al., 2016). In the investigated samples, among the remains of fish which could be classified as belonging to Cyprinidae, no particular species could be identified, although the most common findings were fragments of pharyngeal bones. However, this group of fish can be a permanent ingredient of the diet of seals due to its all-year presence in the Vistula River mouth. Among Percidae, the species most commonly detected in the tested samples were perch and pikeperch, which seems to be justified, as both species are considered as the most frequently and abundantly present in the lower Vistula River. It is also crucial to mention that the obtained results might be biased due to the detectability of different hard parts. The study found numerous thick hard structures of perch, pikeperch, lamprey, cod or cyprinids, and fewer or none of those derived from species with thin bones and small otoliths, e.g., smelt, round goby or sprat. However, it is highly probable that thin bones and small otoliths dissolved in the stomachs and guts of seals, and thus the share of fish species in the food may have been larger than what was found in the analysed scats. Therefore, molecular methods may successfully confirm the results obtained in the analysis of hard parts as it was shown for Atlantic herring. Nevertheless, determining the diet composition of marine mammals is always hindered by additional aspects, such as digestive erosion, secondary prey types and contamination. Therefore, in further studies, use of a panel of spe-

cific primers or a more holistic approach (meta-sequencing) should be used in combination with hard part analysis and, where possible, seal stomach and gut content analysis. Our study, characterized by a limited duration of the sampling period, still allowed the conclusion that grey seal is an opportunistic predator that exploits the local ichthyofauna and the variations in the seal's diet reflect the state of exploited habitat. It is also clear that given the grey seal preferred prey, there is an overlap between the seal and human exploitation of marine resources.

5. Conclusions

The obtained results provide new information on the diet of grey seals inhabiting the mouth of the Vistula River. It is demonstrated that the presence of certain fish species in the diet probably depends not only on specific nutritional preferences of seals (associated with, e.g., obtaining high-energy food in the form of fatty fish) but also on the local availability of these fish species. This conclusion is indirectly supported by the absence of salmon in the tested scat samples. Studies providing more detailed knowledge of the diet of grey seals inhabiting the southern Baltic area can contribute to rational fisheries management in this zone. However, further studies are necessary to define the size of possible biases resulting from digestive erosion and abundance of secondary prey species.

Acknowledgements

The study was approved by the Regional Directorate of Environmental Protection in Gdańsk. Permission number: RDOŚ-Gd-PNII.6205.35.2013.MaK.1. This work has been funded by Department of Aquatic Bioengineering and Aquaculture ZUT, from Szczecin funds.

References

- Bartel, R., Bradauskas, B., Ikonen, E., Mitans, A., Borowski, W., Garbaciak-Wesołowska, A., Witkowski, A., Błachuta, J., Morzuch, J., Bernaś, R., Kapusta, A., 2010. Patterns of river lamprey size and sex ratio in the Baltic Sea basin. *Arch. Pol. Fish.* 18, 247–255.
- Beamish, F.W.H., 1980. Osmoregulation in juvenile and adult lampreys. *Can. J. Fish. Aquat. Sci.* 37, 1739–1750, <https://doi.org/10.1139/f80-219>.
- Daneri, G.A., Carlini, A.R., Harrington, A., Balboni, L., Hernández, C.M., 2008. Interannual variation in the diet of non-breeding male Antarctic fur seals, *Arctocephalus gazella*, at Isla 25 de Mayo/King George Island. *Polar Biol.* 31, 1365–1372, <https://doi.org/10.1007/s00300-008-0475-3>.
- Deagle, B.E., Eveson, J.P., Jarman, S.N., 2006. Quantification of damage in DNA recovered from highly degraded samples – a case study on DNA in faeces. *Front. Zool.* 3, art. no. 11, 10 pp., <https://doi.org/10.1186/1742-9994-3-11>.
- Fjälling, A., 2006. The conflict between grey seals (*Halichoerus grypus*) and the Baltic coastal fisheries: new methods for the assessment and reduction of catch losses and gear damage. Ph.D. thesis. Linköping Univ. Electr. Press, Linköping, 32 pp.
- Gosch, M., Hernandez-Milian, G., Rogan, E., Jessopp, M., Cronin, M., 2014. Grey seal diet analysis in Ireland highlights the

- importance of using multiple diagnostic features. *Aquat. Biol.* 20 (2), 155–167, <https://doi.org/10.3354/ab00553>.
- Hammond, P.S., Wilson, L.J., 2016. Grey seal diet composition and prey consumption. *Scot. Mar. Fresh. Sci.* 7 (20), 1–47, <https://doi.org/10.7489/1799-1>.
- Hansson, S., Bergström, U., Bonsdorff, E., Härkönen, T., Jepsen, N., Kautsky, L., Lundström, K., Lunneryd, S.-G., Ovegård, M., Salmi, J., Sendek, D., Vetemaa, M., 2017. Competition for the fish–fish extraction from the Baltic Sea by humans, aquatic mammals, and birds. *ICES J. Mar. Sci.* 75 (3), 999–1008, <https://doi.org/10.1093/icesjms/fsx207>.
- Harding, K.C., Härkönen, T., Helander, B., Karlsson, O., 2007. Status of Baltic grey seals: Population assessment and extinction risk. *Grey seals in the North Atlantic and the Baltic*, 6. NAMMCO Sci. Publ., 33–56.
- Harrington, A., Daneri, G.A., Carlini, A.R., Reyger, D.S., Corbalán, A., 2015. Seasonal variation in the diet of *Arctocephalus gazella* at 25 de Mayo/King George Island, South Shetland Islands. *Antarctica. Pol. Biol.* 40 (2), 471–475, <https://doi.org/10.1007/s00300-016-1959-1>.
- HELCOM, 2018. State of the Baltic Sea – Second HELCOM holistic assessment 2011–2016. *Baltic Sea Environ. Proc.* 155. Summ. Rep., 155 pp., available at: www.helcom.fi/baltic-sea-trends/holistic-assessments/state-of-the-baltic-sea-2018/reports-and-materials.
- HMS, 2017. Seal observation reports for Mewia Łacha Nature Reserve. Hel Marine Station. Online database, available at: <http://www.fokarium.pl/obserwacjefok/obserwacjefokrezerwat.htm>.
- ICES, 2016. Salmon (*Salmo salar*) in subdivisions 22–31 (Baltic Sea, excluding the Gulf of Finland). In: Report of the ICES Advisory Committee 2016, ICES Advice 2016, 16 pp. available at: <http://ices.dk/sites/pub/Publication%20Reports/Advice/2016/2016/sal-2231.pdf>.
- Lundström, K., Hjerne, O., Alexandersson, K., Karlsson, O., 2007. Estimation of grey seal (*Halichoerus grypus*) diet composition in the Baltic Sea. *Grey seals in the North Atlantic and the Baltic*, 6. NAMMCO Sci. Publ., 177–196.
- Lundström, K., Hjerne, O., Lunneryd, S.-G., Karlsson, O., 2010. Understanding the diet composition of marine mammals: grey seals (*Halichoerus grypus*) in the Baltic Sea. *ICES J. Mar. Sci.* 67, 1230–1239, <https://doi.org/10.1093/icesjms/fsq022>.
- Mansfield, A.W., Beck, B., 1977. The grey seal in eastern Canada. *Arctic Biological Station, Fisher. Mar. Service, Dept Fisher. Environ. Tech. Rep. No. 704*.
- Marshall, H.D., Hart, K.A., Yaskowiak, E.S., Stenson, G.B., McKinnon, D., Perry, E.A., 2010. Molecular identification of prey in the stomach contents of harp seals (*Pagophilus groenlandicus*) using species-specific oligonucleotides. *Mol. Ecol. Res.* 10, 181–189, <https://doi.org/10.1111/j.1755-0998.2009.02713.x>.
- Olsen, M.T., Galatius, A., Härkönen, T., 2018. The history and effects of seal-fishery conflicts in Denmark. *Mar. Ecol. Prog. Ser.* 595, 233–243, <https://doi.org/10.3354/meps12510>.
- Parsons, K.M., Piertney, S.B., Middlemas, S.J., Hammond, P.S., Armstrong, J.D., 2005. DNA-based identification of salmonid prey species in seal faeces. *J. Zool.* 266, 275–281, <https://doi.org/10.1017/S0952836905006904>.
- Pawliczka, I., Górski, W., Hylla-Wawryniuk, A., 2013. Ocena stanu ochrony gatunku foka szara *Halichoerus grypus* w obszarach NATURA2000 w rejonie Zatoki Gdańskiej. *Publ. NATURA2000 Project* 32 pp., available at: http://im.gda.pl/images/Projekty/natura_2000/MATERIALY/15_01/Ocena%20stanu%20ochrony%20-%20foka%20szara.pdf.
- Raczyński, M., 2003. Biologiczna i morfologiczna analiza porównawcza minoga rzeczynego (*Lampetra fluviatilis* L.) z Odry i Wisły. Ph.D. thesis. Agricultural Univ. (since 2009 West Pomeranian Univ. Technol.), Szczecin.
- Radtke, G., Bernaś, R., Dębowski, P., Morzuch, J., Skóra, M., 2013. Ichtyofauna małych doptywów dolnej Wisły. Część I – Między Włocławkiem a Świeciem. *Rocz. Nauk. PZW* 26, 99–115.
- Radtke, G., Bernaś, R., Dębowski, P., Morzuch, J., Skóra, M., 2016. Ichtyofauna przyujściowych odcinków dopływów dolnej Wisły. *Chrońmy Przyr. Ojcz.* 72 (5), 323–336.
- Radtke, G., Bernaś, R., Skóra, M., 2015. Występowanie wędrownych i reofilnych gatunków ryb i minogów w rzekach północnej Polski w świetle historycznych materiałów do początku XX wieku. *Rocz. Nauk. PZW* 28, 123–149.
- Rae, B.B., 1960. Seals and Scottish fisheries. *Mar. Res.* 2, 1–39.
- Rosel, P.E., Kocher, T.D., 2002. DNA-based identification of larval cod in stomach contents of predatory fishes. *J. Exp. Mar. Biol. Ecol.* 267, 75–88, [https://doi.org/10.1016/S0022-0981\(01\)00359-8](https://doi.org/10.1016/S0022-0981(01)00359-8).
- Ross, A., Pawliczka, I., 2010. Życie fok – prawdziwa historia. *FRUG – Gdańsk Univ., Gdańsk*, 45 pp.
- Scharff-Olsen, C.H., Galatius, A., Teilmann, J., Dietz, R., Andersen, S.M., Jarnit, S., Kroner, A.M., Botnen, A.B., Lundström, K., Møller, P.R., Olsen, M.T., 2018. Diet of seals in the Baltic Sea region: a synthesis of published and new data from 1968 to 2013. *ICES J. Mar. Sci.* 76 (1), 284–297, <https://doi.org/10.1093/icesjms/fsy159>.
- Skóra, K., Pawliczka, I., Bała, M., Koss, M., Bednarek, P., Miętkiewicz, W., 2014. Nasze foki. In: „Wsparcie ochrony zagrożonych siedlisk i gatunków Morza Bałtyckiego w rejonie Zatoki Gdańskiej” EOG 2009 Operational Programme PL02: “The protection of the biological diversity and ecosystems” Grant Publications.
- Suuronen, P., Lehtonen, E., 2012. The role of salmonids in the diet of grey and ringed seals in the Bothnian Bay, northern. *Baltic Sea. Fish. Res.* 125–126, 283–288, <https://doi.org/10.1016/j.fishres.2012.03.007>.
- Tollit, D.J., Schulze, A.D., Trites, A.W., Olesiuk, P.F., Crockett, S.J., Gelatt, T.S., Ream, R.R., Miller, K.M., 2009. Development and application of DNA techniques for validating and improving pinniped diet estimates. *Publ. U.S. Dept. Comm. Paper no. 205*, available at: <http://digitalcommons.unl.edu/usdeptcommercepub/205>.
- van Beest, F.M., Mews, S., Elkenkamp, S., Schuhmann, P., Tso-lak, D., Wobbe, T., Bartolino, V., Bastardie, F., Dietz, R., von Dorrien, C., Galatius, A., Karlsson, O., McConnell, B., Nabe-Nielsen, J., Olsen, M.T., Teilmann, J., Langrock, R., 2019. Classifying grey seal behaviour in relation to environmental variability and commercial fishing activity – a multivariate hidden Markov model. *Sci. Rep.* 9 (1), art. no. 5642, 14 pp., <https://doi.org/10.1038/s41598-019-42109-w>.
- Westerberg, H., Fjälling, A., Martinsson, A., Haamer, J., 2000. Säl-skadord i det svenska fisket: beskrivning och kostnadsberäkning baserad på loggboksstatistik och journalföring 1996–1997. *Fisk. Rap.* 3, 3–38.
- Witkowski, A., Kotusz, J., Przybylski, M., 2009. Stopień zagrożenia stokowodnej ichtiofauny Polski: Czerwona lista minogów i ryb – stan 2009. *Chrońmy Przyr. Ojcz.* 65 (1), 33–52.

Available online at www.sciencedirect.com

ScienceDirect

journal homepage: www.journals.elsevier.com/oceanologia

SHORT COMMUNICATION

Some probabilistic properties of surf parameter

Dag Myrhaug*

Department of Marine Technology, Norwegian University of Science and Technology (NTNU), Trondheim, Norway

Received 26 August 2019; accepted 13 February 2020

Available online 28 February 2020

KEYWORDS

Surf parameter;
Spectral surf
parameter;
Phillips spectrum;
JONSWAP spectrum;
Joint frequency
tables;
Wave runup;
Wave statistics

Summary This article is supplementary to Myrhaug (2018) and presents some probabilistic properties of the surf parameter for individual waves and the spectral surf parameter for sea states by using distributions based on data from the Norwegian continental shelf. The average statistical features given by the mean value and the standard deviation of the two surf parameters are considered. Examples of results for the surf parameter are provided for a Phillips spectrum and a family of JONSWAP spectra for wind sea, and for sea states using a joint frequency table of significant wave height and mean zero-crossing wave period for combined wind sea and swell. The spectral surf parameter results are obtained by using a joint distribution of significant wave height and spectral surf parameter, and the mean statistical properties are given for joint frequency tables of significant wave height and mean zero-crossing wave period from three deep water locations on the Norwegian continental shelf. It is also demonstrated how the results can be applied to calculate the vertical wave runup elevation for breaking waves.

© 2020 Institute of Oceanology of the Polish Academy of Sciences. Production and hosting by Elsevier B.V. This is an open access article under the CC BY-NC-ND license (<http://creativecommons.org/licenses/by-nc-nd/4.0/>).

The surf parameter, also denoted as the Iribarren number or the surf similarity parameter, is used frequently to characterize physical processes in the surf zone. It is defined as

the ratio between the slope of a beach or a coastal structure and the square root of the deep water wave steepness, as introduced originally by Iribarren and Nogales (1949) and later applied by Battjes (1974). The surf zone refers to shallow water regions where wave breaking takes place, and types of breakers on slopes are classified by using the surf parameter (Battjes, 1974). Wave breaking in addition to turbulence and heat due to dissipation of the offshore wave energy flux lead to loss of energy, which causes the wave height to decrease towards the shoreline within the surf zone. The nearshore circulation is also affected by wave breaking as it leads to strong currents along shorelines. Intense sediment transport in the surf zone is caused by the high turbulence level due to breaking waves. Wave runup

* Corresponding author at: Department of Marine Technology, Norwegian University of Science and Technology (NTNU), Otto Nielsens vei 10, NO-7491 Trondheim, Norway.

E-mail address: dag.myrhaug@ntnu.no

Peer review under the responsibility of the Institute of Oceanology of the Polish Academy of Sciences.



Production and hosting by Elsevier

<https://doi.org/10.1016/j.oceano.2020.02.003>

0078-3234/© 2020 Institute of Oceanology of the Polish Academy of Sciences. Production and hosting by Elsevier B.V. This is an open access article under the CC BY-NC-ND license (<http://creativecommons.org/licenses/by-nc-nd/4.0/>).

and wave rundown on beaches and coastal structures like breakwaters, seawalls, sand barriers and artificial reefs are also assessed by using the surf parameter; see e.g. Atkinson et al. (2017) for a review and summary of wave runup formulae. The surf parameter is mostly defined in terms of individual wave parameters, but characteristic surf parameters are also defined in terms of sea state wave parameters; the spectral surf parameter defined subsequently is often used in coastal work (see e.g. Kim (2010); EurOtop (2018)). The surf parameter enters in many empirical formulae and theoretical models which are used to describe many of the processes referred to; the importance and relevant examples of applications are provided in e.g. Kim (2010); EurOtop (2018).

Earlier works on statistical properties of the surf parameter for individual waves include Tayfun (2006), Myrhaug and Fouques (2007, 2012), Myrhaug and Rue (2009), Myrhaug and Leira (2011), Myrhaug et al. (2016). Tayfun (2006) presented a lognormal distribution of the surf parameter, while Myrhaug and Fouques (2007) provided a distribution given by the combined Fréchet and lognormal distributions. Myrhaug and Fouques (2012) presented a joint distribution of wave height and surf parameter. The statistics of two successive surf parameters were addressed by Myrhaug and Rue (2009) as well as by Myrhaug and Leira (2011). Myrhaug et al. (2016) presented a comparative study of joint distributions of wave height and surf parameter including finite bandwidth effects. Statistical aspects of the spectral surf parameter were addressed in Myrhaug and Fouques (2010) by providing a joint distribution of significant wave height and spectral surf parameter. Furthermore, statistical properties of the spectral surf parameter were used by Myrhaug (2015), Myrhaug and Leira (2017) and Myrhaug and Sunde (2018, 2019) to estimate wave runup and wave rundown by adopting some of the formulae reviewed by Atkinson et al. (2017). More specifically, Myrhaug (2015) and Myrhaug and Leira (2017) based their results on applying the de la Pena et al. (2014) wave runup formulae and the Blenkinsopp et al. (2016) wave runup and wave rundown formulae, respectively. Myrhaug and Sunde (2018, 2019) based their results on applying runup and rundown formulae together with long-term wind statistics (2018) and long-term wave statistics (2019).

The recent years research focus on wave runup and wave rundown is driven by the attention to climate change and consequences of the possible increase of sea level and more extreme weather. For shorelines and coastal structures it is therefore crucial to be able to make reliable assessments of extreme wave runup and wave rundown events for safe and cost-efficient coastal protections. In this context statistical properties of the surf parameter are an important building stone.

This article presents some statistical properties of the surf parameter for individual waves and the spectral surf parameter representing a sea state characteristic. Here the focus is on the average statistical properties of these parameters expressed in terms of the mean value and the standard deviation, and thus these results are new and complementary to previous results. The Myrhaug and Fouques (2007) surf parameter distribution is used to calculate the statistical values of the surf parameter for individual waves within a sea state; i.e. for a given value of the spectral

surf parameter for a sea state. Results are exemplified for a Phillips spectrum, for a family of JONSWAP spectra, and for sea states provided by a joint frequency table of significant wave height H_s and mean zero-crossing wave period T_z . The statistical properties of the spectral surf parameter defined in terms of H_s and T_z are given by using a joint distribution of H_s and spectral surf parameter. This article is supplementary to Myrhaug (2018) that provided similar results for the deep water wave steepness for individual waves and the deep water spectral wave steepness representing a sea state characteristic. It should be noted that the outline of this paper follows closely that in Myrhaug (2018).

The article is organized as follows. This introduction is followed by summarizing the Myrhaug and Fouques (2007) surf parameter distribution and the joint distribution of H_s and spectral surf parameter. Then examples of estimating the surf parameter and the spectral surf parameter are presented together with an example of application of calculating the vertical wave runup elevation above the still water level for breaking waves. Finally, a summary and the main conclusions are provided.

The surf parameter is defined as $\xi = m/\sqrt{S}$ where $m = \tan \theta$ is the slope with an angle θ with the horizontal, $S = H/((g/2\pi)T^2)$ is the deep water wave steepness, H is the wave height, T is the wave period, and $g = 9.81 \text{ ms}^{-2}$ is the acceleration due to gravity. Myrhaug and Fouques (2007) provided the probability density function (*pdf*) of the normalized surf parameter $\hat{\xi} = \xi/\xi_{rms}$ given by the following combined Fréchet and lognormal *pdfs*

$$p(\hat{\xi}) = \begin{cases} p_1(\hat{\xi}) = k\nu^k \hat{\xi}^{-(k+1)} \exp\left[-\left(\frac{\hat{\xi}}{\nu}\right)^{-k}\right]; & 0 \leq \hat{\xi} \leq \hat{\xi}_1 = 0.913 \\ p_2(\hat{\xi}) = \frac{1}{\sqrt{2\pi}\sigma \hat{\xi}} \exp\left[-\frac{1}{2}\left(\frac{\ln \hat{\xi} - \mu}{\sigma}\right)^2\right]; & \hat{\xi} > \hat{\xi}_1 = 0.913 \end{cases} \quad (1)$$

Here the Fréchet parameters are $\nu = 1.09$, $k = 2.80$, and $\mu = 0.1285$, $\sigma = 0.2615$ are the mean value and the standard deviation, respectively, of $\ln \hat{\xi}$. Furthermore, $\xi_{rms} = m/\sqrt{S_{rms}}$ where $S_{rms} = 0.7s_m$, $s_m = H_s/((g/2\pi)T_z^2)$ is the spectral wave steepness, $H_s = 4\sqrt{m_0}$ is the significant wave height, $T_z = 2\pi\sqrt{m_0/m_2}$ is the mean zero-crossing wave period, $m_n = \int_0^\infty \omega^n S(\omega) d\omega$; $n = 0, 1, 2, \dots$ are the spectral moments, $S(\omega)$ is the single-sided wave spectrum, and $\omega = 2\pi/T$ is the wave frequency. As a consequence, the *pdf* of $\hat{\xi}$ is a conditional *pdf* of $\hat{\xi}$ for a given sea state in terms of H_s and T_z . Thus, statistical values of the surf parameter can be obtained for a given sea state. It should be noted that Eq. (1) as well as the relationship $S_{rms} = 0.7s_m$ are based upon data taken from a larger database measured with Waverider buoys located at the deep water sites Utsira, Halten and Tromsøflaket on the Norwegian continental shelf during the years 1974–1978 (more details are given in Myrhaug and Fouques (2007) and the references therein). Thus, Eq. (1) is applicable to the Norwegian continental shelf but not necessarily to other ocean locations since a priori such data do not belong to the same statistical population, i.e. that they have different statistical properties. However, a similar analysis can be applied for other ocean locations with different statistical properties to obtain the statistical features of the surf parameter at these locations.

Here the expected (mean) value, $E[\hat{\xi}]$, and the variance, $Var[\hat{\xi}] = E[\hat{\xi}^2] - (E[\hat{\xi}])^2$ of the surf parameter are considered, which requires the calculation of $E[\hat{\xi}^n]$ for $n = 1$ and

$n = 2$

$$E[\hat{\xi}^n] = \int_0^\infty \hat{\xi}^n p(\hat{\xi}) d\hat{\xi} = \int_0^{\hat{\xi}_1} \hat{\xi}^n p_1(\hat{\xi}) d\hat{\xi} + \int_{\hat{\xi}_1}^\infty \hat{\xi}^n p_2(\hat{\xi}) d\hat{\xi}. \tag{2}$$

Here (Eq. (A1) in Appendix A)

$$\int_0^{\hat{\xi}_1} \hat{\xi}^n p_1(\hat{\xi}) d\hat{\xi} = v^n \left\{ \Gamma\left(1 - \frac{n}{k}\right) - \Gamma\left(1 - \frac{n}{k}, \frac{\hat{\xi}_1^2}{\sigma^2}\right) \right\} \tag{3}$$

and (Bury, 1975)

$$\int_{\hat{\xi}_1}^\infty \hat{\xi}^n p_2(\hat{\xi}) d\hat{\xi} = e^{n\mu + \frac{1}{2}n^2\sigma^2} \left(1 + \Phi\left[\frac{\ln \hat{\xi}_1 - (\mu + n\sigma^2)}{\sigma}\right] \right), \tag{4}$$

where Φ is the standard Gaussian cumulative distribution function (cdf)

$$\Phi(t) = \frac{1}{\sqrt{2\pi}} \int_{-\infty}^t e^{-x^2/2} dx. \tag{5}$$

Then, by using the results in Eqs. (1) to (5):

$$E[\hat{\xi}] = 2.139, \tag{6}$$

$$\text{Var}[\hat{\xi}] = 0.139. \tag{7}$$

Thus, the ratio between the standard deviation of the surf parameter and the mean value of the surf parameter, i.e. the coefficient of variation, is $\sqrt{\text{Var}[\hat{\xi}]/E[\hat{\xi}]} = 0.174$.

Then, it follows that

$$E[\xi] = E[\hat{\xi}] \cdot \xi_{rms} = E[\hat{\xi}] \cdot \frac{m}{\sqrt{0.7} s_m} = 3.195 m \frac{T_z}{H_s^{1/2}} \tag{8}$$

with the coefficient of variation of ξ equal to 0.174.

The joint pdf of H_s and the spectral surf parameter $\xi_m = m/\sqrt{s_m}$ is obtained from the joint pdf of H_s and s_m given by Myrhaug (2018), which is based on the Mathisen and Bitner-Gregersen (1990) joint pdf of H_s and T_z representing wave data from the three deep water sites Utsira, Halten and Tromsøflaket on the Norwegian continental shelf referred to previously. Furthermore, the Utsira data are the same as those referred to subsequently. The joint pdf of significant wave height and spectral surf parameter is given in Appendix B. Thus, as Eq. (1), this joint pdf of H_s and ξ_m is applicable to the Norwegian continental shelf but not necessarily to other ocean locations. One should notice that the spectral surf parameter is introduced as an alternative to the parameter $\hat{\xi}_{rms}$ due to the relationship $\hat{\xi}_{rms} = m/\sqrt{0.7s_m} = \xi_m/\sqrt{0.7}$.

Now estimates of the surf parameter and the spectral surf parameter are outlined similarly to Sections 3.1 and 3.2 in Myrhaug (2018), respectively. First, estimates of the surf parameter are provided by using the Phillips spectrum as given by Eqs. (16) and (17) in Myrhaug (2018). By using the definition of the spectral moments $m_n, T_z/H_s^{1/2} = \pi m_0^{1/4} m_2^{-1/2} = \pi \alpha^{-1/4} g^{-1/2} = 3.34$ where $\alpha = 0.0081$ is the Phillips constant, which substituted in Eq. (8) yields

$$E[\xi] = 10.67 m. \tag{9}$$

Then, by using the coefficient of variation of ξ equal to 0.174, the mean value (m.v.) plus and minus (\pm) one standard deviation (1SD) of ξ is given by

$$m.v. \pm 1SD = (8.81m, 12.53m) \tag{10}$$

Second, estimates of the surf parameter are provided by adopting the results in Eqs. (A5)–(A7) in Myrhaug (2018) for a family of JONSWAP spectra, giving the following results for the mean value \pm one standard deviation according to Eq. (8)

$$\gamma = 1 (T_p = 5\sqrt{H_s}, T_p = 1.40 T_z) : E[\xi] = 11.41 m, \tag{11}$$

$$m.v. \pm 1SD = (9.42 m, 13.40 m), \tag{12}$$

$$\gamma = 3 (T_p = 4\sqrt{H_s}, T_p = 1.29 T_z) : E[\xi] = 9.91 m, \tag{13}$$

$$m.v. \pm 1SD = (8.19 m, 11.63 m), \tag{14}$$

$$\gamma = 5 (T_p = 3.6\sqrt{H_s}, T_p = 1.24 T_z) : E[\xi] = 9.28 m, \tag{15}$$

$$m.v. \pm 1SD = (7.67 m, 10.89 m). \tag{16}$$

Here γ is the spectral peakedness parameter, and $\gamma = 1$ represents the Pierson-Moskowitz spectrum (see Myrhaug (2018) for more details). Moreover, T_p is the spectral peak period and $\omega_p = 2\pi/T_p$ is the spectral peak frequency. It should be noted that similar parameterizations of the JONSWAP spectrum exist in the literature. For example, the one given in Gran (1992) gives the same results for $\gamma = 1$; for $\gamma = 3 : T_p = 4.1\sqrt{H_s}, T_p = 1.32 T_z$; for $\gamma = 5 : T_p = 3.7\sqrt{H_s}, T_p = 1.26 T_z$, which overall are consistent with the values given in Eqs. (13) and (15), respectively.

The results demonstrate that $E[\xi]$ is smaller for the Phillips spectrum than for the Pierson-Moskowitz spectrum; the reason is that the Phillips spectrum includes waves with higher frequencies than the Pierson-Moskowitz spectrum, i.e. steeper waves and consequently waves with smaller ξ – values. It should be noted, however, that for $\gamma = 3$ and $\gamma = 5$, $E[\xi]$ is smaller than for the Phillips spectrum; the reason is that overall these spectra contain steeper waves than the Phillips spectrum and thus waves with smaller ξ – values. These results are consistent with those in Myrhaug (2018) where further details are provided.

The Phillips and JONSWAP spectra represent wind-generated waves. Thus, other spectral formulations, e.g. the Torsethaugen spectrum (Torsethaugen, 1996), or joint frequency tables of H_s and T_z , have to be used in order to include swell and combined wind sea and swell in addition to wind sea. As in Myrhaug (2018), results are exemplified by using the Mathisen and Bitner-Gregersen (1990) joint frequency table of H_s and T_z from the Utsira location. Table 1 yields estimates of $E[\xi]/m$ according to Eq. (8) together with the mean value plus and minus one standard deviation for each class of H_s, T_z for which there is data. According to Eq. (8) the results show the expected features consistent with those in Table 1 in Myrhaug (2018): $E[\xi]/m$ increases as T_z increases for a given value of H_s ; $E[\xi]/m$ decreases as H_s increases for a given value of T_z ; the values of $E[\xi]/m$ cover a wide range from 5.65 for $H_s = 2 m, T_z = 2.5 s$ to 27.20 s for $H_s = 1 m, T_z = 8.5 s$.

Types of breaking waves on slopes can also be assessed by using the Battjes (1974) classification in terms of the surf parameter ξ :

- spilling (SP) if $0 \leq \xi \leq 0.5$
- plunging (PL) if $0.5 < \xi \leq 3$
- collapsing (CO) if $3 < \xi \leq 3.5$
- surging (SU) if $3.5 < \xi$. (17)

Table 1 Conditional mean value \pm one standard deviation of $E[\xi]/m$ for given sea states at Utsira.

| $T_z(s)$ | 2.5 | 3.5 | 4.5 | 5.5 | 6.5 | 7.5 | 8.5 | 9.5 | 10.5 |
|----------|-----------------|------------------|------------------|------------------|------------------|------------------|------------------|------------------|------------------|
| $H_s(m)$ | | | | | | | | | |
| 1 | 8.00 \pm 1.39 | 11.20 \pm 1.95 | 14.40 \pm 2.50 | 17.60 \pm 3.06 | 20.80 \pm 3.61 | 24.00 \pm 4.17 | 27.20 \pm 4.73 | | |
| 2 | 5.65 \pm 0.98 | 7.92 \pm 1.38 | 10.18 \pm 1.77 | 12.44 \pm 2.16 | 14.70 \pm 2.56 | 16.96 \pm 2.95 | 19.23 \pm 3.35 | 21.49 \pm 3.74 | |
| 3 | | | 8.31 \pm 1.45 | 10.16 \pm 1.78 | 12.00 \pm 2.10 | 13.85 \pm 2.42 | 15.70 \pm 2.74 | 17.54 \pm 3.07 | 19.39 \pm 3.39 |
| 4 | | | 7.19 \pm 1.25 | 8.78 \pm 1.53 | 10.38 \pm 1.80 | 11.98 \pm 2.08 | 13.57 \pm 2.36 | 15.17 \pm 2.64 | 16.77 \pm 2.92 |
| 5 | | | | 7.86 \pm 1.37 | 9.29 \pm 1.62 | 10.71 \pm 1.87 | 12.14 \pm 2.12 | 13.57 \pm 2.37 | 15.00 \pm 2.62 |
| 6 | | | | | 8.48 \pm 1.47 | 9.79 \pm 1.69 | 11.09 \pm 1.92 | 12.40 \pm 2.15 | 13.70 \pm 2.37 |
| 7 | | | | | | 9.06 \pm 1.58 | 10.27 \pm 1.79 | 11.48 \pm 2.00 | 12.68 \pm 2.21 |
| 8 | | | | | | | 9.61 \pm 1.67 | 10.74 \pm 1.87 | 11.87 \pm 2.06 |
| 9 | | | | | | | 9.15 \pm 1.59 | 10.23 \pm 1.78 | 11.31 \pm 1.97 |
| 10 | | | | | | | | 9.61 \pm 1.67 | 10.62 \pm 1.85 |
| 11 | | | | | | | | 9.06 \pm 1.58 | 10.01 \pm 1.74 |
| 12 | | | | | | | | | 9.68 \pm 1.69 |

Table 2 Types of breaking waves classified in terms of ξ/m for the slopes $m=0.10, 0.30, 0.50$.

| m | 0.10 | 0.30 | 0.50 |
|-----|-----------------|-------------------|----------------|
| SP | [0, 5] | [0, 1.7] | [0, 1] |
| PL | < 5, 30] | <1.7, 10] | <1, 6] |
| CO | <30, 35] | <10, 11.7] | <6, 7] |
| SU | <35, ∞ > | <11.7, ∞ > | <7, ∞ > |

Table 3 Types of breaking waves for Phillips and JONSWAP spectra for $m=0.10, 0.30, 0.50$; the three types for each m represent the classification based on $E[\xi] - 1SD, E[\xi], E[\xi] + 1SD$, respectively.

| Spectrum | $m=0.10$ | $m=0.30$ | $m=0.50$ |
|---------------------------------------|------------|------------|------------|
| Phillips Eqs. (9), (10) | PL, PL, PL | PL, CO, SU | SU, SU, SU |
| JONSWAP, $\gamma = 1$ Eqs. (11), (12) | PL, PL, PL | PL, CO, SU | SU, SU, SU |
| JONSWAP, $\gamma = 3$ Eqs. (13), (14) | PL, PL, PL | PL, PL, CO | SU, SU, SU |
| JONSWAP, $\gamma = 5$ Eqs. (15), (16) | PL, PL, PL | PL, PL, CO | SU, SU, SU |

Here the slopes $m = 0.10, 0.30, 0.50$ are used as examples. Thus, the classification of breaking waves in terms of ξ/m is as given in Table 2. It should be noted that the spectral surf parameter is not used to classify breaking waves.

Based on this, the breaker types corresponding to the Phillips and JONSWAP spectra are given in Table 3. The three breaker types in each of the columns for m represent those corresponding to $E[\xi] - 1SD, E[\xi], E[\xi] + 1SD$, respectively. For each spectrum it is referred to the equations which the classification is based on. Based on $E[\xi] - 1SD, E[\xi], E[\xi] + 1SD$ it appears that all the waves break as plunging and surging breakers for $m=0.10$ and 0.50 , respectively, for all the spectra. For $m=0.30$ it is more complex since the classification changes based on the three values of the surf parameter. More specifically, for the JONSWAP spectrum $E[\xi]$ decreases as γ increases from 1 to 3 and

from 3 to 5 (see Eqs. (11), (13), (15)), leading to that the breaker type changes from collapsing to plunging. Based on $E[\xi] - 1SD$ this reduced value of the surf parameter leads to a change from collapsing to plunging breakers for JONSWAP, $\gamma = 1$; while there is no change for JONSWAP, $\gamma = 3$ and $\gamma = 5$. Based on $E[\xi] + 1SD$ this increased value of the surf parameter leads to a change from collapsing to surging breakers for JONSWAP, $\gamma = 1$; from plunging to collapsing breakers for JONSWAP, $\gamma = 3$ and $\gamma = 5$. For the Phillips spectrum $E[\xi]$ is smaller (larger) than $E[\xi]$ for JONSWAP, $\gamma = 1$ ($\gamma = 3$) (see Eqs. (9), (11), (13)), leading to that the waves break as collapsing breakers, i.e. as for JONSWAP, $\gamma = 1$. Based on $E[\xi] \pm 1SD$ the result is also the same as for JONSWAP, $\gamma = 1$.

Next, the classification of breakers in Table 2 based on the values of $E[\xi]/m$ given in Table 1 is provided in Table 4. The breaker types in each class of H_s, T_z represent those corresponding to the slopes $m = 0.10, 0.30, 0.50$, respectively. It appears that for most sea states the waves break as plunging and surging breakers; collapsing breakers occur in some H_s, T_z classes for $m=0.30$; while spilling breakers do not occur. For $m=0.10$ plunging breakers occur in all classes as well as in some classes for $m=0.30, 0.50$. Surging breakers occur in all classes (except for $H_s = 2m, T_z = 2.5s$); in some classes for both $m=0.30, 0.50$ and in some classes only for $m=0.50$. One should notice that the classification may be altered if it is based on $E[\xi] \pm 1SD$.

Example estimates of the spectral surf parameter are obtained by using the joint pdf of H_s and T_z representing sea states from the three deep water sites Utsira, Halten and Tromsøflaket provided by Mathisen and Bitner-Gregersen (1990); see Appendix B in Myrhaug (2018) for details. The results are given in Table 5, where $E[H_s]$ is calculated using Eq. (B6) with the Weibull parameters in Table B1 in Myrhaug (2018), i.e. equal to the same values as in Table 2 in Myrhaug (2018). Next, $E[\hat{\xi}_m | E[H_s]]$ and the coefficient of variation R are calculated using Eqs. (B7) and (B8), respectively. It appears that the differences are small between the results for the three sites; $E[H_s]$ is in the range 2.11 m–2.34 m, $E[\hat{\xi}_m | E[H_s]]$ is in the range 4.8–4.9 with R in the range 0.15–0.16. The values of $E[\hat{\xi}_m | E[H_s]] \pm 1SD$ are also given. The reason for these small differences is probably due to that the joint pdfs of H_s and T_z at the three locations can

Table 4 Types of breaking waves classified in terms of $E[\xi]$; the three types in each class of H_s , T_z correspond to $m = 0.10, 0.30, 0.50$, respectively.

| T_z (s) | 2.5 | 3.5 | 4.5 | 5.5 | 6.5 | 7.5 | 8.5 | 9.5 | 10.5 |
|-----------|------------|------------|------------|------------|------------|------------|------------|------------|------------|
| H_s (m) | | | | | | | | | |
| 1 | PL, PL, SU | PL, CO, SU | PL, SU, SU | | |
| 2 | PL, PL, PL | PL, PL, SU | PL, CO, SU | PL, SU, SU | |
| 3 | | | PL, PL, SU | PL, CO, SU | PL, SU, SU |
| 4 | | | PL, PL, SU | PL, PL, SU | PL, CO, SU | PL, SU, SU | PL, SU, SU | PL, SU, SU | PL, SU, SU |
| 5 | | | | PL, PL, SU | PL, PL, SU | PL, CO, SU | PL, SU, SU | PL, SU, SU | PL, SU, SU |
| 6 | | | | | PL, PL, SU | PL, PL, SU | PL, CO, SU | PL, SU, SU | PL, SU, SU |
| 7 | | | | | | PL, PL, SU | PL, CO, SU | PL, CO, SU | PL, SU, SU |
| 8 | | | | | | | PL, PL, SU | PL, CO, SU | PL, SU, SU |
| 9 | | | | | | | PL, PL, SU | PL, CO, SU | PL, CO, SU |
| 10 | | | | | | | | PL, PL, SU | PL, CO, SU |
| 11 | | | | | | | | PL, PL, SU | PL, CO, SU |
| 12 | | | | | | | | | PL, PL, SU |

Table 5 Statistical results for H_s and $\hat{\xi}_m$ at Usira, Halten and Tromsøflaket based on the Mathisen and Bitner-Gregersen (1990) joint pdf of H_s and T_z .

| Location | Usira | Halten | Tromsøflaket |
|--------------------------------------|------------|------------|--------------|
| $E[H_s]$ (m), Eq. (B6) | 2.11 | 2.30 | 2.34 |
| $E[\hat{\xi}_m E[H_s]]$, Eq. (B7) | 4.81 | 4.88 | 4.86 |
| R, Eq. (B8) | 0.154 | 0.155 | 0.155 |
| m.v.± 1SD | 4.07, 5.55 | 4.12, 5.64 | 4.11, 5.61 |

be regarded as belonging to the same statistical population, i.e. that the statistical properties obtained from the statistical distributions are representative for the wave dynamics in this ocean area (see e.g. Myrhaug and Kjeldsen (1986)).

As referred to in the introduction there are many formulae for wave runup, where some of the formulae have been applied to estimate random wave-induced runup (Myrhaug (2015); Myrhaug and Leira (2017); Myrhaug and Sunde (2018, 2019)). However, this example applies a simple formula where the main purpose is to demonstrate how the present results can be used. Thus, as a compromise between simplicity and accuracy the Hunt (1959) formula for the vertical runup elevation, RU, above the still water level for breaking waves is adopted (see e.g. Baldock et al. (2009)):

$$\frac{RU}{H_0} = K\xi. \tag{18}$$

Here H_0 is the deep water wave height, and K is an empirical coefficient which is taken as $K=1$ (as originally used by Hunt). The results are exemplified by calculating the expected value of ξ by taking $H_0 = E[H_s]$. By using Eqs. (6) and (8), i.e. $E[\xi] = E[\hat{\xi}] \xi_{rms} = 2.139 m / \sqrt{0.7 s_m}$, together with $\hat{\xi}_m = \xi_m / m$ and $\xi_m = m / \sqrt{s_m}$, this yields $E[\xi] = 2.139 m \hat{\xi}_m / \sqrt{0.7}$. Thus, by using the results at Utsira given in Table 5, the vertical runup elevation for a slope $m = 0.10$ is obtained from Eq. (18) as (with $K=1$)

$$RU = E[\xi]E[H_s] = 2.139(0.10/\sqrt{0.7})E[\hat{\xi}_m | E[H_s] = 2.11m]E[H_s]$$

$$= 2.139(0.10/\sqrt{0.7}) \cdot 4.81 \cdot 2.11m = 2.59m. \tag{19}$$

For $m = 0.30$ and 0.50 the results are obtained by multiplying this with the factors 3 and 5, respectively, i.e. giving $RU = 7.77$ m and $RU = 12.95$ m, respectively.

From Eq. (19) it follows that $E[\xi] = 2.59/2.11 = 1.23$, which according to Eq. (17) corresponds to plunging breakers. Consequently, the results for $m = 0.30$ and $m = 0.50$ are obtained by multiplying this with the factors 3 and 5, giving $E[\xi] = 3.69$ and $E[\xi] = 6.15$, corresponding to surging breakers according to Eq. (17).

Finally, there are several uncertainties related to the present analysis such as those related to the wave data upon which the results are based as well as to the spectral formulations which are used. First, the wave data represent two different data bases, but it is reasonable to believe that they overall represent the same wave conditions since they are measured at the same locations and partly in the same periods. Second, the results based on the Phillips and the JONSWAP spectra are only valid for wind sea but is supplemented by using the joint frequency table of H_s and T_z from the Utsira location representing wind sea, swell, and combined wind sea and swell. Other wave data and spectral formulations may alter the present results, but the methodology is still valid.

A summary and the main conclusions of this work are as follows:

Average statistical properties of the surf parameter for individual random waves and the spectral surf parameter for sea states expressed in terms of the mean values and the standard deviations are presented. Results are exemplified by using distributions representing deep water waves based on data from the Norwegian continental shelf.

Estimates of the surf parameter for individual random waves within a sea state are obtained by using the Myrhaug and Fouques (2007) distribution together with a Phillips spectrum and a family of JONSWAP spectra for wind sea, and by a joint frequency table of H_s and T_z for combined wind sea and swell. For wind sea, based on the mean values of the surf parameter, the waves break as plunging and surging breakers for the slopes 0.10 and 0.50, respectively, while for the slope 0.30 they break as plunging breakers for JONSWAP,

$\gamma = 3$ and $\gamma = 5$; as collapsing breakers for Phillips and JON-SWAP, $\gamma = 1$. For combined wind sea and swell, based on the mean values of the surf parameter, most of the waves break as plunging and surging breakers, while collapsing breakers occur in some H_s , T_z classes for the slope 0.30. Plunging breakers occur in all classes for the slope 0.10, while surging breakers occur in all classes (except for one) depending on the slopes 0.30 and/or 0.50. One should notice that the classification of breakers may be altered if it is based on the mean values of the surf parameter plus and minus one standard deviation.

The spectral surf parameter is estimated by using a joint distribution of significant wave height and spectral surf parameter. Examples of results are obtained by using joint frequency tables of H_s and T_z from the deep water locations Utsira, Halten and Tromsøflaket on the Norwegian continental shelf. The differences between the results for the three locations are small with a coefficient of variation of about 15%.

A simple example is also included, demonstrating how the results can be applied to calculate the vertical wave runup elevation above the still water level for breaking waves.

Although there are uncertainties related to the presented analysis which may alter the results, the strength of this work is that it demonstrates how deep water wave statistics can be applied to provide probabilistic properties of the surf parameter for individual random waves within a sea state and for the spectral surf parameter representing a sea state characteristic. This should be useful to serve the purpose of assessing many physical processes in the coastal zone and in coastal protection work.

Appendix A

The first integral in Eq. (2), where the pdf is given by the Fréchet distribution, can be obtained by transformation of variables from $x = (y/v)^{-k/2}$ to y where x is Rayleigh distributed with the pdf $p(x) = 2x \exp(-x^2)$ valid for $x \geq 0$ (see e.g. Myrhaug and Leira (2011)). Thus, it follows, by using the results given in Abramowitz and Stegun (1972, Chs. 6.5 and 26.4), that

$$E[y^n] = \int_0^{x_1} y^n(x) p(x) dx = v^n \int_0^{x_1} x^{-\frac{2}{k}n} 2x \exp(-x^2) dx = v^n \left\{ \Gamma\left(1 - \frac{n}{k}\right) - \Gamma\left(1 - \frac{n}{k}, x_1^2\right) \right\}, \tag{A1}$$

where Γ is the gamma function, $\Gamma(\cdot, \cdot)$ is the incomplete gamma function, and n is a real number (not necessarily an integer).

Appendix B

Here the joint pdf of significant wave height and the spectral surf parameter is obtained from the joint pdf of significant wave height and the spectral wave steepness given by Myrhaug (2018). First, $\hat{\xi}_m$ is defined as $\hat{\xi}_m \equiv \xi_m/m = s_m^{-1/2}$. Then, the joint pdf of H_s and $\hat{\xi}_m$ is obtained by a change of variables from H_s, s_m to $H_s, \hat{\xi}_m$ which yields

$$p(H_s, \hat{\xi}_m) = p(\hat{\xi}_m|H_s)p(H_s), \tag{B1}$$

where $p(H_s)$ is the marginal pdf of H_s given in Eq. (B2) in Myrhaug (2018). The reason is that the change of variables only affects the conditional pdf of s_m given H_s , $p(s_m|H_s)$, since $s_m = \hat{\xi}_m^{-2}$. Thus, by using the Jacobian $|ds_m/d\hat{\xi}_m| = 2\hat{\xi}_m^{-3}$, this gives the conditional pdf of $\hat{\xi}_m$ given H_s as

$$p(\hat{\xi}_m|H_s) = p(s_m = \hat{\xi}_m^{-2}|H_s) \cdot 2\hat{\xi}_m^{-3}. \tag{B2}$$

By combining Eq. (B2) with Eqs. (10) to (12) in Myrhaug (2018), this gives the following lognormal pdf of $\hat{\xi}_m$ given H_s

$$p(\hat{\xi}_m|H_s) = \frac{1}{\sqrt{2\pi}\sigma_{\hat{\xi}_m}} \exp\left[-\frac{1}{2}\left(\frac{\ln \hat{\xi}_m - \mu_{\hat{\xi}_m}}{\sigma_{\hat{\xi}_m}}\right)^2\right]. \tag{B3}$$

Here $\mu_{\hat{\xi}_m}$ and $\sigma_{\hat{\xi}_m}$ are the mean value and the standard deviation, respectively, of $\ln \hat{\xi}_m$, given by

$$\mu_{\hat{\xi}_m} = a_1 + a_2 H_s^{a_3} - \frac{1}{2} \ln\left(\frac{H_s}{g/2\pi}\right), \tag{B4}$$

$$\sigma_{\hat{\xi}_m} = b_1 + b_2 e^{b_3 H_s}, \tag{B5}$$

where the coefficients (a_1, a_2, a_3) and (b_1, b_2, b_3) are given in Table B1 in Myrhaug (2018).

Results are exemplified in terms of the statistical quantities $E[H_s]$, $E[\hat{\xi}_m|H_s]$ and the coefficient of variation $R = \sigma[\hat{\xi}_m|H_s]/E[\hat{\xi}_m|H_s]$ given by (Bury, 1975)

$$E[H_s] = \varepsilon_h + \rho_h \Gamma\left(1 + \frac{1}{\theta_h}\right), \tag{B6}$$

$$E[\hat{\xi}_m|H_s] = \exp\left(\mu_{\hat{\xi}_m} + \frac{1}{2} \sigma_{\hat{\xi}_m}^2\right), \tag{B7}$$

$$R = (e^{\sigma_{\hat{\xi}_m}^2} - 1)^{1/2}, \tag{B8}$$

where ε_h , ρ_h and θ_h are the Weibull parameters in $p(H_s)$ given in Table B1 in Myrhaug (2018).

References

Abramowitz, M., Stegun, I.A., 1972. Handbook of Mathematical Functions. Dover Publications, Inc., New York, 1046 pp.

Atkinson, A.L., Power, H.E., Monra, T., Callaghan, D.P., Baldock, T.E., 2017. Assessment of runup predictions by empirical models on non-truncated beaches on the south-east Australian coast. Coast. Eng. 119, 15–31, <https://doi.org/10.1016/j.coastaleng.2016.10.001>.

Baldock, T.E., Cox, D., Maddux, K., Killian, J., Fayler, L., 2009. Kinematics of breaking tsunami wave fronts: A data set from large scale laboratory experiments. Coast. Eng. 56 (5–6), 506–516, <https://doi.org/10.1016/j.coastaleng.2008.10.011>.

Battjes, J.A., 1974. Surf similarity. In: Proceedings 14th Int. Conf. on Coastal Engineering, 1, New York. ASCE, 466–479.

Blenkinsopp, C.E., Matias, A., Howe, D., Castelle, B., Marieu, V., Turner, I.L., 2016. Wave runup and overwash on a prototype-scale sand barrier. Coast. Eng. 113, 88–103, <https://doi.org/10.1016/j.coastaleng.2015.08.006>.

Bury, K.V., 1975. Statistical Models in Applied Science. John Wiley & Sons, New York, 646 pp.

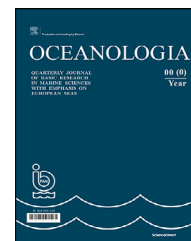
de la Pena, J.M., Sanches-Gonzales, J.F., Diaz-Sanches, R., 2014. Wave runup in a sand bed physical model. J. Waterw. Port Coast. 140 (4), [https://doi.org/10.1061/\(ASCE\)ww.1943-5460.0000246](https://doi.org/10.1061/(ASCE)ww.1943-5460.0000246).

EurOtop, 2018. Manual on wave overtopping of sea defences and related structures. In: Van der Meer, J.W., Allsop, N.W.H., Bruce, T., De Rouck, J., Kortenhaus, A., Pullen, T., Schuttrumpf, H., Troch, P., Zanuttigh, B. (Eds.), An overtopping manual based on European research, but for worldwide application 2nd edn., 320 pp., www.overtopping-manual.com.

- Gran, S., 1992. *A Course in Ocean Engineering*. Elsevier, Amsterdam, 583 pp.
- Hunt, I.A., 1959. Design of seawalls and breakwaters. *Proceedings of the American Society of Civil Engineers* 85, 123–152.
- Iribarren, C.R., Nogales, C., 1949. Protection des ports (Sect. 2, Comm. 4. In: 17th Int. Nav. Congress, Lisbon, 31–80.
- Kim, Y.C., 2010. *Handbook of Coastal and Ocean Engineering*. World Scientific, Singapore, 1163 pp.
- Mathisen, J., Bitner-Gregersen, E., 1990. Joint distribution for significant wave height and wave zero-up-crossing period. *Appl. Ocean Res.* 12 (2), 93–103.
- Myrhaug, D., 2015. Estimation of wave runup on shorelines based on long-term variation of wave conditions. *J. Ocean Eng. Mar. Energy* 1 (2), 193–197, <https://doi.org/10.1007/S40722-015-0016-4>.
- Myrhaug, D., 2018. Some probabilistic properties of deep water wave steepness. *Oceanologia* 60 (2), 187–192, <https://doi.org/10.1016/j.oceano.2017.10.003>.
- Myrhaug, D., Fouques, S., 2007. Discussion of “Distributions of wave steepness and surf parameter” by M. Aziz Tayfun. *J. Waterw. Port Coast.* 133 (3), 242–243, [https://doi.org/10.1061/\(ASCE\)0733-950X\(2007\)133:3\(242\)](https://doi.org/10.1061/(ASCE)0733-950X(2007)133:3(242)).
- Myrhaug, D., Fouques, S., 2010. A joint distribution of significant wave height and characteristic surf parameter. *Coast. Eng.* 57 (10), 948–952, <https://doi.org/10.1016/j.coastaleng.2010.05.001>.
- Myrhaug, D., Fouques, S., 2012. Joint distributions of wave height with surf parameter and breaker index for individual waves. *Coast. Eng.* 60, 235–247, <https://doi.org/10.1016/j.coastaleng.2011.10.008>.
- Myrhaug, D., Kjeldsen, S.P., 1986. Steepness and asymmetry of extreme waves and the highest waves in deep water. *Ocean Eng.* 13 (6), 549–568.
- Myrhaug, D., Leira, B.J., 2011. A bivariate Fréchet distribution and its application to the statistics of two successive surf parameters. *Proceedings Institute Mechanical Engineers, Pt. M: J. Eng. Mar. Environ.* 225 (1), 67–74, <https://doi.org/10.1243/14750902JEME205>.
- Myrhaug, D., Leira, B.J., 2017. Application of wave runup and wave rundown formulae based on long-term variation of wave conditions. *Coast. Eng.* 120, 75–77, <https://doi.org/10.1016/j.coastaleng.2016.11.013>.
- Myrhaug, D., Li, H., Wang, H., 2016. Comparative study of joint distributions of wave height and surf parameter for individual waves including spectral bandwidth effects. *Coast. Eng.* 114, 341–346, <https://doi.org/10.1016/j.coastaleng.2016.05.002>.
- Myrhaug, D., Rue, H., 2009. On a joint distribution of two successive surf parameters. In: Brebbia, C.A., Benassai, G., Rodriguez, G. (Eds.), *Coastal Processes*. Wit Press, Southampton, Hampshire, UK, 85–96.
- Myrhaug, D., Sunde, T., 2018. Wave runup and wave rundown estimation based on long-term variation of wind statistics. *Proceedings of the Institution of Civil Engineers – Mar. Eng.* 171 (1), 40–46, <https://doi.org/10.1680/jmaen.2017.12>.
- Myrhaug, D., Sunde, T., 2019. Assessment of wave runup and wave rundown estimation based on observed long-term wave conditions. *IOP Conf. Ser.: Material Science and Engineering* 700 (1), <https://doi.org/10.1088/1757-899X/700/1/012006>.
- Tayfun, M.A., 2006. Distributions of wave steepness and surf parameter. *J. Waterw. Port Coast.* 132 (1), 1–9, [https://doi.org/10.1061/\(ASCE\)0733-950X\(2006\)132:1\(1\)](https://doi.org/10.1061/(ASCE)0733-950X(2006)132:1(1)).
- Torsethaugen, K., 1996. Model for doubly peaked wave spectra. In: *Tech. Rep. No. STF22A96204*, Civ. Env. Eng., Trondheim, Norway.

Available online at www.sciencedirect.com

ScienceDirect

journal homepage: www.journals.elsevier.com/oceanologia

SHORT COMMUNICATION

Low-active high-density *Noctiluca scintillans* cells in surface seawater

Kuninao Tada^{a,b,*}, Toshimasa Asahi^a, Saho Kitatsuji^{a,c}, Mika Nomura^a, Hitomi Yamaguchi^a, Kazuhiko Ichimi^d

^a Faculty of Agriculture, Kagawa University, Ikenobe, Japan

^b Seto Inland Sea Regional Research Center, Kagawa University, Saiwai-cho, Takamatsu, Kagawa, Japan

^c National Research Institute of Fisheries and Environment of Inland Sea, Japan Fisheries Research and Education Agency, Maruishi, Hatsukaichi, Hiroshima, Japan

^d Aji Marine Station, Seto Inland Sea Regional Research Center, Kagawa University, Kamano, Aji, Takamatsu, Kagawa, Japan

Received 10 November 2019; accepted 29 February 2020

Available online 13 March 2020

KEYWORDS

Noctiluca scintillans;
Heterotrophic
dinoflagellate;
Cell density;
Coastal water;
ATP;
Activity

Summary *Noctiluca scintillans* is an important member of the mesozooplankton in terms of biomass and production in the Seto Inland Sea, Japan. The densities and adenosine triphosphate (ATP) contents of *N. scintillans* cells were measured. Vertical profiles of *N. scintillans* cellular activity in the coastal water were determined and the ATP contents were high at middle layers, with a maximum depth of 10 m. ATP contents were low in the surface and lower layers. These results suggest that active *N. scintillans* cells in subsurface layers with low density play an important role in the coastal ecosystem, and high-density cells in the surface water are not active.

© 2020 Institute of Oceanology of the Polish Academy of Sciences. Production and hosting by Elsevier B.V. This is an open access article under the CC BY-NC-ND license (<http://creativecommons.org/licenses/by-nc-nd/4.0/>).

* Corresponding author at: Faculty of Agriculture, Kagawa University, 2393 Ikenobe, Miki, Kagawa 761–0795, Japan.

E-mail address: tada@ag.kagawa-u.ac.jp (K. Tada).

Peer review under the responsibility of the Institute of Oceanology of the Polish Academy of Sciences.



Production and hosting by Elsevier

Noctiluca scintillans is a large heterotrophic dinoflagellate that has a worldwide distribution (e.g. Elbrächter and Qi, 1998). *N. scintillans* is also one of the most common red-tide-forming dinoflagellates in temperate and tropical coastal regions, and is a frequent cause of water discoloration. Many field observations have been conducted and long- or short-term variations in *N. scintillans* and phytoplankton abundances have been reported (e.g. Huang and Qi, 1997; Tada et al., 2004; Uhling and Sahling, 1990). Although we showed that the biomass of *N. scintillans* cannot be ignored even when a red tide outbreak is not occurring (Tada et al., 2004), the ecological role of *N. scintillans* is

<https://doi.org/10.1016/j.oceano.2020.02.005>

0078-3234/© 2020 Institute of Oceanology of the Polish Academy of Sciences. Production and hosting by Elsevier B.V. This is an open access article under the CC BY-NC-ND license (<http://creativecommons.org/licenses/by-nc-nd/4.0/>).

still not well understood. Specifically, it is not clear whether *N. scintillans* exists as a large biomass with or without predation among other phytoplankton organisms, mainly phytoplankton. However, some studies have discussed the role of *N. scintillans* in a nutrient environment and aquatic ecosystems: *N. scintillans* can play an important role as a nutrient regenerator and supplier owing to the significant amount of $\text{NH}_4^+\text{-N}$ and $\text{PO}_4^{3-}\text{-P}$ regeneration, the pools within the cells, and its supply to phytoplankton primary production (Ara et al., 2013; Montani et al., 1998; Pithakpol et al., 2000a, b). We believe that it is very important to determine the activity of *N. scintillans* cells in the field.

Adenosine triphosphate (ATP) is the energy material in all organisms, and the amount of ATP in particulate material is a valuable indication of biomass of live microorganisms. Several authors have determined the ATP contents of seawater and marine sediment samples using a luciferin-luciferase reaction (e.g. Holm-Hansen and Booth, 1966). ATP has been used both to estimate biomass (e.g. Holm-Hansen and Booth, 1966) and metabolic activity (e.g. Hobbie et al., 1972; Patterson et al., 1970). Holm-Hansen (1970) reported that during extreme nitrogen or phosphorous deficiency, the algal cellular levels of ATP decreased to 20%–50% of that found in exponentially-growing cells. Brezonik et al. (1975) showed that algal ATP responded rapidly to mercury addition and pH changes, indicating its usefulness as a measurement of toxicity. They also showed that the rapid response of ATP following nutrient additions to starved algal cultures suggests that ATP may be useful as a tool in nutrient bioassay studies. In addition, Skjoldal and Båmstedt (1975) reported that the ATP concentration in zooplankton showed marked seasonal change with increasing values during periods of reproduction, which is assumed to reflect an inherent seasonal rhythm in metabolism. Recently, Hyun et al. (2018) studied ballast water and reported that the ATP concentration of living phytoplankton cells obtained from a mono-culture experiment was much higher than living cells in the field. Moreover, they reported that the ATP concentration in plankton cells in ballast water was low because of a decline in their biological activity under the extended exposure to dark conditions. We applied this method to determine the ATP contents of *N. scintillans* cells to examine the vertical profiles of *N. scintillans* cellular activity in a coastal water column.

The oceanographic observation was conducted on 1 May 2018 at Harima-Nada, the eastern part of the Seto Inland Sea, Japan (using the *r/v Calanus III* (19 tons) of the Seto Inland Sea Regional Research Center, Kagawa University, Japan). On the observation day, we looked for areas where *N. scintillans* occurred at high densities. We collected seawater samples at two points: Stn. SS1 and Stn. SS2 (Fig. 1, Table 1). At Stn. SS2, we observed a minor water discoloration by *N. scintillans* in the surface seawater. At both stations, seawater samples were collected from seven depths (0, 2.5, 5, 7.5, 10, 20, and 30 m), using a clean bucket for the surface layer and 10-L Van Dorn bottles for the other layers. A total of 1 L of seawater from each depth was passed through a 150 μm mesh plankton net, and the cell numbers were counted using a magnifying glass, with or without appropriate dilution to account for high density.

For ATP determination, 0.1 to 2 L of collected seawater was immediately filtered on board ship through a 47 mm

Table 1 Locations and depth of the sampling stations.

| Sampling station | Location | Water depth |
|------------------|------------------------------|-------------|
| Stn.SS1 | 34°25'577"N, 134°19'875"E | 48.3 m |
| Stn.SS2 | 34°25'876"N, 134°21'118"E | 44.7 m |

diameter 200 μm mesh screen (Tanaka Sanjiro Co., Ltd., Japan). The mesh screens were then transferred to glass test tubes which contained 3 mL of boiling Tris buffer. After 3 minutes in boiling water, the glass tubes were cooled in an ice bath and thereafter preserved in a deep freezer until analysis. When *N. scintillans* cells were counted, no large phytoplankton and no other zooplankton except *N. scintillans* were observed. The 200 μm mesh screen samples contained only *N. scintillans* cells, and measured ATP was only produced by *N. scintillans*. For chlorophyll *a* (Chl *a*) determination, 0.2 L of seawater from each depth was filtered through a Whatman GF/F filter (47 mm) and extracted in 90% acetone. Extracts were stored overnight in dark at 4°C until analysis. For particulate organic carbon (POC) determination, 1 L of seawater from each depth was filtered through a pre-combusted Whatman GF/F filter (450°C, 2 h), and the filters were rinsed with a small volume of 1N HCl and re-distilled water.

The ATP contents of *N. scintillans* cells were determined by the method of Holm-Hansen and Booth (1966) with some modifications suggested by Bulleid (1978) using a luminometer (Luminescencer PSN AB-2200, Atto, Japan), as described by Parsons et al. (1984).

Chl *a* concentrations of seawater were determined by the fluorescence method (Holm-Hansen et al., 1965) using a fluorometer (10-AU, Turner Designs, USA), described by Parsons et al. (1984). POC concentrations of seawater were determined using a CHN analyzer (Micro Corder JM10, J-Science Lab, Japan).

On the sampling day, cell densities of *N. scintillans* varied from 0 to 328 cells/L at Stn. SS1, and 0 to 21,500 cells/L at Stn. SS2 (Figs. 2 and 3). As described previously, we observed a minor coloration of surface water by *N. scintillans* at Stn. SS2. The cell densities decreased with depth, and no cells were found at the depth of 30 m at either station. ATP concentrations varied from 2.61 to 124 ng/L at Stn. SS1 and 0 to 15,600 ng/L at Stn. SS2. The ATP concentrations were high in the surface layer and were low in the lower layer, with a maximum concentration of 124 ng/L at the 2.5 m depth at Stn. SS1 and 15,600 ng/L at the 0 m depth at Stn. SS2. As previously mentioned, when *N. scintillans* cells were counted for the seawater samples collected by 150 μm mesh plankton nets, no large phytoplankton and no other zooplankton except *N. scintillans* were observed. Therefore, it was thought these ATP contents that accumulated on the 200 μm mesh screen were produced only by *N. scintillans* cells. The ATP contents of *N. scintillans* varied from 0 to 15.1 ng/cell at Stn. SS1 and 0 to 53.8 ng/cell at Stn. SS2. The ATP contents were high at the middle layer with the maximum at the 10 m depth, and low in surface and deeper layers for both stations. However, Chl

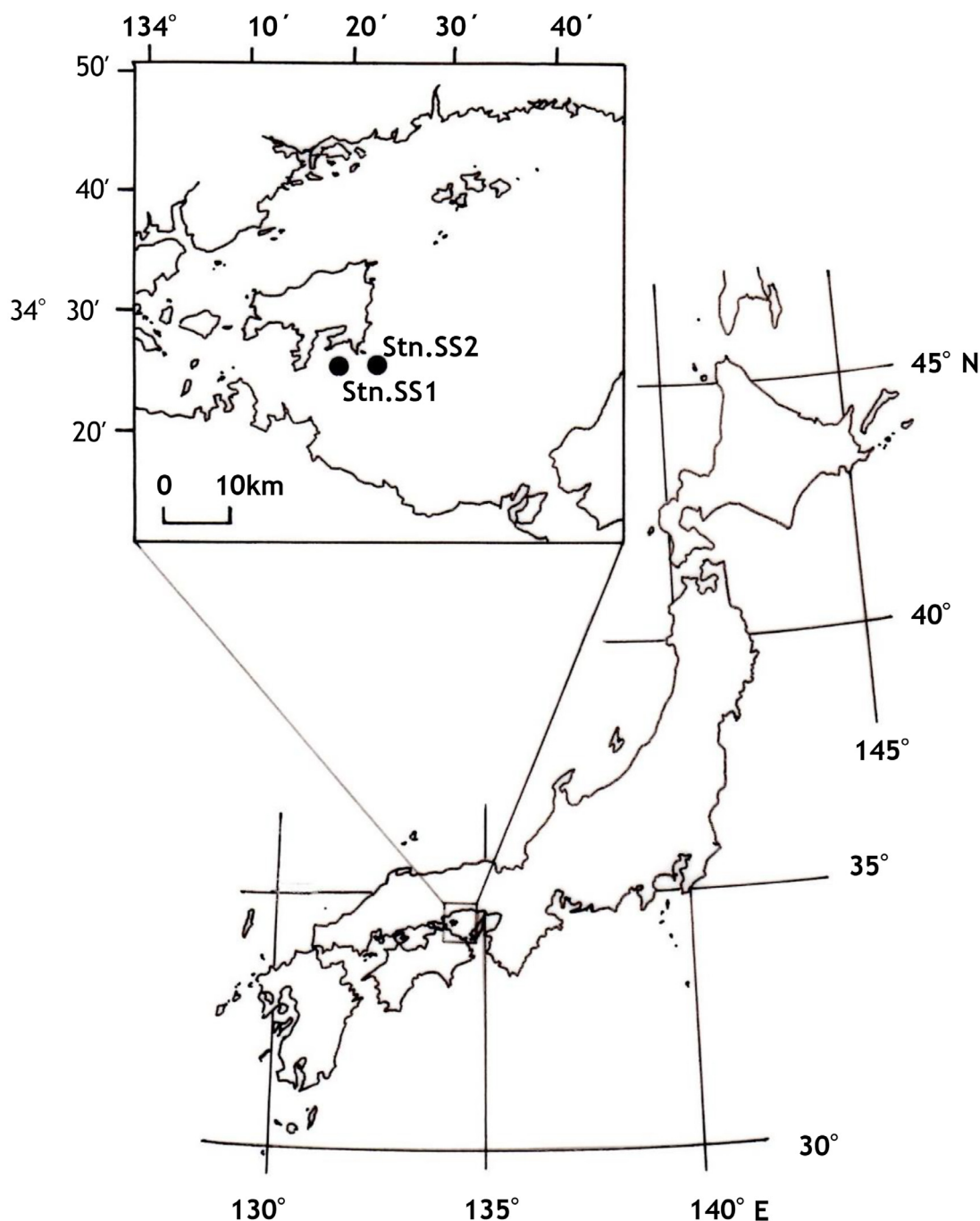


Figure 1 Sampling stations in Harima-Nada, Seto Inland Sea, Japan.

a concentrations varied from 1.88 to 5.02 $\mu\text{g/L}$ and 1.50 to 2.61 $\mu\text{g/L}$ for Stn. SS1 and Stn. SS2, respectively. For both stations, maximum Chl *a* concentrations were observed at the 10 m depth and were lower in surface or deeper layers.

POC concentrations varied from 220 to 351 $\mu\text{g/L}$ at Stn. SS1 and 244 to 12,500 $\mu\text{g/L}$ at Stn. SS2. POC concentrations at both stations tended to decrease with increasing depth.

In the water column at the two stations, POC concentrations varied from 220 to 12,500 $\mu\text{g/L}$, and decreased with increasing depth (Fig. 4). We estimated phytoplankton carbon from the Chl *a* concentration, using the C/Chl *a* ratio of 56.5 reported for this region (Tada and Morishita, 1997).

The biomass of *N. scintillans* was also estimated from its cell density, using the average value for the cellular carbon content (0.353 $\mu\text{g/cell}$) of field samples that were obtained from this region (Tada et al., 2000). The *Noctiluca* carbon biomass varied from 0% to 62% of POC in the water column at both stations. *Noctiluca* carbon biomass was similar to or about 56 times higher than the phytoplankton biomass at 0 m at Stn. SS1 and Stn. SS2. Except for the 0 m level, the *Noctiluca* carbon varied from 0% to 64% of phytoplankton carbon (phytoplankton biomass) at the two stations. Interestingly, the maximum values of Chl *a* concentrations and ATP contents of *N. scintillans* cells were observed at the 10 m depth

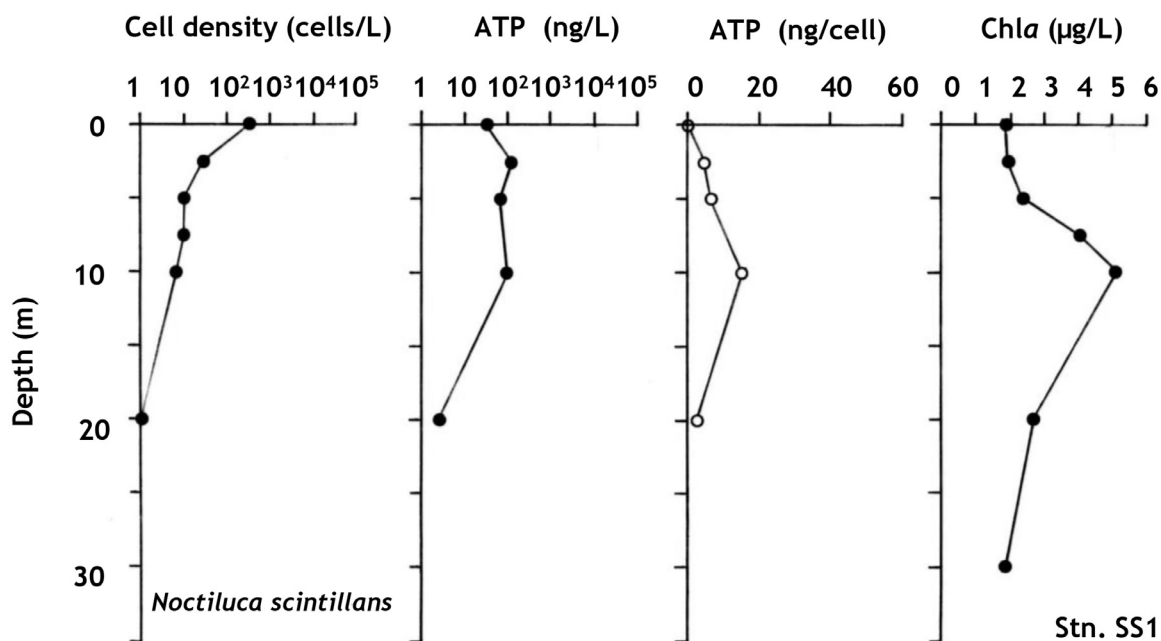


Figure 2 Vertical distributions of the cell density and ATP content of *Noctiluca scintillans* and Chl *a* concentrations in the seawater at Stn. SS1.

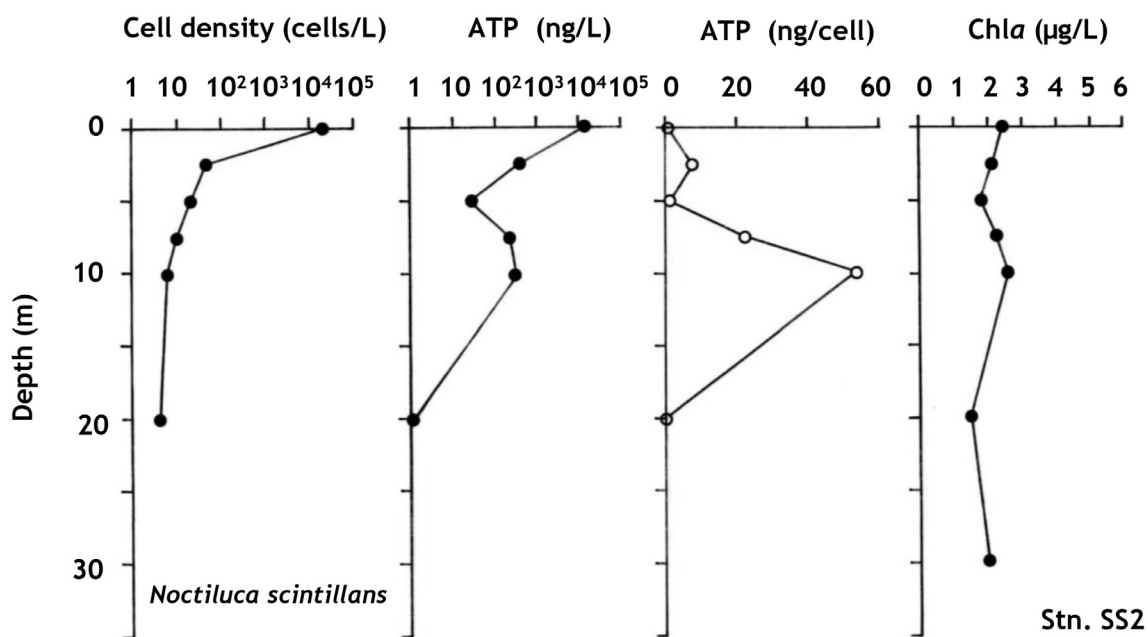


Figure 3 Vertical distributions of the cell density and ATP content of *Noctiluca scintillans* and Chl *a* concentrations in the seawater at Stn. SS2.

at both stations, although maximum cell densities of *N. scintillans* were observed at the 0 m depth. The biomass of *N. scintillans* at the 10 m depth with maximum Chl *a* concentrations at both stations, was about 1% of the phytoplankton biomass, and we believe *N. scintillans* had sufficient food.

Although cell densities decreased with increasing depth, with a maximum density in the surface layer, the ATP contents of *N. scintillans* cells in the surface layer were not high, and the maximum ATP contents were observed at the 10 m for both stations. Our results showed that high

cell densities in the surface layer were not active, and *N. scintillans* cells fed actively at a depth of 10 m. From our results, we believe that *N. scintillans* cells with high intracellular ATP were feeding on phytoplankton actively, and they were associated with the maximum depth of Chl *a*. At both stations, *N. scintillans* abundances were very high at the surface (0 m depth), while Chl *a* concentrations were higher at the 10 m depth. Thus *N. scintillans* at the 10 m depth could feed on more phytoplankton than at the 0 m depth, and consequently intracellular ATP contents at the

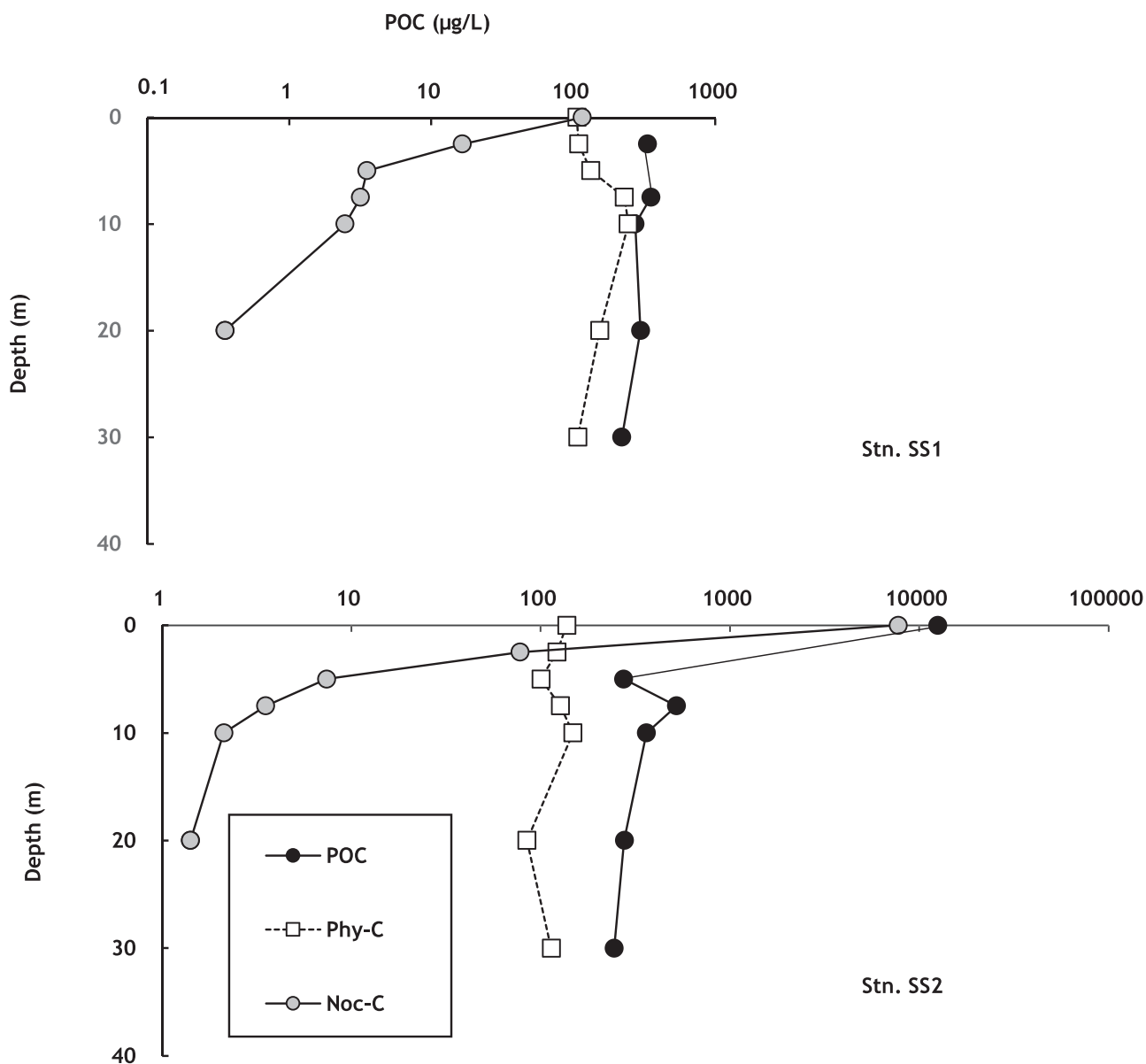


Figure 4 Vertical distributions of POC, estimated *Noctiluca scintillans* and phytoplankton carbon in the seawater at Stn. SS1 and Stn. SS2. Unfortunately, the samples taken at 0 and 5 m at Stn. SS1 and at 2.5 m at Stn. SS2 were lost.

10 m depth were higher than those at the 0 m depth, even if the *N. scintillans* feeding activity at the two stations was similar at the 0 and 10 m depth.

It was thought that the high cell density in surface layer was due to *N. scintillans* growth and accumulations by tidal current and wind. It has been reported that an increase in water temperature during the spring period enhanced the growth rate of *N. scintillans* in the Seto Inland Sea and led to high abundances observed in early summer (Tada et al., 2004). But although the high density of buoyant *Noctiluca* cells in the surface water was a result of their growth, the cells were not active, but they were at least alive.

Red discoloration is observed at *N. scintillans* density of 10,000 cells/L (Kuroda, 1990). However, these high cell densities are thought to be inactive. Furthermore, Tada et al. (2004) reported that the biomass of *N. scintillans* cannot be ignored, even in the absence of a red tide outbreak.

Moreover, Nakamura (1998) suggested that *N. scintillans* was an important member of the mesozooplankton in terms of biomass and production in the Seto Inland Sea during summer. In addition, Kitatsuji et al. (2019) investigated the role of *N. scintillans* on a coastal ecosystem, and they reported that the active feeding ended a diatom bloom in the Seto Inland Sea. On the basis of these findings and the result of this study, it is thought that active *N. scintillans* cells in the subsurface layer with low cell density have a major predatory role in the coastal ecosystem, although high-density cells in the surface water are not active. A field study is needed to assess the activity of *N. scintillans* cells and ATP contents as well as *N. scintillans* cell density.

We determined vertical profiles of both *N. scintillans* cell density and ATP contents. *N. scintillans* cell densities were highest in the surface layer, and decreased with increasing depth. However, the ATP contents of the cells were highest

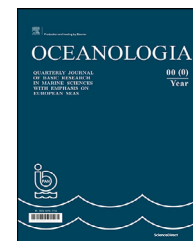
at middle layers with a maximum at a depth of 10 m, and were low in surface and lower layers. These results suggested that the low-active high-density cells of *N. scintillans* in surface seawater is probably due to the cells being in the stationary or death phase. Our results also suggest that active *N. scintillans* cells in subsurface layers with low density have an important role in the coastal ecosystem.

Acknowledgements

The authors thank Mr. Koji Kishimoto of the Aji Marine Station, Seto Inland Sea Regional Research Center, Kagawa University for his kind assistance during the field observations. We are grateful to Mr. Shuzo Sato of Kagawa University for his help in this study. Our gratitude is extended to all members of the Laboratory of Marine Sciences, Kagawa University. Finally, we thank my old friend, Mr. Brian Bigler for reading this manuscript and providing useful suggestions.

References

- Ara, K., Nakamura, S., Takahashi, R., Shiimoto, A., Hiromi, J., 2013. Seasonal variability of the red tide forming heterotrophic dinoflagellate *Noctiluca scintillans* in the neritic area of Sagami Bay, Japan: its role in the nutrient-environment and aquatic ecosystem. *Plankton Benthos Res.* 8 (1), 9–30.
- Brezonik, P.L., Browne, F.X., Fox, J.L., 1975. Application of ATP to plankton biomass and bioassay studies. *Water Res.* 9 (2), 155–162.
- Bulleid, N.C., 1978. An improved method for the extraction of adenosine triphosphate from marine sediment and seawater. *Limnol. Oceanogr.* 23 (1), 174–178.
- Elbrächter, M., Qi, Y.-Z., 1998. *Physiological Ecology of Harmful Algal Blooms*. Springer, Berlin, 315–335.
- Huang, C., Qi, Y., 1997. The abundance cycle and influence of factors on red tide phenomena of *Noctiluca miliaris* (Dinophyceae) in Dapeng Bay, the south China Sea. *J. Plankton Res.* 19 (3), 303–318, <https://doi.org/10.1093/plankt/19.3.303>.
- Hobbie, J.E., Holm-Hansen, O., Packard, T.T., Pomeroy, L.R., Sheldon, R.W., Thomas, J.P., Wiebe, W.J., 1972. A study of the distribution and activity of microorganisms in ocean water. *Limnol. Oceanogr.* 17 (4), 544–555.
- Holm-Hansen, O., 1970. ATP levels in algal cells as influenced by environmental conditions. *Plant. Cell Physiol.* 11 (5), 689–700, <https://doi.org/10.1093/oxfordjournals.pcp.a074557>.
- Holm-Hansen, O., Booth, C.R., 1966. The measurement of adenosine triphosphate in the ocean and its ecological significance. *Limnol. Oceanogr.* 11 (4), 510–519.
- Holm-Hansen, O., Lorenzen, C.J., Holmes, R.W., Strickland, J.D.H., 1965. Fluorometric determination of chlorophyll. *J. Cons. – Cons. Int. Explor. Mer.* 30 (1), 3–15.
- Hyun, B., Cha, H.-G., Lee, N., Yun, S., Baek, S.H., Shin, K., 2018. Development of an ATP assay for rapid onboard testing to detect living microorganisms in ballast water. *J. Sea Res.* 133, 73–80, <http://dx.doi.org/10.1016/j.seares.2017.03003>.
- Kitatsuji, S., Yamaguchi, H., Asahi, T., Ichimi, K., Onizuka, G., Tada, K., 2019. Does *Noctiluca scintillans* end the diatom bloom in coastal water? *J. Exp. Mar. Biol. Ecol.* 510, 10–14, <https://doi.org/10.1016/j.jembe.2018.09.006>.
- Kuroda, K., 1990. *Noctiluca scintillans* (MACARTNEY) EHRENBERG. In: Fukuyo, Y., Takano, H., Chihara, M., Matsuyoka, K. (Eds.), *Red tide organisms in Japan – An Illustrated Taxonomic Guide*. Uchida Rokakuho, Tokyo, 78–79 (in Japanese with English abstract).
- Montani, S., Pithakpol, S., Tada, K., 1998. Nutrient regeneration in coastal seas by *Noctiluca scintillans*, a red tide-causing dinoflagellate. *J. Mar. Biotechnol.* 6, 224–228.
- Nakamura, Y., 1998. Biomass, feeding and production of *N. scintillans* in the Seto Inland Sea. *Japan. J. Plankton Res.* 20 (11), 2213–2222, <https://doi.org/10.1093/plankt/20.11.2213>.
- Parsons, T.R., Maita, Y., Lalli, C.M., 1984. *Determination of Adenosine Triphosphate (ATP) in Particulate Material. A Manual of Chemical and Biological Methods for Seawater Analysis*. Pergamon Press, Oxford, 80–84.
- Patterson, J.W., Brezonik, P.L., Putnam, H.D., 1970. Measurement and significance of adenosine triphosphate in activated sludge. *Envir. Sci. Technol.* 4 (7), 569–575.
- Pithakpol, S., Tada, K., Montani, S., 2000a. Nutrient regeneration during *Noctiluca scintillans* red tide in Harima Nada, the Seto Inland Sea, Japan. In: *Proceedings of the 15th Ocean Engineering Symposium* (ed. the Society of Naval Architects of Japan), 127–134.
- Pithakpol, S., Tada, K., Montani, S., 2000b. Ammonium and phosphate pools of *Noctiluca scintillans* and their supplies to the water column in Harima Nada, the Seto Inland Sea. *Japan. La mer* 37 (4), 153–162.
- Skjoldal, H.R., Båmstedt, U., 1975. Ecobiochemical studies on the deep-water pelagic community of Korsfjorden, Western Norway. Adenine nucleotides in Zooplankton. *Mar. Biol.* 42 (3), 197–211.
- Tada, K., Morishita, M., 1997. The changes of environmental chemical conditions and biomass on lower trophic levels in a coastal bay. *Tech. Bull. Fac. Agric. Kagawa Univ.* 49, 35–47 (in Japanese with English abstract).
- Tada, K., Pithakpol, S., Yano, R., Montani, S., 2000. Carbon and nitrogen content of *Noctiluca scintillans* in the Seto Inland Sea. *Japan. J. Plankton Res.* 22 (6), 1203–1211, <https://doi.org/10.1093/plankt/22.6.1203>.
- Tada, K., Pithakpol, S., Montani, S., 2004. Seasonal variation in the abundance of *Noctiluca scintillans* in the Seto Inland Sea. *Japan. Plankton Biol. Ecol.* 51 (1), 7–14.
- Uhling, G., Sahling, G., 1990. *Noctiluca scintillans*: Zeitliche Deutschen Bucht (Langzeitreihen 1970–1993). *Ber. Biol. Anst. Hegoland* 9, 1–127.



LETTER TO THE EDITOR

Comments on the article “Spatio-temporal variations in sulfur-oxidizing and sulfate-reducing bacterial activities during upwelling, off south-west coast of India”

The recent article “Spatio-temporal variations in sulfur-oxidising and sulfate-reducing bacterial activities during upwelling, off south-west coast of India” (Kamaleson et al., 2019) is the first report on the role of sulphate-reducing and sulphide-oxidising bacteria in the seasonal oxygen minimum zone of the southwestern Indian shelf. Although the study reveals the importance of cryptic sulphur cycle along the southeastern Arabian Sea, I have serious reservations about some aspects of the paper and would like to point out important literature which were not cited.

Reliability of data and experimental methodology are central to any scientific paper. There is no mention of the methodology used for measuring temperature, salinity and pH. There is serious ambiguity w.r.t. the number of samples collected during the cruise – e.g., according to the figure and text (Kamaleson et al., 2019), the study covered 6 stations, while Table 1 shows only 5 stations. There is lack of clarity about the numbers of samples collected (from the stations; five, or six?) during the 3 phases. The paper lacks information on the accuracy / precision of the measurements. The reviewers too appear to have missed these aspects.

The authors have attempted to explain the variations in sulphur-oxidising and sulphate-reducing activities along the two transects off southwest India during the seasonal hypoxic event. Seasonal oxygen deficiency associated with the summer monsoon has long been reported off the west coast of India (Banse, 1959, 1968, 2014; Naqvi et al., 2006, 2009). The intensity of this oxygen depletion varies spatially along the eastern Arabian Sea, which even reaches sulphidic conditions at the central-eastern Arabian Sea (between 12 and 18°N). However, such severe oxygen-depleted conditions have never been reported along the southeastern Arabian Sea (south of 11°N). This is confirmed by the regular monitoring at a time series site off Goa (the Candolim Time Series, CATS by NIO, Goa) and off Kochi (the Kochi Time Series – KoTS by CMLRE, Kochi). There was no evidence

of progressive intensification of hypoxia/anoxia, i.e. ongoing intensification of oxygen-deficient conditions; instead, large inter-annual (and even intra-seasonal) variability was reported (Gupta et al., 2016; Naqvi et al., 2009; Sudheesh et al., 2016). The authors ought to have considered these recent studies before concluding that “the southwest coast of India is becoming more anoxic in recent years”; that too, without proper scientific citations.

The reasoning provided for the activities of sulphate-reducing and sulphide-oxidising bacteria under three different phases of upwelling is note-worthy; but, the experimental protocol used viz., different phases of upwelling being sampled in three different years, 2009, 2010 and 2011 (on the assumption that intra-annual variabilities are negligible; ... is it?) shatters the explanation. Kindly note that 2009 and 2011 were characterised as neutral IOD years and 2010 was a negative IOD year (<http://www.bom.gov.au/climate/iod/>). 2009–10 was a moderate *El Nino* year while 2010–11 was characterised by strong *La Nina* (http://www.cpc.noaa.gov/products/analysis_monitoring/ensostuff/ensoyears.shtml). Recently, Parvathy et al. (2017) have clearly linked this inter-annual variability in seasonal oxygen deficiency to the climatic variabilities like IOD, ENSO events. The intra- and inter-annual variations in upwelling and associated biogeochemical changes along the west coast of India have been well established too (Banse, 1968, 1959; Gupta et al., 2016; Naqvi et al., 2009). I must surmise that the observed changes in the study might be more of a combined effect of intra-seasonal as well as inter-annual variability.

The results and discussion part of the paper are mostly centred on Table 2 (see Kamaleson et al., 2019), which comprises the range and average of different biogeochemical parameters. It would be better and more meaningful if the authors had separated physical and biogeochemical parameters interactions in the surface waters from those in the deeper layers. The data may be cross-checked as some of the values seem to be “abnormally low/high” (when compared to those available in the literature) – e.g., pH max of 8.5 at Trivandrum during phase I, high phosphate values up to 5.6 μM during phase III, the significantly lower silicate values during phase II in both the transects, etc. Use of the same scale and colour palette in figures (Kamaleson et al., 2019) would have rendered the comparison effective. The

<https://doi.org/10.1016/j.oceano.2019.12.003>

0078-3234/© 2020 Institute of Oceanology of the Polish Academy of Sciences. Production and hosting by Elsevier B.V. This is an open access article under the CC BY-NC-ND license (<http://creativecommons.org/licenses/by-nc-nd/4.0/>).

range of chlorophyll *a* in Figure 2 (Kamaleson et al., 2019) is completely out of scale.

The Arabian Sea oxygen minimum zone is well defined by Naqvi (1991), Banse et al. (2014) and many others. In the paper's abstract, the oxygen minimum zone is defined as DO concentration $\leq 2.85 \text{ ml l}^{-1}$, which corresponds to $\sim 127 \mu\text{M}$. However, later, in their discussion, the hypoxia is defined as " $\leq 2.8 \text{ ml l}^{-1}$ or $63 \mu\text{M}$ ", where the conversion is clearly wrong. The later value ($63 \mu\text{M}$) has been used by many researchers to define 'hypoxia', and this corresponds to $\sim 1.4 \text{ ml l}^{-1}$. This error in conversion and the use of different units for DO concentration in different parts of the paper would lead to severe confusion among readers. The use of average values for explaining the ranges of different biogeochemical parameters for the entire area during each phase in the results section, has only compounded the confusion. Taking such average values to explain the statistical significance of various parameters is NOT a recommended procedure. Although the discussion section is generally good, however, comparison of the ocean to a lake samples results (session 4.1) is not appropriate. Instead, the authors could cite other important studies by Jørgensen et al. (2019), Callbeck et al. (2018), Currie et al. (2018), Menezes et al. (2018), Ohde (2018), Johnston et al. (2014), Wright et al. (2012), Brüchert et al. (2006, 2003), Blazejak et al. (2005) and Dannenberg et al. (1992), etc.

On the whole, the paper by Kamaleson et al. (2019) gives the impression that the authors did not consider several important factors while discussing their results. In my opinion, they ought to have been much more careful while citing relevant scientific publications and should have been meticulous while analysing / conveying the results. Their final concluding remark should not have been ambiguous, but ought to have specified the outcome of the study based on the hypothesis introduced.

I have offered these comments to provide readers with a better appreciation of the theme of the paper to improve their understanding of the biogeochemical dynamics of the study area, which is indeed complex.

Sudheesh Valliyodan

Centre for Marine Living Resources and Ecology, Ministry of Earth Sciences, Cochin 682508, India
E-mail address: sudhikeloth13@gmail.com

Available online 28 January 2020

References

- Banse, K., 1968. Hydrography of the Arabian Sea Shelf of India and Pakistan and effects on demersal fishes. *Deep-Sea Res.* 15 (1), 45–48, [https://doi.org/10.1016/0011-7471\(68\)90028-4](https://doi.org/10.1016/0011-7471(68)90028-4).
- Banse, K., 1959. On upwelling and bottom-trawling off the south-west coast of India. *J. Mar. Biol. Assoc. India* 1 (1), 33–49.
- Banse, K., Naqvi, S.W.A., Narvekar, P.V., Postel, J.R., Jayakumar, D.A., 2014. Oxygen minimum zone of the open Arabian Sea: Variability of oxygen and nitrite from daily to decadal timescales. *Biogeosciences* 11, 2237–2261, <https://doi.org/10.5194/bg-11-2237-2014>.
- Blazejak, A., Erséus, C., Amann, R., Dubilier, N., 2005. Coexistence of Bacterial Sulfide Oxidizers, Sulfate Reducers, and Spirochetes in a Gutless Worm (Oligochaeta) from the Peru Margin. *Appl. Environ. Microbiol.* 71 (3), 1553–1561, <https://doi.org/10.1128/AEM.71.3.1553-1561.2005>.
- Brüchert, V., Currie, B., Peard, K.R., Lass, U., Endler, R., Dübecke, A., Julies, E., Leipe, T., Zitzmann, S., 2006. Biogeochemical and physical control on shelf anoxia and water column hydrogen sulphide in the Benguela coastal upwelling system off Namibia. In: Neretin, L. (Ed.), *Past and Present Water Column Anoxia*. Springer, Dordrecht, 161–193, https://doi.org/10.1007/1-4020-4297-3_07.
- Brüchert, V., Jørgensen, B.B., Neumann, K., Riechmann, D., Schlösser, M., Schulz, H., 2003. Regulation of bacterial sulfate reduction and hydrogen sulfide fluxes in the central Namibian coastal upwelling zone. *Geochim. Cosmochim. Acta* 67 (23), 4505–4518, [https://doi.org/10.1016/S0016-7037\(03\)00275-8](https://doi.org/10.1016/S0016-7037(03)00275-8).
- Callbeck, C.M., Lavik, G., Ferdelman, T.G., Fuchs, B., Gruber-Vodicka, H.R., Hach, P.F., Littmann, S., Schoffelen, N.J., Kalvelage, T., Thomsen, S., Schunck, H., Löscher, C.R., Schmitz, R.A., Kuypers, M.M.M., 2018. Oxygen minimum zone cryptic sulfur cycling sustained by offshore transport of key sulfur oxidizing bacteria. *Nat. Commun.* 9, 1–11, <https://doi.org/10.1038/s41467-018-04041-x>.
- Currie, B., Utne-Palm, A.C., Veia Salvanes, A.G., 2018. Winning ways with hydrogen sulphide on the Namibian shelf. *Front. Mar. Sci.* 5 Art. 341, 9 pp, <https://doi.org/10.3389/fmars.2018.00341>.
- Dannenberg, S., Kroder, M., Dilling, W., Cypionka, H., 1992. Oxidation of H₂, organic compounds and inorganic sulfur compounds coupled to reduction of O₂ or nitrate by sulfate-reducing bacteria. *Arch. Microbiol.* 158, 93–99, <https://doi.org/10.1007/BF00245211>.
- Gupta, G.V.M., Sudheesh, V., Sudharma, K.V., Saravanane, N., Dhanya, V., Dhanya, K.R., Lakshmi, G., Sudhakar, M., Naqvi, S.W.A., 2016. Evolution to decay of upwelling and associated biogeochemistry over the southeastern Arabian Sea shelf. *J. Geophys. Res.-Biogeo.* 121 (1), 159–175, <https://doi.org/10.1002/2015JG003163>.
- Johnston, D.T., Gill, B.C., Masterson, A., Beirne, E., Casciotti, K.L., Knapp, A.N., Berelson, W., 2014. Placing an upper limit on cryptic marine. *Nature* 513, 530–533, <https://doi.org/10.1038/nature13698>.
- Jørgensen, B.B., Findlay, A.J., Pellerin, A., 2019. The biogeochemical sulfur cycle of marine sediments. *Front. Microbiol.* 10, 1–27, <https://doi.org/10.3389/fmicb.2019.00849>.
- Kamaleson, S.A., Gonsalves, M.-J., Kumar, S., Jineesh, V.K., LokaBharathi, P.A., 2019. Spatio-temporal variations in sulfur-oxidizing and sulfate-reducing bacterial activities during upwelling, off south-west coast of India. *Oceanologia* 61 (4), 427–444, <https://doi.org/10.1016/j.oceano.2019.03.002>.
- Menezes, L.D., Fernandes, G.L., Mulla, A.B., Meena, R.M., Damare, Samir R., 2018. Diversity of culturable Sulphur-oxidising bacteria in the oxygen minimum zones of the northern Indian Ocean. *Diversity of culturable Sulphur-oxidising bacteria in the oxygen minimum zones of the northern Indian Ocean*. *J. Mar. Syst.* (in press), <https://doi.org/10.1016/j.jmarsys.2018.05.007>.
- Naqvi, S.W.A., 1991. Geographical extent of denitrification in the Arabian Sea in relation to some physical processes. *Oceanol. Acta* 14 (3), 281–290.
- Naqvi, S., Naik, H., Jayakumar, A., Pratihary, A., Narvenkar, G., Kurian, S., Agnihotri, R., Shailaja, M., Narvekar, P.V., 2009. *Seasonal anoxia over the western Indian continental shelf*. *Geophys. Monogr.* 185, 333–345.
- Naqvi, S.W.A., Naik, H., Jayakumar, D.A., Shailaja, M.S., Narvekar, P.A., 2006. Seasonal Oxygen Deficiency over the western continental shelf of India. In: Neretin, L. (Ed.), *Past Present Water Column Anoxia*. Springer, Dordrecht, 195–224, https://doi.org/10.1007/1-4020-4297-3_08.

- Ohde, T., 2018. Coastal Sulfur Plumes off Peru During El Niño, La Niña, and Neutral Phases. *Geophys. Res. Lett.* 45, 7075–7083, <https://doi.org/10.1029/2018GL077618>.
- Parvathy, V., Suresh, I., Matthieu, L., Christian, E., Jérôme, V., Marina, L., Neetu, S., Olivier, A., Laure, R., Hema, N., Naqvi, W., 2017. Positive Indian Ocean Dipole events prevent anoxia off the west coast of India. *Biogeosciences* 14, 1541–1559, <https://doi.org/10.5194/bg-14-1541-2017>.
- Sudheesh, V., Gupta, G.V.M., Sudharma, K.V., Naik, H., Shenoy, D.M., Sudhakar, M., Naqvi, S.W.A., 2016. Upwelling intensity modulates N₂O concentrations over the western Indian shelf. *J. Geophys. Res.-Ocean* 121 (12), 8551–8565, <https://doi.org/10.1002/2016JC012166>.
- Wright, J.J., Konwar, K.M., Hallam, S.J., 2012. Microbial ecology of expanding oxygen minimum zones. *Nat. Rev. Microbiol.* 10, 381–394, <https://doi.org/10.1038/nrmicro2778>.

Available online at www.sciencedirect.com

ScienceDirect

journal homepage: www.journals.elsevier.com/oceanologia

LETTER TO THE EDITOR – REPLY

Response to “Comments on the article «Spatio-temporal variations in sulfur-oxidizing and sulfate-reducing bacterial activities during upwelling, off south-west coast of India»”

The article published in *Oceanologia* 61(4) under the title “Spatio-temporal variations in sulfur-oxidizing and sulfate-reducing bacterial activities during upwelling, off south-west coast of India” by Sam Kamaleson et al. (2019) highlights the interactions between sulphate-reducing and sulphur-oxidising bacterial abundance and their activities, along with the related environmental parameters during upwelling. It emphasizes the importance of the oxidising and reducing bacterial processes involved in the sulphur cycle which decide the general ecological state of upwelled waters in a spatio-temporal framework.

In disagreement with the comments by Sudheesh Valliyodan (Sudheesh Valliyodan, 2020), our manuscript has endeavoured to refer to pertinent literature related to the water column, keeping in mind the journal’s requirement. It has retained only seminal literature to help restrict the number of references. Moreover, the contents of the recent references therein generally cover the earlier literature.

Standard methods have always been used and were not elaborated so as to comply with the required length of the manuscript. Questioning the reliability of data does not arise as the topic of this paper is built on several years of ardent research on the subject some of which have been published in reputed journals earlier. While chemical measurements quantify the end products, the microbial activity measurements indicate the turnover of the product. Thus, these activity measurements are able to capture intermittent/fleeting products.

Moreover, notwithstanding the seasonal and annual variations, the study has been able to discern a pattern in the bacterial processes participating in oxidising and reducing activities to bring about ecological recovery.

Finally, the manuscript does answer the hypothesis and is far from ambiguous. It throws light on how the system evolved from a sulphate-reducing dominated regime in the waxing phase of upwelling to a more sulphide-oxidising regime in the waning phase, thus contributing to the ecological rebound.

A. Sam Kamaleson, Maria-Judith Gonsalves*
CSIR-National Institute of Oceanography, Dona Paula,
Goa, 403004, India

E-mail address: mjudith@nio.org

Swatantar Kumar
Pacific Northwest National Laboratory, US Dept. of
Energy, USA

V.K. Jineesh
Academy of Climate Change, Education and Research,
Agricultural University, Kerala, India

P.A. LokaBharathi
CSIR-National Institute of Oceanography, Dona Paula,
Goa, 403004, India

*Corresponding author.
Available online 21 February 2020

References

- Kamaleson, S.A., Gonsalves, M.-J., Kumar, S., Jineesh, V.K., LokaBharathi, P.A., 2019. Spatio-temporal variations in sulfur-oxidizing and sulfate-reducing bacterial activities during upwelling, off south-west coast of India. *Oceanologia* 61 (4), 427–444, <https://doi.org/10.1016/j.oceano.2019.03.002>.
- Sudheesh, V., 2020. Comments on the article “Spatio-temporal variations in sulfur-oxidizing and sulfate-reducing bacterial activities during upwelling, off south-west coast of India. *Oceanologia* 62 (3), 408–410, <https://doi.org/10.1016/j.oceano.2019.12.003>.

<https://doi.org/10.1016/j.oceano.2020.01.003>

0078-3234/© 2020 Institute of Oceanology of the Polish Academy of Sciences. Production and hosting by Elsevier B.V. This is an open access article under the CC BY-NC-ND license (<http://creativecommons.org/licenses/by-nc-nd/4.0/>).